UNIVERSITY OF CALIFORNIA, SAN DIEGO

FINITE ELEMENT RESPONSE SENSITIVITY, PROBABILISTIC RESPONSE AND RELIABILITY ANALYSES OF STRUCTURAL SYSTEMS WITH APPLICATIONS TO EARTHQUAKE ENGINEERING

A dissertation submitted in partial satisfaction of the requirements for the degree

Doctor of Philosophy

in

Structural Engineering

by

Michele Barbato

Committee in charge:

Professor Joel P. Conte, Chair
Professor Philip E. Gill
Professor John B. Kosmatka
Professor Petr Krysl
Professor Stefan G. Llewellyn Smith

2007

The dissertation of Michele Barbato is approved, and it is acceptable in quality and form for publication on microfilm:

_____

_____

_____

_____

_____
Chair

University of California, San Diego

2007

To my mom and dad, Patrizia and Nicolino,
my sisters, Francesca and Valeria,
and my grandparents, Michele, Gina, Lorenzo and Iolanda.

TABLE OF CONTENTS

LIST OF TABLES

LIST OF FIGURES

ACKNOWLEDGEMENTS

The research for this dissertation was performed at the University of California at San Diego under the direction of Professor Joel P. Conte. I would like to express my deepest and most sincere gratitude to him. He has been for me a rigorous and insightful teacher, a reliable and enlightening guide in the research, an inspiration in my decision to pursue a career in academia, a friend in the difficult moments encountered in the long process of achieving my Ph.D. degree. His guidance and support have been the key to my academic and personal growth over the past five and half years. I will forever be grateful to him and his family, who sustained me when I was missing the most my own family.

Special thanks are given to all the members of my doctoral committee, Professors Philip E. Gill, John B. Kosmatka, Petr Krysl and Stefan G. Llewellyn Smith, who have always been willing to dedicate their time to help me in my research.

In particular, I want to thank Professor Enrico Spacone, without whom I would not have had the opportunity to pursue my Ph.D. in the USA. Based on his unique experience of both the Italian and US academic worlds, Professor Spacone provided me with inestimable support and guidance, for which I will always be grateful. A special thank is also due to Dr. Guido Camata. His friendship, technical suggestions and moral support helped me to overcome very difficult times with renewed energy and enthusiasm.

I wish to thank my fellow students and researchers. My research on sensitivity and reliability analyses has strongly benefited from my collaboration with Mr. Quan Gu and Dr. Alessandro Zona. The quality and joy of my work has been enhanced by my

interactions with Babak Moaveni, Gabriel Acero, Maurizio Gobbato, Yuyi Zhang, Xianfei He, Ozgur Ozcelik, Andre Barbosa, Marco Faggella, Giuseppe Canducci, Chiara Casarotti, Piervincenzo Rizzo, Ivan Bartoli, Stefano Coccia, Salvatore Salamone, Andreas Stavridis, Fabio Matta, Andrea Belleri, Carlo Piotti and many other dear friends who shared with me highs and lows in San Diego and in Pescara. Special thanks go to Professor Francesco Lanza di Scalea and Dr. Gianmario Benzoni, who also helped me to feel at home in San Diego from my first day at UCSD.

Last but not least, I am most grateful to my family for their help, encouragement and support in all these years. I dedicate my work to them.

Chapter 2, in part, is a reprint of the material as it appears in Computer Methods in Applied Mechanics and Engineering (2005), Barbato, M., and Conte, J.P., 194(12-16):1479-1512. The dissertation author was the primary investigator and author of this paper.

Chapter 3, with few minor modifications, is a reprint of the material as it appears in International Journal for Numerical Methods in Engineering (2004), Conte, J.P., Barbato, M., and Spacone, E., 59(13):1781-1820 (Copyright John Wiley & Sons Limited, 2005, reproduced with permission). The dissertation author was second author of this paper. He strongly contributed to the development of the response sensitivity computation algorithm presented and to the preparation of the manuscript. He also is the author of the computer implementation of the algorithm into FEDEASLab used to produce the application examples provided in the paper.

Chapter 4, with minor modifications, is a reprint of the material as it appears in Journal of Engineering Mechanics ASCE (2005), Zona A., Barbato, M., and Conte, J.P., 131(11):1126-1139 (reprinted with permission from ASCE). The dissertation author was second author of this paper. He played a decisive role in the development of the finite element response sensitivity algorithms presented, contributing substantially to the preparation of the manuscript and to the implementation into FEDEASLab of the response sensitivity algorithms for FE response sensitivity computation at the element, section and material constitutive model levels.

Chapter 5, in full, is a reprint of the material as it appears in International Journal for Numerical Methods in Engineering Mechanics (2007), Barbato, M., Zona A., and Conte, J.P., 69(1):114-161 (Copyright John Wiley & Sons Limited, 2007, reproduced with permission). The dissertation author was first author and investigator of this paper.

Chapter 6, in full, is a reprint of the material as it appears in International Journal of Reliability and Safety (2006), Barbato, M., and Conte, J.P., 1(1-2):3-39. The dissertation author was first author and investigator of this paper.

Chapter 8, in full, has been submitted for possible publication to Probabilistic Engineering Mechanics. The dissertation author was first author and investigator of this paper.

Partial supports of this research by the National Science Foundation under Grant No. CMS-0010112 and by the Pacific Earthquake Engineering Research (PEER) Center through the Earthquake Engineering Research Centers Program of the National Science Foundation under Award No. EEC-9701568 are gratefully acknowledged.

VITA

2002	Laurea in Civil Engineering, University of Rome, “La Sapienza”
2002-2007	Research Assistant, University of California, San Diego
2005	Master of Science, University of California, San Diego
2007	Doctor of Philosophy, University of California, San Diego

PUBLICATIONS

Conte J.P., Barbato M., Spacone E (2004). “Finite Element Response Sensitivity Analysis Using Force-Based Frame Models”. *International Journal for Numerical Methods in Engineering*, 59(13):1781-1820.

Barbato M., Conte J.P. (2005) “Finite Element Response Sensitivity Analysis: a Comparison Between Force-Bases and Displacement-Based Frame Elements”. *Computer Methods in Applied Mechanics and Engineering*, 194(12-16):1479-1512.

Zona A., Barbato M., Conte J.P. (2005) “Finite Element Response Sensitivity Analysis of Steel-Concrete Composite Beams with Deformable Shear Connection”. *Journal of Engineering Mechanics* (ASCE), 131(11):1126-1139.

Zona A., Barbato M., Conte J.P. (2006) “Finite Element Response Sensitivity Analysis of Continuous Steel-Concrete Composite Girders”. *Steel and Composite Structures*, 6(3):183-202.

Barbato M., Conte J.P. (2006) “Finite Element Structural Response Sensitivity and Reliability Analyses Using Smooth versus Non-Smooth Material Constitutive Models”. *International Journal of Reliability and Safety*, 1(1-2):3-39.

Barbato M., Zona A., Conte J.P. (2007) “Finite Element Response Sensitivity Analysis Using Three-field Mixed Formulation: General Theory and Application to Frame Structures”. *International Journal for Numerical Methods in Engineering*, 69(1):114-161.

FIELDS OF STUDY

Major Field: Civil Engineering (Structural Engineering)

Studies in Structural Reliability

Professor Joel P. Conte

Studies in Numerical Optimization

Professor Philip E. Gill

ABSTRACT OF THE DISSERTATION

Finite Element Response Sensitivity, Probabilistic Response and Reliability Analyses of Structural Systems with Applications to Earhquake Engineering

by

Michele Barbato

Doctor of Philosophy in Structural Engineering

University of California, San Diego, 2007

Professor Joel P. Conte, Chair

The geometric, mechanical, material and loading parameters used to define the mechanics-based finite element (FE) models of structural systems as well as their seismic input are characterized by significant uncertainties. The rational treatment of uncertainties in computational mechanics has been the object of increasing attention in recent years. Modern design codes indirectly account for parameter and model uncertainties in order to

ensure satisfactory designs. Thus, in addition to accurate deterministic models, methods are needed to propagate uncertainties from the parameters defining the FE model of a structure to the engineering demand parameters.

FE response sensitivities (RSs) to both model and loading parameters represent an essential ingredient in studying this complex uncertainty propagation. New RS algorithms based on the Direct Differentiation Method (DDM) are derived and implemented in general-purpose nonlinear structural analysis frameworks. The use of the DDM is extended to (1) force-based frame elements, (2) steel-concrete composite structures, and (3) three-field mixed FEs. In addition, the effects on RS continuity of using smooth versus non-smooth material constitutive models are thoroughly examined.

An efficient simulation technique for an existing fully non-stationary stochastic earthquake ground motion model is developed. The definition of non-geometric spectral characteristics is extended to general complex-valued non-stationary stochastic processes. Closed-form approximate solutions of the first-passage problem are developed for single- and multi-degree-of-freedom linear elastic systems.

First-order second-moment approximations of the first- and second-order statistics of the response of linear/nonlinear structural systems with random/uncertain parameters and subjected to quasi-static and/or dynamic load(s) are computed efficiently using DDM-based FE RSs. The probability of a structural response quantity exceeding a specified threshold level is obtained by using the First-Order Reliability Method in conjunction with the DDM-based FE RSs in the search for the Design Point(s) (DP). A new method, referred to as Multidimensional Visualization in the Principal Planes, is developed to

explore the geometry of limit-state surfaces near the DP(s) in reduced-spaces defined by planes of major principal curvatures at the DP. A new hybrid reliability analysis method (DP search - Response Surface - Importance Sampling) is developed and tested. Based on pushover and time history analyses, examples of both time-invariant and time-variant reliability analysis of structural systems are presented to illustrate the probabilistic methods developed.

CHAPTER 1

INTRODUCTION

1.1 Background and Motivation

1.1.1 Uncertainties, risk and vulnerability in civil infrastructure systems

Risk is implicit in every engineered system. Natural and man-made hazards are always armed and cannot be deterministically known a-priori. Economic constraints, in general, oblige one to accept in the design process some vulnerability (damage tolerance), which must be carefully evaluated in terms of expected (i.e., uncertain) costs/benefits for single entities and the entire collectivity affected by the engineering system considered. Uncertainties are connatural not only to the hazards which threaten a system, but the systems themselves are known only up to a certain degree of confidence. The higher the complexity of a system, the higher is its uncertainty. Additional uncertainties and unknown errors are introduced when engineering systems are modeled in order to evaluate and simulate their behavior, response and performance. The design of any engineering system clearly needs to address consistently, accurately and efficiently the problem of uncertainties in order to be “satisfactory” in some predefined sense.

1.1.2 Civil structures subjected to seismic hazard

Accounting for uncertainties in the design of an engineered system is particularly crucial for civil structural systems subjected to seismic hazard, which constitute the main focus of the present work. Damage to society from earthquakes can be extremely severe. In the last decade of the 20th century, earthquakes around the world killed almost 100,000 people, affected 14 million people and produced losses estimated at more than $215 billion. In 1999 alone, two strong earthquakes in western Turkey caused the deaths of over 16,000 people, the destruction of more than 60,000 homes and economic losses of about $40 billion (over one quarter of the country's gross domestic product) (National Research Council 2003). In 2001, a magnitude 7.7 earthquake centered near Bhuj in Gujarat, India, killed almost 17,000 people, destroyed 350,000 homes, affected almost 16 million people and caused economic losses estimated at over $4.5 billion with production losses accumulating at a rate of $110 million per day (National Research Council 2003). On December 26, 2004, a massive earthquake of moment magnitude larger than 9.0, the second largest earthquake ever recorded on a seismograph, triggered the deadliest tsunami in the history of the world (Wikipedia 2007). The tsunami was observed worldwide and lasted several days. The death toll was greater than 200,000 people, with Sumatra, Sri Lanka, Thailand and India suffering the highest losses in terms of human lives and damage to constructions. The destructive effects of the waves reached Kenya. This catastrophe is the ninth deadliest natural disaster in modern history (Wikipedia 2007).

The largest part of the death toll in recent earthquakes derives from the collapse of structural systems which were not correctly engineered to survive the seismic event. Nev-

ertheless, most of the economic and life losses suffered subsequently to the earthquakes were experienced or at least aggravated by the failure of engineered civil systems which were designed to withstand seismic events with limited damage.

Although fewer than 150 lives have been lost to earthquakes in the United States since 1975, the cost of damage from just a few moderate events (e.g., 1989 Loma Prieta, 1994 Northridge California earthquakes and 2001 Nisqually Washington earthquake) during that time exceeds $30 billion (Cutter 2001). Today, we are aware that even larger events are likely, and a single catastrophic earthquake could exceed those totals for casualties and economic loss by an order of magnitude. Fortunately, over the past 40 years considerable progress has been made in understanding the nature of earthquakes and how they inflict damage to structures, and in improving the seismic performance of the built environment. Unfortunately, while much has been accomplished, much remains unknown or unproven and much remains to be done to reach the ultimate objective of preventing earthquake disasters in the United States and in the World.

1.1.3 Uncertainties in structural systems and their loading environment

Loading conditions, material and geometric properties and other structural parameters describing the models of structural systems exhibit significant variability, since they are stochastic quantities in nature. Therefore, the complex and still poorly understood interactions between subsurface materials, foundations, and the structure during the passage of seismic waves is further significantly complicated by clouds of uncertainties associated with the various components of a structural system as well as the seismic excitation.

Uncertainties can be formally grouped into inherent or aleatory and epistemic uncertainties. Inherent/aleatory uncertainty is defined as the intrinsic variability (or natural randomness) of engineering/physical quantities such as material properties (e.g., shear modulus of soil material, peak strength of concrete, yield strength of steel), geometric properties (e.g., member cross-section properties, member lengths), seismological variables (earthquake magnitude M and site-to-source distance S), ground motion time history at a specific point, and spatial variation of ground motion. Inherent uncertainties can be viewed as a property of nature. They are irreducible and can be estimated from observations using the frequentist interpretation of probability. In contrast, epistemic uncertainty results from a lack of knowledge and or information and shortcomings in measurement and/or calculation. It arises due to (1) the use of structural, load, and probabilistic models that are idealized, simplified, incorrectly calibrated, and/or of questionable applicability (i.e., modeling uncertainty), and (2) imperfect model parameter estimation due to limited data (i.e., small sampling uncertainty), measurement errors, etc. The predictions made on the basis of these models are inaccurate to some unknown degree. Epistemic uncertainty can usually be reduced by using more accurate/sophisticated models, acquiring additional data, and improving measurement procedures. Thus, inherent and epistemic uncertainties are very different in nature. This difference should be recognized and accounted for by the next generation of seismic design methodologies.

Uncertainties in seismic loading are very large. No methods are currently available (nor does their availability seem feasible in the near future) to determine where and when a seismic event will occur and at what intensity. Seismological variables such as earth-

quake magnitude, M, and site-to-source distance, S, can be modeled only in a probabilistic sense, making use of available statistical data and geological information regarding seismic activity of known faults. The complex combination of reflection, refraction and diffraction phenomena in the wave transmission through the geological medium is not known deterministically. Thus, the ground motion time history at a specific point and its spatial variation can be represented only stochastically.

The intrinsic variability of structural material properties (e.g., Young's modulus of steel/concrete, yield strength of steel, compressive/tensile strength of concrete) has been documented and characterized extensively in the literature (Mirza and MacGregor 1979b; Mirza et al. 1979). Uncertainty in reinforced concrete member geometry has also been studied and documented in the literature (Mirza and MacGregor 1979a).

1.1.4 Current seismic design codes and advent of Performance-Based Earthquake Engineering

Since the late 19th century and until relatively recently, structural safety assurance in civil engineering have relied mainly on Allowable Stress Design (ASD). In ASD, stresses computed through elastic structural analysis from specified nominal loads are checked against some limiting stress divided by a factor of safety. During the past thirty years, both research and practice have stressed out several deficiencies of ASD (Ellingwood 1994). Motivated by these deficiencies, committees on standards and specifications worldwide (AISC 1993; AASHTO 1994; AF&PA/ASCE 1996; AIJ 2000; ASCE 2002;

CEN 1994, 2002) have started to adopt probability-based limit state design procedures, often referred to as Load and Resistance Factor Design (LRFD).

Nevertheless, modern design codes based on LRFD account only indirectly, using probabilistically calibrated design procedures, for parameter and model uncertainties trying to reach implicitly predetermined performance requirements considered satisfactory for society. From this background, Performance-Based Earthquake Engineering (PBEE) has emerged as a new analysis and design philosophy in earthquake engineering (Cornell and Krawinkler 2000; Porter 2003; Moehle and Deierlein 2004) and is leading the way to the new generation of seismic design guidelines (SEAOC 1995; AASHTO 1998; ICC 2003; BSSC 2004; ATC 2005a, 2005b). The PBEE design approach prescribes performance objectives to be achieved by a structure during earthquakes for various hazard levels. PBEE requires a comprehensive understanding of the earthquake response of a structure when damage occurs in the structural system over the course of an earthquake (cracking, yielding, crashing, fracture, and so forth); it requires analysis of progressive damage (collapse) in structures. In the long term, using PBEE, structures will be rated for a given performance level at a given hazard level. However, due to the inherent and epistemic uncertainties characterizing material, mechanical and geometric properties of the structure, the earthquake excitation and the models thereof, the satisfaction of structural performance objectives can only be defined in probabilistic terms (e.g., acceptable annual probability of limit-state exceedance).

1.2 Review of probabilistic methods as applied to Structural Earthquake Engineering

1.2.1 Parameter sensitivities in nonlinear mechanics

Recent years have seen great advances in non-linear FE modeling and analysis of large and complex structural systems. The state-of-the-art in computational simulation of the static and dynamic response of structural systems lies in the non-linear domain to account for material and geometric non-linearities governing the complex behavior of structural systems, especially near their failure range (i.e., collapse analysis).

Maybe even more important than the simulated nonlinear response of a frame structure is its sensitivity to loading parameters and to various geometric, mechanical, and material properties defining the structure. FE response sensitivities represent an essential ingredient for gradient-based optimization methods needed in structural reliability analysis, structural optimization, structural identification, and finite element model updating (Ditlevsen and Madsen 1996; Kleiber et al. 1997). Many researchers have dedicated their attention to the general problem of design sensitivity analysis, among others, Choi and Santos (1987), Arora and Cardoso (1989), Tsay and Arora (1990), Tsai et al. (1990).

Several methods are available for computing FE response sensitivities, such as the Forward/Backward/Central Finite Difference Method (FDM) (Kleiber et al. 1997; Conte et al. 2003, 2004), the Adjoint Method (AM) (Kleiber et al. 1997), the Perturbation Method (Kleiber and Hien 1992) and the Direct Differentiation Method (DDM) (Zhang

and Der Kiureghian 1993, Kleiber et al. 1997; Conte 2001; Conte et al. 2003, 2004; Barbato and Conte 2005, 2006; Zona et al. 2005; Barbato et al. 2006). Among all these methods, the DDM appears to be the more promising in terms of robustness, efficiency and accuracy for application in structural reliability analysis involving nonlinear static and dynamic analyses of real-world structural systems using advanced FE models. Algorithms for consistent FE response sensitivity analysis based on the DDM are already well-documented in the literature for displacement-based finite elements (Zhang and Der Kiureghian 1993; Kleiber et al. 1997; Conte 2001; Conte et al. 2003; Haukaas and Der Kiureghian 2004; Franchin 2004).

1.2.2 Stochastic earthquake ground motion models

The importance of using stochastic processes to model dynamic loads such as earthquake ground motions, wind effects on civil and aerospace structures, and ocean wave induced forces on offshore structures, has been widely recognized in many engineering fields. Extensive research has been devoted to the development of analytical methods and numerical simulation techniques related to modeling of stochastic loads and analysis of their effects on structures (Lin 1967; Priestley 1987; Lutes and Sarkani 1997).

In particular, in earthquake engineering, the non-stationarity in both amplitude and frequency content of earthquake ground motions has been recognized as an essential ingredient to capture realistically the seismic response of structures (Saragoni and Hart 1972; Yeh and Wen 1990; Papadimitriou 1990; Conte 1992). Therefore, significant attention has been given to nonstationary earthquake ground motion models, with particular

emphasis on their accurate but compact representation (Grigoriou et al. 1988; Der Kiureghian and Crempien 1989; Fan and Ahmadi 1990; Conte et al. 1992; Conte and Peng 1997). These models account for the inherent variability of ground motion time histories at a specific point and can be extended to model the random spatial variation of ground motions. There is also the need of incorporating into earthquake ground motion models the uncertainties of seismological variables such as the earthquake magnitude, M, and site-to-source distance, S. A stochastic model able to represent all these sources of uncertainties will enable an end-to-end probabilistic seismic performance analysis of structural systems, integrating seamlessly seismic hazard analysis, probabilistic demand analysis, damage analysis, and reliability analysis.

1.2.3 State-of-the-art in finite element structural reliability methods

The field of structural reliability analysis has seen significant advances in the last two decades (Ditlevsen and Madsen 1996, Der Kiureghian 1996). Analytical and numerical methodologies have been developed and improved for the probabilistic analysis of real structures characterized in general by nonlinear behavior, material and geometric uncertainties and subjected to stochastic loads (Schueller et al. 2004). Reliability analysis methods have been successfully applied to such problems, as the ones encountered in civil engineering and typically analyzed deterministically through the finite element (FE) method (Der Kiureghian and Ke 1988).

Several reliability analysis methods, such as asymptotic methods (First- and Second-Order Reliability Methods) (Breitung 1984; Der Kiureghian and Liu 1986; Der

Kiureghian et al. 1987; Der Kiureghian 1996; Ditlevsen and Madsen 1996) and importance sampling with sampling distribution centered at the design point(s) (Schueller and Stix 1987; Melchers 1989; Au et al. 1999; Au and Beck 2001a) are characterized by the crucial step of finding the design point(s) (DPs), defined as the most likely failure point(s) in the standard normal space. In particular, asymptotic methods can provide reliability analysis results with a relatively small number of simulations (often on the order of 10-100 simulations for FORM analysis) and with a computational effort practically independent of the magnitude of the failure probability. Furthermore, these methods provide important information such as reliability sensitivity measures, as a by-product of the DP search (Hohenbichler and Rackwitz 1986). Other reliability analysis methods, e.g., subset simulation (Au and Beck 2001b; Au and Beck 2003) and importance sampling with sampling distribution not centered at the DP(s) (Bucher 1988; Ang et al. 1992; Au and Beck 1999), do not use the concept of DP. In general, the computational cost of these methods increases for decreasing magnitude of the failure probability. Thus, for very low failure probabilities, these methods could require a very large number of simulations and be computationally prohibitive.

1.3 Research needs, objectives and scope

The future of earthquake engineering is closely tied to high-fidelity model-based simulation and probabilistic/reliability analysis. With future progress in predictive modeling and simulation capabilities, inherent/aleatory uncertainties will still be present and will have to be dealt with. Therefore, basic research needs in earthquake engineering and structural reliability analysis include: (1) consistent modeling of all significant sources of

uncertainty affecting analytical seismic response predictions of structural systems, and (2) accurate and efficient analytical tools to propagate these uncertainties through advanced large-scale nonlinear seismic response analyses of structural systems to obtain probabilistic estimates of the predicted seismic response performance. Sensitivity analysis of the simulated response with respect to both system and loading parameters is a key component in studying this complex propagation of uncertainties and thus requires particular attention from the research community.

The objective of the research work presented in this thesis is to develop a comprehensive and efficient analytical methodology for studying the complex propagation of inherent uncertainties in nonlinear static and dynamic analysis of structural systems in the context of performance-based earthquake engineering. This aim is sought through merging state-of-the-art FE formulations for modeling and seismic response analysis of large-scale structural systems with modern advanced reliability analysis methods. This innovative integration requires (1) the advancement of accurate and efficient algorithms for FE response sensitivity analysis, (2) the enhancement of simulation capabilities for stochastic earthquake ground motion models, (3) the development of benchmark solutions for reliability problems involving random stochastic input, (4) the adaptation of state-of-the-art computational optimization methods to exploit the physics and geometry of the problem to be solved, (5) the development of visualization tools to gain physical and geometrical insight into structural reliability problems involving large numbers of random parameters, and (6) the development of new robust and efficient reliability methods specifically designed for FE reliability analysis.

The research work presented in this dissertation addresses how input uncertainties propagate and how they translate into the variability of the predicted structural response. Nonlinear dynamic analysis of structural systems is the only realistic means of predicting performance with respect to an ensemble of design earthquakes. These analyses are generally complex and computationally demanding. Thus, only the availability of efficient and robust computational tools and of clear guidelines on how to use them will eventually open the way to widespread use of model-based simulations in performance-based engineering. The research presented here represents a fundamental step in this direction.

This research makes use and extends the capabilities of two computational simulation components of the NEESgrid software, in order to increase the visibility and to encourage widespread use of the products of this research. The physical modeling, numerical simulation, and networking tools developed through NEES can be utilized to study and solve problems in an entire spectrum of geotechnical and structural engineering applications, such as the effect of construction and traffic vibrations on structures, the preservation and repair of historic structures, the impact forces of large debris such as cars and trees transported by floods, and the effect of intense heat and explosions on structural performance.

1.4 Computational platforms

The research developed and presented herein has a strong computational component. Therefore, the choice of the computational platforms in which the research results are implemented assumes a particular importance in determining its availability and visi-

bility to the structural engineering community. Two complementary computational platforms, both components of the NEESgrid software, are used and extended in this work.

1.4.1 First computational platform: FEDEASLab-FERUM

The first platform consists of the tandem FEDEASLab-FERUM. FEDEASLab (Finite Elements in Design, Evaluation and Analysis of Structures using Matlab) was originally developed by Prof. Filippou at the University of California, Berkeley (Filippou and Constantinides 2004). It is a Matlab (The Mathworks 1997) toolbox suitable for linear and nonlinear, static and dynamic structural analysis, which has the advantage to provide a general framework for physical parameterization of FE models and response sensitivity computation using the DDM (Franchin 2004). One of the key features of FEDEASLab is its strict modularity, that keeps separate the different hierarchical levels encountered in structural analysis (i.e., structure, element, section and fiber or material levels). It is an integral simulation component of NEESgrid that is particularly suitable for concept/algorithm development, for educational purposes, and for analysis of small structural systems.

FERUM (Finite Element Reliability Using Matlab) is a Matlab toolbox to perform FE reliability analysis, which was originally developed by Prof. Der Kiureghian and his students at the University of California, Berkeley (Haukaas 2001). The coupling between FEDEASLab and FERUM was first established by Franchin (2004). FEDEASLab-FERUM has proven to be an excellent and versatile research tool for concept/algorithm developments in nonlinear FE reliability analysis. However, due to the intrinsic limitations of Matlab as an interpretive language, it is limited to small-scale problems.

1.4.2 Second computational platform: OpenSees

The second computational platform consists of OpenSees (Open System for Earthquake Engineering Simulation) (Mazzoni et al. 2005), an open source software framework to model structural and/or geotechnical systems and simulate their response to earthquakes. OpenSees has been under development by the Pacific Earthquake Engineering Research Center since 1997 through the National Science Foundation engineering and education centers program. OpenSees supports a wide range of simulation models, solution procedures, and distributed computing models. It also has very attractive capabilities for physical parameterization of structural and geotechnical FE models, probabilistic modeling, response sensitivity analysis and reliability analysis (Haukaas and Der Kiureghian 2004). OpenSees has been adopted as a NEESgrid simulation component since 2004.

The combination of FEDEASLab-FERUM as research prototyping as well as educational tool and OpenSees as framework for large-scale seismic response simulation and reliability analysis provides an ideal research platform.

1.5 Organization of the thesis

The research presented in this thesis can be partitioned into three topics. A variable number of chapters is devoted to each of these topics.

The first research topic is FE response sensitivity analysis of structural systems and is covered in Chapters 2 through 6. Chapter 2 introduces FE response sensitivity analysis, its application fields and the existing methodologies for FE response sensitivity computation. Then, the Direct Differentiation Method (DDM) is presented in details for the

classical displacement-based finite element formulation. Chapter 3 presents the algorithm extending DDM to force-based frame elements. Chapter 4 extends the DDM for response sensitivity analysis of steel-concrete composite frame structures. In Chapter 5, a DDM-based FE response sensitivity algorithm is developed for three-field mixed-formulation elements based on the Hu-Washizu functional. Chapter 6 studies the conditions to be imposed on smoothness of material constitutive models to assure continuity of FE response sensitivities.

The second research topic, covered in Chapters 7 through 9, consists of the stochastic modeling of earthquake ground motions and random vibration analysis of structural systems subjected to stochastic ground motion excitation. Chapter 7 describes an existing fully non-stationary stochastic ground motion model and presents a new efficient simulation technique for this model. Chapters 8 and 9 extend the definition of spectral characteristics to general complex-valued non-stationary stochastic processes and employ these newly defined spectral characteristics for time-variant reliability analysis based on linear elastic structural models.

The third research topic, which is the subject of Chapters 10 through 13, is the study of probabilistic and reliability methods applied to structural systems. Chapter 10 presents the DDM-based First-Order Second-Moment method for approximate probabilistic response analysis. Chapter 11 presents a review of structural reliability methods based on the design point concept together with new improvements made as part of this work to existing FE structural reliability analysis methods. Chapter 12 presents a new methodology for visualization of hyper-surfaces defined in high-dimensional spaces, such as the

limit-state surfaces that are commonly considered in FE structural reliability analysis. Chapter 13 focuses on the development of a new hybrid FE reliability method which improves significantly the accuracy of classical reliability methods at a reasonable additional computational cost. Finally, Chapter 14 summarizes the work done, highlights important research findings and provides some suggestions for future research.

REFERENCES

AASHTO (1994) *AASHTO LRFD Bridge Design Specification*. American Association of State Highway and Transportation Officials, Washington D.C., USA.

AASHTO (1998) *AASHTO LRFD Bridge Design Specification*. American Association of State Highway and Transportation Officials, Washington D.C., USA.

AF&PA/ASCE (1996) "Standard for load and resistance factor design for engineered wood construction." *AF&PA/ASCE Standard 16-95*, American Society of Civil Engineers, New York, USA.

AIJ (2000) *Tentative recommendations for limit state design of buildings*. Architectural Institute of Japan (Committee of Limit State Design), Tokyo, Japan.

AISC (1993) *Load and resistance factor design specification for structural steel buildings.* American Institute of Steel Construction, Chicago, USA.

Ang G.L., Ang A.H.-S., Tang W.H. (1992) "Optimal importance sampling density estimator" *Journal of Engineering Mechanics* (ASCE), 118(6):1146–1163.

Arora J.S., Cardoso J.B. (1989) "A design sensitivity analysis principle and its implementation into ADINA." *Computers and Structures*, 32:691-705.

ASCE (2002) “Minimum design loads for buildings and other structures.” *ASCE Standard 7-02*, American Society of Civil Engineers, Reston, VA, USA.

ATC (2005a) *ATC-55: Evaluation and Improvement of Inelastic Seismic Analysis Procedures*, Advanced Technology Council, Redwood City, CA, USA.

ATC (2005b) *ATC-58: Development of Next-Generation Performance-Based Seismic Design Procedures for New and Existing Buildings*, Applied Technology Council, CA, USA.

Au S.K., Beck J.L. (1999) “A new adaptive importance sampling scheme” *Structural Safety*, 21(2):135–158.

Au S.K., Papadimitriou C., Beck J.L. (1999) “Reliability of uncertain dynamical systems with multiple design points” *Structural Safety*, 21(2):113–133.

Au S.K., Beck J.L. (2001a) “First excursion probabilities for linear systems by very efficient importance sampling” *Probabilistic Engineering Mechanics*, 16(3):193–207.

Au S.K., Beck J.L. (2001b) “Estimation of small failure probabilities in high dimensions by subset simulation” *Probabilistic Engineering Mechanics*, 16(4):263–277.

Au S.K., Beck J.L. (2003) “Subset simulation and its application to seismic risk based on dynamic analysis” *Journal of Engineering Mechanics* (ASCE), 129(8):901–917.

Barbato M., Conte J.P. (2005) “Finite element response sensitivity analysis: a comparison between force-based and displacement-based frame element models.” *Computer Methods in Applied Mechanics and Engineering*, 194(12-16):1479-1512.

Barbato M., Conte J.P. (2006) “Finite element structural response sensitivity and reliability analyses using smooth versus non-smooth material constitutive models” *International Journal of Reliability and Safety*, 1(1-2):3-39.

Barbato M., Gu Q., Conte J.P. (2006) “Response Sensitivity and Probabilistic Response

Analyses of Reinforced Concrete Frame Structures" *Proceeding* of 8th National Conference on Earthquake Engineering, San Francisco, CA, USA.

Breitung K. (1984) "Asymptotic approximations for multinormal integrals" *Journal of the Engineering Mechanics Division* (ASCE), 110(3):357–366.

Bucher C.G. (1988) "Adaptive importance sampling – an iterative fast Monte Carlo procedure" *Structural Safety*, 5(2):119–126.

BSSC (2004) *The 2003 NEHRP Recommended Provisions for New Buildings And Other Structures Part 1: Provisions (FEMA 450)*, Building Seismic Science Council, Washington D.C., USA.

CEN (1994) *Eurocode 1 - actions on structures*. Comite Europeen de Normalization 250, Brussels, Belgium.

CEN (2002) *EC1/ EN1991 - actions on structures*. Comite Europeen de Normalization, Brussels, Belgium.

Choi K.K., Santos J.L.T. (1987) "Design sensitivity analysis of nonlinear structural systems. Part I: Theory." *International Journal for Numerical Methods in Engineering*, 24:2039-2055.

Conte J.P. (1992) "Effects of Earthquake Frequency Nonstationarity on Inelastic Structural Response." *Proceedings of the 10th World Conference on Earthquake Engineering*, Madrid, Spain. Rotterdam: AA Balkema, 3645-3651.

Conte J.P., Pister K.S., Mahin S.A. (1992) "Nonstationary ARMA Modeling of Seismic Motions". *Journal of Soil Dynamics and Earthquake Engineering*, 11(7):411-426.

Conte J.P., Peng B.-F. (1997) "Fully nonstationary analytical earthquake ground-motion model". *Journal of Engineering Mechanics* (ASCE), 123(1):15-24.

Conte J.P. (2001) "Finite Element Response Sensitivity Analysis in Earthquake Engineer-

ing" *Earthquake Engineering Frontiers in the New Millennium*, Spenser and Hu, Swets and Zeitlinger, 395-401.

Conte J.P., Vijalapura P.K., Meghella M. (2003) "Consistent Finite-Element Response Sensitivity Analysis" *Journal of Engineering Mechanics* (ASCE), 129:1380-1393.

Conte J.P., Barbato M., Spacone E. (2004) "Finite element response sensitivity analysis using force-based frame models" *International Journal for Numerical Methods in Engineering*, 59(13):1781–1820.

Cornell C.A., Krawinkler H. (2000) "Progress and Challenges in Seismic Performance Assessment" *PEER Center News*, Berkeley, CA, USA.

Cutter S.L. (2001) *American Hazardscapes: The Regionalization of Hazards and Disasters*, Joseph Henry Press, Washington D.C., USA.

Der Kiureghian A., Liu P.-L. (1986) "Structural reliability under incomplete probability information" *Journal of the Engineering Mechanics Division* (ASCE), 111(EM1):85–104.

Der Kiureghian A., Lin H.-Z., Hwang S.-J. (1987) "Second-order reliability approximations" *Journal of the Engineering Mechanics Division* (ASCE), 113(EM8):1208–1225.

Der Kiureghian A., Ke B.-J. (1988) "The stochastic finite element method in structural reliability" *Probabilistic Engineering Mechanics*, 3(2):83–91.

Der Kiureghian A., Crempien J. (1989) "An Evolutionary Model for Earthquake Ground Motion". *Structural Safety*, 6:235-246.

Der Kiureghian A. (1996) "Structural reliability methods in seismic safety assessment: a review" *Journal of Engineering Structures*, 18(6):412–424.

Ditlevsen O., Madsen H.O. (1996) *Structural Reliability Methods*. Wiley, New York, NY, USA.

Ellingwood B. (1994) “Probability-based codified design: Past accomplishments and future challenges.” *Structural Safety,* 13(3):159-176.

Fan F.-G., Ahmadi G. (1990) “Nonstationary Kanai-Tajimi Models for El Centro 1940 and Mexico City 1985 Earthquakes.” *Probabilistic Engineering Mechanics,* 5(4):171-181.

Filippou F.C., Constantinides M. (2004) “FEDEASLab getting started guide and simulation examples” *Technical Report NEESgrid-2004-22,* 31 August, Available at: http:// fedeaslab. berkeley.edu/.

Franchin P. (2004) “Reliability of uncertain inelastic structures under earthquake excitation” *Journal of Engineering Mechanics* (ASCE), 130(2):180–191.

Grigoriu M., Ruiz S.E., Rosenblueth E. (1988) “The Mexico Earthquake of September 19, 1985 - Nonstationary Models of Seismic Ground Acceleration”. *Earthquake Spectra,* 4(3):551-568.

Haukaas T. (2001) “FERUM (Finite Element Reliability Using Matlab)” *User’s Guide*, Available at: http://www.ce.berkeley.edu/~haukaas/FERUM/ferum.html.

Haukaas T., Der Kiureghian A. (2004) “Finite element reliability and sensitivity methods for performance-based engineering” *Report PEER 2003/14*, Pacific Earthquake Engineering Research Center, University of California, Berkeley.

Hohenbichler M., Rackwitz R. (1986) “Sensitivity and importance measures in structural reliability” *Civil Engineering Systems*, 3(4):203–209.

ICC (2003) *International Building Code 2003*. International Code Council.

Kleiber M., Hien T.D. (1992) *The Stochastic Finite Element Method, Basic Perturbation Technique and Computer Implementation.* Wiley.

Kleiber M., Antunez H., Hien T.D., Kowalczyk P. (1997) *Parameter Sensitivity in Nonlinear Mechanics: Theory and Finite Element Computation*, New York, Wiley.

Lin Y.K. (1967) “Probabilistic Theory of Structural Dynamics”. New York, NY: McGraw-Hill, 1967, Huntington: Krieger Pub, 1976.

Lutes L.D., Sarkani S. (1997) “Stochastic analysis of structural and mechanical vibration”. Upple Saddle River, NJ: Prentice Hall.

Mazzoni S., McKenna F., Fenves G.L. (2005) *OpenSees Command Language Manual.* Pacific Earthquake Engineering Center, University of California, Berkeley. <http://opensees.berkeley.edu/>

Melchers R.E. (1989) “Importance sampling in structural systems” *Structural Safety*, 6(1):3–10.

Mirza S.A., MacGregor J.G. (1979a) “Variations of Dimensions of Reinforced Concrete Members” *Journal of the Structural Division* (ASCE), 105(4):751-765.

Mirza S.A., MacGregor J.G. (1979b) “Variability of Mechanical Properties of Reinforcing Bars” *Journal of the Structural Division* (ASCE), 105(4):921-937.

Mirza S.A., Hatzinikolas M., MacGregor J.G. (1979) “Statistical Descriptions of Strength of Concrete,” *Journal of the Structural Division* (ASCE), 105(6):1021-1035.

Moehle J., Deierlein G.G., (2004) “A Framework Methodology for Performance-Based Earthquake Engineering” *Proceedings 13WCEE*, Vancouver, Canada, August 1-6, 2004.

National Research Council (2004) *Preventing Earthquake Disasters – The Grand Challenge in Earthquake Engineering: A Research Agenda for the Network for Earthquake Engineering Simulation (NEES)*, The National Academies Press, Washington D.C., USA.

Papadimitriou C. (1990) “Stochastic Characterization of Strong Ground Motion and Applications to Structural Response”. *Report No. EERL 90-03*, California Institute of Technology, Pasadena, CA.

Porter K.A. (2003) “An Overview of PEER’s performance-based earthquake engineering methodology” *Proceedings ICASP9*, A. Der Kiureghian et al. Eds., San Francisco, CA, USA.

Priestley M.B. (1987) “Spectral Analysis and Time Series, Volume 1: Univariate Series, Volume 2: Multivariate Series, Prediction and Control”. London: Academic Press, Fifth Printing.

Saragoni G. R., Hart G. C. (1972) “Nonstationary Analysis and Simulation of Earthquake Ground Motions.” *Report No. UCLA-ENG-7238*, Earthquake Engineering and Structures Laboratory, University of California at Los Angeles, Los Angeles, CA.

SEAOC (1995) “Performance Based Seismic Engineering of Buildings” Structural Engineers Association of California, Sacramento, CA, USA.

Schueller G.I., Stix R. (1987) “A critical appraisal of methods to determine failure probabilities” *Structural Safety*, 4(4):293-309.

Schueller G.I., Pradlwarter H.J., Koutsourelakis P.S. (2004) “A critical appraisal of reliability estimation procedures for high dimensions” *Probabilistic Engineering Mechanics*, 19(4):463-474.

The MathWorks (1997) “Matlab – high performance numeric computation and visualization software” *User’s Guide*, Natick, MA, USA

Tsay J.J., Arora J.S. (1990) “Nonlinear structural design sensitivity analysis for path dependent problems. Part I: General theory.” *Computer Methods in Applied Mechanics and Engineering*, 81:183-208.

Tsay J.J., Cardoso J.B., Arora J.S. (1990) “Nonlinear structural design sensitivity analysis for path dependent problems. Part II: Analytical examples.” *Computer Methods in Applied Mechanics and Engineering*, 81:209-228.

Wikipedia (2007), Website (accessed on August 26 2007): <http://en.wikipedia.org/wiki/2004_Indian_Ocean_earthquake>.

Yeh C.-H., Wen Y. K. (1990) “Modeling of Nonstationary Ground Motion and Analysis of Inelastic Structural Response.” *Structural Safety*, 8:281-298.

Zhang Y., Der Kiureghian A. (1993) “Dynamic response sensitivity of inelastic structures” *Computer Methods in Applied Mechanics and Engineering*, 108(1-2):23–36.

Zona A., Barbato M., Conte J.P. (2005) “Finite element response sensitivity analysis of steel-concrete composite beams with deformable shear connection” *Journal of Engineering Mechanics* (ASCE), 131(11):1126–1139.

Zona A., Barbato M., Conte J.P. (2006) “Finite Element Response Sensitivity Analysis of Continuous Steel-Concrete Composite Girders” *Steel and Composite Structures*, 6(3):183-202.

CHAPTER 2

COMPUTATIONAL FRAMEWORK FOR FINITE ELEMENT RESPONSE SENSITIVITY ANALYSIS: THE DIRECT DIFFERENTIATION METHOD

2.1 INTRODUCTION

Recent years have seen great advances in the nonlinear finite element (FE) analysis of structural models. The state-of-the-art in computational simulation of the static and dynamic response of structural models lies in the nonlinear domain to account for material and geometric nonlinearities governing the complex behavior of structural systems, especially near their failure range (i.e., collapse analysis).

Maybe even more important than the simulated nonlinear response of a structural system is its sensitivity to loading parameters and to various geometric, mechanical, and material properties defining the structure. FE response sensitivities represent an essential ingredient for gradient-based optimization methods needed in structural reliability analysis, structural optimization, structural identification, and FE model updating (Ditlevsen and Madsen 1996; Kleiber et al. 1997). Many researchers have dedicated their attention to the general problem of design sensitivity analysis, among others, Choi and Santos (1987),

Arora and Cardoso (1989), Tsay and Arora (1990), Tsai et al. (1990). Consistent FE response sensitivity analysis methods have already been formulated for displacement-based FEs (Zhang and Der Kiureghian 1993; Kleiber et al. 1997; Conte et al. 2001, 2002).

2.2 METHODS AVAILABLE FOR FINITE ELEMENT RESPONSE SENSITIVITY COMPUTATION

Several methods are available for computing FE response sensitivities, such as the Forward/Backward/Central Finite Difference Method (FDM) (Zhang and Der Kiureghian 1993; Kleiber et al. 1997; Conte et al. 2003, 2004), the Adjoint Method (AM) (Kleiber et al. 1997), the Perturbation Method (Kleiber and Hien 1992) and the Direct Differentiation Method (DDM) (Kleiber et al. 1997; Conte 2001; Conte et al. 2003, 2004; Barbato and Conte 2005, 2006; Zona et al. 2005; Barbato et al. 2006).

The FDM is the simplest method for response sensitivity computation and consist of performing, in addition to the FE analysis with all sensitivity parameters $\boldsymbol{\vartheta}$ set at their nominal values, a FE response analysis for each parameter θ_i (i = 1, ..., n) in which its nominal value is perturbed by a small but finite amount. Each response sensitivity is then obtained as the ratio of the variation of the response quantity of interest over the parameter perturbation. This method is computationally expensive and approximate in nature and can suffer from numerical inaccuracies (Haftka and Gurdal 1993; Conte et al. 2003, 2004; Zona et al. 2005).

The AM consists in adding as many variables as the number of response sensitivities to be computed (i.e., the number of parameters considered) and solving this adjoint

problem at the same time of the response computation. The AD is extremely efficient for linear and nonlinear elastic systems, but is not competitive with other methods for path-dependent problems (i.e., analysis models involving nonlinear inelastic material constitutive models) (Kleiber et al. 1997).

The PM consists in computing the response sensitivities as a first order perturbation of the response of the model considered. This method is very efficient but, in general, not very accurate.

On the other hand, the DDM is an accurate and efficient way to perform response sensitivity analysis of FE models with nonlinear hysteretic behavior. This method consists of differentiating analytically the space- and time-discretized equations of motion/equilibrium of the FE model of the structural system considered. The response sensitivity computation algorithm affects the various hierarchical layers of FE response calculation, namely the structure, element, integration point (section for frame elements), and material levels. The advantage of the DDM over the FDM is that, at the one-time cost of implementing in a FE code the algorithms for analytical differentiation of the numerical response, the response sensitivities to any of the modeling parameters considered can be computed exactly (up to a numerical tolerance defined by the user) at a relatively small fraction (depending on the number of iterations required in the nonlinear FE analysis of the model considered and on the specific implementation, see Lupoi et al. 2006) of the cost of an additional FE analysis, which is required for computing response sensitivities to each of the parameters considered when the Forward/Backward FDM is employed. In the case of Central FDM, computing the response sensitivities to modeling parameters requires two

additional nonlinear FE analyses for each parameter considered, which makes this method very expensive computationally.

2.3 FINITE ELEMENT RESPONSE SENSITIVITY ANALYSIS AT THE STRUCTURE LEVEL: THE DIRECT DIFFERENTIATION METHOD (DDM)

The computation of FE response sensitivities to material and loading parameters requires extension of the FE algorithms for response computation only. Let r(t) denote a generic scalar response quantity (displacement, acceleration, local or resultant stress, etc.). By definition, the sensitivity of r(t) with respect to the material or loading parameter θ is expressed mathematically as the (absolute) partial derivative of r(t) with respect to the variable θ evaluated at $\theta = \theta_0$, i.e., $\partial r(t)/\partial\theta\big|_{\theta = \theta_0}$ where θ_0 denotes the nominal value taken by the sensitivity parameter θ for the FE response analysis.

In the sequel, following the notation proposed by Kleiber, the scalar response quantity $r(\boldsymbol{\vartheta}) = r(\mathbf{f}(\boldsymbol{\vartheta}), \boldsymbol{\vartheta})$ depends on the parameter vector $\boldsymbol{\vartheta}$ (defined by n time-independent sensitivity parameters, i.e., $\boldsymbol{\vartheta} = [\theta_1, \ldots, \theta_n]^T$), both explicitly and implicitly through the vector function $\mathbf{f}(\boldsymbol{\vartheta})$. It is assumed that $\frac{dr}{d\boldsymbol{\vartheta}}$ denotes the sensitivity gradient or total derivative of r with respect to $\boldsymbol{\vartheta}$, $\frac{dr}{d\theta_i}$ is the absolute partial derivative of the argument r with respect to the scalar variable θ_i, i = 1, ..., n, (i.e., the derivative of the quantity r with respect to the parameter θ_i considering explicit and implicit dependencies), while

$\left.\frac{\partial r}{\partial \theta_i}\right|_{\mathbf{z}}$ is the partial derivative of r with respect to parameter θ_i when the vector of variables $\mathbf{z}$ is kept constant/fixed. In the particular, but important case in which $\mathbf{z} = \mathbf{f}(\boldsymbol{\vartheta})$, the expression $\left.\frac{\partial r}{\partial \theta_i}\right|_{\mathbf{z}}$ reduces to the partial derivative of r considering only the explicit dependency of r on parameter θ_i. For $\boldsymbol{\vartheta} = \theta_1 = \theta$ (single sensitivity parameter case), the adopted notation reduces to the usual elementary calculus notation. The derivations in the sequel consider the case of a single (scalar) sensitivity parameter θ without loss of generality, due to the uncoupled nature of the sensitivity equations with respect to multiple sensitivity parameters.

It is assumed herein that the response of a structural/geotechnical system is computed using a general-purpose nonlinear FE analysis program based on the direct stiffness method, employing suitable numerical integration schemes at both the structure and the element level. At each time step, after convergence of the incremental-iterative response computation, the consistent response sensitivities are calculated. According to the DDM (see Conte 2001; Conte et al. 2002), this requires the exact differentiation of the FE numerical scheme for the response computation (including the numerical integration scheme for the material constitutive laws) with respect to the sensitivity parameter θ in order to obtain the “exact” sensitivities of the computationally simulated system response. Notice that the computationally simulated system response is itself an approximation of the exact but unknown system response. Indeed, the exact system response would require the exact solution of the (time continuous - space continuous) governing nonlinear partial

differential equations for the physical model of the structure under consideration. The DDM consists in computing first the conditional derivatives of the element and material history/state variables, forming the right-hand-side (RHS) of the response sensitivity equation at the structure level, solving it for the nodal displacement response sensitivities and updating the unconditional derivatives of all the history/state variables. The response sensitivity computation algorithm affects the various hierarchical layers of FE response calculation, namely: (1) the structure level, (2) the element level, (3) the section level, and (4) the material level.

After spatial discretization using the FE method, the equations of motion of a materially-nonlinear-only structural system take the form of the following nonlinear matrix differential equation:

$$\mathbf{M}(\theta)\ddot{\mathbf{u}}(t, \theta) + \mathbf{C}(\theta)\dot{\mathbf{u}}(t, \theta) + \mathbf{R}(\mathbf{u}(t, \theta), \theta) = \mathbf{F}(t, \theta) \tag{2.1}$$

where t = time, θ = scalar sensitivity parameter (material or loading variable), $\mathbf{u}(t)$ = vector of nodal displacements, $\mathbf{M}$ = mass matrix, $\mathbf{C}$ = damping matrix, $\mathbf{R}(\mathbf{u}, t)$ = history dependent internal (inelastic) resisting force vector, $\mathbf{F}(t)$ = applied dynamic load vector, and a superposed dot denotes one differentiation with respect to time. In the formulation presented herein, the possible dependency of the internal inelastic resisting force vector $\mathbf{R}$ on the vector of nodal displacement is neglected. This dependency exists when the material constitutive models employed account for viscous (strain rate dependent) effects. The formulation taking in account the viscous effects can be found in Haukaas and Der Kiureghian (2004).

We assume without loss of generality that the time continuous - spatially discrete equation of motion (2.1) is integrated numerically in time using the well-known Newmark-β time-stepping method of structural dynamics (Chopra 2001), yielding the following nonlinear matrix algebraic equation in the unknowns $\mathbf{u}_{n+1} = \mathbf{u}(t_{n+1})$:

$$\boldsymbol{\Psi}(\mathbf{u}_{n+1}) = \tilde{\mathbf{F}}_{n+1} - \left[\frac{1}{\beta(\Delta t)^2}\mathbf{M}\mathbf{u}_{n+1} + \frac{\alpha}{\beta(\Delta t)}\mathbf{C}\mathbf{u}_{n+1} + \mathbf{R}(\mathbf{u}_{n+1})\right] = \mathbf{0} \tag{2.2}$$

where

$$\begin{aligned}\tilde{\mathbf{F}}_{n+1} = \mathbf{F}_{n+1} + \mathbf{M}\left[\frac{1}{\beta(\Delta t)^2}\mathbf{u}_n + \frac{1}{\beta(\Delta t)}\dot{\mathbf{u}}_n - \left(1 - \frac{1}{2\beta}\right)\ddot{\mathbf{u}}_n\right] + \\ \mathbf{C}\left[\frac{\alpha}{\beta(\Delta t)}\mathbf{u}_n - \left(1 - \frac{\alpha}{\beta}\right)\dot{\mathbf{u}}_n - (\Delta t)\left(1 - \frac{\alpha}{2\beta}\right)\ddot{\mathbf{u}}_n\right]\end{aligned} \tag{2.3}$$

α and β are parameters controlling the accuracy and stability of the numerical integration algorithm and Δt is the time increment. Eq. (2.2) represents the set of nonlinear algebraic equations for the unknown response quantities $\mathbf{u}_{n+1}$ that has to be solved at each time step $[t_n, t_{n+1}]$. In general, the subscript $(\ldots)_{n+1}$ indicates that the quantity to which it is attached is evaluated at discrete time t_{n+1}.

We assume that $\mathbf{u}_{n+1}$ is the converged solution (up to some iteration residuals satisfying a specified tolerance usually taken in the vicinity of the machine precision) for the current time step $[t_n, t_{n+1}]$. Then, we differentiate Eq. (2.2) with respect to θ using the chain rule, recognizing that $\mathbf{R}(\mathbf{u}_{n+1}) = \mathbf{R}(\mathbf{u}_{n+1}(\theta), \theta)$ (i.e., the structure inelastic

resisting force vector depends on θ both implicitly, through $\mathbf{u}_{n+1}$, and explicitly), which yields the following response sensitivity equation at the structure level:

$$\left[\frac{1}{\beta(\Delta t)^2}\mathbf{M} + \frac{\alpha}{\beta(\Delta t)}\mathbf{C} + (\mathbf{K}_T^{stat})_{n+1}\right]\frac{d\mathbf{u}_{n+1}}{d\theta} = -\left(\frac{1}{\beta(\Delta t)^2}\frac{d\mathbf{M}}{d\theta} + \frac{\alpha}{\beta(\Delta t)}\frac{d\mathbf{C}}{d\theta}\right)\mathbf{u}_{n+1} - \frac{\partial \mathbf{R}(\mathbf{u}_{n+1}(\theta), \theta)}{\partial \theta}\bigg|_{\mathbf{u}_{n+1}} + \frac{d\tilde{\mathbf{F}}_{n+1}}{d\theta} \tag{2.4}$$

where

$$\begin{aligned}\frac{d\tilde{\mathbf{F}}_{n+1}}{d\theta} = {} & \frac{d\mathbf{F}_{n+1}}{d\theta} + \frac{d\mathbf{M}}{d\theta}\left[\frac{1}{\beta(\Delta t)^2}\mathbf{u}_n + \frac{1}{\beta(\Delta t)}\dot{\mathbf{u}}_n - \left(1-\frac{1}{2\beta}\right)\ddot{\mathbf{u}}_n\right] + \\ & \mathbf{M}\left[\frac{1}{\beta(\Delta t)^2}\frac{d\mathbf{u}_n}{d\theta} + \frac{1}{\beta(\Delta t)}\frac{d\dot{\mathbf{u}}_n}{d\theta} - \left(1-\frac{1}{2\beta}\right)\frac{d\ddot{\mathbf{u}}_n}{d\theta}\right] + \\ & \frac{d\mathbf{C}}{d\theta}\left[\frac{\alpha}{\beta(\Delta t)}\mathbf{u}_n - \left(1-\frac{\alpha}{\beta}\right)\dot{\mathbf{u}}_n - (\Delta t)\left(1-\frac{\alpha}{2\beta}\right)\ddot{\mathbf{u}}_n\right] + \\ & \mathbf{C}\left[\frac{\alpha}{\beta(\Delta t)}\frac{d\mathbf{u}_n}{d\theta} - \left(1-\frac{\alpha}{\beta}\right)\frac{d\dot{\mathbf{u}}_n}{d\theta} - (\Delta t)\left(1-\frac{\alpha}{2\beta}\right)\frac{d\ddot{\mathbf{u}}_n}{d\theta}\right]\end{aligned} \tag{2.5}$$

The term $(\mathbf{K}_T^{stat})_{n+1}$ in Eq. (2.4) denotes the static consistent tangent stiffness matrix of the structure at time t_{n+1}. The second term on the RHS of Eq. (2.4) represents the partial derivative of the internal resisting force vector, $\mathbf{R}(\mathbf{u}_{n+1})$, with respect to sensitivity parameter θ under the condition that the displacement vector $\mathbf{u}_{n+1}$ remains fixed, and is computed through direct stiffness assembly of the element resisting force derivatives as

$$\frac{\partial \mathbf{R}(\mathbf{u}_{n+1}(\theta), \theta)}{\partial \theta}\bigg|_{\mathbf{u}_{n+1}} = \sum_{e=1}^{N_{el}}\left((\mathbf{A}_b^{(e)})^T \cdot \boldsymbol{\Gamma}_{REZ}^{(e)T} \cdot \boldsymbol{\Gamma}_{ROT}^{(e)T} \cdot \boldsymbol{\Gamma}_{RBM}^{(e)T} \cdot \frac{\partial \mathbf{Q}_{n+1}}{\partial \theta}\bigg|_{\mathbf{q}_{n+1}}\right) \tag{2.6}$$

In the above equation, $\mathbf{A}_b^{(e)}$ is the Boolean localization matrix for element "e"; $\mathbf{\Gamma}_{REZ}^{(e)}$, $\mathbf{\Gamma}_{ROT}^{(e)}$, and $\mathbf{\Gamma}_{RBM}^{(e)}$ are kinematic transformation matrices to account for rigid end zones (REZ), rotation from global to local reference system (ROT), and rigid body modes (RBM), respectively; $\mathbf{q}_{n+1}$ and $\mathbf{Q}_{n+1}$ denote the vectors of basic element deformations and forces, respectively; and N_{el} denotes the number of frame elements in the structural model.

The above formulation, derived explicitly for dynamic response sensitivity analysis, contains the quasi-static case as a particular case, obtained by simply equating to zero in Eqs. (2.2) through (2.5) all terms containing the mass and damping matrices as well as their derivatives with respect to the sensitivity parameter θ.

2.4 DDM-BASED RESPONSE SENSITIVITY ANALYSIS AT THE ELEMENT LEVEL: DISPLACEMENT-BASED FORMULATION

The basic formulation for FEs is the displacement-based formulation, in which the displacement fields are interpolated on each FE of the meshed domain by using proper shape functions. In the displacement-based formulation, compatibility is enforced in strong form, while equilibrium is expressed in weak form for each FE. The corresponding relations, for a single FE and for the case of linear geometry (small strains and small generalized displacements) are

$$\mathbf{u}(\mathbf{X}) = \mathbf{N}(\mathbf{X})\mathbf{q} \quad : \quad \text{FE interpolation} \tag{2.7}$$

$$\boldsymbol{\epsilon}(\mathbf{X}) = \mathscr{D}\mathbf{u}(\mathbf{X}) = \mathbf{B}(\mathbf{X})\mathbf{q} \quad \text{: compatibility (strong form)} \tag{2.8}$$

$$\boldsymbol{\sigma}(\mathbf{X}) = \boldsymbol{\sigma}(\boldsymbol{\epsilon}(\mathbf{X})) \quad \text{: constitutive model} \tag{2.9}$$

$$\mathbf{Q} = \int_{\Omega} (\mathbf{B}(\mathbf{X}))^{\mathrm{T}} \boldsymbol{\sigma}(\mathbf{X}) d\Omega \quad \text{: equilibrium (weak form)} \tag{2.10}$$

in which $\mathbf{X} = [x, y, z]^{\mathrm{T}}$ = spatial coordinates, $\mathbf{u}$, $\boldsymbol{\epsilon}$, $\boldsymbol{\sigma}$ = displacement, strain and stress fields, respectively, $\mathbf{q}$, $\mathbf{Q}$ = nodal displacement and force vectors, respectively, $\mathbf{N}$ = shape functions, $\mathscr{D}$ = differential operator matrix defined as

$$\mathscr{D} = \begin{bmatrix} \frac{\partial}{\partial x} & 0 & 0 & 0 & \frac{\partial}{\partial z} & \frac{\partial}{\partial y} \\ 0 & \frac{\partial}{\partial y} & 0 & \frac{\partial}{\partial z} & 0 & \frac{\partial}{\partial x} \\ 0 & 0 & \frac{\partial}{\partial z} & \frac{\partial}{\partial y} & \frac{\partial}{\partial x} & 0 \end{bmatrix}^{\mathrm{T}} \tag{2.11}$$

$\mathbf{B}(\mathbf{X}) = \mathscr{D}\mathbf{N}(\mathbf{X})$, Ω = FE domain, and the superscript T denotes the matrix transpose operator.

The response sensitivities equations at the element level are obtained differentiating Eqs. (2.7) through (2.10) with respect to the sensitivity parameter θ as follows

$$\frac{d\mathbf{u}(\mathbf{X})}{d\theta} = \mathbf{N}(\mathbf{X})\frac{d\mathbf{q}}{d\theta} \tag{2.12}$$

$$\frac{d\boldsymbol{\epsilon}(\mathbf{X})}{d\theta} = \mathbf{B}(\mathbf{X})\frac{d\mathbf{q}}{d\theta} \tag{2.13}$$

$$\frac{d\boldsymbol{\sigma}(\mathbf{X})}{d\theta} = \mathbf{E}(\mathbf{X})\frac{d\boldsymbol{\epsilon}(\mathbf{X})}{d\theta} + \left.\frac{\partial\boldsymbol{\sigma}(\mathbf{X})}{\partial\theta}\right|_{\mathbf{q}} \tag{2.14}$$

$$\frac{d\mathbf{Q}}{d\theta} = \int_{\Omega} (\mathbf{B}(\mathbf{X}))^{T} \frac{d\boldsymbol{\sigma}(\mathbf{X})}{d\theta} d\Omega \tag{2.15}$$

in which $\mathbf{E}$ denotes the consistent tangent stiffness matrix at the material level.

2.5 DDM-BASED RESPONSE SENSITIVITY ANALYSIS FOR DISPLACEMENT-BASED FRAME ELEMENTS

A frame element is a FE commonly used to model frame structures, such as most of the civil buildings. Frame elements are commonly based on the Euler-Bernoulli beam theory and are used to model structural elements having one dimension (length) dominant with respect to the other two (describing the cross-section). Due to the large use of frame elements in the work presented in this dissertation, the specialization of the response sensitivity algorithm for a general displacement-based FE is presented here in detail.

In a displacement-based frame element, the relationships between element and section deformations on one hand, and between element and section forces on the other hand are given by

$$\mathbf{d}(x, \theta) = \mathbf{B}(x) \cdot \mathbf{q}(\theta) \quad \text{(compatibility in strong form)} \tag{2.16}$$

$$\mathbf{Q}(\theta) = \int_{0}^{L} \mathbf{B}^{T}(x) \cdot \mathbf{D}(x, \theta) \cdot dx \quad \text{(equilibrium in weak form)} \tag{2.17}$$

where $\mathbf{B}(x)$ is a transformation matrix between element deformations and section deformations, which is independent of the sensitivity parameter θ.

After introducing the normalized coordinate ξ (with $-1 \leq \xi \leq 1$) and performing numerical integration, Eqs. (2.16) and (2.17) become

$$\mathbf{d}(\xi_i, \theta) = \mathbf{B}(\xi_i) \cdot \mathbf{q}(\theta) \quad (i = 1, ..., n_{IP}) \tag{2.18}$$

$$\mathbf{Q}(\theta) = \frac{L}{2} \cdot \sum_{i=1}^{n_{IP}} \{ \mathbf{B}^T(\xi_i) \cdot \mathbf{D}(\xi_i, \theta) \cdot w_i \} \tag{2.19}$$

where ξ_i and w_i denote the sampling points and their integration weights, respectively, while n_{IP} represents the number of integration points along the beam axis.

Differentiation of the above relations is straightforward and yields

$$\frac{d\mathbf{d}(\xi_i, \theta)}{d\theta} = \mathbf{B}(\xi_i) \cdot \frac{d\mathbf{q}(\theta)}{d\theta} \quad (i = 1, ..., n_{IP}) \tag{2.20}$$

$$\frac{d\mathbf{Q}(\theta)}{d\theta} = \frac{L}{2} \cdot \sum_{i=1}^{n_{IP}} \left\{ \mathbf{B}^T(\xi_i) \cdot \frac{d\mathbf{D}(\xi_i, \theta)}{d\theta} \cdot w_i \right\} \tag{2.21}$$

Therefore, the element response sensitivity computation is easily accomplished using the following procedure (where the dependence of the various quantities on θ is not shown explicitly for the sake of brevity).

2.5.1 Conditional derivatives (for $\mathbf{q}_{n+1}$ fixed)

(1) Set derivatives of the basic element deformations $\mathbf{q}_{n+1}$ to zero as

$$\left. \frac{\partial \mathbf{q}_{n+1}}{\partial \theta} \right|_{\mathbf{q}_{n+1}} = \mathbf{0} \tag{2.22}$$

It follows that

$$\left.\frac{\partial \mathbf{d}_{n+1}(\xi_i)}{\partial \theta}\right|_{\mathbf{q}_{n+1}} = \mathbf{B}(\xi_i) \cdot \left.\frac{\partial \mathbf{q}_{n+1}}{\partial \theta}\right|_{\mathbf{q}_{n+1}} = \mathbf{0} \quad (i = 1, ..., n_{IP}) \tag{2.23}$$

(2) From the constitutive law integration scheme (during loop over the element integration points for pre-response sensitivity calculations), compute $\left.\frac{\partial \mathbf{D}_{n+1}(\xi_i)}{\partial \theta}\right|_{\mathbf{q}_{n+1}}$ $(i = 1, \ldots, n_{IP})$.

(3) Integrate the conditional derivatives of the sections forces over the element as

$$\left.\frac{\partial \mathbf{Q}_{n+1}}{\partial \theta}\right|_{\mathbf{q}_{n+1}} = \frac{L}{2} \cdot \sum_{i=1}^{n_{IP}} \left\{ \mathbf{B}^T(\xi_i) \cdot \left.\frac{\partial \mathbf{D}_{n+1}(\xi_i)}{\partial \theta}\right|_{\mathbf{q}_{n+1}} \cdot w_i \right\} \tag{2.24}$$

(4) Form the RHS of the response sensitivity equation at the structure level, Eq. (2.4), through direct stiffness assembly.

(5) Solve Eq. (2.4) for the nodal response sensitivities, $\frac{d\mathbf{u}_{n+1}}{d\theta}$.

2.5.2 Unconditional derivatives

(1) Compute unconditional derivatives $\frac{d\mathbf{q}_{n+1}}{d\theta}$ from the solution of the response sensitivity equation at the structure level, Eq. (2.4), as

$$\frac{d\mathbf{q}_{n+1}}{d\theta} = \mathbf{\Gamma}^{(e)}_{RBM} \cdot \mathbf{\Gamma}^{(e)}_{ROT} \cdot \mathbf{\Gamma}^{(e)}_{REZ} \cdot \frac{d\mathbf{p}_{n+1}}{d\theta} = \mathbf{\Gamma}^{(e)}_{RBM} \cdot \mathbf{\Gamma}^{(e)}_{ROT} \cdot \mathbf{\Gamma}^{(e)}_{REZ} \cdot \mathbf{A}^{(e)}_{b} \frac{d\mathbf{u}_{n+1}}{d\theta}$$
$$(e = 1, ..., N_{el}) \tag{2.25}$$

The section deformation sensitivities are given by

$$\frac{d\mathbf{d}_{n+1}(\xi_i)}{d\theta} = \mathbf{B}(\xi_i) \cdot \frac{d\mathbf{q}_{n+1}}{d\theta} \quad (i = 1, ..., n_{IP}) \tag{2.26}$$

(2) From the constitutive law integration scheme, compute and save the unconditional derivatives of the material and section history/state variables $\frac{dr_{n+1}(\xi_i)}{d\theta}$ and compute $\frac{d\mathbf{D}(\xi_i)}{d\theta}$.

(3) Integrate the derivatives of the section forces over the element to obtain

$$\frac{d\mathbf{Q}}{d\theta} = \frac{L}{2} \cdot \sum_{i=1}^{n_{IP}} \left\{ \mathbf{B}^T(\xi_i) \cdot \frac{d\mathbf{D}(\xi_i)}{d\theta} \cdot w_i \right\} \tag{2.27}$$

2.6 DDM-BASED RESPONSE SENSITIVITY AT THE INTEGRATION POINT (SECTION) AND MATERIAL LEVELS

As already seen for response sensitivity computation at the element level, response sensitivity algorithms at the integration point and material levels are dependent on the specific integration point and material constitutive models implemented and employed.

Some specific implementations and their corresponding sensitivity algorithms will be presented and used in the following chapters of this dissertation and many other examples can be found in the literature (see Choi and Santos 1987; Arora and Cardoso 1989; Tsay and Arora 1990; Tsai et al. 1990; Zhang and Der Kiureghian 1993; Conte 2001; Conte et al. 2003, 2004; Barbato and Conte 2005, 2006; Zona et al. 2005; Barbato et al. 2006).

2.7 CONCLUSIONS

In this Chapter, finite element response sensitivity analysis is introduced and available methods for computing FE response sensitivities with respect to modeling and loading parameters are illustrated. Then, the Direct Differentiation Method is described in detail at the structural level and at the element level for the classical displacement-based formulation. The material presented here is the state-of-the-art in FE response sensitivity analysis and forms the basis for the developments presented in Chapters 3 through 6 of this dissertation.

2.8 ACKNOWLEDGEMENTS

Chapter 2 contains some material as it appears in Computer Methods in Applied Mechanics and Engineering (2005), Barbato, M., and Conte, J.P., 194(12-16):1479-1512. The dissertation author was the primary investigator and author of this paper.

REFERENCES

Arora J.S., Cardoso J.B. (1989) “A design sensitivity analysis principle and its implementation into ADINA.” *Computers and Structures*, 32:691-705.

Barbato M., Conte J.P. (2005) “Finite element response sensitivity analysis: a comparison between force-based and displacement-based frame element models.” *Computer Methods in Applied Mechanics and Engineering*, 194(12-16):1479-1512.

Barbato M., Conte J.P. (2006) “Finite element structural response sensitivity and reliability analyses using smooth versus non-smooth material constitutive models.” *International Journal of Reliability and Safety,* 1(1-2):3-39.

Choi K.K., Santos J.L.T. (1987) “Design sensitivity analysis of nonlinear structural systems. Part I: Theory.” *International Journal for Numerical Methods in Engineering*, 24:2039-2055.

Chopra A.K. (2001) *Dynamics of Structures: Theory and Applications to Earthquake Engineering.* Second Edition, Prentice Hall.

Conte J.P. (2001) “Finite element response sensitivity analysis in earthquake engineering.” *Earthquake Engineering Frontiers in the New Millennium.* Spencer & Hu, Swets & Zeitlinger, 395-401.

Conte J.P., Vijalapura P.K., Meghella M. (2003) “Consistent finite element response sensitivity analysis.” *Journal of Engineering Mechanics* (ASCE), 129(12) 1380-1393.

Conte J.P., Barbato M., Spacone E. (2004) “Finite element response sensitivity analysis using force-based frame models”. *International Journal of Numerical Methods in Engineering*, 59(13) 1781-1820.

Ditlevsen O., Madsen H.O. (1996) *Structural Reliability Methods.* Wiley.

Kleiber M., Antunez H., Hien T.D., Kowalczyk P. (1997) *Parameter Sensitivity in Nonlinear Mechanics: Theory and Finite Element Computations.* Wiley.

Kleiber M., Hien T.D. (1992) *The Stochastic Finite Element Method, Basic Perturbation Technique and Computer Implementation.* Wiley.

Haftka R.T., Gurdal Z. (1993) *Elements of Structural Optimization.* Third edition, Kluver Academic Publishers, Dordrecht.

Haukaas T., Der Kiureghian A. (2004) "Finite Element Reliability and Sensitivity Methods for Performance-Based Engineering" *Report PEER 2003/14*, Pacific Earthquake Engineering Research Center, University of California, Berkeley, CA.

Lupoi G., Franchin P., Lupoi A., Pinto P.E. (2006) "Seismic fragility analysis of structural systems", *Journal of Engineering Mechanics* (ASCE), 132(4):385-395.

Tsay J.J., Arora J.S. (1990) "Nonlinear structural design sensitivity analysis for path dependent problems. Part I: General theory." *Computer Methods in Applied Mechanics and Engineering*, 81:183-208.

Tsay J.J., Cardoso J.B., Arora J.S. (1990) "Nonlinear structural design sensitivity analysis for path dependent problems. Part II: Analytical examples." *Computer Methods in Applied Mechanics and Engineering*, 81:209-228.

Zhang Y., Der Kiureghian A. (1993) "Dynamic response sensitivity of inelastic structures." *Computer Methods in Applied Mechanics and Engineering*, 108:23-36.

Zona A., Barbato M., Conte J.P. (2005) "Finite Element Response Sensitivity Analysis of Steel-Concrete Composite Beams with Deformable Shear Connection." *Journal of Engineering Mechanics* (ASCE), 131(11):1126-1139.

CHAPTER 3

DDM-BASED FINITE ELEMENT RESPONSE SENSITIVITY ANALYSIS USING FORCE-BASED FRAME ELEMENTS

3.1 INTRODUCTION

In the last decade, great advances have taken place in the nonlinear analysis of frame structures. Advances were led by the development and implementation of force-based elements, which are superior to classical displacement-based elements in tracing material nonlinearities such as those encountered in reinforced concrete beams and columns (Spacone et al. 1996a, 1996b, 1996c; Neuenhofer and Filippou 1997). Force-based elements are the state-of-the-art tool in computational simulation of the static and dynamic response of frame structures in the presence of material and geometric nonlinearities.

As seen in Chapter 2, maybe even more important than the simulated nonlinear response of a frame structure is its sensitivity to loading parameters and to various geometric, mechanical, and material properties defining the structure. In this chapter, algorithms for FE response sensitivity computation are developed for frame structures modeled using force-based finite elements, also called flexibility-based finite elements in

the literature. The objective of this work is to extend the benefits of force-based frame elements for nonlinear structural analysis to FE response sensitivity analysis.

The formulation presented here is based on the DDM and it assumes the use of a general-purpose nonlinear FE analysis program based on the direct stiffness method. In this work, the focus is on materially-nonlinear-only static and dynamic structural response sensitivity analysis.

3.2 NONLINEAR STATIC AND DYNAMIC RESPONSE ANALYSIS OF STRUCTURES USING FORCE-BASED FRAME ELEMENTS

The last few years have seen the rapid development of force-based elements for the nonlinear analysis of frame structures. In a classical displacement-based element, the cubic and linear Hermitian polynomials used to interpolate the transverse and axial frame element displacements, respectively, are only approximations of the actual displacement fields in the presence of non-uniform beam cross-section and/or nonlinear material behavior. On the other hand, force-based frame element formulations stem from equilibrium between section and nodal forces, which can be enforced exactly in the case of a frame element. The exact flexibility matrix can be computed for an arbitrary variation of the cross-section and for any section constitutive law. The main issue with force-based frame elements is their implementation in a general-purpose nonlinear FE program, typically based on the stiffness method. Spacone et al. (1996b, 1996c) presented a consistent solu-

tion to this problem. They propose a state determination based on an iterative procedure that is basically a Newton-Raphson scheme under constant nodal displacements. During the iterations, the deformation fields inside the element (mainly curvature and axial strains) are adjusted until they become compatible (in an integral sense) with the imposed nodal deformations. Neuenhofer and Filippou (1997) showed that the iterations are not necessary at the element level at each global (structure level) iteration step, since the element eventually converges as the structure iteration scheme converges. The first (full iteration) procedure is more robust near limit points and computationally more demanding at the element level, but may save iterations at the global level. The second procedure is generally faster.

The force-based element formulation proposed by Spacone et al. (1996b, 1996c) is totally independent of the section constitutive law. The section state determination is identical to that required for a displacement-based element. The section module must return the section stiffness and the section resisting forces corresponding to the current section deformations. Different section models have been implemented, notably layer and fiber sections and section with nonlinear resultant force-deformation laws. Appendix 3.A presents the features of the force-based frame element formulation, which are needed in deriving the analytical sensitivities of force-based FE models of structural frame systems.

Geometric nonlinearities are not included in this study, whose focus is on material nonlinearities. Two frameworks for including geometric nonlinearities in a force-based

beam formulation have been proposed, one by de Souza (2000) with earlier work by Neuenhofer and Filippou (1998), who uses a corotational formulation to include large displacements, the other by Sivaselvan and Reinhorn (2002), who modify the shape of the force interpolation functions to include the geometric effects.

3.3 RESPONSE SENSITIVITY ANALYSIS AT THE ELEMENT LEVEL

3.3.1 Formulation

This section presents the algorithm developed for response sensitivity analysis of force-based frame elements. Within the direct stiffness assembly formulation at the global level, at every time (or load) step, the element receives as input from the structure level the element nodal displacements $\mathbf{p}$, which are transformed into the basic element deformations $\mathbf{q}$ (see Appendix 3.A.1), and returns as output the nodal resisting force vector $\mathbf{P} = \boldsymbol{\Gamma}_{\mathrm{REZ}}^{\mathrm{T}} \cdot \boldsymbol{\Gamma}_{\mathrm{ROT}}^{\mathrm{T}} \cdot \boldsymbol{\Gamma}_{\mathrm{RBM}}^{\mathrm{T}} \cdot \mathbf{Q}$ (see Appendix 3.A.1) and the element consistent tangent stiffness matrix. The element interacts with the section level (or integration point level) transforming the element nodal deformations $\mathbf{q}$ into section deformations $\mathbf{d}$ and computing the basic element resisting forces $\mathbf{Q}$ from the section forces $\mathbf{D}$, themselves obtained through the material constitutive integration scheme. In a displacement-based formula-

tion, the relationship between element deformations and forces and section deformations and forces is straightforward, namely:

$$\mathbf{d}(x) = \mathbf{B}(x) \cdot \mathbf{q} \tag{3.1}$$

$$\mathbf{Q} = \int_0^L \mathbf{B}^T(x) \cdot \mathbf{D}(x) \cdot dx \tag{3.2}$$

where $\mathbf{B}(x)$ is a transformation matrix between element deformations and section deformations, which is independent of the sensitivity parameter θ. In contrast, in the force-based formulation, there is no simple direct relation between the section deformations $\mathbf{d}$ and the basic element deformations $\mathbf{q}$, and an iterative procedure (although a non-iterative one can also be used) is used to perform the element state determination as described in Appendix A.2 (Spacone et al. 1996b). This fact complicates the derivation of the sensitivities of force-based element response quantities as compared to the case of displacement-based elements (Conte et al. 2002). While for displacement-based elements, the derivative of the section deformations-element deformations relation given in Equation (3.1) is straightforward, since $\mathbf{B}(x)$ is independent of the sensitivity parameter θ, i.e., $\mathbf{d}(x) = \mathbf{d}(x, \mathbf{q}(\theta))$, for force-based elements, the section deformations are function of θ both explicitly and implicitly (through the element deformations $\mathbf{q}(\theta)$), i.e., $\mathbf{d}(x) = \mathbf{d}(x, \mathbf{q}(\theta), \theta)$.

In general, the dependence of section deformations, $\mathbf{d}$, and section forces, $\mathbf{D}$, on the element deformations, $\mathbf{q}$, and sensitivity parameter, θ, can be expressed as

$$\mathbf{d} = \mathbf{d}(\mathbf{q}(\theta), \theta) \tag{3.3}$$

$$\mathbf{D} = \mathbf{D}(\mathbf{d}(\mathbf{q}(\theta), \theta), \theta) \tag{3.4}$$

By the chain rule of differentiation, we determine the sensitivity of these quantities to parameter θ as

$$\frac{d\mathbf{d}}{d\theta} = \left.\frac{\partial \mathbf{d}}{\partial \mathbf{q}}\right|_{\theta} \cdot \frac{d\mathbf{q}}{d\theta} + \left.\frac{\partial \mathbf{d}}{\partial \theta}\right|_{\mathbf{q}} = \mathbf{B}(\theta) \cdot \frac{d\mathbf{q}}{d\theta} + \left.\frac{\partial \mathbf{d}}{\partial \theta}\right|_{\mathbf{q}} \tag{3.5}$$

where

$$\mathbf{B}(x, \theta) = \left.\frac{\partial \mathbf{d}}{\partial \mathbf{q}}\right|_{\theta} = \mathbf{f}_s(x, \theta) \cdot \mathbf{b}(x) \cdot \mathbf{k}_T^{(e)}(\theta) \tag{3.6}$$

The expression for $\mathbf{B}(x, \theta)$ is obtained from

$$\left.\frac{\partial \mathbf{d}}{\partial \mathbf{q}}\right|_{\theta} = \left.\frac{\partial \mathbf{d}}{\partial \mathbf{D}}\right|_{\theta} \cdot \left.\frac{\partial \mathbf{D}}{\partial \mathbf{Q}}\right|_{\theta} \cdot \left.\frac{\partial \mathbf{Q}}{\partial \mathbf{q}}\right|_{\theta} \tag{3.7}$$

$$\left.\frac{\partial \mathbf{d}}{\partial \mathbf{D}}\right|_{\theta} = \mathbf{f}_s(x, \theta) \tag{3.8}$$

$$d\mathbf{D}(x, \theta) = \mathbf{b}(x) \cdot d\mathbf{Q}(\theta) \tag{3.9}$$

$$\left.\frac{\partial \mathbf{Q}}{\partial \mathbf{q}}\right|_{\theta} = \mathbf{k}_T^{(e)}(\theta) \tag{3.10}$$

and substituting (3.8) through (3.10) in Equation (3.7).

From (3.3) through (3.5), again by the chain rule of differentiation, we have

$$\frac{d\mathbf{D}}{d\theta} = \mathbf{k}_s(x, \theta) \cdot \frac{d\mathbf{d}}{d\theta} + \left.\frac{\partial \mathbf{D}}{\partial \theta}\right|_{\mathbf{d}} = \mathbf{k}_s \cdot \left[\mathbf{B}(x, \theta) \cdot \frac{d\mathbf{q}}{d\theta} + \left.\frac{\partial \mathbf{d}}{\partial \theta}\right|_{\mathbf{q}}\right] + \left.\frac{\partial \mathbf{D}}{\partial \theta}\right|_{\mathbf{d}} \tag{3.11}$$

where

$$\mathbf{k}_s(x, \theta) = \left.\frac{\partial \mathbf{D}}{\partial \mathbf{d}}\right|_{\theta} \tag{3.12}$$

is the section consistent tangent stiffness matrix.

Differentiating the (strong form) equilibrium equations, $\mathbf{D}(x, \theta) = \mathbf{b}(x) \cdot \mathbf{Q}(\theta)$ (see Equation (3.59) in Appendix 3.A), at the section level with respect to parameter θ, in the hypothesis of zero element distributed loads (i.e., $\mathbf{D}_p(x) = \mathbf{0}$), yields

$$\frac{d\mathbf{D}}{d\theta} = \mathbf{b}(x) \cdot \frac{d\mathbf{Q}}{d\theta} \tag{3.13}$$

Compatibility between basic element deformations $\mathbf{q}$ and section deformations $\mathbf{d}$ is expressed in weak form through the principle of virtual forces as

$$\mathbf{q} = \int_0^L \mathbf{b}^T(x) \cdot \mathbf{d}(x) \cdot dx \tag{3.14}$$

which, after introducing the normalized coordinate ξ (with $-1 \leq \xi \leq 1$) and performing numerical integration becomes

$$\mathbf{q} = \frac{L}{2} \cdot \sum_{i=1}^{n_{IP}} \{ \mathbf{b}^T(\xi_i) \cdot \mathbf{d}(\xi_i) \cdot w_i \} \tag{3.15}$$

Differentiating the above relation with respect to parameter θ, we obtain

$$\frac{d\mathbf{q}}{d\theta} = \frac{L}{2} \cdot \sum_{i=1}^{n_{IP}} \left\{ \mathbf{b}^T(\xi_i) \cdot \frac{d\mathbf{d}(\xi_i)}{d\theta} \cdot w_i \right\} \tag{3.16}$$

Contrary to the displacement-based formulation (in which $\mathbf{d}(x, \theta) = \mathbf{B}(x) \cdot \mathbf{q}(\theta)$), $\left.\frac{\partial \mathbf{d}}{\partial \theta}\right|_{\mathbf{q}} \neq \mathbf{0}$ in the case of the present force-based formulation for which $\mathbf{B} = \mathbf{B}(x, \theta)$ as shown in Equation (3.6).

It is necessary to derive the conditional (with $\mathbf{q}$ fixed) derivatives of the basic element forces, $\mathbf{Q}$, and section deformations, $\mathbf{d}(x)$, (needed to assemble the RHS of the response sensitivity equation) and the unconditional derivatives of all the history/state variables at the element, section, and material levels, respectively (needed in the computation of the conditional derivatives of the history/state variables at the next time step). For this purpose, we merge Equations (3.11) and (3.13) to obtain

$$\mathbf{k}_s \cdot \left[\mathbf{B}(\theta) \cdot \frac{d\mathbf{q}}{d\theta} + \left.\frac{\partial \mathbf{d}}{\partial \theta}\right|_{\mathbf{q}} \right] - \mathbf{b} \cdot \frac{d\mathbf{Q}}{d\theta} = -\left.\frac{\partial \mathbf{D}}{\partial \theta}\right|_{\mathbf{d}} \tag{3.17}$$

For the conditional derivatives (with $\mathbf{q}$ fixed, i.e., with $\frac{d\mathbf{q}}{d\theta} = \mathbf{0}$), Equation (3.17) reduces to

$$\mathbf{k}_s(\xi_i) \cdot \left.\frac{\partial \mathbf{d}(\xi_i)}{\partial \theta}\right|_{\mathbf{q}} - \mathbf{b}(\xi_i) \cdot \left.\frac{\partial \mathbf{Q}}{\partial \theta}\right|_{\mathbf{q}} = -\left.\frac{\partial \mathbf{D}(\xi_i)}{\partial \theta}\right|_{\mathbf{d}} \quad , i = 1, ..., n_{IP} \tag{3.18}$$

while differentiation of the weak form of compatibility expressed by Equation (3.15) yields

$$\sum_{i=1}^{n_{IP}} \left\{ \mathbf{b}^{T}(\xi_i) \cdot \left. \frac{\partial \mathbf{d}(\xi_i)}{\partial \theta} \right|_{\mathbf{q}} \cdot w_i \right\} = \mathbf{0} \tag{3.19}$$

Thus, in (3.18) and (3.19), we have obtained a set of $(2n_{IP} + 3)$ equations with $(2n_{IP} + 3)$ scalar unknowns where n_{IP} denotes the number of integration points per element. These scalar unknowns are $\left. \frac{\partial \mathbf{d}(\xi_i)}{\partial \theta} \right|_{\mathbf{q}}$ (2 unknowns for each integration point), and $\left. \frac{\partial \mathbf{Q}}{\partial \theta} \right|_{\mathbf{q}}$ (3 unknowns for each element). Equation (3.18) provides 2 scalar equations per integration point, while Equation (3.19) gives 3 scalar equations for each element. The conditional derivatives $\left. \frac{\partial \mathbf{D}(\xi_i)}{\partial \theta} \right|_{\mathbf{d}}$ on the RHS of Equation (3.18) can be obtained through conditional differentiation (with $\mathbf{d}(x)$ fixed) of the constitutive law integration scheme at the numerical integration point level (i.e., section level), requiring the computation of the conditional (with $\mathbf{d}(x)$ fixed) derivatives of all the history/state variables at the section and material levels, as will be shown in Section 6.

The proposed scheme to compute the conditional derivatives $\left. \frac{\partial \mathbf{D}_{n+1}(\xi_i)}{\partial \theta} \right|_{\mathbf{d}_{n+1}}$, $\left. \frac{\partial \mathbf{d}_{n+1}(\xi_i)}{\partial \theta} \right|_{\mathbf{q}_{n+1}}$, and $\left. \frac{\partial \mathbf{Q}_{n+1}}{\partial \theta} \right|_{\mathbf{q}_{n+1}}$, which are needed to form the RHS of the response sensitivity equation at the structure level, at time step t_{n+1}, is described in the sections below.

3.3.1.1 Conditional derivatives (for $\mathbf{q}_{n+1}$ fixed):

(1) Set derivatives of the basic element deformations $\mathbf{q}_{n+1}$ and section deformations $\mathbf{d}_{n+1}(\xi_i)$ to zero (i.e., consider $\mathbf{q}_{n+1}$ and $\mathbf{d}_{n+1}(\xi_i)$, respectively, as fixed quantities):

$$\left.\frac{\partial \mathbf{q}_{n+1}}{\partial \theta}\right|_{\mathbf{q}_{n+1}} = \mathbf{0} \tag{3.20}$$

$$\left.\frac{\partial \mathbf{d}_{n+1}}{\partial \theta}\right|_{\mathbf{d}_{n+1}} = \mathbf{0} \tag{3.21}$$

(2) From the constitutive law integration scheme (during loop over the element integration points for pre- response sensitivity calculations), compute $\left.\frac{\partial \mathbf{D}_{n+1}}{\partial \theta}\right|_{\mathbf{d}_{n+1}}$ and then set up the following linear system of $(2n_{IP}+3)$ equations (after looping over the integration points):

$$\begin{cases} \mathbf{k}_{s,\,n+1}(\xi_i)\cdot\left.\frac{\partial \mathbf{d}_{n+1}(\xi_i)}{\partial \theta}\right|_{\mathbf{q}_{n+1}} - \mathbf{b}(\xi_i)\cdot\left.\frac{\partial \mathbf{Q}_{n+1}}{\partial \theta}\right|_{\mathbf{q}_{n+1}} = -\left.\frac{\partial \mathbf{D}_{n+1}(\xi_i)}{\partial \theta}\right|_{\mathbf{d}_{n+1}} \\ \sum_{i=1}^{n_{IP}} \left\{ \mathbf{b}^T(\xi_i)\cdot\left.\frac{\partial \mathbf{d}_{n+1}(\xi_i)}{\partial \theta}\right|_{\mathbf{q}_{n+1}} \cdot w_i \right\} = \mathbf{0} \end{cases}$$

$$i = 1, \ldots, n_{IP} \tag{3.22}$$

(3) Solve (3.22) for $\left.\frac{\partial \mathbf{d}_{n+1}(\xi_i)}{\partial \theta}\right|_{\mathbf{q}_{n+1}}$ and $\left.\frac{\partial \mathbf{Q}_{n+1}}{\partial \theta}\right|_{\mathbf{q}_{n+1}}$, $i = 1,\ldots, n_{IP}$.

(4) Form the RHS of the response sensitivity equation at the structure level through direct stiffness assembly. For example, the term $\left.\frac{\partial \mathbf{R}(\mathbf{u}_{n+1}(\theta), \theta)}{\partial \theta}\right|_{\mathbf{u}_{n+1}}$ is computed as, using Equation (3.75),

$$\left.\frac{\partial \mathbf{R}(\mathbf{u}_{n+1}(\theta), \theta)}{\partial \theta}\right|_{\mathbf{u}_{n+1}} = \sum_{e=1}^{N_{el}} \left((\mathbf{A}_b^{(e)})^T \cdot \mathbf{\Gamma}_{REZ}^{(e)T} \cdot \mathbf{\Gamma}_{ROT}^{(e)T} \cdot \mathbf{\Gamma}_{RBM}^{(e)T} \cdot \left.\frac{\partial \mathbf{Q}_{n+1}}{\partial \theta}\right|_{\mathbf{q}_{n+1}} \right) \tag{3.23}$$

(5) Solve the response sensitivity equation at the structural level for the nodal response sensitivities, $\frac{d\mathbf{u}_{n+1}}{d\theta}$.

3.3.1.2 Unconditional derivatives:

(1) Compute unconditional derivative $\frac{d\mathbf{q}_{n+1}}{d\theta}$ from the solution of the response sensitivity equation at the structure level as

$$\frac{d\mathbf{q}_{n+1}^{(e)}}{d\theta} = \mathbf{\Gamma}_{RBM}^{(e)} \cdot \mathbf{\Gamma}_{ROT}^{(e)} \cdot \mathbf{\Gamma}_{REZ}^{(e)} \cdot \frac{d\mathbf{p}_{n+1}^{(e)}}{d\theta} = \mathbf{\Gamma}_{RBM}^{(e)} \cdot \mathbf{\Gamma}_{ROT}^{(e)} \cdot \mathbf{\Gamma}_{REZ}^{(e)} \cdot \mathbf{A}_b^{(e)} \frac{\partial \mathbf{u}_{n+1}}{\partial \theta}, \quad e = 1, ..., N_{el} \tag{3.24}$$

(2) Using the conditional derivatives $\left.\frac{\partial \mathbf{D}_{n+1}}{\partial \theta}\right|_{\mathbf{d}_{n+1}}$ computed during the pre- response sensitivity calculation phase, set up the following linear system of $(2n_{IP} + 3)$ equations:

$$\begin{cases} \mathbf{k}_{s,\,n+1}(\xi_i)\cdot\dfrac{d\mathbf{d}_{n+1}(\xi_i)}{d\theta} - \mathbf{b}(\xi_i)\cdot\dfrac{d\mathbf{Q}_{n+1}}{d\theta} = -\left.\dfrac{\partial\mathbf{D}_{n+1}(\xi_i)}{\partial\theta}\right|_{\mathbf{d}_{n+1}} \\ \dfrac{L}{2}\cdot\sum_{i=1}^{n_{IP}}\left\{\mathbf{b}^T(\xi_i)\cdot\dfrac{d\mathbf{d}_{n+1}(\xi_i)}{d\theta}\cdot w_i\right\} = \dfrac{d\mathbf{q}_{n+1}}{d\theta} \end{cases}, \; i = 1, \ldots, n_{IP} \quad (3.25)$$

(3) Solve Equation (3.25) for the unconditional derivatives $\dfrac{d\mathbf{d}_{n+1}(\xi_i)}{d\theta}$, i = 1, ... , n_{IP}, and $\dfrac{d\mathbf{Q}_{n+1}}{d\theta}$.

(4) Perform a loop over the frame element integration points, entering with $\dfrac{d\mathbf{d}_{n+1}(\xi_i)}{d\theta}$ in the differentiated constitutive law integration scheme, compute and save the unconditional derivatives of the material and section history variables $\dfrac{dr_{n+1}(\xi_i)}{d\theta}$. These unconditional derivatives are needed to compute the conditional derivatives required for response sensitivity computations at the next time step, t_{n+2}, namely $\left.\dfrac{\partial\mathbf{D}_{n+2}(\xi_i)}{\partial\theta}\right|_{\mathbf{d}_{n+2}}$, $\left.\dfrac{\partial\mathbf{d}_{n+2}(\xi_i)}{\partial\theta}\right|_{\mathbf{q}_{n+2}}$, and $\left.\dfrac{\partial\mathbf{Q}_{n+2}}{\partial\theta}\right|_{\mathbf{q}_{n+2}}$

3.3.2 Response sensitivities with respect to discrete loading parameters

Three types of discrete loading parameters are of interest here, namely (1) nodal forces, (2) effective earthquake forces due to ground acceleration, and (3) distributed element loads. The nodal forces and effective earthquake forces at time t_{n+1} affect only the

term $\frac{d\tilde{\mathbf{F}}_{n+1}}{d\theta}$ on the RHS of the response sensitivity equation at the structure level through the part $\frac{d\mathbf{F}_{n+1}}{d\theta}$. Obviously, at all subsequent time steps, $t_k > t_{n+1}$, the last two terms on the RHS of the sensitivity equation at the structural level are indirectly influenced by $\frac{d\mathbf{F}_{n+1}}{d\theta}$, through the temporal propagation of the unconditional response sensitivities at time t_{n+1}.

Element distributed loads affect the formation and solution of the response sensitivity equation at two different levels: (1) at the structure level through the term $\frac{d\mathbf{F}_{n+1}}{d\theta}$ in which $\mathbf{F}_{n+1}$ depends on the element distributed load (i.e., fixed end forces as equivalent nodal forces), and (2) at the section level of each element affected by the distributed load in question through differentiation of the equilibrium equations, see Equation (3.59),

$$\mathbf{D}_{n+1}(x, \theta) = \mathbf{b}(x) \cdot \mathbf{Q}_{n+1}(\theta) + \mathbf{D}_{P,\, n+1}(x, \theta) \tag{3.26}$$

with respect to the distributed load parameter, i.e.,

$$\frac{d\mathbf{D}_{n+1}(x)}{d\theta} = \mathbf{b}(x) \cdot \frac{d\mathbf{Q}_{n+1}}{d\theta} + \frac{d\mathbf{D}_{P,\, n+1}(x)}{d\theta} \tag{3.27}$$

3.4 IMPLEMENTATION IN A GENERAL-PURPOSE NONLINEAR FINITE ELEMENT STRUCTURAL ANALYSIS PROGRAM

For validation purposes, the above formulation for response sensitivity analysis using force-based frame elements was implemented in a general-purpose FE structural analysis program, namely FEDEASLab Release 2.2 (Filippou 2002). FEDEASLab is a Matlab (The MathWorks 1997) toolbox suitable for linear and nonlinear, static and dynamic structural analysis, which already provides a general framework for physical parameterization of finite element models and response sensitivity computation (Franchin 2003). One of the most important features of FEDEASLab is its strict modularity, that keeps separate the different hierarchical levels encountered in structural analysis (i.e., structure, element, section and material levels). Therefore, the implementation of the response sensitivity computation scheme presented in this paper for force-based elements can be used with any section model and/or material constitutive law (properly implemented with provisions for sensitivity analysis) without any change in the code.

Flow-charts of the computer implementation of the present algorithm for response sensitivity analysis are presented in Figs. 3.1 and 3.2, which also highlight the modularity of the general framework. It is worth noting two main differences between displacement-based (Conte et al. 2002) and force-based frame elements: (1) in the displacement-based formulation, there is no need to solve a linear system of equations at the element level in

order to obtain the conditional and unconditional derivatives of the nodal element forces $\left.\frac{\partial \mathbf{Q}_{n+1}}{\partial \theta}\right|_{\mathbf{q}_{n+1}}$ and $\frac{d\mathbf{Q}_{n+1}}{d\theta}$; and (2) while for displacement-based elements, requiring $\mathbf{q}_{n+1}$ fixed is equivalent to requiring $\mathbf{d}_{n+1}(\xi_i)$ (i = 1, 2, ..., n_{IP}) fixed, for force-based elements, it is necessary to compute the conditional derivatives of the history/state variables imposing $\mathbf{d}_{n+1}(\xi_i)$ fixed in order to obtain the conditional (for $\mathbf{q}_{n+1}$ fixed) and unconditional derivatives of the nodal elements forces.

(1) Conditional derivatives:

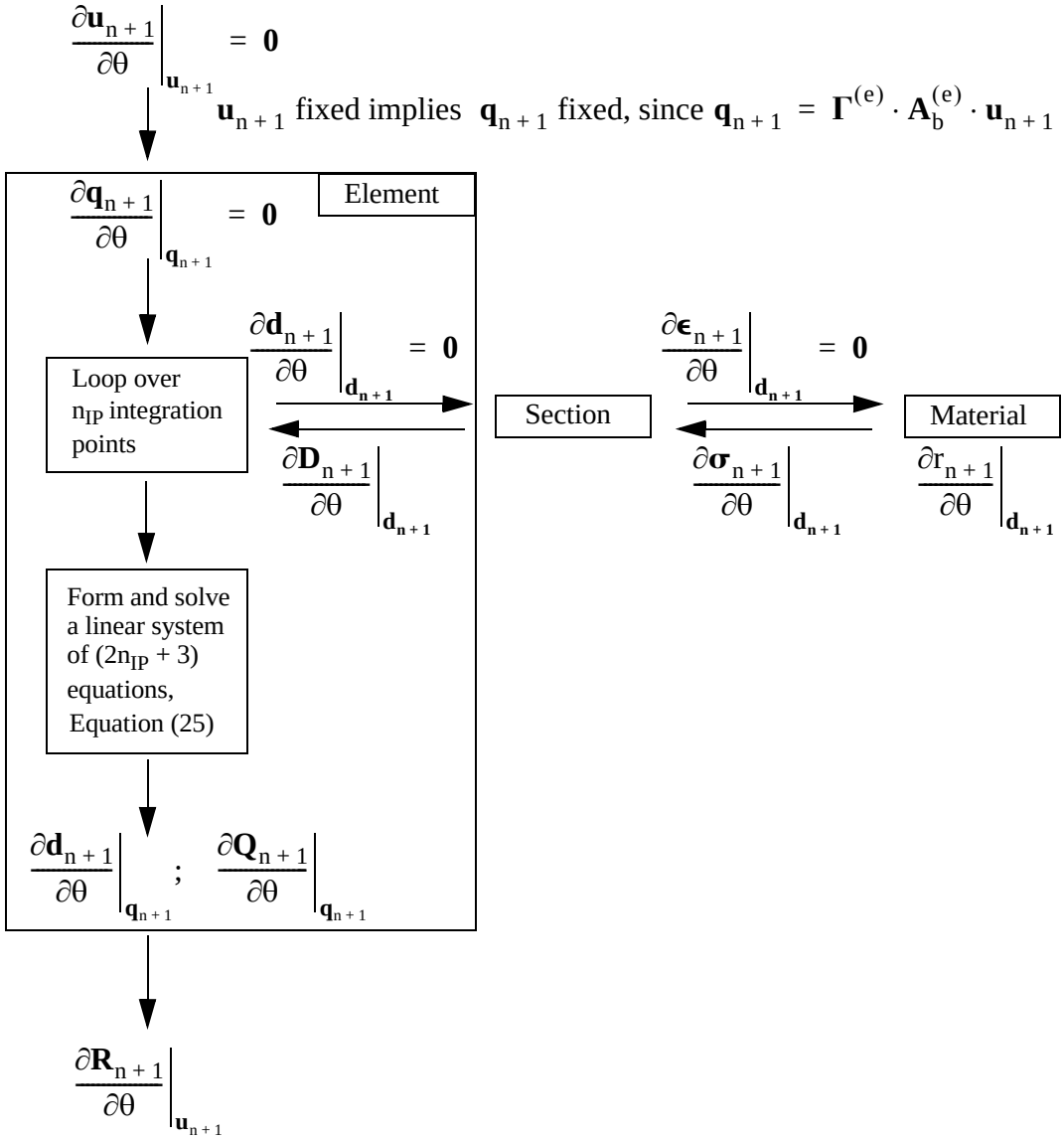

Figure 3.1 Flow chart for the numerical computation of the response sensitivity with a force-based frame element: conditional derivatives.

(2) Unconditional derivatives:

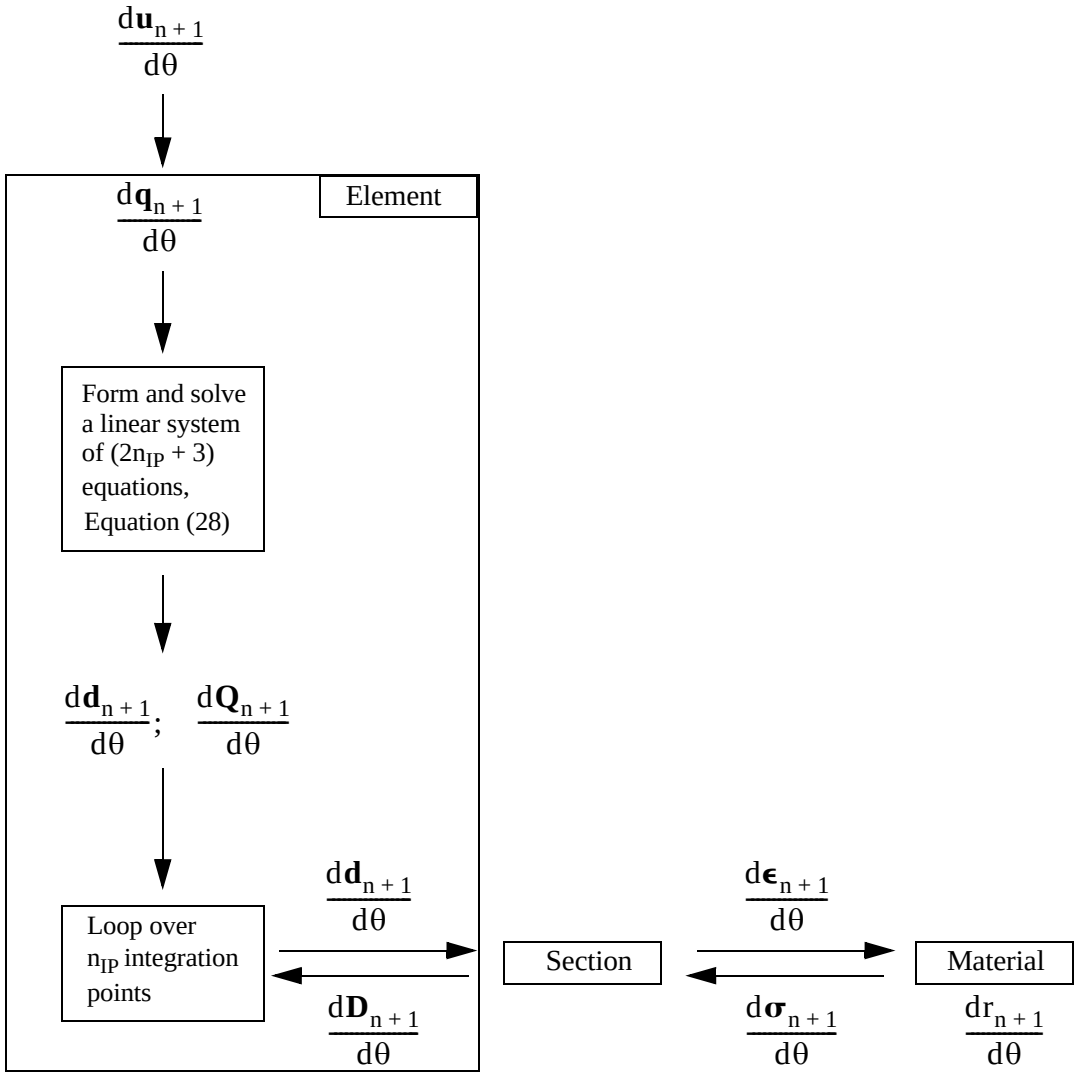

Figure 3.2 Flow chart for the numerical computation of the response sensitivity with a force-based frame element: unconditional derivatives.

3.5 VALIDATION EXAMPLES

3.5.1 Response sensitivity analysis at the section level: homogeneous section with uncoupled axial and flexural response

In the following validation examples, the sectional behavior of the force-based frame element is modeled using a very simple 2-D homogeneous section with uncoupled axial and flexural response. In this case, we have

$$\mathbf{d}_{n+1}(x) = \begin{bmatrix} \varepsilon^{G}_{n+1}(x) \\ \chi_{n+1}(x) \end{bmatrix} \tag{3.28}$$

$$\mathbf{D}_{n+1}(x) = \begin{bmatrix} N_{n+1}(x) \\ M_{n+1}(x) \end{bmatrix} \tag{3.29}$$

$$\mathbf{k}_{s,\,n+1}(x) = \begin{bmatrix} E^{(1)}_{T,\,n+1}(x) \cdot A(x) & 0 \\ 0 & E^{(2)}_{T,\,n+1}(x) \cdot I_z(x) \end{bmatrix} \tag{3.30}$$

where $\varepsilon^{G}_{n+1}(x)$ = axial strain at the reference axis, $\chi_{n+1}(x)$ = curvature, $N_{n+1}(x)$ = axial force, $M_{n+1}(x)$ = bending moment, $A(x)$ = cross-section area, $I_z(x)$ = cross-section moment of inertia, $\mathbf{k}_{s,\,n+1}(x)$ = section consistent tangent stiffness matrix, $E^{(1)}_{T,\,n+1}(x)$ and $E^{(2)}_{T,\,n+1}(x)$ = consistent tangent stiffnesses of the 1-D axial and flexural constitutive laws, respectively.

The numerical section response at time t_{n+1} is given by

$$N_{n+1}(x) = A(x) \cdot \sigma^{(1)}_{n+1}(x) \tag{3.31}$$

$$M_{n+1}(x) = I_z(x) \cdot \sigma^{(2)}_{n+1}(x) \tag{3.32}$$

where $\sigma^{(1)}_{n+1}(x)$ and $\sigma^{(2)}_{n+1}(x)$ are defined as the axial force and bending moment normalized by the cross-section area and moment of inertia, respectively.

The section response sensitivities are

$$\frac{dN_{n+1}(x)}{d\theta} = \frac{dA(x)}{d\theta} \cdot \sigma^{(1)}_{n+1}(x) + A(x) \cdot \frac{d\sigma^{(1)}_{n+1}(x)}{d\theta} \tag{3.33}$$

$$\frac{dM_{n+1}(x)}{d\theta} = \frac{dI_z(x)}{d\theta} \cdot \sigma^{(2)}_{n+1}(x) + I_z(x) \cdot \frac{d\sigma^{(2)}_{n+1}(x)}{d\theta} \tag{3.34}$$

In the present study, the flexural constitutive law is defined as the 1-D J_2 plasticity model, while the axial behavior is taken as linear elastic.

3.5.2 Response sensitivity analysis at the material level:

linear elastic constitutive law

The relations describing both the response and response sensitivities for a 1-D linear elastic material model are

$$\sigma_{n+1} = E \cdot \varepsilon_{n+1} \tag{3.35}$$

$$\frac{d\sigma_{n+1}}{d\theta} = \frac{dE}{d\theta} \cdot \varepsilon_{n+1} + E \cdot \frac{d\varepsilon_{n+1}}{d\theta} \tag{3.36}$$

Note that the terms σ_{n+1}, E and ε_{n+1} in the above equations correspond to the terms $\sigma^{(1)}_{n+1}(x)$, $E^{(1)}_{T,\,n+1}(x)$ and $\varepsilon^{G}_{n+1}(x)$ in (3.28), (3.30), (3.31) and (3.33).

3.5.3 Response sensitivity analysis at the material level: 1-D J_2 plasticity model

In the validation examples presented below, the simple 1-D J_2 (or von Mises) plasticity model is used to describe the nonlinear material flexural behavior. This rate-independent analytical constitutive model can be found in the literature (Simo and Hughes 1998). The discrete constitutive integration algorithm is provided in Appendix 3.B and its consistent differentiation with respect to the sensitivity parameter θ is presented below.

The computation of sensitivities of material history/state variables remains unchanged for both displacement-based (Conte et al. 2002) and force-based frame elements, because the unconditional derivatives of the history/state variables are obtained from the exact differentiation of the same constitutive law integration scheme and the conditional derivatives are computed for the strain ε_{n+1} fixed. Therefore, the conditional derivatives of the history/state variables, $\left.\frac{\partial(\ldots)}{\partial\theta}\right|_{\varepsilon_{n+1}}$, are simply obtained by substituting with zero all the occurrences of the derivative $\frac{d\varepsilon_{n+1}}{d\theta}$ in the expressions for the unconditional derivatives of the history/state variables, $\frac{d(\ldots)}{d\theta}$.

The only difference between the displacement-based and force-based formulations at the material level is that a force-based frame element requires the computation of the derivatives of the history/state variables under the condition that the section deformations

$\mathbf{d}_{n+1}$ remain fixed in order to obtain the term $\left.\frac{\partial \mathbf{D}_{n+1}}{\partial \theta}\right|_{\mathbf{d}_{n+1}}$ in (3.22) and (3.25). For a displacement-based element, fixing the element nodal displacements, $\mathbf{p}(t_{n+1}) = \mathbf{p}_{n+1}$, or the element deformations in the basic system, $\mathbf{q}(t_{n+1}) = \mathbf{q}_{n+1}$, is equivalent to fixing the section deformations $\mathbf{d}_{n+1}$ and therefore the strain ε_{n+1} at the material level, which is not the case for a force-based element (see remark below Equation (3.16)).

If no plastic deformation takes place during the current time/load step $[t_n, t_{n+1}]$, the trial solutions for the state variables given by the elastic predictor step are also the correct solutions, i.e., the elastic predictor step is not followed by a plastic corrector step. Hence, dropping the superscript 'Trial' from (3.83) and differentiating them with respect to the sensitivity parameter θ, we obtain

$$\frac{d(\Delta\lambda)_{n+1}}{d\theta} = 0 \tag{3.37}$$

$$\frac{d\varepsilon^{p}_{n+1}}{d\theta} = \frac{d\varepsilon^{p}_{n}}{d\theta} \tag{3.38}$$

$$\frac{d\alpha_{n+1}}{d\theta} = \frac{d\alpha_{n}}{d\theta} \tag{3.39}$$

$$\frac{d\bar{\varepsilon}^{p}_{n+1}}{d\theta} = \frac{d\bar{\varepsilon}^{p}_{n}}{d\theta} \tag{3.40}$$

$$\frac{d\sigma_{n+1}}{d\theta} = E \cdot \left(\frac{d\varepsilon_{n+1}}{d\theta} - \frac{d\varepsilon^{p}_{n}}{d\theta} \right) + \frac{dE}{d\theta} \cdot (\varepsilon_{n+1} - \varepsilon^{p}_{n}) \tag{3.41}$$

$$\frac{d\sigma_{y,\,n+1}}{d\theta} = \frac{d\sigma_{y,\,n}}{d\theta} \tag{3.42}$$

If plastic deformation takes place during the current time/load step $[t_n, t_{n+1}]$, the discrete elasto-plastic constitutive equations in Appendix 3.A are differentiated exactly with respect to the sensitivity parameter θ in order to compute the derivatives of the history/state variables at time t_{n+1}. The final results are (Conte et al. 2002):

$$\frac{d\sigma_{n+1}^{Trial}}{d\theta} = E \cdot \left(\frac{d\varepsilon_{n+1}}{d\theta} - \frac{d\varepsilon_n^p}{d\theta} \right) + \frac{dE}{d\theta} \cdot (\varepsilon_{n+1} - \varepsilon_n^p) \tag{3.43}$$

$$\frac{d(\Delta\lambda)_{n+1}}{d\theta} = \frac{(E + H_{iso} + H_{kin}) \cdot \left[\left(\frac{d\sigma_{n+1}^{Trial}}{d\theta} - \frac{d\alpha_n}{d\theta} \right) \cdot n_{n+1} - \frac{d\sigma_{y,\,n}}{d\theta} \right]}{(E + H_{iso} + H_{kin})^2} - \frac{\left(\frac{dE}{d\theta} + \frac{dH_{iso}}{d\theta} + \frac{dH_{kin}}{d\theta} \right) \cdot [(\sigma_{n+1}^{Trial} - \alpha_n) \cdot n_{n+1} - \sigma_{y,\,n}]}{(E + H_{iso} + H_{kin})^2} \tag{3.44}$$

$$\frac{d\varepsilon_{n+1}^p}{d\theta} = \frac{d\varepsilon_n^p}{d\theta} + \frac{d(\Delta\lambda)_{n+1}}{d\theta} \cdot n_{n+1} \tag{3.45}$$

$$\frac{d\sigma_{n+1}}{d\theta} = E \cdot \left(\frac{d\varepsilon_{n+1}}{d\theta} - \frac{d\varepsilon_{n+1}^p}{d\theta} \right) + \frac{dE}{d\theta} \cdot (\varepsilon_{n+1} - \varepsilon_{n+1}^p) \tag{3.46}$$

The derivatives of the remaining history/state variables, $\bar{\varepsilon}_{n+1}^p$, $\sigma_{y,\,n+1}$, and α_{n+1}, with respect to the sensitivity parameter θ are obtained by differentiating (3.81) as

$$\frac{d\bar{\varepsilon}_{n+1}^p}{d\theta} = \frac{d\bar{\varepsilon}_n^p}{d\theta} + \frac{d(\Delta\lambda)_{n+1}}{d\theta} \tag{3.47}$$

$$\frac{d\sigma_{y,\,n+1}}{d\theta} = \frac{d\sigma_{y,\,n}}{d\theta} + \frac{dH_{iso}}{d\theta} \cdot (\Delta\lambda)_{n+1} + H_{iso} \cdot \frac{d(\Delta\lambda)_{n+1}}{d\theta} \tag{3.48}$$

$$\frac{d\alpha_{n+1}}{d\theta} = \frac{d\alpha_{n}}{d\theta} + \frac{dH_{kin}}{d\theta} \cdot (\Delta\lambda)_{n+1} \cdot n_{n+1} + H_{kin} \cdot \frac{d(\Delta\lambda)_{n+1}}{d\theta} \cdot n_{n+1} \tag{3.49}$$

3.5.4 Application example: cantilever beam with distributed plasticity

The first test structure considered in this study consists of a cantilever $W21 \times 50$ steel I-beam 8 meters in length. The cross-sectional properties of the beam are: $A = 9.484 \times 10^{-3}$ $[m^2]$ and $I_z = 4.096 \times 10^{-4}$ $[m^4]$, while its initial yield moment is $M_{y0} = 384.2$ [kN-m]. A 20 percent post-yield to initial flexural stiffness ratio is assumed.

The axial behavior is assumed linear elastic, while the flexural behavior is described by a 1-D J_2 plasticity section constitutive law with the following material parameters: Young's modulus $E = 2 \times 10^8$ [kPa], and isotropic and kinematic hardening moduli $H_{iso} = 0$ [kPa], $H_{kin} = 5 \times 10^7$ [kPa], respectively. A material mass density of four times the mass density of steel (i.e., $\rho = 31600$ $[kg/m^3]$) is used to account for typical additional masses (i.e., permanent loads). The beam is modeled with a single 2-D Euler-Bernoulli frame element, see Figure 3.3, with lumped masses at the end nodes (m_i = m/2 = 1200 [kg], i = 1, 2). Five Gauss-Lobatto integration points are used along the beam. No damping is included in the model.

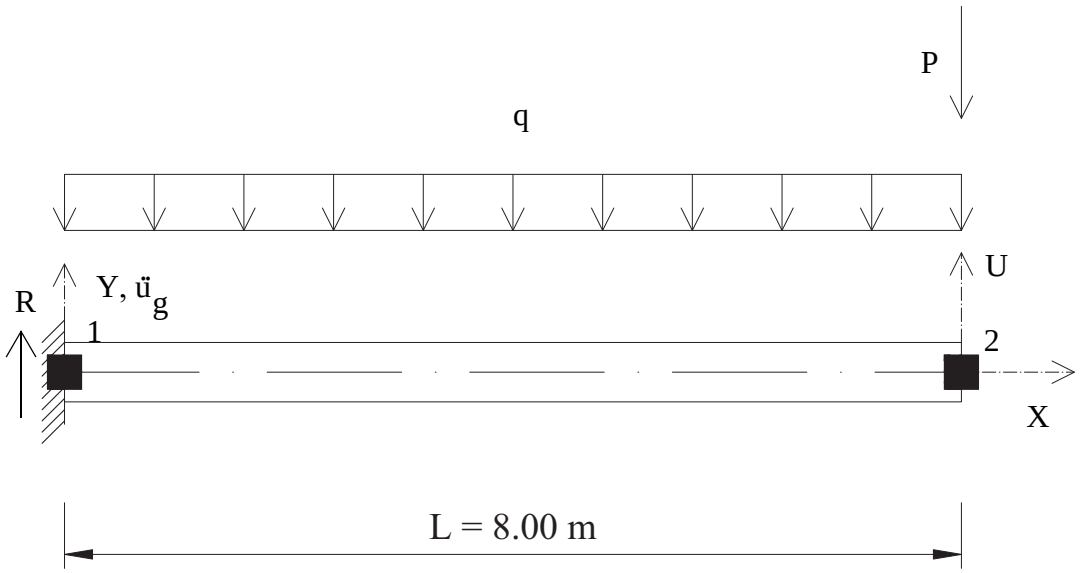

Figure 3.3 Cantilever beam model: geometry, static and quasi-static loads, and global response quantities.

After application of gravity loads (modeled as distributed load q) due to self-weight and permanent loads, the beam is subjected to (1) a nonlinear quasi-static analysis for a cyclic point load applied at the free end, as shown in Figure 3.4, and (2) a nonlinear dynamic analysis for a ground acceleration history taken as the balanced 1940 El Centro earthquake record scaled by a factor 3 (Figure 3.10). The equation of motion and the response sensitivity equation were integrated using the constant average acceleration method with a constant time step of $\Delta t = 0.02$ sec.

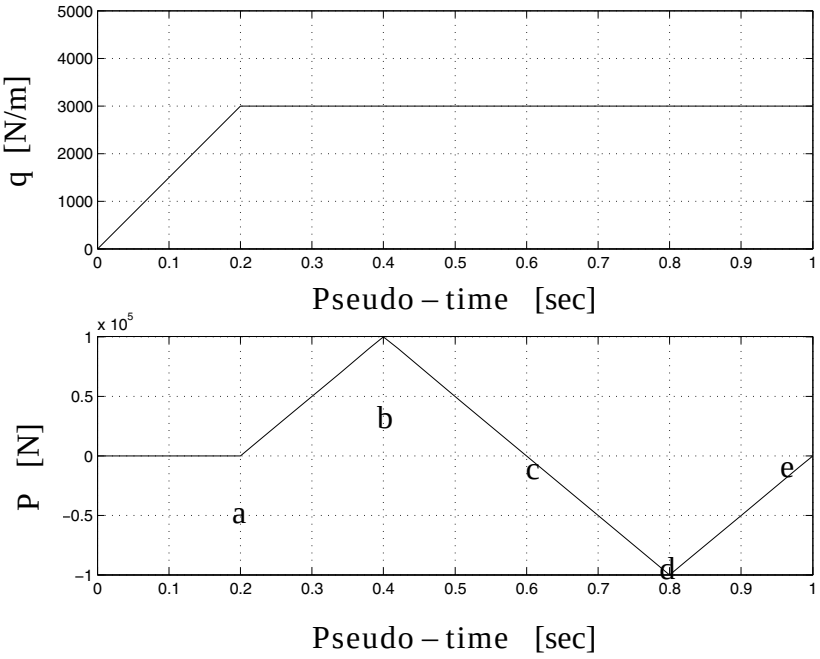

Figure 3.4 Loading histories for the quasi-static cyclic analysis.

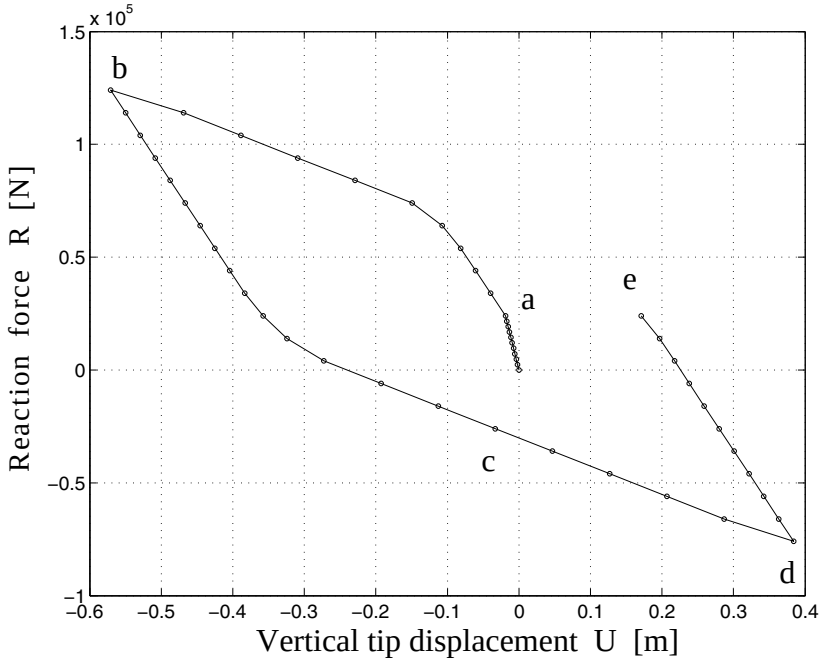

Figure 3.5 Global response of the cantilever beam model for quasi-static cyclic analysis: reaction force versus tip vertical displacement.

The system response is highly nonlinear as shown in Figs. 3.5, 3.11 and 3.12. Figs. 3.6 and 3.7 and Figs. 3.13 and 3.14 plot sensitivities to different material parameters (H_{kin} and M_{y0}) of a global response quantity taken as the tip vertical displacement, for static and dynamic analysis, respectively. Sensitivities of a local response quantity, namely the cumulative plastic curvature ($\bar{\chi}^{p}$) at the fixed end section, to material parameters, are displayed in Figs. 3.8 and 3.9 for static analysis and in Figs. 3.15 and 3.16 for dynamic analysis. Note that all these response sensitivity results are scaled by the sensitivity parameter itself and can therefore be interpreted as 100 times the change in the response quantity per percent change in the sensitivity parameter. To improve the readability of the quasi-static cyclic analysis results in Figs. 3.4 through 3.9, lower-case roman letters were added corresponding to key loading points. Furthermore, global and local response sensitivities to a discrete loading parameter (namely the ground motion acceleration at time $t = 6.00 \ \text{sec}$) are computed and plotted in Figs. 3.17 and 3.18. In all these figures, the response sensitivity results obtained using the consistent Direct Differentiation Method (DDM) are compared directly with their counterparts obtained through Forward Finite Difference (FFD) analysis for three different values of perturbation of the sensitivity parameter, carefully selected to clearly show the asymptotic convergence of the FFD results towards the analytical DDM results. This convergence is further evidenced by the zoom views shown in the insets of Figs. 3.6 through 3.9 and 3.13 through 3.18. For this example, it can be con-

cluded that the FFD results validate both the response sensitivity analysis procedure presented in this paper and its implementation in FEDEASLab.

For quasi-static analysis, it is worth noting the presence of discontinuities in the response sensitivities to the initial yield moment M_{y0} for both global and local response quantities. These discontinuities occur in time/load steps during which elastic-to-plastic material state transitions take place at some integration points (Figs. 3.7 and 3.9). The response sensitivity algorithm developed propagates consistently the discontinuities in response sensitivities from the material, to the section, to the element, and to the structure level, as confirmed by the FFD computations in this example. The sensitivity results obtained for this example also show that, among the sensitivity parameters considered, both the global and local response quantities selected are most sensitive to the initial yield moment M_{y0}

.

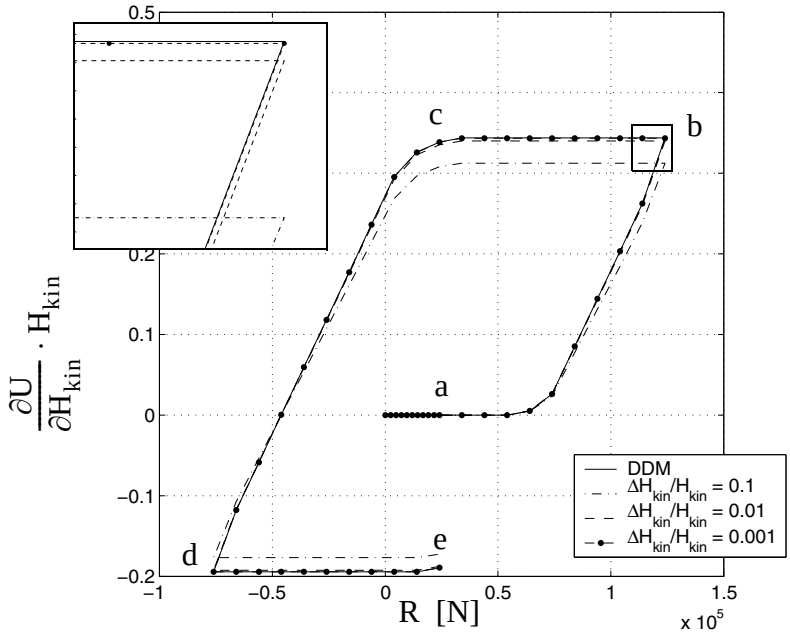

Figure 3.6 Global response sensitivities to material parameters: tip vertical displacement sensitivity to kinematic hardening modulus, H_{kin}.

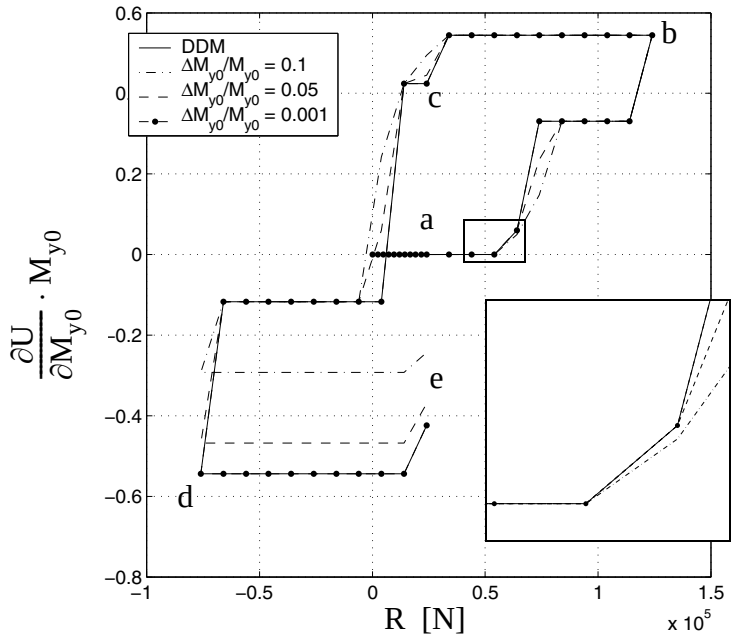

Figure 3.7 Global response sensitivities to material parameters: tip vertical displacement sensitivity to initial yield moment, M_{y0}.

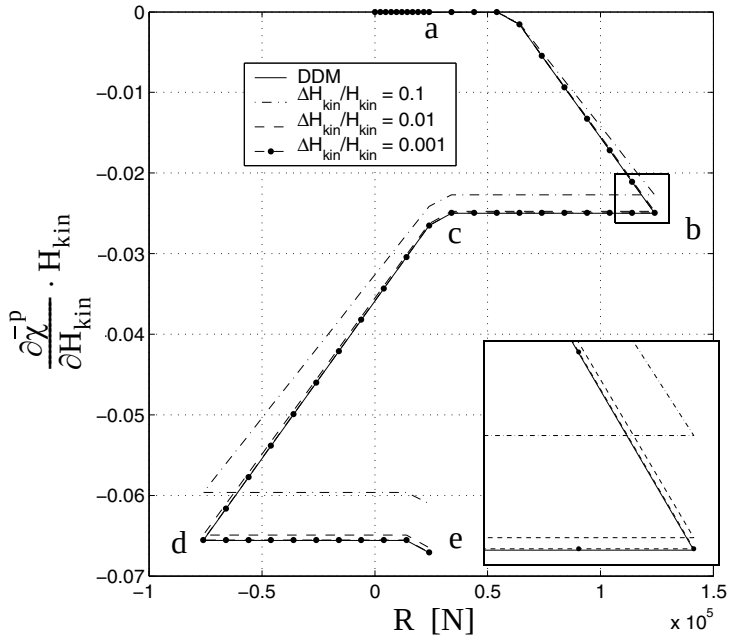

Figure 3.8 Local response sensitivities to material parameters: cumulative plastic curvature sensitivity to kinematic hardening modulus, H_{kin}.

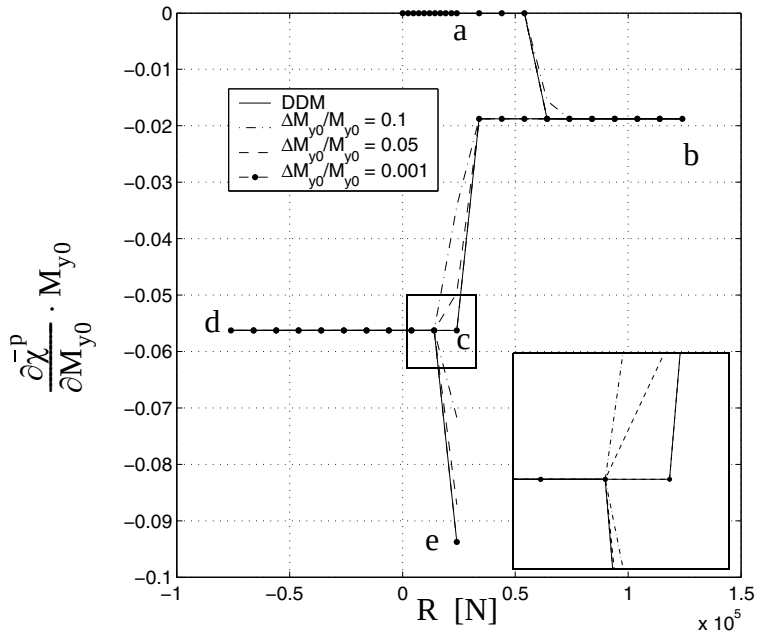

Figure 3.9 Local response sensitivities to material parameters: cumulative plastic curvature sensitivity to initial yield moment, M_{y0}.

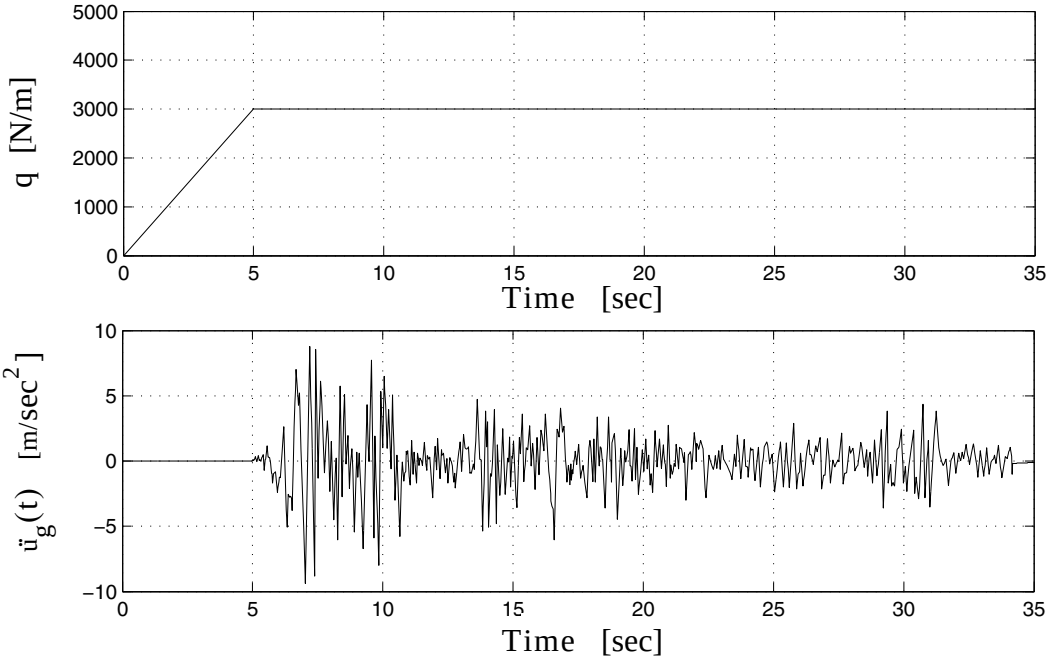

Figure 3.10 Loading histories for the dynamic analysis.

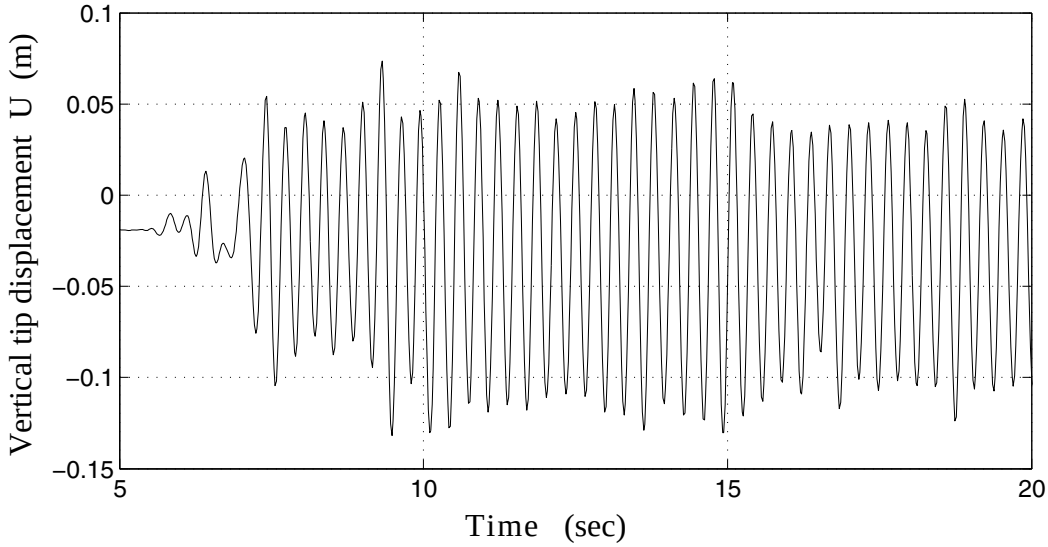

Figure 3.11 Global response of the cantilever beam model for dynamic analysis: tip vertical displacement history.

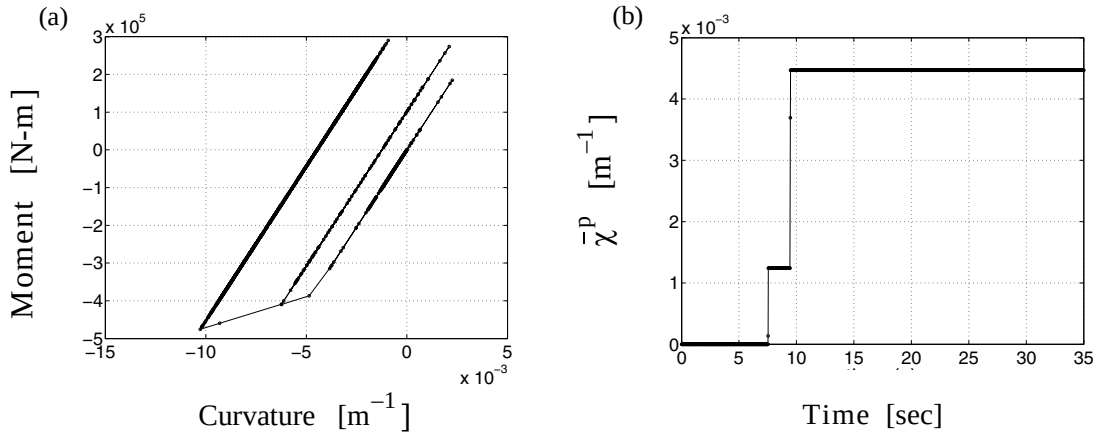

Figure 3.12 Local response of the cantilever beam model for dynamic analysis: (a) moment-curvature and (b) cumulative plastic curvature history, at the fixed end.

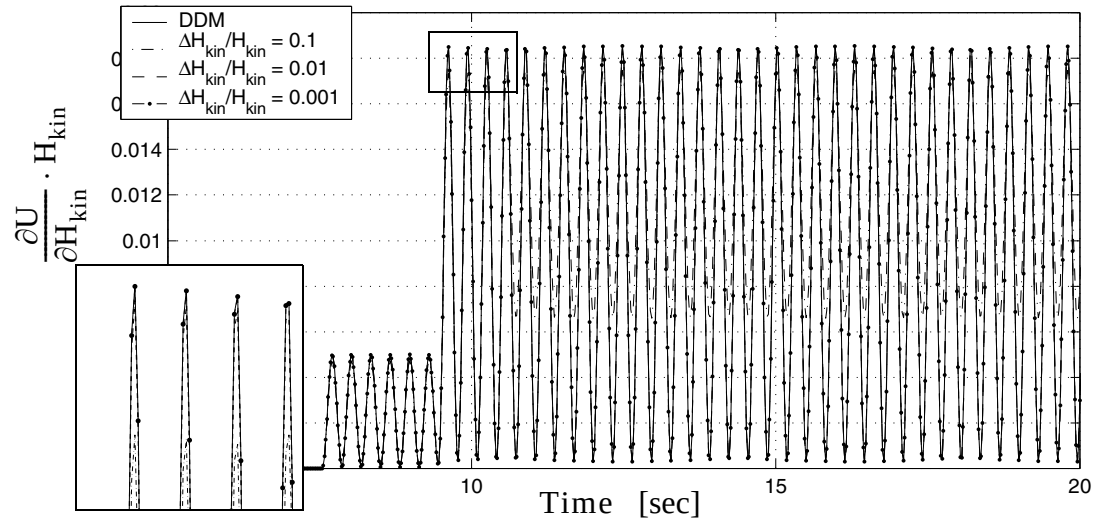

Figure 3.13 Global response sensitivities to material parameters: tip vertical displacement sensitivity to kinematic hardening modulus, H_{kin}.

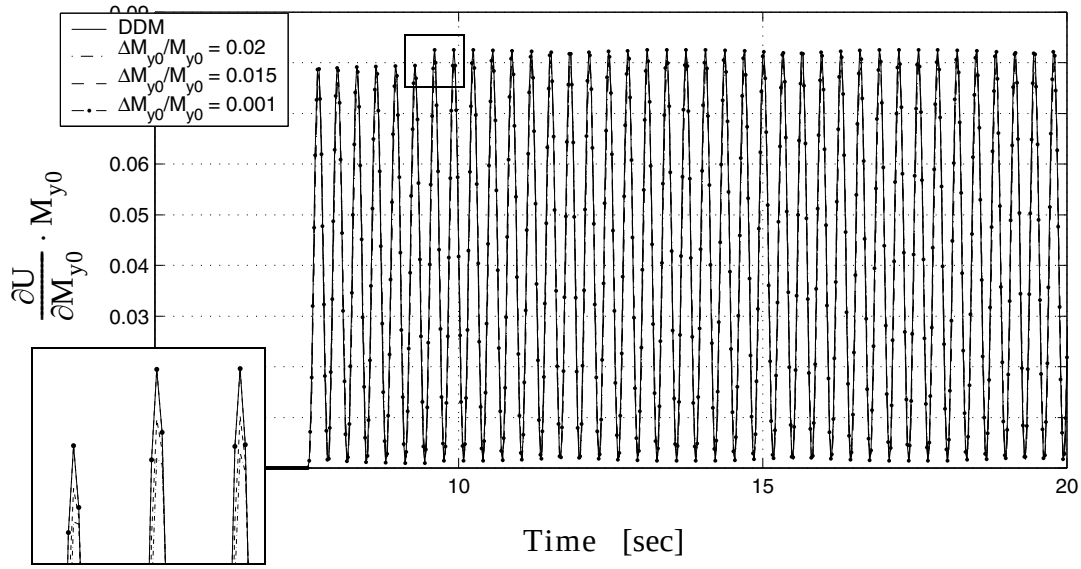

Figure 3.14 Global response sensitivities to material parameters: tip vertical displacement sensitivity to initial yield moment, M_{y0}.

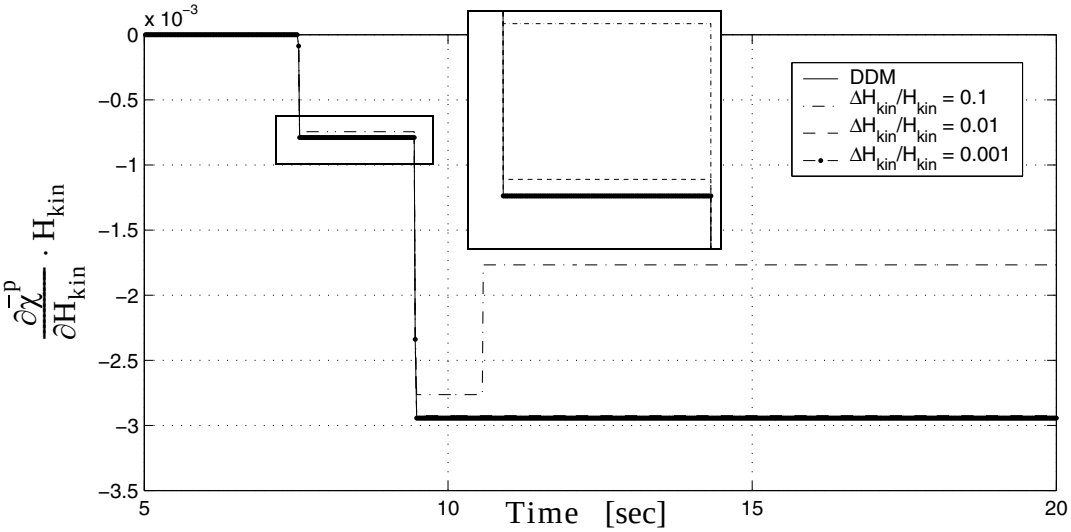

Figure 3.15 Local response sensitivities to material parameters: cumulative plastic curvature sensitivity to kinematic hardening modulus, H_{kin}.

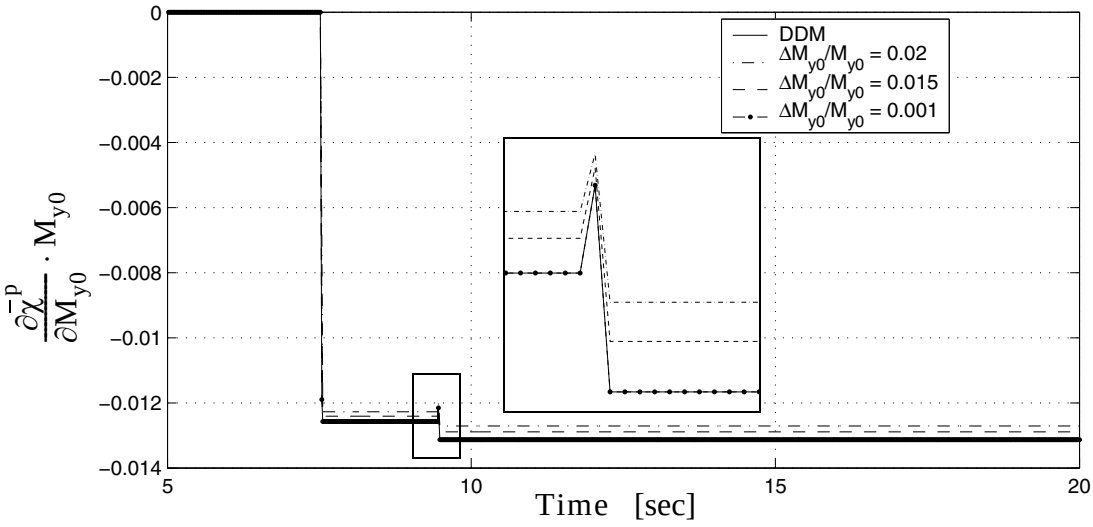

Figure 3.16 Local response sensitivities to material parameters: cumulative plastic curvature sensitivity to initial yield moment, M_{y0}.

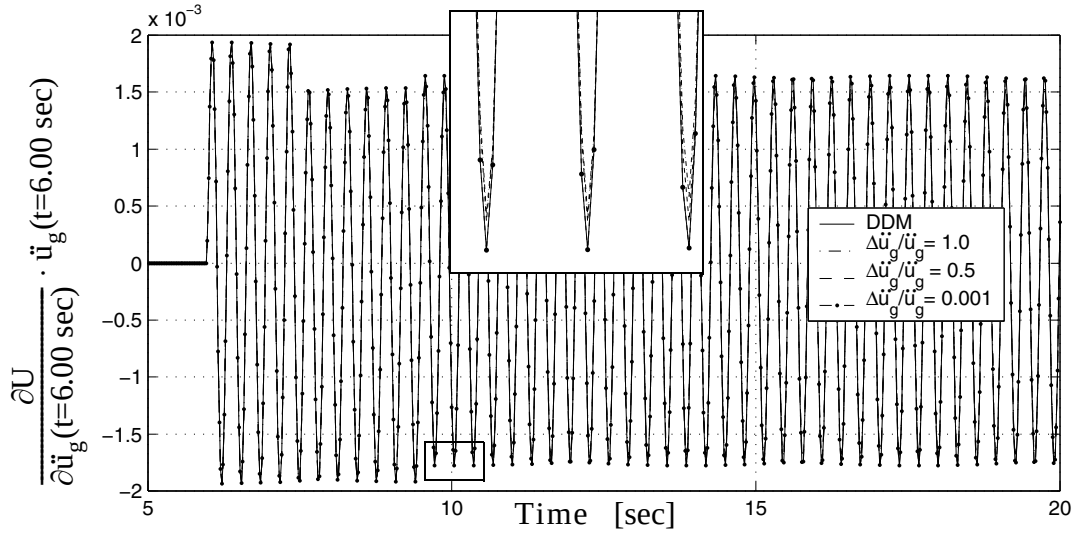

Figure 3.17 Global response sensitivities to loading parameters: tip vertical displacement sensitivity to earthquake ground acceleration at time t = 6.00sec.

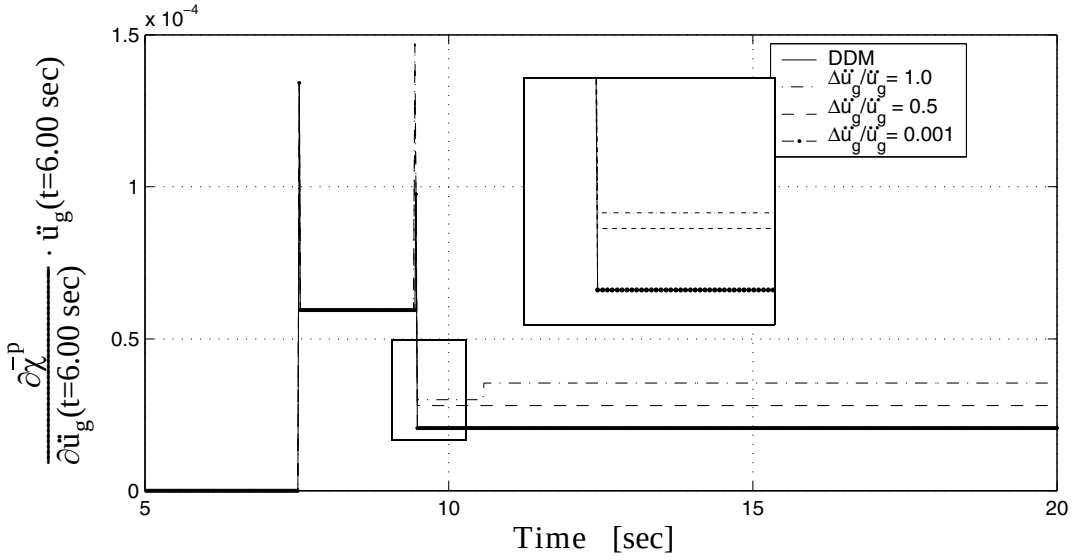

Figure 3.18 Local response sensitivities to loading parameters: cumulative plastic curvature sensitivity to earthquake ground acceleration at time t = 6.00sec.

3.5.5 Application example: 2-D frame with distributed plasticity

The second structure used as validation example is a five-story single-bay steel moment-resisting frame, a FE model of which is shown in Figure 3.19. All columns and beams are $W21 \times 50$ steel I-beams with an initial yield moment of $M_{y0} = 384.2$ [kN-m]. The material behavior is modeled as in the previous example (i.e., 1-D J_2 plasticity model for bending and linear elastic model for axial behavior). The mechanical properties and effective mass density of the material are the same as in the previous model. It is worth mentioning that, even though it is assumed here that a single set of material parameters characterizes all beams and columns of the frame, the DDM presented

in this study is capable to account for multiple sets of material parameters for each material model used.

Each of the physical structural elements is modeled by a simplified Euler-Bernoulli force-based, distributed plasticity, 2-D frame element. The inertia properties of the system are modeled through (translational) lumped masses applied at the nodes, each element contributing half of its effective mass to each of its two nodes. The frame has an initial fundamental period of 0.52 sec.

After application of gravity loads, this frame is subjected to (1) a nonlinear static pushover analysis under an inverted triangular pattern of horizontal lateral loads applied at floor levels as shown in Figure 3.19, with the time history described in Figure 3.20, and (2) a nonlinear response history analysis for earthquake base excitation, with the same seismic input, see Figure 3.10, as for the previous cantilever beam model. In the dynamic analysis, the unconditionally stable constant average acceleration integration method is used with a constant time step of $\Delta t = 0.02$ sec.

Global response quantities (floor horizontal displacements) in the quasi-static pushover analysis are given in Figs. 3.21. Figs. 3.22 through 3.27 show response sensitivity analysis results for the pushover analysis of the present frame structure. In Figs. 3.22 through 3.24, sensitivities to different material parameters (E, H_{kin}, and M_{y0}) of the roof horizontal displacement (global response quantity) obtained through application of the

DDM developed in this paper are compared with the corresponding FFD results. Figs. 3.25 through 3.27 show the sensitivities of the cumulative plastic curvature (local response quantity) at the fixed section of the left base column (section A) to the same material parameters as above, again with their FFD counterparts.

For the dynamic analysis, the response histories of the same global and local response quantities considered previously are shown in Figs. 3.28 and 3.29. Figs. 3.30 through 3.32 display the roof horizontal displacement sensitivities to Young's modulus, E, the kinematic hardening modulus, H_{kin}, and the initial yield moment, M_{y0}, respectively; while the sensitivities of the cumulative plastic curvature at section A to the material sensitivity parameters E, H_{kin} and M_{y0} are plotted in Figs. 3.33 through 3.35. Finally, global and local response sensitivities to the ground motion acceleration value at time $t = 6.00$ sec are given in Figs. 3.36 and 3.37, respectively. Notice that the global response sensitivity becomes non-zero directly at the time of perturbation of the ground acceleration history, while the specific local response sensitivity considered here becomes non-zero only after the first yielding subsequent to the time at which the ground acceleration perturbation is applied.

As in the first application example, the asymptotic convergence of the FFD results (for decreasing perturbation $\Delta\theta$ of the sensitivity parameter) towards the response sensitivities evaluated analytically through the DDM is highlighted by zoom views inserted in

Figs. 3.22 through 3.27 and Figs. 3.30 through 3.37. All the response sensitivity results are scaled by the sensitivity parameter itself according as in Section 5.4. The discontinuities in the response sensitivities for both global and local quantities can be appreciated easily in the quasi-static analysis results and with more careful inspection in the dynamic analysis results. The discontinuities in the dynamic local response sensitivities often appear as spikes. In this second more general application example, it can also be concluded that the asymptotic convergence of the FFD results towards the DDM results validates both the response sensitivity analysis procedure developed in this paper and its computer implementation in FEDEASLab.

The response sensitivity results obtained for this specific application example also show that: (1) in the quasi-static pushover analysis, the roof displacement is most sensitive to changes in the initial yield moment, M_{y0}, while the cumulative plastic curvature at section A is most affected by perturbations in the value of the kinematic hardening modulus, H_{kin}, and (2) in the dynamic analysis, the Young's modulus, E, is the sensitivity parameter that affects most, among the sensitivity parameters considered, both the global and local response sensitivities considered.

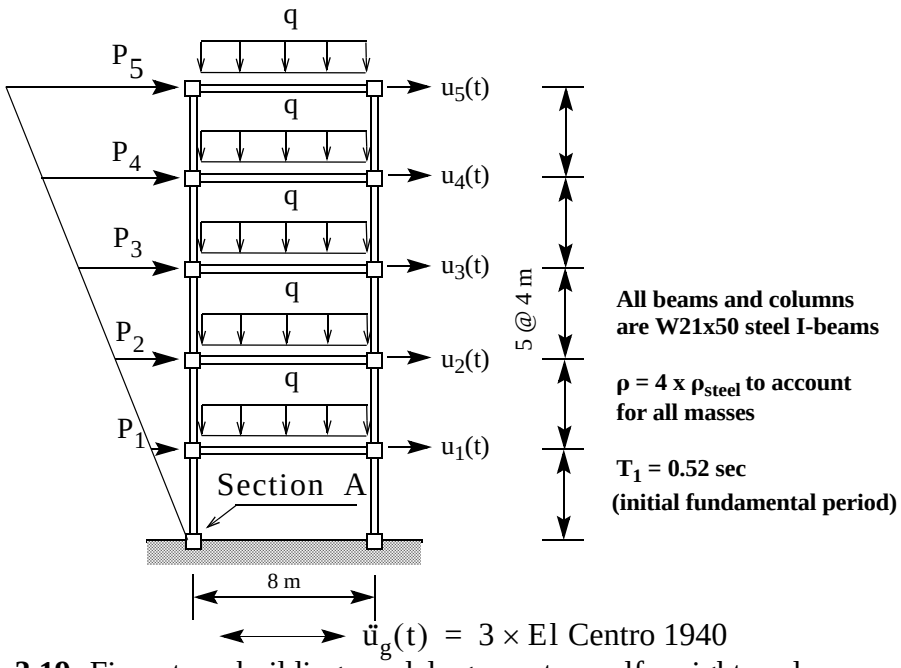

Figure 3.19 Five story building model: geometry, self-weight and permanent loads, quasi-static horizontal lateral load and floor displacements.

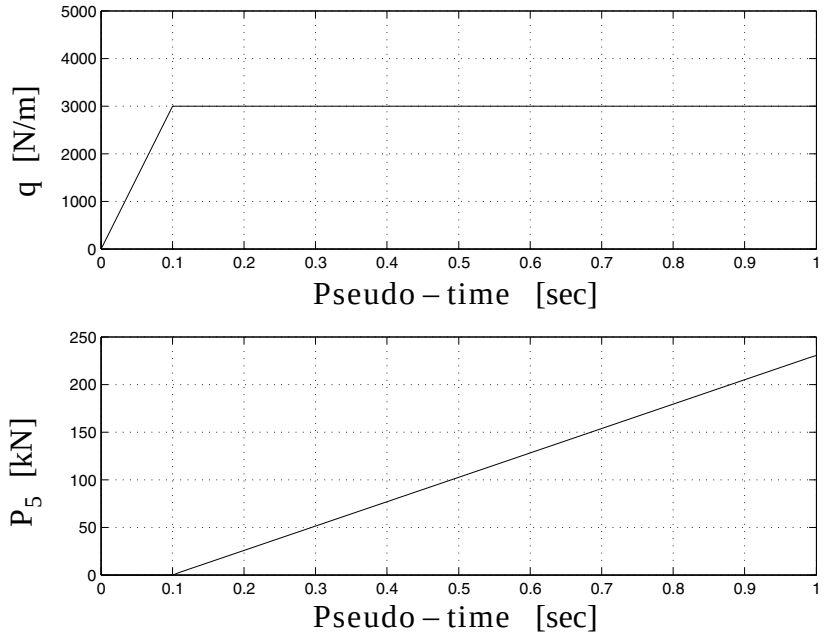

Figure 3.20 Loading histories for pushover analysis.

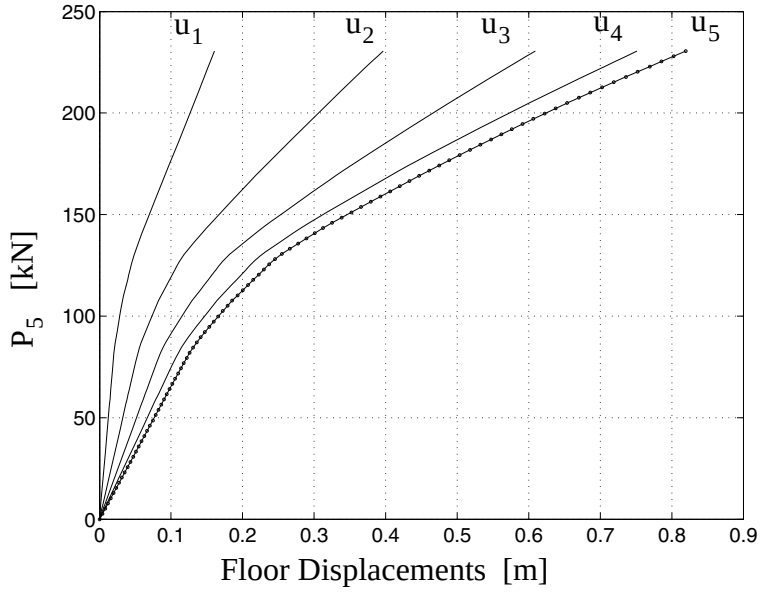

Figure 3.21 Global response of the five story building model for pushover analysis: force at the roof level versus floor horizontal displacements.

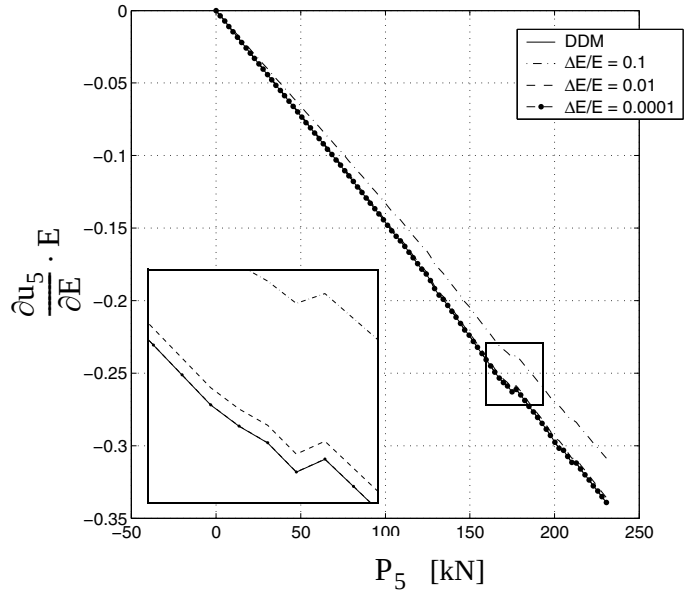

Figure 3.22 Global response sensitivities to material parameters: roof displacement sensitivity to Young's modulus, E.

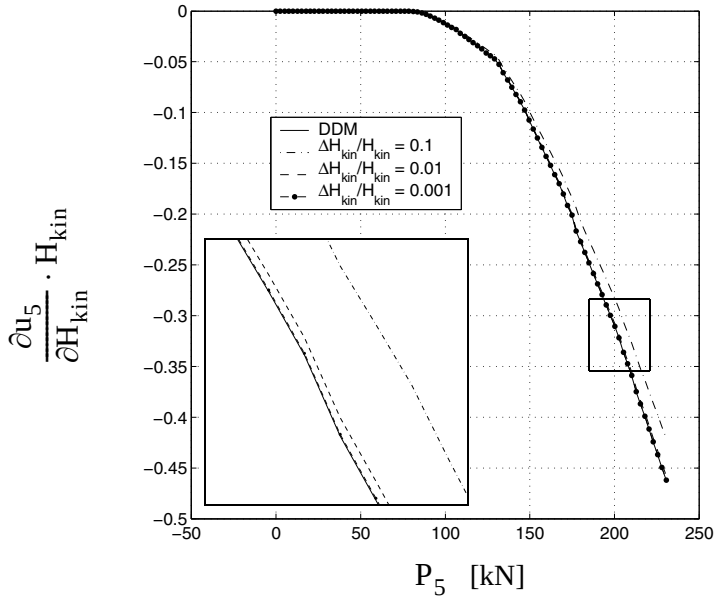

Figure 3.23 Global response sensitivities to material parameters: roof displacement sensitivity to kinematic hardening modulus, H_{kin}.

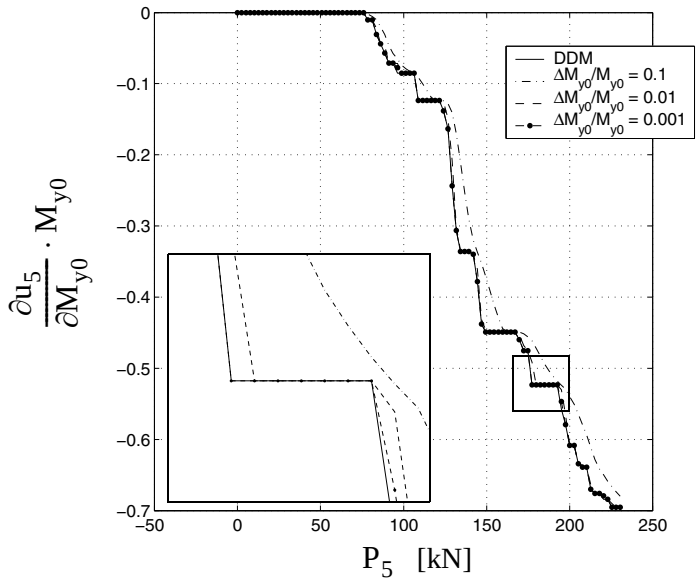

Figure 3.24 Global response sensitivities to material parameters: roof displacement sensitivity to initial yield moment, M_{y0}.

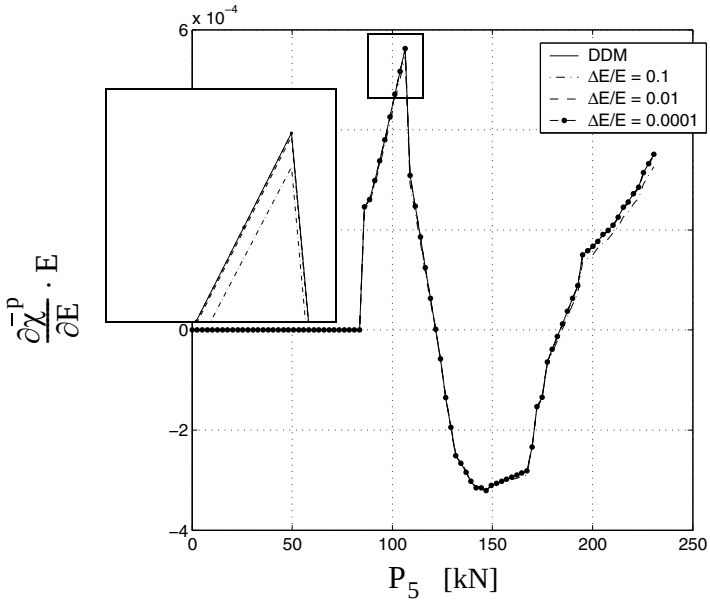

Figure 3.25 Local response sensitivities to material parameters: sensitivity of cumulative plastic curvature at section A to Young's modulus, E.

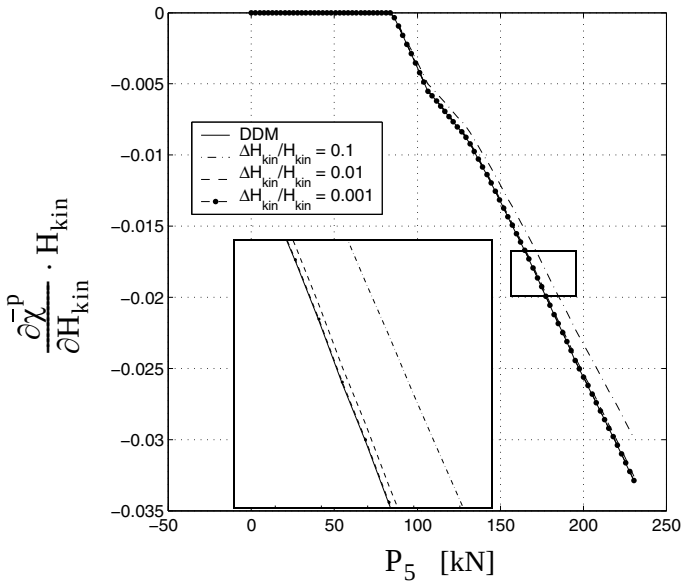

Figure 3.26 Local response sensitivities to material parameters: sensitivity of cumulative plastic curvature at section A to kinematic hardening modulus, H_{kin}.

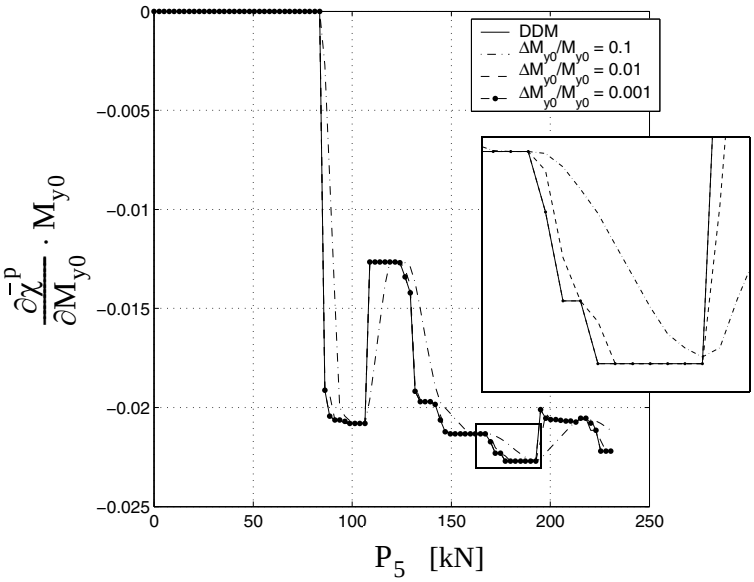

Figure 3.27 Local response sensitivities to material parameters: sensitivity of cumulative plastic curvature at section A to initial yield moment, M_{y0}.

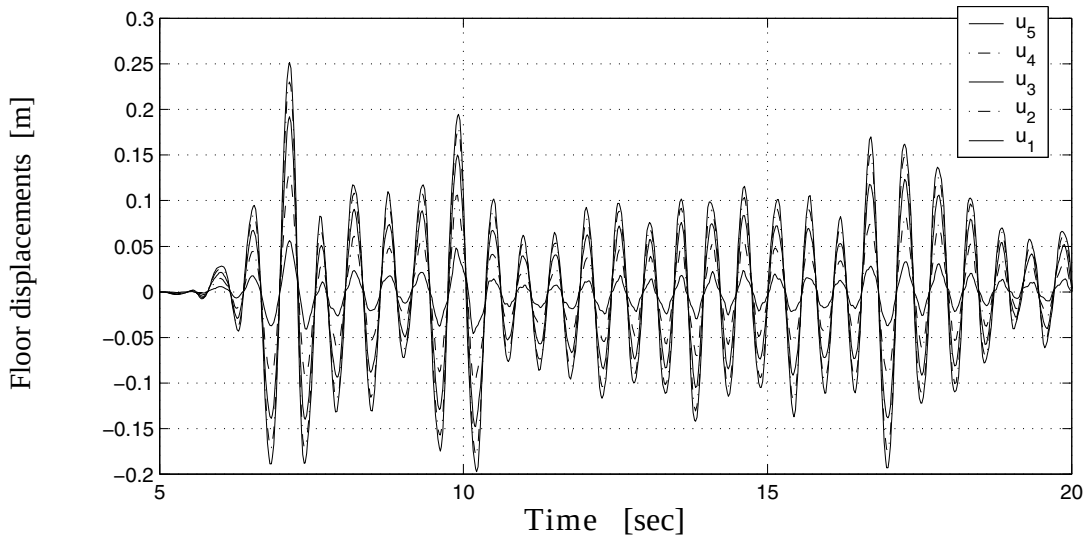

Figure 3.28 Global response of the five story building model for dynamic analysis: floor displacement histories.

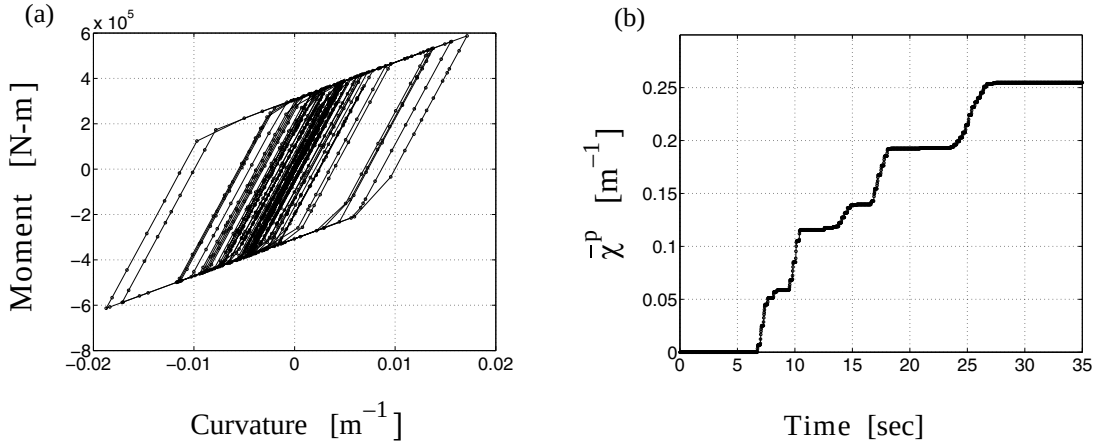

Figure 3.29 Local response of the five story building model for dynamic analysis: (a) moment-curvature and (b) cumulative plastic curvature history, at section A.

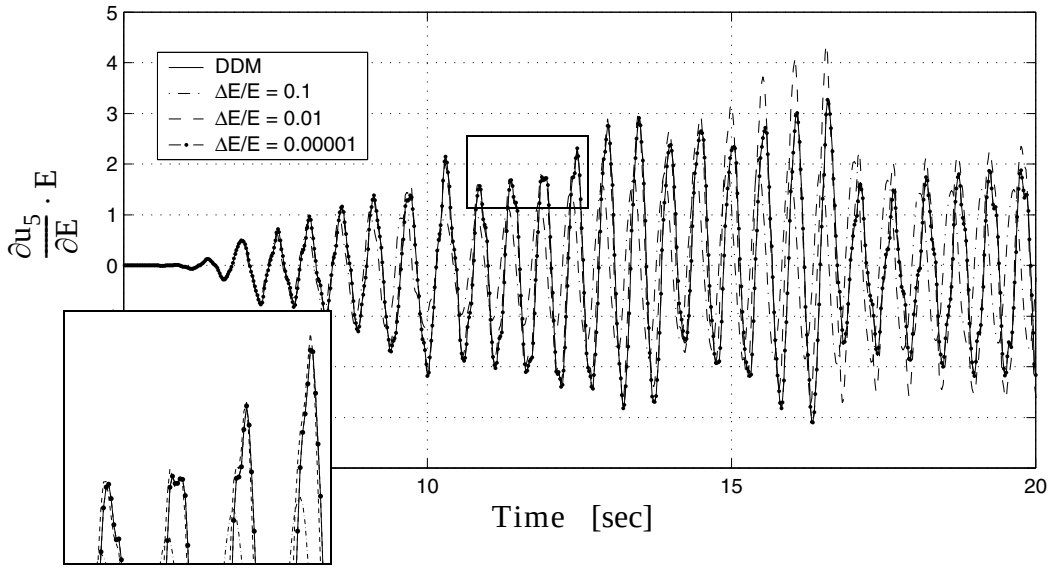

Figure 3.30 Global response sensitivities to material parameters: roof displacement sensitivity to Young's modulus, E.

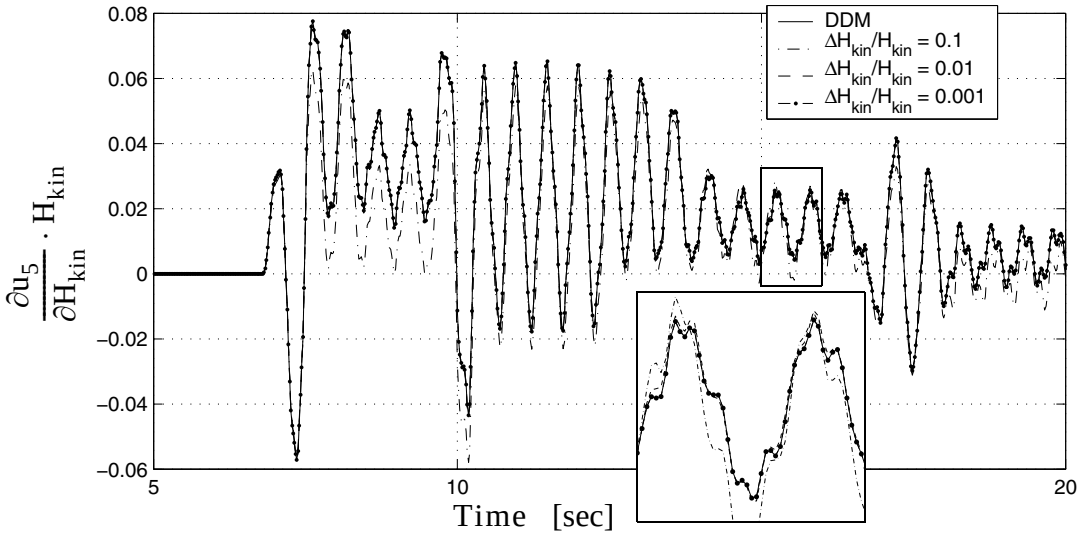

Figure 3.31 Global response sensitivities to material parameters: roof displacement sensitivity to kinematic hardening modulus, H_{kin}.

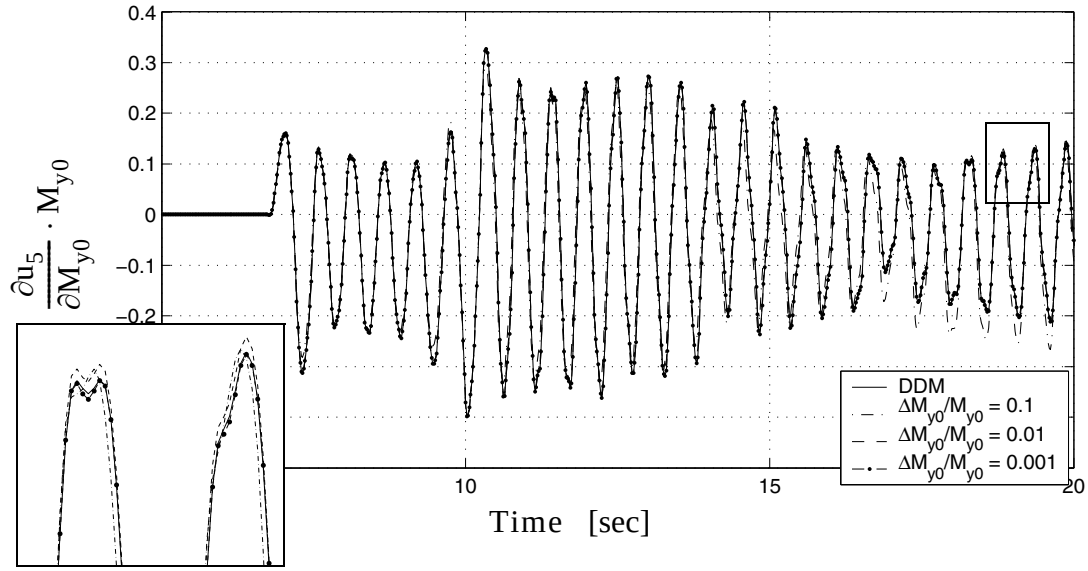

Figure 3.32 Global response sensitivities to material parameters: roof displacement sensitivity to initial yield moment, M_{y0}.

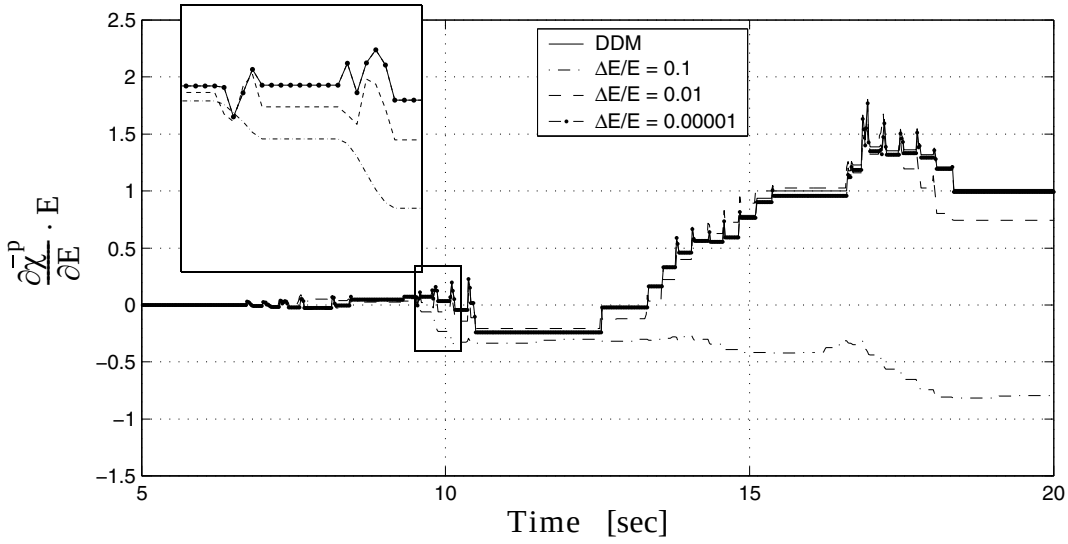

Figure 3.33 Local response sensitivities to material parameters: sensitivity of cumulative plastic curvature at section A to Young's modulus, E.

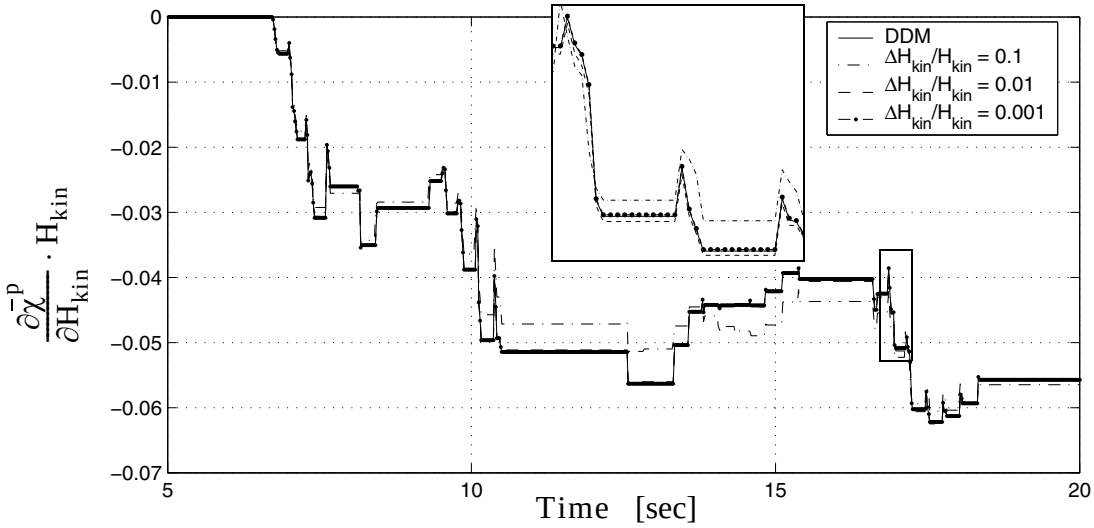

Figure 3.34 Local response sensitivities to material parameters: sensitivity of cumulative plastic curvature at section A to kinematic hardening modulus, H_{kin}.

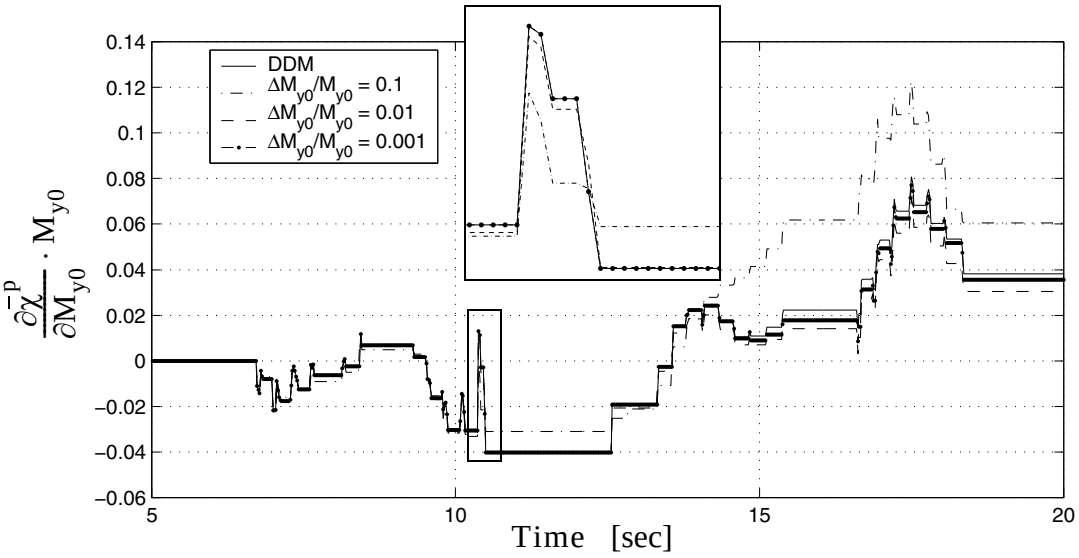

Figure 3.35 Local response sensitivities to material parameters: sensitivity of cumulative plastic curvature at section A to initial yield moment, M_{y0}.

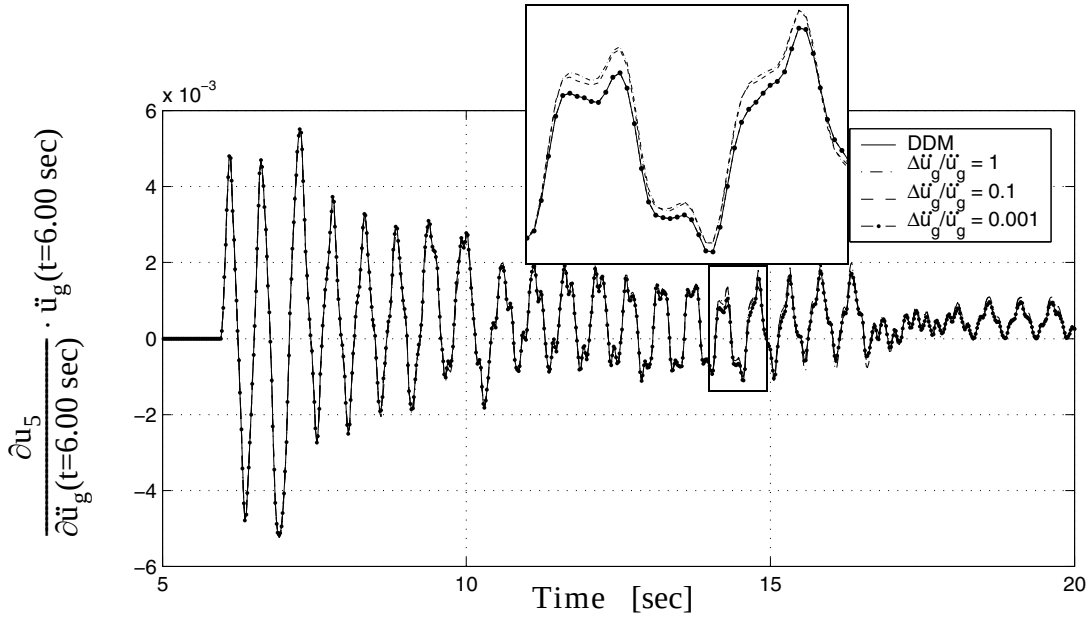

Figure 3.36 Global response sensitivities to loading parameters: roof displacement sensitivity to earthquake ground acceleration at time t = 6.00sec.

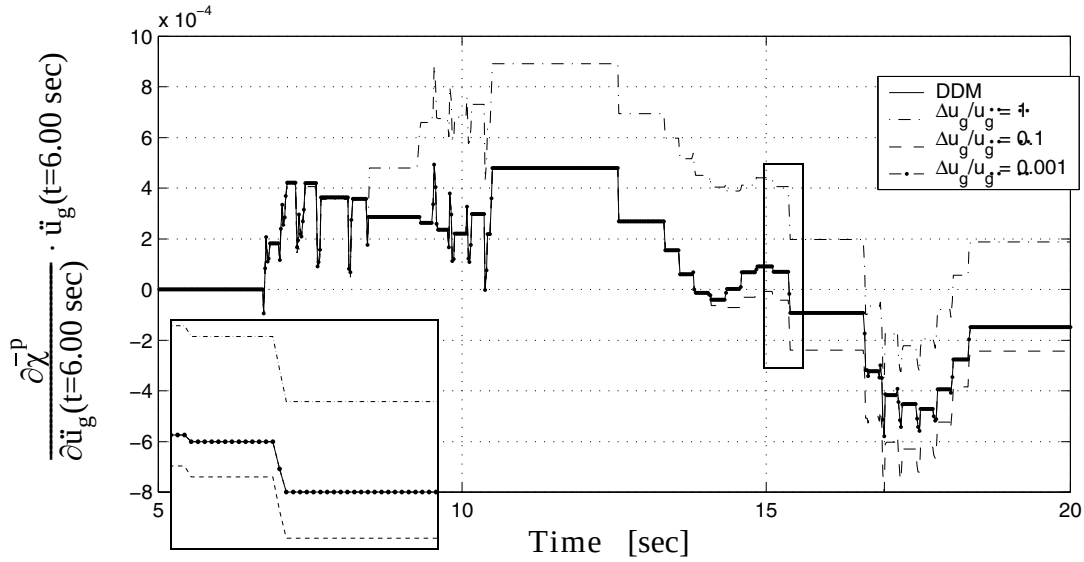

Figure 3.37 Local response sensitivities to loading parameters: sensitivity of cumulative plastic curvature at section A to earthquake ground acceleration at time t = 6.00sec.

3.6 CONCLUSIONS

The formulation of a new procedure to compute response sensitivities to material constitutive parameters and discrete loading parameters for force-based materially-nonlinear-only FE models of structural frame systems is presented. This formulation is based on the consistent differentiation of the discrete equilibrium, compatibility, and constitutive equations at the element and section (or integration point) levels. Key comparisons are made between the existing displacement-based and the newly developed force-based FE response sensitivity analysis procedures. Ample details about the implementation of the formulated approach in a general-purpose nonlinear FE analysis program (FEDEASLab)

based on the direct stiffness method are provided. The formulation is general and applies to linear and nonlinear, static and dynamic structural analysis.

Two application examples are presented, including a cantilever steel beam and a five-story one bay steel frame, both subjected to static and dynamic loading. Without loss of generality, the nonlinear inelastic material model used in the examples consists of the 1-D J_2 plasticity model, which describes the section moment-curvature constitutive law. The method developed applies to any material model that can be formulated analytically. Global and local response sensitivity results obtained analytically using the method developed are compared to their counterparts computed using forward finite difference analysis. It is found that the finite difference results approach asymptotically (for decreasing perturbation $\Delta\theta$ of the sensitivity parameter) the analytical response sensitivity results, which validates both the new formulation for force-based structural response sensitivity analysis as well as its implementation in a general-purpose nonlinear structural analysis program (FEDEASLab).

The superior force-based structural analysis methodology with the addition of the method presented here for analytical sensitivity computation offers a powerful tool for any kind of applications in which finite element response sensitivity analysis results are needed. These applications include structural reliability, structural optimization, structural identification, and finite element model updating. The extension of the work presented

here to include geometric nonlinearities will be the subject of future research by the authors.

3.7 ACKNOWLEDGEMENTS

Chapter 3, with few minor modifications, is a reprint of the material as it appears in International Journal for Numerical Methods in Engineering (2004), Conte, J.P., Barbato, M., and Spacone, E., 59(13):1781-1820 (Copyright John Wiley & Sons Limited, 2005, reproduced with permission). The dissertation author was second author of this paper. He strongly contributed to the development of the response sensitivity computation algorithm presented and to the preparation of the manuscript. He also is the author of the computer implementation of the algorithm into FEDEASLab used to produce the application examples provided in the paper.

APPENDIX A: FORCE-BASED FRAME ELEMENT FORMULATION

A.1 Notation

The algorithmic developments in this paper are based on the following notation for a 2-D frame element also shown in Figure 3.38

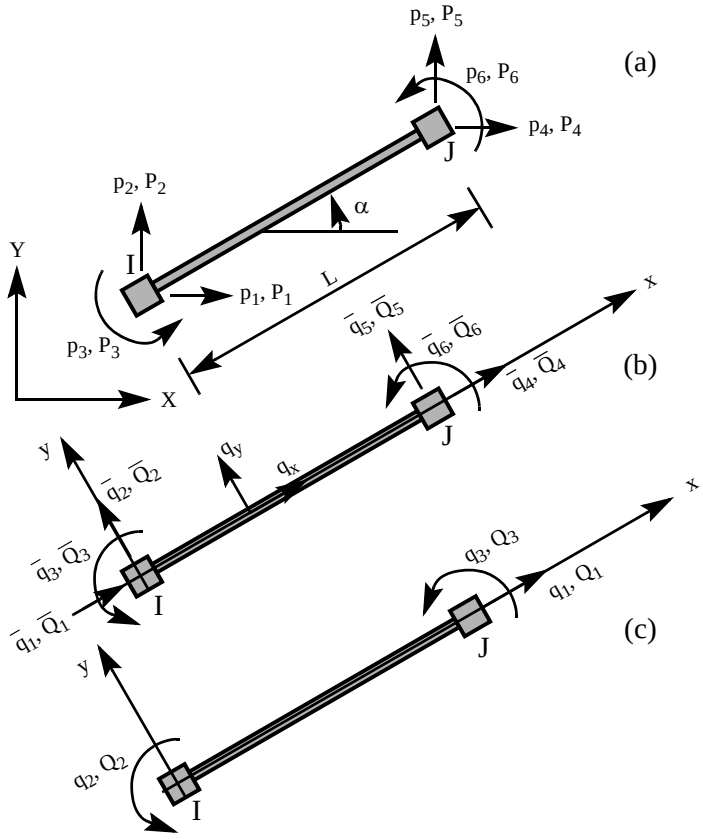

Figure 3.38 Notation used for element end forces and degrees of freedom in (a) global coordinates, (b) local element coordinates including rigid body modes, and (c) local element coordinates without rigid body modes (basic system coordinates).

u: structure nodal displacement vector in global coordinates;

R: structure resisting force vector in global coordinates;

Element nodal displacements in global coordinates: $\mathbf{p}^{(e)} = \left[p_1 \; p_2 \; p_3 \; p_4 \; p_5 \; p_6 \right]^T$

Element nodal forces in global coordinates: $\mathbf{P}^{(e)} = \left[P_1 \; P_2 \; P_3 \; P_4 \; P_5 \; P_6 \right]^T$

$$\mathbf{p}^{(e)} = \mathbf{A}_b^{(e)} \cdot \mathbf{u}; \quad \mathbf{R} = \sum_{e=1}^{N_{el}} \left\{ (\mathbf{A}_b^{(e)})^T \cdot \mathbf{P}^{(e)} \right\}$$

$\mathbf{A}_b^{(e)}$: "Boolean displacement address" matrix (displacement extracting operator).

$(\mathbf{A}_b^{(e)})^T$: "Boolean force address" matrix (force assembling operator).

Element nodal displacements in local coordinates (with rigid body modes):

$$\bar{\mathbf{q}}^{(e)} = \left[\bar{q}_1 \; \bar{q}_2 \; \bar{q}_3 \; \bar{q}_4 \; \bar{q}_5 \; \bar{q}_6 \right]^T$$

Element nodal forces in local coordinates: $\bar{\mathbf{Q}}^{(e)} = \left[\bar{Q}_1 \; \bar{Q}_2 \; \bar{Q}_3 \; \bar{Q}_4 \; \bar{Q}_5 \; \bar{Q}_6 \right]^T$

$$\bar{\mathbf{q}}^{(e)} = \mathbf{\Gamma}_{ROT}^{(e)} \cdot \mathbf{\Gamma}_{REZ}^{(e)} \cdot \mathbf{p}^{(e)}; \quad \mathbf{P}^{(e)} = \mathbf{\Gamma}_{REZ}^{(e)T} \cdot \mathbf{\Gamma}_{ROT}^{(e)T} \cdot \bar{\mathbf{Q}}^{(e)};$$

$$\mathbf{\Gamma}_{ROT}^{(e)} = \begin{bmatrix} \mathbf{R}^{(e)} & \mathbf{0} \\ \mathbf{0} & \mathbf{R}^{(e)} \end{bmatrix}; \quad \mathbf{R}^{(e)} = \begin{bmatrix} \cos\alpha & \sin\alpha & 0 \\ -\sin\alpha & \cos\alpha & 0 \\ 0 & 0 & 1 \end{bmatrix};$$

$\mathbf{\Gamma}_{REZ}^{(e)}$: rigid-end-zone transformation matrix;

$\mathbf{\Gamma}_{ROT}^{(e)}$: global-local rotation matrix;

Element deformations in basic system: $\mathbf{q}^{(e)} = \left[q_1\ q_2\ q_3\right]^T = \left[\delta\ \theta_1\ \theta_2\right]^T$

where δ represents the overall axial deformation of the member, while θ_1 and θ_2 denote the element end rotations relative to the chord.

Element end forces in basic system: $\mathbf{Q}^{(e)} = \left[Q_1\ Q_2\ Q_3\right]^T = \left[N\ M_1\ M_2\right]^T$

where N represents the element axial force (constant in the absence of element distributed axial loads), and M_1 and M_2 denote the element end moments.

$$\mathbf{q}^{(e)} = \mathbf{\Gamma}_{RBM}^{(e)} \cdot \bar{\mathbf{q}}^{(e)}; \quad \bar{\mathbf{Q}}^{(e)} = \mathbf{\Gamma}_{RBM}^{(e)T} \cdot \mathbf{Q}^{(e)}; \quad \mathbf{\Gamma}_{RBM}^{(e)} = \begin{bmatrix} -1 & 0 & 0 & 1 & 0 & 0 \\ 0 & \frac{1}{L} & 1 & 0 & -\frac{1}{L} & 0 \\ 0 & \frac{1}{L} & 0 & 0 & -\frac{1}{L} & 1 \end{bmatrix}$$

$\mathbf{\Gamma}_{RBM}^{(e)}$: transformation matrix that removes the rigid body modes

A.2 Newton-Raphson incremental-iterative procedure

This section summarizes the structure state determination procedure performed at the end of the (i+1)-th global Newton-Raphson iteration (at the structure level) for the (n+1)-th load step, according to the force-based frame element methodology (Spacone et al. 1996a; Neuenhofer and Filippou 1997). This procedure is needed in formulating the response sensitivity algorithm, since the latter is developed through exact differentiation of the space and the time discrete equations for the finite element response. The structure

state determination procedure is obtained through direct stiffness assembly of the results of the element state determination procedure which is summarized below. The element state determination procedure is iterative in nature and the superscript j is used to denote the iteration number for the element state determination. The superscript i is used to denote the iteration number of the global Newton-Raphson procedure at the structure level.

A.2.1 Element state determination:

(1) Initialization:

$\mathbf{k}_T^{j=0} = \mathbf{k}_T^i$: element consistent tangent stiffness matrix; (3.50)

$\mathbf{Q}^{j=0} = \mathbf{Q}^i$: element end forces in the basic system; (3.51)

$\mathbf{D}^{j=0}(x) = \mathbf{D}^i(x)$: section forces; (3.52)

$\mathbf{d}^{j=0}(x) = \mathbf{d}^i(x)$: section deformations; (3.53)

$\mathbf{r}^{j=0}(x) = \mathbf{0}$: residual section deformation vector; (3.54)

$\mathbf{f}_s^{j=0}(x) = \mathbf{f}_s^i(x)$: section (consistent) tangent flexibility matrix. (3.55)

(2) Iterations (j = 1, 2, 3, ...):

Given the last incremental structure nodal displacement vector for the (n+1)-th load step, $\delta\mathbf{u}_{n+1}^{i+1}$, we obtain the last incremental basic element deformation vector, $\delta\mathbf{q}_{n+1}^{i+1}$, as[1]

$$\delta\mathbf{q}^{j=1} = (\boldsymbol{\Gamma}^{(e)}_{RBM} \cdot \boldsymbol{\Gamma}^{(e)}_{ROT} \cdot \boldsymbol{\Gamma}^{(e)}_{REZ}) \cdot \mathbf{A}^{(e)}_{b} \cdot \delta\mathbf{u}^{i+1} = \boldsymbol{\Gamma}^{(e)} \cdot \mathbf{A}^{(e)}_{b} \cdot \delta\mathbf{u}^{i+1} \tag{3.56}$$

We then compute:

$\delta\mathbf{Q}^{j} = \mathbf{k}_{T}^{j-1}\delta\mathbf{q}^{j}$: increment of element end forces in the basic system; (3.57)

$\mathbf{Q}^{j} = \mathbf{Q}^{j-1} + \delta\mathbf{Q}^{j}$: updated element end forces in the basic system; (3.58)

$\mathbf{D}^{j}(x) = \mathbf{b}(x)\mathbf{Q}^{j} + \mathbf{D}_{p}(x)$: updated section forces at section x (3.59)

in which $\mathbf{b}(x)$ is the matrix of internal force interpolation functions (satisfying equilibrium locally) and $\mathbf{D}_{p}(x)$ is the vector of the section forces due to external forces applied along the statically determined basic system;

$\delta\mathbf{D}^{j}(x) = \mathbf{D}^{j}(x) - \mathbf{D}^{j-1}(x)$: section force increments; (3.60)

$\delta\mathbf{d}^{j}(x) = \mathbf{f}_{s}^{j-1}(x) \cdot \delta\mathbf{D}^{j}(x) + \mathbf{r}^{j-1}(x)$: section deformation increments; (3.61)

$\mathbf{d}^{j}(x) = \mathbf{d}^{j-1}(x) + \delta\mathbf{d}^{j}(x)$: updated total section deformations; (3.62)

(2.1) Section state determination:

$\mathbf{D}_{R}^{j}(x) = \mathbf{D}_{R}[\mathbf{d}^{j}(x)]$: section resisting forces; (3.63)

$\mathbf{f}_{s}^{j}(x) = \mathbf{f}_{s}[\mathbf{d}^{j}(x)]$: updated section tangent flexibility matrix; (3.64)

$\mathbf{r}^{j}(x) = \mathbf{f}_{s}^{j}(x) \cdot [\mathbf{D}^{j}(x) - \mathbf{D}_{R}^{j}(x)]$: updated residual section deformations; (3.65)

---

1. To simplify the notation in this section, we drop both the subscript $(\ldots)_{n+1}$ representing the time/load step and the superscript $(\ldots)^{i+1}$ representing the iteration number of the global (structure level) Newton-Raphson iteration cycle.

$$\mathbf{f}_T^j = \int_0^L \mathbf{b}^T(x) \cdot \mathbf{f}_s^j(x) \cdot \mathbf{b}(x) \cdot dx \; : \text{ updated element tangent flexibility matrix;} \quad (3.66)$$

$$\mathbf{k}_T^j = [\mathbf{f}_T^j]^{-1} \; : \qquad \text{updated element tangent stiffness matrix;} \quad (3.67)$$

$$\mathbf{s}^j = \int_0^L \mathbf{b}^T(x) \cdot \mathbf{r}^j(x) \cdot dx \; : \quad \text{element residual deformations.} \quad (3.68)$$

where the section resisting forces $\mathbf{D}_R^j(x)$ and section tangent flexibility matrix $\mathbf{f}_s^j(x)$ are evaluated through the section force-deformation relation.

(2.2) Checking convergence:

If $\dfrac{(\mathbf{s}^j)^T \cdot \mathbf{k}_T^j \cdot \mathbf{s}^j}{(\delta\mathbf{q}^{j=1})^T \cdot \mathbf{k}_T^{j=0} \cdot \delta\mathbf{q}^{j=1}} \leq$ tolerance , the element iterative state determination procedure is converged: update section and element variables and build the consistent tangent stiffness matrix and the internal resisting force vector of the structure through direct stiffness assembly. Otherwise (if not converged), perform another iteration (j+1) of element state determination using:

$$\delta\mathbf{q}^{j+1} = -\mathbf{s}^j \quad (3.69)$$

go to (3.57) with $j = j + 1$ and repeat (3.57) through (3.69) until convergence is achieved.

(3) Updating:

$$\mathbf{k}_T^{i+1} = \mathbf{k}_{T,\,conv}^j \; : \qquad \text{updated element consistent tangent stiffness matrix;} \quad (3.70)$$

$$\mathbf{Q}^{i+1} = \mathbf{Q}_{conv}^j \; : \qquad \text{updated element end forces in the basic system;} \quad (3.71)$$

$$\mathbf{D}^{i+1}(x) = \mathbf{D}^{j}_{conv}(x) : \quad \text{updated section forces;} \tag{3.72}$$

$$\mathbf{d}^{i+1}(x) = \mathbf{d}^{j}_{conv}(x) : \quad \text{updated section deformations;} \tag{3.73}$$

$$\mathbf{f}_{s}^{i+1}(x) = \mathbf{f}^{j}_{s,\,conv}(x) : \quad \text{updated section consistent tangent flexibility matrix} \tag{3.74}$$

(4) Direct stiffness assembly:

$$\mathbf{R}(\mathbf{u}^{i+1}_{n+1}) = \sum_{e=1}^{N_{el}} ((\mathbf{A}^{(e)}_{b})^{T} \cdot \mathbf{\Gamma}^{(e)T}_{REZ} \cdot \mathbf{\Gamma}^{(e)T}_{ROT} \cdot \mathbf{\Gamma}^{(e)T}_{RBM} \cdot \mathbf{Q}^{i+1}_{n+1}) : \tag{3.75}$$

current structure resisting force vector;

$$(\mathbf{K}^{stat}_{T})^{i+1}_{n+1} = \sum_{e=1}^{N_{el}} ((\mathbf{A}^{(e)}_{b})^{T} \cdot \mathbf{\Gamma}^{(e)T} \cdot [\mathbf{f}^{i+1}_{T,\,n+1}]^{-1} \cdot \mathbf{\Gamma}^{(e)} \cdot \mathbf{A}^{(e)}_{b}) : \tag{3.76}$$

current structure consistent tangent stiffness matrix, where

$$\mathbf{\Gamma}^{(e)} = \mathbf{\Gamma}^{(e)}_{RBM} \cdot \mathbf{\Gamma}^{(e)}_{ROT} \cdot \mathbf{\Gamma}^{(e)}_{REZ} \tag{3.77}$$

As already mentioned before, a non-iterative alternative of the above (iterative) element state determination procedure has been proposed by Neuenhofer and Filippou (1997), which reduces the computational cost of nonlinear finite element analyses using force-based frame elements. The algorithm developed below for finite element response sensitivity analysis using force-based frame models applies to both the iterative and non-iterative element state determination procedures.

APPENDIX B: MATERIAL RESPONSE INTEGRATION SCHEME FOR 1-D J_2 PLASTICITY MODEL

The 1-D J_2 rate constitutive equations must be integrated numerically to obtain the stress history for a given strain history. Using the implicit backward Euler scheme to time-discretize the rate equations over the time step $[t_n, t_{n+1}]$, with step size $\Delta t = t_{n+1} - t_n$, we obtain the following discretized material constitutive equations:

(1) Additive split of the total strain:

$$\varepsilon_{n+1} = \varepsilon^e_{n+1} + \varepsilon^p_{n+1} \tag{3.78}$$

(2) Elastic stress-strain relation:

$$\sigma_{n+1} = E \cdot \varepsilon^e_{n+1} \tag{3.79}$$

(3) Flow rule:

$$\varepsilon^p_{n+1} = \varepsilon^p_n + (\Delta\lambda)_{n+1} \cdot \operatorname{sgn}(\sigma_{n+1} - \alpha_{n+1}) \tag{3.80}$$

where $(\Delta\lambda)_{n+1} = \int_{t_n}^{t_{n+1}} \dot{\lambda} \cdot dt \cong \dot{\lambda}_{n+1} \cdot \Delta t$ is the discrete consistency parameter.

(4) Hardening laws (linear kinematic and linear isotropic hardening):

$$\begin{aligned} \alpha_{n+1} &= \alpha_n + H_{kin} \cdot (\Delta\lambda)_{n+1} \cdot \operatorname{sgn}(\sigma_{n+1} - \alpha_{n+1}) \\ \bar{\varepsilon}^p_{n+1} &= \bar{\varepsilon}^p_n + (\Delta\lambda)_{n+1} \\ \sigma_{y,\,n+1} &= \sigma_{y,\,n} + H_{iso} \cdot (\Delta\lambda)_{n+1} \end{aligned} \tag{3.81}$$

(5) Kuhn-Tucker loading/unloading and plastic consistency conditions:

$$(\Delta\lambda)_{n+1} \geq 0, \quad f(\sigma_{n+1}, \alpha_{n+1}, \bar{\varepsilon}^{p}_{n+1}) \leq 0 \quad \text{and}$$

$$(\Delta\lambda)_{n+1} \cdot f(\sigma_{n+1}, \alpha_{n+1}, \bar{\varepsilon}^{p}_{n+1}) = 0 \tag{3.82}$$

As a particular 1-D application of the very effective elastic-plastic operator split method with a concept of return map which is based on the notion of closest-point-projection in the stress space (Simo and Hughes 1998), the above discretized constitutive equations are solved for stress component σ_{n+1} in two steps, namely (1) a trial elastic step and (2) a plastic corrector step. In the trial elastic step, the plastic response is frozen and, consequently, all of the current total strain increment ($\Delta\varepsilon_{n+1} = \varepsilon_{n+1} - \varepsilon_n$) is assumed to be elastic. If the stress computed under this assumption satisfies the yield condition, then the current step is elastic and the integration of the material constitutive law over time step [t_n, t_{n+1}] is complete. Otherwise, the above discrete constitutive equations are solved for the discrete consistency parameter $(\Delta\lambda)_{n+1}$ and finally for σ_{n+1} (by the return map algorithm). The procedure is summarized below.

Trial Elastic State:

$$\begin{aligned} (\Delta\lambda)_{n+1}^{Trial} &= 0 \\ (\varepsilon_{n+1}^{p})^{Trial} &= \varepsilon_{n}^{p} \\ \alpha_{n+1}^{Trial} &= \alpha_{n} \\ (\bar{\varepsilon}_{n+1}^{p})^{Trial} &= \bar{\varepsilon}_{n}^{p} \\ \sigma_{n+1}^{Trial} &= E(\varepsilon_{n+1} - \varepsilon_{n}^{p}) \\ \sigma_{y,\,n+1}^{Trial} &= \sigma_{y,\,n} \end{aligned} \tag{3.83}$$

IF $\{ f(\sigma_{n+1}^{Trial}, \alpha_{n+1}^{Trial}, (\bar{\varepsilon}_{n+1}^{p})^{Trial}) \leq 0 \}$ THEN

Update all the history/state variables at time t_{n+1} by assigning the corresponding trial values to them, i.e., $(\ldots)_{n+1} = (\ldots)_{n+1}^{Trial}$.

Compute the consistent material tangent stiffness:

$$E_{T,\,n+1} = E \tag{3.84}$$

and EXIT.

ELSE

Plastic Corrector Step Using the Return Map Algorithm:

The plastic corrector step is based upon satisfying the consistency condition in discrete form:

$$f_{n+1} = \left|\sigma_{n+1} - \alpha_{n+1}\right| - \sigma_{y,\,n+1} = 0 \tag{3.85}$$

where

$$\begin{aligned}\sigma_{n+1} &= E \cdot (\varepsilon_{n+1} - \varepsilon^{p}_{n+1}) \\ &= E \cdot \{\ \varepsilon_{n+1} - \varepsilon^{p}_{n} - [(\Delta\lambda)_{n+1} \cdot \operatorname{sgn}(\sigma_{n+1} - \alpha_{n+1})]\} \\ &= \sigma^{Trial}_{n+1} - E \cdot (\Delta\lambda)_{n+1} \cdot \operatorname{sgn}(\sigma_{n+1} - \alpha_{n+1})\end{aligned} \tag{3.86}$$

$$\begin{aligned}\alpha_{n+1} &= \alpha_{n} + H_{kin} \cdot (\Delta\lambda)_{n+1} \cdot \operatorname{sgn}(\sigma_{n+1} - \alpha_{n+1}) \\ &= \alpha^{Trial}_{n+1} + H_{kin} \cdot (\Delta\lambda)_{n+1} \cdot \operatorname{sgn}(\sigma_{n+1} - \alpha_{n+1})\end{aligned} \tag{3.87}$$

$$\sigma_{y,\,n+1} = \sigma_{y,\,n} + H_{iso} \cdot (\Delta\lambda)_{n+1} \tag{3.88}$$

From (3.86) and (3.87), it can be shown that

$$\operatorname{sgn}(\sigma_{n+1} - \alpha_{n+1}) = \operatorname{sgn}(\sigma^{Trial}_{n+1} - \alpha^{Trial}_{n+1}) \equiv n_{n+1} \tag{3.89}$$

and

$$\left|\sigma_{n+1} - \alpha_{n+1}\right| = \left|\sigma^{Trial}_{n+1} - \alpha^{Trial}_{n+1}\right| - (E + H_{kin}) \cdot (\Delta\lambda)_{n+1} \tag{3.90}$$

Substituting (3.88) and (3.90) in Equation (3.85), the discrete consistency condition can be rewritten as

$$\left|\sigma^{Trial}_{n+1} - \alpha^{Trial}_{n+1}\right| - (E + H_{kin}) \cdot (\Delta\lambda)_{n+1} - \sigma_{y,\,n} - H_{iso} \cdot (\Delta\lambda)_{n+1} = 0 \tag{3.91}$$

The discrete consistency parameter $(\Delta\lambda)_{n+1}$ can be obtained from the above equation as

$$(\Delta\lambda)_{n+1} = \frac{\left|\sigma^{Trial}_{n+1} - \alpha^{Trial}_{n+1}\right| - \sigma_{y,\,n}}{E + H_{iso} + H_{kin}} \tag{3.92}$$

It can be shown that the consistent tangent material stiffness is given by

$$E_{T,\,n+1} = E \cdot \frac{H_{iso} + H_{kin}}{E + H_{iso} + H_{kin}} \tag{3.93}$$

Given ε_{n+1} and once $(\Delta\lambda)_{n+1}$ is known, the material history/state variables at time t_{n+1} (i.e., ε^{p}_{n+1}, σ_{n+1}, α_{n+1}, $\bar{\varepsilon}^{p}_{n+1}$, $\sigma_{y,\,n+1}$) are obtained from (3.80), (3.81), and (3.86). The above discrete constitutive integration scheme for 1-D J_2 plasticity is represented graphically in Figure 3.39 for an elasto-plastic step.

Note that the terms σ_{n+1} and ε_{n+1} in the above equations correspond to the terms $\sigma^{(2)}_{n+1}(x)$ and $\chi_{n+1}(x)$ in (3.28), (3.32) and (3.34), while the term $E^{(2)}_{T,\,n+1}(x)$ in Equation (3.30) corresponds to $E_{T,\,n+1}$, given by Equation (3.84) or Equation (3.93) depending on the material state (i.e., elastic or plastic, respectively).

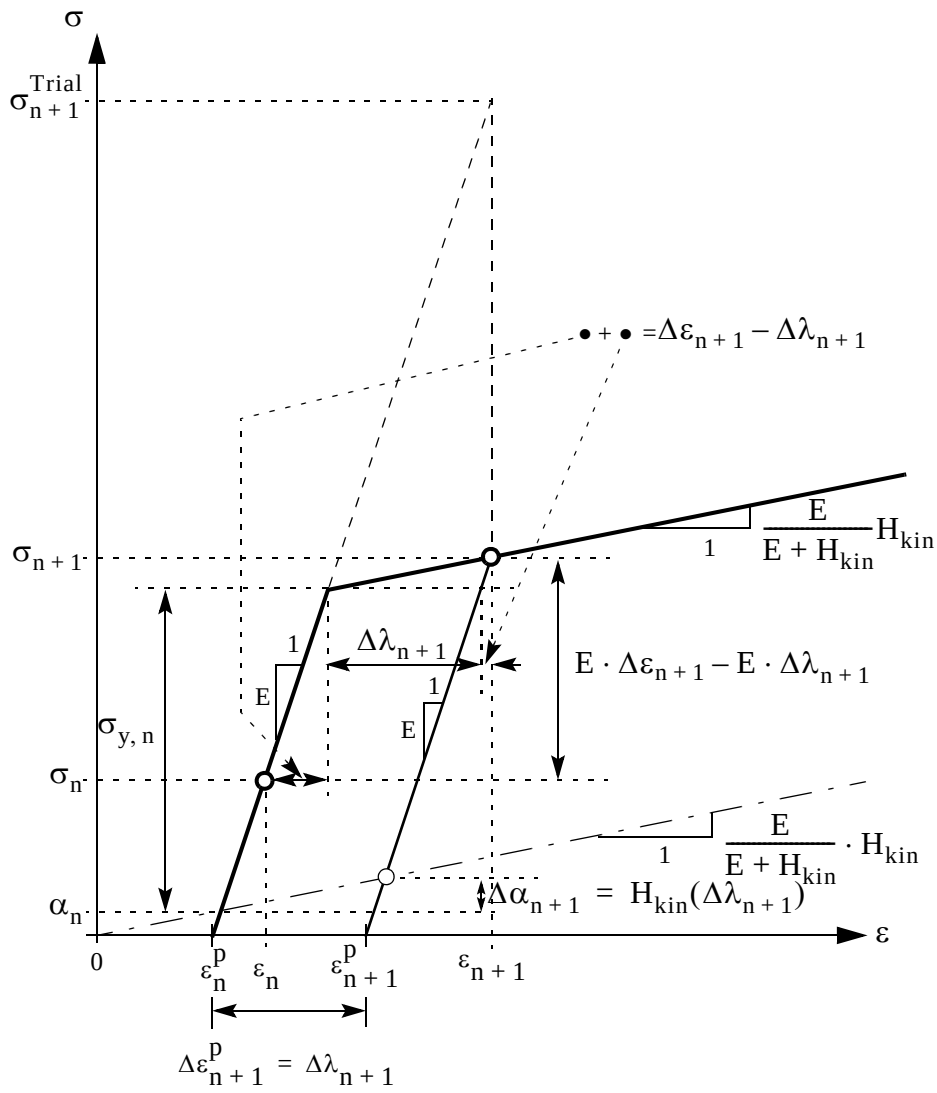

Figure 3.39 Return map algorithm for 1-D J_2 (von Mises) plasticity model with pure kinematic hardening ($H_{iso} = 0$).

REFERENCES

Arora J.S., Cardoso J.B. (1989) “A design sensitivity analysis principle and its implementation into ADINA.” *Computers and Structures*, 32:691-705.

Choi K.K., Santos J.L.T. (1987) “Design sensitivity analysis of nonlinear structural systems. Part I: Theory.” *International Journal for Numerical Methods in Engineering*, 24:2039-2055.

Chopra A.K. (2001) *Dynamics of Structures: Theory and Applications to Earthquake Engineering.* Second Edition, Prentice Hall.

Conte J.P. (2001) “Finite element response sensitivity analysis in earthquake engineering.” *Earthquake Engineering Frontiers in the New Millennium.* Spencer & Hu, Swets & Zeitlinger, 395-401, 2001.

Conte J.P., Vijalapura P.K., Meghella M. (2003) “Consistent finite element response sensitivity analysis”. *Journal of Engineering Mechanics* (ASCE), 129(12):1380-1393.

De Souza R.M. (2000) “Force-based finite element for large displacement inelastic analysis of frames.” *Ph.D. Dissertation*. Department of Civil and Environmental Engineering, University of California, Berkeley, CA.

Ditlevsen O., Madsen H.O. (1996) *Structural Reliability Methods.* Wiley.

Filippou F.C. (2002) “FEDEASLab: a Matlab toolbox for linear and nonlinear structural analysis.” *Private communication.*

Franchin P. (2004) “Reliability of uncertain inelastic structures under earthquake excitation.” *Journal of Engineering Mechanics* (ASCE), 130(2):180-191.

Kleiber M., Antunez H., Hien T.D., Kowalczyk P. (1997) *Parameter Sensitivity in Nonlinear Mechanics: Theory and Finite Element Computations.* Wiley.

Neuenhofer A., Filippou F.C. (1997) “Evaluation of nonlinear frame finite-element models. *Journal of Structural Engineering* (ASCE), 123:958-966.

Neuenhofer A., Filippou F.C. (1998) “Geometrically nonlinear flexibility-based frame finite element.” *Journal of Structural Engineering* (ASCE), 124(6):704-711.

Simo J.C., Hughes T.J.R. (1998) *Computational Inelasticity.* Springer-Verlag.

Sivaselvan M.V. (2002) “Collapse analysis: large inelastic deformations analysis of planar frames.” *Journal of Structural Engineering* (ASCE), 128(12):1575-1583.

Spacone E., Ciampi V., Filippou F.C. (1996a) “Mixed formulation of nonlinear beam finite element.” *Computers and Structures*, 58:71-83.

Spacone E., Filippou F.C., Taucer F.F. (1996b) “Fibre beam-column element for nonlinear analysis of R/C frames. Part I: Formulation.” *Earthquake Engineering and Structural Dynamics*, 25:711-725.

Spacone E., Filippou F.C., Taucer F.F. (1996c) “Fibre beam-column element for nonlinear analysis of R/C frames. Part II: Application.” *Earthquake Engineering and Structural Dynamics*, 25:727-742.

The MathWorks (1997) “Matlab - High performance numeric computation and visualization software.” *User’s Guide*. Natick, MA.

Tsay J.J., Arora J.S. (1990) “Nonlinear structural design sensitivity analysis for path dependent problems. Part I: General theory.” *Computer Methods in Applied Mechanics and Engineering*, 81:183-208.

Tsay J.J., Cardoso J.B., Arora J.S. (1990) “Nonlinear structural design sensitivity analysis for path dependent problems. Part II: Analytical examples.” *Computer Methods in Applied Mechanics and Engineering*, 81:209-228.

Zhang Y., Der Kiureghian A. (1993) “Dynamic response sensitivity of inelastic structures.” *Computer Methods in Applied Mechanics and Engineering*, 108:23-36.

CHAPTER 4

DDM-BASED FINITE ELEMENT RESPONSE SENSITIVITY ANALYSIS FOR STEEL-CONCRETE COMPOSITE FRAME STRUCTURES

4.1 INTRODUCTION

The last decade has seen a growing interest in finite element modeling and analysis of steel-concrete composite structures, with applications to seismic resistant frames and bridges (Spacone and El-Tawil 2004). The behavior of composite beams, made of two components connected through shear connectors to form an interacting unit, is significantly influenced by the type of connection between the steel beam and the concrete slab. Flexible shear connectors allow development of partial composite action (Oehlers and Bradford 2000) and, for accurate analytical response predictions, structural models of composite structures must account for the interlayer slip between the steel and concrete components. Thus, a composite beam finite element able to capture the interface slip is an essential tool for model-based response simulation of steel-concrete composite structures. The three-dimensional model for composite beams with deformable shear connection under general state of stress developed by Dall'Asta (2001) simplifies to the model introduced by Newmark et al. (1951) if only the in-plane bending behavior is considered. In the Newmark's model, the geometrically linear Euler-Bernoulli beam theory (i.e., small dis-

placements, rotations and strains) is used to model the two parts of the composite beam; the effects of the deformable shear connection are accounted for by using an interface model with distributed bond, while the contact between the steel and concrete components is enforced (Fig. 4.1). The interface slip is small since it is given by the difference in longitudinal displacements of the steel and concrete fibers at the steel-concrete interface.

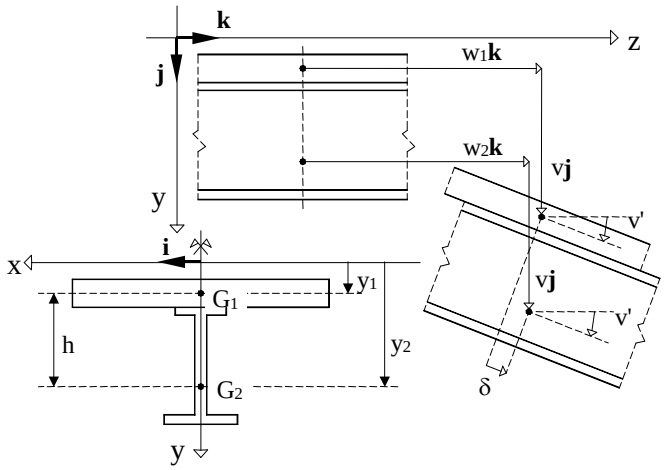

Figure 4.1 Kinematics of 2-D composite beam model

Compared to common monolithic beams, composite beams with deformable shear connection present additional difficulties. Even in very simple structural systems (e.g., simply supported beams), complex distributions of the interface slip and force can develop; furthermore these distributions can be very sensitive to the shear connection properties. Different finite elements representing composite beams with deformable shear connection have been proposed in the literature (Dall'Asta and Zona 2004a, Spacone and El-Tawil 2004). Despite the difficulties encountered in the nonlinear range of structural behavior, locking-free displacement-based elements (such as the one used in this study)

produce accurate global and local results provided that the structure is properly discretized (Dall'Asta and Zona 2002, 2003, 2004a, 2004b, 2004c). Locking-free displacement-based elements were used successfully for accurate analysis of steel-concrete composite beam structures even in the case of very high gradients of the interface slip due for example to horizontal concentrated forces produced by external prestressing cables (Dall'Asta and Zona 2005).

Beyond research activities in model-based simulation of structures, recent years have seen a growing interest in the analysis of structural response sensitivity to various geometric, mechanical, and material properties defining the structure, and to loading parameters. Indeed, finite element response sensitivities represent an essential ingredient for gradient-based optimization methods needed in various sub-fields of structural engineering such as structural optimization, structural reliability analysis, structural identification, and finite element model updating (Ditlevsen 1996; Kleiber et al. 1997). In addition, finite element response sensitivities are invaluable for gaining deeper insight into the effect and relative importance of system and loading parameters in regards to structural response behavior.

This study focuses on materially-nonlinear-only static response sensitivity analysis using displacement-based, locking-free finite elements for composite beams with deformable shear connection (Dall'Asta and Zona 2002). Realistic uniaxial cyclic constitutive laws are adopted for the steel and concrete materials of the beam and for the shear connection. The monotonic and cyclic responses of these material and resulting finite element models are validated through comparison with experimental test results available in the

literature (Ansourian 1981, Bursi and Gramola 2000). The finite element response sensitivity analysis is performed following the Direct Differentiation Method (DDM) and validated by means of Forward Finite Difference (FFD) analysis (Conte 2001, Conte et al. 2003) in the context of two realistic steel-concrete testbed structures considered in this study. The first benchmark structure consists of a non-symmetric two-span continuous beam subjected to a monotonically increasing concentrated force, while the second benchmark structure is a frame sub-assemblage under cyclic loading. Results of sensitivity analysis are used to investigate and quantify the effect and relative importance of the various material parameters in regards to the monotonic and cyclic nonlinear response of the two testbed structures considered.

4.2 RESPONSE SENSITIVITY ANALYSIS AT THE ELEMENT LEVEL

The calculation of the conditional derivative of the element resisting force vector on the RHS of the sensitivity equation is performed at the element level. Since displacement-based locking-free frame elements for composite beams with deformable shear connection have internal nodes (Dall'Asta and Zona 2004b), the element internal resisting force vector needed to assemble the structure resisting force vector is obtained after static condensation of the internal degrees of freedom (DOFs). The static condensation of the internal DOFs is an algebraic procedure (Bathe 1995), corresponding to a partial Gauss elimination, commonly used in finite elements with internal nodes (or DOFs) in order to reduce the size of the system of equilibrium equations to be solved at the structure level.

The element nodal displacement vector $\mathbf{q}$ and element nodal resisting force vector $\mathbf{Q}$ can be partitioned according to the external (subscript e) and internal (subscript i) DOFs as

$$\mathbf{q} = \begin{bmatrix} \mathbf{q}_e \\ \mathbf{q}_i \end{bmatrix} \quad \text{and} \quad \mathbf{Q} = \begin{bmatrix} \mathbf{Q}_e \\ \mathbf{Q}_i \end{bmatrix} \tag{4.1}$$

The linearized incremental equilibrium equations at the element level can be written in partitioned form as

$$\begin{bmatrix} \mathbf{K}_{ee} & \mathbf{K}_{ei} \\ \mathbf{K}_{ie} & \mathbf{K}_{ii} \end{bmatrix} \begin{bmatrix} \delta\mathbf{q}_e \\ \delta\mathbf{q}_i \end{bmatrix} = \begin{bmatrix} \mathbf{F}_e - \mathbf{Q}_e \\ \mathbf{F}_i - \mathbf{Q}_i \end{bmatrix} \tag{4.2}$$

where $\delta\mathbf{q}_e$ and $\delta\mathbf{q}_i$ represent linearized increments of $\mathbf{q}_e$ and $\mathbf{q}_i$, respectively, $\mathbf{F}_e$ and $\mathbf{F}_i$ denote the quasi-static load vectors corresponding to the external and internal DOFs, respectively, and the sub-matrices of the element tangent stiffness matrix are defined as

$$\mathbf{K}_{ee} = \left.\frac{\partial \mathbf{Q}_e}{\partial \mathbf{q}_e}\right|_\theta, \quad \mathbf{K}_{ei} = \left.\frac{\partial \mathbf{Q}_e}{\partial \mathbf{q}_i}\right|_\theta, \quad \mathbf{K}_{ie} = \left.\frac{\partial \mathbf{Q}_i}{\partial \mathbf{q}_e}\right|_\theta = \mathbf{K}_{ei}^T, \quad \mathbf{K}_{ii} = \left.\frac{\partial \mathbf{Q}_i}{\partial \mathbf{q}_i}\right|_\theta \tag{4.3}$$

where the conditioning on θ expresses the fact that these vector function derivatives are evaluated for the unperturbed sensitivity parameter θ. In Eq. (4.2), it should be noted that $\mathbf{F}_e$ also includes the effects of external distributed loads and internal resisting forces acting over and within adjacent finite elements. After condensation of the internal DOFs, Eq. (4.2) reduces to

$$\mathbf{K}_c \delta\mathbf{q}_c = \mathbf{F}_c - \mathbf{Q}_c \tag{4.4}$$

where $\mathbf{q}_c = \mathbf{q}_e$ ($\rightarrow \delta\mathbf{q}_c = \delta\mathbf{q}_e$), and

$$\begin{aligned}
\mathbf{K}_c &= \mathbf{K}_{ee} - \mathbf{K}_{ei}\mathbf{K}_{ii}^{-1}\mathbf{K}_{ie} \\
\mathbf{F}_c &= \mathbf{F}_e - \mathbf{K}_{ei}\mathbf{K}_{ii}^{-1}\mathbf{F}_i \\
\mathbf{Q}_c &= \mathbf{Q}_e - \mathbf{K}_{ei}\mathbf{K}_{ii}^{-1}\mathbf{Q}_i
\end{aligned} \tag{4.5}$$

In the above equations, $\mathbf{K}_c$ is the condensed element tangent stiffness matrix, $\mathbf{F}_c$ is the condensed quasi-static load vector, and $\mathbf{Q}_c$ is the condensed internal resisting force vector. At convergence of the response calculation at time t_{n+1}, the incremental quantities $\delta\mathbf{q}_e$, $\delta\mathbf{q}_i$, and $\delta\mathbf{q}_c$ in Eqs. (4.2) and (4.4) reduce to zero (within a small finite precision dependent on the prescribed tolerance) and the quantities appearing in Eq. (4.5) must be considered as computed at time t_{n+1}. In particular, this implies that the matrices $\mathbf{K}_{ee}$, $\mathbf{K}_{ei}$, $\mathbf{K}_{ie}$, $\mathbf{K}_{ii}$, and $\mathbf{K}_c$ are the consistent tangent stiffness matrices obtained through consistent linearization of the equilibrium equations at time t_{n+1}. Thus, they must be considered as constant quantities with respect to $\mathbf{q}_e$, $\mathbf{q}_i$, $\mathbf{q}_c$ (since they are linearizing constants) and θ (since evaluated at $\theta = \theta_0$).

After static condensation, the conditional sensitivities of the nonlinear inelastic resisting forces reduces to

$$\left.\frac{\partial \mathbf{R}_c(\mathbf{u}_{n+1}(\theta), \theta)}{\partial \theta}\right|_{\mathbf{u}_{n+1}} = \mathop{\mathbf{A}}_{e=1}^{N_{el}} \left\{ \left.\frac{\partial \mathbf{Q}_{n+1}^{(e)}(\mathbf{q}_{n+1}^{(e)}(\theta), \theta)}{\partial \theta}\right|_{\mathbf{q}_{n+1}^{(e)}} \right\} \tag{4.6}$$

where $\mathbf{R}_c$ denotes the condensed vector of structure resisting forces. In the following, the subscript "n+1" is omitted for the sake of brevity.

Differentiating Eq. $(4.5)_3$ with respect to $\mathbf{q}_i$ for θ fixed and using Eq. (4.3) yields

$$\left.\frac{\partial \mathbf{Q}_c}{\partial \mathbf{q}_i}\right|_\theta = \left.\frac{\partial \mathbf{Q}_e}{\partial \mathbf{q}_i}\right|_\theta - \mathbf{K}_{ei}\mathbf{K}_{ii}^{-1}\left.\frac{\partial \mathbf{Q}_i}{\partial \mathbf{q}_i}\right|_\theta = \mathbf{K}_{ei} - \mathbf{K}_{ei}\mathbf{K}_{ii}^{-1}\mathbf{K}_{ii} = \mathbf{0} \tag{4.7}$$

The above equation indicates that $\mathbf{Q}_c$ is independent of $\mathbf{q}_i$ for θ fixed. Thus,

$$\mathbf{Q}_c = \mathbf{Q}_c(\mathbf{q}_e(\theta), \theta) \tag{4.8}$$

Differentiating Eq. $(4.5)_3$ with respect to θ gives

$$\frac{d\mathbf{Q}_c}{d\theta} = \frac{d\mathbf{Q}_e}{d\theta} - \mathbf{K}_{ei}\mathbf{K}_{ii}^{-1}\frac{d\mathbf{Q}_i}{d\theta} \tag{4.9}$$

Differentiating Eq. (4.8) with respect to θ using the implicit function theorem of differentiation results in

$$\frac{d\mathbf{Q}_c}{d\theta} = \left.\frac{\partial \mathbf{Q}_c}{\partial \mathbf{q}_e}\right|_\theta \frac{dq_e}{d\theta} + \left.\frac{\partial \mathbf{Q}_c}{d\theta}\right|_{\mathbf{q}} \tag{4.10}$$

which can be rewritten as, using Eqs. $(4.5)_1$ and $(4.5)_3$,

$$\frac{d\mathbf{Q}_c}{d\theta} = \mathbf{K}_c\frac{d\mathbf{q}_e}{d\theta} + \left.\frac{\partial \mathbf{Q}_c}{d\theta}\right|_{\mathbf{q}} \tag{4.11}$$

In Eq. (4.11), the only term that remains to be derived is $\left.\frac{\partial \mathbf{Q}_c}{d\theta}\right|_{\mathbf{q}}$. This term is extremely important, since it is needed to assemble the conditional derivative/sensitivity of the condensed internal resisting force vector at the structure level as expressed in Eq. (4.6). It is computed through substituting Eq. (4.9) into Eq. (4.11) after solving for $\frac{d\mathbf{Q}_e}{d\theta}$ and $\frac{d\mathbf{Q}_i}{d\theta}$ as follows.

In general, we have the following functional dependence of vectors $\mathbf{Q}_e$ and $\mathbf{Q}_i$ on the sensitivity parameter θ:

$$\begin{aligned} \mathbf{Q}_e &= \mathbf{Q}_e(\mathbf{q}_e(\theta), \mathbf{q}_i(\theta), \theta) \\ \mathbf{Q}_i &= \mathbf{Q}_i(\mathbf{q}_e(\theta), \mathbf{q}_i(\theta), \theta) \end{aligned} \tag{4.12}$$

Applying the implicit function theorem of differentiation to Eq. (4.12) yields

$$\begin{aligned} \frac{d\mathbf{Q}_e}{d\theta} &= \left.\frac{\partial \mathbf{Q}_e}{\partial \mathbf{q}_e}\right|_\theta \frac{d\mathbf{q}_e}{d\theta} + \left.\frac{\partial \mathbf{Q}_e}{\partial \mathbf{q}_i}\right|_\theta \frac{d\mathbf{q}_i}{d\theta} + \left.\frac{\partial \mathbf{Q}_e}{\partial \theta}\right|_{\mathbf{q}} = \mathbf{K}_{ee}\frac{d\mathbf{q}_e}{d\theta} + \mathbf{K}_{ei}\frac{d\mathbf{q}_i}{d\theta} + \left.\frac{\partial \mathbf{Q}_e}{\partial \theta}\right|_{\mathbf{q}} \\ \frac{d\mathbf{Q}_i}{d\theta} &= \left.\frac{\partial \mathbf{Q}_i}{\partial \mathbf{q}_e}\right|_\theta \frac{d\mathbf{q}_e}{d\theta} + \left.\frac{\partial \mathbf{Q}_i}{\partial \mathbf{q}_i}\right|_\theta \frac{d\mathbf{q}_i}{d\theta} + \left.\frac{\partial \mathbf{Q}_i}{\partial \theta}\right|_{\mathbf{q}} = \mathbf{K}_{ie}\frac{d\mathbf{q}_e}{d\theta} + \mathbf{K}_{ii}\frac{d\mathbf{q}_i}{d\theta} + \left.\frac{\partial \mathbf{Q}_i}{\partial \theta}\right|_{\mathbf{q}} \end{aligned} \tag{4.13}$$

After solving the matrix sensitivity equation at the structure level, only the unconditional derivatives, $\frac{d\mathbf{q}_e}{d\theta}$, of the element external DOFs in local coordinates are known. Thus, it is necessary to compute at the element level the unconditioned derivatives, $\frac{d\mathbf{q}_i}{d\theta}$, of the element internal DOFs in local coordinates. In fact, the unconditioned sensitivities of the history/state variables at the section level can be updated only if the unconditional derivatives of all the element DOFs (external and internal) are known.

The equilibrium equation written at the element level implies that the following relations are verified at convergence, up to a small numerical tolerance:

$$\begin{aligned} \mathbf{Q}_e - \mathbf{F}_e &= \mathbf{0} \\ \mathbf{Q}_i - \mathbf{F}_i &= \mathbf{0} \end{aligned} \tag{4.14}$$

where the zero equalities are satisfied up to some iteration residuals. Differentiating Eq. $(4.14)_2$ with respect to θ yields

$$\frac{d\mathbf{Q}_i}{d\theta} - \frac{d\mathbf{F}_i}{d\theta} = \mathbf{0} \tag{4.15}$$

The term $\frac{d\mathbf{F}_i}{d\theta}$ depends only on the distributed and/or concentrated external forces applied on the internal nodes. Therefore, $\frac{d\mathbf{F}_i}{d\theta}$ and consequently $\frac{d\mathbf{Q}_i}{d\theta}$ can be considered as known and if the parameter θ is not related to the element distributed loads, we have

$$\frac{d\mathbf{F}_i}{d\theta} = \frac{d\mathbf{Q}_i}{d\theta} = \mathbf{0} \tag{4.16}$$

Substituting Eq. (4.16) into Eq. $(4.13)_2$ and solving for $\frac{d\mathbf{q}_i}{d\theta}$ yields

$$\frac{d\mathbf{q}_i}{d\theta} = \mathbf{K}_{ii}^{-1}\left(\frac{d\mathbf{Q}_i}{d\theta} - \mathbf{K}_{ie}\frac{d\mathbf{q}_e}{d\theta} - \left.\frac{\partial \mathbf{Q}_i}{\partial \theta}\right|_{\mathbf{q}}\right) \tag{4.17}$$

Substituting Eq. (4.17) into Eq. $(4.13)_1$ and performing some algebraic manipulations yield

$$\frac{d\mathbf{Q}_e}{d\theta} - \mathbf{K}_{ei}\mathbf{K}_{ii}^{-1}\frac{d\mathbf{Q}_i}{d\theta} = (\mathbf{K}_{ee} - \mathbf{K}_{ei}\mathbf{K}_{ii}^{-1}\mathbf{K}_{ie})\frac{d\mathbf{q}_e}{d\theta} + \left(\left.\frac{\partial \mathbf{Q}_e}{\partial \theta}\right|_{\mathbf{q}} - \mathbf{K}_{ei}\mathbf{K}_{ii}^{-1}\left.\frac{\partial \mathbf{Q}_i}{\partial \theta}\right|_{\mathbf{q}}\right) \tag{4.18}$$

By comparing Eq. (4.18) with Eq. (4.11), using Eq. (4.9), we deduce that

$$\left.\frac{\partial \mathbf{Q}_c}{\partial \theta}\right|_{\mathbf{q}} = \left.\frac{\partial \mathbf{Q}_e}{\partial \theta}\right|_{\mathbf{q}} - \mathbf{K}_{ei}\mathbf{K}_{ii}^{-1}\left.\frac{\partial \mathbf{Q}_i}{\partial \theta}\right|_{\mathbf{q}} \tag{4.19}$$

The conditional derivatives $\left.\frac{\partial \mathbf{Q}_e}{\partial \theta}\right|_{\theta}$ and $\left.\frac{\partial \mathbf{Q}_i}{\partial \theta}\right|_{\theta}$ are obtained as

$$\begin{bmatrix} \left.\frac{\partial \mathbf{Q}_e}{\partial \theta}\right|_{\mathbf{q}} \\ \left.\frac{\partial \mathbf{Q}_i}{\partial \theta}\right|_{\mathbf{q}} \end{bmatrix} = \left.\frac{\partial \mathbf{Q}(\mathbf{q}(\theta), \theta)}{\partial \theta}\right|_{\mathbf{q}} = \int_0^L \mathbf{B}^T(z) \left.\frac{\partial \mathbf{D}(\mathbf{B}(z) \cdot \mathbf{q}(\theta), \theta)}{\partial \theta}\right|_{\mathbf{q}} dz \tag{4.20}$$

where **D** denotes the vector of active stress resultants at the section level and **B** is the transformation matrix between the vector of element nodal displacements **q** and the vector of generalized section deformations **d** (i.e., compatibility equation $\mathbf{d}(z, \theta) = \mathbf{B}(z) \cdot \mathbf{q}(\theta)$). The calculation of the conditional derivative on the RHS of Eq. (4.20) is carried out at the section level.

4.3 RESPONSE SENSITIVITY ANALYSIS AT THE SECTION LEVEL

In the case of a composite beam with deformable shear connection, the vector of generalized section deformations is defined as (Dall'Asta and Zona 2004a)

$$\mathbf{d}^T(z, \theta) = \left[\varepsilon_1(z, \theta) \; \varepsilon_2(z, \theta) \; \chi(z, \theta) \; \delta(z, \theta)\right] \tag{4.21}$$

where ε_1 and ε_2 are the axial strains at the reference points G_1 (concrete slab) and G_2 (steel beam), respectively (Fig. 4.1), χ is the curvature (same for concrete slab and steel beam) and δ is the slip at the interface between the concrete slab and the steel beam. The vector of section stress resultants is defined as (Dall'Asta and Zona 2004a)

$$\mathbf{D}^T(z, \theta) = \left[N_1(z, \theta) \; N_2(z, \theta) \; M_{12}(z, \theta) \; f_s(z, \theta)\right] \tag{4.22}$$

where N_1 is the axial force in the concrete slab, N_2 is the axial force in the steel beam, M_{12} is the summation of the bending moments in the concrete slab and steel beam, and f_s is the interface shear force per unit length. The stress resultants N_1, N_2 and M_{12} are calculated through numerical integration over the concrete and steel parts of the beam cross-section, which are discretized using a fiber model.

The calculation of the conditional derivative (for **q** fixed and therefore for **d** fixed) of the vector of section stress resultants in Eq. (4.20) is carried out as

$$\left.\frac{\partial N_\alpha}{\partial \theta}\right|_{\mathbf{d}} = \int_{A_\alpha} \left.\frac{\partial \sigma(y, \varepsilon_\alpha(z, \theta), \chi(z, \theta), \theta)}{\partial \theta}\right|_{\mathbf{d}} dA, \quad \alpha = 1, 2 \tag{4.23}$$

$$\left.\frac{\partial M_{12}}{\partial \theta}\right|_{\mathbf{d}} = \sum_{\alpha = 1}^{2} \left\{ \int_{A_\alpha} (y - y_\alpha) \left.\frac{\partial \sigma(y, \varepsilon_\alpha(z, \theta), \chi(z, \theta), \theta)}{\partial \theta}\right|_{\mathbf{d}} dA \right\} \tag{4.24}$$

where σ is the normal stress; y_1 and y_2 are the reference points of the two components of the composite beam (Fig. 4.1); and A_1 and A_2 are the cross-section areas of the concrete slab and steel beam, respectively. The conditional derivative on the RHS of Eqs. (4.23) and (4.24) and the conditional derivative of f_s (given **d**) are calculated at the material level, hence the (discretized) material constitutive equations must be defined and differentiated analytically with respect to the sensitivity parameter θ.

After solving the sensitivity equations at the structure level in condensed form for $d\mathbf{u}_{n+1}/d\theta$ and calculating the unconditional derivatives of the displacements at the (external and internal) nodes, $d\mathbf{q}_e/d\theta$ and $d\mathbf{q}_i/d\theta$, the unconditioned sensitivities of the generalized section deformations and section stress resultants are updated. The sensitivi-

ties of the section deformations are obtained using the compatibility relations, while the sensitivities of the section stress resultants are evaluated using the unconditional derivatives (with respect to the sensitivity parameter θ) of the material constitutive relations, i.e.,

$$\frac{dN_\alpha}{d\theta} = \int_{A_\alpha} \frac{d\sigma(y, \varepsilon_\alpha(z, \theta), \chi(z, \theta), \theta)}{d\theta} dA, \quad \alpha = 1, 2 \tag{4.25}$$

$$\frac{dM_{12}}{d\theta} = \sum_{\alpha = 1}^{2} \left\{ \int_{A_\alpha} (y - y_\alpha) \frac{d\sigma(y, \varepsilon_\alpha(z, \theta), \chi(z, \theta), \theta)}{d\theta} dA \right\} \tag{4.26}$$

4.4 RESPONSE SENSITIVITY ANALYSIS AT THE MATERIAL LEVEL

For every (discretized) material constitutive model, the conditional and unconditional derivatives of the material state/history variables must be evaluated analytically with respect to the relevant material (sensitivity) parameters. This can be a challenging task when complex cyclic constitutive models are adopted, as is the case in this study.

The constitutive law used for the steel of the beam and for the reinforcements in the concrete slab is a uniaxial cyclic plasticity model with the von Mises yield criterion in conjunction with linear kinematic and isotropic hardening laws. This is the well-known bilinear inelastic material constitutive model. Detailed formulation and differentiation of this model can be found in Conte et al. (2003). The parameters of this material model consist of (1) Young's modulus of elasticity E, (2) the initial yield stress f_y, (3) the linear kinematic hardening modulus H_k, and (4) the linear isotropic hardening modulus H_i.

The selected constitutive law for the concrete material is a uniaxial cyclic law with monotonic envelope given by the Popovics-Saenz law (Balan et al. 1997, 2001, Kwon and Spacone 2002). A typical cyclic response of the concrete material model adopted herein is given in Fig. 4.2. Detailed formulation and differentiation of this model can be found in Zona et al. (2004). The parameters of this material model consists of (1) the initial modulus of elasticity E_c, (2) the compressive strength f_c and (3) the corresponding strain ε_0, (4) the stress f_f and (5) the corresponding strain ε_f of the control point (inflection point) of the softening branch.

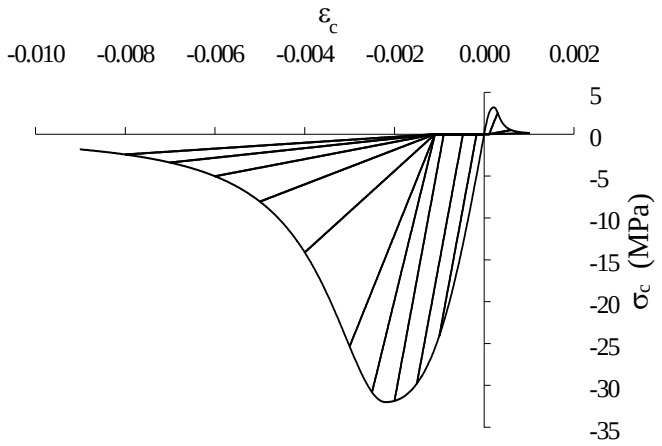

Figure 4.2 Hysteretic concrete material model

The constitutive law used for the shear connectors is a slip-force cyclic law with monotonic envelope given by the Ollgaard et al. (1971) law. The cyclic response of the shear connectors is a modified version of the model proposed by Eligehausen et al. (1983) and is similar to the model used by Salari and Spacone (2001). A typical cyclic response of the constitutive model for the shear connectors used in this study is shown in Fig. 4.3.

Detailed formulation and differentiation of this model can be found in Zona et al. (2004). The parameters of the connection "material" model consist of (1) the connection strength f_{smax}, (2) the ultimate slip δ_{ult}, and (3) the friction parameter τ_{fr}, see Fig. 4.3.

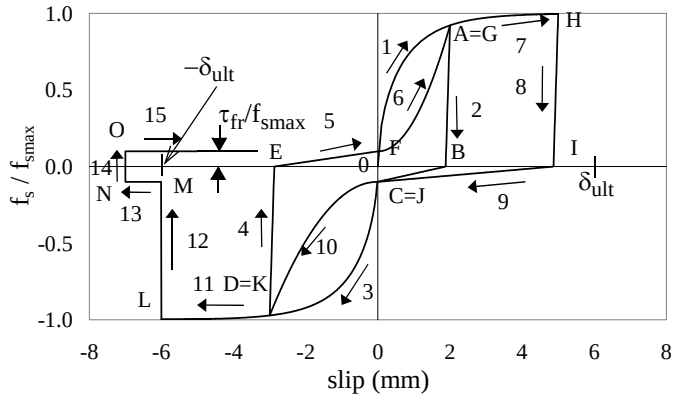

Figure 4.3 Hysteretic model of shear connection

4.5 COMPUTER IMPLEMENTATION

The above formulation for finite element response sensitivity analysis using composite beam elements with deformable shear connection was implemented in FEDEASLab (Filippou 2002), a general-purpose nonlinear finite element structural analysis program. FEDEASLab is a Matlab (MathWorks 1997) toolbox suitable for linear and nonlinear, static and dynamic structural analysis, which provides a general framework for physical parameterization of finite element models and response sensitivity computation (Franchin 2004).

4.6 VALIDATION EXAMPLES

4.6.1 Nonlinear monotonic quasi-static test

The first benchmark problem considered is a non-symmetric two-span continuous beam (Figure 4.4), tested by Ansourian (1981) under monotonic quasi-static loading. The beam, denoted CTB1 in (Ansourian 1981), has two spans 4.00 m and 5.00 m long and is subjected to a vertical concentrated load P applied at the mid-point of the shorter span. The joist section is an European IPE200; the reinforced concrete slab section is 100×800 mm^2. Due to the relatively narrow width of the concrete slab, shear lag effects are neglected in its modeling. The reader is referred to (Ansourian 1981) for all details regarding the geometry and material properties. This problem presents all the main difficulties typically encountered in the analysis of steel-concrete composite structures, such as concrete softening in compression, concrete cracking in tension, and high gradients of slip and shear force along the connection (Dall'Asta and Zona 2002, 2004c). The structure is discretized uniformly into 18 10-DOF elements, see Fig. 4.4, with 5 Gauss-Lobatto points each (Dall'Asta and Zona 2003, 2004c).

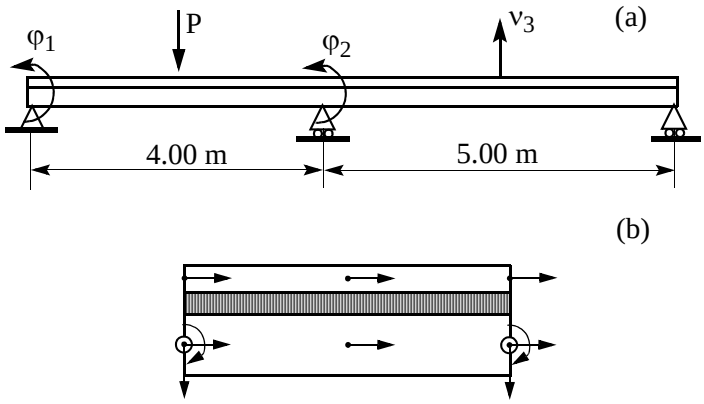

Figure 4.4 (a) Configuration of the Ansourian CTB1 continuous beam,
(b) degrees of freedom of the 10-DOF composite beam element used

A quasi-static, monotonic, materially-nonlinear-only analysis of the beam structure is performed using the incremental-iterative procedure defined above in displacement-control mode with the vertical displacement at the point of application of the load taken as the controlled DOF, thus mimicking the physical experiment. The computed load-deflection curves for the two spans are shown in Fig. 4.5, where they are compared with the experimental results. It is observed that the analytical predictions are in very good agreement with the experimental results. It is worth mentioning that in spite of the fact that the loading is monotonic, small unloading and reloading events are experienced at a few Gauss-Lobatto points due to internal stress redistribution. However, these events do not significantly affect the overall response, i.e., practically the same results are obtained with nonlinear elastic constitutive laws with the same monotonic envelope neglecting the cyclic behavior (Dall'Asta and Zona 2003, 2004c).

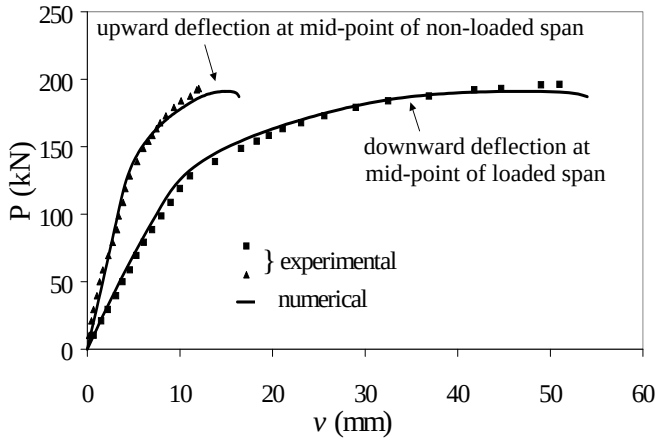

Figure 4.5 Beam CTB1: load-deflection curves

Sensitivities of various global and local response quantities to all material parameters were computed using DDM and FFD. Due to space limitation, only the sensitivities to the most important material parameters (i.e., the parameters to which the response in question is most sensitive) are shown below. The reader is referred to Zona et al. (2004) for an exhaustive presentation of the response sensitivity analysis. The sensitivity results are presented in normalized form, i.e., multiplied by the value of the sensitivity parameter and divided by the value of the response quantity itself. Thus, the normalized sensitivities represent the percent variation of the subject response quantity for a unitary percent variation of the sensitivity parameter. In this way, the normalized response sensitivities reveal directly the relative importance of all the material parameters considered in regards to a given response quantity at various loading stages of the structure.

Sensitivities of three global response quantities (i.e., rotation φ_1 at the left support, rotation φ_2 at the intermediate support and deflection v_3 at mid-point of the non-loaded

span, see Figure 4.4) to the four most important parameters (i.e., modulus of elasticity E_0 and yield stress f_y of the steel beam material, compressive strength f_c of the concrete, and strength f_{smax} of the shear connection) are shown in Figs. 4.6 through 4.9. The sensitivities are plotted as functions of the ratio of the deflection *v* at mid-point of the loaded span to its value at collapse v_{ult} predicted analytically (collapse being defined as the point at which the ultimate strain or the ultimate slip is reached for the first time along any of the material fibers or along the shear connection, respectively). It can be observed that the response sensitivities to f_y are null before yielding occurs for the first time (Fig. 4.6) as expected since prior to first yield, f_y does not affect the response. Some of the response sensitivities are characterized by strong discontinuities, due to material state transitions from the elastic to the plastic regime at Gauss-Lobatto point (Conte 2001, Conte et al. 2001, 2003). These discontinuities appear to be strongly dependent on the load level. The jagged response sensitivities obtained are the manifestation of a complex structural behavior in which important redistributions of deformation and stress occur between the steel beam and the reinforced concrete slab through the shear connection, which behaves nonlinearly from very small slip values. Among the three degrees of freedom considered, the vertical deflection v_3 at mid-point of the non-loaded span is the most sensitive response quantity for every parameter considered. This can be explained in part by the fact that v_3 is more distant from the controlled degree of freedom than the other two degrees of freedom considered. The sensitivities of the displacement along the controlled degree of freedom (i.e., vertical displacement at the point of application of the load) are always zero.

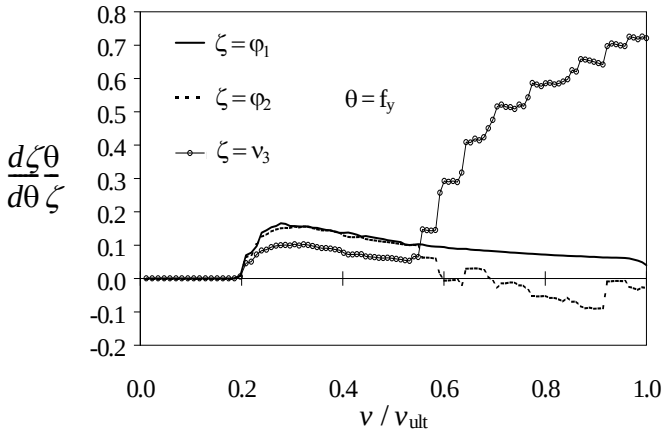

Figure 4.6 Beam CTB1: global response sensitivities to f_y

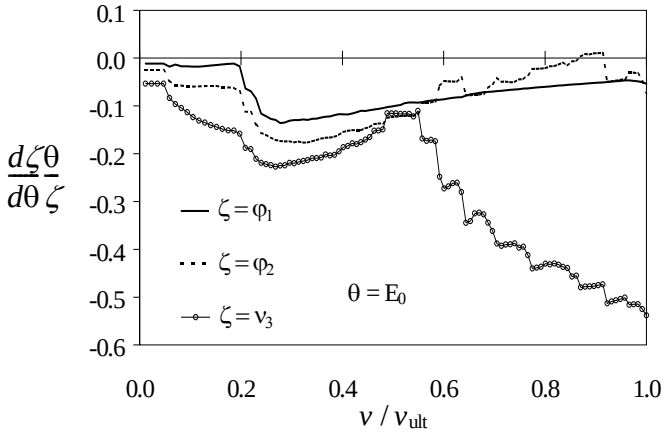

Figure 4.7 Beam CTB1: global response sensitivities to E_0

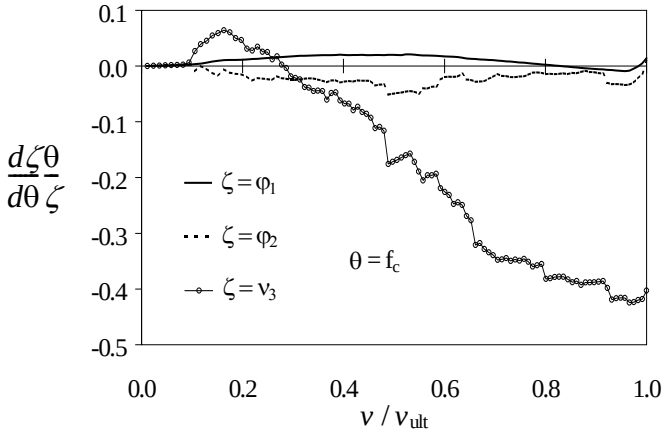

Figure 4.8 Beam CTB1: global response sensitivities to f_c

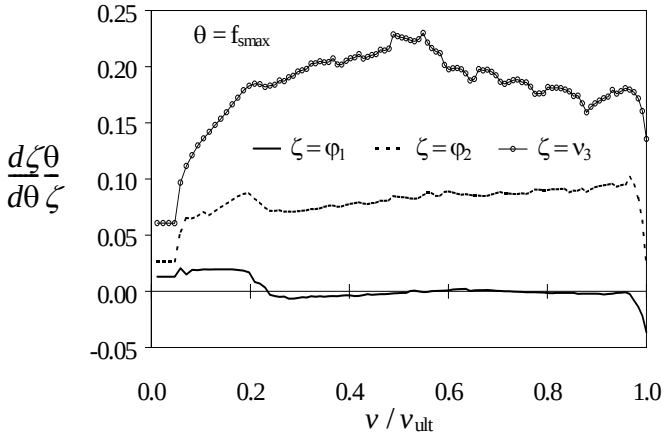

Figure 4.9 Beam CTB1: global response sensitivities to f_{smax}

The normalized sensitivities of ν_3 to the four material parameters considered are compared in Fig. 4.10. In this way, it is possible to clearly highlight and quantify the relative importance of the various material parameters at different load levels. For example, it can be observed that the sensitivities to E_0 and f_{smax} are the most important at the early

stage of the loading history, while as yielding spreads along the steel beam, material parameter f_y becomes increasingly important relative to the other parameters. Similar considerations apply to material parameter f_c, to which the sensitivity of v_3 increases significantly with increasing load level, even though the strength parameter f_c remains less important than the strength parameter f_y at high load levels.

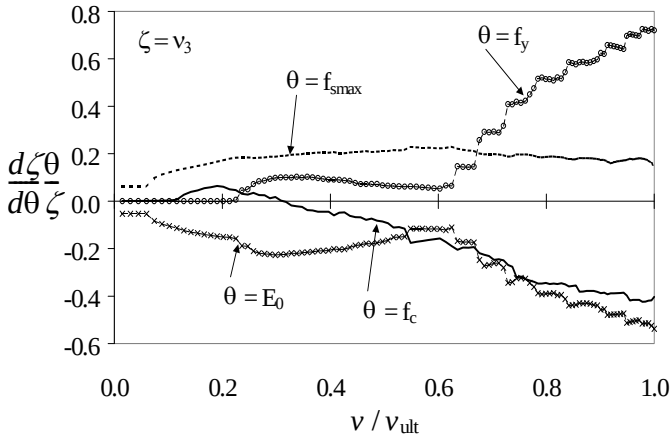

Figure 4.10 Beam CTB1: Sensitivity of global response v_3 to f_y, E_0, f_c and f_{smax}

Sensitivities of a local response quantity (i.e., shear force per unit length f_s) at three locations (i.e., mid-point of the loaded span at z = 2.00 m, intermediate support at z = 4.00 m and mid-point of the non-loaded span at z = 6.50 m) to the three most important material parameters (i.e., yield stress f_y of the steel beam, compressive strength f_c of the concrete, shear connection strength f_{smax}) are plotted in Figs. 4.11 through 4.13. The sensitivities of f_s (at z = 6.50 m) to the three material parameters f_y, f_c, and f_{smax} are plotted together in Fig. 4.14, clearly highlighting the relative importance of these three parameters. It is noteworthy that the discontinuities due to material state transitions (elastic-to-

plastic) are more pronounced than at the global response level. It is also observed that at high load level ($\nu/\nu_{ult} > 0.7$), the sensitivities of the local response f_s increase more strongly with the load level than the global response sensitivities previously considered (see Figs. 4.6 to 4.10).

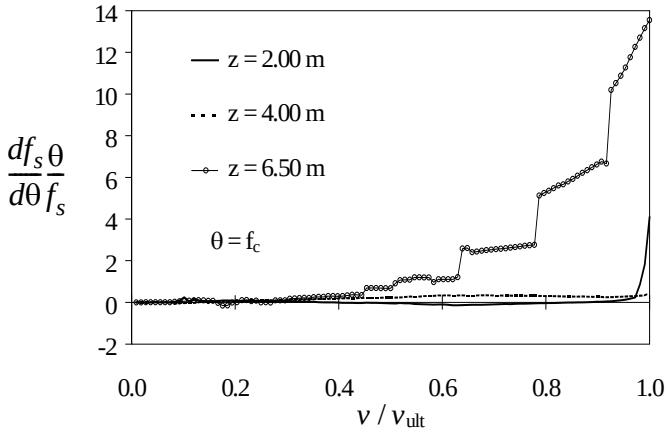

Figure 4.11 Beam CTB1: sensitivity of shear force f_s (at different locations) to f_c

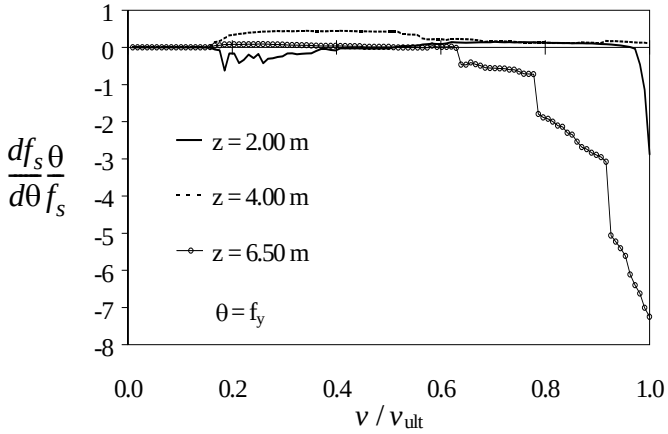

Figure 4.12 Beam CTB1: sensitivity of shear force f_s (at different locations) to f_y

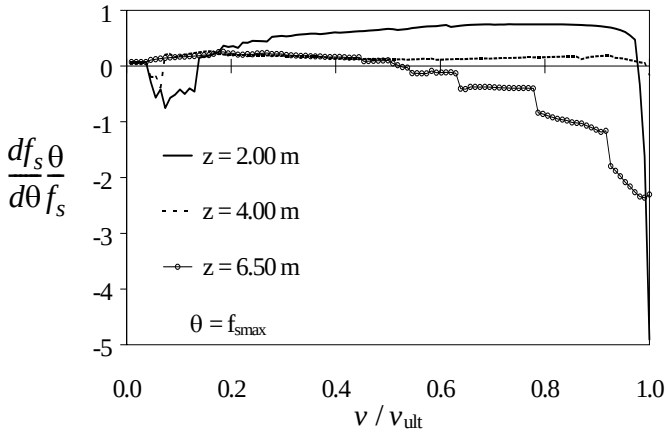

Figure 4.13 Beam CTB1: sensitivity of shear force f_s (at different locations) to f_{smax}

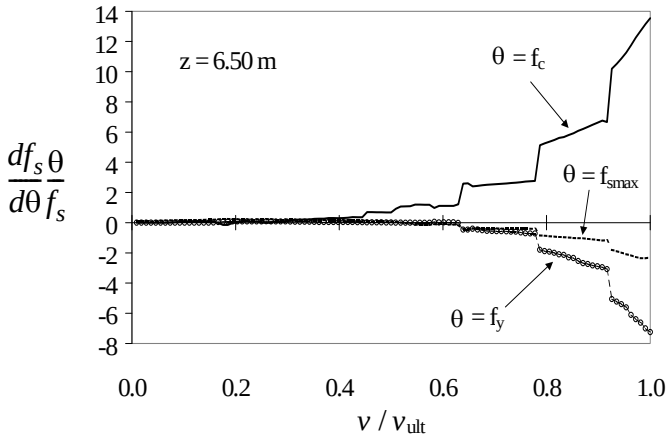

Figure 4.14 Beam CTB1: sensitivity of shear force f_s (at z = 6.50 m) to f_c, f_y and f_{smax}.

All the sensitivity results shown were computed using the DDM and validated by the FFD method using increasingly small perturbations of the sensitivity parameter. Due to space limitation, the comparison between DDM and FFD results is shown herein only for two cases. The first case considered is the sensitivity of the deflection v_3 of the non-

loaded span to the shear connection strength f_{smax} (Fig. 4.15 and close-up in Fig. 4.16); four levels of perturbation of parameter f_{smax} were considered, namely $\Delta\theta/\theta = 10^{-1}$, 10^{-2}, 10^{-3}, 10^{-6}. The second case considered is the sensitivity of the interface shear force f_s at mid-span of the non-loaded span (z = 6.50 m) to the concrete compressive strength f_c (Fig. 4.17 with close-up in Fig. 4.18). The same four levels of perturbation were considered for parameter f_c ($\Delta\theta/\theta = 10^{-1}$, 10^{-2}, 10^{-3}, 10^{-6}). In both cases, it is shown that the FFD results converge asymptotically to the DDM results as $\Delta\theta/\theta$ becomes increasingly small, and that the FFD results for $\Delta\theta/\theta = 10^{-3}$ are close to the DDM results.

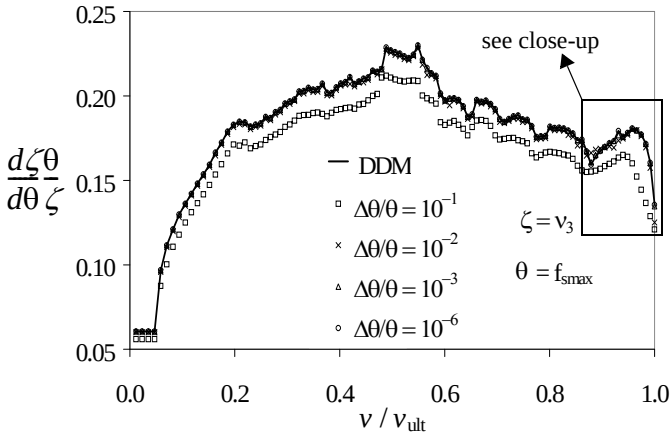

Figure 4.15 Beam CTB1: sensitivity of mid-span deflection v_3 to f_{smax} using DDM and FFD

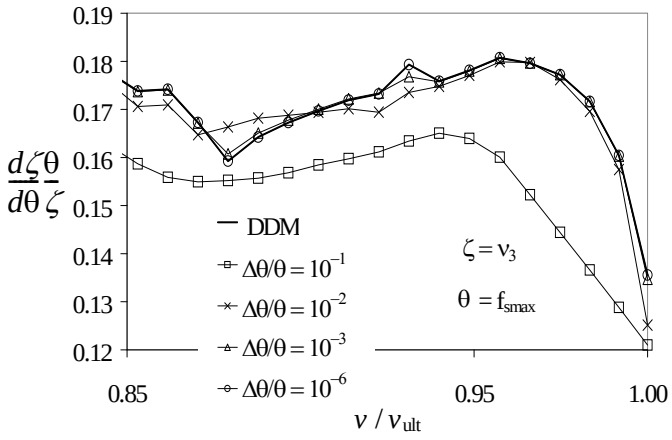

Figure 4.16 Beam CTB1: sensitivity of mid-span deflection v_3 to f_{smax} using DDM and FFD (close-up)

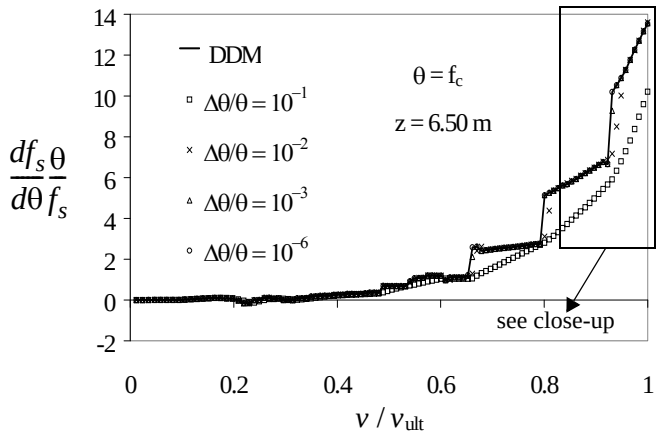

Figure 4.17 Beam CTB1: sensitivity of shear force f_s to f_c using DDM and FFD

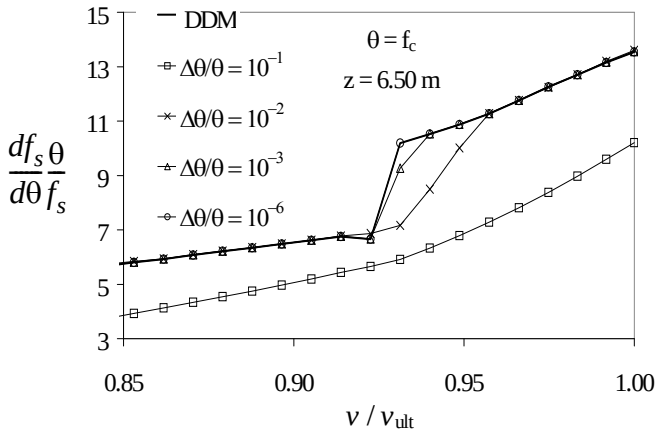

Figure 4.18 Beam CTB1: sensitivity of shear force f_s to f_c using DDM and FFD (close-up)

Figs. 4.19, 4.20, and 4.21 show the effects of the prescribed tolerance δ (used in the energy-based convergence criterion for response calculation) upon convergence of the FFD sensitivity results to their DDM counterparts. In these figures, the response quantity of interest is the rotation φ_1 of the left end node of the two-span continuous beam and the sensitivity parameter θ is the shear connection strength f_{smax}. The sensitivity results are plotted for $v / v_{ult} > 0.6$. Global and local response sensitivities might present irregularities such as the one plotted in Fig. 4.19 where the sensitivity is plotted for an insufficiently small tolerance ($\delta = 10^{-8}$) and for the small tolerance $\delta = 10^{-16}$, which was found to be the largest tolerance leading to the correct DDM results. Fig. 4.20 shows the sensitivity results obtained through FFD analysis with a perturbation $\Delta f_{smax}/f_{smax} = 10^{-2}$ with $\delta = 10^{-8}$ and $\delta = 10^{-16}$, respectively, compared with the DDM results (obtained using $\delta = 10^{-16}$); in this case, no difference can be noticed between the FFD results obtained using two different

values of the tolerance δ (i.e., $\delta = 10^{-8}$ and $\delta = 10^{-16}$). Fig. 4.21 shows the same sensitivity results, but using a perturbation $\Delta f_{smax}/f_{smax} = 10^{-3}$ for the FFD analysis. In this case, it is noticed that the FFD results are not in good agreement with the DDM results when an insufficiently small tolerance ($\delta = 10^{-8}$) is adopted for the iterative response calculation. This example and other examples in Zona et al. (2004) show that the choice of a strict enough convergence tolerance for the iterative response calculation is important for response sensitivity analysis, since the equilibrium equation (or the equation of motion for the dynamic case) is the starting point of the DDM. Use of an inadequate convergence tolerance for response calculation may lead to loss of agreement between response sensitivity results obtained using the DDM and FFD analysis (e.g., an insufficiently small convergence tolerance δ can lead to erroneous DDM results and very inaccurate FFD results if the perturbation of the sensitivity parameter is "too small" in relation to δ).

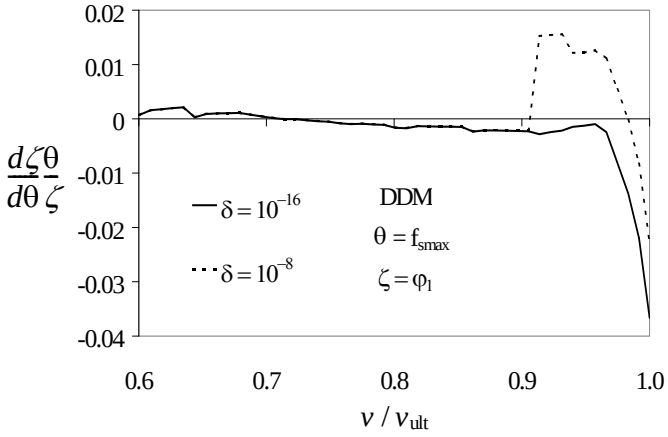

Figure 4.19 Beam CTB1: effect of convergence tolerance for response calculation on DDM results

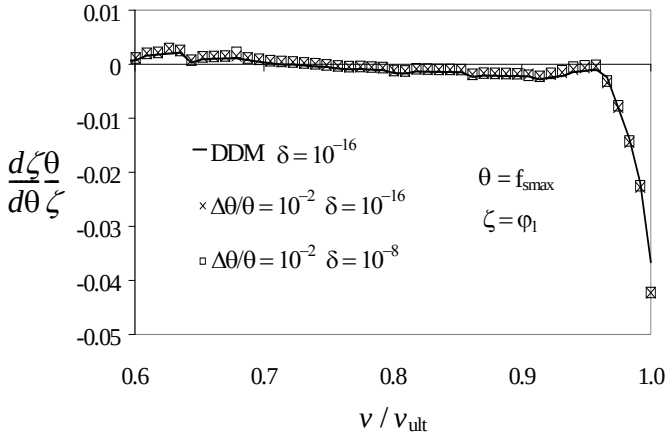

Figure 4.20 Beam CTB1: effect of convergence tolerance for response calculation on agreement between response sensitivity results obtained using DDM and FFD (case in which FFD results converge to DDM)

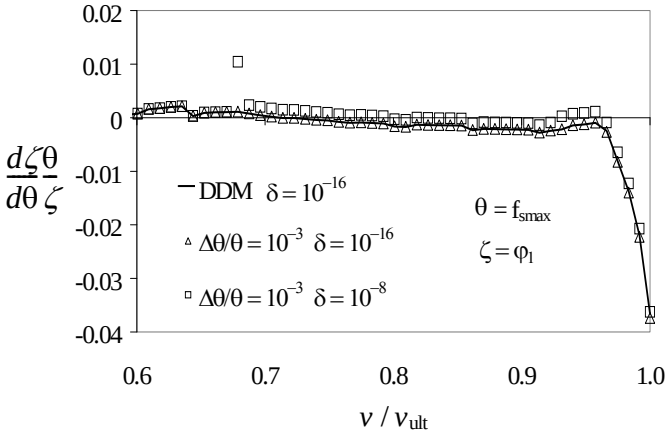

Figure 4.21 Beam CTB1: effect of convergence tolerance for response calculation on agreement between response sensitivity results obtained using DDM and FFD (case in which FFD results do not converge to DDM)

4.6.2 Nonlinear cyclic quasi-static test

The second benchmark problem considered is a frame sub-assemblage tested by Bursi and Gramola (2000) subjected to quasi-static cyclic loading (Fig. 4.22). The frame sub-assemblage, denoted as IPC (intermediate partial connection) in Bursi and Gramola (2000), has a steel-concrete composite beam 4.00 m long made of a European IPE300 steel section and a reinforced concrete slab 1200 mm wide. The shear-lag effects are considered in a simplified way by reducing the slab width to 820 mm over the entire length of the beam (Bursi and Gramola 2000). The steel column is a European HE360B section. The reader is referred to Bursi and Gramola (2000) for all details regarding the geometry, material properties, and the loading history. This sub-assemblage is representative of the behavior of steel-concrete composite frames adopted for seismic-resistant buildings. In addition to the difficulties encountered in the previous example, this case includes problems related to the more complex loading history which is cyclic.

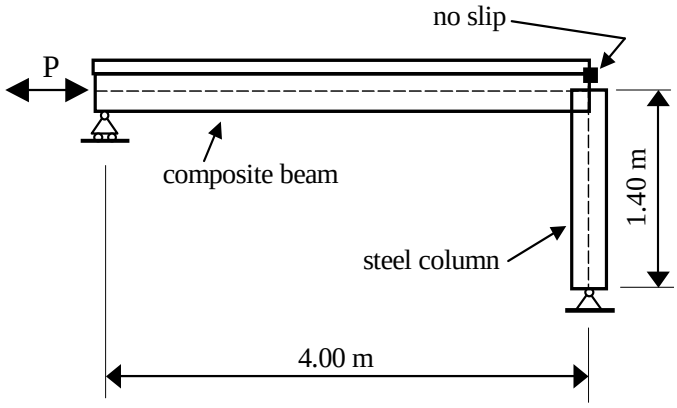

Figure 4.22 Frame IPC: configuration of test specimen

The frame sub-assemblage is uniformly discretized into 5 10-DOF composite frame elements for the beam and one frame element for the column. A materially-nonlinear-only cyclic, quasi-static analysis of the frame sub-assemblage is performed using the incremental-iterative procedure defined above in displacement control mode with the horizontal displacement of the steel beam centroid at the left end of the beam selected as the controlled DOF (as in the experimental tests). The computed load-deflection curve is displayed in Fig. 4.23, where it is compared with the experimental results. It is observed that analytical and experimental results are in good agreement, despite the fact that the finite element model does not include the effects of local buckling (nonlinear geometry) in the steel beam during the push phase of the cyclic loading in the last set of cycles. The extra "fatness" of the computed hysteresis loops is due to the bilinear shape and lack of smoothness of the 1-D J_2 plasticity model used for the steel beam and the steel reinforcements in the concrete slab.

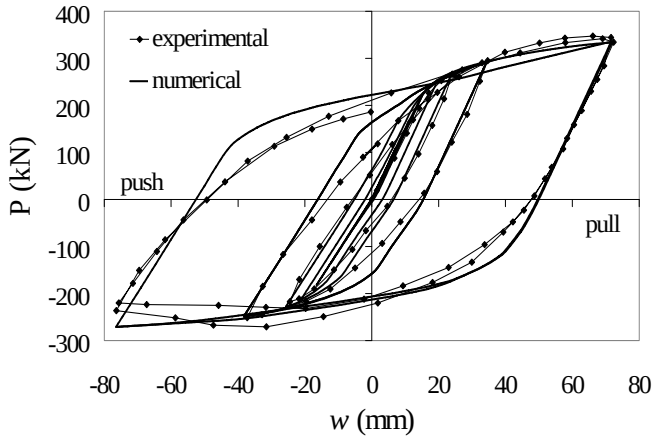

Figure 4.23 Frame IPC: load-deflection curves

Sensitivities of various global and local response quantities to all material parameters were computed using DDM and FFD. Here, for the sake of brevity, only selected sensitivity results are presented. The response sensitivities are only multiplied by the value of the sensitivity parameter (and not divided by the value of the response which can be very small due to its cyclic nature). The normalized sensitivities can thus be interpreted as hundred times the change in the subject response quantity for a unitary percent variation of the sensitivity parameter.

The global response quantities considered in this example are the horizontal displacement *w* of the steel beam centroid at the right-end of the beam and the vertical deflection *v* of the beam at mid-span; their analytical predictions are plotted in Fig. 4.24 as functions of the load step number. The sensitivities of *v* are shown in Fig. 4.25 for the steel beam material parameters (i.e., θ = yield stress f_y, modulus of elasticity E_0, and kinematic hardening modulus H_k) and in Fig. 4.26 for material parameters related to the concrete slab and the shear connection (θ = shear connection strength f_{smax}, concrete compressive strength f_c, and modulus of elasticity E_{0r} of the steel reinforcements). Similarly, the sensitivities of *w* are shown in Fig. 4.27 ($\theta = f_y, E_0, H_k$) and in Fig. 4.28 ($\theta = f_{smax}, f_c, E_{0r}$). It was found (Zona et al. 2004) that the two DOFs *v* and *w* are most sensitive to the steel beam parameters (f_y, E_0, H_k) and the shear connection strength f_{smax}.

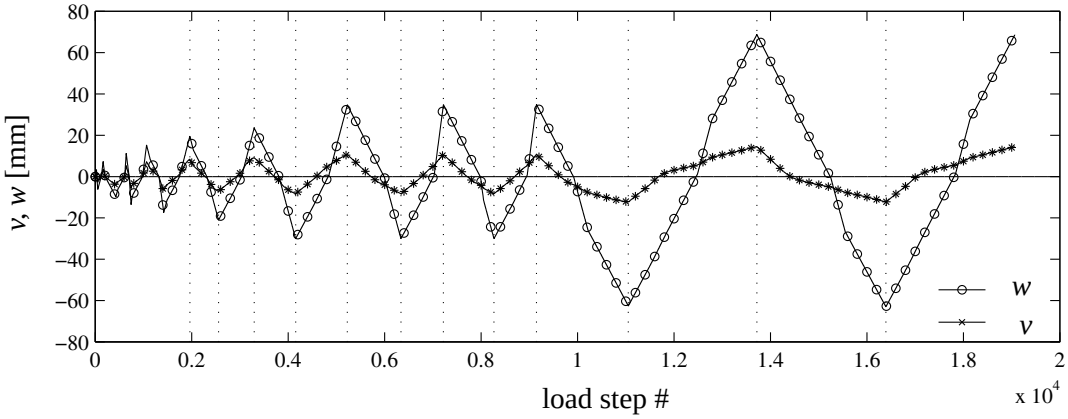

Figure 4.24 Frame IPC: vertical displacement *v* at mid-span and horizontal displacement *w* at the right end of the beam as functions of the load step number

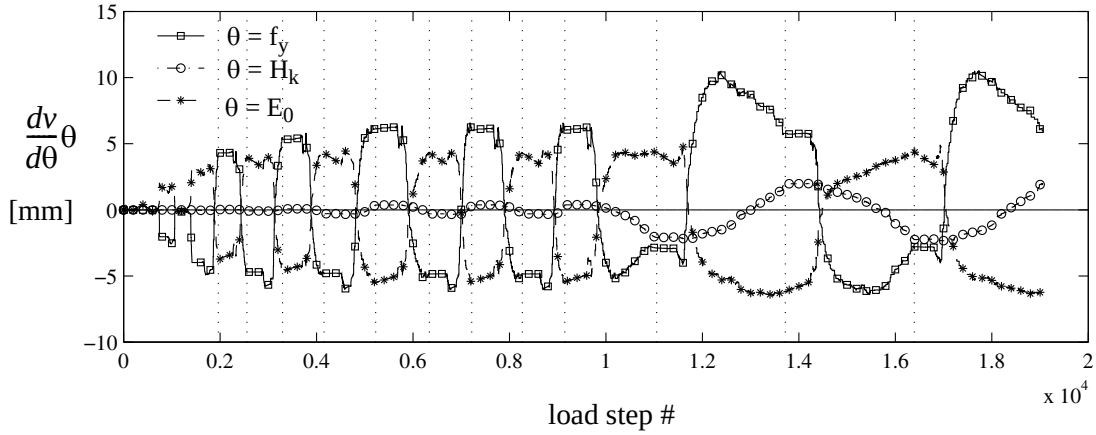

Figure 4.25 Frame IPC: sensitivities of the beam mid-span vertical deflection *v* to steel beam material parameters

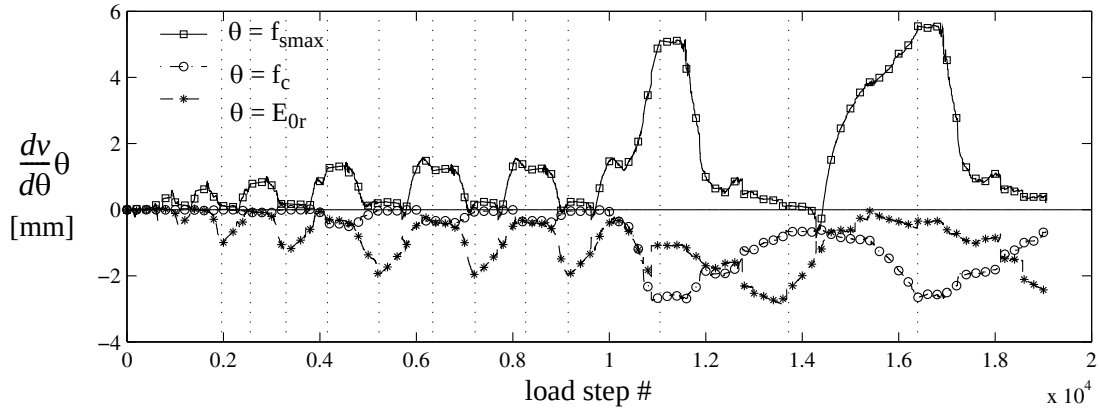

Figure 4.26 Frame IPC: sensitivities of the beam mid-span deflection *v* to parameters related to concrete slab and shear connection

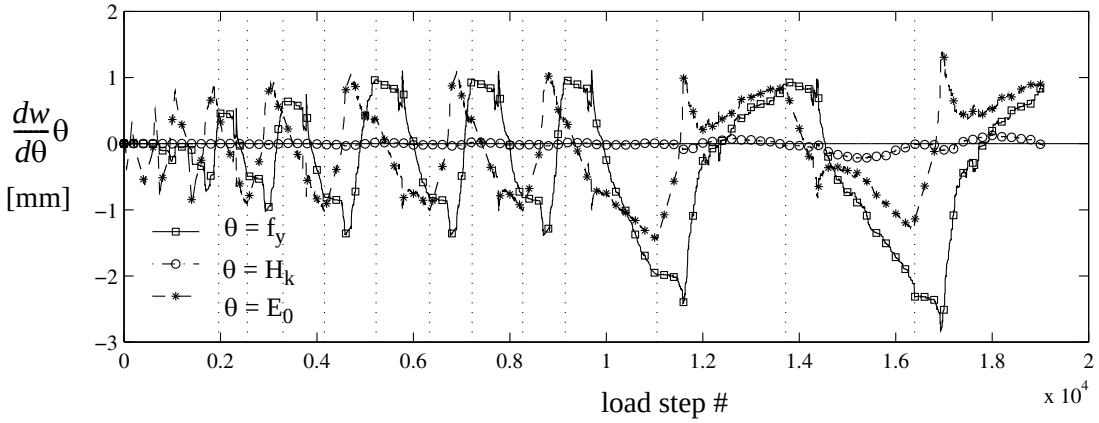

Figure 4.27 Frame IPC: sensitivities of the beam horizontal displacement *w* to steel beam material parameters

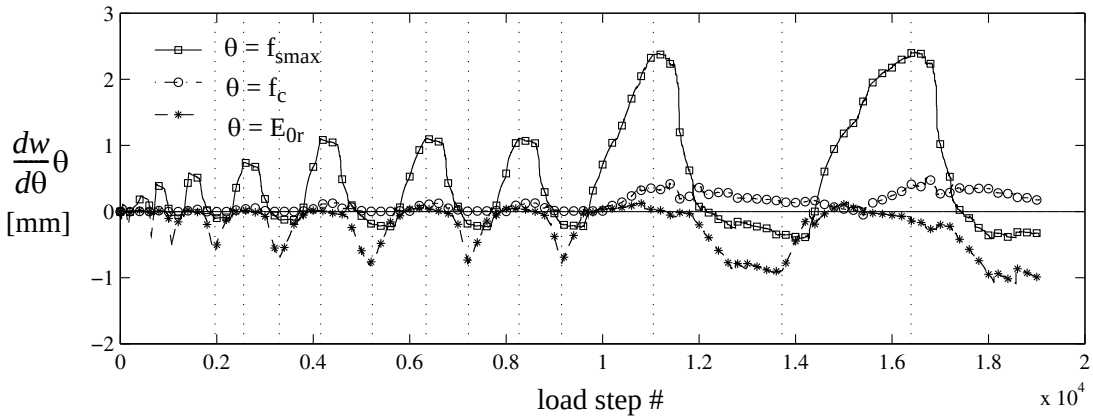

Figure 4.28 Frame IPC: sensitivities of the beam horizontal displacement *w* to parameters related to concrete slab and shear connection

The local response quantity considered here is the axial force N_2 in the steel beam at mid-span which is plotted in Fig. 4.29 as a function of the load step number. The sensitivities of this local response quantity to $\theta = f_y, f_{smax}, f_c$ are shown in Fig. 4.30. These three material parameters control the inelastic behavior of each component (steel beam, shear connection, and concrete slab) of the composite beam and thus influence the diffusion of the applied axial force from the steel beam to the concrete slab. It was found that for N_2, f_y is once again the most important response parameter (Zona et al. 2004). The sensitivities of N_2 as well as other internal forces (shear, bending moment) to most of the material parameters were found to be very erratic (high frequency spikes and discontinuities).

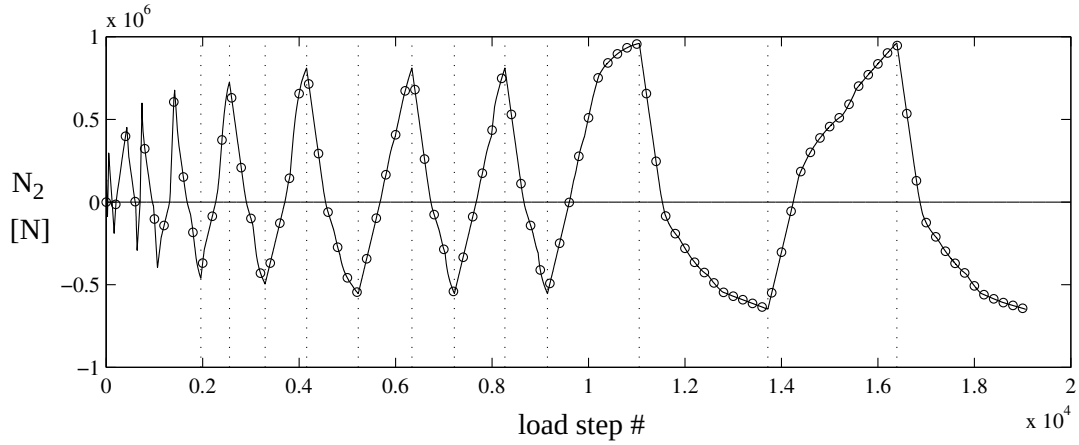

Figure 4.29 Frame IPC: axial force N_2 in the steel beam at mid-span as a function of the load step number

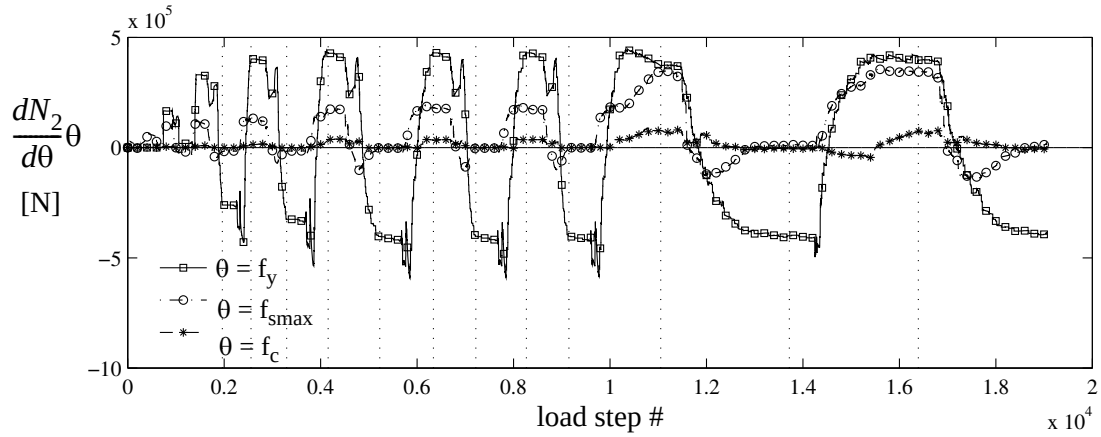

Figure 4.30 Frame IPC: sensitivities of axial force N_2 in the steel beam at mid-span to f_y, f_{smax}, f_c

The vertical dotted lines in Figures 4.24 to 4.30 mark the end of the last loading step or beginning of the first unloading step. Careful examination of the results revealed that no discontinuities occurred exactly at unloading events. This is consistent with prior

results on simpler benchmark problems (Conte et al. 2003). It thus appears that discontinuities in finite element response sensitivities are due to material state transitions from elastic to plastic and not vice versa.

All the sensitivity results presented were computed using the DDM and validated by FFD using increasingly small perturbations of the sensitivity parameters. Due to space limitation, the comparison between DDM and FFD results is shown here only for two cases. The first case consists of the sensitivity of the vertical deflection *v* at mid-span to the concrete strength f_c (Fig. 4.31). For the FFD analysis, three levels of perturbation of parameter f_c were considered, namely $\Delta\theta/\theta = 10^{-2}, 10^{-3}, 10^{-5}$. The second case consists of the sensitivity of the axial force N_2 in the steel beam at mid-span to the shear connection strength f_{smax} (Fig. 4.32). The same three levels of perturbation (i.e., $\Delta\theta/\theta = 10^{-2}, 10^{-3}, 10^{-5}$) were considered for parameter f_{smax}. From these two figures and their close-ups, the FFD results are shown to converge asymptotically to their DDM counterparts as the perturbation of the sensitivity parameter becomes increasingly small. In these two cases, the FFD results are converged to the DDM results for $\Delta\theta/\theta = 10^{-5}$.

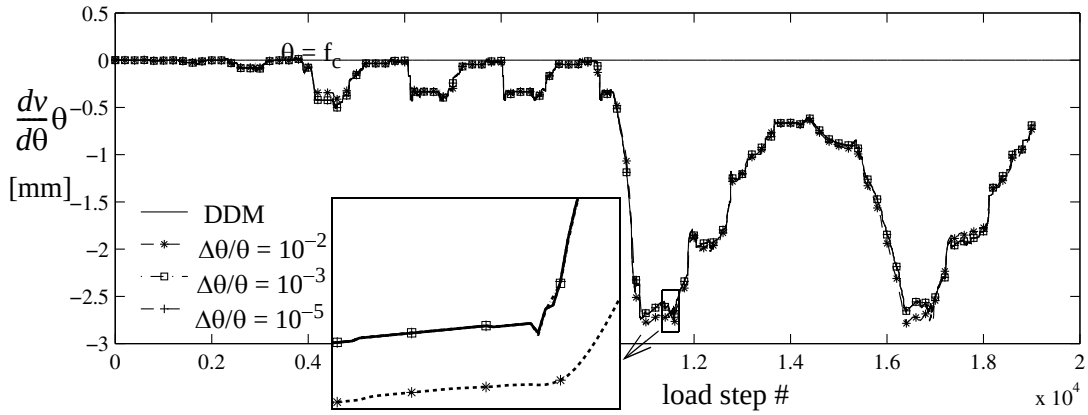

Figure 4.31 Frame IPC: sensitivities of vertical deflection v to f_c using DDM and FFD

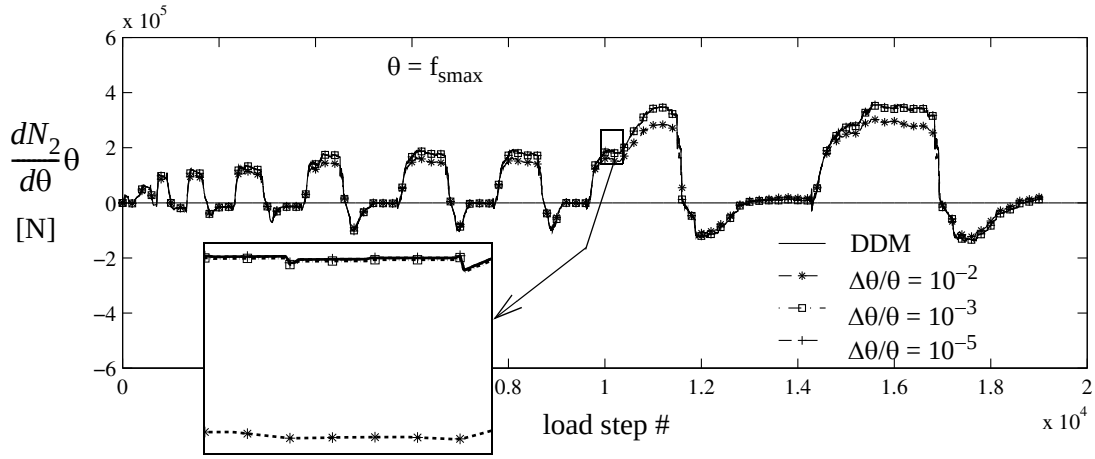

Figure 4.32 Frame IPC: sensitivities of the axial force N_2 to f_{smax} using DDM and FFD

4.7 CONCLUSIONS

This chapter focuses on materially-nonlinear-only analytical response sensitivity analysis, using displacement-based finite elements in conjunction with the Direct Differentiation Method (DDM), of composite beams with deformable shear connection under

quasi-static monotonic and cyclic loading conditions. Realistic uniaxial constitutive models are used for the steel and concrete materials as well as for the shear connection. The concrete and shear connection material models as well as the static condensation procedure at the element level are extended for response sensitivity computations using the DDM. Two benchmark problems that have been the object of experimental testing are used to illustrate the proposed methodology for response sensitivity analysis. The first benchmark problem consists of a two-span asymmetric continuous beam subjected to monotonic loading with a concentrated force. The second benchmark problem consists of a frame sub-assemblage subjected to quasi-static cyclic loading. The finite element response prediction is validated using experimental results available in the literature for the two benchmark problems. The response sensitivity analysis results obtained according to the Direct Differentiation Method (DDM) are validated by means of Forward Finite Difference (FFD) analysis. Selected results of response sensitivity analysis are presented in an effort to quantify the effect and relative importance of various material constitutive model parameters in regards to the nonlinear quasi-static monotonic and cyclic response of a tested steel-concrete composite beam. Using the benchmark problem considered, it is also shown that use of an inadequate convergence tolerance in the nonlinear finite element response calculation may introduce numerical errors in response sensitivity analysis results obtained using both the DDM and FFD analysis.

The algorithms developed in this study for nonlinear finite element response sensitivity analysis of steel-concrete composite structures have direct applications in structural

optimization, structural reliability analysis, and nonlinear finite element model updating for this type of structures.

4.8 ACKNOWLEDGEMENTS

Chapter 4, with minor modifications, is a reprint of the material as it appears in Journal of Engineering Mechanics ASCE (2005), Zona A., Barbato, M., and Conte, J.P., 131(11):1126-1139 (reprinted with permission from ASCE). The dissertation author was second author of this paper. He played a decisive role in the development of the finite element response sensitivity algorithms presented, contributing substantially to the preparation of the manuscript and to the implementation into FedeasLab of the response sensitivity algorithms for FE response sensitivity computation at the element, section and material constitutive model levels.

REFERENCES

Ansourian P. (1981) “Experiments on continuous composite beams”. *Proceedings of the Institution of Civil Engineers* Part 2, 71(Dec.):25-51.

Balan T.A., Filippou F.C., Popov E.P., (1997) “Constitutive model for 3D cyclic analysis of concrete structures”. *Journal of Engineering Mechanics* (ASCE), 123(2):143-153.

Balan T.A., Spacone E., Kwon M. (2001) “A 3D hypoplastic model for cyclic analysis of concrete structures”. *Engineering Structures*, 23:333-342.

Bathe K.J. (1995) *Finite Element Procedures*. Prentice Hall.

Bursi O.S., Gramola G. (2000) “Behaviour of composite substructures with full and partial shear connection under quasi-static cyclic and pseudo-dynamic displacements”. *Material and Structures* (RILEM), 33:154-163.

Conte J.P. (2001) “Finite element response sensitivity analysis in earthquake engineering”. *Earthquake Engineering Frontiers in the New Millennium*. Spencer & Hu, Swets & Zeitlinger, 395-401.

Conte J.P., Vijalapura P.K., Meghella M. (2003) “Consistent finite element response sensitivity analysis”. *Journal of Engineering Mechanics* (ASCE), 129(12):1380-1393.

Conte J.P., Barbato M., Spacone E. (2004) “Finite element response sensitivity analysis using force-based frame models”. *International Journal of Numerical Methods in Engineering*, 59(13):1781-1820.

Dall'Asta A. (2001) “Composite beams with weak shear connection”. *International Journal of Solids and Structures*, 38:5605-5624.

Dall'Asta A., Zona A. (2002) “Non-linear analysis of composite beams by a displacement approach”. *Computers and Structures*, 80(27-30):2217-2228.

Dall'Asta A., Zona A. (2003) “Evaluation of finite elements for the study of the ultimate behaviour of steel-concrete composite beams”. *Proceedings of the International Conference of Advances in Structures: Steel, Concrete, Composites and Aluminium*, June 23-25 2003, Sydney, Australia, 703-709.

Dall'Asta A., Zona A. (2004a) “Three-field mixed formulation for the non-linear analysis of composite beams with deformable shear connection”. *Finite Elements in Analysis and Design*, 40(4):425-448.

Dall'Asta A., Zona A. (2004b) “Slip locking in finite elements for composite beams with deformable shear connection”. *Finite Elements in Analysis and Design*, 40(13-14):1907-1930.

Dall'Asta A., Zona A. (2004c) “Comparison and validation of displacement and mixed elements for the non-linear analysis of continuous composite beams”. *Computers*

and Structures, 82(23-26):2117-2130.

Dall'Asta A., Zona A. (2005) "A finite element model for externally prestressed composite beams with deformable connection", *Journal of Structural Engineering* (ASCE), 131(5):706-714.

Ditlevsen O., Madsen H.O. (1996) *Structural Reliability Methods*. Wiley.

Eligehausen R., Popov E.P., Bertero V.V. (1983) "Local bond stress-slip relationships of deformed bars under generalized excitations". *Report No. 83/23*, EERC Earthquake Engineering Research Center, University of California, Berkeley, CA.

Filippou F.C. (2002) FEDEASLab Releases 2.2. *Private Communication*.

Franchin P. (2004) "Reliability of uncertain inelastic structures under earthquake excitations". *Journal of Engineering Mechanics* (ASCE), 130(2):180-191.

Johnson R.P., Molenstra N. (1991) "Partial shear connection in composite beams for buildings", *Proceedings of the Institution of Civil Engineers*, Part 2, 91(Apr).

Kleiber M., Antunez H., Hien T.D., Kowalczyk P. (1997) *Parameter Sensitivity in Nonlinear Mechanics: Theory and Finite Element Computations*. Wiley.

Kwon M., Spacone E. (2002) "Three-dimensional finite element analyses of reinforced concrete columns". *Computers and Structures*, 80:199-212.

Newmark N.M., Siess C.P., Viest I.M. (1951) "Tests and analysis of composite beams with incomplete interaction". *Proc. Soc. Exp. Stress Anal.*, 9(1):75-92.

Oehlers D.J., Bradford M.A. (2000) *Elementary Behaviour of Composite Steel and Concrete Structural Members*, Butterworth-Heinemann.

Ollgaard J.G., Slutter R.G., Fisher J.W. (1971) "Shear strength of stud connectors in lightweight and normal weight concrete". *AISC Engineering Journal*, 55-64.

Salari M.R., Spacone E. (2001) “Analysis of steel-concrete composite frames with bond-slip”. *Journal of Structural Engineering* (ASCE), 127(11):1243-1250.

Spacone E., El-Tawil S. (2004) "Nonlinear analysis of steel-concrete composite structures: state-of-the-art". *Journal of Structural Engineering* (ASCE), 130(2):159-168.

The MathWorks (1997) “Matlab - High performance numeric computation and visualization software”. *User's Guide*. Natick, MA.

Zona A., Barbato M., Conte J.P. (2004) “Finite element response sensitivity analysis of steel-concrete composite structures”. *Report SSRP-04/02*, Department of Structural Engineering, University of California, San Diego, CA.

CHAPTER 5

DDM-BASED RESPONSE SENSITIVITY ANALYSIS FOR THREE-FIELD MIXED FINITE ELEMENT FORMULATION

5.1 INTRODUCTION

As seen in previous chapters, sensitivity analysis is a very active research field in nonlinear structural analysis. FE response sensitivity formulations have been developed for displacement-based finite element models (Zhang and Der Kiureghian 1993; Conte 2001; Conte et al. 2003) and, recently, for force-based frame elements (Conte et al. 2004; Scott et al. 2004). The advantages gained in response analysis by using finite element formulations more advanced than the classical displacement-based formulation can be further extended to the realm of response sensitivity analysis (Barbato and Conte 2005).

A large body of research has been devoted to mixed finite element formulations since they were first introduced in the pioneering work of Pian (1964). Several finite elements based on different variational principles have been developed (Chien 1983; Washizu 1975; Malkus and Hughes 1978; Noor 1983; Belytschko et al. 2000) and relationships among them have been established (De Veubeke 1965; Stolarski and Belytschko 1987). Accuracy and performance have been thoroughly analyzed and improved and important properties have been recognized and explained, such as equivalence between various stress recovery techniques (Mota and Abel 2000) and ability to eliminate shear-locking

effects for specific applications (Belytschko et al. 2000). After more than three decades of research in the field, mixed finite elements are well established and largely adopted tools in a wide range of structural mechanics applications. However, to the authors knowledge, attempts of extending mixed finite element formulations to response sensitivity analysis by using the Direct Differentiation Method (DDM) are limited to linear elastic and quasi-static analysis (Pandey and Bakshi 1999).

Multi-field mixed finite element formulations were proposed, among others, for finite elements widely used in the structural engineering community such as frame elements. Mixed frame elements are more accurate in nonlinear analysis than displacement-based elements and are a possible alternative to the recently established force-based elements (Spacone et al. 1995). Examples are available in the recent literature for monolithic beams (Spacone et al. 1995, 1996; Taylor et al. 2003) and for composite beams with deformable shear connection (Ayoub and Filippou 2000; Dall'Asta and Zona 2004a).

This study focuses on the formulation of finite element response sensitivity analysis in the case of a nonlinear three-field mixed approach derived from the Hu-Washizu variational principle, considering both quasi-static and dynamic loadings. The formulation presented here is based on the general Direct Differentiation Method (DDM), which consists of differentiating consistently the space (finite element) and time (finite difference) discrete equations governing the structural response (Conte et al. 2003, 2004). The general formulation for finite element response sensitivity analysis using the three-field mixed formulation is then specialized and applied to frame finite element models. The results of the DDM are validated through Forward Finite Difference (FFD) analysis using as appli-

cation example a realistic steel-concrete composite frame structure subjected to quasi-static and dynamic loading, respectively. Both monolithic frame elements (Taylor et al. 2003) and composite frame elements with deformable shear connection (Dall'Asta and Zona 2004a) based on the three-field mixed formulation are included in this application example.

5.2 RESPONSE SENSITIVITY ANALYSIS AT THE ELEMENT LEVEL

5.2.1 General geometric and material nonlinear theory including shape sensitivity

The general formulation is presented for a structural model including geometric and material nonlinearities and considering material, shape, and loading sensitivities. An isoparametric finite element in Total Lagrangian formulation is considered.

Following Belytschko et al. (2000), three different domains need to be introduced:

(1) the parent domain, denoted by the symbol $\square$, with element coordinates $\boldsymbol{\xi} = [\xi_1, \xi_2, \xi_3]^T$;

(2) the reference (or initial configuration) domain, Ω_0, with coordinates $\mathbf{X} = [X_1, X_2, X_3]^T$;

(3) the current configuration domain, $\Omega(t)$, with coordinates $\mathbf{x}(t) = [x_1(t), x_2(t), x_3(t)]^T$, where t denotes time (or pseudo-time in quasi-static analysis).

Correspondingly, the following one-to-one mappings are defined:

(1) from parent domain to current configuration: $\mathbf{x} = \mathbf{x}(\boldsymbol{\xi}, t)$;

(2) from parent domain to reference configuration: $\mathbf{X} = \mathbf{X}(\boldsymbol{\xi})$;

(3) from reference configuration to current configuration: $\mathbf{x} = \mathbf{x}(\mathbf{X}, t)$.

It is supposed that the above mappings satisfy certain conditions of regularity such that the inverse mappings exist and the motion is well defined and sufficiently smooth.

As measure of strain, the Green-Lagrange strain is adopted, defined in tensorial form using the index notation as

$$E_{ij}^{G} = \frac{1}{2}\left(\frac{\partial u_i}{\partial X_j} + \frac{\partial u_j}{\partial X_i} + \frac{\partial u_k}{\partial X_i}\frac{\partial u_k}{\partial X_j}\right), \quad i, j = 1, 2, 3 \tag{5.1}$$

Using Voigt notation, the vector form of the Green-Lagrange strain tensor is defined as

$$\mathbf{E}_G = [E_{11}^{G}, E_{22}^{G}, E_{33}^{G}, 2E_{23}^{G}, 2E_{13}^{G}, 2E_{12}^{G}]^T \tag{5.2}$$

The work conjugate stress measure of the Green-Lagrange strain tensor is the second Piola-Kirchhoff stress tensor, S_{ij}^{PK2}, that can be expressed in vector form using Voigt notation as

$$\mathbf{S}_{PK2} = [S_{11}^{PK2}, S_{22}^{PK2}, S_{33}^{PK2}, S_{23}^{PK2}, S_{13}^{PK2}, S_{12}^{PK2}]^T, \tag{5.3}$$

The Hu-Washizu functional in Total Lagrangian formulation is (Belytschko et al. 2000)

$$\Pi_{HW}(\mathbf{u}, \mathbf{S}_{PK2}, \mathbf{E}_G) = \int_{\Omega_0} \varphi(\mathbf{E}_G) d\Omega_0 + \int_{\Omega_0} \mathbf{S}_{PK2}^{T}(\mathscr{H}\mathbf{u} - \mathbf{E}_G) d\Omega_0 - \Pi_{ext}(\mathbf{u}) \tag{5.4}$$

in which $\mathbf{u}$, $\mathbf{S}_{\mathrm{PK2}}$ and $\mathbf{E}_{\mathrm{G}}$ are the assumed displacement, stress and strain fields, respectively, $\varphi(\mathbf{E}_{\mathrm{G}})$ is the internal strain energy and $\mathscr{H}$ is a differential matrix operator defined as

$$\mathscr{H} = \mathscr{H}_{l} + \frac{1}{2}\mathscr{H}_{nl} \tag{5.5}$$

$$\mathscr{H}_{l} = \begin{bmatrix} \frac{\partial}{\partial X_1} & 0 & 0 & 0 & \frac{\partial}{\partial X_3} & \frac{\partial}{\partial X_2} \\ 0 & \frac{\partial}{\partial X_2} & 0 & \frac{\partial}{\partial X_3} & 0 & \frac{\partial}{\partial X_1} \\ 0 & 0 & \frac{\partial}{\partial X_3} & \frac{\partial}{\partial X_2} & \frac{\partial}{\partial X_1} & 0 \end{bmatrix}^{\mathrm{T}} \tag{5.6}$$

$$\mathscr{H}_{nl} = \begin{bmatrix} \frac{\partial u_1}{\partial X_1}\frac{\partial}{\partial X_1} & \frac{\partial u_2}{\partial X_1}\frac{\partial}{\partial X_1} & \frac{\partial u_3}{\partial X_1}\frac{\partial}{\partial X_1} \\ \frac{\partial u_1}{\partial X_2}\frac{\partial}{\partial X_2} & \frac{\partial u_2}{\partial X_2}\frac{\partial}{\partial X_2} & \frac{\partial u_3}{\partial X_2}\frac{\partial}{\partial X_2} \\ \frac{\partial u_1}{\partial X_3}\frac{\partial}{\partial X_3} & \frac{\partial u_2}{\partial X_3}\frac{\partial}{\partial X_3} & \frac{\partial u_3}{\partial X_3}\frac{\partial}{\partial X_3} \\ \left(\frac{\partial u_1}{\partial X_2}\frac{\partial}{\partial X_3} + \frac{\partial u_1}{\partial X_3}\frac{\partial}{\partial X_2}\right) & \left(\frac{\partial u_2}{\partial X_2}\frac{\partial}{\partial X_3} + \frac{\partial u_2}{\partial X_3}\frac{\partial}{\partial X_2}\right) & \left(\frac{\partial u_3}{\partial X_2}\frac{\partial}{\partial X_3} + \frac{\partial u_3}{\partial X_3}\frac{\partial}{\partial X_2}\right) \\ \left(\frac{\partial u_1}{\partial X_1}\frac{\partial}{\partial X_3} + \frac{\partial u_1}{\partial X_3}\frac{\partial}{\partial X_1}\right) & \left(\frac{\partial u_2}{\partial X_1}\frac{\partial}{\partial X_3} + \frac{\partial u_2}{\partial X_3}\frac{\partial}{\partial X_1}\right) & \left(\frac{\partial u_3}{\partial X_1}\frac{\partial}{\partial X_3} + \frac{\partial u_3}{\partial X_3}\frac{\partial}{\partial X_1}\right) \\ \left(\frac{\partial u_1}{\partial X_1}\frac{\partial}{\partial X_2} + \frac{\partial u_1}{\partial X_2}\frac{\partial}{\partial X_1}\right) & \left(\frac{\partial u_2}{\partial X_1}\frac{\partial}{\partial X_2} + \frac{\partial u_2}{\partial X_2}\frac{\partial}{\partial X_1}\right) & \left(\frac{\partial u_3}{\partial X_1}\frac{\partial}{\partial X_2} + \frac{\partial u_3}{\partial X_2}\frac{\partial}{\partial X_1}\right) \end{bmatrix} \tag{5.7}$$

where $\mathscr{H}_{l}$ and $\mathscr{H}_{nl}$ denote the linear and nonlinear parts, respectively, and the superposed T indicates the transpose operator. The term $\Pi_{\mathrm{ext}}(\mathbf{u})$ denotes the potential energy of the external forces and is defined as

$$\Pi_{ext}(\mathbf{u}) = \int_{\Omega_0} \rho_0 \mathbf{b}^T \mathbf{u} d\Omega_0 + \int_{\partial\Omega_{0\mathbf{t}}} \mathbf{t}_0^T \mathbf{u} d\Gamma_0 \tag{5.8}$$

where ρ denotes the mass density per unit volume, $\mathbf{b}$ are the body forces per unit mass, $\mathbf{t}$ are the surface tractions, $\partial\Omega_{\mathbf{t}}$ denotes the part of the boundary $\partial\Omega$ of Ω where the surface tractions are prescribed, $d\Omega$ and $d\Gamma$ denote an infinitesimal volume and surface element, respectively, and the subscript "0" indicates that the quantities to which it is attached are computed in the reference configuration. For the sake of brevity, the term representing the kinetic energy is not included in the Hu-Washizu functional Eq. (5.4). Notice that the kinetic energy term depends only on the displacement field and thus has the same form as in the case of the single-field (displacement-based) principle of virtual work (Belytschko et al. 2000).

Imposing the stationarity of the functional $\Pi_{HW}(\mathbf{u}, \mathbf{S}_{PK2}, \mathbf{E}_G)$ with respect to the three fields $\mathbf{u}$, $\mathbf{S}_{PK2}$ and $\mathbf{E}_G$, we obtain

$$\delta_{\mathbf{u}}\Pi_{HW} = 0 \Rightarrow \int_{\Omega_0} (\mathscr{H}^T \mathbf{S}_{PK2} - \rho_0 \mathbf{b})^T \delta\mathbf{u} \, d\Omega_0 - \int_{\partial\Omega_{0\mathbf{t}}} \mathbf{t}_0{}^T \delta\mathbf{u} \, d\Gamma_0 = 0 \tag{5.9}$$

$$\delta_{\mathbf{S}_{PK2}}\Pi_{HW} = 0 \Rightarrow \int_{\Omega_0} (\mathscr{H}\mathbf{u} - \mathbf{E}_G)^T \delta\mathbf{S}_{PK2} \, d\Omega_0 = 0 \tag{5.10}$$

$$\delta_{\mathbf{E}_G}\Pi_{HW} = 0 \Rightarrow \int_{\Omega_0} \left(\frac{\partial\varphi(\mathbf{E}_G)}{\partial\mathbf{E}_G} - \mathbf{S}_{PK2} \right)^T \delta\mathbf{E}_G \, d\Omega_0 = 0 \tag{5.11}$$

The classical Hu-Washizu formulation is limited to the case in which the internal energy $\varphi(\mathbf{E}_G)$ is a potential, as for elastic materials. Eqs. (5.9) through (5.11) assume the mean-

ing of weak forms of equilibrium, compatibility and constitutive law, respectively. In order to generalize the Hu-Washizu functional to the case of nonlinear inelastic materials, it is necessary to substitute the term $\frac{\partial \varphi(\mathbf{E}_G)}{\partial \mathbf{E}_G}$ of the variation $\delta_{\mathbf{E}_G}\Pi_{HW}$ in Eq. (5.11) with an expression for the second Piola-Kirchhoff stresses as a function of the Green-Lagrange strain history, i.e., $\hat{\mathbf{S}}_{PK2}(\mathbf{E}_G) = \hat{\mathbf{S}}_{PK2}(\mathbf{E}_G(\tau), \tau \in [0, t])$ obtained through any material constitutive law. In the sequel, superposed hats, i.e. $\hat{\bullet}$, are placed on stress and stress-derived fields evaluated in terms of other independently interpolated variables through the constitutive relations, while symbols without a superposed hat denote the assumed displacement, stress and strain fields. Thus, Eq. (5.11) becomes

$$\delta_{\mathbf{E}_G}\Pi_{HW} = 0 \Rightarrow \int_{\Omega_0} (\hat{\mathbf{S}}_{PK2}(\mathbf{E}_G) - \mathbf{S}_{PK2})^T \delta\mathbf{E}_G \, d\Omega_0 = 0 \tag{5.12}$$

Introducing the finite element discretization and considering explicitly the dependencies on the sensitivity parameter θ, the mapping from the parent domain to the current configuration is given by

$$\mathbf{x}(\boldsymbol{\xi}, \theta, t) = \mathbf{N}^e(\boldsymbol{\xi})\mathbf{x}_I^e(\theta, t) \tag{5.13}$$

and the mapping from the parent domain to the reference configuration is given by

$$\mathbf{X}(\boldsymbol{\xi}, \theta) = \mathbf{N}^e(\boldsymbol{\xi})\mathbf{X}_I^e(\theta) \tag{5.14}$$

where $\mathbf{x}_I^e(\theta, t)$ and $\mathbf{X}_I^e(\theta)$ denote the coordinates of node I of element “e” in the current configuration and reference configuration, respectively. In Eqs. (5.13) and (5.14), the

parameter θ could represent a nodal coordinate in the reference configuration (shape parameter), for example. In the sequel, the dependency on time is not expressed explicitly in order to avoid a heavy notation and because it can be easily understood from the context. From the finite element discretization, the displacement, stress and strain fields are expressed as

$$\begin{aligned} \mathbf{u}^e(\boldsymbol{\xi}, \theta) &= \mathbf{N}^e(\boldsymbol{\xi})\mathbf{q}^e(\theta) \\ \mathbf{S}^e_{PK2}(\boldsymbol{\xi}, \theta) &= \mathbf{S}^e(\boldsymbol{\xi})\mathbf{s}^e(\theta) \qquad e = 1, ..., N_{el} \\ \mathbf{E}^e_G(\boldsymbol{\xi}, \theta) &= \mathbf{E}^e(\boldsymbol{\xi})\mathbf{e}^e(\theta) \end{aligned} \tag{5.15}$$

where $\mathbf{q}^e(\theta)$, $\mathbf{s}^e(\theta)$, and $\mathbf{e}^e(\theta)$ denote the nodal displacement, stress and strain parameters, respectively; $\mathbf{N}^e(\boldsymbol{\xi})$, $\mathbf{S}^e(\boldsymbol{\xi})$, and $\mathbf{E}^e(\boldsymbol{\xi})$ are the shape (interpolation) functions for the displacement, stress and strain fields, respectively, all quantities being referred to element "e"; and N_{el} denotes the number of finite elements used discretizing the structure.

Substituting Eqs. (5.15) in Eqs. (5.9), (5.10) and (5.12), and recognizing that

$$\Omega_0 = \bigcup_{e=1}^{N_{el}} \Omega_0^e \tag{5.16}$$

where $\cup$ denotes the union operator and Ω_0^e is the volume of the element "e" in the reference configuration, we obtain the following weak forms of equilibrium, compatibility and constitutive law, respectively:

$$\sum_{e=1}^{N_{el}} \left(\int_{\Omega_0^e} (\mathscr{H}^T \mathbf{S}^e(\mathbf{X}) \mathbf{s}^e(\theta) - \rho_0(\mathbf{X}, \theta) \mathbf{b}(\mathbf{X}, \theta))^T \cdot \mathbf{N}^e(\mathbf{X}) d\Omega_0 \right) \delta \mathbf{q}^e - \sum_{e=1}^{N_{el}} \left(\int_{\partial \Omega_{0t}^e} \mathbf{t}_0^T(\mathbf{X}, \theta) \mathbf{N}^e(\mathbf{X}) d\Gamma_0 \right) \delta \mathbf{q}^e = 0 \tag{5.17}$$

$$\sum_{e=1}^{N_{el}} \left(\int_{\Omega_0^e} (\mathbf{E}^e(\mathbf{X}) \mathbf{e}^e(\theta) - \mathscr{H} \mathbf{N}^e(\mathbf{X}) \mathbf{q}^e(\theta))^T \cdot \mathbf{S}^e(\mathbf{X}) d\Omega_0 \right) \delta \mathbf{s}^e = 0 \tag{5.18}$$

$$\sum_{e=1}^{N_{el}} \left(\int_{\Omega_0^e} (\mathbf{S}^e(\mathbf{X}) \mathbf{s}^e(\theta) - \hat{\mathbf{S}}_{PK2}^e(\mathbf{E}^e(\mathbf{X}) \mathbf{e}^e(\theta), \theta))^T \cdot \mathbf{E}^e(\mathbf{X}) d\Omega_0 \right) \delta \mathbf{e}^e = 0 \tag{5.19}$$

Let us refer to a single element and drop the suffix "e" in the sequel. Considering the arbitrary (virtual) nature of $\delta \mathbf{q}^e$, $\delta \mathbf{s}^e$, and $\delta \mathbf{e}^e$ in the above three equations, we obtain the following governing equations for each of the finite elements used in the discretization of the structural system:

$$\bar{\mathbf{B}}^T(\theta) \mathbf{s}(\theta) - \mathbf{Q}(\theta) = \mathbf{0} \tag{5.20}$$

$$\bar{\mathbf{E}}(\theta) \mathbf{e}(\theta) - \bar{\mathbf{B}}(\theta) \mathbf{q}(\theta) = \mathbf{0} \tag{5.21}$$

$$\mathbf{a}(\mathbf{e}(\theta), \theta) - \bar{\mathbf{E}}^T(\theta) \mathbf{s}(\theta) = \mathbf{0} \tag{5.22}$$

in which

$$\begin{aligned} \mathbf{Q}(\theta) &= \int_{\Omega_0(\theta)} \rho_0(\mathbf{X}, \theta) \mathbf{b}^T(\mathbf{X}, \theta) \mathbf{N}(\mathbf{X}) d\Omega_0 + \int_{\partial \Omega_{0t}(\theta)} \mathbf{t}_0^T(\mathbf{X}, \theta) \mathbf{N}(\mathbf{X}) d\Gamma_0 \\ &= \int_{\square} \rho_0(\boldsymbol{\xi}, \theta) \mathbf{b}^T(\boldsymbol{\xi}, \theta) \mathbf{N}(\boldsymbol{\xi}) J(\boldsymbol{\xi}, \theta) d\square + \int_{\partial \square} \mathbf{t}_0^T(\boldsymbol{\xi}, \theta) \mathbf{N}(\boldsymbol{\xi}) J(\boldsymbol{\xi}, \theta) d(\partial \square) \end{aligned} \tag{5.23}$$

$$\bar{\mathbf{B}}(\theta) = \int_{\Omega_0(\theta)} \mathbf{S}^T(\mathbf{X})\mathbf{B}(\mathbf{X}, \theta)d\Omega_0 = \int_{\square} \mathbf{S}^T(\boldsymbol{\xi})\mathbf{B}(\boldsymbol{\xi}, \theta)J(\boldsymbol{\xi}, \theta)d\square \tag{5.24}$$

$$\mathbf{B}(\boldsymbol{\xi}, \theta) = \mathscr{H}(\boldsymbol{\xi}, \theta)\, \mathbf{N}(\boldsymbol{\xi}) \tag{5.25}$$

$$\bar{\mathbf{E}}(\theta) = \int_{\Omega_0(\theta)} \mathbf{S}^T(\mathbf{X})\mathbf{E}(\mathbf{X})d\Omega_0 = \int_{\square} \mathbf{S}^T(\boldsymbol{\xi})\mathbf{E}(\boldsymbol{\xi})J(\boldsymbol{\xi}, \theta)d\square \tag{5.26}$$

$$\begin{aligned} \mathbf{a}(\mathbf{e}(\theta), \theta) &= \int_{\Omega_0(\theta)} \mathbf{E}^T(\mathbf{X})\hat{\mathbf{S}}_{PK2}(\mathbf{E}(\mathbf{X})\mathbf{e}(\theta), \theta)d\Omega_0 \\ &= \int_{\square} \mathbf{E}^T(\boldsymbol{\xi})\hat{\mathbf{S}}_{PK2}(\mathbf{E}(\boldsymbol{\xi})\mathbf{e}(\theta), \theta)J(\boldsymbol{\xi}, \theta)d\square \end{aligned} \tag{5.27}$$

where the symbol $\mathscr{H}(\boldsymbol{\xi}, \theta)$ is used to highlight the dependency of the operator $\mathscr{H}$ on $\boldsymbol{\xi}$ and θ and $J(\boldsymbol{\xi}, \theta)$ denotes the Jacobian of the transformation between the parent domain $\square$ and the reference domain Ω_0 such that $d\Omega_0 = J(\boldsymbol{\xi}, \theta) \cdot d\square$, $\boldsymbol{\xi} \in \square$. Eqs. (5.20) through (5.22) constitute a system of $n_q+n_s+n_e$ coupled equations in $n_q+n_s+n_e$ unknowns, where n_q, n_s and n_e denotes the number of displacement, stress and strain parameters, respectively. Eq. (5.22) is nonlinear if any of the used material models is non-linear, Eqs. (5.20) and (5.21) are nonlinear since $\bar{\mathbf{B}}(\theta)$ depends on $\mathbf{q}(\theta)$ through the non-linear part of the operator $\mathscr{H}(\boldsymbol{\xi}, \theta)$ and $\mathbf{Q}(\theta)$ depends implicitly on $\mathbf{q}(\theta)$ when $\mathbf{t}_0$ is displacement-dependent. Notice that the surface tractions $\mathbf{t}_0$ at the element boundaries also contain the reactions of adjacent elements and thus are generally functions of the nodal displacements, i.e., $\mathbf{t}_0 = \mathbf{t}_0(\mathbf{q}(\theta), \theta)$. The nonlinear problem is solved using an incremental-iterative procedure, such as the Newton-Raphson method.

Differentiating Eq. (5.21) exactly with respect to θ and performing some algebraic manipulations (see Appendix A), we obtain

$$\frac{d\mathbf{e}(\theta)}{d\theta} = \bar{\mathbf{D}}_t^{-1}(\theta)\bar{\mathbf{E}}^T(\theta)\bar{\bar{\mathbf{D}}}_t^{-1}(\theta)\left(\bar{\mathbf{B}}(\theta)\frac{d\mathbf{q}(\theta)}{d\theta} + \frac{d\bar{\mathbf{B}}(\theta)}{d\theta}\mathbf{q}(\theta) - \frac{d\bar{\mathbf{E}}(\theta)}{d\theta}\mathbf{e}(\theta)\right) \tag{5.28}$$

in which the following matrices are introduced:

$$\bar{\mathbf{D}}_t(\theta) = \int_{\Omega_0(\theta)} \mathbf{E}^T(\mathbf{X})\mathbf{k}_{IP}(\mathbf{X})\mathbf{E}(\mathbf{X})d\Omega_0 \tag{5.29}$$

$$\bar{\bar{\mathbf{D}}}_t(\theta) = \bar{\mathbf{E}}(\theta) \cdot \bar{\mathbf{D}}_t^{-1}(\theta) \cdot \bar{\mathbf{E}}^T(\theta) \tag{5.30}$$

where $\mathbf{k}_{IP}(\mathbf{X})$ denotes the material consistent (or algorithmic) tangent moduli at the integration point. Matrices $\bar{\mathbf{D}}_t(\theta)$ and $\bar{\bar{\mathbf{D}}}_t(\theta)$ are required in the element state determination for the response and in the response sensitivity computation. The reader is referred to Stolarski and Belytschko (1987) for the conditions under which these two matrices are invertible assuming that $\mathbf{k}_{IP}(\mathbf{X})$ is not singular.

Differentiating Eq. $(5.15)_3$ and the material constitutive relation with respect to θ yields, respectively

$$\frac{d\mathbf{E}_G(\boldsymbol{\xi}, \theta)}{d\theta} = \mathbf{E}(\boldsymbol{\xi})\frac{d\mathbf{e}(\theta)}{d\theta} \tag{5.31}$$

$$\begin{aligned}\frac{d\hat{\mathbf{S}}_{PK2}(\boldsymbol{\xi}, \theta)}{d\theta} &= \left.\frac{\partial\hat{\mathbf{S}}_{PK2}(\boldsymbol{\xi}, \theta)}{\partial\mathbf{E}_G}\right|_{\theta} \frac{d\mathbf{E}_G(\boldsymbol{\xi}, \theta)}{d\theta} + \left.\frac{\partial\hat{\mathbf{S}}_{PK2}(\boldsymbol{\xi}, \theta)}{\partial\theta}\right|_{\mathbf{E}_G} \\ &= \mathbf{k}_{IP}(\boldsymbol{\xi})\mathbf{E}(\boldsymbol{\xi})\frac{d\mathbf{e}(\theta)}{d\theta} + \left.\frac{\partial\hat{\mathbf{S}}_{PK2}(\boldsymbol{\xi}, \theta)}{\partial\theta}\right|_{\mathbf{e}}\end{aligned} \tag{5.32}$$

Differentiating Eq. (5.27) with respect to θ gives

$$\begin{aligned}\frac{d\mathbf{a}(\mathbf{e}(\theta),\theta)}{d\theta} = &\int_{\square} \mathbf{E}^{T}(\boldsymbol{\xi})\frac{d\hat{\mathbf{S}}_{PK2}(\boldsymbol{\xi},\theta)}{d\theta}J(\boldsymbol{\xi},\theta)d\square \\ &+ \int_{\square} \mathbf{E}^{T}(\boldsymbol{\xi})\hat{\mathbf{S}}_{PK2}(\boldsymbol{\xi},\theta)\frac{dJ(\boldsymbol{\xi},\theta)}{d\theta}d\square\end{aligned} \tag{5.33}$$

Eq. (5.33) is obtained noting that, if $f(\mathbf{X},\theta)$ is a function defined in $\Omega_0(\theta)$ and $I(\theta)$ denotes the integral of this function over the reference domain, then

$$I(\theta) = \int_{\Omega_0(\theta)} f(\mathbf{X},\theta)d\Omega_0 = \int_{\square} f(\boldsymbol{\xi},\theta)J(\boldsymbol{\xi},\theta)d\square \tag{5.34}$$

from which

$$\begin{aligned}\frac{dI(\theta)}{d\theta} = \frac{d}{d\theta}\left(\int_{\square} f(\boldsymbol{\xi},\theta)J(\boldsymbol{\xi},\theta)d\square\right) = \int_{\square}\frac{d}{d\theta}[f(\boldsymbol{\xi},\theta)J(\boldsymbol{\xi},\theta)]d\square \\ = \int_{\square}\frac{df(\boldsymbol{\xi},\theta)}{d\theta}J(\boldsymbol{\xi},\theta)d\square + \int_{\square} f(\boldsymbol{\xi},\theta)\frac{dJ(\boldsymbol{\xi},\theta)}{d\theta}d\square\end{aligned} \tag{5.35}$$

Finally, by differentiating Eqs. (5.22) and (5.20) with respect to θ and performing some algebraic manipulations (see Appendix A), we obtain, respectively,

$$\frac{d\mathbf{s}(\mathbf{e}(\theta),\theta)}{d\theta} = \bar{\bar{\mathbf{D}}}_t^{-1}(\theta)\bar{\mathbf{E}}(\theta)\bar{\mathbf{D}}_t^{-1}(\theta)\left(\frac{d\mathbf{a}(\mathbf{e}(\theta),\theta)}{d\theta} - \frac{d(\bar{\mathbf{E}}^{T}(\theta))}{d\theta}\mathbf{s}(\mathbf{e}(\theta),\theta)\right) \tag{5.36}$$

$$\frac{d\mathbf{Q}(\mathbf{e}(\theta),\theta)}{d\theta} = \bar{\mathbf{B}}^{T}(\theta)\frac{d\mathbf{s}(\mathbf{e}(\theta),\theta)}{d\theta} + \frac{d(\bar{\mathbf{B}}^{T}(\theta))}{d\theta}\mathbf{s}(\mathbf{e}(\theta),\theta) \tag{5.37}$$

In order to compute the conditional response sensitivities (for $\mathbf{q}$ fixed, thus with $\left.\frac{\partial \mathbf{q}(\theta)}{\partial \theta}\right|_{\mathbf{q}} = \mathbf{0}$), Eqs. (5.28), (5.31) through (5.33), (5.36) and (5.37) are modified as

$$\left.\frac{\partial \mathbf{e}(\theta)}{\partial \theta}\right|_{\mathbf{q}} = \bar{\mathbf{D}}_{\mathrm{t}}^{-1}(\theta)\bar{\mathbf{E}}^{\mathrm{T}}(\theta)\bar{\bar{\mathbf{D}}}_{\mathrm{t}}^{-1}(\theta)\left(\left.\frac{\partial \bar{\mathbf{B}}(\theta)}{\partial \theta}\right|_{\mathbf{q}} \mathbf{q}(\theta) - \frac{\mathrm{d}\bar{\mathbf{E}}(\theta)}{\mathrm{d}\theta}\mathbf{e}(\theta)\right) \tag{5.38}$$

$$\left.\frac{\partial \mathbf{E}_{\mathrm{G}}(\boldsymbol{\xi}, \theta)}{\partial \theta}\right|_{\mathbf{q}} = \mathbf{E}(\boldsymbol{\xi})\left.\frac{\partial \mathbf{e}(\theta)}{\partial \theta}\right|_{\mathbf{q}} \tag{5.39}$$

$$\left.\frac{\partial \hat{\mathbf{S}}_{\mathrm{PK2}}(\boldsymbol{\xi}, \theta)}{\partial \theta}\right|_{\mathbf{q}} = \mathbf{k}_{\mathrm{IP}}(\boldsymbol{\xi})\mathbf{E}(\boldsymbol{\xi})\left.\frac{\partial \mathbf{e}(\theta)}{\partial \theta}\right|_{\mathbf{q}} + \left.\frac{\partial \hat{\mathbf{S}}_{\mathrm{PK2}}(\boldsymbol{\xi}, \theta)}{\partial \theta}\right|_{\mathbf{e},\,\mathbf{q}} \tag{5.40}$$

$$\begin{aligned}\left.\frac{\partial \mathbf{a}(\mathbf{e}(\theta), \theta)}{\partial \theta}\right|_{\mathbf{q}} = &\int_{\square} \mathbf{E}^{\mathrm{T}}(\boldsymbol{\xi})\left.\frac{\partial \hat{\mathbf{S}}_{\mathrm{PK2}}(\boldsymbol{\xi}, \theta)}{\partial \theta}\right|_{\mathbf{q}} \mathrm{J}(\boldsymbol{\xi}, \theta)\mathrm{d}\square \\ &+ \int_{\square} \mathbf{E}^{\mathrm{T}}(\boldsymbol{\xi})\hat{\mathbf{S}}_{\mathrm{PK2}}(\boldsymbol{\xi}, \theta)\frac{\mathrm{dJ}(\boldsymbol{\xi}, \theta)}{\mathrm{d}\theta}\mathrm{d}\square\end{aligned} \tag{5.41}$$

$$\left.\frac{\partial \mathbf{s}(\mathbf{e}(\theta), \theta)}{\partial \theta}\right|_{\mathbf{q}} = \bar{\bar{\mathbf{D}}}_{\mathrm{t}}^{-1}(\theta)\bar{\mathbf{E}}(\theta)\bar{\mathbf{D}}_{\mathrm{t}}^{-1}(\theta)\left(\left.\frac{\partial \mathbf{a}(\mathbf{e}(\theta), \theta)}{\partial \theta}\right|_{\mathbf{q}} - \frac{\mathrm{d}(\bar{\mathbf{E}}^{\mathrm{T}}(\theta))}{\mathrm{d}\theta}\mathbf{s}(\mathbf{e}(\theta), \theta)\right) \tag{5.42}$$

$$\left.\frac{\partial \mathbf{Q}(\mathbf{e}(\theta), \theta)}{\partial \theta}\right|_{\mathbf{q}} = \bar{\mathbf{B}}^{\mathrm{T}}(\theta)\left.\frac{\partial \mathbf{s}(\mathbf{e}(\theta), \theta)}{\partial \theta}\right|_{\mathbf{q}} + \left.\frac{\partial(\bar{\mathbf{B}}^{\mathrm{T}}(\theta))}{\partial \theta}\right|_{\mathbf{q}} \mathbf{s}(\mathbf{e}(\theta), \theta) \tag{5.43}$$

where the quantity $\left.\frac{\partial \hat{\mathbf{S}}_{\mathrm{PK2}}(\boldsymbol{\xi}, \theta)}{\partial \theta}\right|_{\mathbf{e},\,\mathbf{q}}$ in Eq. (5.40) is computed through conditional differentiation (at the material level) of the material constitutive law. Note that $\bar{\mathbf{E}}(\theta)$ depends on θ only through $\Omega_0(\theta)$, and thus $\frac{\mathrm{d}\bar{\mathbf{E}}(\theta)}{\mathrm{d}\theta} = \left.\frac{\partial \bar{\mathbf{E}}(\theta)}{\partial \theta}\right|_{\mathbf{q}}$. Furthermore, $\mathbf{e}(\theta)$ depends on θ

both explicitly and implicitly through $\mathbf{q}(\theta)$, i.e., $\mathbf{e}(\theta) = \mathbf{e}(\mathbf{q}(\theta), \theta)$, as shown in Eq. (5.28). The quantities $\mathbf{s}(\theta)$ and $\mathbf{Q}(\theta)$ also depend on θ both explicitly and implicitly through $\mathbf{e}(\theta)$, since they are functions of $\mathbf{a}(\mathbf{e}(\theta), \theta)$ as shown in Eqs. (5.36) and (5.37).

5.2.2 Specialization to geometric linear formulation

If linear geometry (i.e., small displacements and small strains) is assumed, the three-field mixed finite element formulation can be obtained from the stationarity conditions of the Hu-Washizu functional, that can be written as (Washizu 1975)

$$\Pi_{\mathrm{HW}}(\mathbf{u}, \boldsymbol{\sigma}, \boldsymbol{\epsilon}) = \int_{\Omega} \varphi(\boldsymbol{\epsilon}) \mathrm{d}\Omega + \int_{\Omega} \boldsymbol{\sigma}^{\mathrm{T}} (\mathscr{D}\mathbf{u} - \boldsymbol{\epsilon}) \mathrm{d}\Omega - \Pi_{\mathrm{ext}}(\mathbf{u}) \tag{5.44}$$

where $\mathbf{u}$, $\boldsymbol{\sigma}$ and $\boldsymbol{\epsilon}$ are the assumed displacement, stress and (small) strain fields, respectively, $\varphi(\boldsymbol{\epsilon})$ is the internal strain energy, $\mathscr{D}$ is a linear differential operator matrix defined as

$$\mathscr{D} = \begin{bmatrix} \dfrac{\partial}{\partial \mathrm{X}_1} & 0 & 0 & 0 & \dfrac{\partial}{\partial \mathrm{X}_3} & \dfrac{\partial}{\partial \mathrm{X}_2} \\ 0 & \dfrac{\partial}{\partial \mathrm{X}_2} & 0 & \dfrac{\partial}{\partial \mathrm{X}_3} & 0 & \dfrac{\partial}{\partial \mathrm{X}_1} \\ 0 & 0 & \dfrac{\partial}{\partial \mathrm{X}_3} & \dfrac{\partial}{\partial \mathrm{X}_2} & \dfrac{\partial}{\partial \mathrm{X}_1} & 0 \end{bmatrix}^{\mathrm{T}} \tag{5.45}$$

As in the previous section, matrix notation and Voigt notation are used (Belytschko et al. 2000) here. The term $\Pi_{\mathrm{ext}}(\mathbf{u})$ denotes the potential energy of the external forces and is defined as

$$\Pi_{ext}(\mathbf{u}) = \int_{\Omega} \mathbf{b}^T \mathbf{u} d\Omega + \int_{\partial\Omega_t} \mathbf{t}^T \mathbf{u} d\Gamma \tag{5.46}$$

As in the general formulation presented in previous section, the term representing the kinetic energy is not included in the Hu-Washizu functional in Eq. (5.44).

Imposing stationarity of the Hu-Washizu functional in Eq. (5.44) with respect to the three fields **u**, $\boldsymbol{\sigma}$ and $\boldsymbol{\epsilon}$, yields

$$\delta_{\mathbf{u}}\Pi_{HW} = 0 \Rightarrow \int_{\Omega} (\mathscr{D}^T \boldsymbol{\sigma} - \mathbf{b})^T \delta\mathbf{u} d\Omega - \int_{\partial\Omega_t} \mathbf{t}^T \delta\mathbf{u} d\Gamma = 0 \tag{5.47}$$

$$\delta_{\boldsymbol{\sigma}}\Pi_{HW} = 0 \Rightarrow \int_{\Omega} (\mathscr{D}\,\mathbf{u} - \boldsymbol{\epsilon})^T \delta\boldsymbol{\sigma} d\Omega = 0 \tag{5.48}$$

$$\delta_{\boldsymbol{\epsilon}}\Pi_{HW} = 0 \Rightarrow \int_{\Omega} \left(\frac{\partial\varphi(\boldsymbol{\epsilon})}{\partial\boldsymbol{\epsilon}} - \boldsymbol{\sigma} \right)^T \delta\boldsymbol{\epsilon} d\Omega = 0 \tag{5.49}$$

The classical Hu-Washizu formulation is limited to the case in which the internal energy $\varphi(\boldsymbol{\epsilon})$ is a potential, as for elastic materials. Eqs. (5.47) through (5.49) assume the meaning of weak forms of equilibrium, compatibility and constitutive law, respectively. In order to generalize the Hu-Washizu functional to the case of nonlinear inelastic materials, it is necessary to substitute the term $\frac{\partial\varphi(\boldsymbol{\epsilon})}{\partial\boldsymbol{\epsilon}}$ of the variation $\delta_{\boldsymbol{\epsilon}}\Pi_{HW}$ in Eq. (5.49) with an expression for the stresses as a function of the strain history, i.e., $\hat{\boldsymbol{\sigma}}(\boldsymbol{\epsilon}) = \hat{\boldsymbol{\sigma}}(\boldsymbol{\epsilon}(\tau), \tau \in [0, t])$, obtained through any material constitutive law.

The finite element approximations of the three independently interpolated fields **u**, $\boldsymbol{\sigma}$ and $\boldsymbol{\epsilon}$ take the form, respectively,

$$\begin{aligned} \mathbf{u}^e(\mathbf{X}, \theta) &= \mathbf{N}^e(\mathbf{X})\mathbf{q}^e(\theta) \\ \boldsymbol{\sigma}^e(\mathbf{X}, \theta) &= \mathbf{S}^e(\mathbf{X})\mathbf{s}^e(\theta) \qquad e = 1, ..., N_{el} \\ \boldsymbol{\epsilon}^e(\mathbf{X}, \theta) &= \mathbf{E}^e(\mathbf{X})\mathbf{e}^e(\theta) \end{aligned} \tag{5.50}$$

Henceforth, the dependencies of the different quantities on the sensitivity parameter θ and on the position vector $\mathbf{X} = [X_1, X_2, X_3]^T$ are shown explicitly because of their important role in the derivation of the response sensitivity equations. Unlike in the previous section, relations for shape sensitivity computations are not derived; they would require considering the dependencies of shape functions and integration domains on the sensitivity parameter θ.

Substituting Eqs. (5.50) in Eqs. (5.47) through (5.49), we obtain the following weak forms of equilibrium, compatibility and constitutive law, respectively,

$$\sum_{e=1}^{N_{el}} \left(\int_{\Omega^e} (\mathscr{D}^T \mathbf{S}^e(\mathbf{X})\mathbf{s}^e(\theta) - \mathbf{b}^e(\mathbf{X}))^T \cdot \mathbf{N}^e(\mathbf{X}) d\Omega - \int_{\partial\Omega_t^e} \mathbf{t}^T(\mathbf{X})\mathbf{N}^e(\mathbf{X}) d\Gamma \right) \delta\mathbf{q}^e = 0 \tag{5.51}$$

$$\sum_{e=1}^{N_{el}} \left(\int_{\Omega^e} (\mathbf{E}^e(\mathbf{X})\mathbf{e}^e(\theta) - \mathscr{D}\mathbf{N}^e(\mathbf{X})\mathbf{q}^e(\theta))^T \cdot \mathbf{S}^e(\mathbf{X}) d\Omega \right) \delta\mathbf{s}^e = 0 \tag{5.52}$$

$$\sum_{e=1}^{N_{el}} \left(\int_{\Omega^e} (\mathbf{S}^e(\mathbf{X})\mathbf{s}^e(\theta) - \hat{\boldsymbol{\sigma}}^e(\mathbf{E}^e(\mathbf{X})\mathbf{e}^e(\theta), \theta))^T \cdot \mathbf{E}^e(\mathbf{X}) d\Omega \right) \delta\mathbf{e}^e = 0 \tag{5.53}$$

Let us define $\mathbf{B}^e(\mathbf{X}) = \mathscr{D}\mathbf{N}^e(\mathbf{X})$ and drop the suffix "e" in the sequel. Considering the arbitrary (virtual) nature of $\delta\mathbf{q}^e$, $\delta\mathbf{s}^e$, and $\delta\mathbf{e}^e$ in Eqs. (5.51) through (5.53), we

obtain the following governing equations for each of the finite elements used in the discretization of the structural system:

$$\bar{\mathbf{B}}^{\mathrm{T}}\mathbf{s}(\theta) - \mathbf{Q}(\theta) = \mathbf{0} \tag{5.54}$$

$$\bar{\mathbf{E}}\mathbf{e}(\theta) - \bar{\mathbf{B}}\mathbf{q}(\theta) = \mathbf{0} \tag{5.55}$$

$$\mathbf{a}(\mathbf{e}(\theta), \theta) - \bar{\mathbf{E}}^{\mathrm{T}}\mathbf{s}(\theta) = \mathbf{0} \tag{5.56}$$

where

$$\mathbf{Q}(\theta) = \int_{\Omega} \mathbf{b}^{\mathrm{T}}(\mathbf{X}, \theta)\mathbf{N}(\mathbf{X})\mathrm{d}\Omega + \int_{\partial\Omega_{\mathbf{t}}} \mathbf{t}^{\mathrm{T}}(\mathbf{X}, \theta)\mathbf{N}(\mathbf{X})\mathrm{d}\Gamma \tag{5.57}$$

$$\bar{\mathbf{B}} = \int_{\Omega} \mathbf{S}^{\mathrm{T}}(\mathbf{X})\mathbf{B}(\mathbf{X})\mathrm{d}\Omega \tag{5.58}$$

$$\bar{\mathbf{E}} = \int_{\Omega} \mathbf{S}^{\mathrm{T}}(\mathbf{X})\mathbf{E}(\mathbf{X})\mathrm{d}\Omega \tag{5.59}$$

$$\mathbf{a}(\mathbf{e}(\theta), \theta) = \int_{\Omega} \mathbf{E}^{\mathrm{T}}(\mathbf{X})\hat{\boldsymbol{\sigma}}(\mathbf{E}(\mathbf{X})\mathbf{e}(\theta), \theta)\mathrm{d}\Omega \tag{5.60}$$

Eqs. (5.54) through (5.56) represent a system of $n_q+n_s+n_e$ (generally) coupled equations in $n_q+n_s+n_e$ unknowns, where n_q, n_s and n_e denote the number of displacement, stress and strain parameters, respectively. Eqs. (5.54) and (5.55) are linear, while Eq. (5.56) is nonlinear if any of the used material models is nonlinear. The nonlinear problem is solved using an incremental-iterative scheme, such as the Newton-Raphson method. In some special cases the matrix $\bar{\mathbf{E}}$ is invertible (e.g., when the stress shape functions $\mathbf{S}(\mathbf{X})$ and strain shape functions $\mathbf{E}(\mathbf{X})$ are identical) and Eqs. (5.54) through (5.56) can be uncoupled and

solved sequentially. However, the general case is considered hereunder, while a special case for which the matrix $\bar{\mathbf{E}}$ is invertible will be presented later for a specific finite element implementation.

Differentiating Eq. (5.55) with respect to θ and pre-multiplying by $\bar{\mathbf{D}}_t^{-1}\bar{\mathbf{E}}^T\bar{\bar{\mathbf{D}}}_t^{-1}$ yields the following relation, after some algebraic manipulations (see Appendix A):

$$\frac{d\mathbf{e}(\theta)}{d\theta} = \bar{\mathbf{D}}_t^{-1}\bar{\mathbf{E}}^T\bar{\bar{\mathbf{D}}}_t^{-1}\bar{\mathbf{B}}\frac{d\mathbf{q}(\theta)}{d\theta} \tag{5.61}$$

where, similarly as in the previous section, matrices $\bar{\mathbf{D}}_t$ and $\bar{\bar{\mathbf{D}}}_t$ are defined as

$$\bar{\mathbf{D}}_t = \int_\Omega \mathbf{E}^T(\mathbf{X})\mathbf{k}_{IP}(\mathbf{X})\mathbf{E}(\mathbf{X})d\Omega \tag{5.62}$$

$$\bar{\bar{\mathbf{D}}}_t = \bar{\mathbf{E}}\bar{\mathbf{D}}_t^{-1}\bar{\mathbf{E}}^T \tag{5.63}$$

These matrices are required in the element state determination for the response and in the response sensitivity computation. The reader is referred to Stolarski and Belytschko (1987) for the conditions under which these two matrices are invertible assuming that $\mathbf{k}_{IP}(\mathbf{X})$ is not singular.

Differentiating Eq. $(5.50)_3$ and the material constitutive relation with respect to θ yields, respectively,

$$\frac{d\boldsymbol{\epsilon}(\mathbf{X},\theta)}{d\theta} = \mathbf{E}(\mathbf{X})\frac{d\mathbf{e}(\theta)}{d\theta} \tag{5.64}$$

$$\begin{aligned}\frac{d\hat{\boldsymbol{\sigma}}(\mathbf{X},\theta)}{d\theta} &= \left.\frac{\partial\hat{\boldsymbol{\sigma}}(\mathbf{X},\theta)}{\partial\boldsymbol{\epsilon}}\right|_{\theta}\frac{d\boldsymbol{\epsilon}(\mathbf{X},\theta)}{d\theta} + \left.\frac{\partial\hat{\boldsymbol{\sigma}}(\mathbf{X},\theta)}{\partial\theta}\right|_{\boldsymbol{\epsilon}} \\ &= \left(\mathbf{k}_{\mathrm{IP}}(\mathbf{X})\mathbf{E}(\mathbf{X})\frac{d\mathbf{e}(\theta)}{d\theta} + \left.\frac{\partial\hat{\boldsymbol{\sigma}}(\mathbf{X},\theta)}{\partial\theta}\right|_{\mathbf{e}}\right)\end{aligned} \tag{5.65}$$

Differentiating Eq. (5.60) with respect to θ and substituting Eqs. (5.65) and (5.62) in the resulting equation gives

$$\frac{d\mathbf{a}(\mathbf{e}(\theta),\theta)}{d\theta} = \int_{\Omega}\mathbf{E}^{\mathrm{T}}(\mathbf{X})\frac{d\hat{\boldsymbol{\sigma}}(\mathbf{X},\theta)}{d\theta}d\Omega = \bar{\mathbf{D}}_{\mathrm{t}}\frac{d\mathbf{e}(\theta)}{d\theta} + \int_{\Omega}\mathbf{E}^{\mathrm{T}}(\mathbf{X})\left.\frac{\partial\hat{\boldsymbol{\sigma}}(\mathbf{X},\theta)}{\partial\theta}\right|_{\mathbf{e}}d\Omega \tag{5.66}$$

Finally, by differentiating Eqs. (5.56) and (5.54) with respect to θ and performing some algebraic manipulations (see Appendix A), we obtain, respectively,

$$\frac{d\mathbf{s}(\mathbf{e}(\theta),\theta)}{d\theta} = \bar{\bar{\mathbf{D}}}_{\mathrm{t}}^{-1}\bar{\bar{\mathbf{E}}}\bar{\mathbf{D}}_{\mathrm{t}}^{-1}\frac{d\mathbf{a}(\mathbf{e}(\theta),\theta)}{d\theta} \tag{5.67}$$

$$\frac{d\mathbf{Q}(\mathbf{e}(\theta),\theta)}{d\theta} = \bar{\mathbf{B}}^{\mathrm{T}}\frac{d\mathbf{s}(\mathbf{e}(\theta),\theta)}{d\theta} \tag{5.68}$$

In order to compute the conditional response sensitivities (for $\mathbf{q}$ fixed, thus with $\left.\frac{\partial\mathbf{q}(\theta)}{\partial\theta}\right|_{\mathbf{q}} = \mathbf{0}$), Eqs. (5.61) and (5.64) through (5.68) are modified as

$$\left.\frac{\partial\mathbf{e}(\theta)}{\partial\theta}\right|_{\mathbf{q}} = \mathbf{0} \tag{5.69}$$

$$\left.\frac{\partial\boldsymbol{\epsilon}(\mathbf{X},\theta)}{\partial\theta}\right|_{\mathbf{q}} = \mathbf{0} \tag{5.70}$$

$$\left.\frac{\partial\hat{\boldsymbol{\sigma}}(\mathbf{X},\theta)}{\partial\theta}\right|_{\mathbf{q}} = \left.\frac{\partial\hat{\boldsymbol{\sigma}}(\mathbf{X},\theta)}{\partial\theta}\right|_{\mathbf{e}} \tag{5.71}$$

$$\left.\frac{\partial \mathbf{a}(\mathbf{e}(\theta), \theta)}{\partial \theta}\right|_{\mathbf{q}} = \int_{\Omega} \mathbf{E}^{\mathrm{T}}(\mathbf{X}) \left.\frac{\partial \hat{\hat{\boldsymbol{\sigma}}}(\mathbf{X}, \theta)}{\partial \theta}\right|_{\mathbf{q}} d\Omega \tag{5.72}$$

$$\left.\frac{\partial \mathbf{s}(\mathbf{e}(\theta), \theta)}{\partial \theta}\right|_{\mathbf{q}} = \bar{\bar{\mathbf{D}}}_{\mathrm{t}}^{-1} \bar{\bar{\mathbf{E}}} \bar{\mathbf{D}}_{\mathrm{t}}^{-1} \left.\frac{\partial \mathbf{a}(\mathbf{e}(\theta), \theta)}{\partial \theta}\right|_{\mathbf{q}} \tag{5.73}$$

$$\left.\frac{\partial \mathbf{Q}(\mathbf{e}(\theta), \theta)}{\partial \theta}\right|_{\mathbf{q}} = \bar{\mathbf{B}}^{\mathrm{T}} \left.\frac{\partial \mathbf{s}(\mathbf{e}(\theta), \theta)}{\partial \theta}\right|_{\mathbf{q}} \tag{5.74}$$

where the quantity $\left.\frac{\partial \hat{\boldsymbol{\sigma}}(\mathbf{X}, \theta)}{\partial \theta}\right|_{\mathbf{e}}$ in Eq. (5.71) is computed by conditional differentiation (at the material level) of the material constitutive law. It is noteworthy that, in the case of linear geometry, assuming **q** fixed is equivalent to assuming **e** fixed (**e** and **q** are linearly related as shown by Eqs. (5.55) and (5.61)), while this equivalence does not apply in the case of nonlinear geometry (see Eqs. (5.21) and (5.28)).

5.2.3 Specialization to 2-D frame structures

As already discussed in the introduction, the frame element is an important class of finite elements for which the beneficial effects of a multi-field mixed formulation have been studied, proved and employed. The specialization of the above three-field mixed formulation to 2-D frame elements requires the definition of the section deformation vector, **d**, and section stress resultant vector, **D**. The explicit definition of the above vectors depends on the specific frame element considered. In general, a matrix $\mathbf{A}_{\mathrm{s}}(\mathbf{X})$ can be defined such that

$$\boldsymbol{\epsilon}(\mathbf{X}, \theta) = \mathbf{A}_{\mathrm{s}}(\mathbf{X}) \mathbf{d}(\mathrm{x}, \theta) \tag{5.75}$$

$$\mathbf{D}(x, \theta) = \int_{A(x)} \mathbf{A}_s(\mathbf{X})^T \boldsymbol{\sigma}(\mathbf{X}, \theta) dA \tag{5.76}$$

where x denotes the abscissa along the frame axis ($x \in [0, L]$, L = length of the frame element) and A(x) denotes the cross-section at abscissa x. Explicit expressions for **d**, **D**, and $\mathbf{A}_s(\mathbf{X})$ corresponding to common frame models presented in the literature are given in Appendix B. In this section and in Appendix B, the notation $\mathbf{X} = [X_1, X_2, X_3]^T = [x, y, z]^T$ is employed for consistency with the majority of the literature on frame elements.

For frame finite elements, it is common to use shape functions directly for the previously defined quantities **d** and **D** and to obtain the complete displacement fields from the displacements $\mathbf{u}(x, \theta)$ of the reference axis of the frame. Thus, Eq. (5.50) can be rewritten as

$$\begin{aligned} \mathbf{u}(x, \theta) &= \mathbf{N}(x)\mathbf{q}(\theta) \\ \mathbf{D}(x, \theta) &= \mathbf{S}(x)\mathbf{s}(\theta) \\ \mathbf{d}(x, \theta) &= \mathbf{E}(x)\mathbf{e}(\theta) \end{aligned} \tag{5.77}$$

Accounting for Eqs. (5.75) through (5.77), all the theoretical developments presented in the previous sections for both response and response sensitivity analysis can be directly applied to any frame element treated in the context of a three-field mixed formulation. In particular, the governing equations for a frame element are formally identical to Eqs. (5.54)-(5.56), when the following specialized definitions are used

$$\mathbf{Q}(\theta) = \int_0^L \mathbf{b}^T(x)\mathbf{N}(x)dx + [\mathbf{t}^T(x)\mathbf{N}(x)]\Big|_{x=0}^{x=L} \tag{5.78}$$

$$\bar{\mathbf{B}} = \int_0^L \mathbf{S}^T(x)\mathbf{B}(x)dx \tag{5.79}$$

$$\bar{\mathbf{E}} = \int_0^L \mathbf{S}^T(x)\mathbf{E}(x)dx \tag{5.80}$$

$$\mathbf{a}(\mathbf{e}(\theta), \theta) = \int_0^L \mathbf{E}^T(x)\hat{\mathbf{D}}(\mathbf{E}(x)\mathbf{e}(\theta), \theta)dx \tag{5.81}$$

$$\bar{\mathbf{D}}_t = \int_0^L \mathbf{E}^T(x)\mathbf{k}_s(x)\mathbf{E}(x)dx \tag{5.82}$$

where $\mathbf{k}_s(x)$ denotes the consistent tangent stiffness matrix of the section at the abscissa x.

The sensitivity Eqs. (5.61) and (5.64) through (5.68) specialize to

$$\frac{d\mathbf{e}(\theta)}{d\theta} = \bar{\mathbf{D}}_t^{-1}\bar{\mathbf{E}}^T\bar{\bar{\mathbf{D}}}_t^{-1}\bar{\mathbf{B}}\ \frac{d\mathbf{q}(\theta)}{d\theta} \tag{5.83}$$

$$\frac{d\mathbf{d}(x, \theta)}{d\theta} = \mathbf{E}(x)\frac{d\mathbf{e}(\theta)}{d\theta} \tag{5.84}$$

$$\frac{d\hat{\mathbf{D}}(x, \theta)}{d\theta} = \mathbf{k}_s(x)\mathbf{E}(x)\frac{d\mathbf{e}(\theta)}{d\theta} + \frac{\partial\hat{\mathbf{D}}(x, \theta)}{\partial\theta}\bigg|_{\mathbf{e}} \tag{5.85}$$

$$\frac{d\mathbf{a}(\mathbf{e}(\theta), \theta)}{d\theta} = \bar{\mathbf{D}}_t\frac{d\mathbf{e}(\theta)}{d\theta} + \int_0^L \mathbf{E}^T(x)\frac{\partial\hat{\mathbf{D}}(x, \theta)}{\partial\theta}\bigg|_{\mathbf{e}} dx \tag{5.86}$$

$$\frac{d\mathbf{s}(\mathbf{e}(\theta),\theta)}{d\theta} = \bar{\bar{\mathbf{D}}}_t^{-1}\bar{\bar{\mathbf{E}}}\bar{\bar{\mathbf{D}}}_t^{-1}\frac{d\mathbf{a}(\mathbf{e}(\theta),\theta)}{d\theta} \tag{5.87}$$

$$\frac{d\mathbf{Q}(\mathbf{e}(\theta),\theta)}{d\theta} = \bar{\mathbf{B}}^T\frac{d\mathbf{s}(\mathbf{e}(\theta),\theta)}{d\theta} \tag{5.88}$$

The equations for conditional response sensitivity computation are readily obtained from Eqs. (5.83) through (5.88) imposing $\left.\frac{\partial \mathbf{q}(\theta)}{\partial\theta}\right|_{\mathbf{q}} = \mathbf{0}$ and computing all the derivatives for $\mathbf{q}$ fixed, as seen in Section 5.2.2 (Eqs. (5.69) through (5.74)).

5.3 VALIDATION EXAMPLES

5.3.1 Finite element modeling of steel-concrete composite frame structures

Composite frames made of steel-concrete beams and steel columns are nowadays common solutions in the design of seismic resistant frames. As a consequence, in the last ten years, a growing attention has been given to finite element modeling and analysis of steel-concrete composite structures (Spacone and El-Tawil 2004). The behavior of composite beams, consisting of two components connected through shear connectors to form an interacting unit, is significantly influenced by the type of connection between the steel beam and the concrete slab. Partial composite action develops when using flexible shear connectors (Oehlers and Bradford 2000). Thus, for accurate analytical predictions, structural models of composite structures must account for the interlayer slip between the steel and concrete components. For this reason, a composite beam finite element able to model the effects of the interface slip is required. The three-dimensional model for composite beams with deformable shear connection under general state of stress (Dall'Asta 2001)

simplifies to the model introduced by Newmark et al. (1951) if only the in-plane bending behavior is considered. In the Newmark's model, the geometrically linear Euler-Bernoulli beam theory (i.e., small displacements, rotations and strains) is used to model each of the two parts of the composite beam; the effects of the deformable shear connection are accounted for by using an interface model with distributed bond, and the contact between the steel and concrete components is enforced (Fig. 5.1). The interface slip is small, since it corresponds to the difference in longitudinal displacements of the steel and composite fibers at the steel-concrete interface.

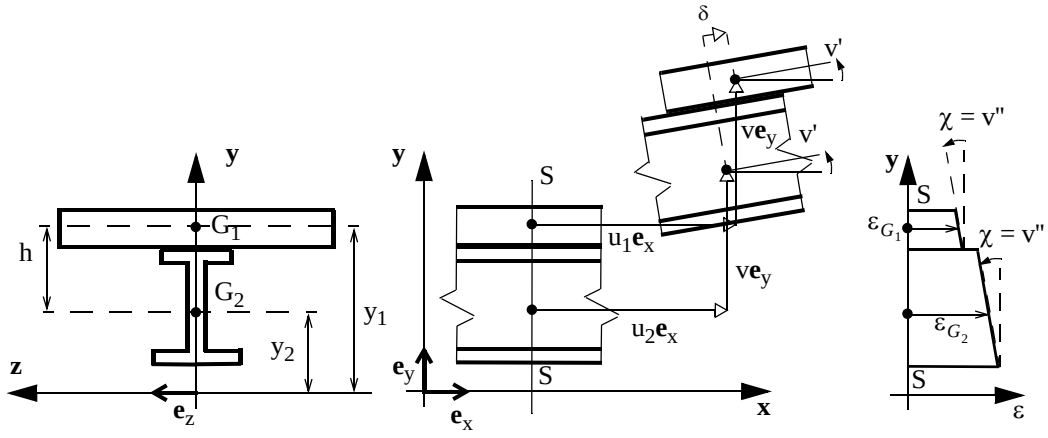

Figure 5.1 Kinematics of 2D composite beam model (Newmark's model).

Compared to common monolithic beams, composite beams with deformable shear connection raise more challenging modeling and numerical difficulties, e.g., complex distributions of the interface slip and force can develop (Dall'Asta and Zona 2002) and special measures are necessary to avoid shear-locking phenomena (Dall'Asta and Zona 2004b). Despite some difficulties, three-field mixed elements (Dall'Asta and Zona 2004a)

can be successfully adopted for numerical simulation of the behavior of steel-concrete composite beams, producing accurate global and local results when a proper discretization of the structure is used (Dall'Asta and Zona 2004c).

In the present study, a 2-D steel-concrete composite frame element with deformable shear connection, previously developed in (Dall'Asta and Zona 2004a), is used for response simulation and is augmented with the response sensitivity computation procedure presented above. The finite element used is based on the three-field mixed formulation and assumes Newmark's kinematics (Fig. 5.1). It has 10 nodal degrees-of-freedom (DOFs) in total: 8 DOFs are external, while 2 DOFs are internal and are condensed out before assembly at the structure level (Fig. 5.2). The procedure for response sensitivity calculation in presence of static condensation has been previously derived by the authors and can be found elsewhere (Zona et al. 2005).

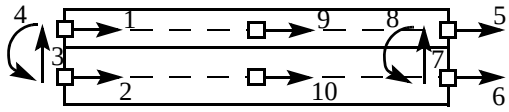

Figure 5.2 Degrees of freedom of the 2D composite beam finite element.

This finite element was proven to provide accurate response simulations and to be superior in the evaluation of local quantities (e.g., section deformations, section stress resultants, shear force distribution at the steel-concrete interface, etc.) to equivalent displacement-based finite elements when meshes requiring similar computational effort are

used. Furthermore, this element presents a useful feature: it is able to model a standard monolithic steel-only or reinforced concrete-only frame element without any modification in the code. This is achieved simply by considering at the section level a concrete slab or a steel beam of null cross-section area, obtaining a monolithic steel frame or a reinforced concrete frame, respectively. The only precaution is to apply constraints to the eliminated DOFs. The obtained three-field mixed monolithic frame element is characterized by exact distributions of section stress resultants (as for force-based frame elements, see Spacone et al. 1995), while the assumed displacement fields have the same form as for standard displacement-based frame elements. The above useful feature allows to assemble easily monolithic and composite frame elements in frame models, representing correctly the connections between steel columns and steel beams or reinforced concrete columns and concrete slabs (Zona et al. 2005).

Regarding the development of the sensitivity analysis, this element presents also a favorable feature: the response sensitivity computation procedure, developed for a general three-field mixed finite element and particularized to a frame element, can be further simplified significantly by taking advantage of the properties of the employed shape functions for the section deformation and section stress resultant fields. This condition derives from the fact that the shape functions used for approximating the section deformations and the section stress resultants are the same (i.e., $\mathbf{E}(x) = \mathbf{S}(x)$). This choice for the shape functions produces a matrix $\bar{\mathbf{E}}$ that is positive definite and, therefore, invertible (Stolarski and Belytschko 1987). Using this property, Eqs. (5.83) and (5.87) simplify to

$$\frac{d\mathbf{e}(\theta)}{d\theta} = \bar{\mathbf{E}}^{-1}\bar{\mathbf{B}}\,\frac{d\mathbf{q}(\theta)}{d\theta} \tag{5.89}$$

$$\frac{d\mathbf{s}(\mathbf{e}(\theta),\theta)}{d\theta} = \bar{\mathbf{E}}^{-T}\,\frac{d\mathbf{a}(\mathbf{e}(\theta),\theta)}{d\theta} \tag{5.90}$$

In this way, inversion of the two matrices $\bar{\mathbf{D}}_t$ and $\bar{\bar{\mathbf{D}}}_t$ (required in Eqs. (5.83) and (5.87)) is avoided and only matrix $\bar{\mathbf{E}}$ has to be inverted. It is noteworthy that, in this special case for which $n_s = n_e$, the three matrices $\bar{\mathbf{D}}_t$, $\bar{\bar{\mathbf{D}}}_t$, and $\bar{\mathbf{E}}$ have the same dimension $n_s \times n_s = n_e \times n_e$.

5.3.2 Implementation of composite frame element and response sensitivity analysis scheme in a general-purpose nonlinear finite element structural analysis program

For validation purposes, the steel-concrete composite frame element and the response sensitivity computation scheme for three-field mixed formulation were implemented in a general-purpose nonlinear finite element structural analysis program, FEDEASLab (Filippou and Constantinides 2004). FEDEASLab is a Matlab toolbox (The MathWorks 1997) for linear and nonlinear, static and dynamic structural analysis, which also provides a general framework for parameterization of finite element models and response sensitivity computation (Franchin 2003).

Taking advantage of the modularity of FEDEASLab, a variety of suitable cross-sections (e.g., composite cross-section with symmetric and unsymmetric steel I-beams) and material constitutive models (e.g., Kent-Scott-Park concrete model, Popovics-Saenz

concrete model with nonlinear tension stiffening) were also implemented for response and response sensitivity computation. Thus, a library of material and element models was implemented in FEDEASLab, which allows accurate response and response sensitivity analyses of steel-concrete composite frame structures. This library can be easily updated and/or extended to follow the state-of-the-art in modeling such structures.

5.3.3 Benchmark example: one-story one-bay steel-concrete composite frame

The benchmark problem considered is a one-story one-bay frame, made of two steel columns and a steel-concrete composite beam (Fig. 5.3). The column steel section is a European HE360A; the composite beam consists of a European IPE300 steel section coupled to a reinforced concrete slab 1000 mm wide and 120 mm thick through two rows of Nelson stud connectors (Fig. 5.4). Two identical layers of steel reinforcement with a total area A_s = 1000 mm^2 are present in the slab. Two loading conditions are considered: (1) pushover analysis (after static application of a uniform distributed vertical load of 46 kN/m on the beam, representing self-weight, permanent loads and live loads, a horizontal load of increasing magnitude is applied quasi-statically at the beam-column nodes at the roof level, see Fig. 5.3), and (2) earthquake base excitation (after static application of a uniform distributed vertical load of 46 kN/m on the beam, the frame is subjected to a horizontal ground motion corresponding to the N90W (W-E) component of the Loma Prieta earthquake of October 17, 1989, recorded at the Capitola site, scaled by a factor 4).

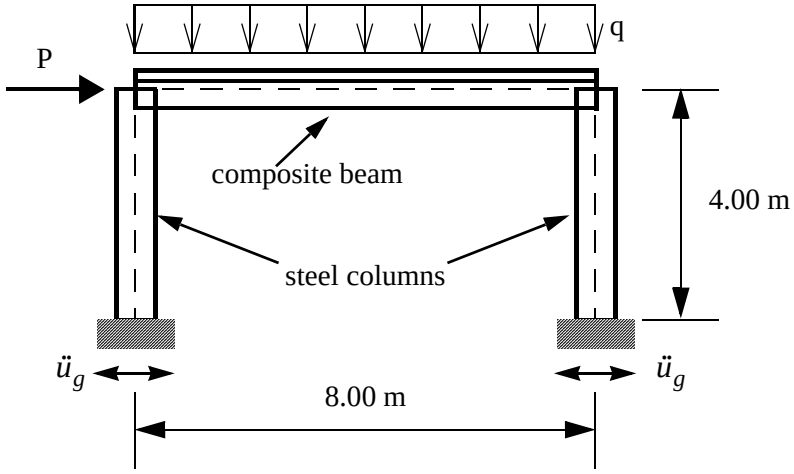

Figure 5.3 Steel-concrete composite frame structure.

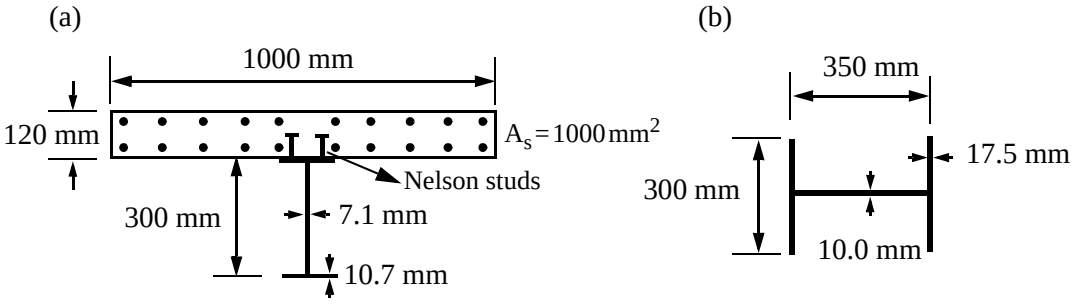

Figure 5.4 Cross-section properties of the steel-concrete frame structure: (a) composite beam cross-section, and (b) steel column cross-section.

The structure is discretized into 6 finite elements, i.e., 4 elements for the steel-concrete composite beam and 1 element for each steel column. The constitutive law used for the steel material of the beam and of the two columns as well as for the reinforcement steel is a uniaxial cyclic J_2 plasticity model with the von Mises yield criterion in conjunction with linear kinematic and isotropic hardening laws (Conte et al. 2003). The selected con-

stitutive law for the concrete material is a uniaxial cyclic law with monotonic envelope given by the Popovics-Saenz law (Balan et al 1997, 2001). The constitutive law used for the shear connectors is a slip-force cyclic law with monotonic envelope given by the Ollgaard et al. (1971) law and a cyclic response following a modified version of the model proposed by Eligenhausen et al. (1983). Detailed formulation and differentiation of the concrete and connection constitutive laws can be found in Zona et al. (2004). The values of the material constitutive parameters are given in Table 5.1. Zona et al. (2004) and Zona et al. (2005) also provide comparisons between analytical predictions and experimental results of structural response.

Table 5.1 Material Constitutive Parameters

Material	Parameter	Value	SI unit	Description
Concrete	f_c	33.0	MPa	Peak compressive strength
	E_c	32000	MPa	Initial tangent stiffness
	ε_c	0.0022	-	Strain at peak strength
	f_f	15	MPa	Strength at inflection point
	ε_f	0.039	-	Strain at inflection point
Beam-and-column steel	f_{ys}	275	MPa	Yield strength
	E_s	210000	MPa	Young's modulus
	$H_{kin,s}$	2100	MPa	Kinematic hardening modulus
	$H_{iso,s}$	0	MPa	Isotropic hardening modulus
	α_{0s}	0	MPa	Initial back-stress
	b_s	0.01	-	Strain hardening ratio
Reinforcement steel	f_{yr}	430	MPa	Yield strength
	E_r	210000	MPa	Young's modulus
	$H_{kin,r}$	2100	MPa	Kinematic hardening modulus
	$H_{iso,r}$	0	MPa	Isotropic hardening modulus
	α_{0r}	0	MPa	Initial back-stress
	b_r	0.01	-	Strain hardening ratio
Shear connectors	f_{smax}	423	kN/m	Shear strength
	τ_{fr}	42.3	kN/m	Residual frictional stress
	δ_{ult}	6.0	mm	Slip at rupture

In the following, numerical simulations of important global and local response quantities as well as of their consistent sensitivities to various material parameters are pre-

sented for each of the two loading conditions defined above. In this paper, the response sensitivity results are presented in normalized form, i.e., they are multiplied by the nominal value of the sensitivity parameter and divided by a factor 100. In this way, the normalized response sensitivities represent the variation of the response quantity considered due to 1 percent change in the sensitivity parameter. These normalized sensitivities can thus be used to compare (in the deterministic sense, or considering that 1 percent change in the various sensitivity parameters are equally likely) the relative effects/importance of the sensitivity parameters on the response quantities considered.

5.3.3.1 Response and response sensitivity analysis for quasi-static load case

The quasi-static pushover analysis of the testbed structure defined above is performed using the force control method. First, a vertical distributed load q = 46 kN/m along the beam is applied statically to the structural model. Subsequently, a horizontal load P (Fig. 5.3) of increasing magnitude is applied quasi-statically to the two horizontal degrees of freedom (DOFs) of the left-end node of the composite beam, until the ultimate horizontal resisting force of the structure is reached (collapse state). The load P is equally distributed between the two DOFs (i.e., P/2 to each DOF), in order to simulate an equivalent earthquake loading for assumed equal tributary masses of the concrete slab and steel beam.

In Fig. 5.5, the applied horizontal load P (representing also the total shear force at the base of the columns) is plotted versus the horizontal displacement u_1 (concrete slab DOF) of the left-end of the composite beam. Fig. 5.6 shows the relation between the load

P and the vertical displacement v at midspan of the composite beam. Figs. 5.7 and 5.8 plot the bending moment - curvature and shear force - slip response curves, respectively, at the left-end section of the composite beam. Fig. 5.5 clearly shows the ductile behavior of the considered structure that reaches a horizontal displacement u_1 of about 30 mm ($P = 300$ kN) without a sensible stiffness degradation (almost linear behavior at the global level, even though the local behavior is strongly nonlinear from the beginning of the analysis, see Fig. 5.8), while the horizontal displacement at collapse is slightly below 150 mm ($P = 575$ kN). The change of stiffness around $u_1 = 45$ mm is mostly due to stiffness degradation of the composite beam, while the change of stiffness around $u_1 = 100$ mm ($P = 545$ kN) is caused primarily by yielding of the columns. This is consistent with the fact that this frame structure has been designed for a “strong column - weak beam” behavior. In Fig. 5.6, the changes in stiffness mentioned above can be observed even more clearly: the vertical displacement v is almost unchanged from the one produced by the vertical loads for an applied horizontal load $P = 95$ kN, then the same stiffness changes as in Fig. 5.5 are visible. It is noteworthy that the concrete never reaches its peak compressive strength and the shear connectors do not fail before the entire structure reaches the collapse state (structure tangent stiffness matrix nearly singular).

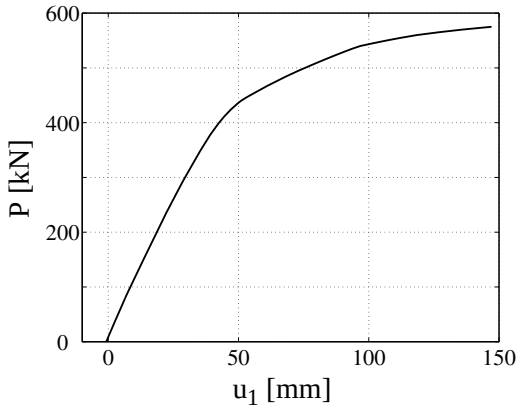

Figure 5.5 Pushover analysis: applied horizontal load P (total base shear) versus horizontal displacement u_1 at the left-end of the concrete slab.

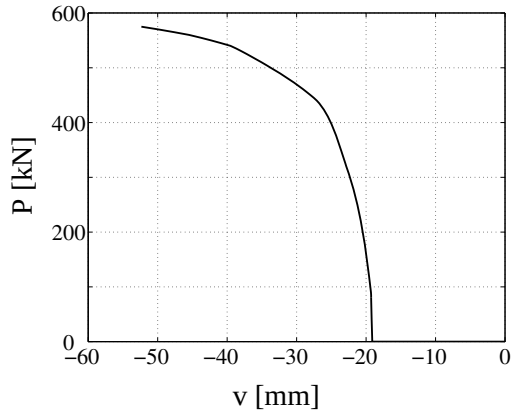

Figure 5.6 Pushover analysis: applied horizontal load P (total base shear) versus vertical displacement v at midspan of the composite beam.

Figs. 5.9-5.28 present sensitivity results for the pushover analysis of the frame structure regarding the global (u_1 and v) and local (M and f_s) response quantities defined previously. Figs. 5.9-5.12 plot the response sensitivities of the horizontal displacement u_1

to material parameters of the steel material of the beam and columns, the reinforcement steel, the concrete and the shear connection, respectively. Fig. 5.13 shows a direct comparison of the sensitivities of the horizontal displacement u_1 to the strength parameters of the steel of the beam and columns (f_{ys}), the concrete (f_c) and the shear connection (f_{smax}). From these figures, it is observed that the response quantity u_1 is more sensitive to material stiffness parameters (E_s, E_r, E_c) in the first phase of the analysis (in which the global behavior of the structure is almost linear), but becomes dominantly sensitive to strength parameters (f_{ys}, f_{yr}, f_c, f_{smax}) when the structure approaches its collapse state. It can be seen that f_{ys} is the material parameter affecting the most the response quantity u_1, especially near the collapse load. Similarly, the response sensitivities to material parameters of the beam-and-column steel material, the reinforcement steel, the concrete and the shear connection are displayed in Figs. 5.14-5.17 for the vertical displacement v, in Figs. 5.19-5.22 for the bending moment M acting at the left-end composite beam section and in Figs. 5.24-5.27 for the shear force f_s acting at the left-end composite beam section, respectively. Figs. 5.18, 5.23 and 5.28 compare the sensitivities to material strength parameters f_{ys}, f_c and f_{smax} of the vertical displacement v, the bending moment M and the shear force f_s, respectively. Among the material parameters considered, the parameter that affects the most the vertical displacement v and the bending moment M is the yield strength f_{ys} of the beam-and-column steel material, while the shear force f_s is most affected by the shear strength f_{smax} of the shear connection.

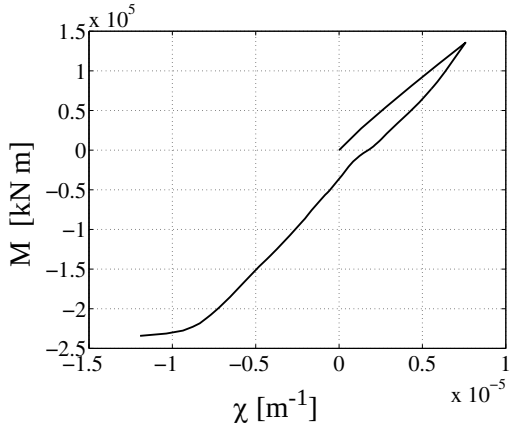

Figure 5.7 Pushover analysis: moment - curvature response at the left-end section of the composite beam.

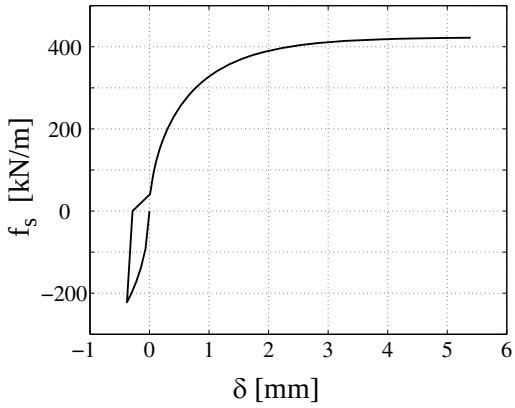

Figure 5.8 Pushover analysis: shear force - slip response at the left-end section of the composite beam.

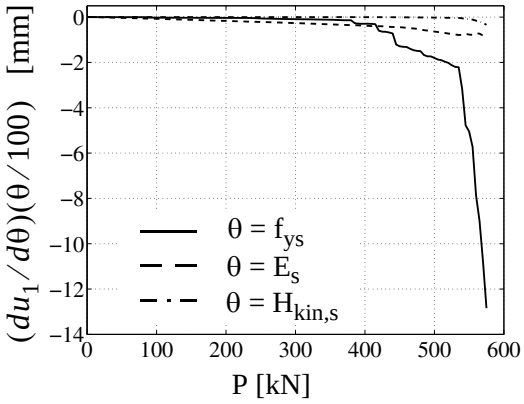

Figure 5.9 Pushover analysis: sensitivities of horizontal displacement u_1 to beam-and-column steel material parameters.

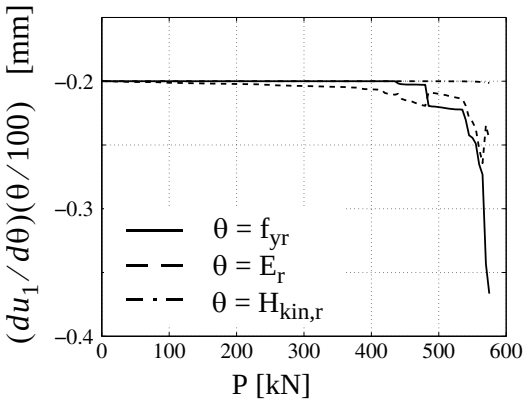

Figure 5.10 Pushover analysis: sensitivities of horizontal displacement u_1 to reinforcement steel material parameters.

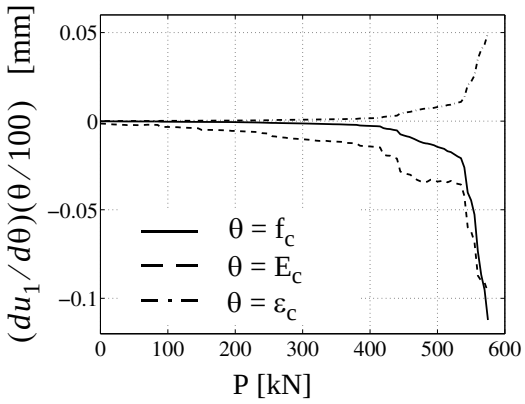

Figure 5.11 Pushover analysis: sensitivities of horizontal displacement u_1 to concrete material parameters.

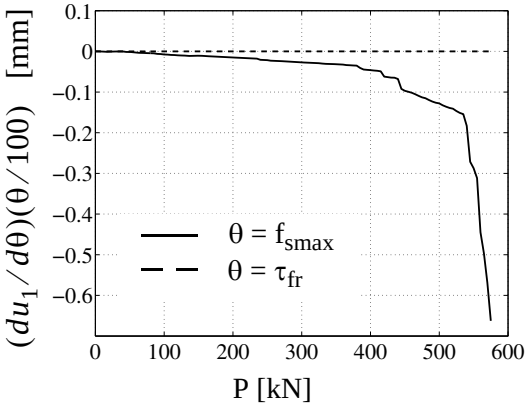

Figure 5.12 Pushover analysis: sensitivities of horizontal displacement u_1 to shear connection material parameters.

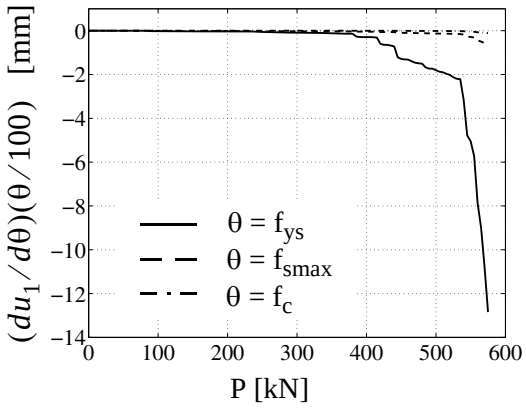

Figure 5.13 Pushover analysis: sensitivities of horizontal displacement u_1 to strength parameters of beam-and-column steel, concrete and shear connection.

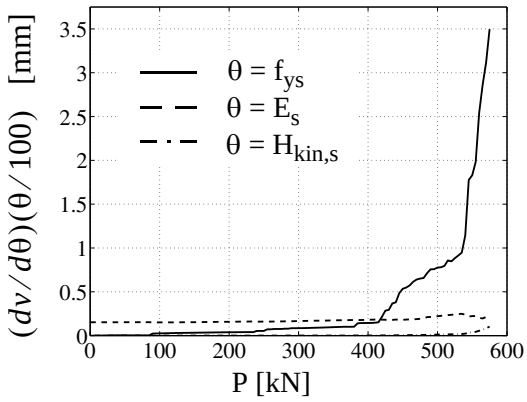

Figure 5.14 Pushover analysis: sensitivities of vertical displacement v at midspan of the composite beam to beam-and-column steel material parameters.

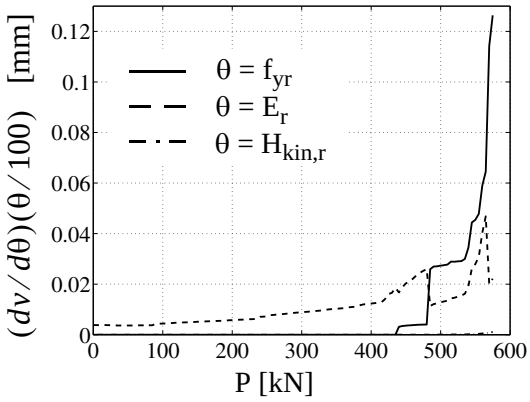

Figure 5.15 Pushover analysis: sensitivities of vertical displacement v at midspan of the composite beam to reinforcement steel material parameters.

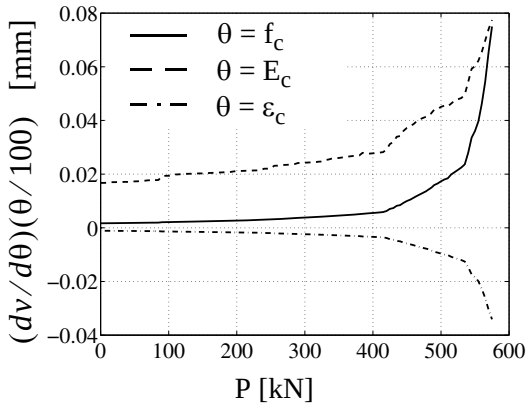

Figure 5.16 Pushover analysis: sensitivities of vertical displacement v at midspan of the composite beam to concrete material parameters.

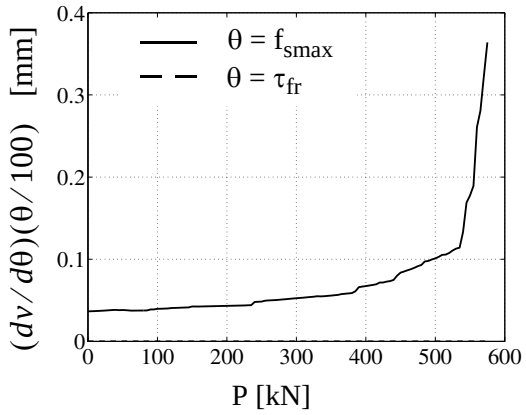

Figure 5.17 Pushover analysis: sensitivities of vertical displacement v at midspan of the composite beam to shear connection material parameters.

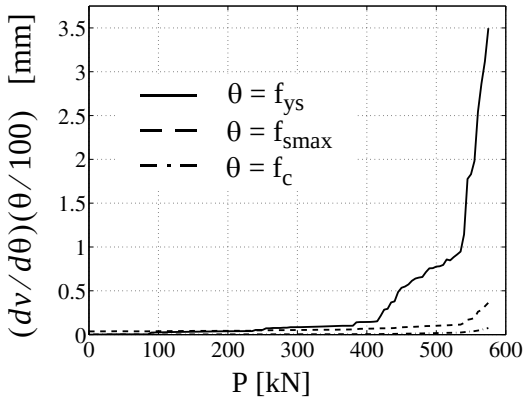

Figure 5.18 Pushover analysis: sensitivities of vertical displacement v at midspan of the composite beam to strength parameters of beam-and-column steel, concrete and shear connection materials.

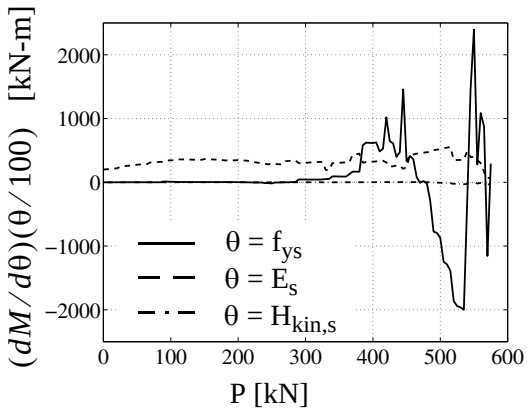

Figure 5.19 Pushover analysis: sensitivities of bending moment M acting at the left-end composite beam section to beam-and-column steel material parameters.

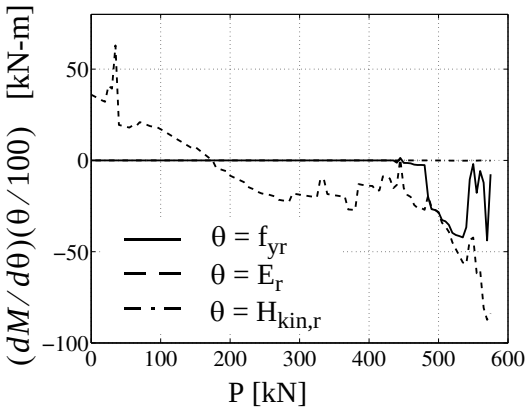

Figure 5.20 Pushover analysis: sensitivities of bending moment M acting at the left-end composite beam section to reinforcement steel material parameters.

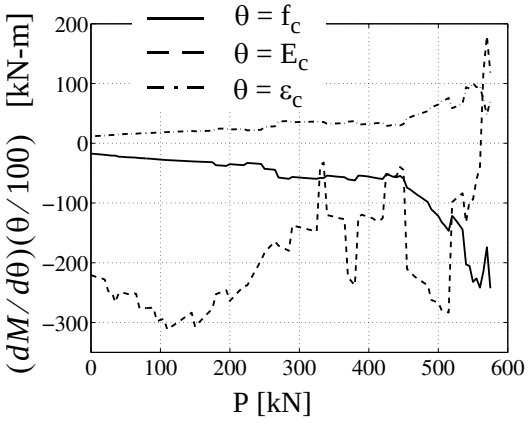

Figure 5.21 Pushover analysis: sensitivities of bending moment M acting at the left-end composite beam section to concrete material parameters.

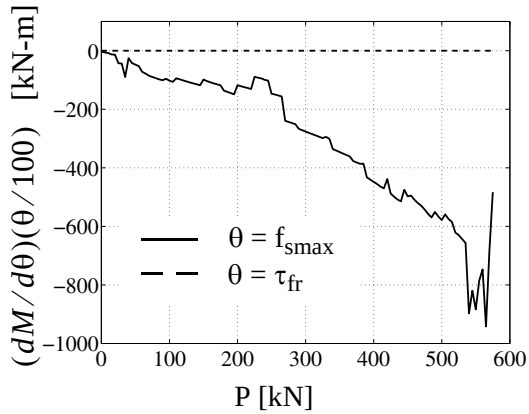

Figure 5.22 Pushover analysis: sensitivities of bending moment M acting at the left-end composite beam section to shear connection material parameters.

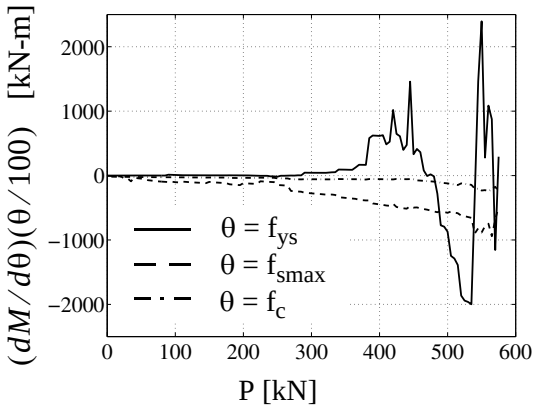

Figure 5.23 Pushover analysis: sensitivities of bending moment M acting at the left-end composite beam section to strength parameters of beam-and-column steel, concrete and shear connection materials.

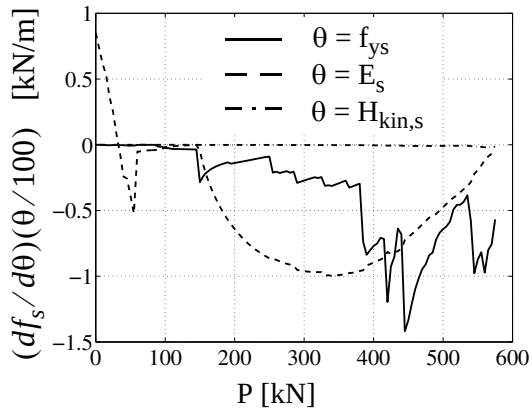

Figure 5.24 Pushover analysis: sensitivities of connection shear force f_s acting at the left-end composite beam section to beam-and-column steel material parameters.

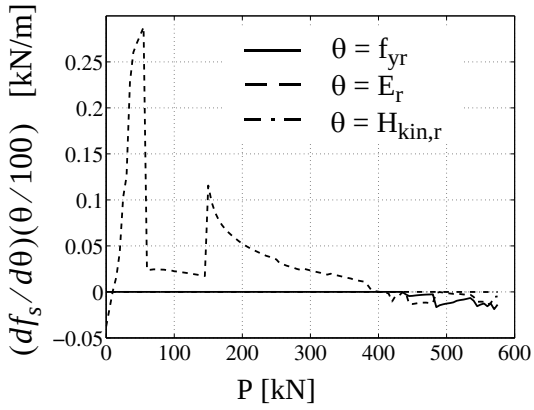

Figure 5.25 Pushover analysis: sensitivities of connection shear force f_s acting at the left-end composite beam section to reinforcement steel material parameters.

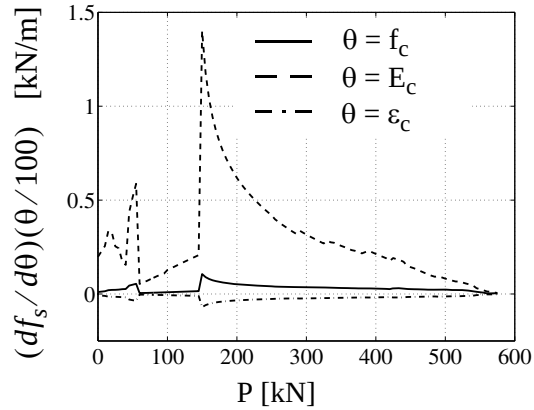

Figure 5.26 Pushover analysis: sensitivities of connection shear force f_s acting at the left-end composite beam section to concrete material parameters.

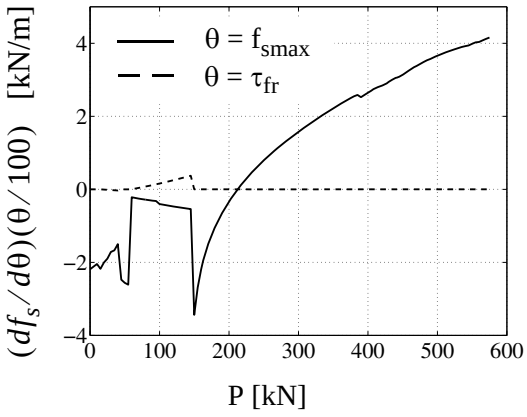

Figure 5.27 Pushover analysis: sensitivities of connection shear force f_s acting at the left-end composite beam section to shear connection material parameters.

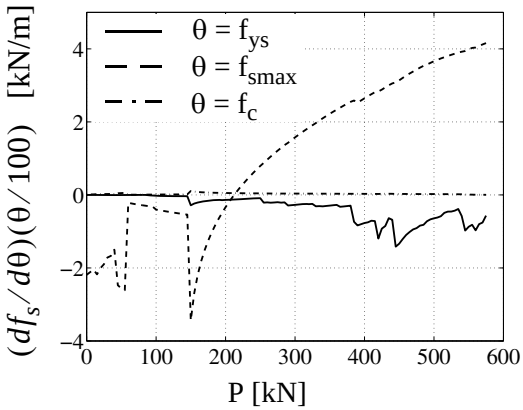

Figure 5.28 Pushover analysis: sensitivities of connection shear force f_s acting at the left-end composite beam section to strength parameters of beam-and column steel, concrete and shear connection materials.

In addition, the above stand-alone sensitivity results allow the following considerations, useful for gaining insight into the nonlinear response behavior of the considered structure to quasi-static pushover:

(1) Parameters ε_f and f_f, describing the degrading branch of the concrete constitutive law, do not affect the response behavior of the considered frame. In fact, the concrete never reaches its peak strength and therefore the response sensitivities with respect to ε_f and f_f are equal to zero for the entire pushover analysis. For this reason, these sensitivities are not plotted in Figs. 5.11, 5.16, 5.21 and 5.26.

(2) Parameter τ_{fr} (residual frictional stress per unit length of the shear connection) does not affect sensibly the response quantities considered (see Figs. 5.12, 5.17, 5.22 and 5.27), consistently with the fact that the shear connection does not reach failure (residual frictional state).

(3) Stiffness related material parameters significantly affect the response at low loading levels, while strength related material parameters become predominant at high loading levels, particularly near failure (see in particular Figs. 5.14-5.16). Sensitivity analysis not only confirms this intuitive result, but also allows to precisely quantify the effects and relative importance of the different material parameters at different loading stages.

Figs. 5.29-5.31 present the results of a convergence study of the sensitivities of the horizontal displacement u_1 computed through Forward Finite Difference (FFD) analysis (using increasingly small $\Delta\theta/\theta$ ratio) to the sensitivity results obtained using the DDM, for material parameters f_{ys}, f_c and f_{smax}, respectively. Results of the same convergence study are shown in Figs. 5.32-5.34 for sensitivities of the connection shear force f_s acting at the left-end composite beam section to the same material parameters f_{ys}, f_c and f_{smax}. The insets in Figs. 5.29-5.34 show zoom views that allow to better appreciate the convergence trends. In these figures, the results corresponding to three different values of param-

eter perturbation (i.e., 10^{-1}, 10^{-2} and 10^{-5} of the nominal value of the considered parameter) are plotted together with the exact DDM sensitivities. These values of the $\Delta\theta/\theta$ ratio have been carefully selected in order to obtain a clear visual display of the convergence trends, and particular attention has been given in choosing the lower value of parameter perturbation so as to avoid numerical problems related to round-off errors ("step-size dilemma", see Haftka and Gurdal 1993; Conte et al. 2003, 2004; Barbato and Conte 2005; Zona et al. 2005).

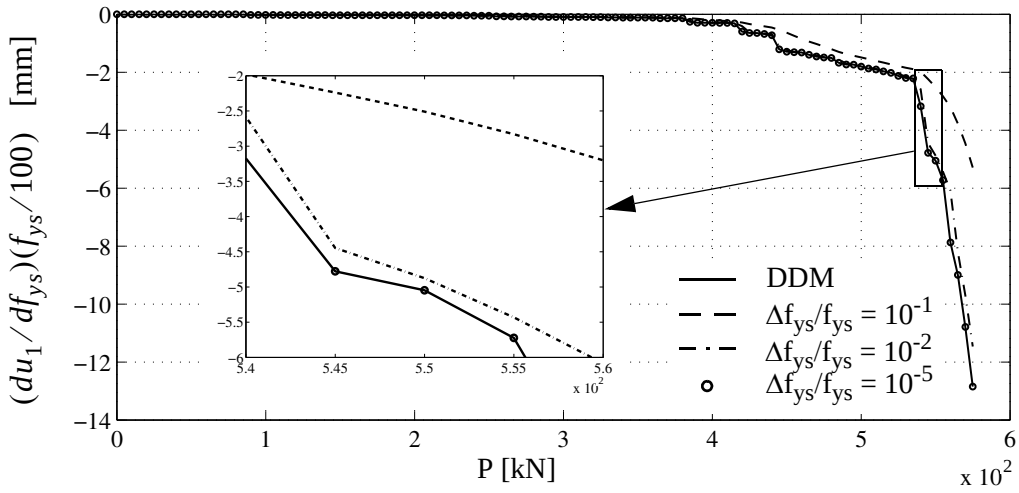

Figure 5.29 Convergence study of FFD to DDM sensitivity results for pushover analysis: sensitivities of horizontal displacement u_1 to yielding strength f_{ys} of beam-and-column steel material.

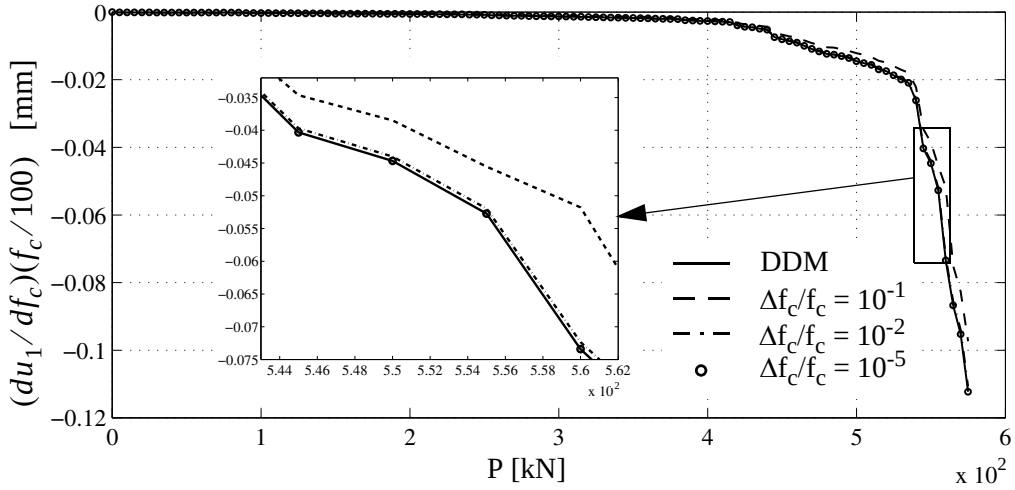

Figure 5.30 Convergence study of FFD to DDM sensitivity results for pushover analysis: sensitivities of horizontal displacement u_1 to peak strength f_c of concrete material.

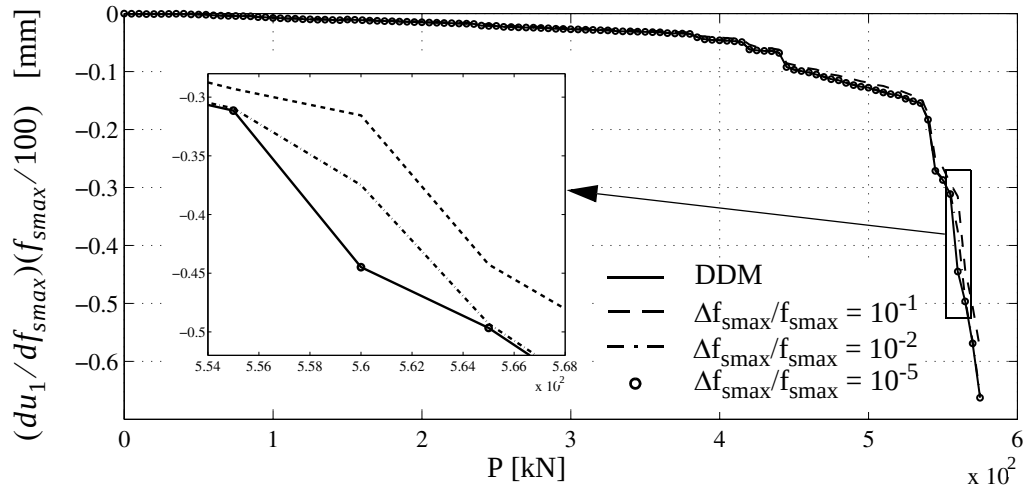

Figure 5.31 Convergence study of FFD to DDM sensitivity results for pushover analysis: sensitivities of horizontal displacement u_1 to shear strength f_{smax} of shear connection material.

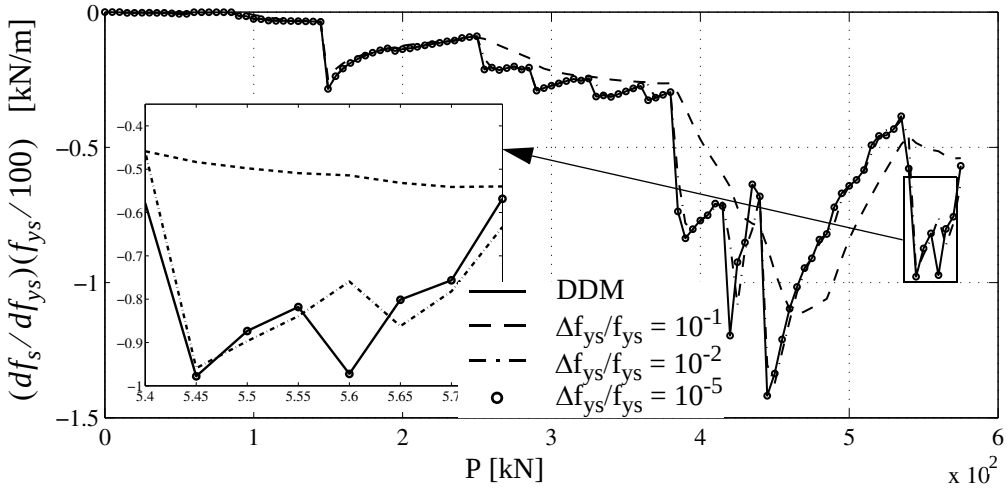

Figure 5.32 Convergence study of FFD to DDM sensitivity results for pushover analysis: sensitivities of connection shear force f_s acting at the left-end composite beam section to yield strength f_{ys} of beam-and-column steel material.

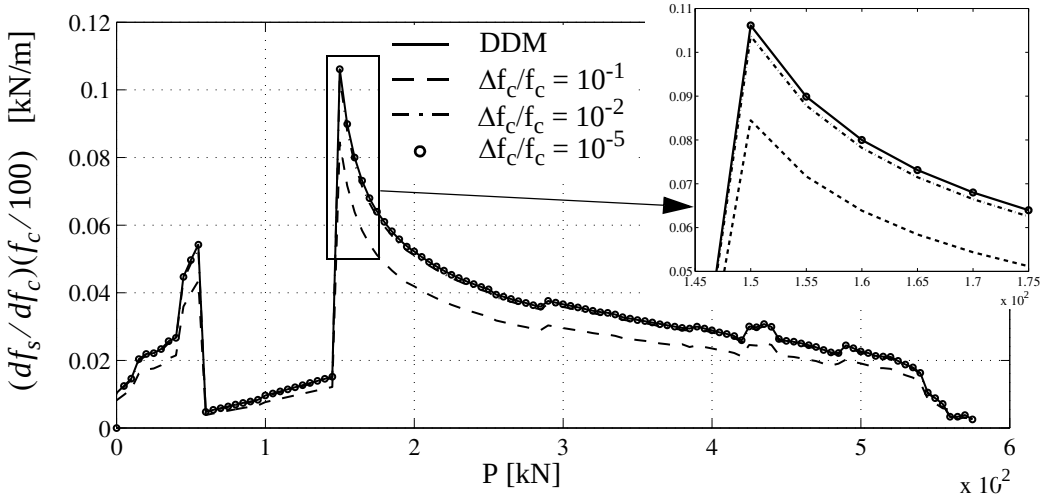

Figure 5.33 Convergence study of FFD to DDM sensitivity results for pushover analysis: sensitivities of connection shear force f_s acting at the left-end composite beam section to peak strength f_c of concrete material.

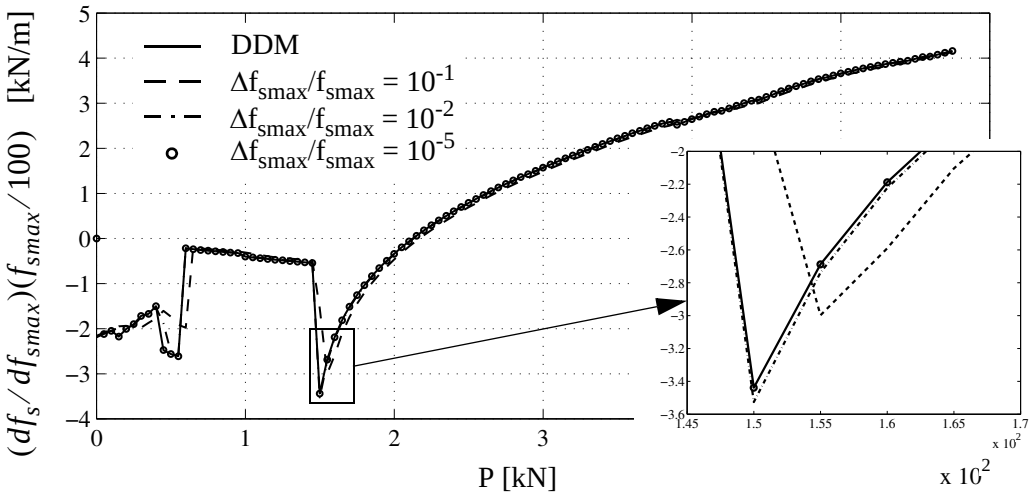

Figure 5.34 Convergence study of FFD to DDM sensitivity results for pushover analysis: sensitivities of connection shear force f_s acting at the left-end composite beam section to shear strength f_{smax} of shear connection material.

Convergence studies for other response quantities and other material parameters have also been performed, giving similar results in terms of convergence of FFD computations to DDM sensitivities for decreasing parameter perturbation values (Zona et al. 2004). These convergence results validate the DDM-based algorithms for response sensitivity computation presented in this paper and their computer implementation for finite elements based on the three-field mixed formulation in the case of quasi-static structural analysis.

5.3.3.2 Response and response sensitivity analysis for dynamic load case

In dynamic analysis, the inertia and damping properties of the structure must also be included in the model. The total mass of the frame has been discretized into translational (horizontal and vertical) masses lumped at the two external nodes of each composite

beam element. The mass corresponding to the permanent and live loads (i.e., total vertical distributed load of 40 kN/m) was distributed evenly between the slab and steel beam and added to the self-weight (5 kN/m for the slab and 1 kN/m for the beam). Half of the mass corresponding to the self-weight of the columns was added to the DOFs at the nodes where steel beam and column are connected. With this assumed distribution of masses, an eigenanalysis was performed using the initial stiffness properties of the structure. The first vibration mode of period $T_1 = 0.30$s corresponds to a horizontal translation of the entire composite beam, while the second and third modes of vibration of period $T_2 = 0.18$s and $T_3 = 0.13$s, respectively, correspond to vertical motions. The other modes of vibration correspond to axial compression-tension modes in the composite beams and vertical modes of the frame; they are all characterized by short periods and small modal participating masses. From the modal analysis results, a Rayleigh-type damping matrix (Chopra 2001) was computed based on an assumed damping ratio $\xi = 0.05$ for the first and third modes.

After static application of a vertical distributed load of 46 kN/m along the beam, the frame is subjected to a horizontal seismic motion corresponding to the first 30s of the N90W (W-E) component of the Loma Prieta earthquake of October 17, 1989, recorded at the Capitola site, scaled by a factor of four to yield a peak ground acceleration of 6160 mm/s^2 or 0.62g (see Fig. 5.35), and with two seconds of zero ground motion acceleration added at the end of the record in order to capture the free-vibration properties of the structure with yielded/degraded material properties at the end of the earthquake. The equation of motion and response sensitivity equation are integrated using the constant-average-

acceleration method (Chopra 2001) with a constant time step of $\Delta t = 0.005 s$. The following figures present results of the response history analysis performed.

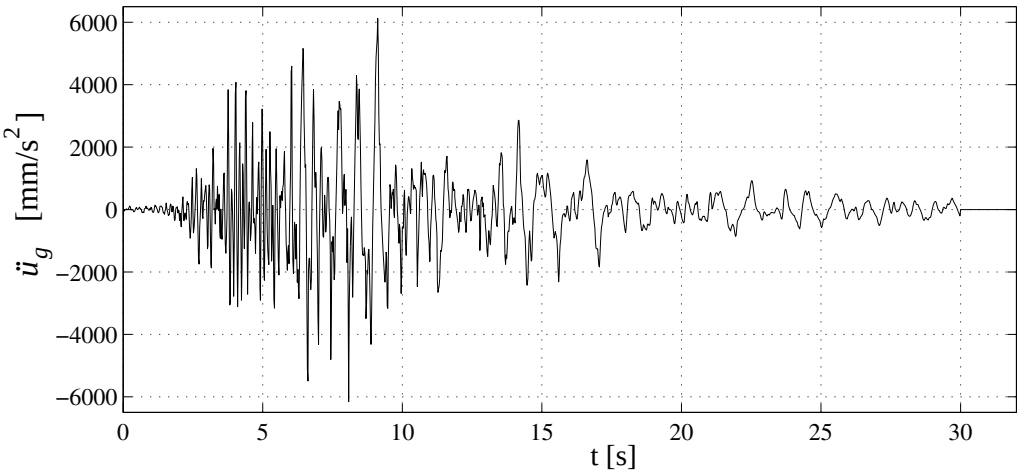

Figure 5.35 N90W (W-E) component of the Loma Prieta earthquake of October 17, 1989, recorded at the Capitola site, scaled by a factor of four.

Figs. 5.36 and 5.37 show the time histories of the horizontal displacement u_1 and vertical displacement v, respectively. The moment - curvature response at the left-end composite beam section is plotted in Fig. 5.38, while the shear force - slip response at the same section is given in Fig. 5.39. During the earthquake ground motion, extensive plastic behavior is developed by the structure. In particular, the vertical displacement v exhibits a large increase due to inelastic deformation at around t = 7s (Fig. 5.37) and the hysteretic behavior of the shear force - slip response is pronounced (Fig. 5.39).

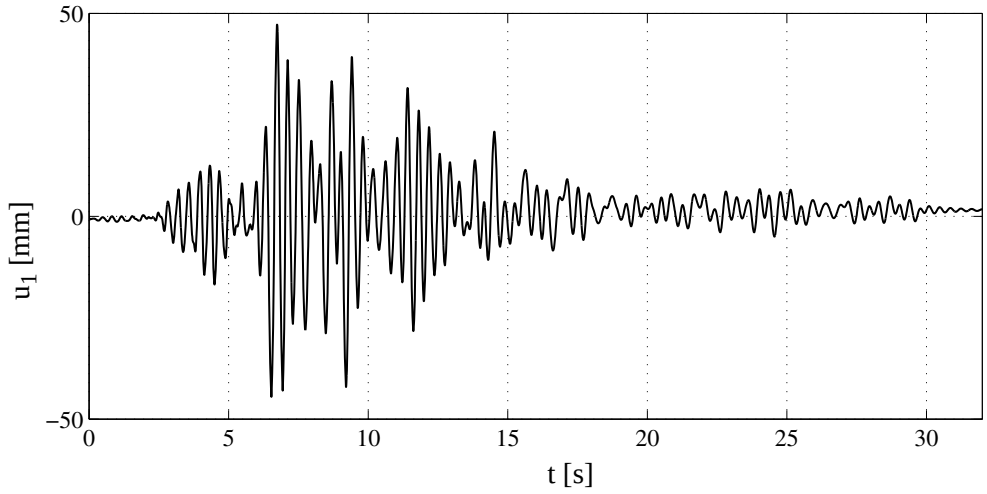

Figure 5.36 Dynamic analysis: horizontal displacement u_1 response history.

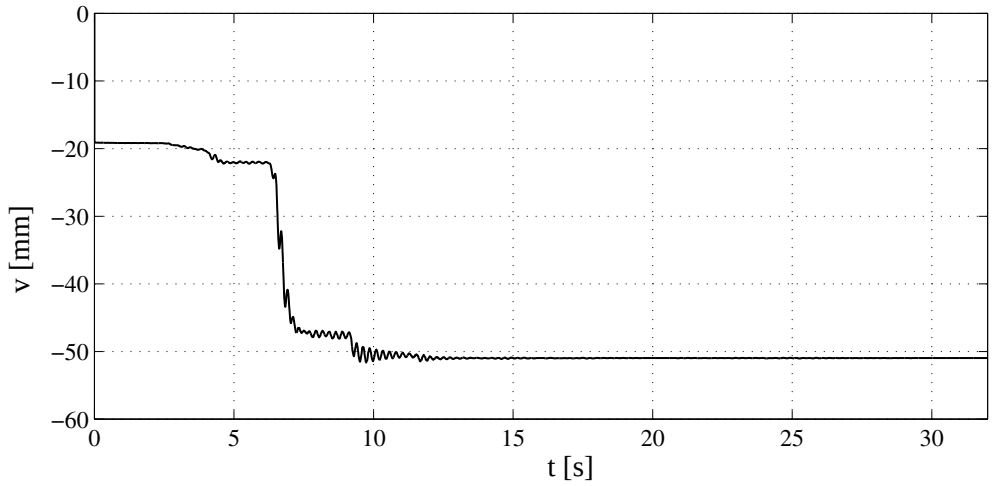

Figure 5.37 Dynamic analysis: vertical displacement v response history.

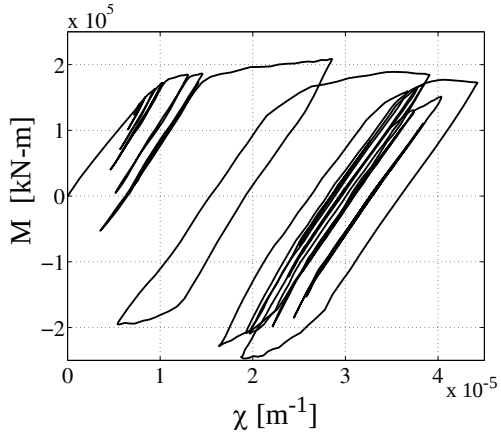

Figure 5.38 Dynamic analysis: moment - curvature response at the left-end section of the composite beam.

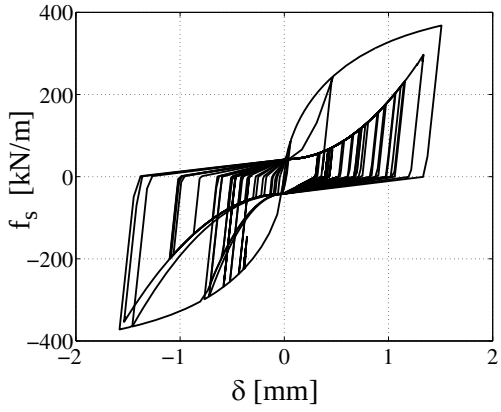

Figure 5.39 Dynamic analysis: shear force - slip response at the left-end section of the composite beam.

Figs. 5.40-5.43 show the normalized sensitivities of the horizontal displacement u_1 to Young's modulus E_s of the beam-and-column steel, Young's modulus E_r of the reinforcement steel, the initial tangent stiffness E_c of concrete, and the strength f_{smax} of the

shear connection, respectively. The choice of plotting these sensitivities is driven by the fact that, for the dynamic case, material stiffness related parameters affect the horizontal displacement u_1 more than strength related parameters. This is shown in Fig. 5.44, which compares the sensitivities of the horizontal displacement u_1 to the material parameters affecting the most this response quantity. The response sensitivity histories are observed to have similar waveforms (frequency content) to that of the time history of u_1 and exhibit a small shift in their mean value. This feature is linked to the material constitutive laws employed: all these constitutive laws (except for the concrete constitutive model beyond the peak strength, which was not reached in the dynamic load case presented here) use the initial tangent stiffness for unloading from plastic branches, and thus the effective first period of vibration of the structure remains close to the initial fundamental period even after large plastic deformations are experienced by the structure (waveform similarity). The small shift in mean value of the response sensitivities is due to the hysteretic nature of the material constitutive laws.

Fig. 5.45 shows the sensitivity of the vertical displacement v at midspan of the composite beam to Young's modulus E_s of the beam-and-column steel material, while Fig. 5.46 compares the sensitivities of v to the material parameters to which this response quantity is most sensitive. Similarly, Fig. 5.47 shows the sensitivity of the bending moment M acting at the left-end composite beam section to Young's modulus E_s of the beam-and-column steel material and Fig. 5.48 compares the sensitivities of M to material parameters to which M is most sensitive. Fig. 5.49 shows the sensitivity of the shear force f_s acting at the left-end composite beam section to Young's modulus E_s of the beam-and-

column steel material, while Fig. 5.50 compares the sensitivities of f_s to material parameters to which f_s is most sensitive. The material parameter affecting the most the bending moment M and the shear force f_s is Young's modulus E_s of the beam-and-column steel material, while the material parameter to which the vertical displacement v is most sensitive is the yield strength f_{ys} of the beam-and-column steel material. The dynamic response sensitivity analysis shows that the global and local responses of the considered structure are most sensitive to the material parameters describing the constitutive law of the beam-and-column steel material, as was already the case for the pushover loading and as expected from design considerations.

Fig. 5.51 shows the sensitivities of the vertical displacement v to the yield strength f_{ys} of the beam-and-column steel material computed using both DDM and FFD analysis for decreasing values of the parameter perturbation. Fig. 5.52 shows a closer view of the convergence of the FFD results to the DDM results. Similarly, the sensitivities of the bending moment M to the yield strength f_{ys}, computed via the FFD method for decreasing values of the parameter perturbation are plotted in Fig. 5.53 together with the corresponding response sensitivity computed using the DDM. Fig. 5.54 offers a zoom view of the previous figure, showing again convergence of the FFD results to the DDM results. These results, together with the results of other convergence studies (not shown here) performed by the authors for the sensitivities of other response quantities to all the material parameters considered in this paper, validate the DDM-based algorithms for response sensitivity computation presented in this paper and their computer implementation for finite elements

based on the three-field mixed formulation in the cases of quasi-static and dynamic structural analysis.

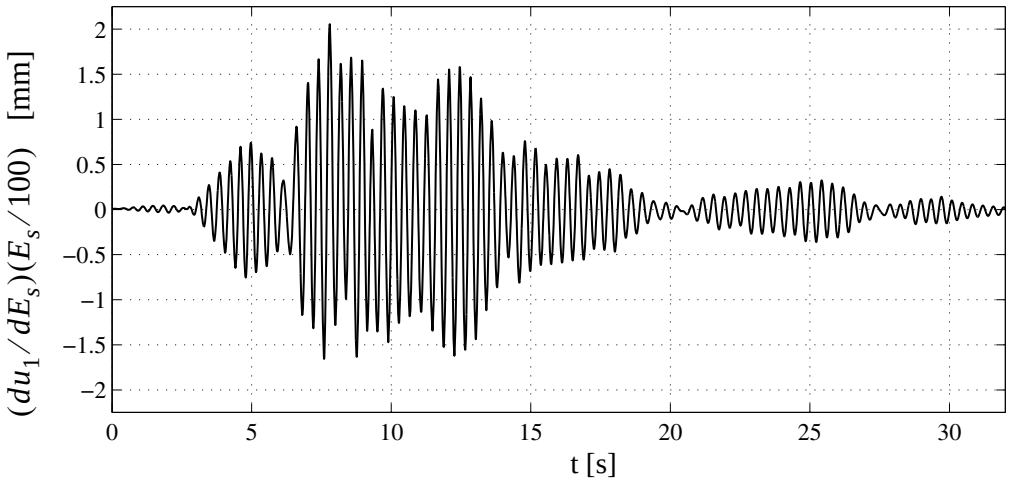

Figure 5.40 Dynamic analysis: sensitivity of horizontal displacement u_1 to Young's modulus E_s of the beam-and-column steel material.

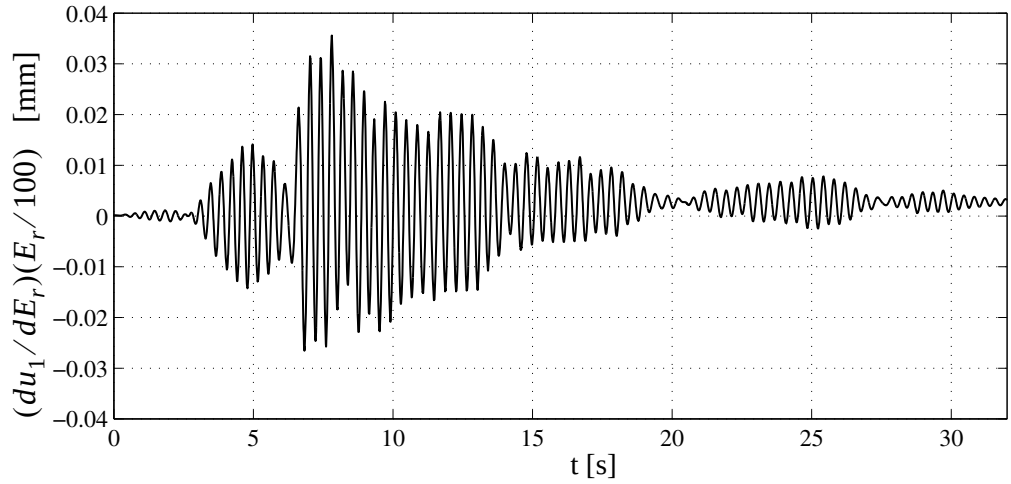

Figure 5.41 Dynamic analysis: sensitivity of horizontal displacement u_1 to Young's modulus E_r of reinforcement steel material.

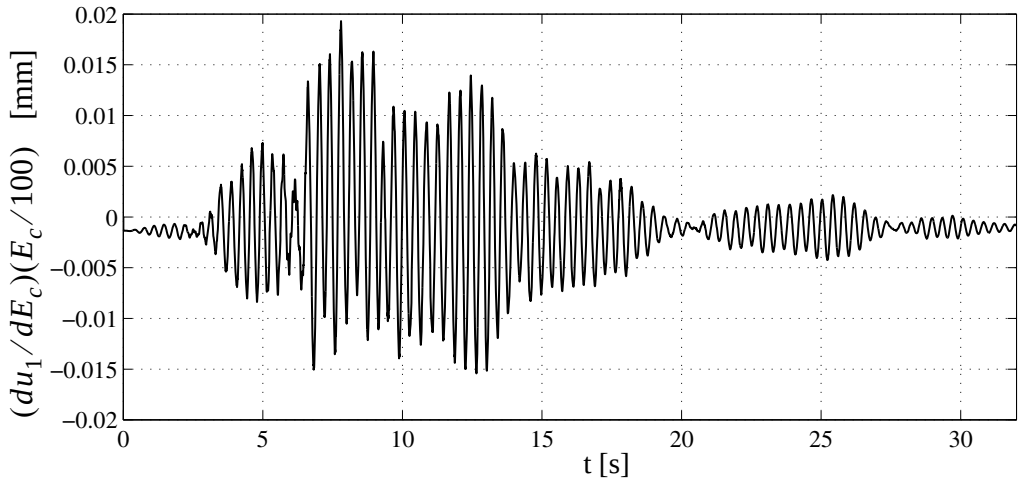

Figure 5.42 Dynamic analysis: sensitivity of horizontal displacement u_1 to initial tangent stiffness E_c of concrete material.

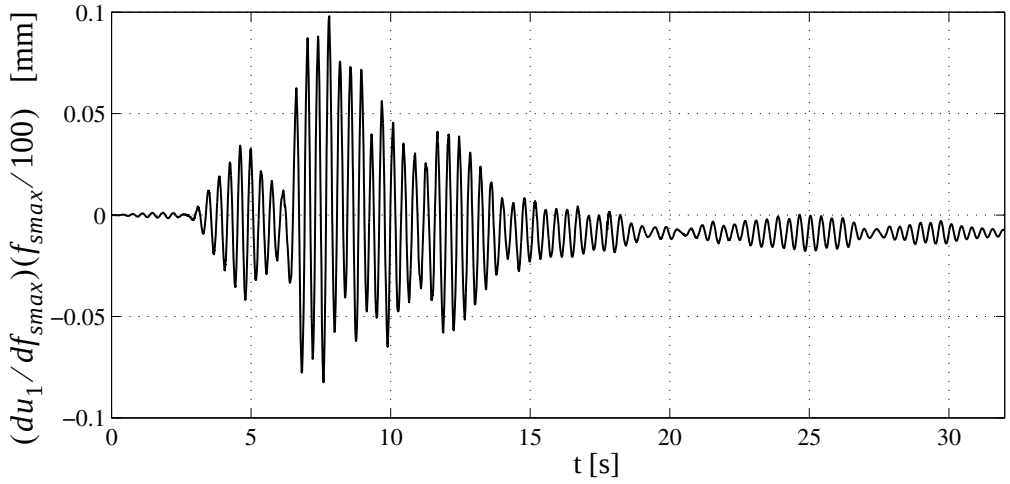

Figure 5.43 Dynamic analysis: sensitivity of horizontal displacement u_1 to shear strength f_{smax} of shear connection material.

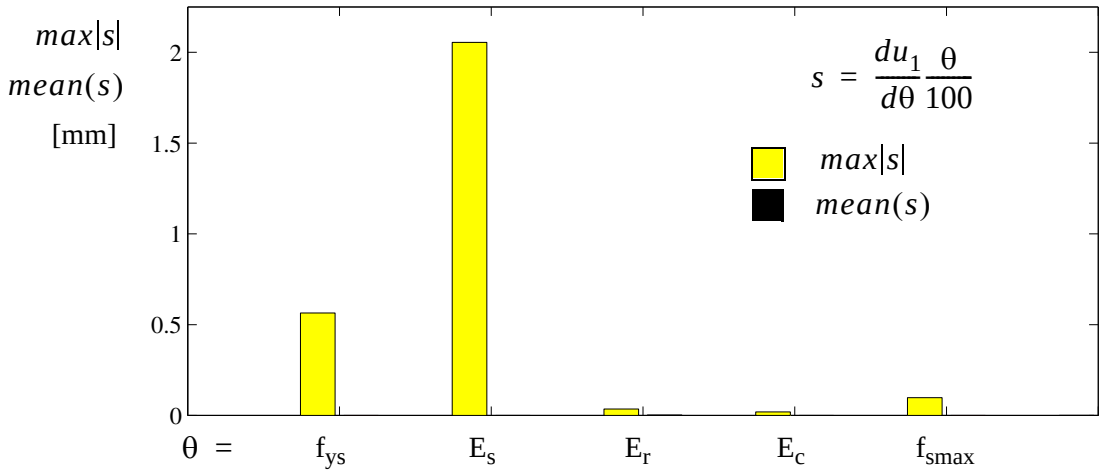

Figure 5.44 Dynamic analysis: comparison of sensitivities of horizontal displacement u_1 to material parameters to which u_1 is most sensitive.

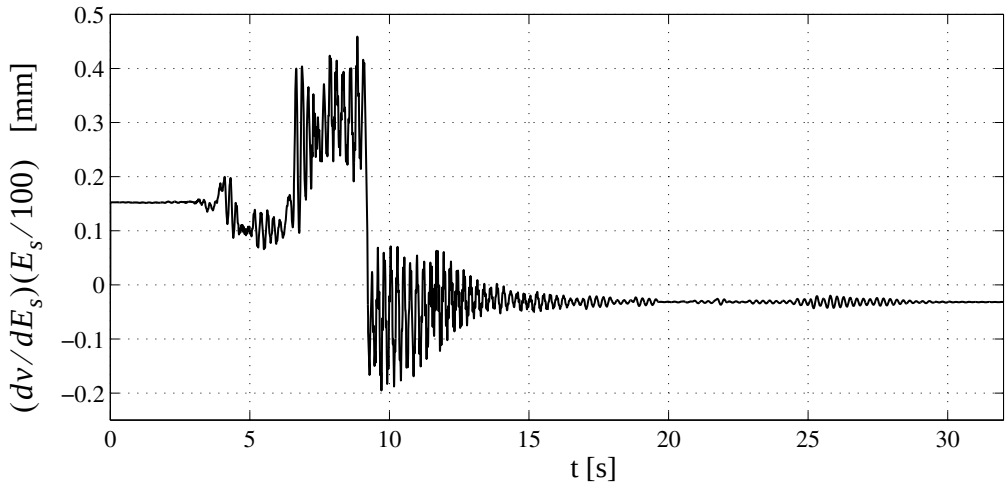

Figure 5.45 Dynamic analysis: sensitivity of vertical displacement v at midspan of composite beam to Young's modulus E_s of the beam-and-column steel material.

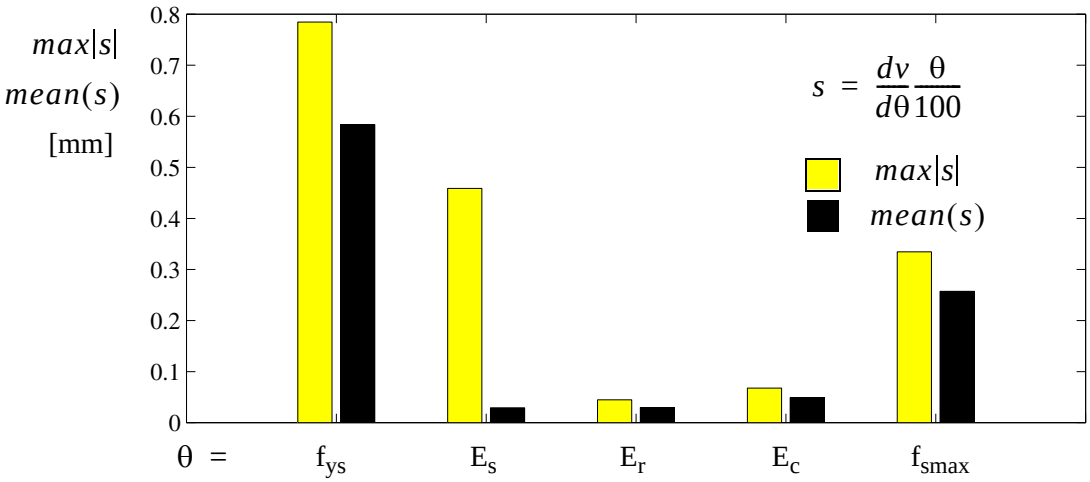

Figure 5.46 Dynamic analysis: comparison of sensitivities of vertical displacement v to material parameters to which v is most sensitive.

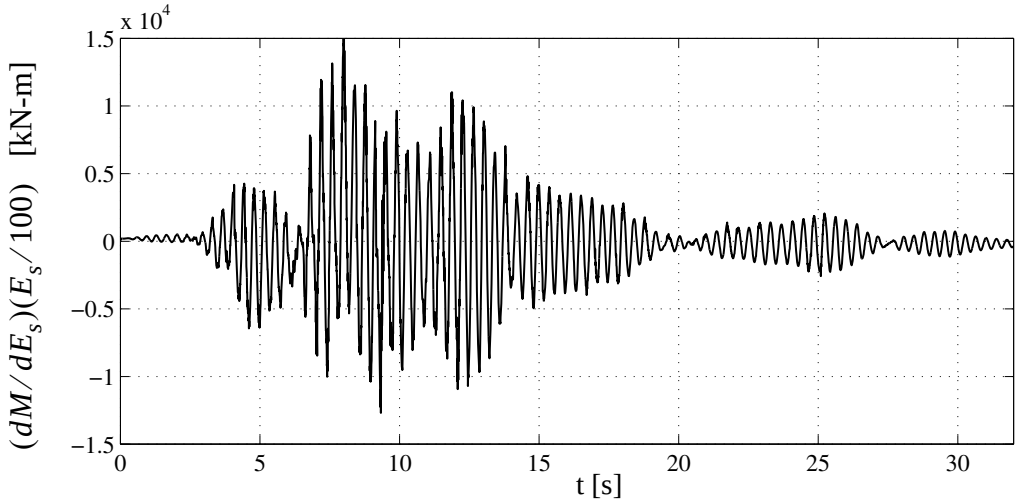

Figure 5.47 Dynamic analysis: sensitivity of bending moment M acting at the left-end section of the composite beam to Young's modulus E_s of the beam-and-column steel material.

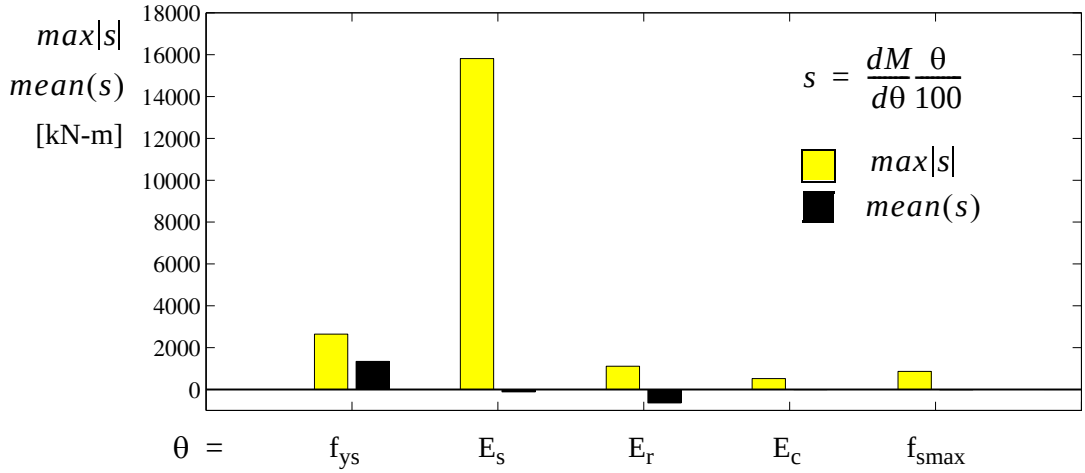

Figure 5.48 Dynamic analysis: comparison of sensitivities of bending moment M acting at the left-end composite beam section to material parameters to which M is most sensitive.

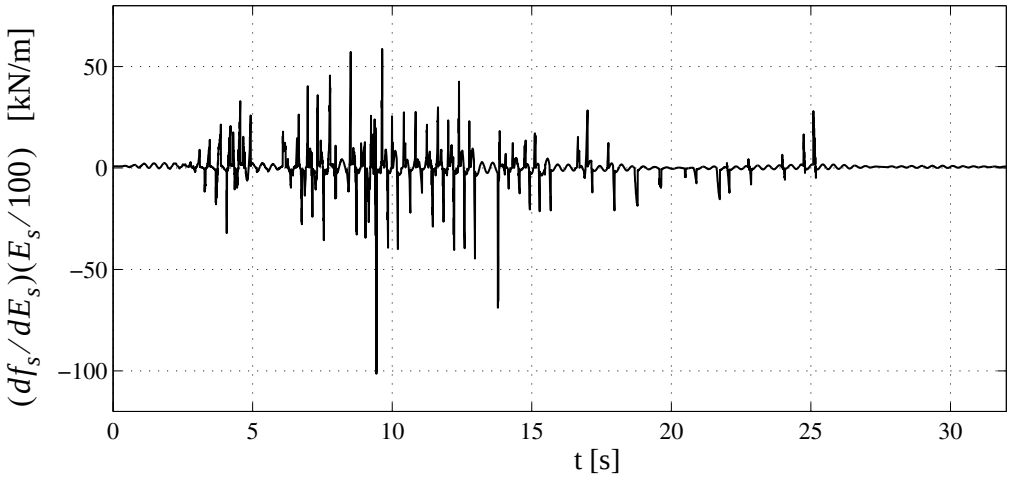

Figure 5.49 Dynamic analysis: sensitivity of connection shear force f_s acting at the left-end section of the composite beam to Young's modulus E_s of the beam-and-column steel material.

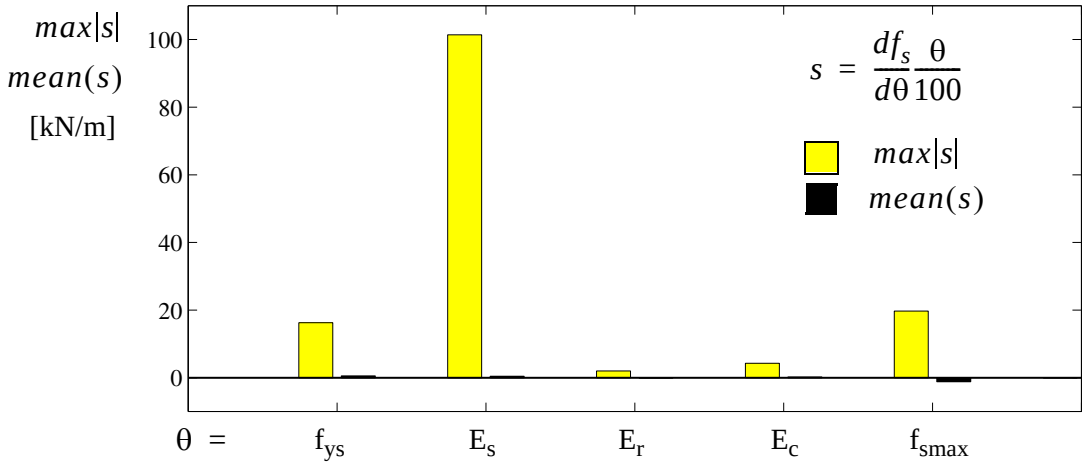

Figure 5.50 Dynamic analysis: comparison of response sensitivities of connection shear force f_s acting at the left-end composite beam section to material parameters to which f_s is most sensitive.

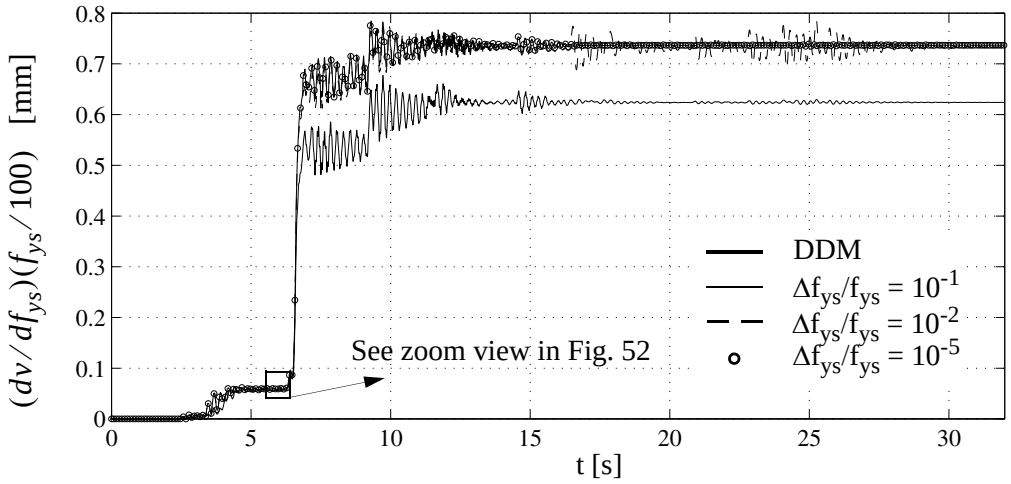

Figure 5.51 Convergence study of FFD to DDM sensitivity results for dynamic analysis: sensitivity of vertical displacement v at midspan of composite beam to yield strength f_{ys} of the beam-and-column steel material.

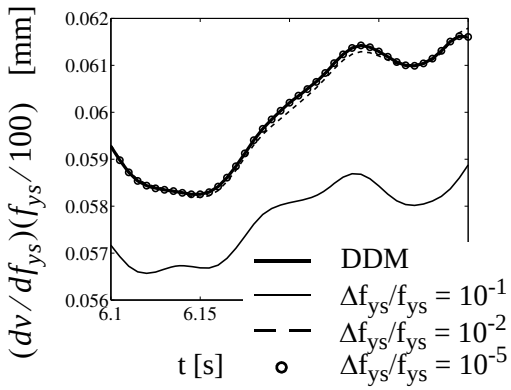

Figure 5.52 Convergence study of FFD to DDM sensitivity results for dynamic analysis: zoom view of sensitivity of vertical displacement v at midspan of composite beam to yield strength f_{ys} of the beam-and-column steel material (see Fig. 5.51).

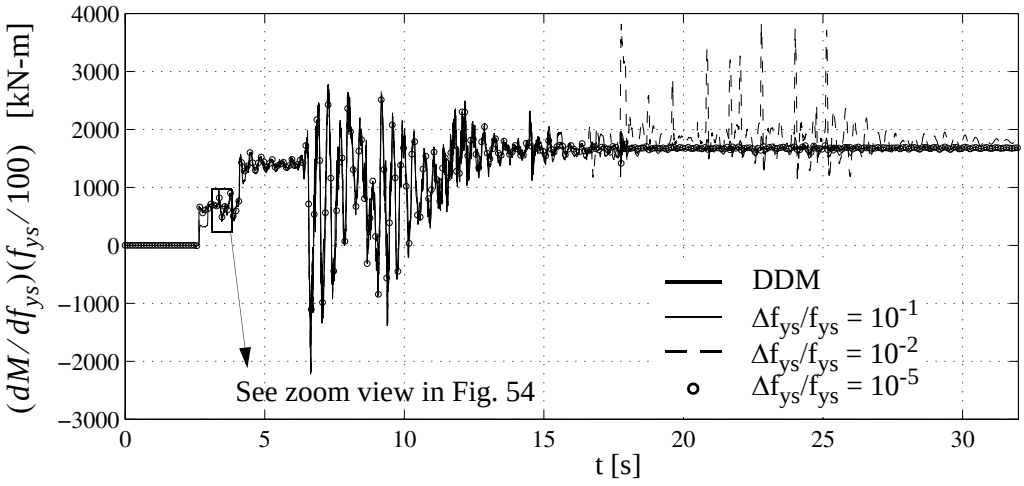

Figure 5.53 Convergence study of FFD to DDM sensitivity results for dynamic analysis: sensitivity of bending moment M acting at the left-end composite beam section to yield strength f_{ys} of beam-and-column steel material.

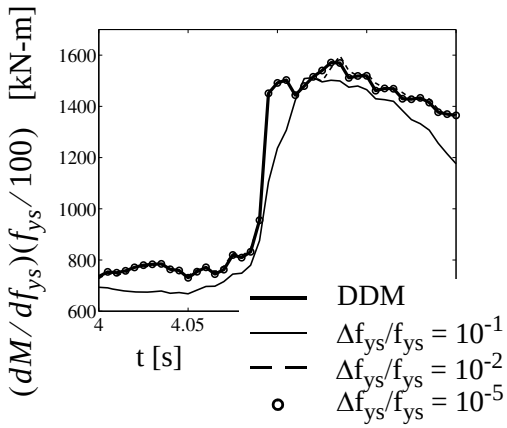

Figure 5.54 Convergence study of FFD to DDM sensitivity computations for dynamic analysis: zoom view sensitivity of bending moment M acting at the left-end composite beam section to yield strength f_{ys} of beam-and-column steel material (see Fig. 5.53).

5.4 CONCLUSIONS

This paper presents a newly developed response sensitivity computation methodology for nonlinear finite element based on a three-field mixed formulation derived from the Hu-Washizu functional. The formulation developed is based on the general Direct Differentiation Method (DDM), which consists of differentiating consistently the space (finite element) and time (finite difference) discrete equations of the structural response. The response sensitivity computation algorithm for three-field mixed finite element formulation is presented for the general case of geometric and material nonlinearities considering response sensitivity to geometric, material and loading parameters. This general algorithm is then specialized for materially-only nonlinear finite element models (i.e., linear geometry) and is presented in detail for 2-D frame finite elements. Particular attention

is given to steel-concrete composite frame finite elements, for which the three-field mixed formulation has been found beneficial in terms of accuracy in the numerical results. The DDM sensitivity computations are validated by comparisons with the Forward Finite Difference (FFD) analysis using as application example a realistic steel-concrete composite frame under quasi-static and dynamic loading. The finite element model of the proposed benchmark structure includes both monolithic beam elements and composite beam elements with deformable shear connection based on the three-field mixed formulation. Insight is gained into the effects and relative importance of the various material parameters upon the response behavior of the benchmark structure.

The addition of the method presented here for analytical sensitivity computation to finite elements based on a three-field mixed formulation offers a powerful tool for any kind of applications in which finite element response sensitivity analysis results are needed. These applications include structural reliability, structural optimization, structural identification, and finite element model updating. Furthermore, finite element response sensitivity analysis offers insight into structural response behavior and its sensitivity to modeling parameters.

5.5 ACKNOWLEDGEMENTS

Chapter 5, in full, is a reprint of the material as it appears in International Journal for Numerical Methods in Engineering Mechanics (2007), Barbato, M., Zona A., and Conte, J.P., 69(1):114-161 (Copyright John Wiley & Sons Limited, 2007, reproduced with permission). The dissertation author was first author and investigator of this paper.

APPENDIX A: DERIVATION OF SENSITIVITY EQUATIONS FOR NODAL DISPLACEMENT AND STRESS PARAMETERS

Eq. (5.61) is obtained by differentiating Eq. (5.55) with respect to θ as

$$\bar{\mathbf{E}}\frac{d\mathbf{e}(\theta)}{d\theta} - \bar{\mathbf{B}}\frac{d\mathbf{q}(\theta)}{d\theta} = \mathbf{0} \quad \Rightarrow \quad \bar{\mathbf{E}}\frac{d\mathbf{e}(\theta)}{d\theta} = \bar{\mathbf{B}}\frac{d\mathbf{q}(\theta)}{d\theta} \tag{5.91}$$

Pre-multiplying both sides of the second of Eqs. (5.91) by $\bar{\mathbf{D}}_t^{-1}\bar{\mathbf{E}}^T\bar{\bar{\mathbf{D}}}_t^{-1}$, we obtain

$$\bar{\mathbf{D}}_t^{-1}\bar{\mathbf{E}}^T\bar{\bar{\mathbf{D}}}_t^{-1}\bar{\mathbf{E}}\,\frac{d\mathbf{e}(\theta)}{d\theta} = \bar{\mathbf{D}}_t^{-1}\bar{\mathbf{E}}^T\bar{\bar{\mathbf{D}}}_t^{-1}\bar{\mathbf{B}}\,\frac{d\mathbf{q}(\theta)}{d\theta} \tag{5.92}$$

Using the definition of $\bar{\bar{\mathbf{D}}}_t$ in Eq. (5.63), we have

$$\mathbf{I}_s = \bar{\bar{\mathbf{D}}}_t\bar{\bar{\mathbf{D}}}_t^{-1} = \bar{\mathbf{E}}\bar{\mathbf{D}}_t^{-1}\bar{\mathbf{E}}^T\bar{\bar{\mathbf{D}}}_t^{-1} \tag{5.93}$$

where $\mathbf{I}_s$ denotes the unit matrix of dimension n_s x n_s.

Post-multiplying the first and last terms of Eq. (5.93) by $\bar{\mathbf{E}}$, we have

$$\mathbf{I}_s\bar{\mathbf{E}} = \bar{\mathbf{E}}\bar{\mathbf{D}}_t^{-1}\bar{\mathbf{E}}^T\bar{\bar{\mathbf{D}}}_t^{-1}\bar{\mathbf{E}} \quad \Rightarrow \quad \bar{\mathbf{E}} = \bar{\mathbf{E}}(\bar{\mathbf{D}}_t^{-1}\bar{\mathbf{E}}^T\bar{\bar{\mathbf{D}}}_t^{-1}\bar{\mathbf{E}}) \tag{5.94}$$

from which it can be deduced that

$$\bar{\mathbf{D}}_t^{-1}\bar{\mathbf{E}}^T\bar{\bar{\mathbf{D}}}_t^{-1}\bar{\mathbf{E}} = \mathbf{I}_e \tag{5.95}$$

where $\mathbf{I}_e$ denotes the unit matrix of dimension n_e x n_e. Thus, Eq. (5.92) reduces to Eq. (5.61).

Eq. (5.67) can be derived following a reasoning similar to the one above. Differentiating Eq. (5.56) with respect to θ yields

$$\bar{\mathbf{E}}^{\mathrm{T}} \frac{\mathrm{d}\mathbf{s}(\mathbf{e}(\theta), \theta)}{\mathrm{d}\theta} = \frac{\mathrm{d}\mathbf{a}(\mathbf{e}(\theta), \theta)}{\mathrm{d}\theta} \tag{5.96}$$

Pre-multiplying both sides of Eq. (5.96) by $\bar{\bar{\mathbf{D}}}_{\mathrm{t}}^{-1}\bar{\mathbf{E}}\bar{\mathbf{D}}_{\mathrm{t}}^{-1}$, we obtain

$$\bar{\bar{\mathbf{D}}}_{\mathrm{t}}^{-1}\bar{\mathbf{E}}\bar{\mathbf{D}}_{\mathrm{t}}^{-1}\bar{\mathbf{E}}^{\mathrm{T}} \frac{\mathrm{d}\mathbf{s}(\mathbf{e}(\theta), \theta)}{\mathrm{d}\theta} = \bar{\bar{\mathbf{D}}}_{\mathrm{t}}^{-1}\bar{\mathbf{E}}\bar{\mathbf{D}}_{\mathrm{t}}^{-1} \frac{\mathrm{d}\mathbf{a}(\mathbf{e}(\theta), \theta)}{\mathrm{d}\theta} \tag{5.97}$$

Using again Eq. (5.63), we can write

$$\mathbf{I}_{\mathrm{s}} = \bar{\bar{\mathbf{D}}}_{\mathrm{t}}^{-1}\bar{\bar{\mathbf{D}}}_{\mathrm{t}} = \bar{\bar{\mathbf{D}}}_{\mathrm{t}}^{-1}\bar{\mathbf{E}}\bar{\mathbf{D}}_{\mathrm{t}}^{-1}\bar{\mathbf{E}}^{\mathrm{T}} \tag{5.98}$$

from which Eq. (5.97) reduces to Eq. (5.67).

Eqs. (5.28) and (5.36) can be derived following the same reasoning used above for Eqs. (5.61) and (5.67), respectively.

APPENDIX B: EXPLICIT EXPRESSIONS FOR SECTION RESULTANT QUANTITIES

In this appendix, explicit expressions for the quantities **d**, **D**, and $\mathbf{A}_s(\mathbf{X})$ introduced in Section 5.2.3 are given for three important 2-D frame models: (1) Euler-Bernoulli monolithic beam; (2) Timoshenko monolithic beam; and (3) composite beam with distributed shear connection and Newmark's kinematic assumptions. The extension to 3-D frames is straightforward for the monolithic beams but more complicated for the composite beam with deformable shear connection (Dall'Asta 2001).

(1) Euler-Bernoulli monolithic beam (Fig. 5.55):

$$\mathbf{A}_s(x, y, \theta) = [1 \quad -y] \tag{5.99}$$

$$\boldsymbol{\epsilon}(\mathbf{X}, \theta) \equiv \varepsilon_x(x, y, \theta); \quad \boldsymbol{\sigma}(\mathbf{X}, \theta) \equiv \sigma_x(x, y, \theta) \tag{5.100}$$

$$\mathbf{d}(x, \theta) = \begin{bmatrix} \varepsilon_G(x, \theta) \\ \chi(x, \theta) \end{bmatrix} \tag{5.101}$$

$$\mathbf{D}(x, \theta) = \begin{bmatrix} N(x, \theta) \\ M(x, \theta) \end{bmatrix} \tag{5.102}$$

(2) Timoshenko monolithic beam (Fig. 5.56):

$$\mathbf{A}_s(x, y, \theta) = \begin{bmatrix} 1 & -y & 0 \\ 0 & 0 & 1 \end{bmatrix} \tag{5.103}$$

$$\boldsymbol{\epsilon}(\mathbf{X}, \theta) \equiv \begin{bmatrix} \varepsilon_x(x, y, \theta) \\ \gamma_{xy}(x, y, \theta) \end{bmatrix}; \quad \boldsymbol{\sigma}(\mathbf{X}, \theta) \equiv \begin{bmatrix} \sigma_x(x, y, \theta) \\ \tau_{xy}(x, y, \theta) \end{bmatrix} \tag{5.104}$$

$$\mathbf{d}(x, \theta) = \begin{bmatrix} \varepsilon_G(x, \theta) \\ \chi(x, \theta) \\ \gamma(x, \theta) \end{bmatrix} \tag{5.105}$$

$$\mathbf{D}(x, \theta) = \begin{bmatrix} N(x, \theta) \\ M(x, \theta) \\ V(x, \theta) \end{bmatrix} \tag{5.106}$$

(3) Newmark composite beam (Fig. 5.1):

$$\mathbf{A}_s(x, y, \theta) = \begin{bmatrix} 1 & 0 & (y_1 - y) & 0 \\ 0 & 1 & (y_2 - y) & 0 \\ 0 & 0 & 0 & 1 \end{bmatrix} \tag{5.107}$$

$$\boldsymbol{\epsilon}(\mathbf{X}, \theta) \equiv \begin{bmatrix} \varepsilon_{x1}(x, y, \theta) \\ \varepsilon_{x2}(x, y, \theta) \\ \delta_s(x, \theta) \end{bmatrix}; \quad \boldsymbol{\sigma}(\mathbf{X}, \theta) \equiv \begin{bmatrix} \sigma_{x1}(x, y, \theta) \\ \sigma_{x2}(x, y, \theta) \\ f_s(x, \theta)/A(x) \end{bmatrix} \tag{5.108}$$

$$\mathbf{d}(x, \theta) = \begin{bmatrix} \varepsilon_{x1}(x, \theta) \\ \varepsilon_{x2}(x, \theta) \\ \chi(x, \theta) \\ \delta_s(x, \theta) \end{bmatrix} \tag{5.109}$$

$$\mathbf{D}(x, \theta) = \begin{bmatrix} N_1(x, \theta) \\ N_2(x, \theta) \\ M_{12}(x, \theta) \\ f_s(x, \theta) \end{bmatrix} \tag{5.110}$$

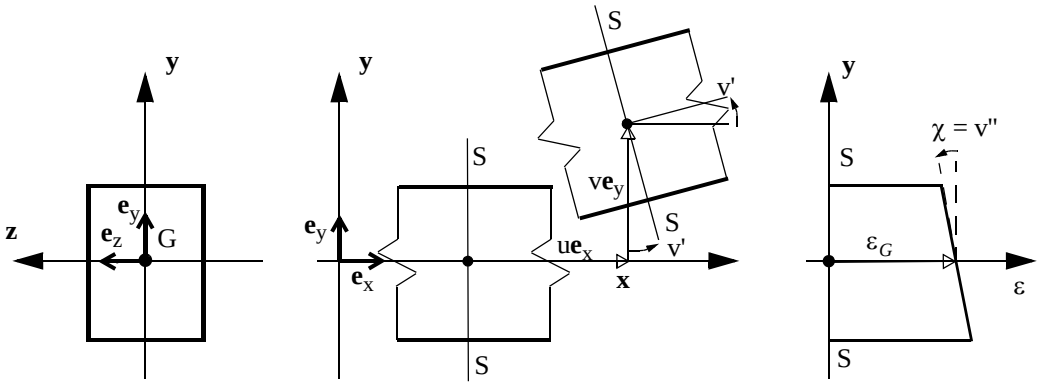

Figure 5.55 Kinematics of 2D monolithic Euler-Bernoulli beam model.

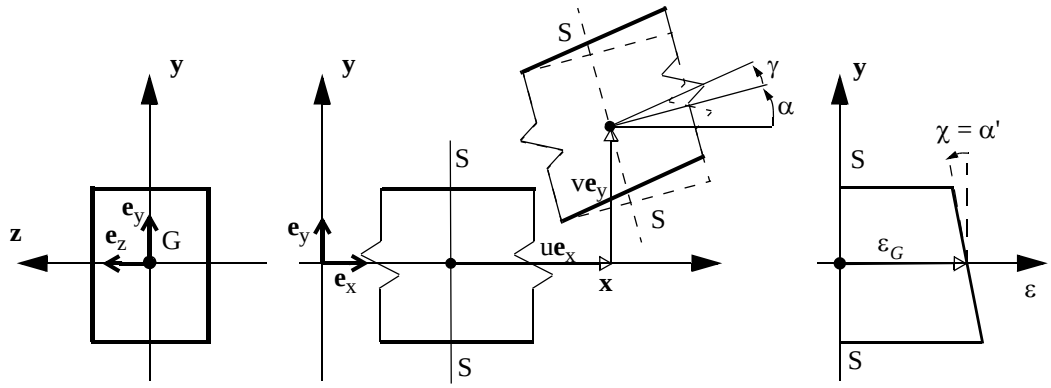

Figure 5.56 Kinematics of 2D monolithic Timoshenko beam model.

REFERENCES

Ayoub A., Filippou F.C. (2000) “Mixed formulation of nonlinear steel-concrete composite beam element.” *Journal of Structural Engineering* (ASCE), 126(3):371-381.

Balan T.A., Spacone E., Kwon M. (2001) “A 3D hypoplastic model for cyclic analysis of concrete structures.” *Engineering Structures*, 23(4):333-342.

Balan T.A., Filippou F.C., Popov E.P. (1997) “Constitutive model for 3D cyclic analysis of concrete structures.” *Journal of Engineering Mechanics* (ASCE), 123(2):143-153.

Barbato M., Conte J.P. (2005) “Finite element response sensitivity analysis: a comparison between force-based and displacement-based frame element models.” *Computer Methods in Applied Mechanics and Engineering*, 194(12-16):1479-1512.

Belytschko T., Liu W.K., Moran B. (2000) *Nonlinear Finite Elements for Continua and Structures*. Wiley, New York.

Chien W.Z. (1983) “Method of high-order Lagrange multiplier and generalized variational principles of elasticity with more general forms of functionals.” *Applied Mathematics and Mechanics*, 4(2):137-150.

Chopra A.K. (2001) *Dynamics of Structures: Theory and Applications to Earthquake Engineering.* Second Edition, Prentice Hall, Englewood Cliffs, New Jersey.

Conte J.P. (2001) “Finite element response sensitivity analysis in earthquake engineering.” *Earthquake Engineering Frontiers in the New Millennium.* Spencer & Hu, Swets & Zeitlinger, Lisse, The Netherlands, 395-401.

Conte J.P., Vijalapura P.K., Meghella M. (2003) “Consistent finite-element response sensitivity analysis.” *Journal of Engineering Mechanics* (ASCE), 129(12):1380-1393.

Conte J.P., Barbato M., Spacone E. (2004) “Finite element response sensitivity analysis using force-based frame models.” *International Journal for Numerical Methods in Engineering*, 59(13):1781-1820.

Dall'Asta A. (2001) “Composite beams with weak shear connection.” *International Journal of Solids and Structures*, 38(32-33):5605-5624.

Dall'Asta A., Zona A. (2002) “Non-linear analysis of composite beams by a displacement approach.” *Computers and Structures*, 80(27-30): 2217-2228.

Dall'Asta A., Zona A. (2004) “Slip locking in finite elements for composite beams with deformable shear connection.” *Finite Elements in Analysis and Design*, 40(13-14):1907-1930.

Dall'Asta A., Zona A. (2004a) “Comparison and validation of displacement and mixed elements for the non-linear analysis of continuous composite beams.” *Computers and Structures*, 82(23-26):2117-2130.

Dall'Asta A., Zona A. (2004b) “Three-field mixed formulation for the non-linear analysis of composite beams with deformable shear connection.” *Finite Elements in Analysis and Design*, 40(4):425-448.

Ditlevsen O., Madsen H.O. (1996) *Structural Reliability Methods*. Wiley, New York.

Eligenhausen R., Popov E.P., Bertero V.V. (1983) “Local bond stress-slip relationships of deformed bars under generalized excitations.” *Report No. 83/23*, EERC Earthquake Engineering Research Center, University of California, Berkeley, CA.

Filippou F.C., Constantinides M. (2004) “FEDEASLab getting started guide and simulation examples.” *Technical Report NEESgrid-2004-22*, August 31, 2004. <http://fedeaslab.berkeley.edu/>

Fraeijs De Veubeke B.M. (1965) “Displacement and equilibrium models in the finite element method.” *Stress Analysis* (Zienkiewicz OC, Hollister GS. ed.) John Wiley & Sons, London; 145-196. Reprinted in: *International Journal for Numerical Methods in Engineering* 2001; 52(3):287-342.

Franchin, P. (2003) “Reliability of uncertain inelastic structures under earthquake excitation.” *Journal of Engineering Mechanics* (ASCE), 130(2):180-191.

Haftka R.T., Gurdal Z. (1993) *Elements of Structural Optimization.* Third edition, Kluver Academic Publishers, Dordrecht.

Kleiber M., Antunez H., Hien T.D., Kowalczyk P. (1997) *Parameter Sensitivity in Nonlinear Mechanics: Theory and Finite Element Computations*. Wiley, New York.

Loma Prieta 1989 Accelerograms (1989), *PEER Strong Motion Database*, <http://peer.berkeley.edu/smcat/>

Malkus D.S., Hughes T.J.R. (1978) "Mixed finite element methods-reduced and selective integration techniques: a unification of concepts." *Computer Methods in Applied Mechanics and Engineering*, 15(1):63-81.

Mota A., Abel J.F. (2000) "On mixed finite element formulation and stress recovery techniques." *International Journal for Numerical Methods in Engineering*, 47(1-3):191-204.

Newmark N.M., Siess C.P., Viest I.M. (1951) "Tests and analysis of composite beams with incomplete interaction." *Proceedings, Society for Experimental Stress Analysis*, 9(1):75-92.

Newmark N.M. (1959) "A method of computation for structural dynamics." *Journal of the Engineering Mechanics Division* (ASCE), 85:67-94.

Noor A.K. (1983) "Multifield (mixed and hybrid) finite element models." *State-of-the-art surveys on finite element technology.* A.K. Noor and W.D. Pilkey eds., ASME, New York, 127-156.

Oehlers D.J., Bradford M.A. (2000) *Elementary Behaviour of Composite Steel and Concrete Structural Members*. Butterworth-Heinemann, Oxford.

Ollgaard J.G., Slutter R.G., Fisher J.W. (1971) "Shear strength of stud connectors in lightweight and normal weight concrete." *Engineering Journal* (AISC), 2Q:55-64.

Pandey P.C., Bakshi P. (1999) "Analytical response sensitivity computation using hybrid

finite elements.” *Computers and Structures*, 71(5):525-534.

Pian T.H.H. (1964) “Derivation of element stiffness matrices by assumed stress distribution. *AIAA J*, 2(7):1333-1336.

Scott M.H., Franchin P., Fenves G.L., Filippou F.C. (2004) “Response sensitivity for nonlinear beam-column elements.” *Journal of Structural Engineering* (ASCE), 130(9):1281-1288.

Spacone E., Ciampi V., Filippou F.C. (1995) “Mixed formulation of nonlinear beam finite element.” *Computers and Structures*, 58(1):71-83.

Spacone E., Filippou F.C., Taucer F.F. (1996) “Fibre beam-column element for nonlinear analysis of R/C frames. Part I: Formulation.” *Earthquake Engineering and Structural Dynamics*, 25(7):711-725.

Spacone E., El-Tawil S. (2004) “Nonlinear analysis of steel-concrete composite structures: state of the art.” *Journal of Structural Engineering* (ASCE), 130(2):159-168.

Stolarski H., Belytschko T. (1987) “Limitation principles for mixed finite elements based on the Hu-Washizu variational formulation.” *Computer Methods in Applied Mechanics and Engineering*, 60(2):195-216.

Taylor R.L., Filippou F.C., Saritas A., Auricchio F. (2003) “A mixed element method for beam and frame problems.” *Computational Mechanics*, 31(1-2):192-103.

The MathWorks (1997) “Matlab - High performance numeric computation and visualization software.” *User’s Guide*. Natick, MA.

Washizu K. (1975) *Variational methods in elasticity and plasticity.* Pergamon Press, Oxford.

Zhang Y., Der Kiureghian A. (1993) “Dynamic response sensitivity of inelastic structures.” *Computers Methods in Applied Mechanics and Engineering*, 108(1-2):23-36.

Zona A., Barbato M., Conte J.P. (2004) “Finite element response sensitivity analysis of steel-concrete composite structures.” *Report SSRP-04/02*, Department of Structural Engineering, University of California, San Diego, CA.

Zona A., Barbato M., Conte J.P. (2005) “Finite element response sensitivity analysis of steel-concrete composite beams with deformable shear connection.” *Journal of Engineering Mechanics* (ASCE), 131(11):1126-1139.

CHAPTER 6

SMOOTHNESS PROPERTIES OF FINITE ELEMENT RESPONSE SENSITIVITIES

6.1 INTRODUCTION

The field of structural reliability analysis has seen significant advances in the last two decades (Ditlevsen and Madsen 1996). Analytical and numerical methodologies have been developed and improved for the probabilistic analysis of real structures characterized in general by nonlinear behavior, material and geometric uncertainties and subjected to stochastic loads (Schueller et al. 2004). Reliability analysis methods have been successfully applied to problems such as the ones encountered in civil engineering and typically analyzed deterministically through the finite element method (Der Kiureghian and Ke 1988).

Several reliability analysis methods, such as asymptotic methods (First- and Second-Order Reliability Methods) (Breitung 1984; Der Kiureghian and Liu 1986; Der Kiureghian et al. 1987; Der Kiureghian 1996; Ditlevsen and Madsen 1996) and importance sampling with sampling distribution centered on the design point(s) (Schueller and Stix 1987; Melchers 1989; Au et al. 1999; Au and Beck 2001a) are characterized by the crucial step of finding the design point(s). In particular, asymptotic methods can provide reliability analysis results with a relatively small number of simulations (often of the order of 10-100 simulations for FORM analysis) and with a computational effort practically

independent of the magnitude of the failure probability. Furthermore, these methods provide important information such as reliability sensitivity measures, as a by-product of the design point search (Hohenbichler and Rackwitz 1986). Other reliability analysis methods, e.g., subset simulation (Au and Beck 2001b; Au and Beck 2003) and importance sampling with sampling distribution not centered at the design point(s) (Bucher 1988; Ang et al. 1992; Au and Beck 1999), do not use the concept of design point, do not require computation of response sensitivities, and therefore are not affected by smoothness or non-smoothness of the material constitutive models used. In general, the computational cost of these methods increases for decreasing magnitude of the failure probability. Thus, for very low failure probabilities, these methods could require a very large number of simulations.

In general, the design point(s) is(are) found as the solution(s) of a constrained optimization problem, in which the number of variables corresponds to the number of material, geometric and loading parameters modeled as random variables (Ditlevsen and Madsen 1996). The most effective optimization algorithms for high-dimensional problems are gradient-based methods coupled with algorithms for efficient and precise computation of response sensitivities to material, geometric and loading parameters (Liu and Der Kiureghian 1991). Moreover, these methods assume some smoothness properties of the objective and constraint functions, on which the convergence properties are dependent. Constraint function(s) that arise in structural engineering problems often do not possess second-order differentiability, as required by gradient-based optimization methods in order to achieve quadratic convergence rates (Gill et al. 1981). In general, they present discontinuities in the first derivatives (e.g., J_2 plasticity model, contact problems) or even

in the response (e.g., crack propagation), and further discontinuities are introduced by numerical solution methodologies (e.g., finite element, finite difference, numerical integration).

Significant research efforts have been devoted to the development of smooth nonlinear material constitutive models, in order to better describe actual material behavior. Important characteristics such as Baushinger's effect for steel and hysteresis loops for concrete are most accurately described by smooth material models. Other smooth versus non-smooth material behavioral properties (e.g., shape of relation for concrete in tension) may have a negligible effect on simulated structural response, but a significant effect on response sensitivities to material parameters.

This chapter describes some features of response sensitivity analysis using smooth and non-smooth material constitutive laws. The response sensitivity computation algorithm is presented for the Menegotto-Pinto smooth constitutive model typically used for structural steel (Menegotto and Pinto 1973). Continuity of finite element response sensitivities is analyzed and a sufficient condition on the smoothness properties of material constitutive models to obtain such continuity is stated and proved for the quasi-static case. Based on application examples, remarks are made on the continuity (or lack thereof) of response sensitivities for the dynamic case, which is more difficult to study mathematically. The Direct Differentiation Method (DDM) (Zhang and Der Kiureghian 1993; Kleiber et al. 1997; Conte 2001; Conte et al. 2003) is used for finite element response sensitivity analysis.

The implications of using smooth versus non-smooth material constitutive models on finite element response and response sensitivity analyses are discussed. Based on the results obtained, conclusions are drawn on the need to use existing or develop new inelastic material constitutive models with specified smoothness properties both in the monotonic as well as cyclic hysteretic behavior for applications requiring continuous response sensitivities such as gradient-based optimization.

It is worth mentioning that response sensitivity analysis finds application not only in reliability analysis, which is the focus of this study, but also in structural optimization, structural identification, finite element model updating and any other field in which gradient-based optimization techniques are used. The results presented in this chapter are general and apply to any situation for which response sensitivity analysis is required.

6.2 MATERIAL CONSTITUTIVE MODELS

In this work, two different material constitutive models typically used to describe the behavior of structural steel are considered: the one-dimensional J_2 plasticity model (also more commonly known as bilinear inelastic model), for which the sensitivity computation algorithm is presented elsewhere (Conte et al. 2003), and the Menegotto-Pinto model (1973) in the version extended by Filippou et al. (1983) to account for isotropic strain hardening, for which the response sensitivity computation algorithm is developed and presented in the following sections.

The J_2 plasticity model with Von Mises yield surface is a well-known non-smooth plasticity model for metallic materials. Its one-dimensional version presents a kink at the

yielding point of the $\sigma - \varepsilon$ relation, leading to discontinuities in response sensitivities at elastic-to-plastic state transition events (Conte 2001).

The Menegotto-Pinto (M-P) one-dimensional plasticity model is a computationally efficient smooth inelastic model typically used for structural steel, showing very good agreement with experimental results, particularly from cyclic tests on reinforcing steel bars. A typical cyclic stress-strain response behavior of steel modeled using the Menegotto-Pinto model is presented in Figure 6.1. It presents two favorable features for finite element response, response sensitivity and reliability analyses: (a) the model expresses explicitly the current stress as a function of the current strain, so that it is computationally more efficient than competing models such as the Ramberg-Osgood model (Ramberg and Osgood 1943); (b) the constitutive law is smooth and continuously differentiable (with respect to strain and constitutive material parameters), therefore producing response sensitivities continuous everywhere. Furthermore, the M-P model can accommodate modifications in order to account for local buckling of steel bars in reinforced concrete members (Monti and Nuti 1992), and can be used for macroscopic modeling of hysteretic behavior of structures or substructures with an appropriate choice of the modeling parameters. It is also noteworthy that the Menegotto-Pinto model is a physically motivated model of structural material hysteresis, and its performance in representing structural physical behavior is not undermined by mathematical features that can lead to non-physical analysis results. Such non-physical results have been documented for widely used models such as the Bouc-Wen hysteretic model based on nonlinear differential equations (Thyagarajan and Iwan 1990). Caution is needed in the use of such mathematically-based models in order to

avoid non-physical analysis results, and preference should be granted to physically-based models such as the Menegotto-Pinto model used in this work.

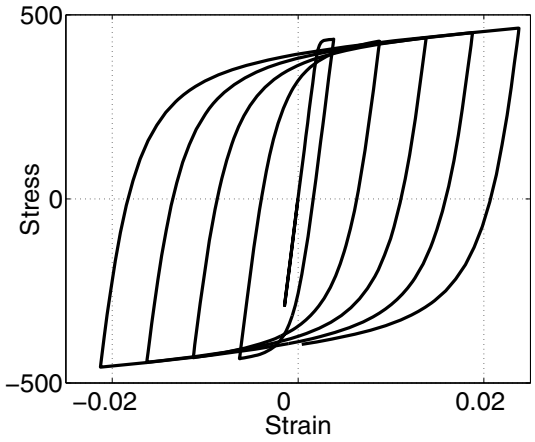

Figure 6.1 Cyclic stress-strain response behavior of structural steel modeled using the Menegotto-Pinto model.

6.2.1 Response computation for the Menegotto-Pinto smooth constitutive model

The M-P model is described by the following equations

$$\sigma^* = b\varepsilon^* + \frac{(1-b)\varepsilon^*}{(1+|\varepsilon^*|^R)^{1/R}} \tag{6.1}$$

$$\varepsilon^* = \frac{\varepsilon - \varepsilon_r}{\varepsilon_y - \varepsilon_r} \tag{6.2}$$

$$\sigma^* = \frac{\sigma - \sigma_r}{\sigma_y - \sigma_r} \tag{6.3}$$

Eq. (6.1) represents a smooth curved transition from an asymptotic straight line with slope E_0 to another asymptotic straight line with slope E_1, where b is the ratio between E_1 and E_0; ε^* and σ^* are the normalized strain and stress, respectively; ε_y and σ_y are the

coordinates in the strain-stress plane of the intersection of the two asymptotes; ε_r and σ_r are the coordinates in the strain-stress plane of the point where the last strain reversal took place; ε and σ are the current strain and stress, respectively; R is a parameter describing the curvature of the transition curve between the two asymptotes. This model is completed by updating rules for ε_r , σ_r, ε_y , σ_y, and R at each strain reversal event. For example, parameter R is obtained as

$$R = R_0 - \frac{a_1 \cdot \xi}{a_2 + \xi} \tag{6.4}$$

in which R_0 is the value of the parameter R during the first loading; a_1 and a_2 are experimentally determined parameters; ξ is the ratio between the maximum plastic strain, $\varepsilon^p_{max} = \max\left|\varepsilon_{max} - \varepsilon_y\right|$, and the initial yielding strain, ε_{y0}.

To account for isotropic hardening, Filippou et al. (1983) proposed a stress shift σ_{sh} in the linear yield asymptote depending on the maximum plastic strain as

$$\frac{\sigma_{sh}}{\sigma_{y0}} = a_3 \cdot \left(\frac{\varepsilon_{max}}{\varepsilon_{y0}} - 1\right) \tag{6.5}$$

in which a_3 and a_4 are experimentally determined parameters and ε_{max} is the absolute maximum total strain at the instant of strain reversal. For this model, the updating rules at the instant of strain reversal (detected in the time step $[t_n, t_{n+1}]$) are

$$\varepsilon_{r,\,n+1} = \varepsilon_n; \quad \sigma_{r,\,n+1} = \sigma_n \tag{6.6}$$

$$\varepsilon^{p}_{max,\,n+1} = \begin{cases} \varepsilon^{p}_{max,\,n}; \text{ if } \varepsilon^{p}_{max,\,n} > |\varepsilon_n - \varepsilon_{y,\,n}| \\ |\varepsilon_n - \varepsilon_{y,\,n}|; \quad \text{otherwise} \end{cases} \tag{6.7}$$

$$\xi_{n+1} = \frac{\varepsilon^{p}_{max,\,n+1}}{\varepsilon_{y0}} \tag{6.8}$$

$$\varepsilon_{max,\,n+1} = \begin{cases} \varepsilon_{max,\,n}; \text{ if } \varepsilon_{max,\,n} > |\varepsilon_n| \\ |\varepsilon_n|; \quad \text{otherwise} \end{cases} \tag{6.9}$$

$$\sigma_{sh,\,n+1} = \max[a_3 \cdot (\varepsilon_{max,\,n+1} - a_4 \cdot \varepsilon_{y0}) \cdot E;\, 0] \tag{6.10}$$

$$\varepsilon_{y,\,n+1} = \frac{\sigma_{r,\,n+1} - E \cdot \varepsilon_{r,\,n+1} \pm [(1-b) \cdot \sigma_{y0} + \sigma_{sh,\,n+1}]}{(b-1) \cdot E} \tag{6.11}$$

$$\sigma_{y,\,n+1} = b \cdot E \cdot \varepsilon_{y,\,n+1} \pm [(1-b) \cdot \sigma_{y0} + \sigma_{sh,\,n+1}] \tag{6.12}$$

In Eqs. (19) and (20), the "+" sign has to be used for strain inversion from positive strain increment (tensile increment) to negative strain increment (compressive increment), while the " – " sign is required for strain inversion from negative strain increment to positive strain increment.

6.2.2 Response sensitivity computation for the Menegotto-Pinto smooth constitutive model

Following the Direct Differentiation Method (DDM), the exact response sensitivities of the discretized material constitutive laws are required in finite element response sensitivity analysis. As already seen in previous Chapters, the DDM consists of differentiating analytically the space- and time-discretized equations of motion/equilibrium of the

finite element model of the structural system considered. It involves (1) computing the derivatives (with respect to the sensitivity parameters) of the element and material history/ state variables conditional on fixed nodal displacements at the structure level (conditional sensitivities), (2) forming the right-hand-side of the response sensitivity equation at the structure level, (3) solving the resulting equation for the nodal displacement response sensitivities, and (4) updating the unconditional derivatives of all history/state variables (unconditional sensitivities). The response sensitivity computation algorithm affects the various hierarchical layers of finite element response calculation, namely the structure, element, section, and material levels. This section presents the algorithm for computing the response sensitivities of the M-P material constitutive model over a single time step.

(1) Sensitivity parameters

The material constitutive parameters selected as sensitivity parameters are: elastic Young's modulus (E); initial yield stress (σ_{y0}); plastic-to-elastic material stiffness ratio (b).

(2) Input at time $t = t_{n+1}$

The input information for response sensitivity computation at time $t = t_{n+1}$ consists of:

- Current strain (ε_{n+1}) and stress (σ_{n+1}) and history variables *h* ($\varepsilon_{r,\,n+1}$, $\sigma_{r,\,n+1}$, $\varepsilon^{p}_{max,\,n+1}$, ξ_{n+1}, $\varepsilon_{max,\,n+1}$, $\sigma_{sh,\,n+1}$, $\varepsilon_{y,\,n+1}$, $\sigma_{y,\,n+1}$) after convergence for the response computation at time t_{n+1}.

- Unconditional sensitivities at time t_n: $(d\varepsilon/d\theta)_n$, $(d\sigma/d\theta)_n$, $(d\varepsilon_r/d\theta)_n$, $(d\sigma_r/d\theta)_n$, $(d\varepsilon^p_{max}/d\theta)_n$, $(d\xi/d\theta)_n$, $(d\varepsilon_{max}/d\theta)_n$, $(d\sigma_{sh}/d\theta)_n$, $(d\varepsilon_y/d\theta)_n$, $(d\sigma_y/d\theta)_n$.

(3) Algorithm

IF strain reversal took place in time step $[t_n, t_{n+1}]$,

THEN compute the sensitivities of all history variables, $(dh/d\theta)_{n+1}$, consistently with the constitutive law integration scheme, i.e.,

$$\left(\frac{d\varepsilon_r}{d\theta}\right)_{n+1} = \left(\frac{d\varepsilon}{d\theta}\right)_n ; \quad \left(\frac{d\sigma_r}{d\theta}\right)_{n+1} = \left(\frac{d\sigma}{d\theta}\right)_n \tag{6.13}$$

$$\left(\frac{d\varepsilon^p_{max}}{d\theta}\right)_{n+1} = \begin{cases} \left(\frac{d\varepsilon^p_{max}}{d\theta}\right)_n ; & \text{if } \varepsilon^p_{max,\,n} > |\varepsilon_n - \varepsilon_{y,\,n}| \\ \text{sign}(\varepsilon_n - \varepsilon_{y,\,n}) \cdot \left[\left(\frac{d\varepsilon}{d\theta}\right)_n - \left(\frac{d\varepsilon_y}{d\theta}\right)_n\right]; & \text{otherwise} \end{cases} \tag{6.14}$$

$$\left(\frac{d\xi}{d\theta}\right)_{n+1} = \frac{\left(\frac{d\varepsilon^p_{max}}{d\theta}\right)_{n+1} \cdot \varepsilon_{y0} - \varepsilon^p_{max,\,n+1} \cdot \frac{d\varepsilon_{y0}}{d\theta}}{\varepsilon^2_{y0}} \tag{6.15}$$

$$\left(\frac{d\varepsilon_{max}}{d\theta}\right)_{n+1} = \begin{cases} \left(\frac{d\varepsilon_{max}}{d\theta}\right)_n ; & \text{if } \varepsilon_{max,\,n} > |\varepsilon_n| \\ \text{sign}(\varepsilon_n) \cdot \left(\frac{d\varepsilon}{d\theta}\right)_n ; & \text{otherwise} \end{cases} \tag{6.16}$$

$$\left(\frac{d\sigma_{sh}}{d\theta}\right)_{n+1} = \begin{cases} a_3 \cdot \left\{ (\varepsilon_{max,\,n+1} - a_4 \cdot \varepsilon_{y0}) \cdot \frac{dE}{d\theta} + \left[\left(\frac{d\varepsilon_{max}}{d\theta}\right)_{n+1} - a_4 \cdot \frac{d\varepsilon_{y0}}{d\theta} \right] \cdot E \right\} & \text{if } \sigma_{sh,\,n+1} > 0 \\ 0; & \text{otherwise} \end{cases} \tag{6.17}$$

$$\left(\frac{d\varepsilon_y}{d\theta}\right)_{n+1} = \frac{\left(\frac{d\sigma_r}{d\theta}\right)_{n+1} - \varepsilon_{r,\,n+1} \cdot \frac{dE}{d\theta} - E \cdot \left(\frac{d\varepsilon_r}{d\theta}\right)_{n+1}}{(b-1) \cdot E} \pm \frac{\left[(1-b) \cdot \frac{d\sigma_{y0}}{d\theta} - \sigma_{y0} \cdot \frac{db}{d\theta} + \left(\frac{d\sigma_{sh}}{d\theta}\right)_{n+1} \right]}{(b-1) \cdot E} - \frac{\{\sigma_{r,\,n+1} - E \cdot \varepsilon_{r,\,n+1} \pm [(1-b) \cdot \sigma_{y0} + \sigma_{sh,\,n+1}]\} \cdot \left[E\frac{db}{d\theta} - (1-b)\frac{dE}{d\theta} \right]}{(1-b)^2 \cdot E^2} \tag{6.18}$$

$$\left(\frac{d\sigma_y}{d\theta}\right)_{n+1} = \frac{db}{d\theta} \cdot E \cdot \varepsilon_{y,\,n+1} + b \cdot \frac{dE}{d\theta} \cdot \varepsilon_{y,\,n+1} + b \cdot E \cdot \left(\frac{d\varepsilon_y}{d\theta}\right)_{n+1} \pm \left[(1-b) \cdot \frac{d\sigma_{y0}}{d\theta} - \sigma_{y0} \cdot \frac{db}{d\theta} + \left(\frac{d\sigma_{sh}}{d\theta}\right)_{n+1} \right] \tag{6.19}$$

In Eqs. (26) and (27), the “+” sign has to be used for strain inversion from positive strain increment (tensile increment) to negative strain increment (compressive increment), while the “ – ” sign is required for strain inversion from negative strain increment to positive strain increment.

ELSE $(dh/d\theta)_{n+1} = (dh/d\theta)_n$ (since all the above history variables h remain fixed between two consecutive strain reversal events).

END IF

COMPUTE

$$\left(\frac{dR}{d\theta}\right)_{n+1} = -\left(\frac{d\xi}{d\theta}\right)_{n+1} \cdot \frac{a_1 \cdot a_2}{(a_2 + \xi_{n+1})^2} \tag{6.20}$$

$$\left(\frac{d\varepsilon^*}{d\theta}\right)_{n+1} = \frac{\left(\frac{d\varepsilon}{d\theta}\right)_{n+1} - \left(\frac{d\varepsilon_r}{d\theta}\right)_{n+1}}{\varepsilon_{y,\,n+1} - \varepsilon_{r,\,n+1}} - \frac{\left[\left(\frac{d\varepsilon_y}{d\theta}\right)_{n+1} - \left(\frac{d\varepsilon_r}{d\theta}\right)_{n+1}\right] \cdot (\varepsilon_{n+1} - \varepsilon_{r,\,n+1})}{(\varepsilon_{y,\,n+1} - \varepsilon_{r,\,n+1})^2} \tag{6.21}$$

$$\begin{aligned}\left(\frac{d\sigma^*}{d\theta}\right)_{n+1} &= b \cdot \left(\frac{d\varepsilon^*}{d\theta}\right)_{n+1} + \frac{db}{d\theta} \cdot \varepsilon^*_{n+1} \\ &\quad + \frac{\left(\frac{dR}{d\theta}\right)_{n+1}}{R_{n+1}}\left[\frac{\ln\left|\varepsilon^*_{n+1}\right|\left|\varepsilon^*_{n+1}\right|^{R_{n+1}}}{(1 + \left|\varepsilon^*_{n+1}\right|^{R_{n+1}})} - \frac{\ln(1 + \left|\varepsilon^*_{n+1}\right|^{R_{n+1}})}{R_{n+1}}\right] \\ &\quad + \frac{(1-b) \cdot \left[\left(\frac{d\varepsilon^*}{d\theta}\right)_{n+1} - \varepsilon^*_{n+1}\right] - \frac{db}{d\theta} \cdot \varepsilon^*_{n+1}}{(1 + \left|\varepsilon^*_{n+1}\right|^{R_{n+1}})^{1/R_{n+1}}} \\ &\quad + \frac{\mathrm{sign}(\varepsilon^*_{n+1}) \cdot R_{n+1} \cdot \left(\frac{d\varepsilon^*}{d\theta}\right)_{n+1}}{\left|\varepsilon^*_{n+1}\right|}\end{aligned} \tag{6.22}$$

$$\begin{aligned}\left(\frac{d\sigma}{d\theta}\right)_{n+1} &= \left(\frac{d\sigma^*}{d\theta}\right)_{n+1} \cdot (\sigma_{y,\,n+1} - \sigma_{r,\,n+1}) \\ &\quad + \sigma^*_{n+1} \cdot \left[\left(\frac{d\sigma_y}{d\theta}\right)_{n+1} - \left(\frac{d\sigma_r}{d\theta}\right)_{n+1}\right] + \left(\frac{d\sigma_r}{d\theta}\right)_{n+1}\end{aligned} \tag{6.23}$$

END

The DDM requires computing at each analysis step, after convergence is achieved for the response calculation, the structure resisting force sensitivities for nodal displacements kept fixed (i.e., conditional sensitivities). At the material level, the required condi-

tional sensitivities (for ε_{n+1} fixed) can be obtained from Eqs. (28) through (31) after setting $(d\varepsilon/d\theta)_{n+1} = 0$.

6.3 APPLICATION EXAMPLE

6.3.1 Description of the benchmark structure

A three-story one-bay steel shear-frame is considered as application example in this study (Figure 6.2). The structure has been chosen simple enough to allow for closed-form computation of the design point (for pushover analysis and in the case of J_2 plasticity), yet realistic and complex enough to illustrate the main features and difficulties encountered in the general class of problems under study. In fact, the same structure example has been also used to illustrate the detrimental effects that discontinuities in finite element response sensitivities could have on the search for the design point(s). More complex examples or more complete and advanced reliability analyses would not achieve this objective as simply and as clearly. In fact, problems of dimension higher than two in the parameter space do not allow simple visualization of the limit-state function and limit-state surface (visualization is still possible for limit-state surfaces of three parameter problems). Moreover, other not easily recognizable difficulties for the design point search could be superimposed to the detrimental effects of response sensitivity discontinuities (e.g., multiple design points, saddle points).

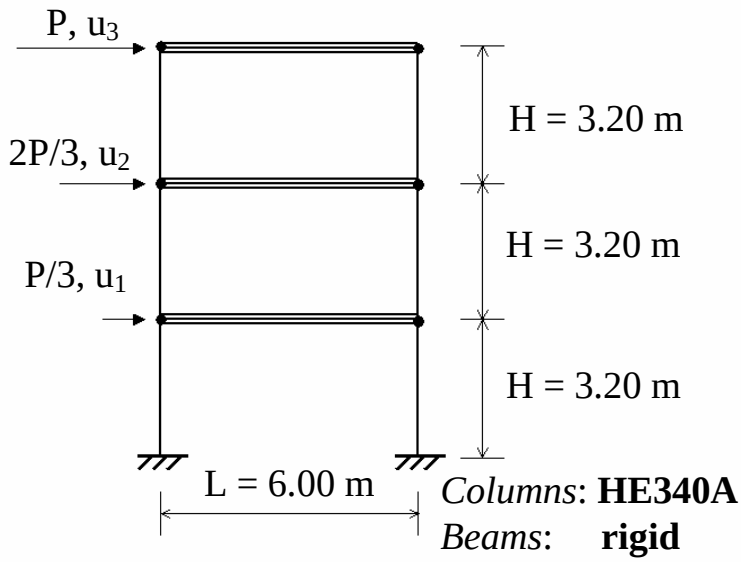

Figure 6.2 Shear-frame structure: geometry, floor displacements and quasi-static horizontal loads.

The shear-frame has three stories of height H = 3.20m each, and one bay of length L = 6.00m. The columns are European HE340A steel columns with moment of inertia along the strong axis $I = 27690.0\text{cm}^4$. The steel material has a Young's modulus $E = 2 \times 10^5 \text{N/mm}^2$ and an initial yield stress $f_{y0} = 350\text{N/mm}^2$. The initial yield moment of the columns is $M_{y0} = 587.3\text{kN} - \text{m}$. The beams are considered rigid to enforce a typical shear building behavior. Under this assumption, the initial yield shear force for each story is $F_{y0} = 734\text{kN}$.

The frame described above is assumed to be part of a building structure with a distance between frames L' = 6.00m. The tributary mass per story, M, is obtained assuming a distributed gravity load of $q = 8\text{kN/m}^2$, accounting for the structure own weight, as

well as for permanent and live loads, and is equal to $M = 28.8 \times 10^3 kg$. The fundamental period of the linear elastic undamped shear-frame is T_1 = 0.38s. Natural frequencies, natural periods and effective modal mass ratios for the undamped structure are given in Table 6.1. Viscous damping in the form of Rayleigh damping is assumed with a damping ratio $\xi = 0.05$ for the first and third modes of vibration.

Table 6.1 Modal analysis results for the linear elastic undamped three-story one-bay shear-frame

Mode #	Natural circular frequencyω (rad/s)	Natural period T (s)	Effective modal mass ratio (%)
1	16.70	0.38	91.41
2	46.80	0.13	7.49
3	67.62	0.09	1.10

The story shear force - interstory drift relation is modeled using three different hysteretic models, which have in common the initial stiffness K = 40.56kN/mm, the initial yield force F_{y0} = 734kN and the post-yield stiffness to initial stiffness ratio b = 0.10. The three models are: (a) Menegotto-Pinto model with parameters R_0 = 20, a_1 = 18.5, a_2 = 0.15, $a_3 = a_4 = 0$, denoted as 'M-P (R_0 = 20)' in the sequel; (b) Menegotto-Pinto model with parameters R_0 = 80, a_1 = 18.5, a_2 = 0.15, $a_3 = a_4 = 0$, denoted as 'M-P (R_0 = 80)' hereafter; (c) uni-axial J_2 plasticity model with $H_{kin} = K/9 = 4.057 kN/mm^2$ (kinematic hardening modulus), $H_{iso} = 0 kN/mm^2$ (isotropic hardening modulus), and $\alpha_0 = 0 kN/mm^2$ (initial back-stress), denoted as 'J_2 plasticity' hereafter. The M-P (R_0 =

20) model is characterized by typical values of the parameters used for common structural steel, while the M-P ($R_0 = 80$) model is used only for the purpose of reproducing as closely as possible with a smooth inelastic model the behavior of the non-smooth J_2 plasticity model.

In the following examples, finite element response and response sensitivity analyses are performed using the general-purpose nonlinear finite element structural analysis program FEDEASLab (Filippou and Constantinides 2004). FEDEASLab is a Matlab (The Mathworks 1997) toolbox suitable for linear and non-linear, static and dynamic structural analysis, which also incorporates a general framework for parameterization of finite element models and for response sensitivity computation using the DDM (Franchin 2004).

6.3.2 Finite element response and response sensitivity analysis results

Response sensitivity analysis can be used to gain insight into the effects and relative importance of the loading and material parameters θ on the response behavior of a structural system. The example structure presented above is subjected to a response and response sensitivity analysis for quasi-static cyclic loading and dynamic loading in the form of seismic base excitation, respectively. Some response quantities and their sensitivities to various material and loading parameters are presented and carefully examined below.

In the quasi-static analysis, horizontal loads are applied at floor levels with an upper triangular distribution, with a maximum load $P = P_{max}$ at roof level and a total

horizontal load (= total base shear) $P_{tot} = 2P$ (see Figure 6.2). The loading history is presented in Figure 6.3.

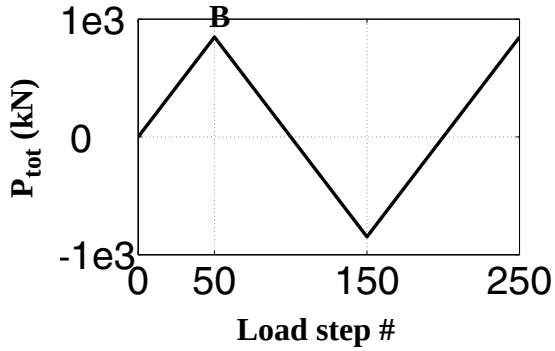

Figure 6.3 Quasi-static cyclic loading.

In Figure 6.4, the relation between the total base shear P_{tot} and the roof horizontal displacement u_3 is plotted for the three constitutive models considered. After the first unloading (point B), the response of the M-P ($R_0 = 20$) model deviates significantly from the responses corresponding to the J_2 plasticity and M-P ($R_0 = 80$) models.

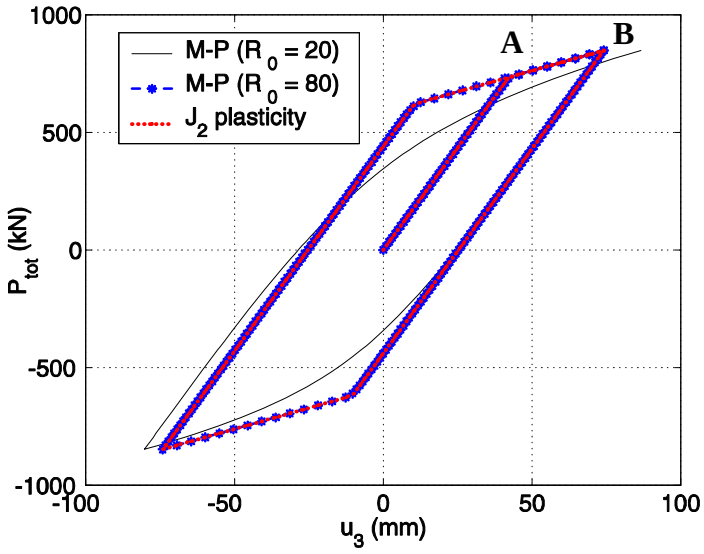

Figure 6.4 Total base shear, P_{tot}, versus roof displacement, u_3, for quasi-static cyclic loading and different constitutive models.

Figs. 6.5 and 6.6 display the normalized sensitivities of the roof displacement u_3 to the initial yield force F_{y0} and the load parameter P_{max}, respectively. The normalized sensitivities are obtained by multiplying the response sensitivities with the nominal value of the corresponding sensitivity parameters and dividing the results by one hundred. Thus, these normalized sensitivities represent the total change in the response quantity of interest due to one percent change in the sensitivity parameter value and can be used for assessing quantitatively the relative importance of the sensitivity parameters in the deterministic sense. Similar to the response results, the response sensitivities obtained from the J_2 plasticity model are very close to the ones produced by the M-P ($R_0 = 80$) model and quite different from the ones given by the M-P ($R_0 = 20$) model. It is important to note that, while the response sensitivities for the J_2 plasticity model are discontinuous at elastic-to-plastic

material state transition events, the response sensitivities produced by the M-P models are continuous everywhere (see for example the inset in Figure 6.5, corresponding to point A in Figure 6.4). These conclusions are consistent with previous findings of other researchers (Haukaas and Der Kiureghian 2004).

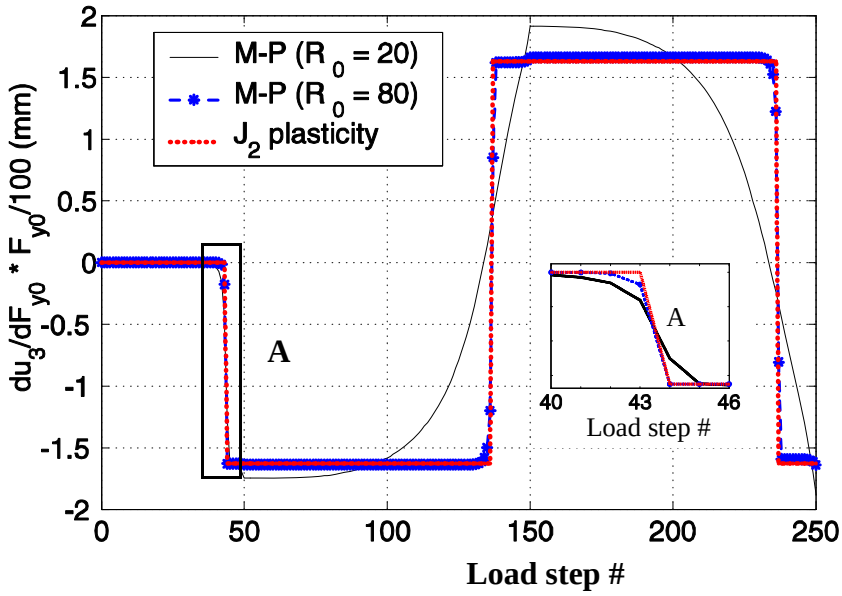

Figure 6.5 Normalized sensitivity of roof displacement u_3 to initial yield force F_{y0} (quasi-static cyclic loading).

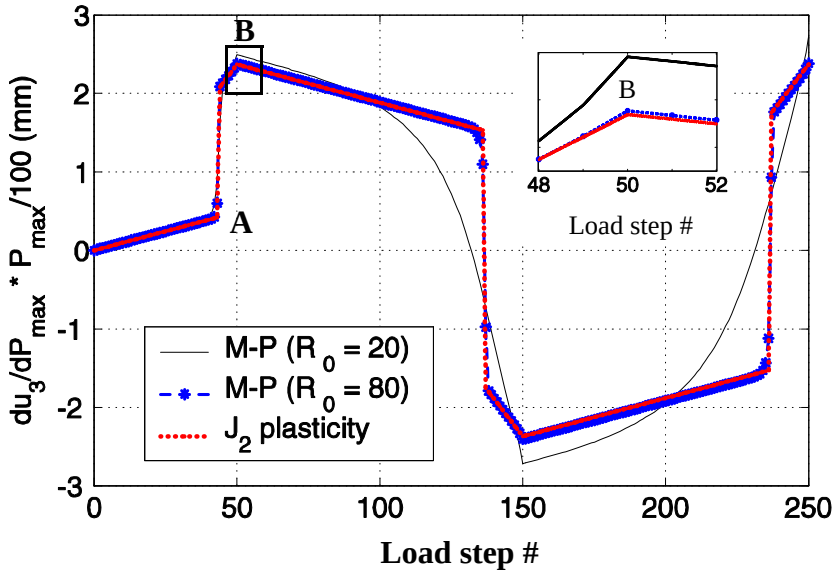

Figure 6.6 Normalized sensitivity of roof displacement u_3 to loading parameter P_{max} (quasi-static cyclic loading).

The absence of discontinuities in the response sensitivities for all three constitutive models at unloading events is noteworthy (see for example the inset in Figure 6.6, corresponding to point B in Figure 6.4). It has been proven (Haukaas and Der Kiureghian 2004) that no discontinuities arise from elastic unloading events. This proof assumes explicitly a linear elastic unloading branch in the material constitutive law (as for the uniaxial J_2 plasticity model considered herein) and implicitly that the entire structure (i.e., all yielded integration points) undergoes elastic unloading at the same load/time step. The M-P model presented herein does not have a linear elastic unloading branch; nevertheless, it does not exhibit discontinuities at unloading events as well. It can be proven (see Appendix) that, if only one-dimensional constitutive models are employed, unloading events in quasi-static finite element analysis do not produce response sensitivity discontinuities provided that

the unloading branches of the material constitutive laws can be expanded in Taylor series about the unloading points. A physical explanation of this statement is that any material unloading event can be seen as connecting two stress-strain points on the same (unloading) branch of the constitutive model, as opposed to a material yielding event which connects two stress-strain points belonging to two different branches in the case of a non-smooth constitutive model (see Figure 6.7).

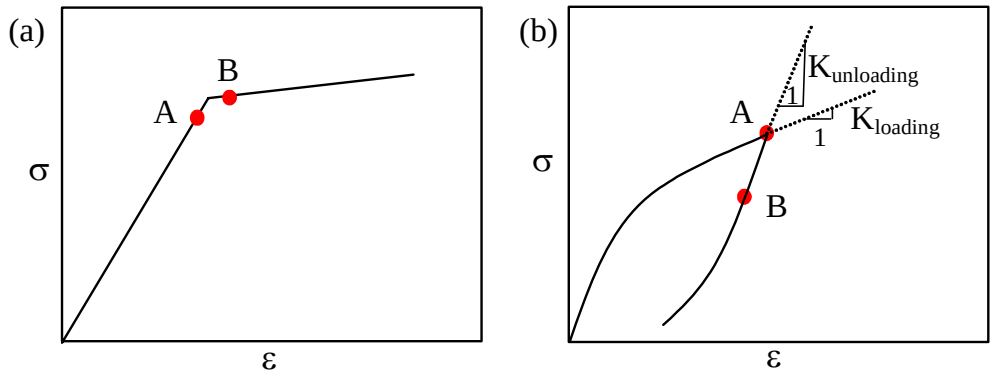

Figure 6.7 Examples of branches of material constitutive models: (a) loading branch with elastic-to-plastic material state transition (discontinuous response sensitivities), and (b) smooth loading and unloading branches at unloading event (continuous response sensitivities).

The same example structure is subjected to finite element response and response sensitivity analyses for dynamic seismic loading. The balanced 1940 El Centro earthquake record scaled by a factor 3 is taken as input ground motion with a resulting peak ground acceleration $a_{g,\max} = \max_t(|u_g(t)|) = 0.96g$. The structure is modeled with the J_2 plasticity, the M-P ($R_0 = 20$), and the M-P ($R_0 = 80$) constitutive law, respectively. Time integration is performed using the constant average acceleration method (special case of the Newmark-beta family of time stepping algorithms that is unconditionally stable, see

Appendix for more details). The computed time histories of the roof displacement u_3 are plotted in Figure 6.8. The results corresponding to the M-P ($R_0 = 80$) model are not shown, being very close to the ones obtained from the J_2 plasticity model. For all three constitutive models, the structure undergoes large plastic deformations as shown in Figure 6.8 by the non-zero centered oscillations of the response.

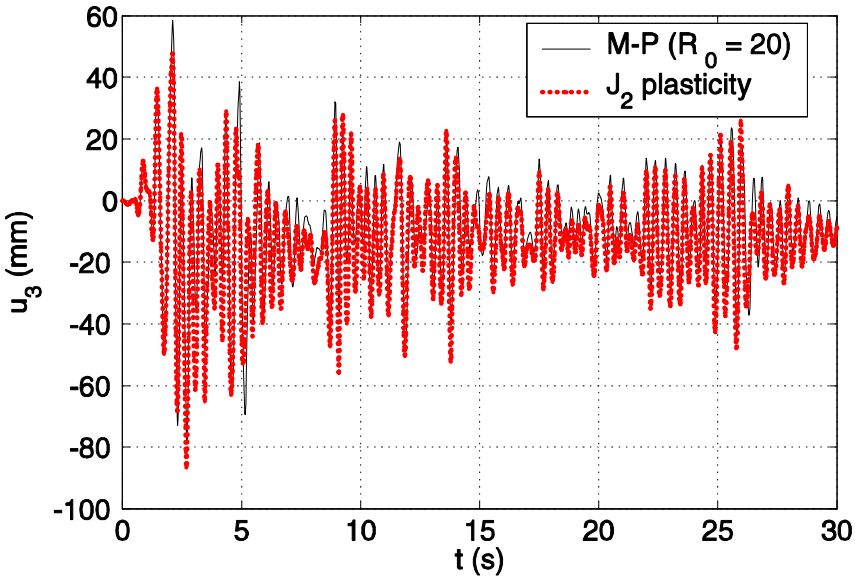

Figure 6.8 Response histories of roof displacement u_3 for different constitutive models (dynamic analysis).

Figures 6.9 and 6.10 display the time histories of the normalized sensitivities of the roof displacement u_3 to the initial yield force F_{y0} and the peak ground acceleration $a_{g,\,max}$, respectively. Again, the results for the M-P ($R_0 = 80$) model are very similar to those for the J_2 plasticity model and are not shown in Figs. 6.9 and 6.10. Even a close inspection of these time histories does not reveal any discontinuities in the response sensi-

tivities along the time axis. In fact, both the smoothing effect of the inertia terms in the sensitivity equation of the structure (Haukaas and Der Kiureghian, 2004) and the oscillatory behavior of the sensitivities contribute to hide discontinuities of small magnitude.

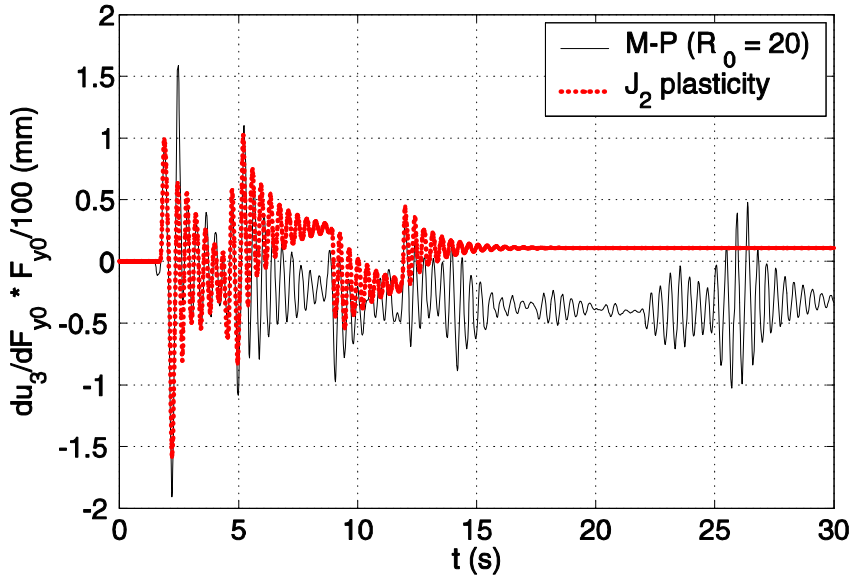

Figure 6.9 Normalized sensitivity of roof displacement u_3 to initial yield force F_{y0} (dynamic analysis).

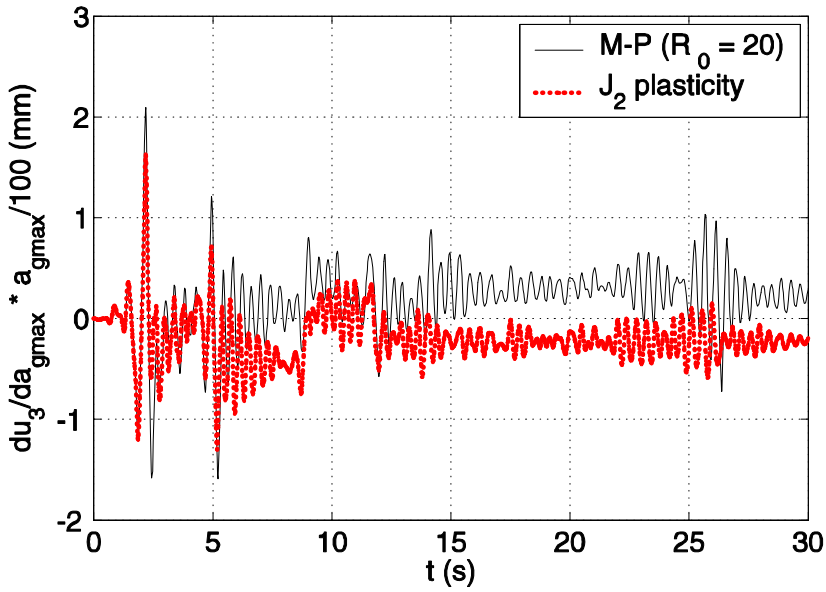

Figure 6.10 Normalized sensitivity of roof displacement u_3 to peak ground acceleration $a_{g,max}$ (dynamic analysis).

However, examining response sensitivity results along the sensitivity parameter axis (for a fixed time step Δt sufficiently small, herein $\Delta t = 0.001s$) reveals a very different behavior: discontinuities arise clearly in the response sensitivities obtained from the non-smooth J_2 plasticity model, while the M-P models response sensitivities are smooth along the parameter axis, as shown in Figure 6.10. Figs. 6.11 and 6.12 plot the time histories (for $0 \le t \le 5s$) of the displacement u_3 for fixed peak ground acceleration $a_{g,\,max}$ and variable initial yield force F_{y0} obtained using the M-P ($R_0 = 20$) model and the J_2 plasticity model, respectively, and the integration time step $\Delta t = 0.001s$. It is observed that the response surfaces are continuous in both time and parameter F_{y0} and present small differences overall between the two different constitutive models. Figs. 6.14 and 6.15 show the time histories (for $0 \le t \le 5s$) of the normalized sensitivities of the displacement u_3 to the

initial yield force F_{y0} for fixed peak ground acceleration $a_{g,\,max}$ and variable initial yield force F_{y0} obtained using the M-P ($R_0 = 20$) model and the J_2 plasticity model, respectively, and the integration time step $\Delta t = 0.001 s$. The response sensitivity surface obtained for the M-P ($R_0 = 20$) constitutive model is continuous in both time and parameter F_{y0}, while the response sensitivity surface obtained using the J_2 plasticity model exhibits clear discontinuities along the parameter axis. It is important to notice that continuity along the parameter axis is obtained only for a sufficiently small integration time step Δt. (see Appendix). If the time step used to integrate the equations of motion of the system is not small enough, spurious discontinuities can be introduced by the time stepping scheme employed, as illustrated in Figure 6.16, which shows the surface of the normalized sensitivities of the displacement u_3 to the initial yield force F_{y0} for fixed peak ground acceleration $a_{g,\,max}$ and variable initial yield force F_{y0} obtained using the M-P ($R_0 = 20$) model and the integration time step $\Delta t = 0.02 s$.

In finite element reliability analysis, response sensitivity discontinuities in the parameter space can be detrimental to the convergence of the computational optimization procedure to find the design point(s). Therefore, the use of smooth constitutive laws is also beneficial in the dynamic case for avoiding discontinuities in the response sensitivities along the parameter axes, provided that the integration time step is small enough.

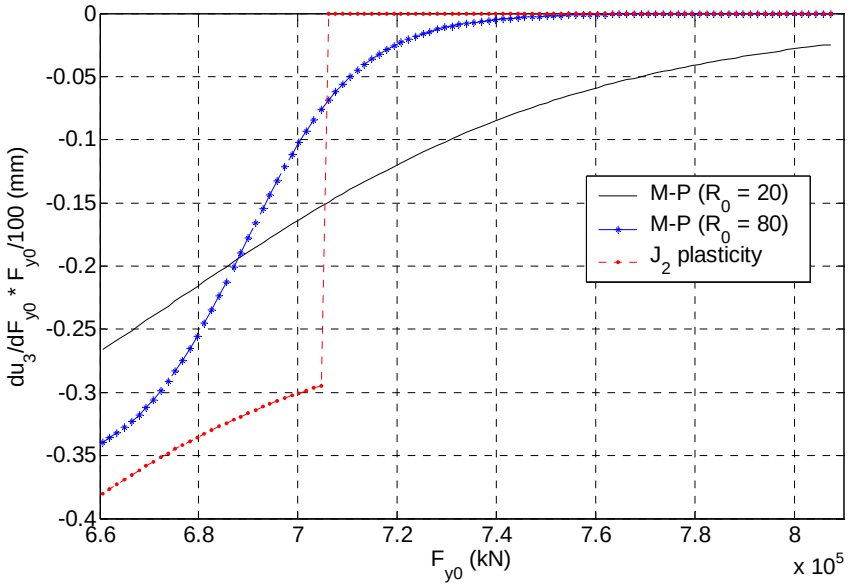

Figure 6.11 Normalized sensitivity of roof displacement u_3 to initial yield force F_{y0} at time t = 1.66s with fixed peak ground acceleration $a_{g,max}$.

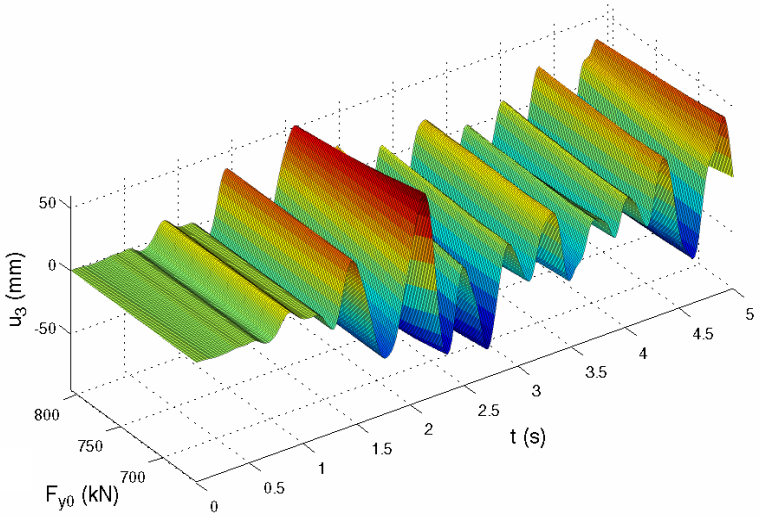

Figure 6.12 Time histories (for $0 \le t \le 5s$) of displacement u_3 for fixed peak ground acceleration $a_{g,max}$ and variable initial yield force F_{y0}: dynamic analysis using the M-P ($R_0 = 20$) model and $\Delta t = 0.001s$

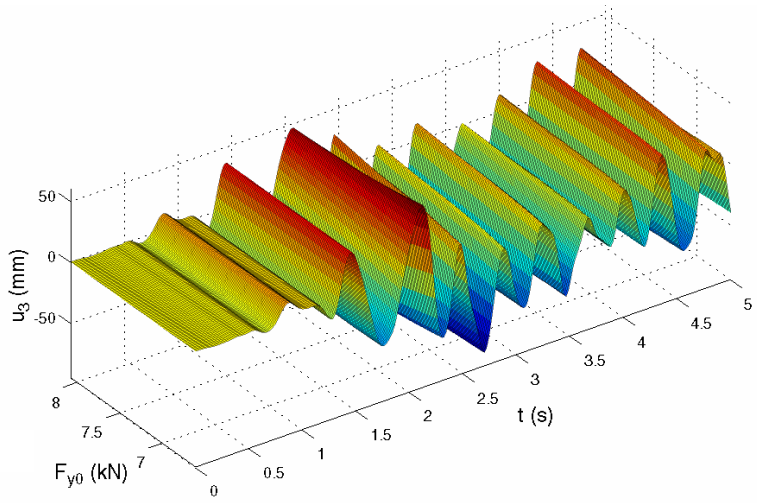

Figure 6.13 Time histories (for $0 \le t \le 5s$) of displacement u_3 for fixed peak ground acceleration $a_{g,max}$ and variable initial yield force F_{y0}: dynamic analysis using the J_2 plasticity model and $\Delta t = 0.001s$

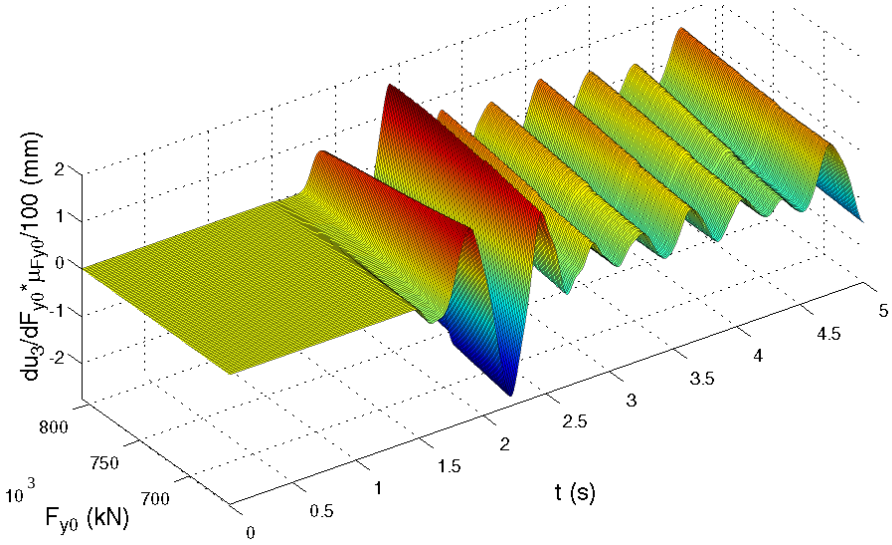

Figure 6.14 Time histories (for $0 \le t \le 5s$) of normalized sensitivities of the displacement u_3 to initial yield force F_{y0} for fixed peak ground acceleration $a_{g,max}$ and variable initial yield force F_{y0}: dynamic analysis using the M-P ($R_0 = 20$) model and $\Delta t = 0.001s$

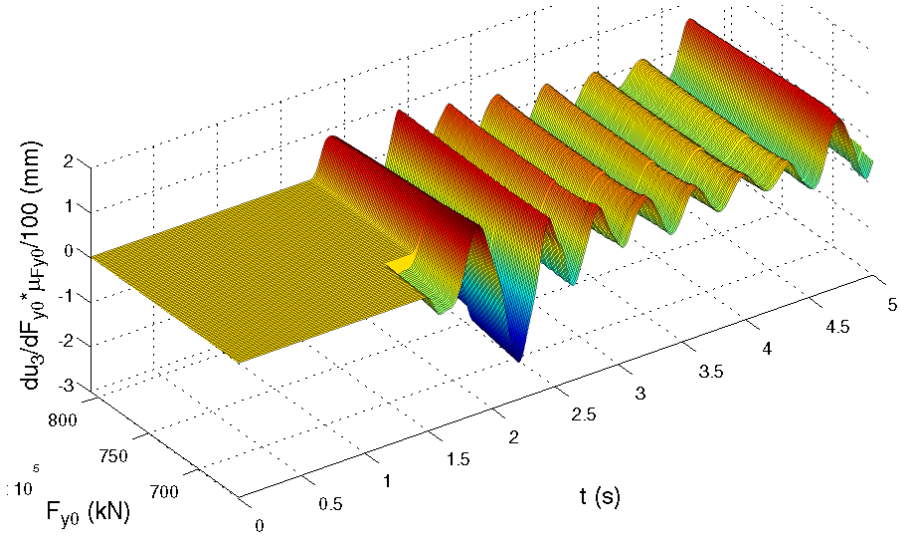

Figure 6.15 Time histories (for $0 \le t \le 5s$) of normalized sensitivities of the displacement u_3 to initial yield force F_{y0} for fixed peak ground acceleration $a_{g,max}$ and variable initial yield force F_{y0}: dynamic analysis using the J_2 model and $\Delta t = 0.001s$

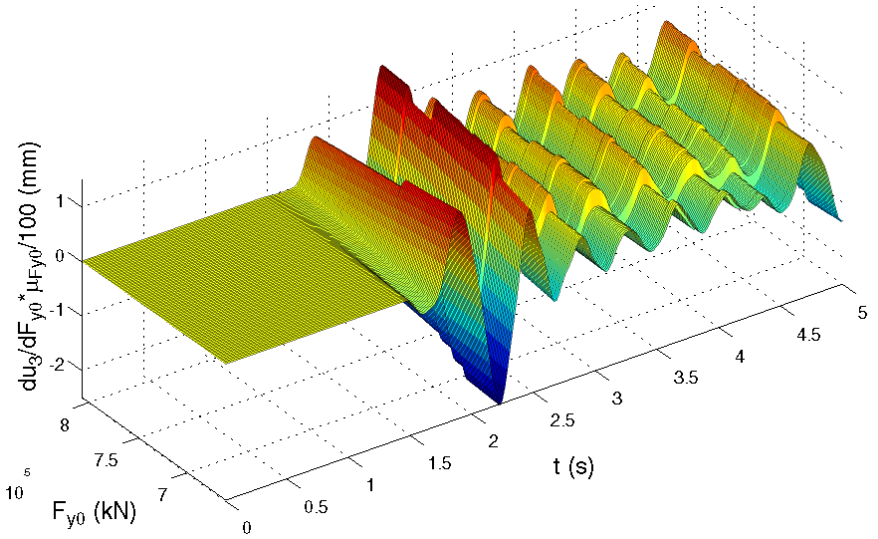

Figure 6.16 Time histories (for $0 \le t \le 5s$) of normalized sensitivities of the displacement u_3 to initial yield force F_{y0} for fixed peak ground acceleration $a_{g,max}$ and variable initial yield force F_{y0}: dynamic analysis using the M-P ($R_0 = 20$) model and $\Delta t = 0.02s$

6.4 CONCLUSIONS

Insight is gained into the analytical behavior of finite element response sensitivities obtained from smooth (Menegotto-Pinto) and non-smooth (J_2 plasticity) material constitutive models. The response sensitivity computation algorithm for the Menegotto-Pinto uni-axial material constitutive model is developed and presented. Focus is on continuity (or discontinuity) of finite element response sensitivities. In particular, important response sensitivity discontinuities are observed along the axes of both pseudotime and sensitivity parameters when using non-smooth material models in quasi-static finite element analysis. A sufficient condition is stated and proved on the smoothness properties of material constitutive laws for obtaining continuous response sensitivities in the quasi-static analysis case. These results about response sensitivity continuity are illustrated using the Menegotto-Pinto material constitutive law to model a simple inelastic steel shear-frame. Comparisons are made between response and response sensitivities obtained using the smooth Menegotto-Pinto and the non-smooth uni-axial J_2 plasticity material constitutive law to model the same example structure. Response and response sensitivity computations are also examined in the dynamic analysis case using both the Menegotto-Pinto and J_2 plasticity models. It is found that the linear inertia and damping terms in the equations of motion have significant smoothing effects on the response sensitivity results along the time axis. Nevertheless, discontinuities along the parameter axes are observed for both non-smooth and smooth constitutive models, if the time discretization of the equations of motion is not sufficiently refined. Important remarks and observations are made about the dynamic analysis case, which suggest that response sensitivity discontinuities can be eliminated by

using smooth material constitutive models and refining the time discretization of the equations of motion. Some of the discontinuities in dynamic response sensitivities obtained using non-smooth material constitutive models are inherent to the constitutive models themselves and cannot be eliminated by reducing the integration time step. Response sensitivity results are presented in support of these conclusions.

Continuity of response sensitivities is extremely important for the design point search using gradient based optimization algorithms. In fact, when discontinuities are present in the response sensitivities, convergence to a (local) design point cannot be ensured by gradient based optimization techniques.

6.5 ACKNOWLEDGEMENTS

Chapter 6, in full, is a reprint of the material as it appears in International Journal of Reliability and Safety (2006), Barbato, M., and Conte, J.P., 1(1-2):3-39. The dissertation author was first author and investigator of this paper.

APPENDIX: SMOOTHNESS CONDITIONS FOR RESPONSE SENSITIVITY CONTINUITY

Continuity is a very desirable property of finite element response sensitivities for applications involving the use of gradient-based optimization algorithms. Herein, a theorem giving a sufficient condition for continuity to hold is stated and proved for the case of quasi-static finite element analysis. Remarks and observations are made for the more complicated dynamic analysis case. In the sequel, the symbol $a\big|_b$ indicates that the quantity "a" has been computed considering the quantity "b" as a constant (i.e., b fixed), and the symbol $a\big|_{b = \bar{b}}$ indicates that the quantity "a" is evaluated for variable "b" equal to the value "$\bar{b}$".

Theorem:

Given a finite element model of a structural system, the sensitivities $\boldsymbol{\nu}$ *of the response quantities* $\mathbf{r}$ *to sensitivity parameter* θ, $\boldsymbol{\nu}(t, \theta) = \dfrac{d\mathbf{r}(t, \theta)}{d\theta}$, *are continuous everywhere as functions of both the ordering parameter* t *(pseudo-time) of a quasi-static analysis and the sensitivity parameter* θ, *if the following conditions are satisfied:*

(a) *All the material constitutive models used for representing the structural behavior are uni-axial constitutive laws, i.e.,* $\sigma = \sigma(\varepsilon)$, *in which* σ *and* ε *denote a scalar stress or stress resultant quantity and a scalar strain or strain resultant quantity, respec-*

tively.

(b) *All the branches of the material constitutive models can be expanded in Taylor series about any of their points, i.e.,* $\left.\frac{d^j\sigma}{d\varepsilon^j}\right|_{\varepsilon = \bar{\varepsilon}}$ *exists and is finite for any* $\bar{\varepsilon}$ *and* $j = 1, 2, \ldots .$

(c) *The material constitutive models are continuously differentiable with respect to the sensitivity parameter* θ*, i.e.,* $\left.\frac{\partial\sigma(\varepsilon, \theta)}{\partial\theta}\right|_{\varepsilon}$ *exists and is a continuous function of* θ*.*

(d) *The components of the external nodal loading vector,* $\mathbf{F}(t, \theta)$*, are continuous in terms of the ordering parameter* t *and continuously differentiable with respect to the sensitivity parameter* θ*.*

Proof:

Without lack of generality, the proof will be presented for $\mathbf{r} = \mathbf{u}$, where $\mathbf{u}$ denotes the nodal displacement vector, and will refer to a single analysis step (i.e., load or displacement increment) after convergence (within a small specified tolerance) is achieved for response calculation.

For quasi-static analysis, the equilibrium equation for the space-discretized system at $t = t_{n+1}$ is expressed as

$$\mathbf{R}_{n+1}(\mathbf{u}_{n+1}(\theta), \theta) = \mathbf{F}_{n+1}(\theta) \tag{6.24}$$

in which $\mathbf{R}(\mathbf{u}(\theta),\theta)$ and $\mathbf{F}(\theta)$ denote the internal and external nodal force vectors, respectively, and where their dependence on the sensitivity parameter θ is shown explicitly; the subscript n+1 indicates the load/time step number (i.e., the quantity to which it is attached is computed at $t = t_{n+1}$).

The response sensitivity equation at the structure level is obtained from Eq. (6.24) using the chain rule of differentiation as

$$\mathbf{K}_{n+1}\frac{d\mathbf{u}_{n+1}}{d\theta} = \frac{d\mathbf{F}_{n+1}}{d\theta} - \left.\frac{\partial \mathbf{R}_{n+1}}{\partial \theta}\right|_{\mathbf{u}_{n+1}} \tag{6.25}$$

where $\mathbf{K}$ denotes the structure (consistent) tangent stiffness matrix. From Eq. (6.25), it follows that

$$\begin{cases} \dfrac{d\mathbf{u}_n}{d\theta} = \mathbf{K}_n^{-1}\left(\dfrac{d\mathbf{F}_n}{d\theta} - \left.\dfrac{\partial \mathbf{R}_n}{\partial \theta}\right|_{\mathbf{u}_n}\right) \\ \dfrac{d\mathbf{u}_{n+1}}{d\theta} = \mathbf{K}_{n+1}^{-1}\left(\dfrac{d\mathbf{F}_{n+1}}{d\theta} - \left.\dfrac{\partial \mathbf{R}_{n+1}}{\partial \theta}\right|_{\mathbf{u}_{n+1}}\right) \end{cases} \tag{6.26}$$

Three different cases must be considered:

(i) *Continuity of response sensitivity,* $\dfrac{d\mathbf{u}}{d\theta}$*, with respect to the ordering parameter* t *for a load step* $t = t_{n+1}$ *in which the strain rate does not change sign, with* θ *kept fixed and equal to its nominal value* θ_0.

We need to prove that

$$\lim_{t_{n+1} \to t_n} \left(\frac{d\mathbf{u}_{n+1}}{d\theta} - \frac{d\mathbf{u}_n}{d\theta} \right) = \mathbf{0} \tag{6.27}$$

The assumed smoothness/continuity properties of the material constitutive models and the external loading functions (assumptions (b), (c) and (d) above) together with Eq. (6.24) imply that

$$\begin{cases} \lim_{t_{n+1} \to t_n} \mathbf{u}_{n+1} = \mathbf{u}_n \\ \lim_{t_{n+1} \to t_n} \mathbf{K}_{n+1} = \mathbf{K}_n \\ \lim_{t_{n+1} \to t_n} \left. \dfrac{\partial \mathbf{R}_{n+1}}{\partial \theta} \right|_{\mathbf{u}_{n+1}} = \left. \dfrac{\partial \mathbf{R}_n}{\partial \theta} \right|_{\mathbf{u}_n} \\ \lim_{t_{n+1} \to t_n} \dfrac{d\mathbf{F}_{n+1}}{d\theta} = \dfrac{d\mathbf{F}_n}{d\theta} \end{cases} \tag{6.28}$$

Thus Eq. (6.27) is proved by substituting Eqs. $(6.26)_{1,2}$ in its left-hand-side and using Eqs. $(6.28)_{2,3,4}$.

(ii) *Continuity of response sensitivity,* $\dfrac{d\mathbf{u}}{d\theta}$*, with respect to the ordering parameter* t *for a load step* $t = t_{n+1}$ *in which the strain rate changes sign (i.e.,* t_n *corresponds exactly to an unloading point), with* θ *kept fixed and equal to its nominal value* θ_0.

We need to prove Eq. (6.27) again. In this sub-case, Eq. $(6.28)_2$ is not satisfied since, in general, $\lim_{t_{n+1} \to t_n} \mathbf{K}_{n+1} = \mathbf{K}_{n,\,\text{unloading}} \neq \mathbf{K}_{n,\,\text{loading}}$ (see Figure 6.7b). The internal and external nodal force vectors at $t = t_{n+1}$ can be written in incremental form as

$$\begin{cases} \mathbf{R}_{n+1} = \mathbf{R}_n + \Delta\mathbf{R}_{n+1} \\ \mathbf{F}_{n+1} = \mathbf{F}_n + \Delta\mathbf{F}_{n+1} \end{cases} \tag{6.29}$$

Equilibrium as expressed in Eq. (6.24) requires also that

$$\begin{cases} \mathbf{R}_n = \mathbf{F}_n \\ \Delta\mathbf{R}_{n+1} = \Delta\mathbf{F}_{n+1} \end{cases} \tag{6.30}$$

Taylor series expansion of the internal nodal force vector **R** (considered as function of the nodal displacement vector **u**) about $\mathbf{u} = \mathbf{u}_{n+1}$ is expressed at $\mathbf{u} = \mathbf{u}_n$ as

$$\mathbf{R}(\mathbf{u}_n) = \mathbf{R}(\mathbf{u}_{n+1}) + \sum_{p=1}^{\infty} \frac{1}{p!} \left\{ [(\mathbf{u}_n - \mathbf{u}_{n+1})^T \cdot \nabla_{\mathbf{u}}]^p \mathbf{R}(\mathbf{u}_n) \right\} \Big|_{\mathbf{u} = \mathbf{u}_{n+1}} \tag{6.31}$$

in which $\nabla_{\mathbf{u}} = \left[\frac{\partial}{\partial u_1} \cdots \frac{\partial}{\partial u_n} \right]^T$, N denotes the number of degrees of freedom of the system, and the superscript T represents the vector/matrix transpose operator. Considering that $\mathbf{R}(\mathbf{u}_n) = \mathbf{R}_n$ and $\mathbf{R}(\mathbf{u}_{n+1}) = \mathbf{R}_{n+1}$, we can also write

$$\mathbf{R}_{n+1} = \mathbf{R}_n - \sum_{p=1}^{\infty} \frac{(-1)^p}{p!} \left\{ [(\mathbf{u}_n - \mathbf{u}_{n+1})^T \cdot \nabla_{\mathbf{u}}]^p \mathbf{R}(\mathbf{u}_n) \right\} \Big|_{\mathbf{u} = \mathbf{u}_{n+1}} \tag{6.32}$$

Differentiating Eq. (6.32) with respect to parameter θ at $\theta = \theta_0$, and recognizing that $\frac{\partial}{\partial\theta} \left(\frac{\partial \mathbf{R}(\mathbf{u})}{\partial u_i} \Big|_{\mathbf{u} = \mathbf{u}_{n+1}} \right) = \mathbf{0}$, i = 1, ..., N (since $\frac{\partial \mathbf{R}(\mathbf{u})}{\partial u_i}$ depends on θ only implicitly through

$\mathbf{u}(\theta)$ and the operation $(\ldots)\big|_{\mathbf{u}=\mathbf{u}_{n+1}}$ removes any dependence on θ since $\mathbf{u}_{n+1}$ has been computed for $\theta = \theta_0$), we obtain

$$\frac{d\mathbf{R}_{n+1}}{d\theta} = \frac{d\mathbf{R}_n}{d\theta} + \sum_{p=1}^{\infty} \frac{(-1)^{p+1}}{(p-1)!} \left\{ \left\{ [(\mathbf{u}_n - \mathbf{u}_{n+1})^T \cdot \nabla_{\mathbf{u}}]^{p-1} \cdot \left(\frac{d\mathbf{u}_{n+1}}{d\theta} - \frac{d\mathbf{u}_n}{d\theta} \right)^T \cdot \nabla_{\mathbf{u}} \right\} \mathbf{R}(\mathbf{u}_n) \right\} \Bigg|_{\mathbf{u}=\mathbf{u}_{n+1}} \tag{6.33}$$

From Eq. (6.33), we obtain the conditional derivative $\left.\frac{\partial \mathbf{R}_{n+1}}{\partial \theta}\right|_{\mathbf{u}_{n+1}}$ as

$$\left.\frac{\partial \mathbf{R}_{n+1}}{\partial \theta}\right|_{\mathbf{u}_{n+1}} = \frac{d\mathbf{R}_n}{d\theta} + \sum_{p=1}^{\infty} \frac{(-1)^{p}}{(p-1)!} \left\{ \left\{ [(\mathbf{u}_n - \mathbf{u}_{n+1})^T \cdot \nabla_{\mathbf{u}}]^{p-1} \cdot \left(\frac{d\mathbf{u}_n}{d\theta} \right)^T \cdot \nabla_{\mathbf{u}} \right\} \mathbf{R}(\mathbf{u}_n) \right\} \Bigg|_{\mathbf{u}=\mathbf{u}_{n+1}} \tag{6.34}$$

recognizing that $\left.\frac{\partial \mathbf{R}_n}{\partial \theta}\right|_{\mathbf{u}_{n+1}} = \frac{d\mathbf{R}_n}{d\theta}$ (since $\frac{d\mathbf{R}_n}{d\theta}$ is independent of the response $\mathbf{u}_{n+1}$ computed at a subsequent analysis step) and $\left.\frac{\partial \mathbf{u}_{n+1}}{\partial \theta}\right|_{\mathbf{u}_{n+1}} = \mathbf{0}$. For $\mathbf{u}_{n+1}$ sufficiently close to $\mathbf{u}_n$, the terms in Eq. (6.34) that are multiplied by $(u_{i,\,n+1} - u_{i,\,n})^j$ $(i = 1, \ldots, N;\ j \geq 1)$ are negligibly small (i.e., infinitesimal quantities) due to assumption (b) which implies that the quantities $\left.\frac{\partial^j \mathbf{R}(\mathbf{u})}{\partial u_1^{j_1} \ldots \partial u_N^{j_N}}\right|_{\mathbf{u}=\mathbf{u}_{n+1}}$ (j = 1, 2, ... and $\sum_{k=1}^{N} j_k = j$ exist and are finite.

Thus, discarding infinitesimal quantities in Eq. (6.34), we obtain that

$$\lim_{t_{n+1}\to t_n}\left.\frac{\partial \mathbf{R}_{n+1}}{\partial\theta}\right|_{\mathbf{u}_{n+1}} = \frac{d\mathbf{R}_n}{d\theta} - \left.\left\{\left[\left(\frac{d\mathbf{u}_n}{d\theta}\right)^{T}\cdot\nabla_{\mathbf{u}}\right]\mathbf{R}(\mathbf{u}_n)\right\}\right|_{\mathbf{u}=\mathbf{u}_{n+1}} = \frac{d\mathbf{R}_n}{d\theta} - \mathbf{K}_{n+1}\frac{d\mathbf{u}_n}{d\theta} \tag{6.35}$$

in which the equivalence between consistent tangent moduli and continuum tangent moduli for uni-axial material constitutive models is used (assumption (a); Simo and Hughes 1998; Conte et al. 2003). Finally, substituting Eq. $(6.26)_2$ in Eq. (6.27) and making use of Eqs. (6.34), $(6.28)_1$, and (6.35) (in this order), we obtain

$$\begin{aligned}\lim_{t_{n+1}\to t_n}\left(\frac{d\mathbf{u}_{n+1}}{d\theta} - \frac{d\mathbf{u}_n}{d\theta}\right) &= \lim_{t_{n+1}\to t_n}\left[\mathbf{K}_{n+1}^{-1}\left(\frac{d\mathbf{F}_{n+1}}{d\theta} - \left.\frac{\partial \mathbf{R}_{n+1}}{\partial\theta}\right|_{\mathbf{u}_{n+1}}\right) - \frac{d\mathbf{u}_n}{d\theta}\right] \\ &= \lim_{t_{n+1}\to t_n}\left[\mathbf{K}_{n+1}^{-1}\left(\frac{d\mathbf{F}_{n+1}}{d\theta} - \frac{d\mathbf{R}_n}{d\theta}\right) + \frac{d\mathbf{u}_n}{d\theta} - \frac{d\mathbf{u}_n}{d\theta}\right] = \mathbf{0}\end{aligned} \tag{6.36}$$

in which we used the relation $\lim_{t_{n+1}\to t_n}\frac{d\mathbf{F}_{n+1}}{d\theta} = \frac{d\mathbf{F}_n}{d\theta} = \frac{d\mathbf{R}_n}{d\theta}$, obtained by differentiating Eq. $(6.30)_1$ and combining the result with Eq. $(6.28)_4$.

(iii) *Continuity of response sensitivity,* $\frac{d\mathbf{u}}{d\theta}$*, with respect to sensitivity parameter* θ *(for* $t = t_{n+1}$ *fixed).*

Let us consider a perturbed value $\tilde{\theta}$ of the sensitivity parameter, i.e., $\tilde{\theta} = \theta_0 + \Delta\theta$, in which θ_0 denotes the nominal value of the parameter and $\Delta\theta$ is a small but finite perturbation of it. Let $\boldsymbol{f} = \boldsymbol{f}(t, \theta)$ denote a response or response sensitivity vector quantity as

function of both the ordering parameter t and sensitivity parameter θ and let $\mathbf{f} = \boldsymbol{f}(t, \theta)\big|_{\theta = \theta_0}$ and $\tilde{\mathbf{f}} = \boldsymbol{f}(t, \theta)\big|_{\theta = \tilde{\theta}}$, respectively. We need to prove that

$$\lim_{\tilde{\theta} \to \theta} \left(\frac{d\tilde{\mathbf{u}}_{n+1}}{d\theta} - \frac{d\mathbf{u}_{n+1}}{d\theta} \right) = \lim_{\Delta\theta \to 0} \left(\frac{d\tilde{\mathbf{u}}_{n+1}}{d\theta} - \frac{d\mathbf{u}_{n+1}}{d\theta} \right) = \mathbf{0} \tag{6.37}$$

From the continuity of the response and the loading function(s) with respect to the sensitivity parameter θ (assumptions (c) and (d)), it follows that

$$\begin{cases} \lim\limits_{\Delta\theta \to 0} \tilde{\mathbf{u}}_{n+1} = \mathbf{u}_{n+1} \\ \lim\limits_{\Delta\theta \to 0} \tilde{\mathbf{K}}_{n+1} = \mathbf{K}_{n+1} \\ \lim\limits_{\Delta\theta \to 0} \tilde{\mathbf{R}}_{n+1} = \mathbf{R}_{n+1} \\ \lim\limits_{\Delta\theta \to 0} \tilde{\mathbf{F}}_{n+1} = \mathbf{F}_{n+1} \end{cases} \tag{6.38}$$

Making use of the static equilibrium equation (34) and assumption (d), we have

$$\lim_{\Delta\theta \to 0} \frac{d\tilde{\mathbf{R}}_{n+1}}{d\theta} = \lim_{\Delta\theta \to 0} \frac{d\tilde{\mathbf{F}}_{n+1}}{d\theta} = \frac{d\mathbf{F}_{n+1}}{d\theta} = \frac{d\mathbf{R}_{n+1}}{d\theta} \tag{6.39}$$

From the chain rule of differentiation applied to the internal force vector $\mathbf{R}$ expressed as function of parameter θ (i.e., $\mathbf{R}(\mathbf{u}(\theta), \theta)$), we also have

$$\begin{cases} \dfrac{d\tilde{\mathbf{R}}_{n+1}}{d\theta} = \tilde{\mathbf{K}}_{n+1} \dfrac{d\tilde{\mathbf{u}}_{n+1}}{d\theta} + \dfrac{\partial \tilde{\mathbf{R}}_{n+1}}{\partial \theta}\bigg|_{\tilde{\mathbf{u}}_{n+1}} \\ \dfrac{d\mathbf{R}_{n+1}}{d\theta} = \mathbf{K}_{n+1} \dfrac{d\mathbf{u}_{n+1}}{d\theta} + \dfrac{\partial \mathbf{R}_{n+1}}{\partial \theta}\bigg|_{\mathbf{u}_{n+1}} \end{cases} \tag{6.40}$$

Furthermore, from assumption (c), it follows that $\lim_{\Delta\theta \to 0} \left.\frac{\partial \tilde{\mathbf{R}}}{\partial \theta}\right|_{\mathbf{u}} = \left.\frac{\partial \mathbf{R}}{\partial \theta}\right|_{\mathbf{u}}$, which when combined with Eq. $(6.38)_1$ gives

$$\lim_{\Delta\theta \to 0} \left.\frac{\partial \tilde{\mathbf{R}}_{n+1}}{\partial \theta}\right|_{\tilde{\mathbf{u}}_{n+1}} = \left.\frac{\partial \mathbf{R}_{n+1}}{\partial \theta}\right|_{\mathbf{u}_{n+1}} \tag{6.41}$$

From Eq. (6.40) and using Eqs. (6.39), $(6.38)_2$, and (6.41), it follows that

$$\lim_{\Delta\theta \to 0} \frac{d\tilde{\mathbf{u}}_{n+1}}{d\theta} = \frac{d\mathbf{u}_{n+1}}{d\theta} \tag{6.42}$$

Remarks on the Sufficient Conditions for Response Sensitivity Continuity:

The sufficient conditions required by the above theorem are easy to satisfy. In particular, condition (b) (requiring that all branches of the material constitutive models used be expandable in Taylor series) is in general satisfied by common smooth material models, provided that branches with infinite stiffness are avoided.

The only condition that actually restricts the application of the above theorem is condition (a) (all material constitutive models need to be uni-axial), which is required by Eq. (6.35), where the identity between continuum and consistent tangent moduli for uniaxial constitutive models is used. Other researchers (Haukaas and Der Kiureghian 2004) found that continuity of finite element response sensitivities can be obtained by using smooth multi-axial constitutive models. Thus, it appears that the above theorem may be extendable to multi-axial material constitutive models.

Remarks and Observations for the Dynamic Analysis Case:

The proof of the above theorem for quasi-static analysis cannot be easily extended to the case of dynamic analysis. The space and time discretized equations of motion of a structural system subjected to dynamic loads can be written as

$$a_1\mathbf{M}(\theta)\mathbf{u}_{n+1}(\theta) + a_5\mathbf{C}(\theta)\mathbf{u}_{n+1}(\theta) + \mathbf{R}_{n+1}(\mathbf{u}_{n+1}(\theta), \theta) = \bar{\mathbf{F}}_{n+1}(\theta) \tag{6.43}$$

in which

$$\begin{aligned}\bar{\mathbf{F}}_{n+1}(\theta) = \mathbf{F}_{n+1}(\theta) &- \mathbf{M}(\theta)\cdot[a_2\mathbf{u}_n(\theta) + a_3\dot{\mathbf{u}}_n(\theta) + a_4\ddot{\mathbf{u}}_n(\theta)] \\ &- \mathbf{C}(\theta)\cdot[a_6\mathbf{u}_n(\theta) + a_7\dot{\mathbf{u}}_n(\theta) + a_8\ddot{\mathbf{u}}_n(\theta)]\end{aligned} \tag{6.44}$$

and the following general one-step time integration scheme is used (Conte et al. 1995; Conte 2001; Conte et al. 2003, 2004; Haukaas and Der Kiureghian 2004; Barbato and Conte 2005)

$$\begin{cases}\ddot{\mathbf{u}}_{n+1} = a_1\mathbf{u}_{n+1} + a_2\mathbf{u}_n + a_3\dot{\mathbf{u}}_n + a_4\ddot{\mathbf{u}}_n \\ \dot{\mathbf{u}}_{n+1} = a_5\mathbf{u}_{n+1} + a_6\mathbf{u}_n + a_7\dot{\mathbf{u}}_n + a_8\ddot{\mathbf{u}}_n\end{cases} \tag{6.45}$$

The above family of time stepping schemes includes well-known algorithms such as the Newmark-beta family of methods (e.g, constant average acceleration method, linear acceleration method, Fox-Goodwin method, central difference method) and the Wilson-theta method (Hughes, 1987).

Differentiating Eq. (6.43) with respect to the sensitivity parameter θ yields the following sensitivity equation:

$$\mathbf{K}_{n+1}^{dyn}\frac{d\mathbf{u}_{n+1}}{d\theta} = \left(\frac{d\mathbf{F}}{d\theta}\right)_{n+1}^{dyn} - \left.\frac{\partial \mathbf{R}_{n+1}}{\partial \theta}\right|_{\mathbf{u}_{n+1}} \tag{6.46}$$

in which the terms $\left(\frac{d\mathbf{F}}{d\theta}\right)_{n+1}^{dyn}$ and $\mathbf{K}_{n+1}^{dyn}$ are defined as

$$\begin{aligned}\left(\frac{d\mathbf{F}}{d\theta}\right)_{n+1}^{dyn} &= \frac{d\mathbf{F}_{n+1}}{d\theta} - \frac{d\mathbf{M}}{d\theta}(a_1\mathbf{u}_{n+1} + a_2\mathbf{u}_n + a_3\dot{\mathbf{u}}_n + a_4\ddot{\mathbf{u}}_n) - \mathbf{M}\left(a_2\frac{d\mathbf{u}_n}{d\theta} + a_3\frac{d\dot{\mathbf{u}}_n}{d\theta} + a_4\frac{d\ddot{\mathbf{u}}_n}{d\theta}\right) \\ &\quad - \frac{d\mathbf{C}}{d\theta}(a_5\mathbf{u}_{n+1} + a_6\mathbf{u}_n + a_7\dot{\mathbf{u}}_n + a_8\ddot{\mathbf{u}}_n) - \mathbf{C}\left(a_6\frac{d\mathbf{u}_n}{d\theta} + a_7\frac{d\dot{\mathbf{u}}_n}{d\theta} + a_8\frac{d\ddot{\mathbf{u}}_n}{d\theta}\right) \\ &= \frac{d\bar{\mathbf{F}}_{n+1}}{d\theta} - \left(a_1\frac{d\mathbf{M}}{d\theta} + a_5\frac{d\mathbf{C}}{d\theta}\right)\mathbf{u}_{n+1}\end{aligned} \tag{6.47}$$

$$\mathbf{K}_{n+1}^{dyn} = a_1\mathbf{M} + a_5\mathbf{C} + \mathbf{K}_{n+1} \tag{6.48}$$

Eq. (6.46) is formally identical to Eq. (6.25). Therefore, if we assume (in addition to the hypotheses of the theorem presented above) that (1) the mass matrix, **M**, and the damping matrix, **C**, are time-invariant, and (2) the term $\left(\frac{d\mathbf{F}}{d\theta}\right)_{n+1}^{dyn}$ is continuous as a function of θ, we could prove the continuity of the response sensitivities $\frac{d\mathbf{u}}{d\theta}$, $\frac{d\dot{\mathbf{u}}}{d\theta}$, and $\frac{d\ddot{\mathbf{u}}}{d\theta}$ in a way that is similar to the one used for the quasi-static case.

Unfortunately, while assumption (1) is generally satisfied for civil structures (i.e., inertial properties remain usually constant within a dynamic load event, and damping properties are typically modeled through a time-invariant viscous damping mechanism), it was found through application examples such as the one shown in Figure 6.16 that assumption (2) is not true in general.

Assuming the same smoothness hypotheses (i.e., assumptions (b), (c), and (d)) used in the above theorem for quasi-static problems, intuition would suggest that response sensitivities are also continuous in the dynamic case that further benefits from the "linearization" (and smoothing) effects of the linear inertial and damping terms (Haukaas and Der Kiureghian 2004). The fact that discontinuities are hard to detect in response sensitivity histories (i.e., along the time axis for θ fixed), as illustrated by Figs. 6.9 and 6.10, further reinforces this intuitive argument. However, finite element response sensitivities computed from the space and time discretized equations of motion, Eq. (6.43), and the corresponding sensitivity equations, Eq. (6.46), are not continuous in general. This statement is clearly illustrated in Figure 6.16 which clearly shows, for the example structure presented in this paper and modeled using the smooth M-P ($R_0 = 20$) material constitutive law, discontinuities in the response sensitivities along the parameter (F_{y0}) axis, even though discontinuities cannot be visually observed along the time axis (for a given value of F_{y0}). Discontinuities in the response sensitivities along the parameter axes are of highest interest, since they can have detrimental effects on the convergence of gradient-based optimization algorithms such as the ones used for the design point search in structural reliability analysis.

Analytical treatment of the observed discontinuities along the parameter axes for the dynamic analysis case and for a smooth material constitutive model (such as the M-P model) is very challenging and is outside the scope of this paper. There are some fundamental differences between the quasi-static case (treated in the above theorem) and the dynamic case discussed here. By comparing the response sensitivity equations for the

quasi-static case, Eq. (6.25), and the dynamic case, Eq. (6.46), we notice the following two significant changes. (1) In the dynamic case, the term $\left(\frac{d\mathbf{F}}{d\theta}\right)_{n+1}^{dyn}$ on the right-hand-side of the sensitivity equation (Eq. (6.46)) depends on both the response and response sensitivity histories up to the current time step as shown in Eq. (6.47), which is not the case for the corresponding term $\frac{d\mathbf{F}_{n+1}}{d\theta}$ on the right-hand-side of the sensitivity equation (Eq. (6.25)) for the quasi-static case. (2) The term $\left(\frac{d\mathbf{F}}{d\theta}\right)_{n+1}^{dyn}$ and the dynamic tangent stiffness matrix, $\mathbf{K}_{n+1}^{dyn}$, depend explicitly on the time step length Δt as shown by Eqs. (6.47) and (6.48). Indeed, the time stepping algorithm in Eq. (6.45) assumes a finite (and fixed) Δt and coefficients a_i (i = 1, ..., 8) are, in general, dependent on Δt, i.e., $a_i = a_i(\Delta t)$ (i = 1, ..., 8). For example, if the Newmark-beta algorithm is used, we have $a_1 = \frac{1}{\beta \cdot (\Delta t)^2} = -a_2$, $a_3 = -\frac{1}{\beta \cdot \Delta t}$, $a_4 = 1 - \frac{1}{2\beta}$, $a_5 = \frac{\alpha}{\beta \cdot \Delta t} = -a_6$, $a_7 = 1 - \frac{\alpha}{\beta}$, $a_8 = \left(1 - \frac{\alpha}{2\beta}\right) \cdot \Delta t$, in which α and β are parameters controlling the accuracy and stability of the numerical integration scheme (for the constant average acceleration method used in this paper, $\alpha = \frac{1}{2}$ and $\beta = \frac{1}{4}$). It has been found through application examples that for some values of the sensitivity parameter θ,

$$\lim_{\Delta\theta \to 0} \left.\frac{d\tilde{\mathbf{u}}_{n+1}}{\partial\theta}\right|_{\Delta t} \neq \left.\frac{d\mathbf{u}_{n+1}}{\partial\theta}\right|_{\Delta t} \tag{6.49}$$

Convergence studies of response sensitivities suggest that such discontinuities expressed in Eq. (6.49) tend to spread (reduce in size and increase in number) for decreasing Δt. A comparison between the results presented in Figure 6.16 (large discontinuities) and the results shown in Figure 6.14 (small discontinuities, not visible at the given scale) shows clearly the effect of reducing the time step length Δt from 0.02s to 0.001s upon the computed response sensitivities for the smooth M-P ($R_0 = 20$) material constitutive law.

Based on the application examples performed, it can be safely concluded that the response sensitivity discontinuities shown in Figure 6.16 are largely due to the discretization in time of the equations of motion, Eq. (6.43). The solution of the time continuous problem for smooth material constitutive models (satisfying the hypotheses of the theorem presented above) appears to have continuous response sensitivities, as suggested by intuition, i.e.,

$$\lim_{\Delta\theta \to 0}\left[\lim_{\Delta t \to 0}\left(\frac{d\tilde{\mathbf{u}}_{n+1}}{\partial\theta}\right)\right] = \lim_{\Delta t \to 0}\left(\frac{d\mathbf{u}_{n+1}}{\partial\theta}\right) \tag{6.50}$$

For practical purposes and finite element applications, the result expressed by Eq. (6.50) requires a fine time discretization in integrating the equation of motion in order to obtain continuous (and therefore converged with respect to Δt) response sensitivities (see Figure 6.14 for converged results and Figure 6.16 for non-converged results). Previous studies show that convergence requirements (with respect to Δt) for response sensitivity computation are stricter than those for response computation only (Gu and Conte 2003). It is noteworthy that non-smooth material constitutive models (such as the J_2 plasticity model considered in this paper) present discontinuities along the parameter axes that are due to the physics of the problem (material state transition from elastic to plastic at integration point(s)), and thus cannot be eliminated through reducing Δt (see Figure 6.15).

REFERENCES

Ang G.L., Ang, A.H-S., Tang W.H. (1992) “Optimal importance sampling density estimator” *Journal of Engineering Mechanics* (ASCE), 118(6):1146–1163.

Au S.K., Beck J.L. (1999) “A new adaptive importance sampling scheme” *Structural Safety*, 21(2):135–158.

Au S.K., Beck J.L. (2001a) “First excursion probabilities for linear systems by very efficient importance sampling” *Probabilistic Engineering Mechanics*, 16(3):193–207.

Au S.K., Beck J.L. (2001b) “Estimation of small failure probabilities in high dimensions by subset simulation” *Probabilistic Engineering Mechanics*, 16(4):263–277.

Au S.K., Beck J.L. (2003) “Subset simulation and its application to seismic risk based on dynamic analysis” *Journal of Engineering Mechanics* (ASCE), 129(8):901–917.

Au S.K., Papadimitriou C., Beck, J.L. (1999) “Reliability of uncertain dynamical systems with multiple design points” *Structural Safety*, 21(2):113–133.

Barbato M., Conte J.P. (2005) “Finite element response sensitivity analysis: a comparison between force-based and displacement-based frame element models” *Computer Methods in Applied Mechanics and Engineering*, 194(12–16):1479–1512.

Breitung K. (1984) “Asymptotic approximations for multinormal integrals” *Journal of the Engineering Mechanics Division* (ASCE), 110(3):357–366.

Bucher C.G. (1988) “Adaptive importance sampling – an iterative fast Monte Carlo procedure” *Structural Safety*, 5(2):119–126.

Conte J.P., Jagannath M.K., Meghella M. (1995) “Earthquake response sensitivity analysis of concrete gravity dams” *Proceedings of Seventh International Conference on Applications of Statistics and Probability*, Paris, France, 10–13 July, 395–402.

Conte J.P. (2001) “Finite element response sensitivity analysis in earthquake engineering” *Earthquake Engineering Frontiers in the New Millennium*, Spenser and Hu, Swets and Zeitlinger, 395–401.

Conte J.P., Vijalapura P.K., Meghella M. (2003) “Consistent finite-element response sensitivity analysis” *Journal of Engineering Mechanics* (ASCE), 129(12):1380–1393.

Conte J.P., Barbato M., Spacone E. (2004) “Finite element response sensitivity analysis using force-based frame models” *International Journal for Numerical Methods in Engineering*, 59(13):1781–1820.

Der Kiureghian A., Liu P.-L. (1986) “Structural reliability under incomplete probability information” *Journal of the Engineering Mechanics Division* (ASCE), 111(EM1):85–104.

Der Kiureghian A., Lin H.-Z., Hwang S.-J. (1987) “Second-order reliability approximations” *Journal of the Engineering Mechanics Division* (ASCE), 113(EM8):1208–1225.

Der Kiureghian A., Ke B.-J. (1988) “The stochastic finite element method in structural reliability” *Probabilistic Engineering Mechanics*, 3(2):83–91.

Der Kiureghian A. (1996) “Structural reliability methods in seismic safety assessment: a review” *Journal of Engineering Structures*, 18(6):412–424.

Ditlevsen O., Madsen H.O. (1996) *Structural Reliability Methods*, New York: Wiley.

Filippou F.C., Popov E.P., Bertero V.V. (1983) “Effects of bond deterioration on hysteretic behavior of reinforced concrete joints” *Report EERC 83–19*, Earthquake Engineering Research Center, University of California, Berkeley.

Filippou F.C., Constantinides M. (2004) “FEDEASLab getting started guide and simulation examples” *Technical Report NEESgrid-2004-22*, 31 August, Available at: http://fedeaslab. berkeley.edu/.

Franchin P. (2004) “Reliability of uncertain inelastic structures under earthquake excitation” *Journal of Engineering Mechanics* (ASCE), 130(2):180–191.

Gill P.E., Murray W., Wright M.H. (1981) *Practical Optimization*, New York: Academic Press.

Gill P.E., Murray W., Saunders M.A. (2002) “SNOPT: an SQP algorithm for large-scale constrained optimization” *SIAM Journal on Optimization*, 12:979–1006.

Gill P.E., Murray W., Saunders M.A. (2005) “User’s guide for SNOPT version 7, a Fortran package for large-scale non-linear programming” *User’s Guide*, Version 7.0, Available at: http://www.scicomp.ucsd.edu/~peg/.

Gu Q., Conte J.P. (2003) “Convergence studies in non-linear finite element response sensitivity analysis” *Applications of Statistics and Probability in Civil Engineering, Proceedings of ICASP9*, San Francisco, CA, 6–9 July, Rotterdam, Netherlands: Millpress.

Hagen O., Tvedt L. (1991) “Vector process out-crossing as parallel system sensitivity measure” *Journal of Engineering Mechanics* (ASCE), 117(10):2201–2220.

Haukaas T. (2001) “FERUM (Finite Element Reliability Using Matlab)” *User’s Guide*, Available at: http://www.ce.berkeley.edu/~haukaas/FERUM/ferum.html.

Haukaas T., Der Kiureghian A. (2004) “Finite element reliability and sensitivity methods for performance-based engineering” *Report PEER 2003/14*, Pacific Earthquake Engineering Research Center, University of California, Berkeley.

Hohenbichler M., Rackwitz R. (1986) “Sensitivity and importance measures in structural reliability” *Civil Engineering Systems*, 3(4):203–209.

Hughes T.J.R. (1987) *The Finite Element Method – Linear Static and Dynamic Finite Element Analysis*, Englewood Cliffs, NJ: Prentice-Hall.

Kleiber M., Antunez H., Hien T.D., Kowalczyk P. (1997) *Parameter Sensitivity in Non-*

linear Mechanics: Theory and Finite Element Computation, New York, Wiley.

Liu P.-L., Der Kiureghian A. (1991) "Optimization algorithms for structural reliability" *Structural Safety*, 9(3):161–177.

Melchers R.E. (1989) "Importance sampling in structural systems" *Structural Safety*, 6(1):3–10.

Menegotto M., Pinto P.E. (1973) "Method for analysis of cyclically loaded reinforced concrete plane frames including changes in geometry and non-elastic behavior of elements under combined normal force and bending" *Proceedings*, *IABSE Symposium on* 'Resistance and Ultimate Deformability of Structures Acted on by Well-Defined Repeated *Loads'*, Lisbon.

Monti G., Nuti C. (1992) "Non-linear cyclic behavior of reinforcing bars including buckling" *Journal of Structural Engineering* (ASCE), 118(12):3268–3284.

Rackwitz R., Fiessler B. (1978) "Structural reliability under combined random load sequences" *Computers and Structures*, 9(5):489–499.

Ramberg W., Osgood W.R. (1943) "Description of stress-strain curves by three parameters" *Technical Note 902*, NACA.

Schueller G.I., Stix R. (1987) "A critical appraisal of methods to determine failure probabilities" *Structural Safety*, 4(4):293–309.

Schueller G.I., Pradlwarter H.J., Koutsourelakis P.S. (2004) "A critical appraisal of reliability estimation procedures for high dimensions" *Probabilistic Engineering Mechanics*, 19(4):463–474.

Simo J.C., Hughes T.J.R. (1998) *Computational Inelasticity*, Springer Verlag.

Thyagarajan R.S., Iwan W.D. (1990) "Performance characteristics of a widely used hysteretic model in structural dynamics" *Proceedings of the Fourth US National Conference on Earthquake Engineering*, *EERI*, Palm Springs, 2:177–186.

The MathWorks (1997) “Matlab – high performance numeric computation and visualization software” *User’s Guide*, Natick, MA.

The MathWorks (2004) “Optimization toolbox for use with Matlab” *User’s Guide*, Natick, MA. Available at: http://www.mathworks.com/access/helpdesk/help/toolbox/optim/.

Zhang Y., Der Kiureghian A. (1993) “Dynamic response sensitivity of inelastic structures” *Computer Methods in Applied Mechanics and Engineering*, 108(1-2):23–36.

Zona A., Barbato M., Conte J.P. (2005) “Finite element response sensitivity analysis of steel-concrete composite beams with deformable shear connection” *Journal of Engineering Mechanics* (ASCE), 131(11):1126–1139.

CHAPTER 7

EFFICIENT SIMULATION OF FULLY NONSTATIONARY STOCHASTIC EARTHQUAKE GROUND MOTION MODEL

7.1 INTRODUCTION

In many engineering fields, the importance of using stochastic processes to model loading such as earthquake ground motion, wind turbulence, ocean wave excitation has become clear. A large amount of research has been devoted to the development of analytical expressions and numerical simulation techniques of stochastic processes adequate to represent those kinds of loading driven by natural variability and many books have been written on the topic (Lin 1967; Priestley 1987; Lutes and Sarkani 1997). In particular in earthquake engineering, the nonstationarity in time and in frequency content has been recognized as an essential ingredient to capture the loading effects on the structural response realistically (Saragoni and Hart 1972; Yeh and Wen 1990; Papadimitriou 1990; Conte 1992). Therefore, attention has been given to nonstationary earthquake ground motion models, with the aim of accurate but computationally inexpensive representation of such

loading (Grigoriu et al. 1988; Der Kiureghian and Crempien 1989; Fan and Ahmadi 1990; Conte et al. 1992; Conte and Peng 1997).

At the same time, Monte Carlo simulation has been widely used for directly solving (often together with variance reduction techniques) and/or checking approximate solutions of random vibration and system stochasticity problems (Shinozuka 1972; Shinozuka and Wen 1972; Bjerager 1988; Bucher 1988; Ditelvsen and Madsen 1996). Monte Carlo simulation is a general and robust method for solving probabilistic problems, but usually is also computationally expensive or even unfeasible. A crucial step in Monte Carlo simulation is the generation of sample functions of the stochastic processes or random fields involved in the problem. Accurate and efficient sampling generation is of paramount importance for a successful application of the Monte Carlo simulation technique. A general method for sampling generation of stochastic processes and/or random fields is the spectral representation method (Rice 1944; Shinozuka and Jan 1972; Shinozuka and Deodatis 1991).

In this chapter, a new simulation methodology is presented for a specific fully non-stationary earthquake ground motion stochastic process which has found wide application in earthquake engineering studies (Conte and Peng 1997; Peng and Conte 1997, 1998; Takewaki 2001a, 2001b, 2001c; Michaelov et al. 2001; Chaudhuri and Chakraborty 2003; 2004; Takewaki 2004; Barbato et al. 2004). This new methodology, based on a “physical”

interpretation of the considered stochastic process, is compared with the more general spectral representation method in terms of accuracy and efficiency.

7.2 FULLY NONSTATIONARY STOCHASTIC EARTHQUAKE GROUND MOTION MODEL

In this work, the stochastic earthquake ground motion model is considered as a sigma-oscillatory process (Conte and Peng 1997), nonstationary in both amplitude and frequency content. This earthquake ground acceleration model, $\ddot{U}_g(t)$, is defined as the sum of a finite number of pair-wise independent, uniformly modulated Gaussian processes. Thus

$$\ddot{U}_g(t) = \sum_{k=1}^{N_p} X_k(t) = \sum_{k=1}^{N_p} A_k(t) S_k(t) \tag{7.1}$$

where N_p represents the number of component processes, $A_k(t)$ is the time modulating function of the k-th sub-process or component process, $X_k(t)$, and $S_k(t)$ is the k-th Gaussian stationary process. The time modulating function $A_k(t)$ is defined as

$$A_k(t) = \alpha_k (t - \theta_k)^{\beta_k} e^{-\gamma_k (t - \theta_k)} H(t - \theta_k) \tag{7.2}$$

where α_k and γ_k are positive constants, β_k is a positive integer, and θ_k represents the "arrival time" of the k-th sub-process, $X_k(t)$; H(t) denotes the Heaviside unit step function.

The k-th zero-mean, stationary Gaussian process, $S_k(t)$, is characterized by its autocorrelation function

$$R_{S_kS_k}(\tau) = e^{-\nu_k|\tau|}\cos(\eta_k\tau) \tag{7.3}$$

and the corresponding power spectral density (PSD) function

$$\Phi_{S_kS_k}(\omega) = \frac{\nu_k}{2\pi}\left[\frac{1}{\nu_k^2 + (\omega + \eta_k)^2} + \frac{1}{\nu_k^2 + (\omega - \eta_k)^2}\right] \tag{7.4}$$

in which ν_k and η_k are the two free parameters representing the frequency bandwidth and the predominant or central frequency of the process $S_k(t)$, respectively.

It can be shown (Conte and Peng 1997) that the mean square function of the above ground acceleration model can be expressed as

$$E[\left|\ddot{U}_g(t)\right|^2] = \int_{-\infty}^{\infty}\sum_{k=1}^{N_p}\left|A_k(t)\right|^2\Phi_{S_kS_k}(\omega)d\omega = \sum_{k=1}^{N_p}\left|A_k(t)\right|^2 \tag{7.5}$$

where $E[\ldots]$ is the expectation operator, and the corresponding evolutionary (time-varying) power spectral density (EPSD) function is given by

$$\Phi_{\ddot{U}_g\ddot{U}_g}(t, \omega) = \sum_{k=1}^{N_p}\left|A_k(t)\right|^2\Phi_{S_kS_k}(\omega) \tag{7.6}$$

The EPSD function gives the time-frequency distribution of the earthquake ground acceleration process.

7.3 DIGITAL SIMULATION OF STOCHASTIC GROUND MOTION MODEL

7.3.1 Simulation using the spectral representation method (SRM)

The spectral representation method (SRM) (Shinozuka and Deodatis 1991) is based on the following infinite series representation of a one-dimensional uni-variate stationary stochastic process $f_0(t)$ with mean value equal to zero, autocorrelation function $R_{f_0 f_0}(\tau)$ and two-sided power spectral density function $S_{f_0 f_0}(\omega)$:

$$f_0(t) = \sqrt{2} \sum_{n=0}^{\infty} [2S_{f_0 f_0}(\omega_n) \cdot \Delta\omega]^{1/2} \cos(\omega_n t + \Phi_n) \tag{7.7}$$

in which $\omega_n = n \cdot \Delta\omega$, with sufficiently small but finite $\Delta\omega$, and Φ_n are independent random phase angles uniformly distributed in the range $[0, 2\pi]$. From the infinite series representation of Eq. (7.7), it follows that the stochastic process $f_0(t)$ can be simulated by the following series as $N \to \infty$:

$$f(t) = \sqrt{2} \sum_{n=0}^{N-1} A_n \cos(\omega_n t + \Phi_n) \tag{7.8}$$

in which $f(t)$ denotes the simulated process and

$$A_n = [2S_{f_0 f_0}(\omega_n) \cdot \Delta\omega]^{1/2}, \quad n = 0, 1, \ldots, N-1 \tag{7.9}$$

$$\omega_n = n \cdot \Delta\omega, \quad n = 0, 1, \ldots, N-1 \tag{7.10}$$

$$\Delta\omega = \omega_u / N \tag{7.11}$$

$$A_0 = 0 \quad \text{or} \quad S_{f_0 f_0}(\omega_n = 0) = 0 \tag{7.12}$$

and ω_u in Eq. (7.11) represents an upper cut-off frequency beyond which the power spectral density function $S_{f_0 f_0}(\omega)$ can be considered negligible. Under the condition of Eq. (7.12), the simulated process $f(t)$ is periodic with period $T_0 = 2\pi/\Delta\omega$ and thus, if the process needs to be simulated over the time interval $[0, T]$, the condition

$$T_0 \geq T \rightarrow N \geq \omega_u T/(2\pi) \tag{7.13}$$

must be imposed. Furthermore, the time interval Δt separating the generated values of a sample function of the process $f(t)$ has to obey the condition:

$$\Delta t = 2\pi/\omega_u \tag{7.14}$$

The simulation formula given in Eq. (7.8) is directly applicable to each of the Gaussian stationary stochastic process, $S_k(t)$ with k = 1,2, ..., N_p, substituting the power spectral density function $S_{f_0 f_0}(\omega)$ with the function $\Phi_{S_k S_k}(\omega)$ of Eq. (7.4). The simulation formula for the i-th sample function $\tilde{S}_k^{(i)}(t)$ of the simulated process $\tilde{S}_k(t)$ becomes

$$\tilde{S}_k^{(i)}(t) = \sqrt{2} \sum_{n=0}^{N-1} [2\Phi_{S_k S_k}(\omega_n) \cdot \Delta\omega]^{1/2} \cos(\omega_n t + \phi_n^{(i)}) \tag{7.15}$$

in which $\phi_n^{(i)}$ denotes the i-th realization of the random phase angle Φ_n (n = 0, 1, ..., N). The computational cost of digital simulation of the sample function $\tilde{S}_k^{(i)}(t)$ can be dramat-

ically reduced by using the fast Fourier transform (FFT) technique. Eq. (7.15) can be rewritten as

$$\tilde{S}_k^{(i)}(p\Delta t) = \mathrm{Re}\left\{\sum_{n=0}^{M-1} B_n \exp(2\pi i n p/M)\right\}, \quad p = 0, 1, \ldots, M-1 \tag{7.16}$$

in which

$$B_n = \sqrt{2}[2\Phi_{S_k S_k}(\omega_n)\cdot\Delta\omega]^{1/2}\exp(i\phi_n^{(i)}), \quad p = 0, 1, \ldots, M-1 \tag{7.17}$$

$$B_0 = 0 \quad \text{and} \quad B_n = 0 \quad (N \le n \le M-1) \tag{7.18}$$

The following condition is established between N and M:

$$M \ge 2N \tag{7.19}$$

Furthermore, in order to take full advantage of the FFT technique, M must be an integer power of two:

$$M = 2^{\mu} \tag{7.20}$$

in which μ is a positive integer.

7.3.2 New efficient simulation method

Herein, a new efficient simulation method is developed and described specifically for the stochastic ground motion model presented in Section 7.1. This simulation technique is denoted in the sequel as physical interpretation-based method (PBM) since it is based on a particular physical interpretation of the Gaussian stationary process used to

describe each of the components $S_k(t)$ (k=1, 2, ..., N_p) constituting the nonstationary ground motion process considered herein. Each of the N_p Gaussian stationary process $S_k(t)$, necessary to determine the given stochastic earthquake ground motion is characterized by the following autocorrelation function

$$R_{S_k S_k}(\tau) = e^{-\nu_k|\tau|}\cos(\eta_k\tau) \tag{7.21}$$

Each of the processes $S_k(t)$ (k=1, 2, ..., N_p) can be viewed as a specific linear combination of the displacement and the velocity responses of a particular linear single-degree-of-freedom (SDOF) system (shaping filter) to two statistically independent Gaussian white noises, i.e.

$$S_k(t) = \alpha_k S_{1k}(t) + \beta_k \dot{S}_{2k}(t) \tag{7.22}$$

Use of Eq. (7.22) requires computing the values of the characteristics of the SDOF system, $\omega_0^{(k)}$: natural circular frequency, and $\zeta^{(k)}$: damping ratio, respectively, and the coefficients α_k and β_k.

The autocorrelation functions of the displacement and velocity response of an SDOF system subjected to white noise excitation are given by (Lutes and Sarkani 1997)

$$R_{S_{1k}S_{1k}}(\tau) = \frac{\pi\phi_0}{2\zeta^{(k)}(\omega_0^{(k)})^3} e^{-\zeta^{(k)}\omega_0^{(k)}|\tau|}\left(\cos(\omega_D^{(k)}|\tau|) + \frac{\zeta^{(k)}}{\sqrt{1-(\zeta^{(k)})^2}}\sin(\omega_D^{(k)}|\tau|)\right) \tag{7.23}$$

$$R_{\dot{S}_{2k}\dot{S}_{2k}}(\tau) = \frac{\pi\phi_0}{2\zeta^{(k)}\omega_0^{(k)}} e^{-\zeta^{(k)}\omega_0^{(k)}|\tau|}\left(\cos(\omega_D^{(k)}|\tau|) - \frac{\zeta^{(k)}}{\sqrt{1-(\zeta^{(k)})^2}}\sin(\omega_D^{(k)}|\tau|)\right) \tag{7.24}$$

where ϕ_0 is the PSD of each of the two statistically independent Gaussian white noises and $\omega_D^{(k)} = \omega_0^{(k)}\sqrt{1-(\zeta^{(k)})^2}$ is the damped circular frequency of the SDOF. The autocorrelation function of each component of the process can be obtained by using the definition as

$$\begin{gathered} R_{S_kS_k}(\tau) = E[S_k(t)S_k(t+\tau)] = \\ E[(\alpha_k S_{1k}(t) + \beta_k \dot{S}_{2k}(t))(\alpha_k S_{1k}(t+\tau) + \beta_k \dot{S}_{2k}(t+\tau))] = \\ \alpha_k^2 E[S_{1k}(t)S_{1k}(t+\tau)] + \alpha_k\beta_k E[S_{1k}(t)\dot{S}_{2k}(t+\tau)] + \\ \alpha_k\beta_k E[\dot{S}_{2k}(t)S_{1k}(t+\tau)] + \beta_k^2 E[\dot{S}_{2k}(t)\dot{S}_{2k}(t+\tau)] = \\ \alpha_k^2 R_{S_{1k}S_{1k}}(\tau) + \beta_k^2 R_{\dot{S}_{2k}\dot{S}_{2k}}(\tau) \end{gathered} \tag{7.25}$$

where we have $E[S_{1k}(t)\dot{S}_{2k}(t+\tau)] = E[\dot{S}_{2k}(t)S_{1k}(t+\tau)] = 0$ because $S_{1k}(t)$ and $S_{2k}(t)$ are statistically independent.

By introducing Eqs. (7.23) and (7.24) into Eq. (7.21) and comparing the resulting expression with Eq. (7.25), we obtain:

$$\begin{cases} \nu_k = \zeta^{(k)}\omega_0^{(k)} \\ \eta_k = \omega_0^{(k)}\sqrt{1-(\zeta^{(k)})^2} \end{cases} \Rightarrow \begin{cases} \zeta^{(k)} = \dfrac{\nu_k}{\sqrt{\eta_k^2+\nu_k^2}} \\ \omega_0^{(k)} = \sqrt{\eta_k^2+\nu_k^2} \end{cases} \tag{7.26}$$

$$\begin{cases} \alpha_k^2 = \dfrac{\zeta^{(k)}(\omega_0^{(k)})^3}{\pi\phi_0} \\ \beta_k^2 = \dfrac{\zeta^{(k)}\omega_0^{(k)}}{\pi\phi_0} \end{cases} \tag{7.27}$$

This interpretation of the stochastic random sub-processes is useful in developing a fast simulation procedure, consisting in (1) generating two independent Gaussian white noises with PSD ϕ_0, (2) integrating in time the SDOF defined by Eq. (7.26) subjected separately to the two independent Gaussian white noises previously generated, and (3) linearly combining (Eq. (7.22)) the obtained displacement and velocity responses using the coefficients given by Eq. (7.27).

An important aspect of this simulation procedure is the generation of the needed discrete white noises and their numerical interpolation shape. A discrete white noise process is realized by generating a sequence of statistically independent random variables positioned at equidistant time instants, i.e., with constant time intervals Δt. Any probability distribution can be selected; in the present case, discrete Gaussian white noises are generated by selecting a Gaussian distribution with zero mean $\mu_w = 0$ and variance $\sigma_w^2 = 1$. Different methods of numerical integration of the equation of motion assume different schemes of interpolation shape between the discrete input values. Here the exact

piece-wise linear integration scheme is adopted; therefore a linear interpolation shape is assumed for the discrete white noise.

The power spectral density of a continuous white noise is a constant:

$$\Phi_{w,\,c}(\omega) = \phi_0 \tag{7.28}$$

On the other hand, the actual power spectral density of a linearly interpolated discrete white noise is:

$$\Phi_{w,\,d}(\omega, \Delta t) = \frac{\sigma_w^2}{2\pi}\frac{6 - 8\cos(\omega\Delta t) + 2\cos(2\omega\Delta t)}{\omega^4(\Delta t)^3} \tag{7.29}$$

Taking the limit as $\Delta t \to 0$, the PSD function of the corresponding continuous white noise is obtained as

$$\lim_{\Delta t \to 0} \Phi_{w,\,d}(\omega, \Delta t) = \frac{1}{(2\pi)} \lim_{\Delta t \to 0} (\sigma_w^2 \Delta t) = \phi_0 \tag{7.30}$$

The value of ϕ_0 given by Eq. (7.30) is the one required to determine the coefficient for the linear combination of the responses of the shaping filters (Eq. (7.27)). Integrating naively the so-defined linearly interpolated discrete Gaussian white noises, it is evident that the result is dependent on the choices of Δt and on the natural frequencies of the shaping filters $\omega_0^{(k)}$. In particular, Eq. (7.29) shows a non-negligible loss of power in the PSD function for large Δt and $\omega_0^{(k)}$. In order to avoid this problem, it is necessary to rescale the variance of the Gaussian random variables used to generate each of the input

discrete white noises for each of the shaping filters. This is accomplished by computing the reduction of the PSD corresponding to the natural frequency of the shaping filter $\omega_0^{(k)}$ and the discretization time interval Δt from Eq. (7.29) as

$$\gamma_k(\Delta t) = \frac{\Phi_{w,d}(\omega_0^{(k)}, \Delta t)}{\phi_0} = \frac{6 - 8\cos(\omega_0^{(k)}\Delta t) + 2\cos(2\omega_0^{(k)}\Delta t)}{(\omega_0^{(k)})^4(\Delta t)^4} \tag{7.31}$$

and using Gaussian random variables with zero mean $\mu_w = 0$ and corrected variance $\hat{\sigma}_w^2$ given as

$$\hat{\sigma}_w^2 = \frac{1}{\gamma_k}\sigma_w^2 = \frac{1}{\gamma_k} \tag{7.32}$$

The proposed simulation method requires that the discretization time interval Δt is chosen such that

$$\gamma_k(\Delta t) > 0, \quad k = 1, 2, \ldots, N_p \tag{7.33}$$

7.3.3 Comparison between the two simulation methods

The SRM reviewed above in this paper is a general and powerful tool for simulating one-dimensional uni-variate Gaussian stochastic processes. In the version making use of the FFT (Eq. (7.16)), the SRM is also extremely efficient. Nevertheless the SRM is subject to some limitations and conditions deriving from the fact that the simulation formulae employed (Eq. (7.15) or Eq. (7.16)) are exact only in the limit as $N \to \infty$ (i.e., as the trun-

cated series in Eqs. (7.15) or (7.16)) approach the corresponding infinite series in Eq. (7.7)).

In particular the following aspects need careful consideration.

(1) The power spectral density of the simulated process obtained through SRM is equal to zero for frequencies greater than the cut-off frequency ω_u. This condition is not verified by any of the components of the stochastic process considered in the paper. The effects of this artificially introduced cut-off frequency is loss in terms of total power of the process. The power loss for each process component is equal to

$$P^{(k)}_{loss,\,1} = 2\int_0^{\infty} \Phi_{S_k S_k}(\omega)d\omega - 2\int_0^{\omega_u} \Phi_{S_k S_k}(\omega)d\omega = \qquad k = 1, 2, \ldots, N_p \qquad (7.34)$$
$$= 2\int_{\omega_u}^{\infty} \Phi_{S_k S_k}(\omega)d\omega$$

From Eq. (7.34), the power loss for the mean square ground acceleration can be computed as

$$P_{loss,\,1}(t) = \sum_{k=1}^{N_p} \left(\left|A_k(t)\right|^2 \cdot P^{(k)}_{loss,\,1}\right) \qquad (7.35)$$

The integral of $P_{loss,\,1}(t)$ over the assumed earthquake duration T is the total energy loss from the original process to the simulated process, i.e.

$$E_{loss,\,1} = \int_0^T P_{loss,\,1}(t)dt \qquad (7.36)$$

This energy loss has an impact that is particularly evident on the response statistics of elastic structures with high frequency modes subject to the earthquake ground motion process considered in the paper. This power (and energy) loss can be reduced increasing the value of the cut-off frequency ω_u, which also implies decreasing the maximum value of the time interval Δt separating the generated values of a sample function, as shown in Eq. (7.14). Given the characteristics of the earthquake ground motion process considered, the same time interval Δt must be used in simulating each of the N_p component processes, leading to different accuracy in simulating the different components and possibly to a choice of a very small Δt in order to achieve a required minimum accuracy.

(2) The autocorrelation function of the digitally simulated process obtained by using the SRM is an approximation of the autocorrelation function of the simulated process. In Shinozuka and Deodatis (1991), the error due to this approximation is shown to be inversely proportional to the number N of components used in the simulation. The power loss for each process component and the total energy loss for the earthquake ground motion process due to this approximation can be expressed as

$$P_{loss,\,2}^{(k)} = 2\int_0^{\omega_u} \Phi_{S_k S_k}(\omega)d\omega - 2\sum_{n=0}^{N-1} \Phi_{S_k S_k}(\omega_n)\Delta\omega, \quad k = 1, 2, \ldots, N_p \tag{7.37}$$

$$E_{loss,\,2} = \sum_{k=1}^{N_p} \left(P_{loss,\,2}^{(k)} \cdot \int_0^T |A_k(t)|^2 dt \right) \tag{7.38}$$

(3) The simulated process is only asymptotically Gaussian (i.e., for $N \to \infty$). When the interest is focused on quantities depending on the tail distribution, biasing could be introduced if the number N of components used in the simulation is not sufficiently large.

(4) The simulated process is periodic with period $T_0 = 2\pi/\Delta\omega$. This characteristic imposes conditions on the number N of components to use for simulation and/or on the time interval Δt and/or on the time length T of the simulation, since the condition $T \geq T_0$ must be satisfied.

(5) When using the FFT technique, the additional condition $M = 2^{\mu}$ must be enforced to obtain the maximum computational efficiency. Furthermore, the relation $M \geq 2N$ must be satisfied. For large N, this condition could require large use of memory storage and may have negative effects on the computational efficiency of the simulation procedure.

(6) If the time length of the simulation is increased from T to $\overline{T} > T$, the realizations of the process must be completely recomputed, i.e., previous realizations cannot be reused.

(7) The process of "zooming-in" (i.e., refining the simulation in a narrow time window using a time step as small as desired) is possible only with SRM using summation of cosines, while zooming-in over the whole period T_0 is necessary when SRM with FFT technique is employed.

The PBS method developed in this work specifically for the earthquake ground motion process presented in Section 7.1 overcomes the limitations of the SRM. In fact, the following considerations hold.

(1) The PBS method does not require to define a cut-off frequency, avoiding power loss in the PSD function of each of the process components.

(2) The autocorrelation function of the simulated process is exact, i.e., equal to the auto-correlation function of the process to simulate.

(3) The simulated process is exactly Gaussian, provided that the random number generator used is able to generate numbers following exactly a Gaussian distribution.

(4) The simulated process is not periodic and the only condition on the time interval Δt used in the simulation is that $\gamma_k(\Delta t) > 0$ $(k = 1, 2, ..., N_p)$. In general, this condition is easy to satisfy.

(5) The computational efficiency of the simulation procedure is independent of the time interval Δt and the simulation time is proportional to the ratio $T/\Delta t = n_{step}$.

(6) Extending the simulation to a time length $\bar{T} > T$ can leverage previous realizations, provided that the final states of the two basic filtered white noises have been previously saved for each component of the process (i.e., $S_{1k}(T)$ and $\dot{S}_{2k}(T)$, $k = 1, 2, ..., N_p$).

(7) Zooming-in is obtained very easily and requires only to change the value of Δt in the time interval of interest.

On the other hand, while the SRM is a general simulation technique, the PBS method can be applied only to stationary Gaussian processes having an autocorrelation function given by Eq. (7.21).

7.4 APPLICATION EXAMPLES

7.4.1 Calibrated stochastic earthquake models

In this study, the stochastic process for the earthquake excitation has been calibrated to model the characteristics of three actual ground motion records: (1) the S00E (N-S) component of the Imperial Valley earthquake of May 18, 1940, recorded at the El Centro site (in short, El Centro earthquake); (2) the N00W (N-S) component of the San Fernando earthquake of February 9, 1971, recorded at the Orion Blvd. site (Orion Blvd. earthquake); and (3) the N90W (W-E) component of the Loma Prieta earthquake of October 17, 1989, recorded at the Capitola site (Capitola earthquake). The parameters for each of these records are estimated using the short-time Thomson multiple-window method described in Conte and Peng (1997), where the parameter values for the El Centro and the Orion Blvd. earthquakes are also given. The model parameters for the Capitola earthquake are given in Barbato et al. (2004). The agreement between the presented model and the ground motion simulation is very good and it has been validated in previous works (Conte and Peng 1997), in which the SRM was used for the simulation of artificial ground motions.

A direct comparison in terms of computational efficiency and accuracy between the SRM and the PBS method is presented for the three earthquakes considered using data from 10000 simulations. Computational efficiency is evaluated comparing the CPU times required for generating the 10000 simulations using the SRM with summation of cosines and the SRM with FFT technique for different number N of components and the PBS method. Accuracy is evaluated computing the energy relative error, ε_{energy}, and the peak relative error, ε_{peak}, in the simulated process obtained using the SRM for different number N of components. Those errors are defined as follows:

$$\varepsilon_{energy} = \frac{E_{loss,\,1} + E_{loss,\,2}}{\sum_{k=1}^{N_p} \left(\int_0^T |A_k(t)|^2 dt \right)} \tag{7.39}$$

$$\varepsilon_{peak} = \frac{\max_{(0 \le t \le T)} \left| E[|\ddot{U}_g(t)|^2] - E[|\tilde{\ddot{U}}_g(t)|^2] \right|}{\max_{(0 \le t \le T)} \{ E[|\ddot{U}_g(t)|^2] \}} \tag{7.40}$$

For the three earthquake models considered, the parameters used in the PBS method are computed for all the component processes and are shown in Table 7.1.

7.4.2 Comparison of simulation methods for the El Centro earthquake model

The earthquake ground motion model used to represent the El Centro earthquake is constituted of 21 different time-modulated components. For this earthquake model, a first

comparison is made between the statistics of the target stochastic model (equal to the one obtained using the PBS method) and the simulated process obtained using the SRM with different values of the number N of components selected for the simulation. The results presented herein refers to an assumed duration of the earthquake T = 35.0s and a time interval of the simulation $\Delta t = 0.02s$, with a number of time steps $n_{step} = 1751$.

The time-variant mean square accelerations of the target ground acceleration process and of the simulated processes for different values of N are shown in Fig. 7.1. It is noteworthy that the simulated processes obtained from (1) the SRM with summation of cosines and (2) the SRM with the FFT technique are identical when using the same number N of simulation components. Fig. 7.2 plots the energy relative error and the peak relative error, defined in Eqs. (7.39) and (7.40), respectively, in the simulated processes obtained using the SRM for different values of N. Figs. 7.1 and 7.2 show that the simulated process approximates better the target process for increasing number N of simulation components, but for N larger than a certain number (in this case $N^* = 2^{11}$), the improvement obtained increasing N is very small and cannot completely eliminate the difference between target and simulated processes. This difference is due to the energy loss related to the introduced cut-off frequency ω_u, as shown in Eq. (7.36).

Fig. 7.3 shows the CPU time required for the simulation of 10000 realizations of the ground acceleration process using (1) the SRM with summation of cosines (denoted in

the sequel as SRM) and (2) the SRM with the FFT technique (SRM_{FFT}) relative to the CPU time required by the simulation of 10000 realizations obtained using the PBS method. In the inset, the relative CPU time for the SRM for different N values is shown separately, due to the different higher order of magnitude. Fig. 7.3 shows clearly that:

(1) The SRM is extremely time-consuming, even for a small number N of simulation components ($t_{CPU}/t_{CPU,PBM} > 20$ for $N = 2^4$).

(2) The SRM_{FFT} is very efficient computationally when the conditions $M = 2^{\mu}$, with μ positive integer, and M = 2N are satisfied. In the present case, simulations using the SRM_{FFT} have been performed also for values of M not satisfying the first of the above conditions (i.e., $M = \alpha \cdot n_{step}$, α = 1, 2, 3, 4, 5). For these values of M, the simulation algorithm is much less efficient than for $M = 2^{\mu}$

(3) For $N = 1024 = 2^{10}$ ($M = 2^{11}$), simulation of the ground motion stochastic model using the SRM_{FFT} requires approximately the same amount of time required by simulation by using the PBS method. On the other hand, in order to satisfy the condition $T \geq T_0$, the condition $N \geq n_{step}$ must also be satisfied. Thus, the minimum value of N for which both the conditions $M = 2^{\mu}$ and M = 2N hold is $N = 2^{11} = 2048$, for which $t_{CPU} / t_{CPU,\,PBM} = 1.926$.

Due to the last of the above considerations, the statistics of the 10000 simulations obtained using the PBS method and the SRM with FFT technique and N = 2048 (in the

following denoted as SRM_{2048}) are directly compared with the closed form solutions of the theoretical statistics of the process which is being simulated. Fig. 7.4 shows the comparison between the target mean square acceleration relative to the El Centro earthquake model and the mean square acceleration computed from the 10000 realizations obtained using the PBS method. The curves representing estimates of the mean value plus and minus the standard deviation of the estimate of the mean are also plotted. The target quantity is almost always contained in the interval between the latter two curves. The worst agreement case between target and estimated mean square accelerations happens in correspondence of the peak about time $t = 2s$ and is shown in the inset of Fig. 7.4. Fig. 7.5 illustrate the comparison between the target mean square acceleration relative to the El Centro earthquake model and the mean square acceleration computed from the 10000 realizations obtained by using the SRM_{2048}, together with the curves representing the estimates of the mean value plus and minus the standard deviation of the estimate of the mean. The agreement between target and estimated mean square accelerations is also very good, but in the inset of Fig. 7.5 the systematic underestimation of the mean square acceleration by the estimate obtained through simulation by SRM_{2048} is evident. This is consistent with the expected power loss previously discussed in the comparison between the two simulations techniques considered and represented in Fig. 7.1 for this application example.

Fig. 7.6 compares the closed-form solution for the mean upcrossing rate of the ground motion acceleration relative to a deterministic threshold $\xi = 3\sigma_{a,\,max} = 3 \cdot max[\sigma_a(t)]$ (see Appendix) with the corresponding simulation estimates obtained through PBM and SRM_{2048}. In Fig. 7.7, the same kind of comparison is presented for the expected value of upcrossings of the ground motion acceleration relative to a deterministic threshold $\xi = 3\sigma_{a,\,max}$. The confidence intervals of plus and minus the standard deviation of the estimate of the quantity of interest are also given. The results obtained from both PBS method and SRM_{2048} are in very good agreement with the theoretical values.

Fig. 7.8 illustrates the comparison between the target mean square displacement for an SDOF system with natural period $T_n = 2s$ and damping ratio $\zeta = 0.10$ subjected to the El Centro earthquake model (closed-form solutions for such a quantity can be found in Peng and Conte 1996) and the same quantity estimate computed from the 10000 realizations obtained using the PBS method. Fig. 7.9 compares the same closed-form solution quantities as in Fig. 7.8 with their estimates obtained through SRM_{2048}. The curves representing the estimates of the mean value plus and minus the standard deviation of the estimate of the mean are also plotted. A behavior similar to the one recognized in Figs. 7.4 and 7.5 is found also in this case: both the PBS method and SRM_{2048} results are overall in good agreement with the theoretical results relative to the target process, but while the

results obtained through PBS method match very well the theoretical values also in correspondence of the peaks in the time-history (see inset of Fig. 7.8), the SRM_{2048} results systematically underestimate the theoretical results at these peaks, as highlighted clearly by the inset of Fig. 7.9.

Figs. 7.10 and 7.11 show the comparison between the closed-form solutions for the mean upcrossing rate and the expected number of upcrossings, respectively, of the SDOF system considered relative to a deterministic threshold $\xi = 3\sigma_{d,\,max} = 3 \cdot max[\sigma_d(t)]$ (see Barbato et al. 2004) and the corresponding estimates obtained through PBS method and SRM_{2048}. For the expected value of upcrossings, the confidence interval of plus and minus one standard deviation of the estimates are also given. The agreement between theoretical values and estimates is overall very good. The theoretical values are contained for the entire simulation interval in the confidence interval obtained through PBS method, while they slightly exceed the confidence interval obtained through SRM_{2048} around t = 3.0s and t = 6.0s. From theoretical considerations (see point 3 of the section “Comparison between the two simulation techniques”), it is believed that the quality of results obtained from SRM_{2048} will deteriorate when considering quantities depending on higher thresholds (i.e., with smaller probability of occurrence), while results obtained from PBS method are not influenced by the probability of occurrence, since the simulated process is exactly Gaussian-distributed.

The results in terms of relative errors and relative CPU time presented in this section are representative only of the considered choice of T = 35.0s and $\Delta t = 0.02s$. Different choices of the time length T of the simulation and/or of the time interval Δt of the simulation will give results that are numerically different but qualitatively similar. In particular, since (1) the computational cost of the PBS method is proportional to the number of time steps n_{step} and the computational cost of the SRM_{FFT} is proportional to the number of simulation components N, (2) the two simulation methods present similar computational cost for $n_{step}/N \approx 1.7$, (3) the condition $N \geq n_{step}$ must hold, (4) the SRM approximates the target process only asymptotically while the PBS method simulates exactly the target process, it can be concluded that the PBS method is more efficient and accurate than the SRM in simulating the target process representing the El Centro earthquake model for any choice of T and Δt.

7.4.3 Comparison of simulation methods for the Orion Blvd. earthquake model

The earthquake ground motion model used to represent the Orion Blvd. earthquake is constituted of 15 different time-modulated components. Also for this earthquake model, the time length of the simulation and the time interval of the simulation are assumed as $T = 35.0s$ and $\Delta t = 0.02s$, respectively, giving a number of time steps $n_{step} = 1751$.

The time-variant mean square acceleration of the target ground acceleration process and of the simulated processes for different values of N are shown in Fig. 7.12. Fig. 7.13 plots the energy relative error and the peak relative error in the simulated processes obtained by using the SRM for different values of N. Figs. 7.12 and 7.13 show that the simulated process approximates better the target process for increasing number N of simulation components. Similarly to the El Centro earthquake process case, for N larger N* = 2^{11} the improvement obtained increasing N is very small and cannot completely eliminate the difference between target and simulated processes, mainly due to the energy loss related to the introduced cut-off frequency ω_u. For the Orion Blvd. earthquake model, the energy and peak relative errors are roughly half of the corresponding errors found for the El Centro earthquake model when using the same number N of simulation components.

Fig. 7.14 provides the CPU time required for the simulation of 10000 realizations of the ground acceleration process using the SRM_{FFT} relative to the CPU time required by the simulation of 10000 realizations obtained by using the PBS method. It is found that also in this case for $N = 1024 = 2^{10}$ ($M = 2^{11}$), simulation of the ground motion stochastic model by using the SRM_{FFT} requires approximately the same amount of time required by simulation by using the PBS method. The minimum value of N that satisfies the conditions $M = 2^{\mu}$, $M = 2N$ and $N \geq n_{step}$ is $N = 2^{11} = 2048$, for which

$t_{CPU}/t_{CPU,\,PBM} = 1.956$. The results in terms of relative CPU time for the simulation of the Orion Blvd. earthquake model are very similar to the ones for the El Centro earthquake models and similar considerations apply. Thus, also in this case the PBS method is more efficient and accurate than the SRM in simulating the target process for any choice of T and Δt.

7.4.4 Comparison of simulation methods for the Capitola earthquake model

The earthquake ground motion model used to represent the Capitola earthquake consists of 11 different time-modulated components. Also for this earthquake model, the time length of the simulation and the time interval of the simulation are assumed as T = 35.0s and $\Delta t = 0.02s$, respectively, giving a number of time steps $n_{step} = 1751$.

Fig. 7.15 compares the time-variant mean square acceleration of the target ground acceleration process and of the simulated processes for different values of N. Fig. 7.16 plots the energy relative error and the peak relative error in the simulated processes obtained by using the SRM for different values of N. Similar considerations apply as for the two earthquake model illustrated above. The energy and peak relative errors found for the Capitola earthquake model are very close to the ones of the Orion Blvd. Earthquake model for the same number N of simulation components.

Fig. 7.17 shows the CPU time required for the simulation of 10000 realizations of the ground acceleration process by using the SRM_{FFT} relative to the CPU time required by the simulation of 10000 realizations obtained by using the PBS method. As in two previous cases, simulation of the ground motion stochastic model using the SRM_{FFT} with $N = 1024 = 2^{10}$ ($M = 2^{11}$) requires approximately the same amount of time required by simulation by using the PBS method. For $N = 2^{11} = 2048$, the relative CPU time is $t_{CPU}/t_{CPU,\,PBM} = 2.010$. The results in terms of relative CPU time are very similar to the ones obtained in the previous two cases and also in this case the PBS method is more efficient and accurate than the SRM in simulating the target process for any choice of T and Δt.

7.4.5 Comparison results based on the three earthquake models considered

The following common observations can be made based on the results obtained from the three earthquake models considered.

(1) The energy relative error and the peak relative error in the simulated processes obtained using the SRM are strongly dependent on the characteristics of the process itself (number N_p of process components, parameters representing the components, etc.) and only slightly on the number N of components used in the simulation for $N \geq n_{step}$. These errors tend to a constant value for $N \to \infty$ depending on the cut-off

frequency ω_u and thus on the time interval Δt used to discretize the simulation. In general, these errors are small for reasonable choices of time length T of the simulation and time interval Δt discretizing the simulation. The PBS method is able to simulate the given stochastic process without introducing any energy and peak relative errors.

(2) The PBS method is more efficient and accurate than the SRM in simulating the target process for any choice of T and Δt. For all the three earthquake models considered, it is found that for $N \approx n_{step}$ the relative CPU time is $t_{CPU}^{(N = n_{step})} / t_{CPU,\,PBM} \approx 1.7$. Considering that $N \geq n_{step}$, the minimum number N* satisfying also the conditions $M = 2^{\mu}$ and M = 2N (i.e., $N = 2^{\mu - 1}$) is such that $n_{step} \leq N^* \leq 2n_{step}$. Thus, the relative CPU time is such that $1.7 \leq (t_{CPU}^{(N^*)} / t_{CPU,\,PBM}) \leq 3.4$, independently of the choice of T and Δt and of the earthquake model to be simulated.

7.5 CONCLUSIONS

A new efficient simulation technique for a specific fully nonstationary earthquake ground motion stochastic model is developed and presented in this work. This new method, based on a physical interpretation of the considered stochastic process, is compared with the more general spectral representation method in terms of both computational efficiency and accuracy. This comparison is performed by using three earthquake ground motion models for which the parameters characterizing the stochastic processes

have been calibrated to represent three different actual recorded earthquakes. The relative CPU time required for generating 10000 samples of the earthquake ground motion is used as measure of computational efficiency. The statistics, estimated from the simulations, of the earthquake ground motion itself and of the response of a linear elastic single-degree-of-freedom system subjected to the earthquake ground motion are compared with the corresponding available closed-form solutions.

It is found that the new proposed simulation method is: (1) at least as accurate as the spectral representation method, (2) more efficient than the spectral representation method in terms of computational time required for simulating samples of the specific stochastic process considered in this work, and (3) more flexible and easy to use, since the time length and the time interval used to discretize the simulation are independent and do not need to satisfy restrictive additional conditions.

Table 7.1 Parameters defining the sub-processes for the stochastic models of three considered earthquakes

	El Centro earthquake			Orion Blvd. earthquake			Capitola earthquake		
	$\omega_0^{(k)}$	$\zeta^{(k)}$	$1/\gamma_k$	$\omega_0^{(k)}$	$\zeta^{(k)}$	$1/\gamma_k$	$\omega_0^{(k)}$	$\zeta^{(k)}$	$1/\gamma_k$
1	6.915	0.2104	1.0032	3.349	0.3768	1.0007	9.346	0.0260	1.0058
2	11.361	0.2190	1.0086	5.147	0.3081	1.0018	7.770	0.1039	1.0040
3	8.075	0.4090	1.0044	4.592	0.4177	1.0014	5.829	0.2284	1.0023
4	13.768	0.1596	1.0127	3.363	0.5679	1.0008	15.672	0.1633	1.0165
5	14.718	0.2123	1.0146	3.661	0.3278	1.0009	18.484	0.1125	1.0231
6	26.039	0.2586	1.0463	11.150	0.1076	1.0083	29.806	0.0706	1.0612
7	48.137	0.0559	1.1685	14.289	0.1463	1.0137	21.771	0.0105	1.0322
8	38.301	0.1882	1.1033	16.671	0.1775	1.0187	39.706	0.0572	1.1114
9	20.398	0.2995	1.0282	9.509	0.1428	1.0060	46.140	0.0338	1.1537
10	9.256	0.2146	1.0057	19.419	0.1277	1.0255	51.372	0.0382	1.1942
11	9.647	0.2509	1.0062	20.249	0.0638	1.0278	60.218	0.1363	1.2773
12	14.189	0.1074	1.0135	31.594	0.0868	1.0690	-	-	-
13	24.105	0.0711	1.0396	28.824	0.0463	1.0571	-	-	-
14	28.426	0.2095	1.0555	43.123	0.0419	1.1329	-	-	-
15	13.064	0.1482	1.0114	37.764	0.1149	1.1002	-	-	-
16	12.153	0.1473	1.0099	-	-	-	-	-	-
17	98.752	0.0500	1.9595	-	-	-	-	-	-
18	61.863	0.0319	1.2949	-	-	-	-	-	-
19	44.028	0.0738	1.1389	-	-	-	-	-	-
20	26.592	0.1382	1.0484	-	-	-	-	-	-
21	37.153	0.0460	1.0969	-	-	-	-	-	-

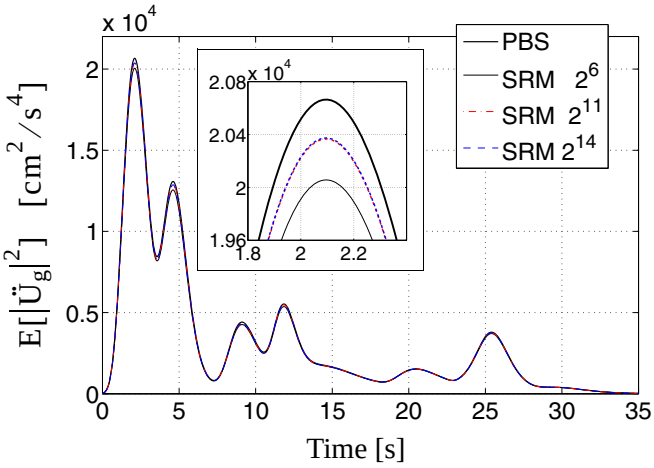

Figure 7.1 Comparison of time-variant mean square acceleration for the El Centro earthquake of target earthquake ground motion process (PBS) with simulated process obtained by using SRM with different N.

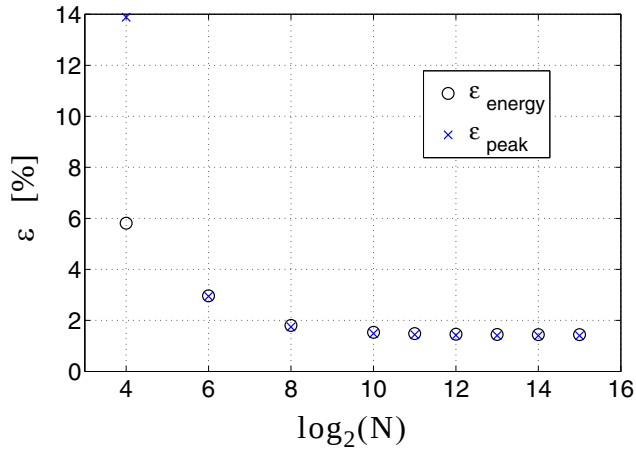

Figure 7.2 Energy relative error and peak relative error in the simulated processes for the El Centro earthquake obtained by using the SRM and various N.

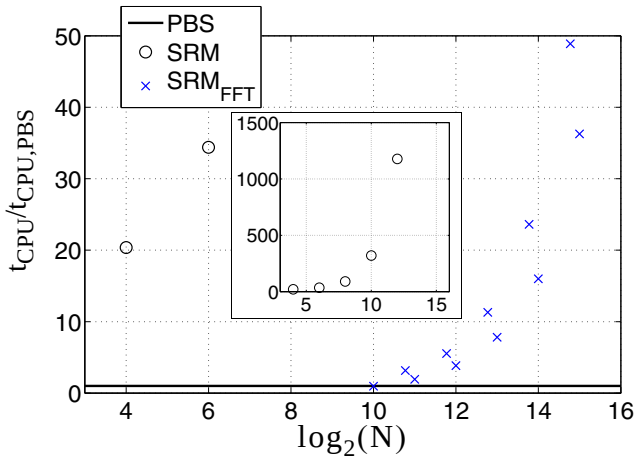

Figure 7.3 Relative CPU time required for simulating 10000 realizations of the El Centro earthquake ground motion stochastic model.

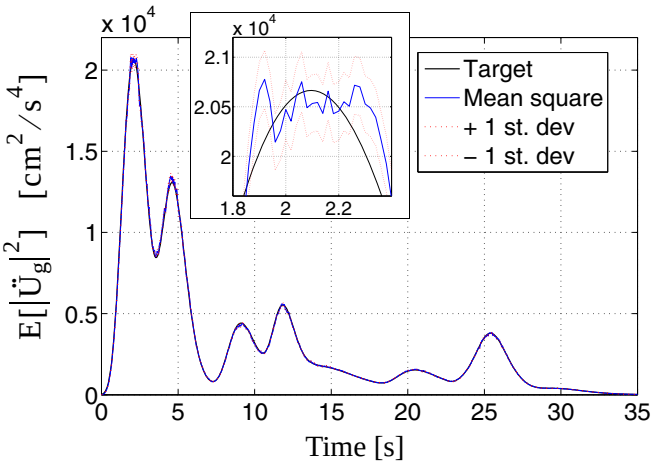

Figure 7.4 Comparison of target mean square acceleration for the El Centro earthquake with mean square acceleration from 10000 realizations obtained by using the PBS method.

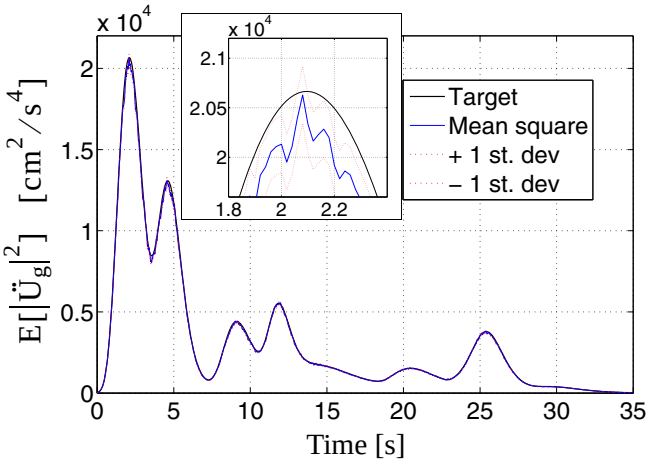

Figure 7.5 Comparison of target mean square acceleration for the El Centro earthquake with mean square acceleration from 10000 realizations obtained by using the SRM with the FFT technique and N = 2048 (SRM_{2048}).

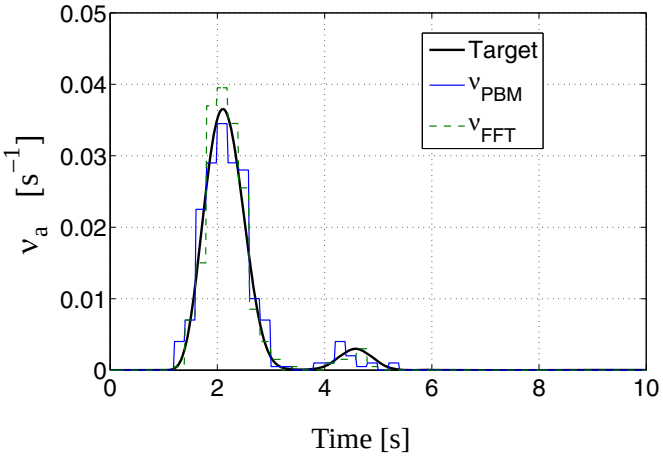

Figure 7.6 Mean upcrossing rate of acceleration for the El Centro earthquake relative to a deterministic threshold $\xi = 3\sigma_{a,\max}$.

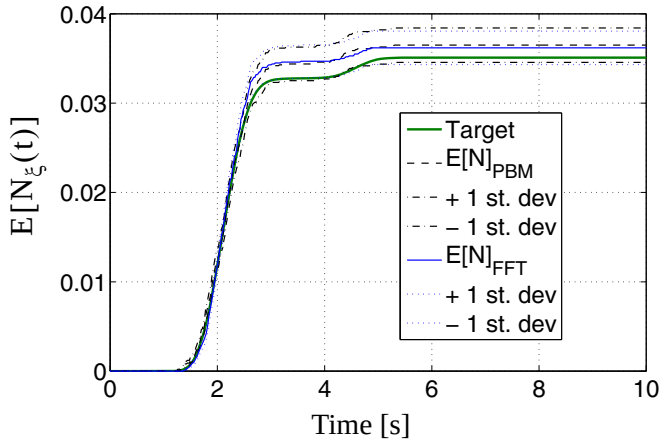

Figure 7.7 Expected values of upcrossings of acceleration for the El Centro earthquake relative to a deterministic threshold $\xi = 3\sigma_{a,\max}$.

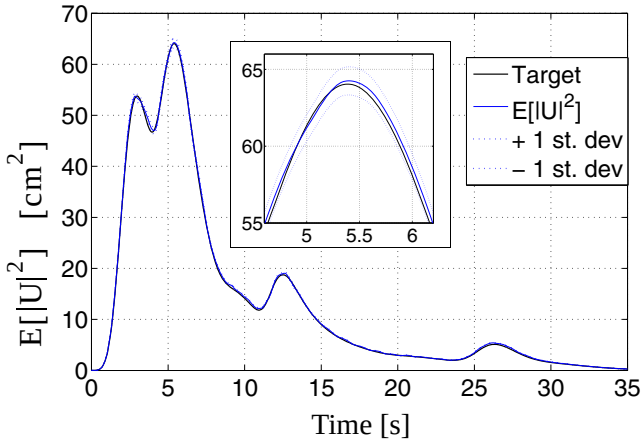

Figure 7.8 Comparison of target mean square displacement for a SDOF oscillator with natural period T_n = 2s and damping ratio $\zeta = 0.10$ subjected to the El Centro earthquake with mean square displacement from 10000 realizations obtained by using the PBS method.

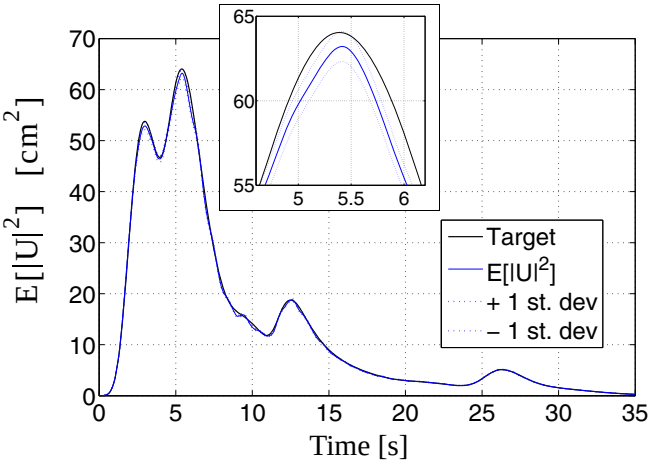

Figure 7.9 Comparison of target mean square displacement for a SDOF oscillator with natural period T_n = 2s and damping ratio $\zeta = 0.10$ subjected to the El Centro earthquake with mean square displacement from 10000 realizations obtained by using the SRM with the FFT technique and N = 2048 (SRM_{2048}).

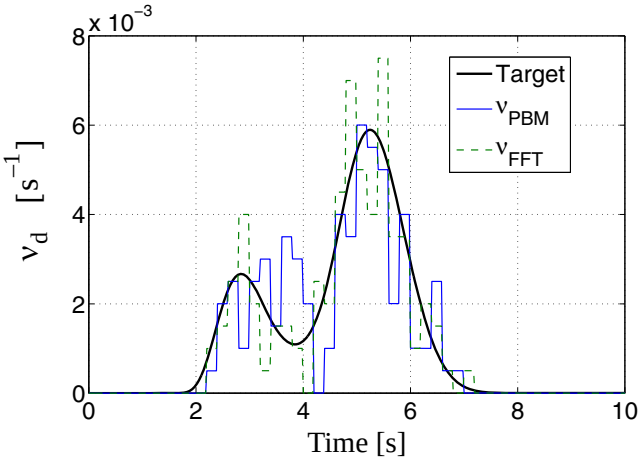

Figure 7.10 Mean upcrossing rate of displacement for a SDOF oscillator with natural period T_n = 2s and damping ratio $\zeta = 0.10$ subjected to the El Centro earthquake relative to a deterministic threshold $\xi = 3\sigma_{d,\max}$.

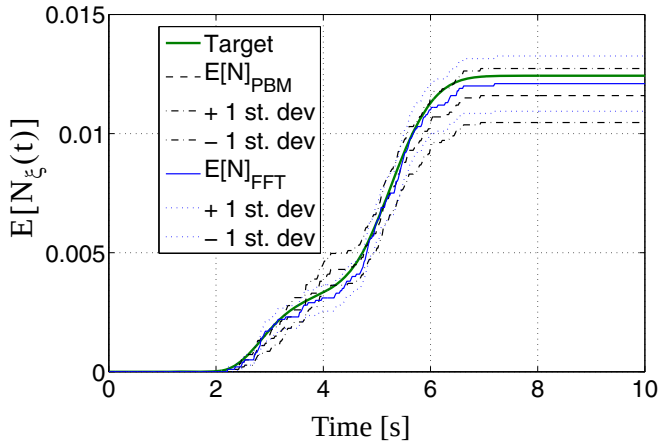

Figure 7.11 Expected values of upcrossings of displacement for a SDOF oscillator with natural period T_n = 2s and damping ratio $\zeta = 0.10$ subjected to the El Centro earthquake relative to a deterministic threshold $\xi = 3\sigma_{d,\max}$.

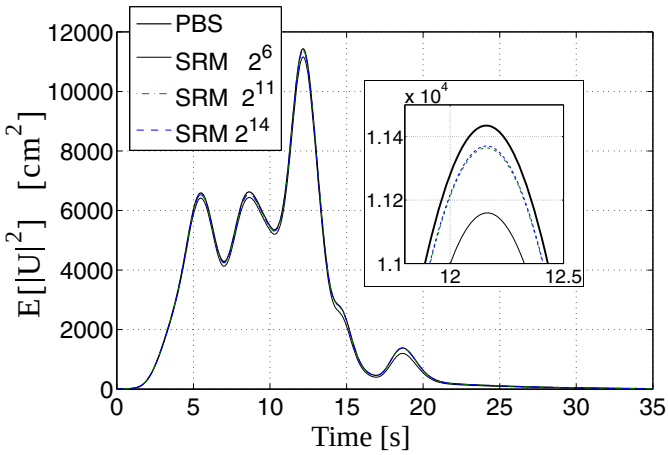

Figure 7.12 Comparison of time-variant mean square acceleration for the Orion Blvd. earthquake of target earthquake ground motion process (PBS) with simulated process obtained by using SRM with different N.

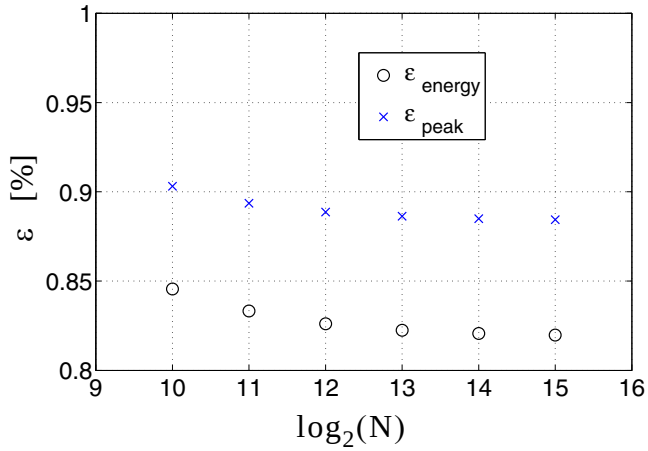

Figure 7.13 Energy relative error and peak relative error in the simulated processes for the Orion Blvd. earthquake obtained by using the SRM and various N.

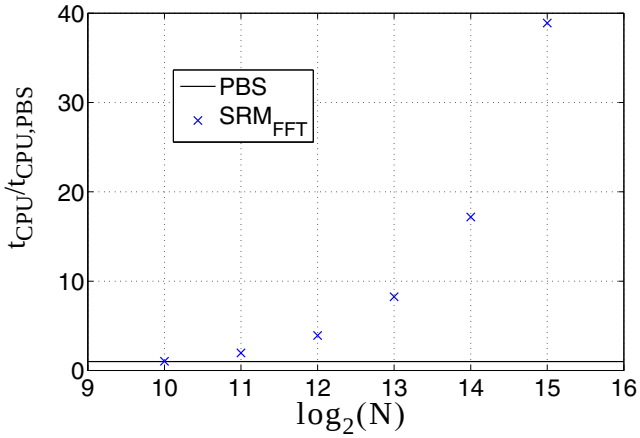

Figure 7.14 Relative CPU time required for simulating 10000 realizations of the Orion Blvd. earthquake ground motion stochastic model.

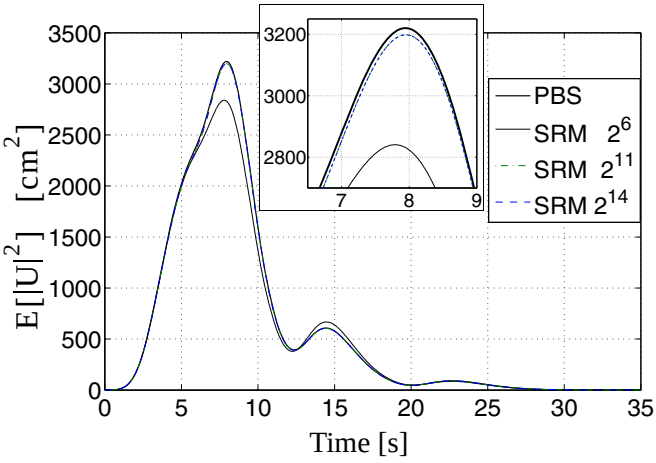

Figure 7.15 Comparison of time-variant mean square acceleration for the Capitola earthquake of target earthquake ground motion process (PBS) with simulated process obtained by using SRM with different N.

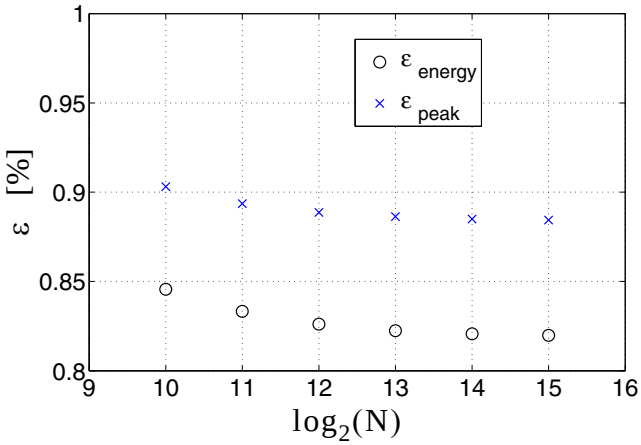

Figure 7.16 Energy relative error and peak relative error in the simulated processes for the Capitola earthquake obtained by using the SRM and various N.

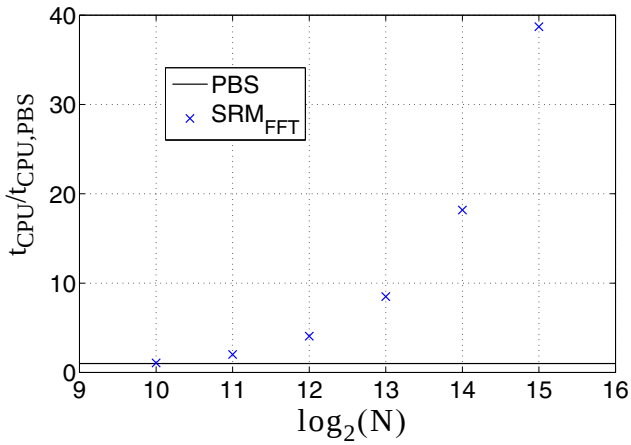

Figure 7.17 Relative CPU time required for simulating 10000 realizations of the Capitola earthquake ground motion stochastic model.

APPENDIX: MEAN UPCROSSING RATE FOR GROUND ACCELERATION PROCESS

The quantities shown in Figs. 7.6 and 7.7 can be expressed in closed form as follows:

$$\nu(\xi^+, t) = \int_0^\infty \ddot{u}_g f_{\ddot{U}_g\ddot{U}_g}(\xi, \ddot{u}_g, t)d\ddot{u}_g = \frac{1}{2\pi}\frac{\sigma_{\ddot{U}_g}}{\sigma_{\ddot{U}_g}}\sqrt{1-\rho^2_{\ddot{U}_g\ddot{U}_g}}\cdot e^{-\frac{1}{2(1-\rho^2_{\ddot{U}_g\ddot{U}_g})}\left(\frac{\xi}{\sigma_{\ddot{U}_g}}\right)^2} \cdot \left\{1 + \frac{\sqrt{\pi}\rho_{\ddot{U}_g\ddot{U}_g}}{\sqrt{2(1-\rho^2_{\ddot{U}_g\ddot{U}_g})}}\left(\frac{\xi}{\sigma_{\ddot{U}_g}}\right)e^{\frac{\rho^2_{\ddot{U}_g\ddot{U}_g}}{2(1-\rho^2_{\ddot{U}_g\ddot{U}_g})}\left(\frac{\xi}{\sigma_{\ddot{U}_g}}\right)^2}\operatorname{erfc}\left(-\frac{\rho_{\ddot{U}_g\ddot{U}_g}}{\sqrt{2(1-\rho^2_{\ddot{U}_g\ddot{U}_g})}}\frac{\xi}{\sigma_{\ddot{U}_g}}\right)\right\} \quad (7.41)$$

$$E[N(t)] = \int_0^t \nu(\xi^+, \tau)d\tau \quad (7.42)$$

where

$$\sigma^2_{\ddot{U}_g} = R_{\ddot{U}_g\ddot{U}_g}(t, 0) = E[|\ddot{U}_g(t)|^2] = \sum_{k=1}^{N_p} |A_k(t)|^2 \quad (7.43)$$

$$\sigma^2_{\dddot{U}_g} = R_{\dddot{U}_g\dddot{U}_g}(t, 0) = E[|\dddot{U}_g(t)|^2] = \sum_{k=1}^{N_p} [|\dot{A}_k(t)|^2 + (\eta_k^2 - \nu_k^2)|A_k(t)|^2] \quad (7.44)$$

$$\rho_{\ddot{U}_g\ddot{U}_g} = \frac{R_{\ddot{U}_g\ddot{U}_g}(t, 0)}{\sigma_{\ddot{U}_g}\sigma_{\ddot{U}_g}} = \frac{\sum_{k=1}^{N_p} [A_k(t)\cdot\dot{A}_k(t)]}{\sigma_{\ddot{U}_g}\sigma_{\ddot{U}_g}} \quad (7.45)$$

REFERENCES

Barbato M., Conte J.P., Peng B.-F. (2004) "Response mean upcrossing rate for linear MDOF systems subjected to fully nonstationary earthquake ground motion model". *Proceedings of the 13th World Conference on Earthquake Engineering*, Vancouver, British Columbia, Canada. Paper No. 2977.

Bjerager P. (1988) "Probability integration by directional simulation". *Journal of Engineering Mechanics* (ASCE), 114(8):1285-1302.

Bucher C.G. (1988) "Adaptive sampling - an iterative fast Monte Carlo procedure". *Journal of Structural Safety,* 5(2):119-126.

Chaudhuri A., Chakraborty S. (2003) "Reliability evaluations of 3-D frame subjected to non-stationary earthquake". *Journal of Sound and Vibration*, 259(4):797-808.

Chaudhuri A., Chakraborty S. (2004) "Sensitivity evaluations in seismic reliability analysis of structures". *Computer Methods in Applied Mechanics and Engineering*, 193(1-2):59-68.

Conte J.P. (1992) "Effects of Earthquake Frequency Nonstationarity on Inelastic Structural Response." *Proceedings of the 10th World Conference on Earthquake Engineering*, Madrid, Spain. Rotterdam: AA Balkema, 3645-3651.

Conte J.P., Pister K.S., Mahin S.A. (1992) "Nonstationary ARMA Modeling of Seismic Motions". *Journal of Soil Dynamics and Earthquake Engineering*, 11(7):411-426.

Conte J.P., Peng B.-F. (1997) "Fully nonstationary analytical earthquake ground-motion model". *Journal of Engineering Mechanics* (ASCE), 123(1):15-24.

Ditlevsen O., Madsen H.O. (1996) *Structural Reliability Methods*, Wiley, New York.

Peng B.-F., Conte J.P. (1997) "Statistical insight into constant-ductility design using a non-stationary earthquake ground motion model". *Earthquake Engineering and Structural Dynamics*, 26(9):895-916.

Peng B.-F., Conte J.P. (1998) “Closed-form solutions for the response of linear systems to fully nonstationary earthquake excitation”. *Journal of Engineering Mechanics* (ASCE), 124(6):684-694.

Der Kiureghian A., Crempien J. (1989) “An Evolutionary Model for Earthquake Ground Motion”. *Structural Safety,* 6:235-246.

Fan F.-G., Ahmadi G. (1990) “Nonstationary Kanai-Tajimi Models for El Centro 1940 and Mexico City 1985 Earthquakes.” *Probabilistic Engineering Mechanics,* 5(4):171-181.

Grigoriu M., Ruiz S.E., Rosenblueth E. (1988) “The Mexico Earthquake of September 19, 1985 - Nonstationary Models of Seismic Ground Acceleration”. *Earthquake Spectra,* 4(3):551-568.

Lin Y.K. (1967) “Probabilistic Theory of Structural Dynamics”. New York, NY: McGraw-Hill, 1967, Huntington: Krieger Pub, 1976.

Lutes L.D., Sarkani S. (1997) “Stochastic analysis of structural and mechanical vibration”. Upple Saddle River, NJ: Prentice Hall.

Michaelov G., Lutes L.D., Sarkani S. (2001) “Extreme value of response to nonstationary excitation”. *Journal of Engineering Mechanics* (ASCE), 127(4):352-363.

Papadimitriou C. (1990) “Stochastic Characterization of Strong Ground Motion and Applications to Structural Response”. *Report No. EERL 90-03,* California Institute of Technology, Pasadena, CA.

Peng B.-F., Conte J.P. (1998) “Closed-form solutions for the response of linear systems to fully nonstationary earthquake excitation”. *Journal of Engineering Mechanics* (ASCE), 124(6):684-694.

Priestley M.B. (1987) “Spectral Analysis and Time Series, Volume 1: Univariate Series, Volume 2: Multivariate Series, Prediction and Control”. London: Academic Press, Fifth Printing.

Rice S.O. (1944). “Mathematical analysis of random noise”. *Bell System Technical Journal*, 23:282-332; 24:46-156.

Saragoni G. R., Hart G. C. (1972) “Nonstationary Analysis and Simulation of Earthquake Ground Motions.” *Report No. UCLA-ENG-7238*, Earthquake Engineering and Structures Laboratory, University of California at Los Angeles, Los Angeles, CA.

Shinozuka M. (1972) “Monte Carlo soluton of structural dynamics”. *Computers and Structures*, 2(5-6):855-874.

Shinozuka M., Jan C.-M. (1972) “Digital simulation of random processes and its application”. *Journal of Sound and Vibration*, 25(1):111-128.

Shinozuka M., Wen Y.-K. (1972) “Monte Carlo soluton of nonlinear vibrations”. *Journal of American Institute of Aeronautics and Astronautics*, 10(1):37-40.

Shinozuka M., Deodatis G. (1991) “Simulation of stochastic processes by spectral representation”. *Applied Mechanics Reviews* (ASME), 44(4):191-203.

Takewaki I. (2001a) “A new method for non-stationary random critical excitation”. *Earthquake Engineering and Structural Dynamics*, 30(4):519-535.

Takewaki I. (2001b) “Nonstationary random critical excitation for nonproportionally damped structural systems”. *Computer Methods in Applied Mechanics and Engineering*, 190(31):3927-3943.

Takewaki I. (2001c) “Nonstationary random critical excitation for acceleration response”. *Journal of Engineering Mechanics* (ASCE), 127(6):544-556.

Takewaki I. (2004) “Critical envelope functions for non-stationary random earthquake input”. *Computers and Structures*, 82(20-21):1671-1683.

Yeh C.-H., Wen Y. K. (1990) “Modeling of Nonstationary Ground Motion and Analysis of Inelastic Structural Response.” *Structural Safety*, 8:281-298.

CHAPTER 8

SPECTRAL CHARACTERISTICS OF STOCHASTIC PROCESSES

8.1 INTRODUCTION

The probabilistic study of the dynamic behavior of structural and mechanical systems requires the characterization of the random processes describing the input excitation and the structural response. This characterization is usually very complex for realistic input processes and structural systems, when non-stationary and non-Gaussian processes are involved.

A very common and powerful methodology for characterizing and describing a random process is spectral analysis, which studies random processes in the frequency domain. In particular, the use of power spectral density (PSD) functions (Priestley 1987) is customary in describing stationary random processes. Definition of functions describing the spectral properties of non-stationary random processes is less simple and not unique. In fact, several non-stationary spectra have been defined in the literature (Bendat and Piersol 1986, Priestley 1988), with different application fields. In addition, direct extension of the definition of spectral characteristics, such as the spectral moments, from stationary to non-stationary processes leads to difficulties in the interpretation and application of these spectral characteristics (Corotis et al. 1972).

Among existing definitions of non-stationary spectra, the most widely used is probably Priestley's evolutionary power spectral density (EPSD) (Priestley 1987). Based on this EPSD, the so-called "non-geometric" spectral characteristics (NGSCs) have been defined for real-valued non-stationary processes (Di Paola 1985; Michaelov et al. 1999a). The NGSCs have been proved appropriate for describing non-stationary processes (Michaelov et al. 1999b) and can be effectively employed in structural reliability applications, such as the computation of the time-variant probability that a random process outcrosses a given limit-state threshold.

In this chapter, the definition of NGSCs is extended to general complex-valued non-stationary random processes. These newly defined quantities provide information consistent with that provided by their counterparts for real-valued stationary and non-stationary processes. These NGSCs are used in this study to solve exactly and in closed-form the classical problem of computing the time-variant central frequency and bandwidth parameter of the response processes of single-degree-of-freedom (SDOF) and both classically and non-classically damped multi-degree-of-freedom (MDOF) linear elastic systems subjected to white noise excitation from at rest initial conditions. In addition, the NGSCs of complex-valued processes are useful in problems which require the use of complex modal analysis, such as random vibrations of non-classically damped MDOF linear structures, and in structural reliability applications (Crandall 1970), for which the existing definitions of spectral characteristics were specifically developed.

For the sake of simplicity and without loss of generality, all random processes considered in this study are zero-mean processes. An important implication is that the auto-

and cross-covariance functions of these random processes coincide with their auto- and cross-correlation functions, respectively.

8.2 STATIONARY STOCHASTIC PROCESSES AND SPECTRAL MOMENTS

A real-valued stationary process $X_S(t)$ is represented by the following spectral decomposition:

$$X_S(t) = \int_{-\infty}^{\infty} e^{j\omega t} dZ(\omega) \tag{8.1}$$

where t = time, ω = frequency parameter, $j = \sqrt{-1}$, and dZ(ω) = zero-mean orthogonal-increment process having the properties

$$\begin{cases} dZ(-\omega) = dZ^*(\omega) \\ E[dZ^*(\omega_1) dZ(\omega_2)] = \Phi(\omega_1)\boldsymbol{\delta}(\omega_1 - \omega_2)d\omega_1 d\omega_2 \end{cases} \tag{8.2}$$

in which Φ(ω) = PSD function of the stationary process $X_S(t)$, $\boldsymbol{\delta}(\ldots)$ = Dirac delta and the superscript $(\ldots)^*$ denotes the complex-conjugate operator. For the stationary process considered, $X_S(t)$, the geometric spectral moments λ_n of order n with $n = 0, 1, \ldots$, are defined as (Corotis et al. 1972)

$$\lambda_n = \int_{-\infty}^{\infty} |\omega|^n \Phi(\omega) d\omega = 2\int_0^{\infty} \omega^n \Phi(\omega) d\omega \tag{8.3}$$

where $|\ldots|$ = absolute value of a real-valued variable (or modulus of a complex-valued variable). The last equality in Eq. (8.3) is obtained noticing that the PSD of a real-valued

stationary process is an even function of the frequency parameter ω. The geometric spectral moments are utilized in random vibration problems to compute several meaningful quantities, such as

(1) The variance of the i-th time-derivative of the process $X_S(t)$:

$$\sigma^2_{X_S^{(i)}} = \lambda_{2i} = 2\int_0^\infty \omega^{2i}\Phi(\omega)d\omega, \quad i = 0, 1, 2, ... \tag{8.4}$$

where $X_S^{(i)}(t) = \dfrac{d^i X_S(t)}{dt^i}$, provided that this i-th time-derivative process exists in the mean-square sense.

(2) The central frequency parameter ω_c of the process $X_S(t)$:

$$\omega_c = \frac{\lambda_1}{\lambda_0} \tag{8.5}$$

For a narrowband process, ω_c indicates the frequency where most of the power is concentrated (i.e., predominant frequency).

(3) The bandwidth parameter q of the process $X_S(t)$:

$$q = \left(1 - \frac{\lambda_1^2}{\lambda_0\lambda_2}\right)^{\frac{1}{2}} \tag{8.6}$$

The bandwidth parameter q is a dimensionless parameter with values $0 \le q \le 1$ defined so that it assumes low values (i.e., near zero) for narrowband processes and high values (i.e., near unity) for broadband processes.

8.3 NONSTATIONARY STOCHASTIC PROCESSES

A real-valued non-stationary (RVNS) process X(t) can be expressed in the general form of a Fourier-Stieltjes integral as (Priestley 1987)

$$X(t) = \int_{-\infty}^{\infty} A_X(\omega, t) e^{j\omega t} dZ(\omega) \tag{8.7}$$

where $A_X(\omega, t)$ = complex-valued deterministic time-frequency modulating function defined such that

$$A_X(-\omega, t) = A_X^*(\omega, t) \tag{8.8}$$

An embedded stationary process $X_S(t)$, with PSD function $\Phi(\omega)$ defined through the zero-mean orthogonal-increment process $dZ(\omega)$ (see Eqs. (8.1) and (8.2)), is associated to the RVNS process X(t). The process X(t) has the following EPSD function $\Phi_{XX}(\omega, t)$:

$$\Phi_{XX}(\omega, t) = A_X^*(\omega, t) \cdot \Phi(\omega) \cdot A_X(\omega, t) \tag{8.9}$$

From Eq. (8.8) and the fact that $\Phi(\omega)$ is an even function of the frequency parameter ω, it can be deduced that the EPSD of a RVNS process is a symmetric function of the frequency parameter ω.

The definition in Eq. (8.7) can be mathematically extended to complex-valued non-stationary (CVNS) processes with a general complex-valued deterministic time-frequency modulating function $A_X(\omega, t)$. In this case, Eq. (8.8) does not hold in general and the EPSD is not a symmetric function of the frequency parameter ω.

8.4 SPECTRAL CHARACTERISTICS OF REAL-VALUED NON-STATIONARY STOCHASTIC PROCESSES

The definition of the geometric spectral moments (Eq. (8.3)) can be mathematically extended to the non-stationary case as

$$\lambda_n(t) = \int_{-\infty}^{\infty} |\omega|^n \Phi_{XX}(\omega, t) d\omega = 2\int_0^{\infty} \omega^n \Phi_{XX}(\omega, t) d\omega \tag{8.10}$$

where $\Phi_{XX}(\omega, t)$ = EPSD of the RVNS process $X(t)$. Using these spectral moments, Corotis et al. (1972) extended consistently the definitions of the central frequency, $\omega_c(t)$, and bandwidth parameter, $q(t)$, in Eqs. (8.5) and (8.6), respectively, to RVNS processes as

$$\omega_c(t) = \frac{\lambda_1(t)}{\lambda_0(t)} \tag{8.11}$$

$$q(t) = \left(1 - \frac{[\lambda_1(t)]^2}{\lambda_0(t) \cdot \lambda_2(t)}\right)^{\frac{1}{2}} \tag{8.12}$$

The geometric spectral moments defined in Eq. (8.10) suffer two severe drawbacks in characterizing non-stationary stochastic processes (Michaelov et al. 1999a), namely

(1) The variance of the i-th time-derivative of the process $X(t)$ for $i > 0$ is not equal to the 2i-th spectral moment.

(2) Even when the variance of the i-th time-derivative of the process is finite, the 2i-th non-stationary geometric spectral moment can be divergent, in which case the central frequency and bandwidth parameter defined in Eqs. (8.11) and (8.12) cannot be com-

puted.

More recently, Di Paola (1985) and Michaelov et al. (1999a, 1999b) introduced a proper definition of spectral characteristics to be used in computing the central frequency and bandwidth parameter for a RVNS process $X(t)$ defined by Eqs. (8.7) through (8.9). For such a process, the so-called "non-geometric" spectral characteristics (NGSCs) $c_{ik}(t)$ are defined as

$$c_{ik}(t) = 2(-1)^k j^{i+k} \int_0^\infty \Phi_{X^{(i)}X^{(k)}}(\omega, t) d\omega, \qquad i, k = 0, 1, ... \tag{8.13}$$

where $\Phi_{X^{(i)}X^{(k)}}(\omega, t)$ is the evolutionary cross-PSD function of the time-derivatives of order i and k of the process $X(t)$, i.e.,

$$\Phi_{X^{(i)}X^{(k)}}(\omega, t) = A_{X^{(i)}}^*(\omega, t) \cdot \Phi(\omega) \cdot A_{X^{(k)}}(\omega, t), \qquad i, k = 0, 1, ... \tag{8.14}$$

in which $X^{(m)}(t) = \dfrac{d^m X(t)}{dt^m}$ (m = i, k), provided that $X^{(m)}(t)$ exists in the mean-square sense, and the modulating function $A_{X^{(m)}}(\omega, t)$ is obtained recursively as

$$\begin{cases} A_{X^{(m)}}(\omega, t) = j\omega A_{X^{(m-1)}}(\omega, t) + \dot{A}_{X^{(m-1)}}(\omega, t), & m = 1, 2, ... \\ A_{X^{(0)}}(\omega, t) = A_X(\omega, t) \end{cases} \tag{8.15}$$

where a superposed dot denotes one differentiation with respect to time. This definition of NGSCs is equivalent to the one derived by Di Paola (1985) from the Rice envelope process.

Using the NGSCs in Eq. (8.13), the time-variant central frequency $\omega_c(t)$ and bandwidth parameter $q(t)$ are defined as (Michaelov et al. 1999a)

$$\omega_c(t) = \frac{(\mathrm{Re}[c_{01}(t)])}{c_{00}(t)} \tag{8.16}$$

$$q(t) = \left(1 - \frac{(\mathrm{Re}[c_{01}(t)])^2}{c_{00}(t)c_{11}(t)}\right)^{\frac{1}{2}} \tag{8.17}$$

where $\mathrm{Re}[\ldots]$ = real part of the quantity in the square brackets and the NGSC $c_{01}(t)$ is expressed as

$$c_{01}(t) = c_{10}^*(t) = -2j\int_0^\infty \Phi_{X\dot{X}}(\omega, t)d\omega \tag{8.18}$$

At this point, it is convenient to define the process $Y(t)$ as the modulation (with modulating function $A_X(\omega, t)$) of the stationary process $Y_S(t)$ defined as the Hilbert transform of the embedded stationary process $X_S(t)$, i.e.,

$$Y(t) = -j\int_{-\infty}^{\infty} \mathrm{sign}(\omega)A_X(\omega, t)e^{j\omega t}dZ(\omega) = \int_{-\infty}^{\infty} A_Y(\omega, t)e^{j\omega t}dZ(\omega) \tag{8.19}$$

in which

$$\begin{aligned} A_Y(\omega, t) &= -j \cdot \mathrm{sign}(\omega) \cdot A_X(\omega, t) \\ Y_S(t) &= -j\int_{-\infty}^{\infty} \mathrm{sign}(\omega)e^{j\omega t}dZ(\omega) \end{aligned} \tag{8.20}$$

Using Eq. (8.19), Eqs. (8.15) to (8.17) can be rewritten as

$$\omega_c(t) = \frac{\sigma_{X\dot{Y}}(t)}{\sigma_X^2(t)} \tag{8.21}$$

$$q(t) = \left(1 - \frac{\sigma_{X\dot{Y}}^2(t)}{\sigma_X^2(t)\sigma_{\dot{X}}^2(t)}\right)^{\frac{1}{2}} \tag{8.22}$$

$$c_{01}(t) = c_{10}^*(t) = \sigma_{X\dot{Y}}(t) - j\sigma_{X\dot{X}}(t) \tag{8.23}$$

where $\sigma_{X\dot{Y}}(t)$ = cross-covariance of $X(t)$ and $\dot{Y}(t)$, and $\sigma_{X\dot{X}}(t)$ = cross-covariance of $X(t)$ and $\dot{X}(t)$.

Eqs. (8.16) and (8.17) apply only to RVNS stochastic processes, since they make use of the symmetry with respect to ω of the evolutionary cross-PSD function $\Phi_{X^{(i)}X^{(k)}}(\omega, t)$. Notice that, in the case of a stationary process, Eqs. (8.16) and (8.17) reduce to Eqs. (8.5) and (8.6), respectively.

The time-variant central frequency and bandwidth parameter are useful in describing the time-variant spectral properties of a RVNS process $X(t)$. The central frequency $\omega_c(t)$ provides the predominant frequency of the process at each instant of time. The bandwidth parameter $q(t)$ provides information on the spectral bandwidth of the process at each instant of time. Notice that a non-stationary process can behave as a narrowband and a broadband process at different instants of time. In addition, the bandwidth parameter $q(t)$ plays an important role in time-variant reliability analysis, since it is an essential ingredient of analytical approximations (Crandall 1970; Vanmarcke 1975) to the time-

variant failure probability for the first-passage reliability problem (Rice 1944, 1945; Lin 1967).

8.5 SPECTRAL CHARACTERISTICS OF COMPLEX-VALUED NONSTATIONARY STOCHASTIC PROCESSES

In this paper, an extension of the definition of NGSCs to CVNS random processes is proposed and presented. For CVNS processes, the real and imaginary parts of the evolutionary cross-PSD function $\Phi_{X^{(i)}X^{(k)}}(\omega, t)$ are not symmetric and anti-symmetric functions, respectively, of the frequency parameter ω. Our interest is limited to CVNS processes with a real-valued embedded stationary process $X_S(t)$ as defined by Eqs. (8.1) and (8.2).

For each CVNS process $X(t)$, two sets of NGSCs are defined as follows

$$\begin{cases} c_{ik,\,XX}(t) = \int_{-\infty}^{\infty} \Phi_{X^{(i)}X^{(k)}}(\omega, t)d\omega = \sigma_{X^{(i)}X^{(k)}}(t) \\ c_{ik,\,XY}(t) = \int_{-\infty}^{\infty} \Phi_{X^{(i)}Y^{(k)}}(\omega, t)d\omega = \sigma_{X^{(i)}Y^{(k)}}(t) \end{cases} \quad i, k = 0, 1, ... \qquad (8.24)$$

where $\sigma_{X^{(i)}X^{(k)}}(t)$ = cross-covariance of random processes $X^{(i)}(t)$ and $X^{(k)}(t)$, and $\sigma_{X^{(i)}Y^{(k)}}(t)$ = cross-covariance of random processes $X^{(i)}(t)$ and $Y^{(k)}(t) = \dfrac{d^k Y(t)}{dt^k}$, i.e.,

$$\begin{cases} \sigma_{X^{(i)}X^{(k)}}(t) = E[(X^{(i)}(t))^* \cdot X^{(k)}(t)] \\ \sigma_{X^{(i)}Y^{(k)}}(t) = E[(X^{(i)}(t))^* \cdot Y^{(k)}(t)] \end{cases} \tag{8.25}$$

The process $Y(t)$ is defined by Eq. (8.19), and the evolutionary cross-PSD functions, $\Phi_{X^{(i)}W^{(k)}}(\omega, t)$ (W = X, Y, and i, k = 0, 1, …), are given by

$$\Phi_{X^{(i)}W^{(k)}}(\omega, t) = A^*_{X^{(i)}}(\omega, t) \cdot \Phi(\omega) \cdot A_{W^{(k)}}(\omega, t); \quad W = X, Y; \quad i, k = 0, 1, ... \tag{8.26}$$

where (Peng and Conte 1998)

$$A_{W^{(i)}}(\omega, t) = e^{-j\omega t} \frac{\partial^i}{\partial t^i}[A_W(\omega, t) \cdot e^{j\omega t}]; \quad W = X, Y; \quad i = 0, 1, ... \tag{8.27}$$

Again, it is assumed that the time-derivative processes in Eqs. (8.24) and (8.25) exist in the mean-square sense.

In the particular case when $i = k = n$, the cross-covariance in Eq. $(8.25)_1$ reduces to the variance of the n-th time-derivative of the process $X(t)$, or in more common notation,

$$\sigma_{X^{(n)}X^{(n)}}(t) = \sigma^2_{X^{(n)}}(t) \tag{8.28}$$

The four NGSCs $c_{00, XX}(t)$, $c_{11, XX}(t)$, $c_{01, XX}(t)$ and $c_{01, XY}(t)$ are particularly relevant to random vibration theory and time-variant reliability applications. In fact, $c_{00, XX}(t)$ and $c_{11, XX}(t)$ represent the variance of the process and its first time-derivative (i.e., $\sigma^2_X(t)$ and $\sigma^2_{\dot{X}}(t)$), respectively, $c_{01, XX}(t)$ denotes the cross-covariance of the pro-

cess and its first time derivative (i.e., $\sigma_{X\dot{X}}(t)$), and $c_{01,\,XY}(t)$ represents the cross-covariance of the process $X(t)$ and the first time-derivative of the process $Y(t)$ (i.e., $\sigma_{X\dot{Y}}(t)$).

Notice that for RVNS processes, the definitions in Eq. (8.24) for $c_{00,\,XX}(t)$, $c_{11,\,XX}(t)$, $c_{01,\,XX}(t)$ and $c_{01,\,XY}(t)$ are equivalent to the definitions in Eq. (8.13) for i, k = 0, 1, since

$$c_{00}(t) = 2(-1)^0 j^0 \int_0^\infty \Phi_{XX}(\omega, t)d\omega = \int_{-\infty}^\infty \Phi_{XX}(\omega, t)d\omega = c_{00,\,XX}(t) \tag{8.29}$$

$$c_{11}(t) = 2(-1)^1 j^2 \int_0^\infty \Phi_{\dot{X}\dot{X}}(\omega, t)d\omega = \int_{-\infty}^\infty \Phi_{\dot{X}\dot{X}}(\omega, t)d\omega = c_{11,\,XX}(t) \tag{8.30}$$

$$\begin{aligned} c_{01}(t) &= 2(-1)^1 j^1 \int_0^\infty \Phi_{X\dot{X}}(\omega, t)d\omega \\ &= -j\left(2\int_0^\infty \Phi_{X\dot{X}}(\omega, t)d\omega + \int_{-\infty}^0 \Phi_{X\dot{X}}(\omega, t)d\omega - \int_{-\infty}^0 \Phi_{X\dot{X}}(\omega, t)d\omega\right) \\ &= \int_{-\infty}^\infty (-j)\,\mathrm{sign}(\omega)\Phi_{X\dot{X}}(\omega, t)d\omega - j\int_{-\infty}^\infty \Phi_{X\dot{X}}(\omega, t)d\omega \\ &= c_{01,\,XY}(t) - jc_{01,\,XX}(t) \end{aligned} \tag{8.31}$$

Eqs. $(8.20)_1$ and (8.26) are used in deriving the last equality in Eq. (8.31). The NGSCs $c_{00,\,XX}(t)$, $c_{11,\,XX}(t)$ and $c_{01,\,XY}(t)$ are used in the definition of the time-variant central frequency, $\omega_c(t)$, and bandwidth parameter, $q(t)$, of the CVNS process $X(t)$ as

$$\omega_c(t) = \frac{c_{01,\,XY}(t)}{c_{00,\,XX}(t)} = \frac{\sigma_{X\dot{Y}}(t)}{\sigma_X^2(t)} \tag{8.32}$$

$$q(t) = \left(1 - \frac{[c_{01,XY}(t)]^2}{\sigma_X^2(t)\sigma_{\dot{X}}^2(t)}\right)^{\frac{1}{2}} = \left(1 - \frac{\sigma_{X\dot{Y}}^2(t)}{\sigma_X^2(t)\sigma_{\dot{X}}^2(t)}\right)^{\frac{1}{2}} \tag{8.33}$$

In the case of RVNS processes, the two definitions in Eqs. (8.32) and (8.33) reduce to the ones given in Eqs. (8.16) and (8.17), respectively. However, for CVNS processes, the complex-valued central frequency and bandwidth parameter defined in Eqs. (8.32) and (8.33) loose the simple physical interpretation available for RVNS processes.

8.6 SPECTRAL CHARACTERISTICS OF THE RESPONSE OF SDOF AND MDOF LINEAR SYSTEMS SUBJECTED TO NON-STATIONARY STOCHASTIC INPUT PROCESSES

8.6.1 Complex modal analysis

A state-space formulation of the equations of motion for a linear MDOF system is useful to describe the response of both classically and non-classically damped systems (Reid 1983). The general (second-order) equations of motion for an n-degree-of-freedom linear system are, in matrix form,

$$\mathbf{M}\ddot{\mathbf{U}}(t) + \mathbf{C}\dot{\mathbf{U}}(t) + \mathbf{K}\mathbf{U}(t) = \mathbf{P}F(t) \tag{8.34}$$

where $\mathbf{M}$, $\mathbf{C}$, and $\mathbf{K}$ = $n \times n$ time-invariant mass, damping and stiffness matrices, respectively; $\mathbf{U}(t)$, $\dot{\mathbf{U}}(t)$, and $\ddot{\mathbf{U}}(t)$ = length-n vectors of nodal displacements, velocities and accelerations, respectively; $\mathbf{P}$ = length-n load distribution vector, and $F(t)$ = scalar function

describing the time-history of the external loading which, in the case of random excitation, is modeled as a random process. Defining the following length-2n state vector

$$\mathbf{Z}(t) = \begin{bmatrix} \mathbf{U}(t) \\ \dot{\mathbf{U}}(t) \end{bmatrix}_{(2n \times 1)}, \tag{8.35}$$

the matrix equation of motion (8.34) can be recast into the following first-order matrix equation

$$\dot{\mathbf{Z}}(t) = \mathbf{G}\mathbf{Z}(t) + \tilde{\mathbf{P}}F(t) \tag{8.36}$$

where

$$\mathbf{G} = \begin{bmatrix} \mathbf{0}_{(n \text{ x } n)} & \mathbf{I}_{(n \text{ x } n)} \\ (-\mathbf{M}^{-1}\mathbf{K}) & (-\mathbf{M}^{-1}\mathbf{C}) \end{bmatrix}_{(2n \times 2n)} \tag{8.37}$$

$$\tilde{\mathbf{P}} = \begin{bmatrix} \mathbf{0}_{(n \text{ x } 1)} \\ \mathbf{M}^{-1}\mathbf{P} \end{bmatrix}_{(2n \times 1)} \tag{8.38}$$

The subscripts in Eqs. (8.35), (8.37) and (8.38) indicate the dimensions of the vectors and matrices to which they are attached. The complex modal matrix, **T**, is formed from the complex eigenmodes of matrix **G** and can be used as an appropriate transformation matrix to decouple the first-order matrix equation (8.36) and introduce the transformed state vector **V**(t) of complex modal coordinates as

$$\mathbf{Z}(t) = \mathbf{T}\mathbf{V}(t) \tag{8.39}$$

Substituting Eq. (8.39) into Eq. (8.36), considering that $\mathbf{T}^{-1}\mathbf{G}\mathbf{T} = \mathbf{D}$ (Reid 1983), where **D** is the diagonal matrix containing the 2n complex eigenvalues, $\lambda_1, \lambda_2, ..., \lambda_{2n}$, of

the system matrix **G**, and $\mathbf{T}^{-1}\tilde{\mathbf{P}} = [\Gamma_1, ..., \Gamma_{2n}]^T$, where Γ_i is the i-th modal participation factor (complex-valued), the normalized complex modal equations are obtained as

$$\dot{S}_i(t) = \lambda_i S_i(t) + F(t), \quad i = 1, 2, ..., 2n \tag{8.40}$$

where the normalized complex modal responses $S_i(t)$ (i = 1, 2, ..., 2n) are defined as

$$S_i(t) = \frac{1}{\Gamma_i} V_i(t), \quad i = 1, 2, ..., 2n \tag{8.41}$$

The impulse response function for the i-th mode, $h_i(t)$, defined as the solution of Eq. (8.40) when $F(t) = \delta(t)$ and for at rest initial conditions at time $t = 0^-$ (i.e., $S_i(0^-) = 0$), is simply given by

$$h_i(t) = e^{\lambda_i t}, \quad t > 0 \tag{8.42}$$

Assuming that the system is initially at rest, the solution of Eq. (8.40) can be expressed by the following Duhamel integral

$$S_i(t) = \int_0^t e^{\lambda_i (t-\tau)} F(\tau) d\tau, \quad i = 1, 2, ..., 2n \tag{8.43}$$

It is worth mentioning that the normalized complex modal responses $S_i(t)$, i = 1, 2, ..., 2n, are complex conjugate by pairs and in this study are ordered so that $S_i(t) = S_{n+i}^*(t)$.

In the case of a non-stationary loading process, the loading function $F(t)$ can be expressed in general as (see Eq. (8.7))

$$F(t) = \int_{-\infty}^{\infty} A_F(\omega, t) e^{j\omega t} dZ(\omega) \tag{8.44}$$

It can be shown that the normalized complex modal responses are given by

$$S_i(t) = \int_{-\infty}^{\infty} A_{S_i}(\omega, t) e^{j\omega t} dZ(\omega), \quad i = 1, 2, ..., 2n \tag{8.45}$$

where

$$A_{S_i}(\omega, t) = \int_0^t \left\{ e^{\lambda_i (t-\tau)} A_F(\omega, \tau) \cdot e^{j\omega(\tau - t)} \right\} d\tau, \quad i = 1, 2, ..., 2n \tag{8.46}$$

Combining Eqs. (8.39) and (8.41) yields

$$\mathbf{Z}(t) = \mathbf{T}\mathbf{V}(t) = \mathbf{T}\boldsymbol{\Gamma}\mathbf{S}(t) = \tilde{\mathbf{T}}\mathbf{S}(t) \tag{8.47}$$

in which $\boldsymbol{\Gamma}$ = diagonal matrix containing the 2n modal participation factors Γ_i, $\tilde{\mathbf{T}} = \mathbf{T}\boldsymbol{\Gamma}$ = effective modal participation matrix and $\mathbf{S} = [S_1(t), S_2(t), \ldots, S_{2n}(t)]^T$ = normalized complex modal response vector.

8.6.2 Spectral characteristics of the response processes of linear MDOF systems using complex modal analysis

The state-space formulation of the equations of motion is also advantageous for the computation of the NGSCs of response processes of both classically and non-classically damped linear MDOF systems. If only Gaussian input processes are considered, only a few spectral characteristics are needed to describe fully the response processes of linear elastic MDOF systems, since these processes are also Gaussian. In particular, if $U_i(t)$

denotes the i-th DOF displacement response process of a linear elastic MDOF system subjected to Gaussian excitation, the only spectral characteristics required, e.g., for reliability applications, are

$$\begin{cases} c_{00,\,U_iU_i}(t) = \sigma^2_{U_i}(t) \\ c_{11,\,U_iU_i}(t) = \sigma^2_{\dot{U}_i}(t) \\ c_{01,\,U_iU_i}(t) = \sigma_{U_i\dot{U}_i}(t) \\ c_{01,\,U_i\Upsilon_i}(t) = \sigma_{U_i\dot{\Upsilon}_i}(t) \end{cases}, \quad i = 1, 2, ..., n \tag{8.48}$$

where $\dot{\Upsilon}_i(t)$ denotes the first time-derivative of the process $\Upsilon_i(t)$ defined as

$$\Upsilon_i(t) = -j\int_{-\infty}^{\infty} \text{sign}(\omega) A_{U_i}(\omega, t) e^{j\omega t} dZ(\omega), \quad i = 1, 2, ..., n \tag{8.49}$$

and $A_{U_i}(\omega, t)$ denotes the time-frequency modulating function of process $U_i(t)$. The process $\Upsilon_i(t)$ is the modulation (with the same modulating function $A_{U_i}(\omega, t)$ as process $U_i(t)$) of the Hilbert transform of the stationary process embedded in the process $U_i(t)$ (see Eq. (8.19)).

Similarly to the response processes (see Eq. (8.35)), the following auxiliary state vector process can be defined

$$\Xi(t) = \begin{bmatrix} \Upsilon(t) \\ \dot{\Upsilon}(t) \end{bmatrix}_{(2n \times 1)} \tag{8.50}$$

Using complex modal decomposition, the cross-covariance matrices of the response processes and the auxiliary processes can be computed as follows

$$E[\mathbf{Z}(t)\mathbf{Z}^T(t)] = E\begin{bmatrix}\mathbf{U}(t)\mathbf{U}^T(t) & \mathbf{U}(t)\dot{\mathbf{U}}^T(t)\\ \dot{\mathbf{U}}(t)\mathbf{U}^T(t) & \dot{\mathbf{U}}(t)\dot{\mathbf{U}}^T(t)\end{bmatrix} = \tilde{\mathbf{T}}^* E[\mathbf{S}^*(t)\,\mathbf{S}^T(t)]\tilde{\mathbf{T}}^T \tag{8.51}$$

$$E[\mathbf{Z}(t)\Xi^T(t)] = E\begin{bmatrix}\mathbf{U}(t)\Upsilon^T(t) & \mathbf{U}(t)\dot{\Upsilon}^T(t)\\ \dot{\mathbf{U}}(t)\Upsilon^T(t) & \dot{\mathbf{U}}(t)\dot{\Upsilon}^T(t)\end{bmatrix} = \tilde{\mathbf{T}}^* E[\mathbf{S}^*(t)\,\Sigma^T(t)]\tilde{\mathbf{T}}^T \tag{8.52}$$

where the components of the vector process $\Sigma = [\Sigma_1(t), \Sigma_2(t), \ldots, \Sigma_{2n}(t)]^T$ are defined as

$$\Sigma_i(t) = -j\int_{-\infty}^{\infty} \mathrm{sign}(\omega) A_{S_i}(\omega, t) e^{j\omega t} dZ(\omega), \quad i = 1, 2, ..., 2n \tag{8.53}$$

(8.51) and (8.52) show that all quantities in Eq. (8.48) can be computed from the following spectral characteristics of complex-valued non-stationary processes

$$\begin{Bmatrix}\sigma_{S_iS_m}(t)\\ \sigma_{S_i\Sigma_m}(t)\end{Bmatrix}, \quad i, m = 1, 2, ..., 2n \tag{8.54}$$

Notice also that knowledge of the spectral characteristics in Eq. (8.54) allows computation of the zeroth to second-order spectral characteristics of the components of any vector response quantity Q(t) linearly related to the displacement response vector $\mathbf{U}(t)$, i.e., $\mathbf{Q}(t) = \mathbf{B}\mathbf{U}(t)$, where B = constant matrix.

8.6.3 Response statistics of MDOF linear systems subjected to modulated Gaussian white noise

Time-modulated Gaussian white noises constitute an important class of non-stationary loading processes. The expression given in Eq. (8.44) describing a general non-stationary loading process reduces to

$$F(t) = A_F(t) \cdot W(t) \tag{8.55}$$

where the time-modulating function $A_F(t)$ is frequency-independent and the white noise process $W(t)$ can be represented as

$$W(t) = \int_{-\infty}^{\infty} e^{j\omega t} dZ(\omega) \tag{8.56}$$

with $E[dZ^*(\omega_1)dZ(\omega_2)] = \phi_0 \boldsymbol{\delta}(\omega_1 - \omega_2)d\omega_1 d\omega_2$ where ϕ_0 = constant value of PSD. Therefore, in this special case, Eq. (8.46) becomes

$$A_{S_i}(\omega, t) = e^{(\lambda_i - j\omega)t} \int_0^t \left\{ A_F(\tau) \cdot e^{-(\lambda_i - j\omega)\tau} \right\} d\tau, \quad i = 1, 2, ..., 2n \tag{8.57}$$

In the sequel, closed-form solutions are derived for the case of the modulating function equal to the unit step function, i.e., $A_F(t) = H(t)$. Notice that even for this very simple modulating function and for a SDOF linear oscillator, to date and to the best of the authors' knowledge, no closed-form solution is available for the first order NGSC $c_{01,UY}(t)$ $(Re[c_{01}(t)]$ with the notation adopted by Michaelov et al. (1999a, b) required for computing the time-variant central frequency and bandwidth parameter of the dis-

placement response process U(t). In Subsection 8.7.1, it will be shown that the presented extension of NGSCs to complex-valued non-stationary stochastic processes enables to derive the closed-form solution for $c_{01,\,UY}(t)$ in an elegant way.

In the case of the unit step modulating function, Eq. (8.57) becomes

$$A_{S_i}(\omega, t) = e^{(\lambda_i - j\omega)t}\int_0^t \{H(\tau)\cdot e^{-(\lambda_i - j\omega)\tau}\}d\tau = \frac{e^{(\lambda_i - j\omega)t} - 1}{\lambda_i - j\omega}, \quad i = 1, 2, ..., 2n \tag{8.58}$$

The spectral characteristics in Eq. $(8.54)_1$ can be computed using Cauchy's residue theorem as (see Appendix A)

$$\sigma_{S_iS_m}(t) = \frac{2\pi\phi_0}{\lambda_i^* + \lambda_m}[e^{(\lambda_i^* + \lambda_m)t} - 1] \ , \quad i, m = 1, 2, ..., 2n \tag{8.59}$$

After extensive algebraic manipulation (see Appendix B), the spectral characteristics in Eq. $(8.54)_2$ are obtained as

$$\begin{aligned}\sigma_{S_i\Sigma_m}(t) = {} & \frac{2\phi_0}{\lambda_i^* + \lambda_m}[E_1(-\lambda_i^* t) + \log(-\lambda_i^*) - E_1(-\lambda_m t) - \log(-\lambda_m)] \\ & + \frac{2\phi_0}{\lambda_i^* + \lambda_m}e^{(\lambda_i^* + \lambda_m)t}[E_1(\lambda_i^* t) + \log(\lambda_i^*) - E_1(\lambda_m t) - \log(\lambda_m)] \\ & \qquad i, m = 1, 2, ..., 2n\end{aligned} \tag{8.60}$$

in which $E_1(x)$ denotes the integral exponential function defined as (Abramowitz and Stegun 1972)

$$E_1(x) = \int_x^\infty \frac{e^{-u}}{u}du \ , \qquad |\arg(x)| < \pi \tag{8.61}$$

where $\arg(\ldots)$ = complex argument function.

The introduction of the spectral characteristics of the complex modal response processes has the following important advantages:

(1) Closed-form integration for variances and cross-covariances of displacement and velocity response processes for linear elastic MDOF systems can be performed using Cauchy's residue theorem provided that the time-frequency modulating functions (see Eq. (8.57)) of these response quantities have at least one pole in the complex plane, which is not a severe restriction.

(2) The time-frequency modulating functions of response processes are obtained by integrating (in closed-form or numerically) Eq. (8.57), in which the time modulating function of the loading process, $A_F(t)$, is multiplied by the impulse response function of a first-order differential equation (i.e., $h(t) = e^{\lambda t}$, $t > 0$, λ = complex constant). In general, this integration is much simpler than its counterpart for real modal response processes, in which the time modulating function of the loading process is multiplied by the impulse response function of a second-order differential equation (i.e., $h(t) = \frac{e^{-Re[\lambda] \cdot t}}{Im[\lambda]} \sin(Im[\lambda] \cdot t)$, $t > 0$, where $Im[\ldots]$ = imaginary part of the quantity in the square brackets).

(3) The use of complex modal decomposition allows computation of the spectral characteristics of response quantities of linear MDOF systems that are non-classically damped.

(4) The presented extension of NGSCs to complex-valued non-stationary stochastic processes enables the derivation of the exact solution in closed-form for the first-order

NGSC, $c_{01,\,U_i Y_i}(t)$ (see Eq. $(8.48)_4$), of response processes of linear SDOF and MDOF systems subjected to white noise excitation modulated by the unit-step function. This closed-form solution cannot be obtained using real-valued responses of second-order modes.

8.7 APPLICATION EXAMPLES

8.7.1 Linear elastic SDOF systems

The first application example consists of a set of linear elastic SDOF systems subjected to a Gaussian white noise time-modulated by the unit-step function (i.e., with at rest initial conditions). In this case, the complex modal matrix **T** is given by

$$\mathbf{T} = \begin{bmatrix} 1 & 1 \\ \lambda_1 & \lambda_2 \end{bmatrix} \tag{8.62}$$

in which

$$\lambda_{1,\,2} = -\xi\omega_0 \pm j\omega_d \tag{8.63}$$

where ξ = viscous damping ratio, ω_0 = natural circular frequency, and $\omega_d = \omega_0\sqrt{1-\xi^2}$ = damped circular frequency of the system. It is assumed that $0 < \xi < 1$, which is usually the case for structural systems.

From Eqs. (8.47), (8.59) and (8.62), the well-known closed form solutions for the variances of the displacement and velocity response processes and the cross-covariance

between the displacement and the velocity response processes (Lutes and Sarkani 2004) are readily obtained as

$$\sigma_{U\dot{U}}(t) = \frac{\pi\phi_0}{2\xi\omega_0^3}\left\{1 - \frac{e^{-(2\xi\omega_0)t}}{1-\xi^2}[1 + \xi\sqrt{1-\xi^2}\sin(2\omega_d t) - \xi^2\cos(2\omega_d t)]\right\} \tag{8.64}$$

$$\sigma_{\dot{U}\dot{U}}(t) = \frac{\pi\phi_0}{2\xi\omega_0}\left\{1 - \frac{e^{-(2\xi\omega_0)t}}{1-\xi^2}[1- \xi\sqrt{1-\xi^2}\sin(2\omega_d t) - \xi^2\cos(2\omega_d t)]\right\} \tag{8.65}$$

$$\sigma_{U\ddot{U}}(t) = \frac{\pi\phi_0}{2\omega_d^2}e^{-(2\xi\omega_0)t}[1 - \cos(2\omega_d t)] \tag{8.66}$$

After some algebraic manipulations (see Appendix C), the first-order NGSC $\sigma_{U\dot{Y}}(t)$ is found as

$$\begin{aligned}\sigma_{U\dot{Y}}(t) = {} & \frac{j\phi_0}{2\xi\omega_0\omega_d}\left[E_1(-\lambda_1 t) - E_1(-\lambda_2 t) - 2j\,\mathrm{arctg}\left(\frac{\sqrt{1-\xi^2}}{\xi}\right)\right] \\ & + \frac{j\phi_0}{2\xi\omega_0\omega_d}e^{-(2\xi\omega_0)t}\left\{E_1(\lambda_1 t) - E_1(\lambda_2 t) + 2j\left[\pi - \mathrm{arctg}\left(\frac{\sqrt{1-\xi^2}}{\xi}\right)\right]\right\}\end{aligned} \tag{8.67}$$

It is noteworthy that Eq. (8.67) can be directly employed for computing the corresponding first-order NGSCs of the response processes of linear MDOF systems that are classically damped, by using real mode superposition and thus avoiding complex modal analysis, which is computationally more expensive and less commonly used. From Eq. (8.67), the stationary value of the spectral characteristic $\sigma_{U\dot{Y}}(t)$ is readily obtained as

$$\sigma_{U\dot{Y},\infty} = \frac{\phi_0}{\xi\omega_0\omega_d}\text{arctg}\left(\frac{\sqrt{1-\xi^2}}{\xi}\right) \tag{8.68}$$

The result provided in Eq. (8.67) is the exact closed-form solution for the NGSC $\sigma_{U\dot{Y}}(t)$. To date and to the best of the authors' knowledge, $\sigma_{U\dot{Y}}(t)$ could only be obtained by evaluating numerically the following exact expression in integral form

$$\begin{aligned}\sigma_{U\dot{Y}}(t) &= \frac{\phi_0}{\xi\omega_0\omega_d}\left[\int_0^t e^{-\xi\omega_0 u}\frac{\sin(\omega_d u)}{u}du - e^{-2\xi\omega_0 t}\int_0^t e^{\xi\omega_0 u}\frac{\sin(\omega_d u)}{u}du\right] \\ &= \text{Re}[c_{01}(t)]\end{aligned} \tag{8.69}$$

Fig. 8.1 plots the variances of the displacement and velocity responses (normalized by their corresponding stationary values) and the square of the correlation coefficient between the displacement and velocity responses for SDOF systems with damping ratio $\xi = 0.10$. Fig. 8.2 shows the first-order NGSC $c_{01,U\dot{Y}}(t) = \sigma_{U\dot{Y}}(t)$ (Eq. (8.67)) normalized by its corresponding stationary value $\sigma_{U\dot{Y},\infty}$ (Eq. (8.68)) for SDOF systems with three different damping ratios (i.e., $\xi = 0.01, 0.05, 0.10$). For comparison purposes, Fig. 8.2 also provides the normalized first-order NGSC $\sigma_{U\dot{Y}}(t)/\sigma_{U\dot{Y},\infty}$ with the numerator evaluated numerically through Eq. (8.69). The two integrals in Eq. (8.69) are evaluated using the trapezoidal rule of integration and a constant integration step $\Delta t = 10^{-4}T_0$, which was found sufficiently small to provide a relative accuracy of $\varepsilon \le 2 \cdot 10^{-4}$ for an integration interval $[0, T_{max}]$ with $T_{max} = 10T_0$. The normalized first-order NGSC

$\sigma_{\dot{U}\dot{U}}(t)/\sigma_{\dot{U}\dot{U},\infty}$ is a function of the damping ratio and the time normalized by the natural period T_0 of the SDOF system considered. As expected, stationarity is reached after a larger number of periods for decreasing values of the damping ratio ξ.

Fig. 8.3 plots the bandwidth parameter q(t) of the displacement response of SDOF systems with $\xi = 0.01, 0.05, 0.10$, obtained by substituting Eqs. (8.64), (8.65), and (8.67) into Eqs. (8.21) and (8.22). From the results in Fig. 8.3, it is observed that:

(1) The value of q(t) for t = 0s is always equal to 0.961. This result implies that, at the beginning of the motion of the system, the SDOF system response is very close to a white noise (for which q(t) = 1), i.e., broadband.

(2) The value of q(t) decreases with time until it reaches its stationary value. This fact implies that the SDOF system response changes from a broadband to a narrowband process.

(3) The bandwidth parameter q(t) is a function only of the damping ratio and the time normalized by the natural period T_0 of the SDOF system. In particular, the stationary value of q(t) depends only on the damping ratio of the SDOF system. In fact, it can be shown from Eqs. (8.33) and (8.67) that

$$q_\infty = \lim_{t \to \infty} q(t) = \left\{ 1 - \frac{4[\text{arctg}(\sqrt{1-\xi^2}/\xi)]^2}{\pi^2(1-\xi^2)} \right\}^{\frac{1}{2}} \tag{8.70}$$

This stationary value decreases with decreasing value of ξ with $\lim_{\xi \to 0} q_\infty = 0$ indicating that the response process after reaching stationarity approaches a single har-

monic component (with random phase and amplitude) as the damping ratio approaches zero.

Fig. 8.4 shows the ratio of the central frequency of the displacement response process over the natural circular frequency, referred to as the normalized central frequency, of SDOF systems with varying damping ratio (ξ = 0.01, 0.05 and 0.10). It is observed that:

(1) The normalized central frequency has a very high value for small (t/T_0), then as (t/T_0) increases it reaches a minimum and finally oscillates until it reaches stationarity. These oscillations remain always below the stationary value.

(2) The normalized central frequency is a function only of the damping ratio and the time normalized by the natural period T_0 of the SDOF system. In particular, the stationary value of the normalized central frequency depends only on the damping ratio. This stationary value is given by

$$\omega_{c\infty}/\omega_0 = \lim_{t\to\infty}[\omega_c(t)/\omega_0] = \frac{2\cdot \operatorname{arctg}(\sqrt{1-\xi^2}/\xi)}{\pi\sqrt{1-\xi^2}} = \frac{1}{\sqrt{1-\xi^2}}\left[1-\frac{2}{\pi}\operatorname{arctg}(\xi/\sqrt{1-\xi^2})\right] \tag{8.71}$$

(see also Lutes and Sarkani 2004). In particular, $\lim_{\xi\to 0}(\omega_{c\infty}/\omega_0) = 1$, which implies that the single harmonic component (with random phase and amplitude) approached for large (t/T_0) by the displacement response process of a lightly damped SDOF system has a frequency equal to the natural frequency of the system.

Fig. 8.5 shows the dependency of the stationary values of the bandwidth parameter and normalized central frequency, respectively, on the damping ratio for a SDOF system, summarizing in graphical form some of the above observations. Fig. 8.6 provides a single realization of a white noise excitation with PSD $\phi_0 = 0.01 \mathrm{m}^2/\mathrm{s}^3$ and the corresponding displacement response histories of linear SDOF systems with natural period $T_0 = 1.0 \mathrm{s}$ and damping ratio ξ = 0.01, 0.05 and 0.10. The displacement time-histories corresponding to ξ = 0.01, after a few seconds of transient behavior, clearly approach a single harmonic component with a mean frequency close to the natural frequency of the system, as indicated by the results shown in Fig. 8.3 for the bandwidth parameter and Fig. 8.4 for the normalized central frequency. For the higher damping ratios of ξ = 0.05 and 0.10, after the initial transient behavior, a predominant harmonic component can also be observed in the displacement response histories. However, for these two higher damping cases and particularly for ξ = 0.10, contributions to the displacement response histories from other frequency components are non-negligible (broadening the frequency bandwidth of the response).

8.7.2 Three-story shear-type building (linear MDOF system)

The three-story one-bay steel shear-frame shown in Fig. 8.7 is considered as application example. This building structure has a uniform story height H = 3.20m and a bay width $L = 6.00 \mathrm{m}$. The steel columns are made of European HE340A wide flange beams with moment of inertia along the strong axis $I = 27690.0 \mathrm{cm}^4$. The steel material is mod-

eled as linear elastic with Young's modulus $E = 200\text{GPa}$. The beams are considered rigid to enforce a typical shear building behavior. Under this assumptions, the shear-frame is modeled as a 3-DOF linear system.

The frame described above is assumed to be part of a building structure with a distance between frames $L' = 6.00\text{m}$. The tributary mass per story, M, is obtained assuming a distributed gravity load of $q = 8\text{kN}/\text{m}^2$, accounting for the structure own weight, as well as for permanent and live loads, and is equal to $M = 28800\text{kg}$. The fundamental period of the linear elastic undamped shear-frame is $T_1 = 0.38\text{s}$. The modal properties of the shear-frame are given in Table 8.1. Viscous damping in the form of Rayleigh damping is assumed with a damping ratio $\xi = 0.02$ for the first and third modes of vibration. The same shear-frame is also considered with the addition of a viscous damper of coefficient $c = 200\text{kN-s/m}$ across the first story as shown in Fig. 8.7. The structure with viscous damper is a non-classically damped system. In both cases (with and without viscous damper), the shear-frame is subjected to base excitation modeled as a Gaussian white noise with PSD $\phi_0 = 0.1\text{m}^2/\text{s}^3$ time-modulated by the unit-step function (i.e., with at rest initial conditions).

Figs. 8.8 and 8.9 show the bandwidth parameter and normalized central frequencies (central frequency divided by the natural circular frequency of the first mode of vibration), respectively, for each of the three modes of vibration of the shear-frame. The stationary values of the bandwidth parameters for the first and third modes are identical, since these two modes have the same damping ratio, see Eq. (8.70). The second mode has

a lower damping ratio ($\xi_2 = 0.017$) and therefore a smaller stationary value for the bandwidth parameter.

Figs. 8.10 through 8.13 show time histories of the variances of the floor displacements and velocities (relative to the ground), and of the bandwidth parameters and central frequencies (normalized by the first mode natural frequency) of the floor relative displacement responses for the classically damped case. These figures show that the floor relative displacement response processes are dominated by the first mode contribution. In particular, the time histories of the bandwidth parameters and normalized central frequencies of the floor (especially the second and third floors) relative displacement responses are very similar to their counterparts for the first mode as shown by comparing Figs. 8.8 and 8.12 and Figs. 8.9 and 8.13, respectively. This comparison also indicates that the first floor relative displacement response has some small higher mode contributions.

Figs. 8.14 through 8.17 provide the same information as Figs. 8.10 through 8.13, but for the shear-frame with viscous damper (i.e., non-classically damped case). The floor relative displacement response processes remain dominated by the first mode contribution. The higher damping ($\xi_1 = 0.037$, $\xi_2 = 0.048$, $\xi_3 = 0.034$) reduces significantly the variances of floor relative displacements and velocities as shown by comparing Figs. 8.10 and 8.14 and Figs. 8.11 and 8.15, respectively. The higher damping has also the effect of raising slightly the stationary value of the bandwidth parameters of the floor relative horizontal displacements.

This second application example shows the capability of the presented extension of spectral characteristics to complex-valued stochastic processes to capture the time-vari-

ant spectral properties in terms of the bandwidth parameter and central frequency of the response of linear MDOF classically and non-classically damped systems.

8.8 CONCLUSIONS

In this chapter, the definition of the non-geometric spectral characteristics (NGSCs) is extended to general complex-valued non-stationary random processes. These newly defined NGSCs are essential for computing the time-variant bandwidth parameter and central frequency of non-stationary response processes of linear systems. The bandwidth parameter is also used in structural reliability applications, e.g., for obtaining analytical approximations of the probability that a structural response process out-crosses a specified limit-state threshold.

Using the non-geometric spectral characteristics of complex-valued non-stationary processes and employing complex modal analysis, closed-form exact solutions are found for the classical problem of deriving the time-variant central frequency and bandwidth parameter of the response of linear SDOF and MDOF systems, both classically and non-classically damped, when subjected to white noise excitation from at rest initial conditions.

The exact closed-form solutions derived for the linear SDOF oscillator are used to investigate the dependency of the stationary and time-variant central frequency and bandwidth parameter on the SDOF system parameters, i.e., natural circular frequency, ω_0, and damping ratio, ξ. A three-story shear-type steel frame building without and with viscous dampers (i.e., classically and non-classically damped, respectively) is used to illustrate the

application of the presented closed-form solutions for linear MDOF systems to the floor response processes of a base excited building structure.

The exact closed-form solutions developed and presented in this paper have their own mathematical merit, since to the best of the authors' knowledge, they are new. These solutions have a direct and important application, since the response of many structures can be approximated by using linear SDOF and MDOF models, and provide valuable benchmark solutions for validating (at the linear structural response level) numerical methods developed to estimate the probabilistic response of non-linear systems subjected to non-stationary excitations.

8.9 ACKNOWLEDGEMENTS

Chapter 8, in full, has been submitted for possible publication to Probabilistic Engineering Mechanics. The dissertation author was first author and investigator of this paper.

Table 8.1 Modal properties of the three-story one-bay shear-frame

Mode #	ω_i [rad/sec]	T [s]	Effective modal mass ratio [%]
1	16.70	0.38	91.41
2	46.80	0.13	7.49
3	67.62	0.09	1.10

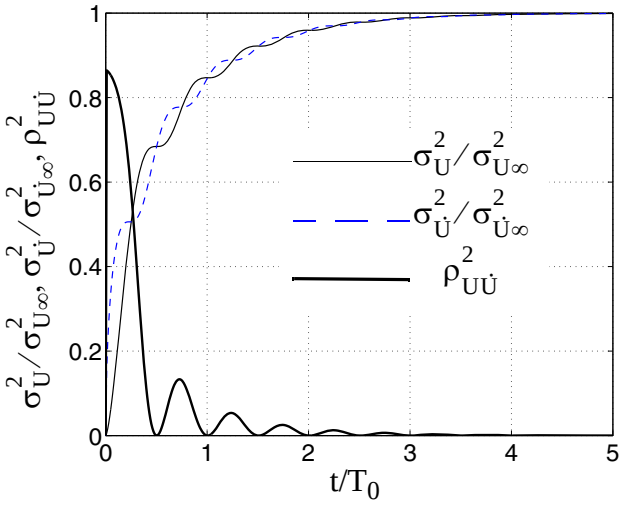

Figure 8.1 Normalized variances and square of correlation coefficient of displacement and velocity responses of linear SDOF systems with damping ratio $\xi = 0.10$.

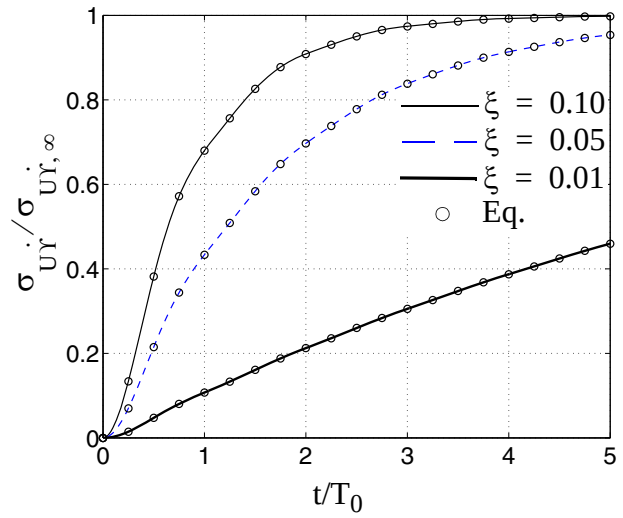

Figure 8.2 Comparison of analytical (Eq. (8.67)) and numerical (Eq. (8.69)) solutions for the normalized first NGSC $\sigma_{U\dot{Y}}(t)/\sigma_{U\dot{Y},\infty}$ of the displacement response of linear SDOF systems with damping ratios $\xi = 0.01$, 0.05 and 0.10.

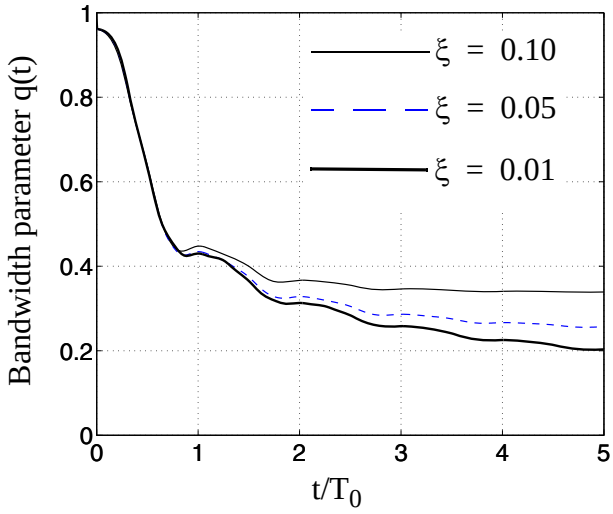

Figure 8.3 Time-variant bandwidth parameter, q(t), of the displacement response of linear SDOF systems with damping ratios ξ = 0.01, 0.05 and 0.10.

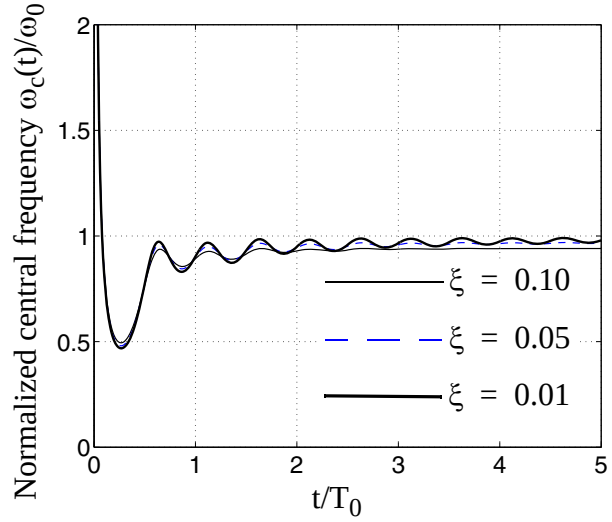

Figure 8.4 Time-variant normalized central frequency of the displacement response of linear SDOF systems with damping ratios ξ = 0.01, 0.05 and 0.10.

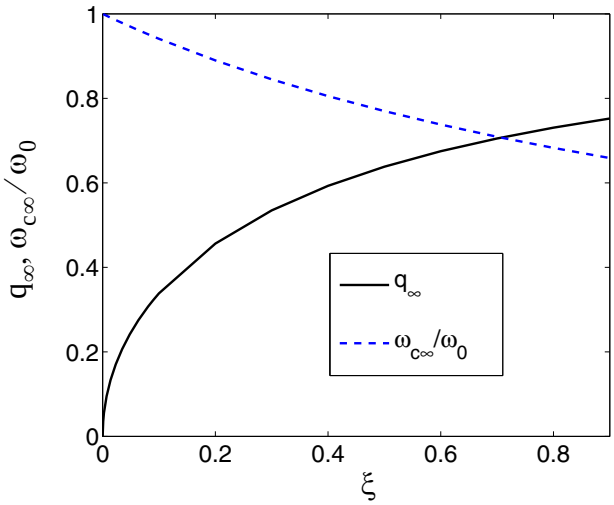

Figure 8.5 Dependency on damping ratio of the stationary values of the bandwidth parameter and normalized central frequency, respectively, of the displacement response of linear SDOF systems.

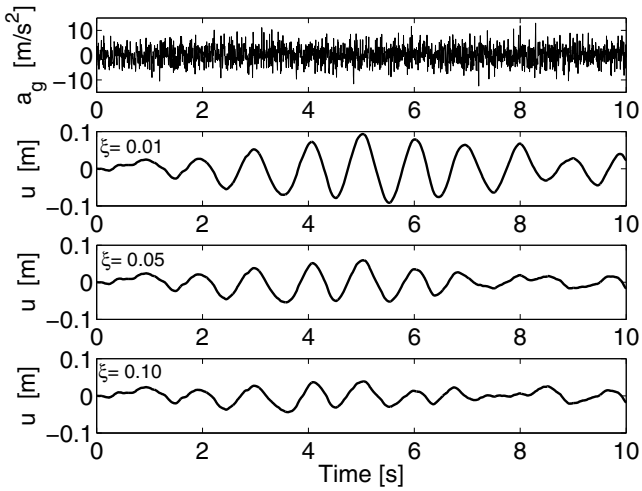

Figure 8.6 Realization of white noise excitation ($\phi_0 = 0.01 m^2/s^3$, $\Delta t = 0.005s$) and corresponding response displacement histories of linear SDOF systems with natural period $T_0 = 1.0s$ and damping ratio $\xi = 0.01$, 0.05 and 0.10.

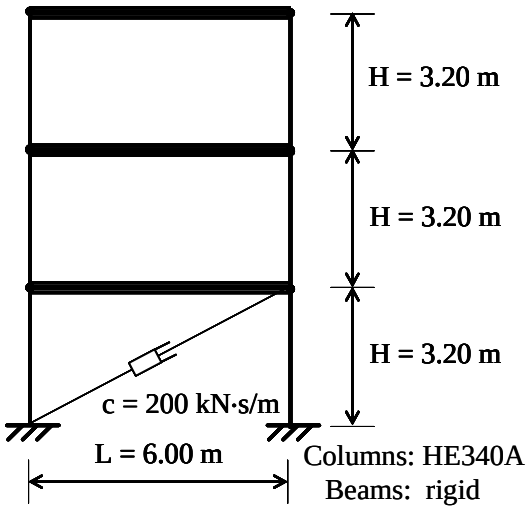

Figure 8.7 Geometric configuration of benchmark three-story one-bay shear-type steel frame.

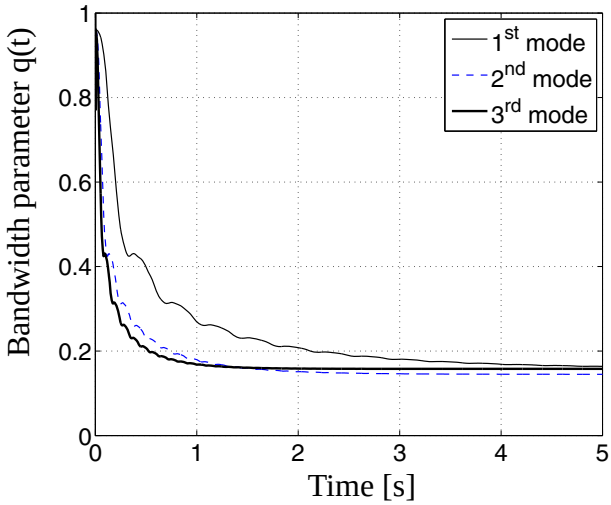

Figure 8.8 Time-variant bandwidth parameters for each of the three vibration mode displacement responses of the (classically damped) three-story shear-frame.

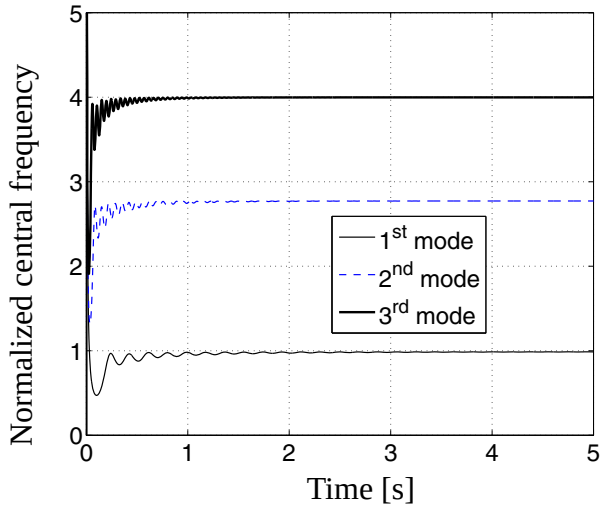

Figure 8.9 Time-variant central frequency (normalized by the circular frequency of the first vibration mode) for each of the three mode displacement responses of the (classically damped) three-story shear-frame.

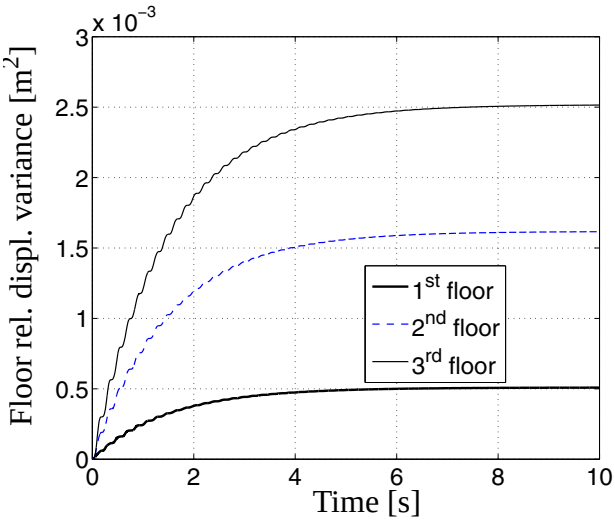

Figure 8.10 Time-variant variances of floor relative displacement responses of three-story shear-frame without damper (i.e., classically damped).

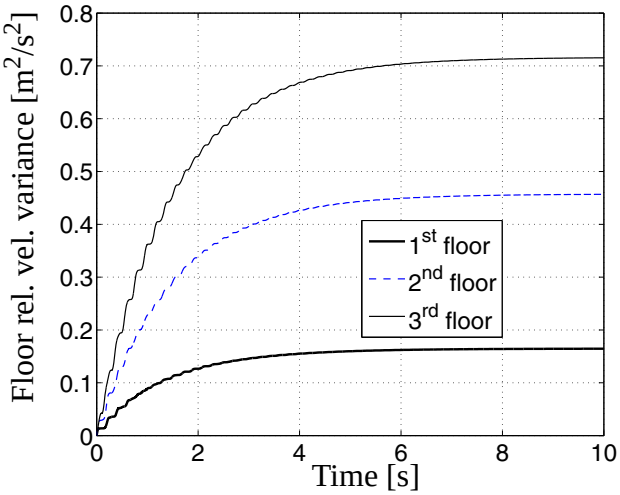

Figure 8.11 Time-variant variances of floor relative velocity responses of three-story shear-frame without damper (i.e., classically damped structure).

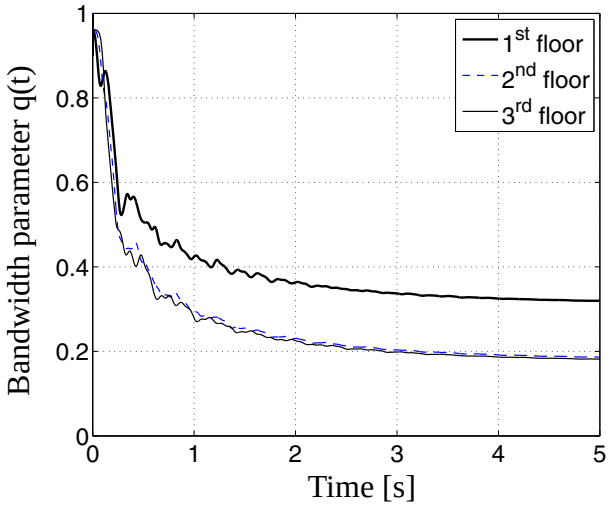

Figure 8.12 Time-variant bandwidth parameters of floor relative displacement responses of three-story shear-frame without damper (i.e., classically damped).

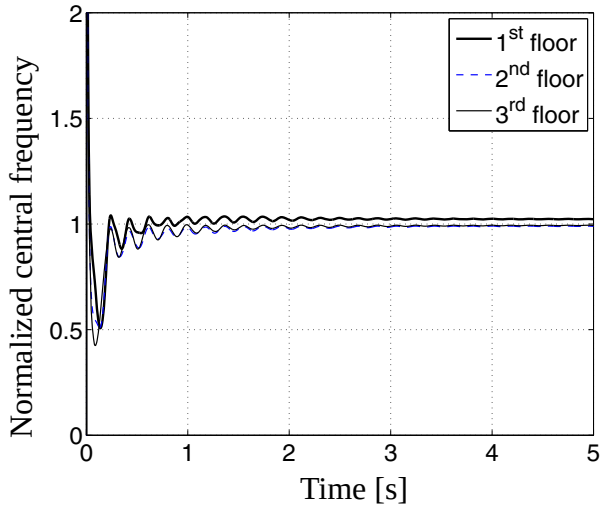

Figure 8.13 Time-variant central frequencies (normalized by first mode natural frequency) of floor relative displacement responses of three-story shear-frame without damper (i.e., classically damped).

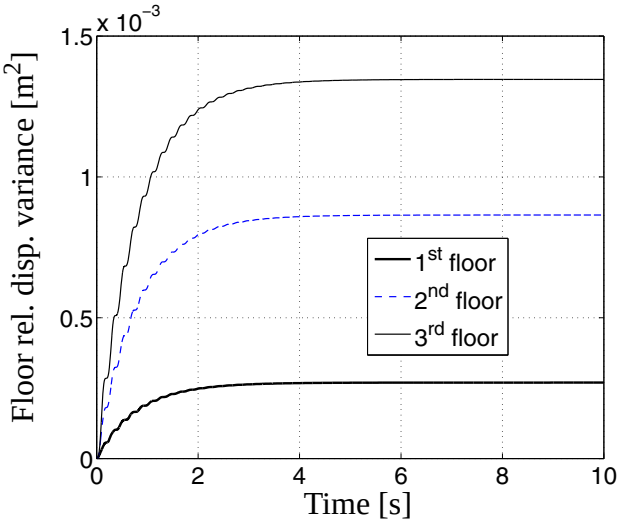

Figure 8.14 Time-variant variances of floor relative displacement responses of three-story shear-frame with damper (i.e., non-classically damped).

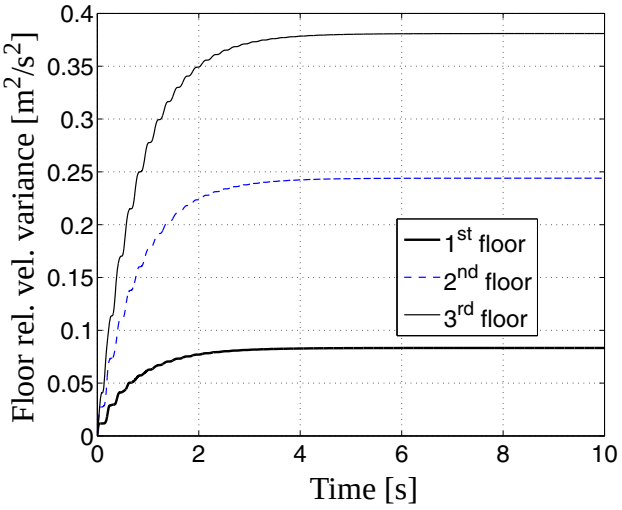

Figure 8.15 Time-variant variances of floor relative velocity responses of three-story shear-frame with damper (i.e., non-classically damped).

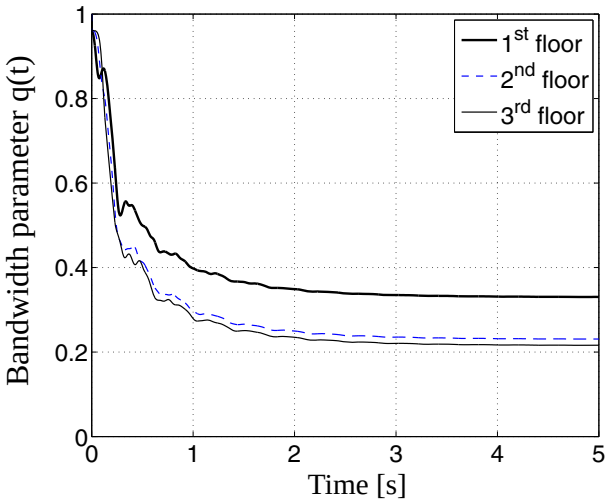

Figure 8.16 Time-variant bandwidth parameters of floor relative displacement responses of three-story shear-frame with damper (i.e., non-classically damped).

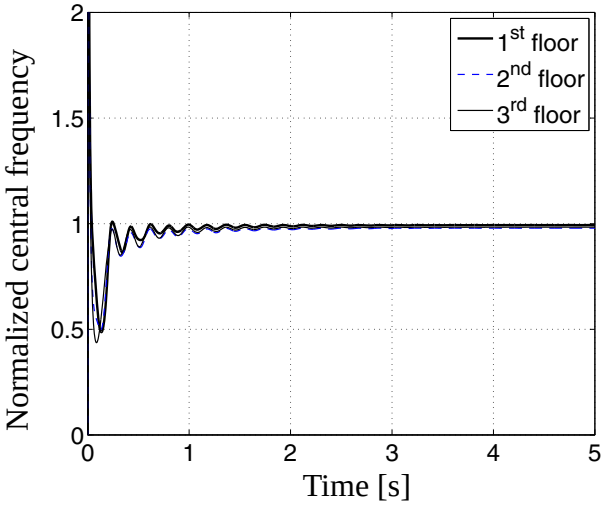

Figure 8.17 Time-variant central frequencies (normalized by first-mode natural frequency) of floor relative displacement responses of three-story shear-frame with damper (i.e., non-classically damped).

APPENDIX A: COMPUTATION OF THE CROSS-COVARIANCES OF NORMALIZED COMPLEX MODAL RESPONSES OF LINEAR SYSTEMS SUBJECTED TO WHITE NOISE EXCITATION FROM AT REST INITIAL CONDITIONS

The spectral characteristics $\sigma_{S_i S_m}(t)$ (i, m = 1, 2, ..., 2n) in Eq. $(8.54)_1$ can be computed as, using Cauchy's residue theorem,

$$\sigma_{S_iS_m}(t) = E[S_i^*(t)S_m(t)] = \phi_0\int_{-\infty}^{\infty} A_{S_i}^*(\omega, t)A_{S_m}(\omega, t)d\omega$$

$$= \phi_0\left\{\left[e^{(\lambda_i^* + \lambda_m)t} + 1\right]\cdot I_1 - e^{\lambda_i^* t}\cdot I_2 - e^{\lambda_m t}\cdot I_3\right\} \quad , \quad i, m = 1, 2, ..., 2n \quad (8.72)$$

in which

$$I_1 = \int_{-\infty}^{\infty}\frac{d\omega}{(\lambda_i^* + j\omega)(\lambda_m - j\omega)} = 2\pi\frac{k_1 - k_2}{\lambda_i^* + \lambda_m}, \quad i, m = 1, 2, ..., 2n \quad (8.73)$$

$$I_2 = \int_{-\infty}^{\infty}\frac{e^{j\omega t}d\omega}{(\lambda_i^* + j\omega)(\lambda_m - j\omega)} = 2\pi\frac{e^{-\lambda_i^* t}\cdot k_1 - e^{\lambda_m t}\cdot k_2}{\lambda_i^* + \lambda_m}, \quad i, m = 1, 2, ..., 2n \quad (8.74)$$

$$I_3 = \int_{-\infty}^{\infty}\frac{e^{-j\omega t}d\omega}{(\lambda_i^* + j\omega)(\lambda_m - j\omega)} = -2\pi\frac{e^{\lambda_i^* t}\cdot k_3 - e^{-\lambda_m t}\cdot k_4}{\lambda_i^* + \lambda_m}, \quad i, m = 1, 2, ..., 2n \quad (8.75)$$

$$k_1 = \begin{cases} 1, & \text{if } \mathrm{Im}[j\lambda_i^*] > 0 \\ 0, & \text{if } \mathrm{Im}[j\lambda_i^*] < 0 \end{cases}, \qquad k_2 = \begin{cases} 1, & \text{if } \mathrm{Im}[-j\lambda_m] > 0 \\ 0, & \text{if } \mathrm{Im}[-j\lambda_m] < 0 \end{cases} \quad (8.76)$$

$$k_3 = \begin{cases} 1, & \text{if } \mathrm{Im}[j\lambda_i^*] < 0 \\ 0, & \text{if } \mathrm{Im}[j\lambda_i^*] > 0 \end{cases}, \qquad k_4 = \begin{cases} 1, & \text{if } \mathrm{Im}[-j\lambda_m] < 0 \\ 0, & \text{if } \mathrm{Im}[-j\lambda_m] > 0 \end{cases} \quad (8.77)$$

Substituting Eqs. (8.73) through (8.75) into Eq. (8.72) yields

$$\sigma_{S_iS_m}(t) = \frac{2\pi\phi_0}{\lambda_i^* + \lambda_m}\left[e^{(\lambda_i^* + \lambda_m)t}(k_1 + k_3) - (k_2 + k_4)\right] = \frac{2\pi\phi_0}{\lambda_i^* + \lambda_m}\left[e^{(\lambda_i^* + \lambda_m)t} - 1\right],$$

$$i, m = 1, 2, ..., 2n \quad (8.78)$$

where the equalities $k_1 + k_3 = k_2 + k_4 = 1$ follow from Eqs. (8.76) and (8.77).

APPENDIX B: COMPUTATION OF THE FIRST-ORDER NGSCS OF NORMALIZED COMPLEX MODAL RESPONSES OF LINEAR SYSTEMS SUBJECTED TO WHITE NOISE EXCITATION FROM AT REST INITIAL CONDITIONS

The spectral characteristics $\sigma_{S_i\Sigma_m}(t)$ (i, m = 1, 2, ..., 2n) in Eq. $(8.54)_2$ can be computed as

$$\sigma_{S_i\Sigma_m}(t) = E[S_i^*(t)\Sigma_m(t)] = -j\phi_0\int_{-\infty}^{\infty} \mathrm{sign}(\omega)A_{S_i}^*(\omega, t)A_{S_m}(\omega, t)d\omega$$

$$= -j\phi_0\left\{\left[e^{(\lambda_i^* + \lambda_m)t} + 1\right]\cdot J_1 - e^{\lambda_i^* t}\cdot J_2 - e^{\lambda_m t}\cdot J_3\right\}$$

$$i, m = 1, 2, ..., 2n \tag{8.79}$$

where

$$J_1 = \int_{-\infty}^{\infty} \frac{\mathrm{sign}(\omega)d\omega}{(\lambda_i^* + j\omega)(\lambda_m - j\omega)}$$

$$\overset{(1)}{=} \frac{-j}{\lambda_i^* + \lambda_m}\left(\int_0^{\infty}\frac{d\omega}{\omega - \omega_i} + \int_0^{\infty}\frac{d\omega}{\omega + \omega_i} - \int_0^{\infty}\frac{d\omega}{\omega - \omega_m} - \int_0^{\infty}\frac{d\omega}{\omega + \omega_m}\right)$$

$$\overset{(2)}{=} \frac{-j}{\lambda_i^* + \lambda_m}\left\{\lim_{\omega\to\infty}\log\left[\frac{(\omega - \omega_i)(\omega + \omega_i)}{(\omega - \omega_m)(\omega + \omega_m)}\right] + \log\left(\frac{-\omega_m\cdot\omega_m}{-\omega_i\cdot\omega_i}\right)\right\},$$

$$\overset{(3)}{=} \frac{-2j}{\lambda_i^* + \lambda_m}\log\left(\frac{-\lambda_m}{\lambda_i^*}\right)$$

$$i, m = 1, 2, ..., 2n \tag{8.80}$$

$$J_2 = \int_{-\infty}^{\infty} \frac{\mathrm{sign}(\omega)e^{j\omega t}d\omega}{(\lambda_i^* + j\omega)(\lambda_m - j\omega)} = \int_{-\infty}^{\infty} \frac{\mathrm{sign}(\omega)e^{j\omega t}d\omega}{(\omega - \omega_i)(\omega - \omega_m)}, \quad i, m = 1, 2, ..., 2n \tag{8.81}$$

$$J_3 = \int_{-\infty}^{\infty} \frac{\text{sign}(\omega)e^{-j\omega t}d\omega}{(\lambda_i^* + j\omega)(\lambda_m - j\omega)} = \int_{-\infty}^{\infty} \frac{\text{sign}(\omega)e^{-j\omega t}d\omega}{(\omega - \omega_i)(\omega - \omega_m)}, \quad i, m = 1, 2, ..., 2n \qquad (8.82)$$

in which the poles ω_i and ω_m in the complex plane are given by

$$\omega_i = j\lambda_i^* \quad \text{and} \quad \omega_m = -j\lambda_m \qquad (8.83)$$

In Eq. (8.80), the successive equalities (each identified by a number in parentheses superposed to the equal sign) are obtained by performing the following operations:

(1) The denominator of the integrand is expressed in terms of poles. The integral is subdivided in contributions from positive and negative ω, respectively. The integrands are decomposed into partial fractions.

(2) Indefinite integration is performed and contributions from lower ($\omega = 0$) and upper ($\omega \to \infty$) integration limits are collected separately.

(3) The contribution from the upper integration limit is obtained solving the corresponding limit for $\omega \to \infty$.

The term $e^{\lambda_i^* t} \cdot J_2$ appearing in Eq. (8.79) can be developed as follows:

$$e^{\lambda_i^* t}\cdot J_2 = e^{\lambda_i^* t}\cdot\int_{-\infty}^{\infty}\frac{e^{j\omega t}\,\mathrm{sign}(\omega)\,d\omega}{(\omega-\omega_i)(\omega-\omega_m)}$$

$$\overset{(1)}{=}\left(e^{\lambda_i^* t}\cdot\int_0^{\infty}\frac{e^{j\omega t}d\omega}{(\omega-\omega_i)(\omega-\omega_m)}\right)-\left(e^{\lambda_i^* t}\cdot\int_0^{\infty}\frac{e^{-j\omega t}d\omega}{(\omega+\omega_i)(\omega+\omega_m)}\right)$$

$$\overset{(2)}{=}\frac{e^{\lambda_i^* t}}{(\omega_i-\omega_m)}\left[\left(\int_0^{\infty}\frac{e^{j\omega t}d\omega}{(\omega-\omega_i)}\right)-\left(\int_0^{\infty}\frac{e^{j\omega t}d\omega}{(\omega-\omega_m)}\right)+\left(\int_0^{\infty}\frac{e^{-j\omega t}d\omega}{(\omega+\omega_i)}\right)-\left(\int_0^{\infty}\frac{e^{-j\omega t}d\omega}{(\omega+\omega_m)}\right)\right]$$

$$\overset{(3)}{=}\frac{je^{\lambda_i^* t}}{(\lambda_i^*+\lambda_m)}\left[e^{-\lambda_i^* t}\left(\int_0^{\infty}\frac{e^{j(\omega-\omega_i)t}d\omega}{(\omega-\omega_i)}\right)-e^{\lambda_m t}\left(\int_0^{\infty}\frac{e^{j(\omega-\omega_m)t}d\omega}{(\omega-\omega_m)}\right)\right]$$

$$+\frac{je^{\lambda_i^* t}}{(\lambda_i^*+\lambda_m)}\left[e^{-\lambda_i^* t}\left(\int_0^{\infty}\frac{e^{-j(\omega+\omega_i)t}d\omega}{(\omega+\omega_i)}\right)-e^{\lambda_m t}\left(\int_0^{\infty}\frac{e^{-j(\omega+\omega_m)t}d\omega}{(\omega+\omega_m)}\right)\right]$$

$$\overset{(4)}{=}\frac{j}{(\lambda_i^*+\lambda_m)}\left[\log(\omega^2-\omega_i^2)+\sum_{r=1}^{\infty}\frac{(jt)^r\cdot(\omega-\omega_i)^r}{r\cdot r!}+\sum_{r=1}^{\infty}\frac{(-jt)^r\cdot(\omega+\omega_i)^r}{r\cdot r!}\right]_0^{\infty} \quad (8.84)$$

$$-\frac{je^{(\lambda_i^*+\lambda_m)t}}{(\lambda_i^*+\lambda_m)}\left[\log(\omega^2-\omega_m^2)+\sum_{r=1}^{\infty}\frac{(jt)^r\cdot(\omega-\omega_m)^r}{r\cdot r!}+\sum_{r=1}^{\infty}\frac{(-jt)^r\cdot(\omega+\omega_m)^r}{r\cdot r!}\right]_0^{\infty}$$

$$\overset{(5)}{=}\frac{j}{(\lambda_i^*+\lambda_m)}\left[\log(-\omega_i^2)+2\sum_{r=1}^{\infty}\frac{(-jt\omega_i)^r}{r\cdot r!}\right]-\frac{je^{(\lambda_i^*+\lambda_m)t}}{(\lambda_i^*+\lambda_m)}\left[\log(-\omega_m^2)+2\sum_{r=1}^{\infty}\frac{(-jt\omega_m)^r}{r\cdot r!}\right]$$

$$+\frac{j}{(\lambda_i^*+\lambda_m)}\lim_{\omega\to\infty}\left[\log(\omega^2-\omega_i^2)+\sum_{r=1}^{\infty}\frac{(jt)^r[(\omega-\omega_i)^r+(-1)^r(\omega+\omega_i)^r]}{r\cdot r!}\right]$$

$$-\frac{je^{(\lambda_i^*+\lambda_m)t}}{(\lambda_i^*+\lambda_m)}\lim_{\omega\to\infty}\left[\log(\omega^2-\omega_m^2)+\sum_{r=1}^{\infty}\frac{(jt)^r[(\omega-\omega_m)^r+(-1)^r(\omega+\omega_m)^r]}{r\cdot r!}\right]$$

In Eq. (8.84), the successive equalities (each identified by a number in parentheses superposed to the equal sign) are obtained by performing the following operations:

(1) The integral is subdivided in contributions from positive and negative ω, respectively. The sign of the integration variable is changed in the integral representing the contribution from negative ω.

(2) The integrands are decomposed into partial fractions.

(3) The integrals obtained are manipulated so to express the integrand as $\frac{e^{cx}}{x}$, with c = constant and x = integration variable.

(4) The numerators of the integrands are expanded in Taylor's series about x = 0 (i.e., $e^{cx} = \sum_{r=0}^{\infty} \frac{c^r x^r}{r!}$). Indefinite integration is performed and similar terms are collected.

(5) The contributions from the lower and upper limits of integration are collected separately.

The term $e^{\lambda_m t} \cdot J_3$ appearing in Eq. (8.79) can be developed as follows

$$e^{\lambda_m t}\cdot J_3 = e^{\lambda_m t}\cdot\int_{-\infty}^{\infty}\frac{\operatorname{sign}(\omega)e^{-j\omega t}d\omega}{(\omega-\omega_i)(\omega-\omega_m)}$$

$$\overset{(1)}{=}\left(e^{\lambda_m t}\cdot\int_0^{\infty}\frac{e^{-j\omega t}d\omega}{(\omega-\omega_i)(\omega-\omega_m)}\right)-\left(e^{\lambda_m t}\cdot\int_0^{\infty}\frac{e^{j\omega t}d\omega}{(\omega+\omega_i)(\omega+\omega_m)}\right)$$

$$\overset{(2)}{=}\frac{e^{\lambda_m t}}{(\omega_i-\omega_m)}\left[\left(\int_0^{\infty}\frac{e^{-j\omega t}d\omega}{(\omega-\omega_i)}\right)-\left(\int_0^{\infty}\frac{e^{-j\omega t}d\omega}{(\omega-\omega_m)}\right)+\left(\int_0^{\infty}\frac{e^{j\omega t}d\omega}{(\omega+\omega_i)}\right)-\left(\int_0^{\infty}\frac{e^{j\omega t}d\omega}{(\omega+\omega_m)}\right)\right]$$

$$\overset{(3)}{=}\frac{j\,e^{\lambda_m t}}{(\lambda_i^{*}+\lambda_m)}\left[e^{\lambda_i^{*}t}\left(\int_0^{\infty}\frac{e^{-j(\omega-\omega_i)t}d\omega}{(\omega-\omega_i)}\right)-e^{-\lambda_m t}\left(\int_0^{\infty}\frac{e^{-j(\omega-\omega_m)t}d\omega}{(\omega-\omega_m)}\right)\right]$$

$$+\frac{j\,e^{\lambda_m t}}{(\lambda_i^{*}+\lambda_m)}\left[e^{\lambda_i^{*}t}\left(\int_0^{\infty}\frac{e^{j(\omega+\omega_i)t}d\omega}{(\omega+\omega_i)}\right)-e^{-\lambda_m t}\left(\int_0^{\infty}\frac{e^{j(\omega+\omega_m)t}d\omega}{(\omega+\omega_m)}\right)\right]$$

$$\overset{(4)}{=}\frac{je^{(\lambda_i^{*}+\lambda_m)t}}{(\lambda_i^{*}+\lambda_m)}\left[\log(\omega^2-\omega_i^2)+\sum_{r=1}^{\infty}\frac{(-jt)^r\cdot(\omega-\omega_i)^r}{r\cdot r!}+\sum_{r=1}^{\infty}\frac{(jt)^r\cdot(\omega+\omega_i)^r}{r\cdot r!}\right]_0^{\infty} \quad (8.85)$$

$$-\frac{j}{(\lambda_i^{*}+\lambda_m)}\left[\log(\omega^2-\omega_m^2)+\sum_{r=1}^{\infty}\frac{(-jt)^r\cdot(\omega-\omega_m)^r}{r\cdot r!}+\sum_{r=1}^{\infty}\frac{(jt)^r\cdot(\omega+\omega_m)^r}{r\cdot r!}\right]_0^{\infty}$$

$$\overset{(5)}{=}\frac{je^{(\lambda_i^{*}+\lambda_m)t}}{(\lambda_i^{*}+\lambda_m)}\left[\log(-\omega_i^2)+2\sum_{r=1}^{\infty}\frac{(jt\omega_i)^r}{r\cdot r!}\right]-\frac{j}{(\lambda_i^{*}+\lambda_m)}\left[\log(-\omega_m^2)+2\sum_{r=1}^{\infty}\frac{(jt\omega_m)^r}{r\cdot r!}\right]$$

$$+\frac{je^{(\lambda_i^{*}+\lambda_m)t}}{(\lambda_i^{*}+\lambda_m)}\lim_{\omega\to\infty}\left[\log(\omega^2-\omega_i^2)+\sum_{r=1}^{\infty}\frac{(jt)^r[(-1)^r(\omega-\omega_i)^r+(\omega+\omega_i)^r]}{r\cdot r!}\right]$$

$$-\frac{j}{(\lambda_i^{*}+\lambda_m)}\lim_{\omega\to\infty}\left[\log(\omega^2-\omega_m^2)+\sum_{r=1}^{\infty}\frac{(jt)^r[(-1)^r(\omega-\omega_m)^r+(\omega+\omega_m)^r]}{r\cdot r!}\right]$$

In Eq. (8.85), the same five operations as in Eq. (8.84) are performed.

Summing the results of (8.84) and (8.85) and simplifying, the following relation is obtained

$$e^{\lambda_i^* t}\cdot J_2 + e^{\lambda_m t}\cdot J_3 =$$

$$= \frac{j}{(\lambda_i^* + \lambda_m)}\left[\log(-\omega_i^2) + 2\sum_{r=1}^{\infty}\frac{(-jt\omega_i)^r}{r\cdot r!} - \log(-\omega_m^2) - 2\sum_{r=1}^{\infty}\frac{(jt\omega_m)^r}{r\cdot r!}\right]$$

$$+ \frac{je^{(\lambda_i^* + \lambda_m)t}}{(\lambda_i^* + \lambda_m)}\left[\log(-\omega_i^2) + 2\sum_{r=1}^{\infty}\frac{(jt\omega_i)^r}{r\cdot r!} - \log(-\omega_m^2) - 2\sum_{r=1}^{\infty}\frac{(-jt\omega_m)^r}{r\cdot r!}\right]$$

$$+ \frac{j}{(\lambda_i^* + \lambda_m)}\lim_{\omega\to\infty}\left[\log\frac{(\omega^2-\omega_i^2)}{(\omega^2-\omega_m^2)}\right] + \frac{je^{(\lambda_i^* + \lambda_m)t}}{(\lambda_i^* + \lambda_m)}\lim_{\omega\to\infty}\left[\log\frac{(\omega^2-\omega_i^2)}{(\omega^2-\omega_m^2)}\right]$$

$$+ \frac{j}{(\lambda_i^* + \lambda_m)}\lim_{\omega\to\infty}\sum_{r=1}^{\infty}\frac{(jt)^r\{(\omega-\omega_i)^r - (\omega+\omega_m)^r + (-1)^r[(\omega+\omega_i)^r - (\omega-\omega_m)^r]\}}{r\cdot r!} \quad (8.86)$$

$$+ \frac{je^{(\lambda_i^* + \lambda_m)t}}{(\lambda_i^* + \lambda_m)}\lim_{\omega\to\infty}\sum_{r=1}^{\infty}\frac{(jt)^r\{(\omega+\omega_i)^r - (\omega-\omega_m)^r + (-1)^r[(\omega-\omega_i)^r - (\omega+\omega_m)^r]\}}{r\cdot r!}$$

$$= \frac{2j}{(\lambda_i^* + \lambda_m)}\left[\log\left(\frac{\omega_i}{\omega_m}\right) + \sum_{r=1}^{\infty}\frac{(jt)^r\cdot[-\omega_m{}^r + (-\omega_i)^r]}{r\cdot r!}\right]$$

$$+ \frac{2je^{(\lambda_i^* + \lambda_m)t}}{(\lambda_i^* + \lambda_m)}\left[\log\left(\frac{\omega_i}{\omega_m}\right) + \sum_{r=1}^{\infty}\frac{(-jt)^r\cdot[-\omega_m{}^r + (-\omega_i)^r]}{r\cdot r!}\right]$$

Notice that the contributions of the upper limit of integration in Eqs. (8.85) and (8.86) (which are divergent if taken separately) cancel each other out.

Substituting the results of Eqs. (8.80) and (8.86) into Eq. (8.79), the following result is obtained

$$\sigma_{S_i\Sigma_m}(t) = \frac{2\phi_0}{\lambda_i^* + \lambda_m}\sum_{r=1}^{\infty}\left\{\frac{t^r}{r\cdot r!}[(\lambda_m)^r - (\lambda_i^*)^r]\cdot\left[1 + (-1)^r e^{(\lambda_i^* + \lambda_m)t}\right]\right\},$$

$$i, m = 1, 2, ..., 2n \quad (8.87)$$

The infinite series in Eq. (8.87) can be expressed in terms of the integral exponential function $E_1(\ldots)$ noticing that (Abramowitz and Stegun 1972)

$$\sum_{r=1}^{\infty} \frac{(-x)^r}{r \cdot r!} = -\gamma - \log(x) - E_1(x) \;, \qquad |\arg(x)| < \pi \tag{8.88}$$

where γ = Euler's constant.

Manipulating Eq. (8.87) by using Eq. (8.88), the closed-form solution for the spectral characteristics $\sigma_{S_i\Sigma_m}(t)$ is finally obtained as

$$\begin{aligned}\sigma_{S_i\Sigma_m}(t) = {} & \frac{2\phi_0}{\lambda_i^* + \lambda_m}[E_1((-\lambda_i^*)t) + \log(-\lambda_i^*) - E_1(-\lambda_m t) - \log(-\lambda_m)] \\ & + \frac{2\phi_0}{\lambda_i^* + \lambda_m} e^{(\lambda_i^* + \lambda_m)t}[E_1(\lambda_i^* t) + \log(\lambda_i^*) - E_1(\lambda_m t) - \log(\lambda_m)] \\ & \qquad i, m = 1, 2, \ldots, 2n\end{aligned} \tag{8.89}$$

APPENDIX C: COMPUTATION OF THE FIRST-ORDER NGSCS OF THE DISPLACEMENT RESPONSE PROCESS OF A LINEAR SDOF SYSTEM SUBJECTED TO WHITE NOISE EXCITATION FROM AT REST INITIAL CONDITIONS

For a linear SDOF system, Eq. (8.52) reduces to

$$\begin{bmatrix} \sigma_{UY}(t) & \sigma_{U\dot{Y}}(t) \\ \sigma_{\dot{U}Y}(t) & \sigma_{\dot{U}\dot{Y}}(t) \end{bmatrix} = \frac{1}{4\omega_d^2} \begin{bmatrix} 1 & -1 \\ \lambda_2 & -\lambda_1 \end{bmatrix} \begin{bmatrix} \sigma_{S_1\Sigma_1}(t) & \sigma_{S_1\Sigma_2}(t) \\ \sigma_{S_2\Sigma_1}(t) & \sigma_{S_2\Sigma_2}(t) \end{bmatrix} \begin{bmatrix} 1 & \lambda_1 \\ -1 & -\lambda_2 \end{bmatrix} \tag{8.90}$$

From Eqs. (8.60) and (8.63), it is found that

$$\sigma_{S_1\Sigma_2}(t) = \sigma_{S_2\Sigma_1}(t) = 0 \tag{8.91}$$

and

$$\sigma_{S_1\Sigma_1}(t) = -\sigma_{S_2\Sigma_2}(t) \tag{8.92}$$

Therefore, $\sigma_{U\dot{Y}}(t)$ can be obtained from Eq. (8.90) as

$$\sigma_{U\dot{Y}}(t) = \frac{j}{2\omega_d}\sigma_{S_1\Sigma_1}(t) \tag{8.93}$$

Eq. (8.60) for $\sigma_{S_1\Sigma_1}(t)$ reduces to

$$\begin{aligned} \sigma_{S_1\Sigma_1}(t) = &-\frac{\phi_0}{\xi\omega}[E_1(-\lambda_2 t) + \log(-\lambda_2) - E_1(-\lambda_1 t) - \log(-\lambda_1)] \\ &-\frac{\phi_0}{\xi\omega} e^{-2\xi\omega t} [E_1(\lambda_2 t) + \log(\lambda_2) - E_1(\lambda_1 t) - \log(\lambda_1)] \end{aligned} \tag{8.94}$$

In addition, the following two equalities hold:

$$\begin{aligned}\log(-\lambda_2) - \log(-\lambda_1) &= \log(\xi\omega + j\omega_d) - \log(\xi\omega - j\omega_d) \\ &= \log(|\omega|) + j\,\mathrm{arctg}\left(\frac{\sqrt{1-\xi^2}}{\xi}\right) - \log(|\omega|) + j\,\mathrm{arctg}\left(\frac{\sqrt{1-\xi^2}}{\xi}\right) \\ &= 2j\,\mathrm{arctg}\left(\frac{\sqrt{1-\xi^2}}{\xi}\right)\end{aligned} \tag{8.95}$$

where the equality $\mathrm{arctg}(x) = -\mathrm{arctg}(-x)$ is used, and

$$\begin{aligned}\log(\lambda_2) - \log(\lambda_1) &= -j\pi + \log(-\lambda_2) - j\pi - \log(-\lambda_1) \\ &= \log(-\lambda_2) - \log(-\lambda_1) - 2j\pi = 2j\,\mathrm{arctg}\left(\frac{\sqrt{1-\xi^2}}{\xi}\right) - 2j\pi\end{aligned} \tag{8.96}$$

where the principal value of the natural logarithm function of complex variable x is considered (with branch cut on $(-\infty, 0]$) so that $|\arg(x)| < \pi$.

Finally, substituting (8.95) and (8.96) into Eq. (8.94), the closed-form solution for $\sigma_{\dot{UY}}(t)$ is obtained as

$$\begin{aligned}\sigma_{\dot{UY}}(t) = \frac{j\phi_0}{2\xi\omega_0\omega_d}&\left[E_1(-\lambda_1 t) - E_1(-\lambda_2 t) - 2j\,\mathrm{arctg}\left(\frac{\sqrt{1-\xi^2}}{\xi}\right)\right] \\ &+ \frac{j\phi_0}{2\xi\omega_0\omega_d} e^{-(2\xi\omega_0)t}\left\{E_1(\lambda_1 t) - E_1(\lambda_2 t) + 2j\left[\pi - \mathrm{arctg}\left(\frac{\sqrt{1-\xi^2}}{\xi}\right)\right]\right\}\end{aligned} \tag{8.97}$$

REFERENCES

Abramowitz M., Stegun I. A. (1972) “Exponential integral and related functions.” Ch. 5 in *Handbook of mathematical functions with formulas, graphs, and mathematical tables*, 9th printing. New York, NY: Dover, 227-233.

Bendat J., Piersol A.G. (1986) *Random data: analysis and measurement procedures.* New York, NY: Wiley.

Corotis R.B., Vanmarke E.H., Cornell C.A. (1972) “First passage of nonstationary random processes.” *Journal of Engineering Mechanics Division* (ASME), 98(EM2):401-414.

Crandall S. H. (1970) “First-crossing probabilities of the linear oscillator.” *Journal of Sounds and Vibrations*, 12(3):285-299.

Di Paola M. (1985) “Transient spectral moments of linear systems.” *SM Archives*, 10:225-243.

Lin Y. K. (1967) *Probabilistic theory of structural dynamics.* New York, NY: McGraw-Hill, 1967, Huntington, UK: Krieger Pub., 1976.

Lutes L.D., Sarkani S. (2004) *Random vibrations - analysis of structural and mechanical systems*. Burlington, MA: Elsevier Butterworth-Heinemann.

Michaelov G., Sarkani S., Lutes L.D. (1999a) “Spectral characteristics of nonstationary random processes- a critical review.” *Structural Safety*, 21:223-244.

Michaelov G., Sarkani S., Lutes L.D. (1999b) “Spectral characteristics of nonstationary random processes- response of a simple oscillator.” *Structural Safety*, 21:245-267.

Peng B.-F., Conte J.P. (1998) “Closed-form solutions for the response of linear systems to fully nonstationary earthquake excitation.” *Journal of Engineering Mechanics* (ASCE), 124(6):684-694.

Priestley M.B. (1987) *Spectral analysis and time series, volume 1: univariate series, volume 2: multivariate series, prediction and control.* London, UK: Academic Press, Fifth Printing.

Priestley M.B. (1988) *Non-linear and non-stationary time series analysis.* London, UK: Academic Press.

Reid, J.G. (1983) *Linear system fundamentals: continuous and discrete, classic and modern.* New York, NY: McGraw-Hill.

Rice S. O. (1944) “Mathematical analysis of random noise.” *Bell System Technical Journal*, 23:282.

Rice S. O. (1945) “Mathematical analysis of random noise.” *Bell System Technical Journal*, 24:46.

Vanmarcke E.H. (1975) “On the distribution of the first-passage time for normal stationary random processes.” *Journal of Applied Mechanics* (ASME), 215-220.

CHAPTER 9

USE OF SPECTRAL CHARACTERISTICS FOR RELIABILITY ANALYSIS OF LINEAR ELASTIC MDOF SYSTEMS

9.1 INTRODUCTION

In many engineering fields, the importance of using stochastic processes to model dynamic loads such as earthquake ground motions, wind effects on civil and aerospace structures, and ocean wave induced forces on offshore structures, has been widely recognized. Extensive research has been devoted to the development of analytical methods and numerical simulation techniques related to modeling of stochastic loads and analysis of their effects on structures (Lin 1976; Priestley 1987; Lutes and Sarkani 1997). These effects are stochastic in nature and, in general, are represented by random processes which are nonstationary in both amplitude and frequency content (Yeh and Wen 1990; Papadimitriou 1990; Conte 1992). Modern design codes consider carefully loading uncertainties (as well as parameter and modeling uncertainties) and account for their stochastic nature to ensure satisfactory designs. The Performance-Based Earthquake Engineering (PBEE) is emerging as new design philosophy (Cornell and Krawinkler 2000; Porter 2003; Moehle and Deierlein 2004) and is leading the way to the new generation of seismic design codes (AASHTO 1998; ICC 2003; BSSC 2004; ATC-55 2005; ATC-58 2005). The PBEE paradigm explicitly abandons the sole use of empirical conventions and prescription formulas

for designing the components of a structure, in favor of the satisfaction of prescribed performance criteria by the complete structure in its particular environment. In this view, paramount importance is gained by time-variant reliability analysis methodologies, which provide a sound analytical basis for evaluating probabilistically the satisfaction of the above mentioned performance criteria.

The probability of failure over a given interval of time (i.e., probability of a response vector process outcrossing a general limit-state surface during an exposure time) is the fundamental result required in a time-variant reliability analysis. For a large class of structural applications, the failure condition can be identified as the exceedance of a deterministic threshold by a linear combination of scalar response quantities. To date, no exact closed-form solution of this problem (also called the first-passage problem in the literature) is available, even for the simplest case of structural model (deterministic linear elastic SDOF system) subjected to the simplest stochastic load model (stationary Gaussian white noise). The Monte Carlo simulation technique is the only general method accommodating for nonstationarity and non-Gaussianess of the excitation as well as nonlinearity in the structural behavior and uncertainty/randomness in the structural parameters. However, it is computationally extremely expensive. Nevertheless, an analytical upper bound of the time-variant probability of failure can be obtained readily when response mean out-crossing rates are available (Lin 1976) and several direct approximations of this failure probability have been developed making use of different statistics of the response quantities of interest (Crandall 1970; Wen 1987). In particular, Poisson and Vanmarcke approximations have been shown to offer a good compromise between accuracy and computational effort

(Rice 1944, 1945; Corotis et al. 1972). Vanmarcke suggested two different approximations (Vanmarcke 1975), called classical and modified Vanmarcke approximation, respectively, which both require the computation of the bandwidth parameter of the stochastic process considered, in addition to the other stochastic moments required for computing the mean out-crossing rate and Poisson approximation. The two Vanmarcke approximations were first derived for stationary problems, and then extended to nonstationary problems (Corotis et al. 1972; Vanmarcke 1975). More recent work by Di Paola (1985) and Michaelov et al. (1999a, 1999b) provided new insight into the nonstationary quantities required by the Vanmarcke approximations, suggesting a more appropriate definition of the bandwidth parameter for real-valued nonstationary random processes.

This work focuses on analytical approximations to the first passage problem in structural reliability. After defining the problem, existing analytical approximations are reviewed and the exact closed-forms of the spectral characteristics of nonstationary random processes are used to define integral representations of such approximations, namely Poisson, classical Vanmarcke and modified Vanmarcke approximations. Finally, two sets of benchmark models, consisting of linear elastic SDOF systems with different natural periods and damping ratios and of a realistic three dimensional unsymmetric three storey building, respectively, are used to compare these analytical approximations with simulation results obtained using the Importance Sampling using Elementary Events (ISEE) method (Au and Beck 2001).

9.2 FIRST-PASSAGE PROBLEM IN STRUCTURAL RELIABILITY ANALYSIS

An extremely important quantity in the reliability analysis of a structure is the probability of failure in a given interval of time. In the present study, the probability of failure is identified as the probability of exceeding a given (deterministic and invariant with time) threshold by a quantity (linearly) related to the response displacements and velocities (as absolute displacement, relative displacement, elastic force, etc.) of a given structural system. The problem of evaluating this time-variant probability of failure is also known as first-passage problem and has been presented in the literature as single-barrier problem (random process up-crossing or down-crossing a given threshold) or as double-barrier problem (absolute value of the random process exceeding a given threshold).

It is known that an analytic upper-bound of the probability of failure $P_{f,X}(\zeta^+, t)$ is obtained by integrating in time the up-crossing rate $\nu_X(\zeta^+, t)$ of the considered process $X(t)$ corresponding to the fixed threshold ζ (single-barrier problem), as

$$P_{f,X}(\zeta^+, t) = P[x(t) \geq \zeta / x(\tau) < \zeta, \tau \in [0, t)] = \sum_{n=1}^{\infty} P[N_{out}(t) = n] \leq \int_0^t \nu_X(\zeta^+, t) d\tau = E[N_{out}(t)] = \sum_{n=1}^{\infty} nP[N_{out}(t) = n] \tag{9.1}$$

where $E[\ ]$ represents the expectation operator and $P(A/B)$ is the probability of event A conditioned to the event B. Moreover, it is common to express the probability of failure $P_{f,X}(\zeta^+, t)$ in the following functional form

$$P_{f,X}(\zeta^+, t) = 1 - P[x(t = 0) < \zeta] \cdot \exp\left\{-\int_0^t h_X(\zeta^+, \tau)d\tau\right\} \tag{9.2}$$

where $P[x(t = 0) < \zeta]$ denotes the probability that, at time t = 0, the realization $x(t)$ of the process $X(t)$ is below the failure threshold ζ (in particular, for at rest initial conditions, $P[x(t = 0) < \zeta] = 1$), and $h_X(\zeta^+, t)$ is the so-called hazard function, i.e., it is the up-crossing rate of threshold ζ conditioned to zero up-crossing before time t. Up to date, no exact closed-form solution is available for the hazard function even for the simplest structure possible (linear elastic SDOF oscillator), even if many approximations have been developed and described in literature (Crandall 1970). Extension of the problem expressed by Eq. (9.2) to double-barrier problems is straightforward and can be formally expressed as

$$P_{f,|X|}(\zeta, t) = 1 - P[|x(t = 0)| < \zeta] \cdot \exp\left\{-\int_0^t h_{|X|}(\zeta, \tau)d\tau\right\} \tag{9.3}$$

where the quantities $P_{f,|X|}(\zeta, t)$ and $h_{|X|}(\zeta, t)$ are the time-variant probability of failure and hazard function referred to the process $|X(t)|$ and to the threshold level ζ. In the following, the case of single-barrier problem will be considered explicitly for derivation of

the failure probability approximations and extensions to the double-barrier will be provided as well.

The most famous and simple approximation for the hazard function is the Poisson hazard function, $h_{X,P}(\zeta^+, t)$, obtained considering the out-crossings as statistically independent events with Poisson distribution (process without memory). This hypothesis leads to

$$h_{X,P}(\zeta^+, t) = \nu_X(\zeta^+, t) \tag{9.4}$$

For low thresholds and/or narrow-band processes, the Poisson hazard function tends to give very conservative values of the probability of failure, while for high barrier levels and broad-band processes it is asymptotically correct. The mean up-crossing rate $\nu_X(\zeta^+, t)$ is given by the well-known Rice formula

$$\nu_X(\zeta^+, t) = \int_0^\infty \dot{x} f_{X\dot{X}}(\zeta, \dot{x}, t) d\dot{x} \tag{9.5}$$

in which $f_{X\dot{X}}(\zeta, \dot{x}, t)$ denotes the joint probability density distribution of the process X(t) and its time-derivative $\dot{X}(t)$ for $x(t) = \zeta$.

A closed-form solution for Eq. (9.5) in the case of nonstationary random process is available only for Gaussian processes. In general, a numerical estimate of the mean up-crossing rate $\nu_X(\zeta^+, t)$ is obtained through the limiting formula (Hagen and Tvedt 1991)

$$\nu_X(\zeta^+, t) = \lim_{\delta t \to 0} \frac{P[(x(t) < \zeta) \cap (x(t + \delta t) \geq \zeta)]}{\delta t} \tag{9.6}$$

If the considered process $X(t)$ is Gaussian, the closed-form solution for the mean upcrossing rate is

$$\nu_X(\zeta^+, t) = \frac{1}{2\pi}\frac{\sigma_{\dot{X}}(t)}{\sigma_X(t)}\sqrt{1-(\rho_{X\dot{X}}(t))^2}\cdot e^{-\left[\frac{Q(t)}{\rho_{X\dot{X}}(t)}\right]^2}\cdot \left\{1+\sqrt{\pi}Q(t)\cdot e^{[Q(t)]^2}\operatorname{erfc}[-Q(t)]\right\} \tag{9.7}$$

where

$$Q(t) = \frac{\rho_{X\dot{X}}(t)}{\sqrt{2[1-(\rho_{X\dot{X}}(t))^2]}}\left(\frac{\zeta}{\sigma_X(t)}\right) \tag{9.8}$$

a superposed dot denotes derivative with respect to time, σ_X, $\sigma_{\dot{X}}$ and $\rho_{X\dot{X}} = \frac{\sigma_{X\dot{X}}}{\sigma_X\sigma_{\dot{X}}}$ denote the standard deviation of the process, the standard deviation of the time-derivative of the process and the correlation coefficient between the process and its time-derivative process, respectively, and $\operatorname{erfc}(\ldots)$ denotes the error function. If the process $X(t)$ is non-stationary, all the quantities previously defined are time-dependent, while in the case of stationary process, these quantities are constant in time and Eq. (9.7) reduces to

$$\nu_X(\zeta^+) = \int_0^\infty \dot{x} f_{X\dot{X}}(\zeta, \dot{x})d\dot{x} = \frac{1}{2\pi}\frac{\sigma_{\dot{X}}}{\sigma_X}\cdot e^{-\frac{1}{2}\left(\frac{\zeta}{\sigma_X}\right)^2} \tag{9.9}$$

An improved estimate of the probability of failure for the stationary case has been developed by Vanmarcke (1975), considering the envelope process as defined by Cramer and Leadbetter (1967). It is based on the two-state Markov process assumption and it takes

in account the fraction of time that the envelope spends above the threshold ζ and the fact that out-crossings of the envelope process are not always associated with an out-crossing of actual process. The first fact is important for low threshold levels, while the second can be relevant for high threshold levels. The obtained relation for the stationary case is

$$h_{X,\,VM}(\zeta^+) = \nu_X(\zeta^+) \cdot \frac{1 - \exp\left(-\sqrt{2\pi}q\frac{\zeta}{\sigma_x}\right)}{1 - \exp\left(-\frac{\zeta^2}{2\sigma_x^2}\right)} \tag{9.10}$$

where $\nu_X(\zeta^+)$ is the up-crossing rate of the threshold ζ for the stationary process $X(t)$ and q is the process bandwidth parameter. An important feature of the Vanmarcke approximation is that, for high thresholds and/or broad-band processes, at the limit it reduces to the Poisson approximation.

The relation for the nonstationary case is obtained substituting in Eq. (9.10) the stationary quantities with their nonstationary counterparts,

$$h_{X,\,VM}(\zeta^+, t) = \nu_X(\zeta^+, t) \cdot \frac{1 - \exp\left[-\sqrt{2\pi}q(t)\frac{\zeta}{\sigma_x(t)}\right]}{1 - \exp\left\{-\frac{\zeta^2}{2[\sigma_x(t)]^2}\right\}} \tag{9.11}$$

Vanmarcke also suggested an empirical modification of Eqs. (9.10) and (9.11), in which the bandwidth parameters q and q(t) are substituted with $q^{1.2}$ and $[q(t)]^{1.2}$, respectively, to account for super-clamping effects, leading to the modified Vanmarcke approximation

$$h_{X,\,mVM}(\zeta^+, t) = \nu_X(\zeta^+, t) \cdot \frac{1 - \exp\left\{-\sqrt{2\pi}[q(t)]^{1.2}\dfrac{\zeta}{\sigma_x(t)}\right\}}{1 - \exp\left\{-\dfrac{\zeta^2}{2[\sigma_x(t)]^2}\right\}} \tag{9.12}$$

The relations for the double-barrier problem corresponding to Eqs. (9.4), (9.11) and (9.12) are

$$h_{|X|,\,P}(\zeta, t) = \nu_{|X|}(\zeta, t) = \nu_X(\zeta^+, t) + \nu_X(\zeta^-, t) = 2\nu_X(\zeta^+, t) \tag{9.13}$$

$$h_{|X|,\,VM}(\zeta, t) = \nu_{|X|}(\zeta, t) \cdot \frac{1 - \exp\left[-\sqrt{\dfrac{\pi}{2}}q(t)\dfrac{\zeta}{\sigma_x(t)}\right]}{1 - \exp\left\{-\dfrac{\zeta^2}{2[\sigma_x(t)]^2}\right\}} \tag{9.14}$$

$$h_{|X|,\,mVM}(\zeta, t) = \nu_{|X|}(\zeta, t) \cdot \frac{1 - \exp\left\{-\sqrt{\dfrac{\pi}{2}}[q(t)]^{1.2}\dfrac{\zeta}{\sigma_x(t)}\right\}}{1 - \exp\left\{-\dfrac{\zeta^2}{2[\sigma_x(t)]^2}\right\}} \tag{9.15}$$

9.3 USE OF SPECTRAL CHARACTERISTICS IN TIME-VARIANT RELIABILITY ANALYSIS

The spectral characteristics of the process $X(t)$ are necessary in order to compute the quantities in Eqs. (9.7) through (9.11). In fact, the non-geometric spectral characteristics of the two random processes $X_1(t)$ and $X_2(t)$ are defined as (Barbato and Conte 2007)

$$c_{ik,\,X_1X_2}(t) = \int_{-\infty}^{\infty} \Phi_{X_1^{(i)}X_2^{(k)}}(\omega, t)d\omega = \sigma_{X_1^{(i)}X_2^{(k)}}(t) \tag{9.16}$$

For the particular case of $X_1(t) = X_2(t) = X(t)$, we have

$$c_{00,\,(XX)}(t) = \sigma_X^2(t) \tag{9.17}$$

$$c_{11,\,(XX)}(t) = \sigma_{\dot{X}}^2(t) \tag{9.18}$$

$$c_{01,\,(XX)}(t) = \sigma_{X\dot{X}}(t) = \rho_{X\dot{X}}(t)\sigma_X(t)\sigma_{\dot{X}}(t) \tag{9.19}$$

For the case of $X_1(t) = X(t)$ and $X_2(t) = Y(t)$, with $X(t)$ and $Y(t)$ defined as

$$X(t) = \int_{-\infty}^{\infty} A_X(\omega, t)\exp(j\omega t)dZ(\omega) \tag{9.20}$$

$$Y(t) = -j\int_{-\infty}^{\infty} \text{sign}(\omega)A_X(\omega, t)\exp(j\omega t)dZ(\omega) \tag{9.21}$$

respectively, we have

$$c_{01,\,(XY)}(t) = \sigma_{X\dot{Y}}(t) \tag{9.22}$$

from which the bandwidth parameter, q(t), can be computed as

$$q(t) = \left(1 - \frac{\sigma_{X\dot{Y}}^2(t)}{\sigma_X^2(t)\sigma_{\dot{X}}^2(t)}\right)^{\frac{1}{2}} \tag{9.23}$$

9.4 APPLICATION EXAMPLES

9.4.1 Linear elastic SDOF systems

The first application example consists of the analysis of linear elastic SDOF systems subjected to a Gaussian white noise time-modulated by a unit-step function, i.e., with at rest initial conditions. For this type of structural system subjected to the given excitation, exact solutions for the time-variant spectral characteristics up to the second order are available in closed-form and have been presented in Chapter 8. Fig. 9.1 plots the normalized second-order statistical moments of the response of a linear elastic SDOF system with natural period $T_0 = 0.5s$ and damping ratio $\xi = 0.05$. These closed-form solutions are here applied to obtain exact time-variant mean up-crossing rates and Poisson and Vanmarcke approximations to the time-variant probability of failure, as defined previously for the double-barrier problem. In this case, the response of the system is a zero-mean Gaussian process (obtained by filtering a zero-mean Gaussian process with a linear filter) for which the closed-form of the time-variant mean up-crossing rate for a given deterministic threshold is given by Eq. (9.13). The effects on the failure probability of different values in the parameters describing the system (namely, natural circular frequency, ω_0, and damping ratio, ξ) and of different threshold levels (normalized with the stationary values of the standard deviation of the response process as $\zeta/\sigma_{X\infty}$) will be considered and analyzed. The effect of different magnitude levels in the excitation is implicitly considered through the different threshold levels, since higher or lower excitation magnitudes will only scale up or down the response, due to the linearity of the system considered.

Figs. 9.2 through 9.9 show some selected analysis results for the out-crossing of given deterministic thresholds by the response of a linear elastic SDOF system with natural period $T_0 = 0.5s$ and damping ratio $\xi = 0.05$ subjected to a white noise excitation with at rest initial conditions. Figs. 9.2, 9.4, 9.6 and 9.8 plot the time-variant mean out-crossing rate, ν, the Vanmarcke hazard function, h_{VM}, and the modified Vanmarcke hazard function, h_{mVM}, for the linear elastic SDOF system described above and threshold levels $\zeta = 2.0 \cdot \sigma_{X\infty}$, $\zeta = 2.5 \cdot \sigma_{X\infty}$, $\zeta = 3.0 \cdot \sigma_{X\infty}$ and $\zeta = 4.0 \cdot \sigma_{X\infty}$, respectively.

Figs. 9.3, 9.5, 9.7 and 9.9 show, for the same linear SDOF system considered above, the time-variant expected number of out-crossings, E[N], and the failure probability estimates given by the Poisson approximation, $P_{f,P}$, the Vanmarcke approximation, $P_{f,VM}$, and the modified Vanmarcke approximation, $P_{f,mVM}$, respectively. The same Figs. 9.3, 9.5, 9.7 and 9.9 also provide the failure probability at different instants of time obtained by Importance Sampling using Elementary Events (ISEE) (Au and Beck 2001) with a coefficient of variation c.o.v. = 0.01.

For the case analysis corresponding to the threshold level $\zeta = 2.0 \cdot \sigma_{X\infty}$, the hazard functions obtained using the Vanmarcke and the modified Vanmarcke approximations give much lower values than the corresponding mean out-crossing rate, as shown in Fig. 9.2. In particular, the values at time T = 5.0s, at which the considered functions have practically reached their stationary values, are $\nu(T) = 0.2707s^{-1}$, $h_{VM}(T) = 0.1439s^{-1} = 0.53\nu(T)$ and $h_{mVM}(T) = 0.1164s^{-1} = 0.43\nu(T)$, respec-

tively. For the very high values of failure probability found in this analysis case, the analytical upper bound provided by E[N] is useless, since the expected number of out-crossings is more than one after less than three seconds of analysis, and the Poisson estimate is largely overestimating the probability of failure (see Fig. 9.3). On the other hand, the two Vanmarcke approximations are both in good agreement with the simulation results, with better agreement of the Vanmarcke approximation for the earlier phase of the analysis ($t \leq 2.5s$) and of the modified Vanmarcke approximation for analysis time larger than three seconds. In this specific case, the failure probability at different instants of time is computed also by using crude Monte Carlo Simulation (MCS), the use of which is possible due to the large values assumed by the time-variant probability of failure. The results obtained by crude MCS are in very good agreement with the ones computed by ISEE.

The results presented in Figs. 9.4 and 9.5, related to a threshold $\zeta = 2.5 \cdot \sigma_{X\infty}$, are qualitatively very similar to the corresponding ones of Figs. 9.2 and 9.3. In fact, we can notice that: (1) the Vanmarcke and the modified Vanmarcke hazard functions assume values much lower than the corresponding mean out-crossing rate values (see Fig. 9.4); (2) the expected number of out-crossings and the Poisson approximation grossly overestimate the probability of failure of the system obtained using ISEE, even though the improvement obtained using the Poisson approximation is significant; (3) the two Vanmarcke approximations are both in good agreement with the simulation results, with better agreement of the Vanmarcke approximation for the earlier phase of the analysis ($t \leq 2.0s$) and of the modified Vanmarcke approximation for $t \geq 2.5s$.

The mean out-crossing rate values relative to the threshold $\zeta = 3.0 \cdot \sigma_{X\infty}$ are larger than the Vanmarcke and the modified Vanmarcke hazard function values (see Fig. 9.6), but the differences are smaller than for lower thresholds. In fact, in this case, we have for $T = 5.0s$: $\nu(T) = 0.0220s^{-1}$, $h_{VM}(T) = 0.0135s^{-1} = 0.61\nu(T)$ and $h_{mVM}(T) = 0.0112s^{-1} = 0.51\nu(T)$. It is also noteworthy that the mean out-crossing rate and hazard functions at time $T = 5.0s$ are not as close to their stationary values as they are for thresholds lower than $\zeta = 3.0 \cdot \sigma_{X\infty}$. The comparison of the analytical approximations of the time-variant failure probability with its estimate obtained through ISEE (see Fig. 9.7) shows: (1) the expected number of out-crossings is almost double the failure probability computed by ISEE and the Poisson approximation improves only slightly this estimate; (2) the two Vanmarcke approximations provides good failure probability estimates, but in this case the Vanmarcke approximation has a better agreement with the ISEE results for the entire time interval considered in the analysis. Nevertheless, it is evident that the ISEE results get closer to the modified Vanmarcke approximation results for larger values of the time.

For the case of a threshold $\zeta = 4.0 \cdot \sigma_{X\infty}$, the differences between the mean out-crossing rate and the Vanmarcke approximations are smaller than for lower thresholds, as shown in Fig. 9.8, and their values at the time instant $T = 5.0s$ are equal to $\nu(T) = 6.61 \cdot 10^{-4}s^{-1}$, $h_{VM}(T) = 4.69 \cdot 10^{-4}s^{-1} = 0.71\nu(T)$ and $h_{mVM}(T) = 4.01 \cdot 10^{-4}s^{-1} = 0.61\nu(T)$, respectively. Fig. 9.9 compares the expected

value of out-crossings, the Poisson, the Vanmarcke and the modified Vanmarcke approximations of the failure probability with the ISEE simulation results. In this case, the expected number of out-crossings and the Poisson approximation are practically coincident and their difference with the ISEE simulation results are small than in the previous cases. The Vanmarcke approximation provides values almost coincident to the ISEE results, while the modified Vanmarcke approximation slightly underestimates the failure probability.

Table 9.1 provides the values of the time-variant failure probability estimated using the Poisson, Vanmarcke and modified Vanmarcke approximations and the ISEE simulation relative to a linear elastic SDOF system with natural period $T_0 = 0.5s$, subjected to a white noise excitation and with at rest initial conditions. Results are given for different normalized thresholds ($\zeta / \sigma_{X\infty} = 2.0, 2.5, 3.0, 4.0$), different damping ratios (ξ = 1%, 5%, 10%) and different instants of time (normalized in terms of the natural period, i.e., $T / T_0 = 5, 10$). From the results given in Table 9.1, the following observations can be made: (1) the two Vanmarcke approximations provide failure probability estimates which are consistently closer to the ISEE simulation results; (2) the modified Vanmarcke approximation performance in estimating the probability of failure is better for increasing time intervals of analysis; (3) the relative performance of the two Vanmarcke approximations in estimating the probability of failure depends on both the order of magnitude of the failure probability (for small failure probability values, i.e., $P_f \leq 10^{-4}$, the Vanmarcke approximation performs better than the modified Vanmarcke approximation) and the

value of the damping ratio ξ (for $\xi = 5\%$, the modified Vanmarcke approximation performs better than the Vanmarcke approximation, for $\xi = 10\%$, the Vanmarcke approximation performs better than the modified Vanmarcke approximation, for $\xi = 1\%$ the relative performance changes for different time instants of analysis and magnitude of the failure probability).

9.4.2 Three-dimensional unsymmetrical building (linear elastic MDOF system)

An idealized three-dimensional unsymmetrical building is considered as linear MDOF system and is shown in Fig. 9.10. This building consists of three floor diaphragms, assumed infinitely rigid in their own plane, supported by wide flange steel columns of size W14x145. Each floor diaphragm is assumed to be made of reinforced concrete with a weight density of 36kN/m^3 and a depth of 18cm. The axial deformations of the columns are neglected. The modulus of elasticity of steel is 200GPa. The motion of each floor diaphragm is completely defined by three DOFs defined at its center of mass, namely the relative displacements with respect to the ground in the x-direction, $U_{X_i}(t)$, in the y-direction, $U_{Y_i}(t)$, and the rotation about the vertical z-axis, $\theta_{Z_i}(t)$. The earthquake ground motion excitation is assumed to act at 45 degrees with respect to the x-axis and is modeled as a white noise with spectral power density $\phi_0 = 1.0\text{m}^2/\text{s}^3$. Both classically and non-classically damped structural models are considered. For the case of classical damping, each modal damping ratio is taken as 2%. To physically realize the non-classical damping case, diagonal viscous damping elements (fluid viscous braces) are added as shown in Fig. 9.10. The damping coefficient of each viscous damping element is taken as

$0.1 kN \cdot s/mm$. The undamped natural circular frequencies of this building are shown in Table 9.2.

Figs. 9.11 through 9.25 show some selected results for the time-variant reliability of the considered structure before and after the application of the viscous dampers. Three quantities are considered: the horizontal displacement, U_{X_3}, at the third floor in the x-direction (Figs. 9.11 through 9.15), which is the weak direction of the building along which the dampers are active, the horizontal displacement, U_{Y_3}, at the third floor in the y-direction (Figs. 9.16 through 9.20), which is the strong direction of the building, and the horizontal drift, $\Delta_{X_3} = U_{X_3} - U_{X_2}$, between the third and second floor in the x-direction (Figs. 9.21 through 9.25).

Fig. 9.11 plots the time histories of the normalized variances and bandwidth parameters of U_{X_3} of both the classically (subscript 'u') and non-classically (subscript 'd') damped three dimensional unsymmetrical building (3-D UB). The normalization of the variances is obtained dividing them by the value of the variance of U_{X_3} at time $T = 5.0s$ for the classically damped system. The addition to the system of the viscous dampers produces two distinct effects on the variance of U_{X_3}: (1) the variance is strongly reduced (at time $T = 5.0s$, $\sigma_d^2/\sigma_u^2 = 0.39$), and (2) stationarity conditions are approximately reached in a shorter analysis time. The effects of the viscous dampers on the time histories of the bandwidth parameter are the reduction of the time before stationarity is reached and reduction of the stationary value, which are consistent with the increase of

damping of the system (see Barbato and Conte 2007, for details on the effects of different levels of damping on the time-variant bandwidth parameter).

Fig. 9.12 shows the time-variant mean out-crossing rate, Vanmarcke and modified Vanmarcke hazard functions for the DOF U_{X_3} corresponding to a deterministic threshold $\zeta = 0.456\text{m}$ (i.e., a displacement over height ratio equal to 4%) and relative to the classically damped 3-D system. The two Vanmarcke hazard functions assume values considerably lower than the mean out-crossing rate function. Fig. 9.13 compares, for the same analysis case considered in Fig. 9.12, analytical approximations of the failure probability (expected number of out-crossings, E[N], Poisson approximation, $P_{f,P}$, Vanmarcke approximation, $P_{f,VM}$, and modified Vanmarcke approximation, $P_{f,mVM}$) with simulation results obtained using the ISEE method, $P_{f,sim}$. In this specific case, the simulation results are almost in perfect agreement with the modified Vanmarcke approximation. The failure probability after 5.0s second of analysis is of the order of 1%. This failure probability (conditional to the given magnitude of ground motion excitation) is quite large and can be considered unsatisfactory for the given threshold, thus suggesting the retrofitting of the building using the viscous damping system previously described.

Figs. 9.14 and 9.15 provides the same quantities shown in Figs. 9.12 and 9.13, respectively, for the case of non-classically damped structure. The mean out-crossing rate and hazard functions are four orders of magnitude smaller and the failure probability estimates seven orders of magnitude smaller than for the classically damped system. The Vanmarcke approximation provides the better agreement with the ISEE results, slightly

underestimating the time-variant failure probability. It is noteworthy the efficacy of the use of the viscous dampers for the considered building in reducing the probability of the DOF U_{X_3} out-crossing the threshold $\zeta = 0.456\text{m}$ when subjected to the given base excitation.

Fig. 9.16 plots the time histories of the normalized variances and bandwidth parameters of U_{Y_3} of both the classically and non-classically damped three dimensional unsymmetrical building. The normalization of the variances is again obtained dividing them by the value of the variance of U_{Y_3} at time $T = 5.0\text{s}$ for the classically damped system. For this degree of freedom, the effects of the application of the viscous dampers are very small and consist in a small reduction of the response variance, while the changes in the time history of the bandwidth parameter are not visible at the scale used in the figure. This result was expected, since the action of the viscous dampers is directed only along the x-direction and affects the y-direction only indirectly, through the coupling with the torsional modes of vibration.

Figs. 9.17 and 9.19 plot the time-variant mean out-crossing rate, Vanmarcke and modified Vanmarcke hazard functions for the DOF U_{Y_3} corresponding to a deterministic threshold $\zeta = 0.456\text{m}$ and relative to the classically and non-classically damped 3-D system, respectively. Figs. 9.18 and 9.20 compare the analytical approximations with the ISEE simulation of the failure probability for the DOF U_{Y_3} and threshold $\zeta = 0.456\text{m}$ relative to the classically and non-classically damped 3-D system, respectively. In this case, out-crossing rate, hazard functions and failure probability are very small already for

the classically damped system and reduce to less than half for the non-classically damped building. The simulation results are always contained between the estimates from Vanmarcke and modified Vanmarcke approximation.

Fig. 9.21 shows the time histories of the normalized variances and bandwidth parameters of Δ_{X_3} for both the classically and non-classically damped 3-D UB. The normalization of the variances is obtained dividing them by the value of the variance of Δ_{X_3} at time $T = 5.0s$ relative to the classically damped system. Computation of variances and bandwidth parameters for drifts and any other response linearly related to displacement and velocity responses can be performed directly from the variances and bandwidth parameters of the latter quantities (see Barbato and Conte, 2007). The normalized variances and bandwidth parameters of Δ_{X_3} present characteristics very similar to the corresponding quantities shown in Fig. 9.11 for DOF U_{X_3}: (1) the displacement variances for the non-classically damped structure are much lower than for the classically damped structure, (2) stationarity is reached faster by the non-classically damped building, and (3) the stationary value of the bandwidth parameter is lower for the non-classically damped building than for the classically damped one.

Figs. 9.22 and 9.24 plot the time-variant mean out-crossing rate, Vanmarcke and modified Vanmarcke hazard functions for the Δ_{X_3} corresponding to a deterministic threshold $\zeta = 0.114m$ (corresponding to an interstory drift equal to 3% of the storey height) and relative to the classically and non-classically damped 3-D system, respectively. Figs. 9.23 and 9.25 compare the analytical approximations with the ISEE simula-

tion of the failure probability for the Δ_{X_3} and threshold $\zeta = 0.114\text{m}$ relative to the classically and non-classically damped 3-D system, respectively. For the classically damped case, all the analytical approximations overestimate the failure probability obtained via ISEE simulation, while, for non-classically damped case, the ISEE simulation results are contained between the Vanmarcke and modified Vanmarcke appoximations. Also for the response quantity Δ_{X_3}, the use of viscous dampers produces a considerable reduction of the time-variant failure probability (five orders of magnitude).

From this second application example, it can be concluded that the two Vanmarcke approximations provide better estimates than the Poisson approximation of the time-variant failure probability of linear elastic systems subjected to white noise excitation and with at rest initial conditions.

9.5 CONCLUSIONS

This Chapter presents the application of spectral characteristics of nonstationary random processes to the time-variant first passage problem in structural reliability. The first passage problem consists in computing the probability of exceeding a given deterministic time-invariant threshold by a quantity (linearly) related to the response displacements and velocities (as absolute displacement, relative displacement, elastic force, etc.) of a given structural system. This quantity is generally known as failure probability.

The so-called Vanmarcke failure probability approximations (i.e., Vanmarcke and modified Vanmarcke approximation) are computed, by numerical integration of the closed-forms of the corresponding hazard functions, for linear elastic single- (SDOF) and

multi-degree-of-freedom (MDOF) systems subjected to a white noise base excitation and with at rest initial conditions. The closed-form of the two Vanmarcke hazard function are obtained using the closed-form solutions, derived and presented in Chapter 8, for the time-variant bandwidth parameter relative to nonstationary stochastic process representing the displacement response. These approximate solutions are compared with the well-known Poisson approximation and simulation results obtained via the Importance Sampling using Elementary Events (ISEE) method for two application examples: (1) linear elastic SDOF systems, for which a parametric study is performed considering different natural periods, damping ratios and threshold levels, and (2) an idealized yet realistic three dimensional unsymmetrical steel building subjected to a white noise base excitation, acting along a direction inclined with respect to the principal axes of the building itself. For this second application example, the retrofit of the given building with viscous dampers is also considered, serving a two-fold purpose: (1) to illustrate the use of the newly available closed-form approximations of the failure probability for non-classically damped linear elastic systems, and (2) to show an example of practical use in structural engineering of the presented analytical derivations.

From the results presented in this study, it can be concluded that the two Vanmarcke approximations provide greatly improved estimates of the failure probability for the first passage problem when compared with the simpler Poisson approximation. On the other hand, the relative performance of the Vanmarcke and modified Vanmarcke approximation can be evaluated only on a case by case basis and deserves further studies to be better understood.

Table 9.1 Time-variant failure probability for a SDOF system with natural period $T_0 = 0.5$s subjected to a white noise and with at rest initial conditions

damping ratio	ζ	2.0σ		2.5σ		3.0σ		4.0σ	
	T_{max}	$5T_0$	$10T_0$	$5T_0$	$10T_0$	$5T_0$	$10T_0$	$5T_0$	$10T_0$
1%	P	0.0300	0.3388	2.01e-3	0.0643	8.06e-5	7.66e-3	2.88e-8	3.82e-5
	VM1	0.0177	0.1659	1.30e-3	0.0315	5.66e-5	4.07e-3	2.27e-8	2.37e-5
	VM2	0.0145	0.1286	1.08e-3	0.0242	4.75e-5	3.14e-3	1.95e-8	1.86e-5
	ISEE	0.0162	0.1229	1.35e-3	0.0246	5.52e-5	3.26e-3	2.51e-8	2.19e-5
5%	P	0.5073	0.8684	0.1711	0.4567	0.0379	0.1337	7.65e-4	3.79e-3
	VM1	0.3457	0.6779	0.1112	0.3006	0.0256	0.0866	5.80e-4	2.74e-3
	VM2	0.3006	0.6065	0.0954	0.2575	0.0221	0.0735	5.08e-4	2.37e-3
	ISEE	0.3233	0.6011	0.0996	0.2654	0.0250	0.0763	6.11e-4	2.72e-3
10%	P	0.6411	0.9072	0.2650	0.5261	0.0698	0.1675	1.91e-3	5.25e-3
	VM1	0.5059	0.7981	0.1957	0.4044	0.0527	0.1262	1.59e-3	4.31e-3
	VM2	0.4619	0.7520	0.1761	0.3671	0.0475	0.1137	1.46e-3	3.94e-3
	ISEE	0.5214	0.8009	0.2030	0.4051	0.0539	0.1224	1.71e-3	4.67e-3

Table 9.2 Undamped Natural Frequencies and Description of Mode Shapes of the Three-Dimensional Unsymmetrical Building Example

Mode #	ω_i [rad/s]	Period [s]	Mode Shape Description
1	15.97	0.393	x-translation
2	24.12	0.261	y-translation + torsion
3	36.56	0.172	x-translation
4	41.21	0.153	y-translation + torsion
5	56.74	0.111	y-translation + torsion
6	56.98	0.110	x-translation
7	73.88	0.085	y-translation + torsion
8	95.15	0.066	y-translation + torsion
9	127.69	0.049	y-translation + torsion

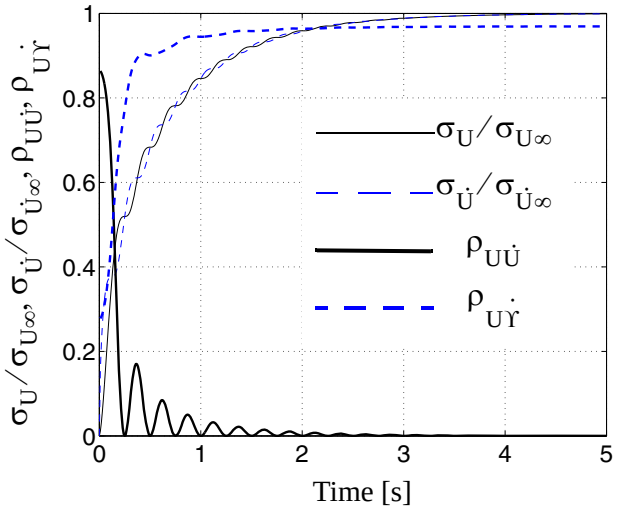

Figure 9.1 Second-order statistical moments of the response of a linear elastic SDOF system with natural period $T_0 = 0.5$s and damping ratio $\xi = 0.05$.

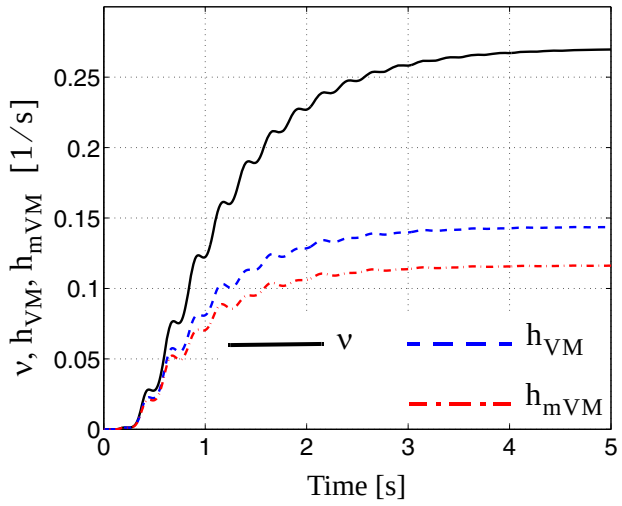

Figure 9.2 Mean up-crossing rate, Vanmarcke hazard and modified Vanmarcke hazard functions of the response of a linear elastic SDOF system with natural period $T_0 = 0.5$s and damping ratio $\xi = 0.05$ relative to a threshold level $\zeta = 2.0 \cdot \sigma_{X\infty}$.

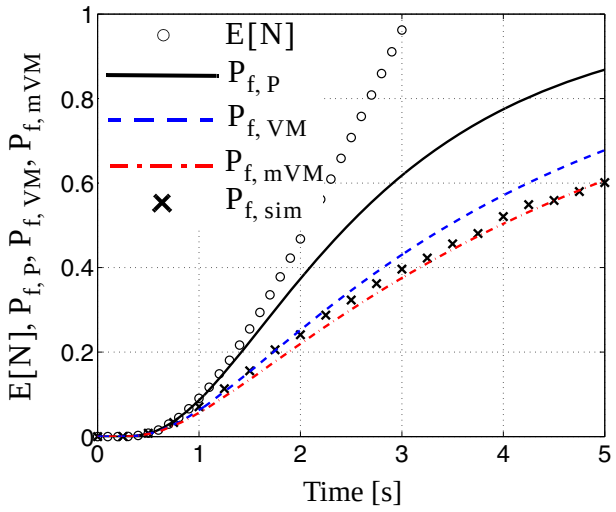

Figure 9.3 Approximations of probability of failure of a linear elastic SDOF system with natural period $T_0 = 0.5s$ and damping ratio $\xi = 0.05$ relative to a threshold level $\zeta = 2.0 \cdot \sigma_{X\infty}$.

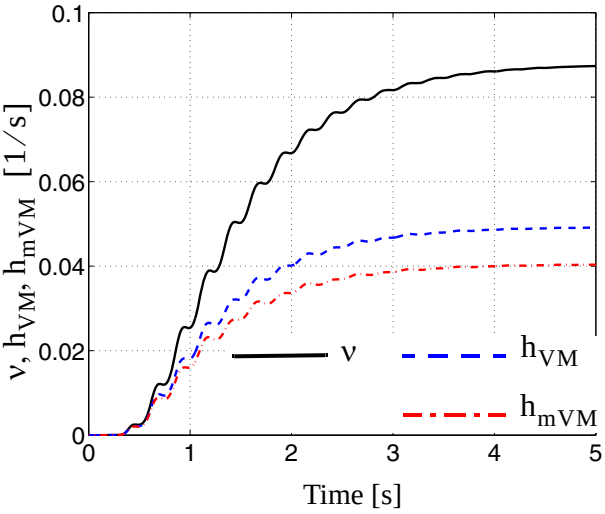

Figure 9.4 Mean up-crossing rate, Vanmarcke hazard and modified Vanmarcke hazard functions of the response of a linear elastic SDOF system with natural period $T_0 = 0.5s$ and damping ratio $\xi = 0.05$ relative to a threshold level $\zeta = 2.5 \cdot \sigma_{X\infty}$.

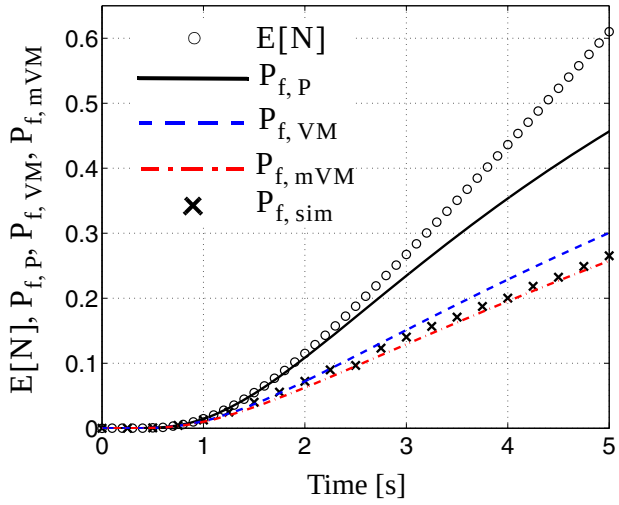

Figure 9.5 Approximations of probability of failure of a linear elastic SDOF system with natural period $T_0 = 0.5s$ and damping ratio $\xi = 0.05$ relative to a threshold level $\zeta = 2.5 \cdot \sigma_{X\infty}$.

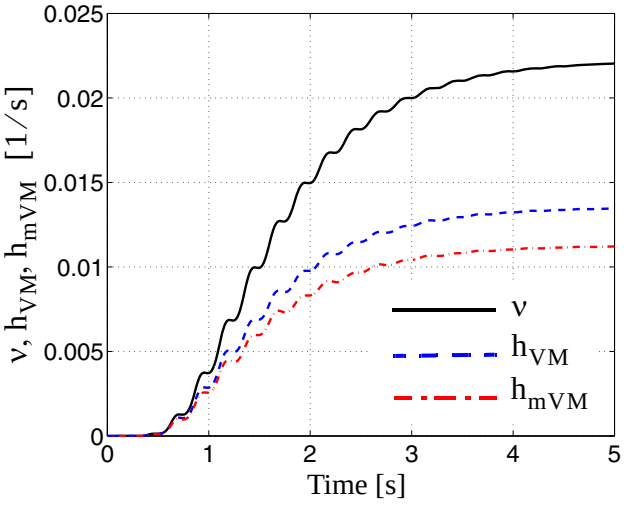

Figure 9.6 Mean up-crossing rate, Vanmarcke hazard and modified Vanmarcke hazard functions of the response of a linear elastic SDOF system with natural period $T_0 = 0.5s$ and damping ratio $\xi = 0.05$ relative to a threshold level $\zeta = 3.0 \cdot \sigma_{X\infty}$.

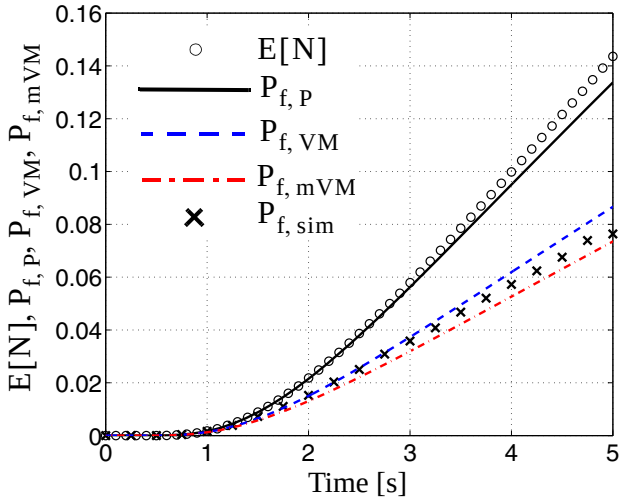

Figure 9.7 Approximations of probability of failure of a linear elastic SDOF system with natural period $T_0 = 0.5s$ and damping ratio $\xi = 0.05$ relative to a threshold level $\zeta = 3.0 \cdot \sigma_{X\infty}$.

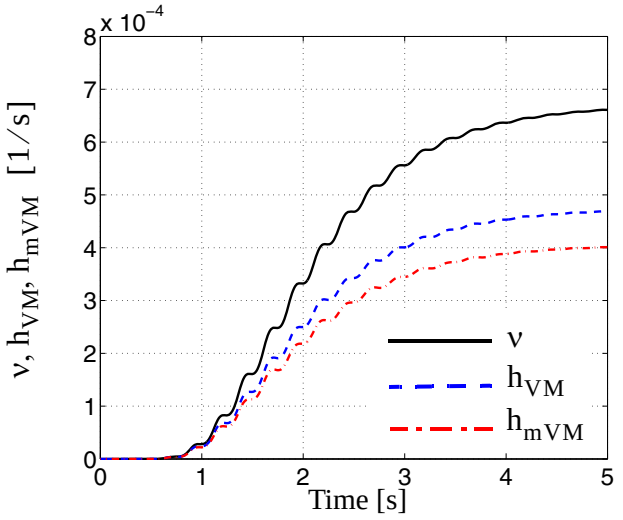

Figure 9.8 Mean up-crossing rate, Vanmarcke hazard and modified Vanmarcke hazard functions of the response of a linear elastic SDOF system with natural period $T_0 = 0.5s$ and damping ratio $\xi = 0.05$ relative to a threshold level $\zeta = 4.0 \cdot \sigma_{X\infty}$.

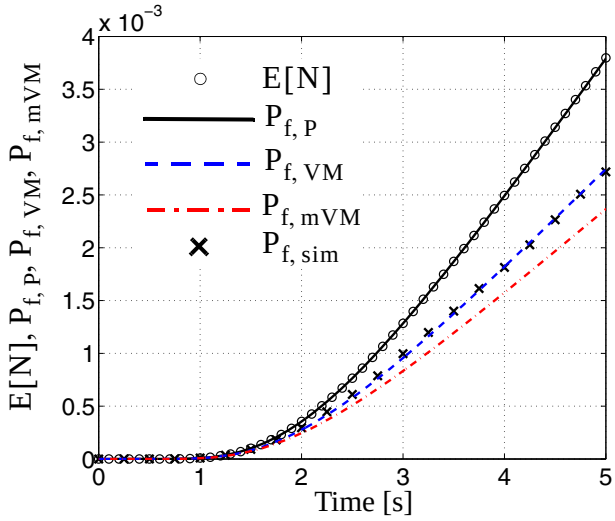

Figure 9.9 Approximations of probability of failure of a linear elastic SDOF system with natural period $T_0 = 0.5s$ and damping ratio $\xi = 0.05$ relative to a threshold level $\zeta = 4.0 \cdot \sigma_{X\infty}$.

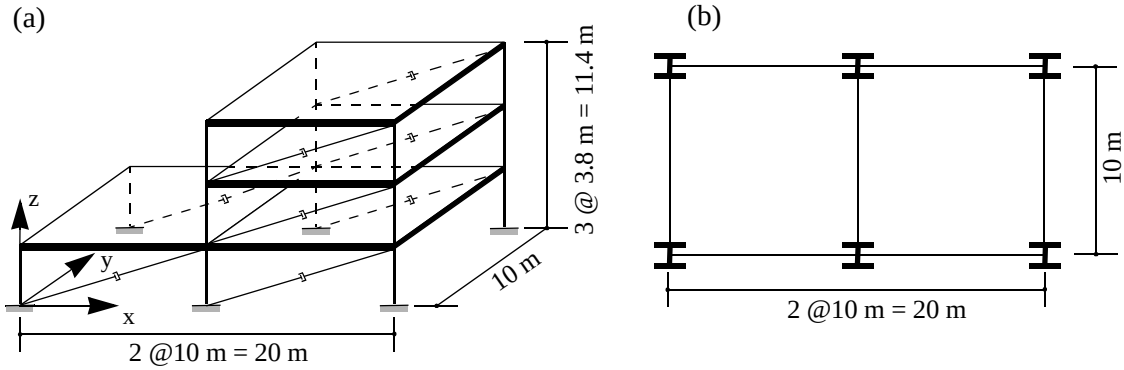

Figure 9.10 Three dimensional unsymmetrical building: (a) geometry, (b) floor view.

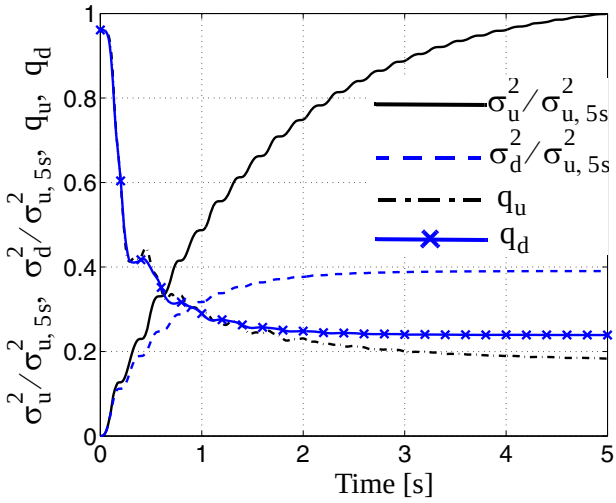

Figure 9.11 Normalized variances and bandwidth parameters of the horizontal displacement in the x-direction at the third floor (DOF U_{X_3}) for the classically (subscript 'u') and non-classically (subscript 'd') damped three dimensional unsymmetrical building (3-D UB).

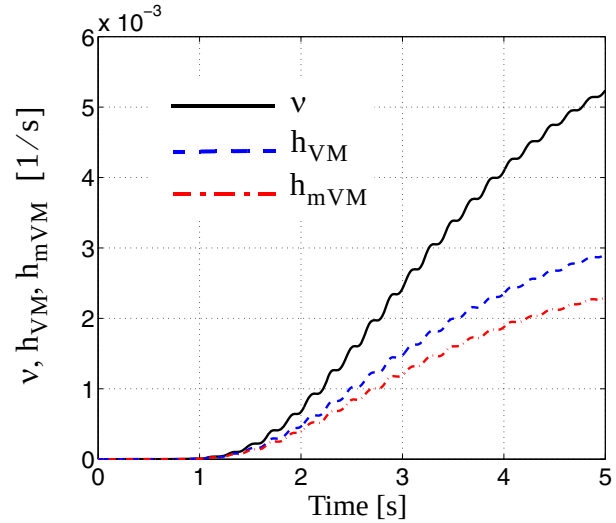

Figure 9.12 Time-variant mean out-crossing rate, Vanmarcke and modified Vanmarcke hazard functions for the DOF U_{X_3} corresponding to a deterministic threshold $\zeta = 0.456\text{m}$ (classically damped 3-D UB).

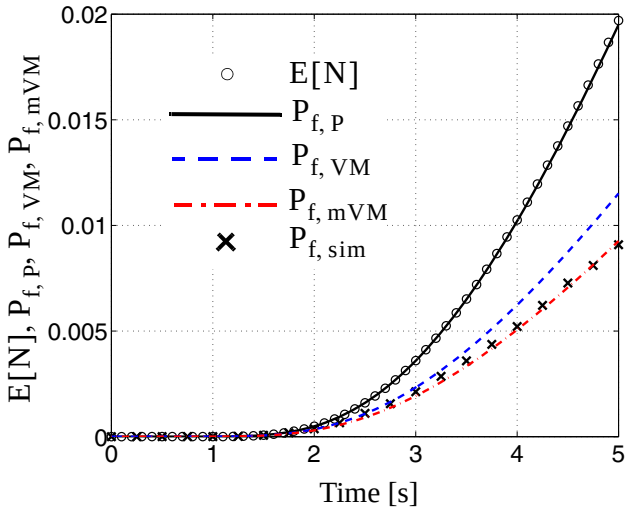

Figure 9.13 Comparison of analytical approximation with ISEE estimate of the time-variant failure probability for DOF U_{X_3} and threshold $\zeta = 0.456\text{m}$ (classically damped 3-D UB).

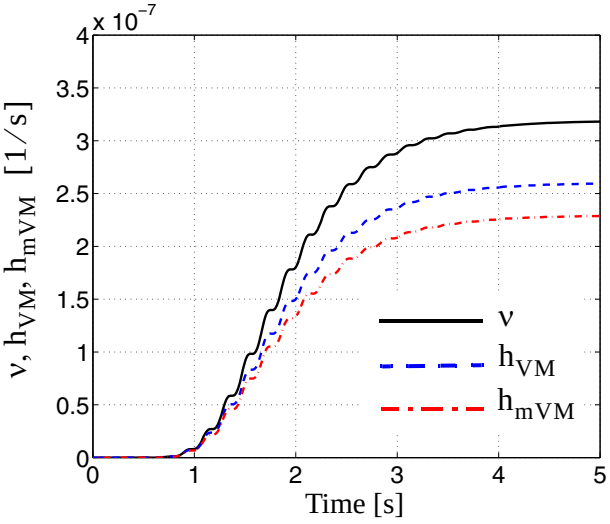

Figure 9.14 Time-variant mean out-crossing rate, Vanmarcke and modified Vanmarcke hazard functions for the DOF U_{X_3} corresponding to a deterministic threshold $\zeta = 0.456\text{m}$ (non-classically damped 3-D UB).

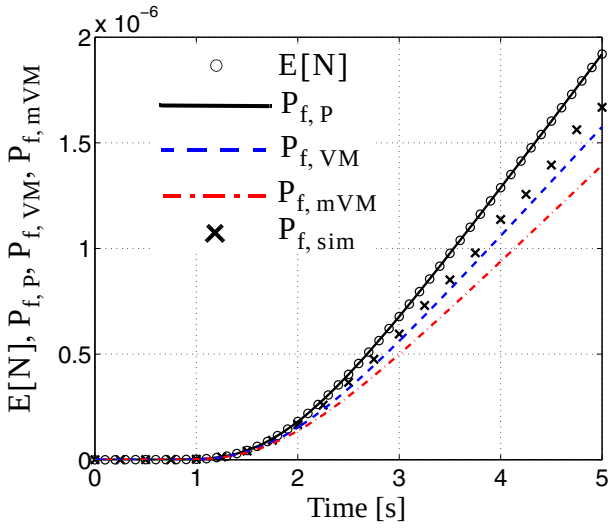

Figure 9.15 Comparison of analytical approximation with ISEE estimate of the time-variant failure probability for DOF U_{X_3} and threshold ζ = 0.456m (non-classically damped 3-D UB).

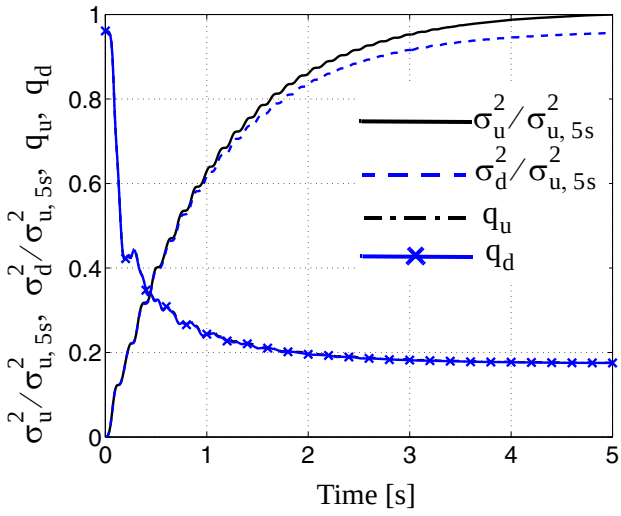

Figure 9.16 Normalized variances and bandwidth parameters of the horizontal displacement in the y-direction at the third floor (DOF U_{Y_3}) for the classically (subscript 'u') and non-classically (subscript 'd') damped 3-D UB.

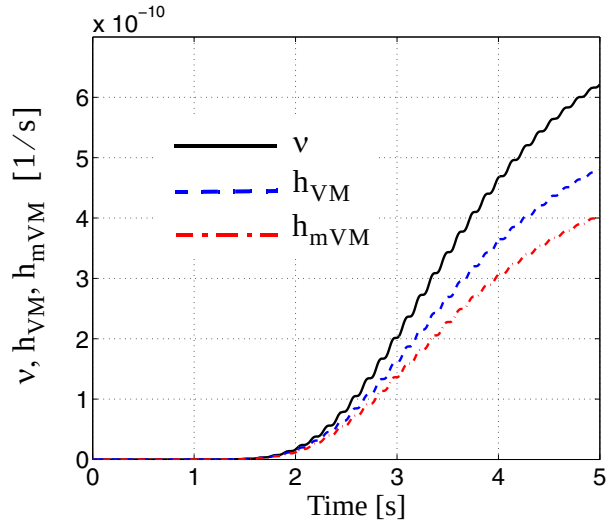

Figure 9.17 Time-variant mean out-crossing rate, Vanmarcke and modified Vanmarcke hazard functions for the DOF U_{Y_3} corresponding to a deterministic threshold $\zeta = 0.456\text{m}$ (classically damped 3-D UB).

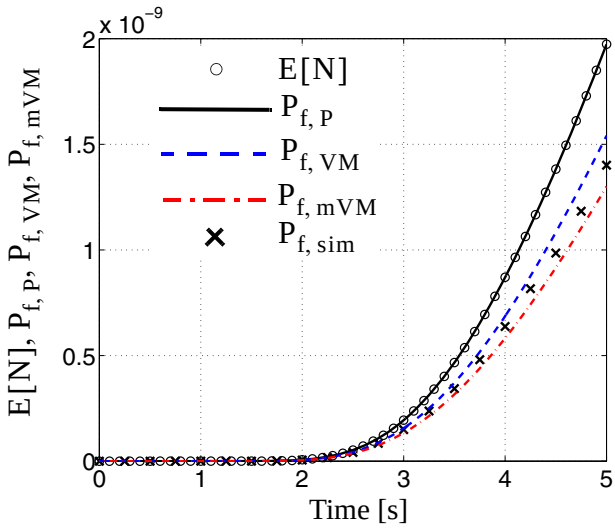

Figure 9.18 Comparison of analytical approximation with ISEE estimate of the time-variant failure probability for DOF U_{Y_3} and threshold $\zeta = 0.456\text{m}$ (classically damped 3-D UB).

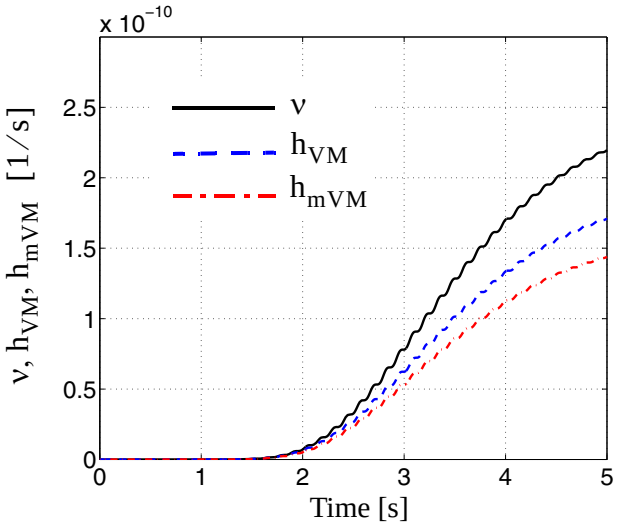

Figure 9.19 Time-variant mean out-crossing rate, Vanmarcke and modified Vanmarcke hazard functions for the DOF U_{Y_3} corresponding to a deterministic threshold $\zeta = 0.456\text{m}$ (non-classically damped 3-D UB).

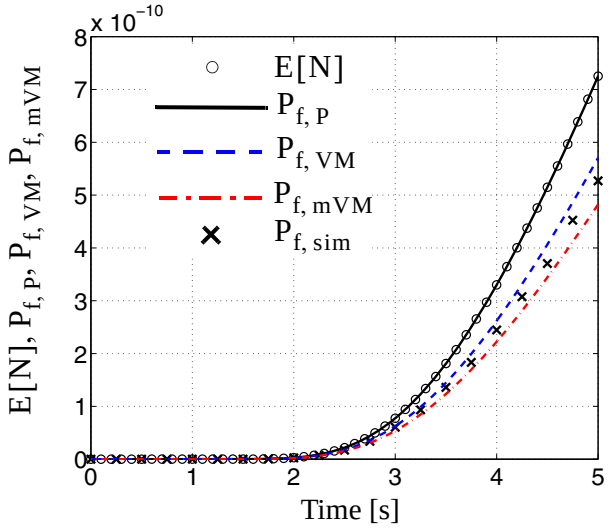

Figure 9.20 Comparison of analytical approximation with ISEE estimate of the time-variant failure probability for DOF U_{Y_3} and threshold $\zeta = 0.456\text{m}$ (non-classically damped 3-D UB).

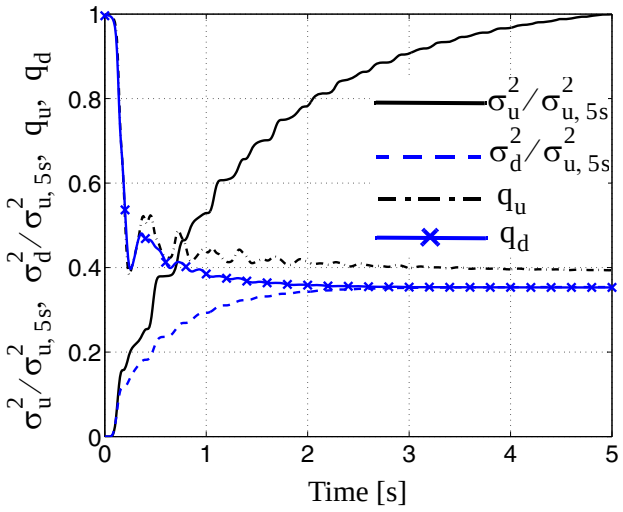

Figure 9.21 Normalized variances and bandwidth parameters of the horizontal drift in the x-direction between third and second floor ($\Delta_{X_3} = U_{X_3} - U_{X_2}$) for the classically (subscript 'u') and non-classically (subscript 'd') damped three dimensional unsymmetrical building.

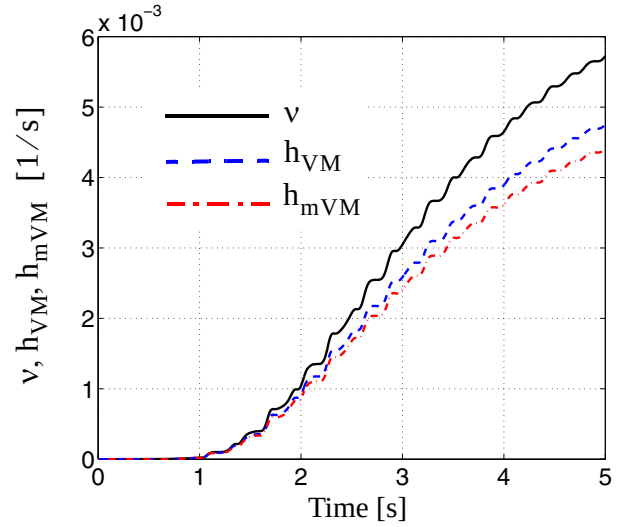

Figure 9.22 Time-variant mean out-crossing rate, Vanmarcke and modified Vanmarcke hazard functions for Δ_{X_3} corresponding to a deterministic threshold $\zeta = 0.114\text{m}$ (classically damped 3-D UB).

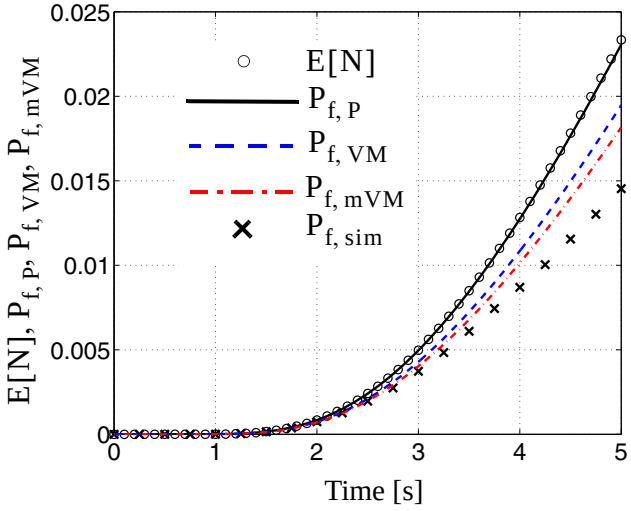

Figure 9.23 Comparison of analytical approximation with ISEE estimate of the time-variant failure probability for Δ_{X_3} corresponding to a deterministic threshold $\zeta = 0.114\text{m}$ (classically damped 3-D UB).

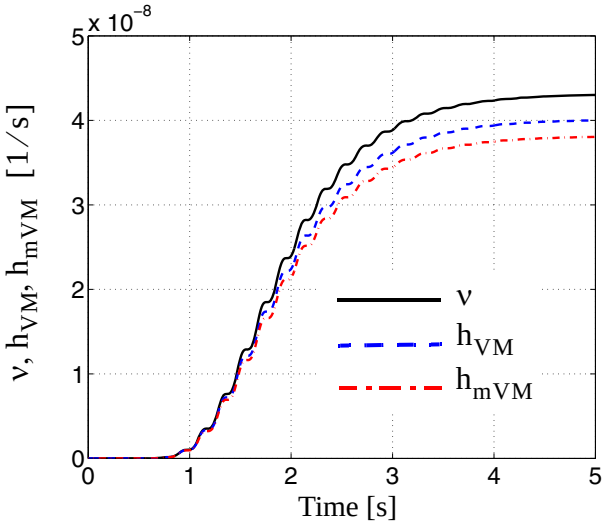

Figure 9.24 Time-variant mean out-crossing rate, Vanmarcke and modified Vanmarcke hazard functions for Δ_{X_3} corresponding to a deterministic threshold $\zeta = 0.114\text{m}$ (non-classically damped 3-D UB).

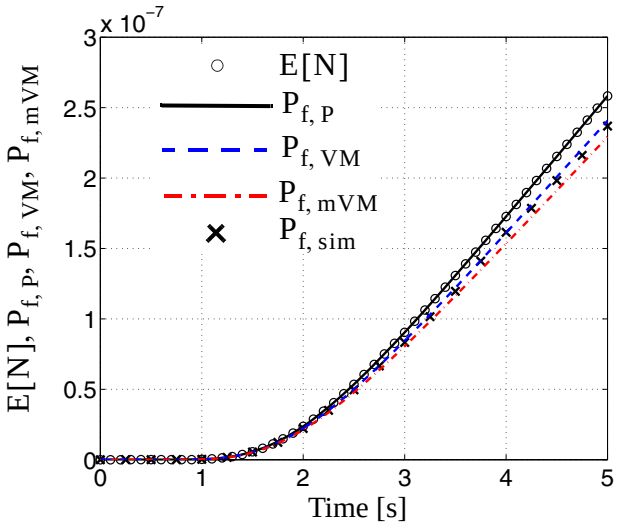

Figure 9.25 Comparison of analytical approximation with ISEE estimate of the time-variant failure probability for Δ_{X_3} corresponding to a deterministic threshold $\zeta = 0.114\text{m}$ (non-classically damped 3-D UB).

REFERENCES

AASHTO (1998) “AASHTO LRFD bridge design specification”, American Association of State Highway and Transportation Officials, 2nd ed.

ATC-55 (2005) “Evaluation and improvement of inelastic seismic analysis procedures.” Advanced Technology Council, Redwood City, CA.

ATC-58 (2005) “Development of next-generation performance-based seismic design procedures for new and existing buildings.” Advanced Technology Council, Redwood City, CA.

Au S. K., Beck J.L. (2001) “First excursion probabilities for linear systems by very efficient importance sampling.” *Probabilistic Engineering Mechanics*, 16:193-207.

Barbato M., Conte J.P. (2007) “Spectral characteristics of non-stationary random processes: theory and applications to linear structural models” *Probabilistic Engineering Mechanics*, submitted.

BSSC (2004) “The 2003 NEHRP recommended provisions for new buildings and other structures. Part 1: provisions (FEMA 450).” Building Seismic Science Council, http://www.bssconline.org/

Conte J.P. (1992) “Effects of Earthquake Frequency Nonstationarity on Inelastic Structural Response.” *Proceedings* of the 10th World Conference on Earthquake Engineering, Madrid, Spain. Rotterdam: AA Balkema, 1992: 3645-3651.

Cornell C.A., Krawinkler H. (2000) “Progress and challenges in seismic performance assessment.” *PEER Center News*, Spring 2000.

Corotis R.B., Vanmarcke E.H., Cornell C.A. (1972) “First passage of nonstationary random processes”. *Journal of the Engineering Mechanics Division* (ASCE), 98(EM2):401-414.

Cramer H., Leadbetter M.R. (1967) *Stationary and related stochastic process.* New York,

NY: Wiley.

Crandall S.H. (1970) “First-crossing probabilities of the linear oscillator”. *Journal of Sounds and Vibrations*, 12(3):285-299.

Di Paola M. (1985) “Transient spectral moments of linear systems”. *SM Archives*, 10:225-243.

Hagen O., Tvedt L. (1991) “Vector process out-crossing as parallel system sensitivity measure” *Journal of Engineering Mechanics* (ASCE), 117(10):2201–2220.

ICC (2003) “International Building Code 2003.” International Code Council, CD-Rom.

Lin Y.K. (1976) “Probabilistic Theory of Structural Dynamics”. New York, NY: McGraw-Hill, 1967, Huntington: Krieger Pub., 1976.

Lutes L.D., Sarkani S. (1997) *Stochastic analysis of structural and mechanical vibration*. Upple Saddle River, NJ: Prentice Hall.

Michaelov G., Sarkani S., Lutes L.D. (1999a). “Spectral characteristics of nonstationary random processes - a critical review”. *Structural Safety*, 21:223-244.

Michaelov G., Sarkani S., Lutes L.D. (1999b). “Spectral characteristics of nonstationary random processes- response of a simple oscillator”. *Structural Safety*, 21:245-267.

Moehle J., Deierlein G.G. (2004) “A framework methodology for Performance-Based Earthquake Engineering.” *Proceedings*, 13th World Conference on Earthquake Engineering, Vancouver, Canada, August 1-6, 2004.

Papadimitriou C. (1990) “Stochastic characterization of strong ground motion and applications to structural response”. *Report No. EERL 90-03*, California Institute of Technology, Pasadena, CA.

Porter K.A. (2003) “An overview of PEER’s performance-based earthquake engineering

methodology." *Proceedings*, 9th International Conference on Applications of Statistics and Probability (ICASP9) in Civil Engineering, San Francisco, CA, July 2003, Der Kiureghian A. et al., Eds., 2:973-980.

Priestley M.B. (1987) *Spectral Analysis and Time Series, Volume 1: Univariate Series, Volume 2: Multivariate Series, Prediction and Control.* London: Academic Press, Fifth Printing.

Rice S. O. (1944) "Mathematical analysis of random noise." *Bell System Technical Journal*, 23:282.

Rice S. O. (1945) "Mathematical analysis of random noise." *Bell System Technical Journal*, 24:46.

Vanmarcke E.H. (1975) "On the distribution of the first-passage time for normal stationary random processes." *Journal of Applied Mechanics* (ASME), 215-220.

Wen Y. K. (1987) "Approximate methods for nonlinear time-variant reliability analysis". *Journal of Engineering Mechanics* (ASCE), 113(12):1826-1839.

Yeh C.-H., Wen Y.K. (1990) "Modeling of Nonstationary Ground Motion and Analysis of Inelastic Structural Response." *Structural Safety*, 8:281-298.

CHAPTER 10

PROBABILISTIC PUSHOVER ANALYSIS OF STRUCTURAL SYSTEMS

10.1 INTRODUCTION

Evaluation of the uncertainty in the computed structural response of civil structures is of paramount importance in order to improve safety and optimize the use of economic resources. In the last two decades, significant research has been devoted to propagating uncertainties from modeling parameters to structural response through the finite element method (Dong et al. 1987; Der Kiureghian and Ke 1988; Bjerager 1990; Ghanem and Spanos 1991; To 2001). Probabilistic methodologies for describing the statistics of the random response of structures with uncertain properties or/and subjected to random loading have been developed and interfaced with the widely used and accepted finite element method. Some of these methods, used in particular for estimating the first- and second-moment statistics, are the Stochastic Equivalent Linearization Method (Crandall 2006; Ghanem and Spanos 1991) and the Stochastic Perturbation Method (Bolotin 1968; Grigoriou 2000).

This paper presents a comparison of two different probabilistic response analysis methods based on non-linear finite element response simulation. A Mean-Centered First-Order Second-Moment (FOSM) approximation (Haukaas and Der Kiureghian 2004) is used to estimate first- and second-moment statistics of finite element response quantities

and these estimates are compared with results obtained using Monte Carlo simulation (MCS) (Liu 2001). Finite element response sensitivities required by FOSM analysis are computed through the Direct Differentiation Method (DDM) (Kleiber et al. 1997) and through forward and backward finite difference analysis using relatively large perturbations of the uncertain parameters. Only material non-linearities and uncertainties in material parameters are considered in this study.

The FOSM is applied to advanced non-linear finite element models of realistic structures and Soil-Structure-Foundation-Interaction (SFSI) systems subjected to non-linear quasi-static pushover analysis. Non-linear quasi-static pushover analysis is a popular procedure in the earthquake engineering community, since it allows one to gain insight into the non-linear seismic response behavior of structures using simplified analysis techniques. Even though this procedure presents several shortcomings and is based more on intuition than on rigorous physical and mathematical modeling of the problem, it has been recognized by international codes (ATC 1996; FEMA 1997) as a possible substitute, under certain conditions, for non-linear dynamic analysis of structural systems.

10.2 FINITE ELEMENT RESPONSE SENSITIVITY ANALYSIS

Finite element response sensitivity analysis is a crucial ingredient in several subfields of structural engineering, such as structural optimization, structural identification, finite element model updating, reliability analysis and probabilistic response analysis. For real-world problems, response simulation (computation of response quantities $\mathbf{r} = [r_1 \; r_2 \; \ldots \; r_m]^T$ for given values of a set of random/variable parameters

$\boldsymbol{\vartheta} = [\theta_1 \ \theta_2 \ \ldots \ \theta_m]^T$) is typically performed using advanced mechanics-based non-linear computational models developed based on the finite element method (Cook et al. 1989). Finite element sensitivity analysis requires augmenting existing (deterministic) finite element formulations for response-only calculation, with the capability of computing the response sensitivities to parameters $\boldsymbol{\vartheta}$, defined as the gradient of the response quantities $\mathbf{r}$ with respect to parameters $\boldsymbol{\vartheta}$, i.e., $\nabla_{\boldsymbol{\vartheta}}\mathbf{r}$, with $[\nabla_{\boldsymbol{\vartheta}}\mathbf{r}]_{ij} = \partial r_i / \partial \theta_j$, $i = 1, 2, \ldots, m$ and $j = 1, 2, \ldots, n$.

Several methods are available for computing finite element response sensitivities, such as the Forward/Backward Finite Difference Method (F-FDM/B-FDM) and the Direct Differentiation Method (DDM) (Kleiber et al. 1997). The F-FDM/B-FDM consist of performing, in addition to the finite element analysis with all sensitivity parameters $\boldsymbol{\vartheta}$ set at their nominal values, a finite element response analysis for each parameter θ_i ($i = 1, ..., n$) in which its nominal value is perturbed by a small but finite amount. Each response sensitivity is then obtained as the ratio of the variation of the response quantity of interest over the parameter perturbation. This method is computationally expensive and approximate in nature and can suffer from numerical inaccuracies (Haftka and Gurdal 1993; Conte et al. 2003, 2004; Zona et al. 2005). On the other hand, the DDM is an accurate and efficient way to perform response sensitivity analysis of finite element models with non-linear hysteretic behavior. This method consists of differentiating analytically the space- and time-discretized equations of motion/equilibrium of the finite element model of the structural system considered. It involves (1) computing the derivatives (with respect to the parame-

ters ϑ) of the element and material history/state variables conditional on fixed nodal displacements at the structure level (conditional sensitivities), (2) forming the right-hand-side of the response sensitivity equation at the structure level, (3) solving the resulting equation for the nodal displacement response sensitivities, and (4) updating the unconditional derivatives of all history/state variables (unconditional sensitivities). For a more detailed explanation of the DDM, the interested reader is referred elsewhere (Kleiber et al. 1997; Conte et al. 1995; Conte 2001; Conte et al. 2003, 2004; Barbato and Conte 2005, 2006; Barbato et al. 2006; Zona et al. 2005, 2006). The response sensitivity computation algorithm affects the various hierarchical layers of finite element response calculation, namely the structure, element, integration point (section for frame elements), and material levels. The advantage of the DDM over the F-FDM/B-FDM is that, at the one-time cost of implementing in a finite element code the algorithms for analytical differentiation of the numerical response, the response sensitivities to any of the modeling parameters considered can be computed exactly (up to a numerical tolerance defined by the user) at a relatively small fraction (depending on the number of iterations required in the non-linear finite element analysis of the model considered and on the specific implementation, see Lupoi et al. 2006) of the cost of an additional finite element analysis, which is required for computing response sensitivities to each of the parameters considered when the F-FDM/B-FDM is employed.

Both the DDM and the F-FDM/B-FDM with small perturbations are intended to compute the "local" response sensitivities of the finite element model of the structure under consideration (the DDM in an analytical way, and the F-FDM/B-FDM in an approx-

imate way). “Global” response sensitivities can be computed through Forward/Backward Finite Difference (FFD/BFD) analysis using a relatively large perturbation of the sensitivity parameter (e.g., perturbation equal to one standard deviation of the random parameter). Such global sensitivities are insensitive to noise in the computed structural response and approximately account for the effect of higher-order terms (of the Taylor series expansion of the response quantities of interest) in the perturbation range (e.g., mean ± 1 standard deviation). They can therefore be used as an alternative to local response sensitivities in probabilistic response analysis. Notice that these global sensitivities do not have the property of “multidimensional averaging” (Saltelli et al. 2000), which is required for proper global sensitivity analysis techniques.

Stand-alone finite element response sensitivities are also invaluable for gaining deeper insight into the effects and relative importance of system and loading parameters in regards to structural response behavior. By scaling the response sensitivities with the nominal (or mean) values or the standard deviations of the considered parameters, the relative importance of each sensitivity parameter in regards to a given structural response quantity can be quantified in a deterministic or probabilistic sense, respectively. This information is of paramount importance, e.g., when design decisions are required or when an efficient experimental program needs to be planned to reduce uncertainties in the modeling parameters of a structure specimen.

10.3 FIRST-ORDER SECOND-MOMENT (FOSM) PROBABILISTIC RESPONSE ANALYSIS

Probabilistic response analysis consists of computing the probabilistic characterization of the response of a specific structure, given as input the probabilistic characterization of material, geometric and loading parameters. An approximate method of probabilistic response analysis is the First-Order Second-Moment (FOSM) method, in which mean values (first-order statistical moments), variances and covariances (second-order statistical moments) of the response quantities of interest are estimated by using a first-order Taylor series expansion of the response quantities in terms of the random or uncertain modeling parameters (Haukaas and Der Kiureghian 2004) about a given point in the space in which the modeling parameters are defined. Thus, this method requires only the knowledge of the first- and second-order statistical moments of the random parameters. It is noteworthy that often statistical information about the random parameters is limited to first and second moments and therefore probabilistic response analysis methods more advanced than FOSM analysis cannot be fully exploited.

In the following, upper case letters $\boldsymbol{\Theta}$, Θ, $\mathbf{R}$ and R will denote random quantities and the corresponding lower case letters $\boldsymbol{\vartheta}$, θ, $\mathbf{r}$ and r will denote specific realizations of the random quantities. Given the vector of n random parameters $\boldsymbol{\Theta}$, defined in a given domain, the corresponding covariance matrix $\boldsymbol{\Sigma}_{\boldsymbol{\Theta}}$ is

$$\boldsymbol{\Sigma}_{\boldsymbol{\Theta}} = [\rho_{ij}\sigma_i\sigma_j]; \quad i, j = 1, 2, \ldots, n \tag{10.1}$$

where ρ_{ij} is the correlation coefficient of random parameters Θ_i and Θ_j ($\rho_{ii} = 1$; i = 1, 2, …, n), and σ_i denotes the standard deviation of random parameter Θ_i. FOSM analysis is based on a linearization of the vector **R** of the m response quantities of interest. In fact, the vector **R** is approximated by the following first-order truncation of its Taylor series expansion in the random parameters $\boldsymbol{\Theta}$ about a given point $\boldsymbol{\vartheta}_0$

$$\mathbf{R}(\boldsymbol{\Theta}) \approx \mathbf{R}_{\text{lin}}(\boldsymbol{\Theta}) = \mathbf{r}(\boldsymbol{\vartheta}_0) + \nabla_{\boldsymbol{\vartheta}}\mathbf{r}\big|_{\boldsymbol{\vartheta} = \boldsymbol{\vartheta}_0}(\boldsymbol{\Theta} - \boldsymbol{\vartheta}_0) \tag{10.2}$$

In general, the linearization point is chosen as the point $\boldsymbol{\mu}_{\boldsymbol{\Theta}}$ of the mean values of the parameters. In fact, this is an optimal point (at least in a local sense) for estimating the mean of a scalar function (e.g., response quantity R_k, with k = 1, 2, …, m) of the parameters by using a linear approximation, independently of the functional relation and of the joint probability distribution of the parameters (see Appendix). Using the Mean-Centered FOSM method, the vector **R** of m response quantities of interest is approximated by a first-order truncation of its Taylor series expansion in the random parameters $\boldsymbol{\Theta}$ about their mean values $\boldsymbol{\mu}_{\boldsymbol{\Theta}}$ as

$$\mathbf{R}(\boldsymbol{\Theta}) \approx \mathbf{R}_{\text{lin}}(\boldsymbol{\Theta}) = \mathbf{r}(\boldsymbol{\mu}_{\boldsymbol{\Theta}}) + \nabla_{\boldsymbol{\vartheta}}\mathbf{r}\big|_{\boldsymbol{\vartheta} = \boldsymbol{\mu}_{\boldsymbol{\Theta}}}(\boldsymbol{\Theta} - \boldsymbol{\mu}_{\boldsymbol{\Theta}}) \tag{10.3}$$

The first- and second-order statistical moments of the response quantities **R** are approximated by the corresponding moments of the linearized response quantities, i.e.,

$$\boldsymbol{\mu}_{\mathbf{R}} \approx \boldsymbol{\mu}_{\mathbf{R}_{\text{lin}}} = \text{E}[\mathbf{R}_{\text{lin}}(\boldsymbol{\Theta})] = \mathbf{r}(\boldsymbol{\mu}_{\boldsymbol{\Theta}}) + \nabla_{\boldsymbol{\vartheta}}\mathbf{r}\big|_{\boldsymbol{\vartheta} = \boldsymbol{\mu}_{\boldsymbol{\Theta}}}\text{E}[\boldsymbol{\Theta} - \boldsymbol{\mu}_{\boldsymbol{\Theta}}] = \mathbf{r}(\boldsymbol{\mu}_{\boldsymbol{\Theta}}) \tag{10.4}$$

$$\begin{aligned}\boldsymbol{\Sigma}_{\mathbf{R}} \approx \boldsymbol{\Sigma}_{\mathbf{R}_{\text{lin}}} &= \mathrm{E}[(\mathbf{R}_{\text{lin}}(\boldsymbol{\Theta}) - \boldsymbol{\mu}_{\mathbf{R}_{\text{lin}}}) \cdot (\mathbf{R}_{\text{lin}}(\boldsymbol{\Theta}) - \boldsymbol{\mu}_{\mathbf{R}_{\text{lin}}})^{\mathrm{T}}] \\ &= \left(\nabla_{\boldsymbol{\vartheta}} \mathbf{r} \big|_{\boldsymbol{\vartheta} = \boldsymbol{\mu}_{\boldsymbol{\Theta}}} \cdot \boldsymbol{\Sigma}_{\boldsymbol{\Theta}} \cdot (\nabla_{\boldsymbol{\vartheta}} \mathbf{r} \big|_{\boldsymbol{\vartheta} = \boldsymbol{\mu}_{\boldsymbol{\Theta}}})^{\mathrm{T}} \right)\end{aligned} \tag{10.5}$$

in which E[…] denotes the mathematical expectation operator. In particular, the explicit form for the covariances between couples of response quantities and the variances of each of the response quantities considered are found from Eq. (10.5) as

$$\mathrm{cov}[\mathrm{R}_{\mathrm{r}}, \mathrm{R}_{\mathrm{s}}] \approx \sum_{\mathrm{i}=1}^{\mathrm{n}} \sum_{\mathrm{j}=1}^{\mathrm{n}} \rho_{\mathrm{ij}} \frac{\partial \mathrm{r}_{\mathrm{r}}}{\partial \theta_{\mathrm{i}}}\bigg|_{\boldsymbol{\vartheta} = \boldsymbol{\mu}_{\boldsymbol{\Theta}}} \frac{\partial \mathrm{r}_{\mathrm{s}}}{\partial \theta_{\mathrm{j}}}\bigg|_{\boldsymbol{\vartheta} = \boldsymbol{\mu}_{\boldsymbol{\Theta}}} \sigma_{\Theta_{\mathrm{i}}} \sigma_{\Theta_{\mathrm{j}}}; \quad \mathrm{r}, \mathrm{s} = 1, ..., \mathrm{m} \tag{10.6}$$

$$\sigma^2_{\mathrm{R}_{\mathrm{k}}} \approx \sum_{\mathrm{i}=1}^{\mathrm{n}} \left(\frac{\partial \mathrm{r}_{\mathrm{k}}}{\partial \theta_{\mathrm{i}}}\bigg|_{\boldsymbol{\vartheta} = \boldsymbol{\mu}_{\boldsymbol{\Theta}}} \right)^2 \sigma^2_{\Theta_{\mathrm{i}}} + 2 \sum_{\mathrm{i}=1}^{\mathrm{n}} \sum_{\mathrm{j}=1}^{\mathrm{i}-1} \rho_{\mathrm{ij}} \frac{\partial \mathrm{r}_{\mathrm{k}}}{\partial \theta_{\mathrm{i}}}\bigg|_{\boldsymbol{\vartheta} = \boldsymbol{\mu}_{\boldsymbol{\Theta}}} \frac{\partial \mathrm{r}_{\mathrm{k}}}{\partial \theta_{\mathrm{j}}}\bigg|_{\boldsymbol{\vartheta} = \boldsymbol{\mu}_{\boldsymbol{\Theta}}} \sigma_{\Theta_{\mathrm{i}}} \sigma_{\Theta_{\mathrm{j}}}; \quad \mathrm{k} = 1, ..., \mathrm{m} \tag{10.7}$$

respectively.

The approximate response statistics computed through Eqs. (10.4) and (10.5) are extremely important in evaluating the variability of the response quantities of interest due to the intrinsic uncertainty of the modeling parameters and provide information on the statistical correlation between the different response quantities. It is noteworthy that these approximate first- and second-order response statistics can be readily obtained when response sensitivities evaluated at the mean values of the random parameters are available. Only a single finite element analysis is needed in order to perform a FOSM probabilistic response analysis, when the finite element response sensitivities are computed using the DDM. In the following, only Mean-Centered FOSM analyses will be considered and denoted as FOSM analyses in short, for the sake of brevity.

10.4 PROBABILISTIC RESPONSE ANALYSIS USING MONTE CARLO SIMULATION

Probabilistic response analysis can also be performed using Monte Carlo Simulation (MCS) (Liu 2001). In this study, MCS is used to assess the accuracy of the FOSM approximations in Eqs. (3) and (4) when applied to non-linear finite element response analysis of R/C building structures characterized with random/uncertain material parameters and subjected to quasi-static pushover. The MCS procedure requires:

(1) Generation of N realizations of the n-dimensional random parameter vector $\boldsymbol{\Theta}$ according to a given n-dimensional joint probability density function (PDF).

(2) Computation by finite element analysis of N pushover curves (i.e., force-response curves) for each component of the response vector **R**, corresponding to the N realizations of the random parameter vector $\boldsymbol{\Theta}$.

(3) Statistical estimation of specified marginal and joint moments of the components of response vector **R** at each load step of the finite element response analysis.

MCS is a general and robust methodology for probabilistic response analysis, but it suffers two significant limitations:

(1) It requires knowledge of the joint PDF of the random parameters $\boldsymbol{\Theta}$. In general, this joint PDF is only partially known and appropriate models, consistent with the incomplete statistical information available, must be used to generate realizations of the vector $\boldsymbol{\Theta}$.

(2) MCS requires performing N finite element response analyses. This number N can be very large for accurate estimates of marginal and joint moments of response quantities **R** and increases rapidly with the order of the moments. For real-world structures, complex non-linear finite element analyses are necessary for accurate prediction of the structural response and repeating such analyses a large number of times could be computationally prohibitive.

In this study, the Nataf model (Ditlevsen and Madsen 1996) is used to generate realizations of the random parameters $\boldsymbol{\Theta}$. It requires specification of the marginal PDFs of the random parameters $\boldsymbol{\Theta}$ and their correlation coefficients. It is therefore able to reproduce the given first- and second-order statistical moments of the random parameters $\boldsymbol{\Theta}$.

10.5 TORNADO AND JAVELIN DIAGRAMS IN RESPONSE SENSITIVITY ANALYSIS

The FOSM method used in this paper allows one to consider the effects of the variability of each random parameter on the variability of the response. Herein, two simplified procedures, based on the response and response sensitivities computed at the mean values of the parameters, are presented to obtain information on the dependency of the response quantities considered on each of the material random parameters.

The first procedure is used to find the relative importance of each material random parameter on the response quantities. Such relative importance is based on a FOSM analysis and is obtained using the response sensitivities computed at the mean values of the parameters and the variances of the parameters. The relative importance using FOSM

results is validated against corresponding results obtained computing the response quantities changing the value of each parameter by ± 1 standard deviation one at a time. Such validation is graphically represented through tornado diagrams (Howard 1983; Porter et al. 2002). Another quantity commonly used to define a relative importance ranking of the uncertain/random parameters in influencing the variability of the response quantities considered is the so-called "swing" (Porter et al. 2002). The term swing denotes the variation in the response quantity of interest due to the variability of only one parameter when all the other parameters are kept fixed at their corresponding mean values. The swing is computed in correspondence of the minimum and maximum values of the parameter considered when its probability distribution is defined over a finite interval (e.g., beta and uniform distributions) or of the 10% and 90% fractiles when the probability distribution of the parameter is defined over an infinite (e.g., normal distribution) or semi-infinite (e.g., lognormal or exponential distributions) interval. The swing is commonly represented by using tornado diagrams.

The second procedure is employed to find an approximation of the cumulative probability functions (CDFs) and probability density functions (PDFs) of the response quantities of interest as functions of each random parameter considered one at a time. These approximations are obtained assuming that the response quantities of interest have the same distribution of the random parameter considered, with mean value and standard deviation given by the Mean-Centered FOSM estimates of mean and standard deviation, respectively. These approximate CDFs and PDFs are validated through the corresponding quantities obtained computing repeatedly the response for several values of the material

parameter considered and keeping all the other random parameters at their mean value. The results of this procedure are graphically represented using the so-called "javelin diagrams" (Felli and Hazen 2004), which are used in the fields of Economics, Management and Decision Analysis but, to the best of authors' knowledge, have not yet been employed by the Structural Engineering community.

10.6 APPLICATION EXAMPLES

10.6.1 Three-dimensional R/C frame building

The first application example considered herein consists of a three-dimensional reinforced concrete frame building on rigid foundation with concrete slabs at each floor as shown in Fig. 10.1. The frame consists of three stories of height $h = 3.66\text{m}$ (12ft) each and one bay of span $L = 6.10\text{m}$ (20ft) in each direction. Beam and column cross-sections are shown in Fig. 10.1.

Beams and columns are modeled using displacement-based Euler-Bernoulli frame elements with four Gauss-Legendre integration points each. Each column and beam is discretized in two and three finite elements, respectively. Beam and column cross-sections are discretized in fibers of confined concrete, unconfined concrete and steel reinforcement. The reinforcement steel is modeled through a bilinear hysteretic model, while the concrete is represented by the Kent-Scott-Park model with zero tension stiffening (Scott et al. 1982), as shown in Fig. 10.1. Different material parameters are used for the confined (core) and unconfined (cover) concrete in the columns and beams. The concrete slabs are modeled through a diaphragm constraint at each floor to enforce rigid in-plane behavior.

Ten material constitutive parameters are used to characterize the various structural materials present in the structure, namely four parameters for the confined concrete ($f_{c,\,core}$: peak strength, $\varepsilon_{c,\,core}$: strain at peak strength, $f_{cu,\,core}$: residual strength, $\varepsilon_{cu,\,core}$: strain at which the residual strength is reached), three parameters for the unconfined concrete ($f_{c,\,cover}$, $\varepsilon_{c,\,cover}$, $\varepsilon_{cu,\,cover}$) with the fourth parameter $f_{cu,\,cover} = 0\text{MPa}$, and three parameters for the reinforcement steel (f_y: yield strength, E_0: initial stiffness, b: post-yield to initial stiffness ratio). Fig. 10.1 shows graphically the meaning of all the material parameters considered. These material parameters are modeled as random fields spatially fully correlated, i.e., each material parameter is modeled with a single random variable (RV). The marginal PDFs of these material parameters are given in Table 1 and were obtained from studies reported in the literature (Mirza and MacGregor 1979; Mirza et al. 1979). The correlation coefficients between the various material parameters are assumed as follows: $\rho = 0.8$ for (1) $f_{c,\,core}$ and $f_{cu,\,core}$, (2) $\varepsilon_{c,\,core}$ and $\varepsilon_{cu,\,core}$, (3) $\varepsilon_{c,\,cover}$ and $\varepsilon_{cu,\,cover}$, (4) $f_{c,\,core}$ and $f_{c,\,cover}$, (5) $\varepsilon_{c,\,core}$ and $\varepsilon_{c,\,cover}$, (6) $\varepsilon_{cu,\,core}$ and $\varepsilon_{cu,\,cover}$; $\rho = 0.64$ for (1) $f_{cu,\,core}$ and $f_{c,\,cover}$, (2) $\varepsilon_{c,\,core}$ and $\varepsilon_{cu,\,cover}$, (3) $\varepsilon_{cu,\,core}$ and $\varepsilon_{c,\,cover}$; and $\rho = 0.0$ for all other pairs of parameters. These correlation coefficients are chosen based on engineering judgement, since to the authors' knowledge, precise values of correlation coefficients are not available in the literature.

After static application of the gravity loads (assumed as uniformly distributed load per unit area $q = 8\text{kN}/\text{m}^2$ at each floor), the structure is subjected to a quasi-static push-

over analysis, in which an upper triangular distribution of horizontal forces is applied on the master nodes of the floor diaphragm constraints in the x-direction (see Figure 1). The total base shear force, $P_{tot} = 2P$, is considered as deterministic and is assumed to increase linearly during the analysis from 0kN to 600kN, using a force-control procedure with load-increments of 6kN. In this analysis, only material non-linearities are taken into account. A response analysis and response sensitivity analysis using the DDM are first performed at the mean values $\boldsymbol{\mu}_{\boldsymbol{\Theta}}$ of the random parameters $\boldsymbol{\Theta}$. A MCS analysis based on 1000 realizations is then carried out based on the Nataf model used as joint PDF of the random parameters $\boldsymbol{\Theta}$. Global sensitivities of the response quantities $\mathbf{R}$ are evaluated through FFD and BFD analysis, perturbing one material parameter at a time by ± 1 standard deviation, respectively. Finally, the swing of the response quantities of interest is computed by performing two additional fine element analyses for each random material parameter at its upper and lower values (as defined in the previous Section). Finite element response, response sensitivity and probabilistic response computations are performed using the finite element analysis framework OpenSees (Mazzoni et al. 2005), in which new classes were added to perform MCS probabilistic response analysis, three-dimensional frame elements were augmented for response sensitivity analysis (Barbato et al. 2007) and the response sensitivity algorithm for imposing multipoint constraints was implemented (Gu et al. 2007b).

Fig. 10.2 shows a comparison of estimates of the mean and mean ± 1 standard deviation of the force - response curve for the roof displacement in the x-direction, u_{x3}, obtained through FOSM analysis using the DDM to compute the response sensitivities

and MCS, respectively. Fig. 10.3 displays the standard deviation estimates of u_{x3} obtained through MCS and FOSM analysis using different methods to compute the response sensitivities. For the given structure subjected to quasi-static pushover, the condition of failure is defined as non-convergence of the finite element analysis or roof displacement in the x-direction, u_{x3}, exceeding 0.4m (i.e., $u_{x3,fail} = 0.4m$, corresponding to a drift over total height ratio equal to 3.65%), whichever happens first. The choice of the value of the roof displacement at failure is driven by the fact that, for the considered level of drift, a building structure is strongly damaged or already physically collapsed. It is found that, until the load level $P_{tot} = 450kN$ is reached, no failure case is observed in the MCS performed, while nearly one third of the Monte Carlo realizations reach failure below load level $P_{tot} = 600kN$. In Figs. 10.2 and 10.3, horizontal dashed lines mark the load levels $P_{tot} = 300kN$ and $P_{tot} = 450kN$, which denote the load levels below which the response is almost linear and no failure occurs, respectively. In Figs. 10.2 and 10.3, for load levels above $P_{tot} = 450kN$, both the unconditional (denoted as "MC") and conditional to survival ("MCS cond. surv.") MCS estimates of the mean value and standard deviation of u_{x3} are plotted. The MCS mean response conditional to survival presents a stiffening behavior at high load levels, since it represents the mean response of only the realizations corresponding to structures with higher stiffness and/or strength. It is clear that MCS results conditional to survival cannot be directly compared with the FOSM approximations, because of the different meaning of the two sets of quantities. On the other hand, the presence of simulations with failure due to singularity of the structure stiffness matrix (i.e., non-convergence of the finite element pushover analysis) introduces

some arbitrarity in the computation and interpretation of the unconditional MCS results. In fact, the value of the displacement u_{x3} at the last converged step of the pushover analysis in these simulations is lower than the value assumed as failure threshold ($u_{x3,fail} = 0.4m$) and thus the value to be used for the unconditional MCS estimates of mean and standard deviation is not clearly and uniquely defined for load levels higher than the one at which failure occurred (denoted here as $P_{tot,fail}$). In this work, for $P_{tot} \geq P_{tot,\,fail}$, $u_{x3} = u_{x3,\,fail} = 0.4m$ is assumed, which is consistent with the failure condition for the simulations reaching the failure threshold and provides unconditional MCS estimates comparable with FOSM results. Notice that another possible choice would be assuming $u_{x3}(P_{tot}) = u_{x3}(P_{tot,\,fail}) \leq 0.4m$ for $P_{tot} \geq P_{tot,\,fail}$. This second choice is not used, since it would decrease significantly and artificially the computed mean and variance of the response quantity considered.

Fig. 10.2 shows clearly that the FOSM approximation is in excellent agreement with the MCS results when the structural response is nearly linear (for load levels below $P_{tot} = 300kN$), while the FOSM results slightly underestimate the MCS results when the structure undergoes low-to-moderate non-linear inelastic deformations (for load levels between $P_{tot} = 300kN$ and $P_{tot} = 450kN$). When MCS realizations start to reach failure as defined above (i.e., for load levels $P_{tot} \geq 450kN$), FOSM results significantly underestimate unconditional MCS results. It can be concluded that, for the first application example considered in this paper, FOSM analysis provides, at very low computational

cost, very good estimates of the mean of response quantities for low-to-moderate levels of material non-linearity in the structural response.

In Fig. 10.3, the different techniques employed for computing response sensitivities used in FOSM are: (1) DDM; (2) BFD analysis with perturbations $\Delta\theta_i = -\sigma_i$ $(i = 1, 2, \ldots, 10)$; (3) FFD analysis with perturbations $\Delta\theta_i = \sigma_i$ $(i = 1, 2, \ldots, 10)$; and (4) FD average of global sensitivities computed using BFD and FFD. It is observed that these four methods produce similar results and in particular the standard deviation estimate obtained using method (4) is very close to the one based on the DDM, except for very high load levels. However, it is important to note that, for each sensitivity parameter, the computational cost of response sensitivities using the DDM is only a fraction of the cost of an additional non-linear finite element analysis, which is required for BFD and FFD analyses. Thus, method (4) requires two additional non-linear finite element analyses for each sensitivity parameter, and is therefore significantly more expensive computationally than the DDM. In addition, the BFD analysis for parameter $f_{c,\,core}$ does not reach the load level $P_{tot} = 600\text{kN}$ and the corresponding structural model fails at $P_{tot} = 582\text{kN}$ and $u_{x3} = 0.344\text{m}$. Therefore, it is not possible to compute the BFD and FD average estimates of the response standard deviation for $P_{tot} \geq 582\text{kN}$. As for the mean of the response, FOSM analysis using DDM provides, at very low computational cost, excellent estimates of the standard deviation of response quantities for low-to-moderate levels of material non-linearity in the structural response.

Fig. 10.4 plots, on a semilogarithmic scale, the coefficient of variation (C.O.V.) of the mean of the response quantity u_{x3} for different load levels as a function of the number of simulations performed. As expected, the C.O.V. is higher for higher load levels, for which the dispersion of the results is higher. At 1000 simulations, the C.O.V. for $P_{tot} = 300\text{kN}, 450\text{kN}, 600\text{kN}$ are 0.59%, 1.04% and 2.85%, respectively, and thus the MCS results are very reliable. Notice also that the number of simulations required to obtain a C.O.V. lower than 10% are less than 10 for $P_{tot} = 300\text{kN}$ and $P_{tot} = 450\text{kN}$, but more than 100 for $P_{tot} = 600\text{kN}$. Fig. 10.5 displays the cumulative density functions (CDFs) of u_{x3} obtained by MCS for load levels $P_{tot} = 300\text{kN}$, 450kN and 600kN. For $P_{tot} = 600\text{kN}$, the CDF conditional to survival and scaled by the probability of survival is also shown, while the CDF conditional to failure (and scaled by the probability of failure) corresponds to the difference between the unconditional CDF and the scaled CDF conditional to survival.

Table 10.2 provides the sensitivities of u_{x3} to the random material parameters computed at the nominal/mean values of the latter and normalized in a deterministic sense, $(\partial u_{x3}/\partial\theta_i)\big|_{\boldsymbol{\vartheta} = \boldsymbol{\mu}_{\boldsymbol{\Theta}}}(\mu_{\Theta_i}/\mu_{u_{x3}})$, and probabilistic sense, $(\partial u_{x3}/\partial\theta_i)\big|_{\boldsymbol{\vartheta} = \boldsymbol{\mu}_{\boldsymbol{\Theta}}}(\sigma_{\Theta_i}/\mu_{u_{x3}})$, respectively (with the mean response $\mu_{u_{x3}}$ computed using FOSM). The sensitivities normalized in a deterministic sense can be interpreted as the percent change in the response due to one percent change in the sensitivity parameter considered. The sensitivities normalized in a probabilistic sense represent the percent change in the mean response due to a change in the mean of the random parameter taken as one percent of the standard devia-

tion of this parameter, assuming this change to be equally likely for all random parameters. It is observed that these normalized sensitivities increase in absolute value for increasing load level P_{tot}, except the normalized sensitivity to $\varepsilon_{c,\,cover}$, which is first positive and relatively large for $P_{tot} = 300\text{kN}$, decreases in absolute value for $P_{tot} = 450\text{kN}$ and becomes negative for $P_{tot} = 600\text{kN}$. Table 10.2 gives also the specific relative contributions (or marginal contributions) to the variance $\sigma^2_{u_{x3}}$ of u_{x3} of each of the material random parameters, expressed as per cent of $\sigma^2_{u_{x3}}$ for different load levels and computed using FORSM analysis. These relative contributions to the variance can be used as measures of relative importance in a probabilistic sense of the various parameters in regards to the response quantity of interest. In this case, it is noted that the most important parameter in the probabilistic sense is $f_{c,\,cover}$ for $P_{tot} = 300\text{kN}$ and $P_{tot} = 450\text{kN}$, while $f_{c,\,core}$ becomes predominant for $P_{tot} = 600\text{kN}$. The steel material parameters f_y and E are found to be relatively less important in the probabilistic sense than in the deterministic sense (for which the relative importance is given by the absolute value of the sensitivities normalized in a deterministic sense), since their coefficients of variation are relatively small compared to other parameters. Note that for equal coefficients of variation of all random parameters, the relative importance of these parameters in the deterministic and probabilistic sense are identical. Table 10.3 provides the contributions to the variance $\sigma^2_{u_{x3}}$ of u_{x3} due to the cross-terms (for all pairs of correlated parameters) expressed as per cent of $\sigma^2_{u_{x3}}$ for different load levels. In this application example,

these normalized (dimensionless) cross-term contributions grow for increasing load level P_{tot} and are of magnitude comparable or even larger than the marginal contributions of the random parameters to the variance of the response given in Table 10.2. In particular, the correlation between the parameters $f_{c,\,core}$ and $f_{c,\,cover}$ provides the highest contribution to the variance $\sigma^2_{u_{x3}}$ of u_{x3} for the load level $P_{tot} = 600\text{kN}$ (i.e. 36.70%). This phenomenon has a physical intuitive explanation. In fact, the value of $f_{c,\,cover}$ determines the force level at which spalling of the cover concrete starts: the lower $f_{c,\,cover}$, the sooner spalling initiates. Also, the sooner and the more extensively the spalling initiates, the more stress is taken by the core concrete. Finally, the lower is the value of $f_{c,\,core}$, the more likely is crushing of the core concrete in compression and consequently the higher is the deformation of the structure. Similar considerations are valid for the case of higher values of $f_{c,\,cover}$ and $f_{c,\,core}$, leading to lower deformations of the structure. The high positive correlation between the values of $f_{c,\,cover}$ and $f_{c,\,core}$ (due to the fact that they represent the same property of the same material in different positions in the structure) justify the importance in terms of contribution to the variance $\sigma^2_{u_{x3}}$ of their correlation term, which takes into account the chain effect described above. Furthermore, the sum of the contributions to the variance $\sigma^2_{u_{x3}}$ for the load level $P_{tot} = 600\text{kN}$ due to the variability of $f_{c,\,core}$ and $f_{c,\,cover}$ and to their correlation accounts for 87.44% of the total variance. It can be concluded that the concrete strength is by large the most influential factor on the strength and the deformability at high load levels for this specific structure.

Figs. 10.6 through 10.8 compare results for evaluating the relative importance and effects on the structural response u_{x3} of the randomness of the material parameters for different load levels by using the tornado diagrams. In particular, the estimate of the relative change in the response (taken as the change in the response normalized with the mean value of the response) due to a variation of ± 1 standard deviation of each parameter considered one at the time is computed by FOSM and by FFD and BFD with changes in the parameters equal to ± 1 standard deviation of the parameter considered, respectively. The response change are computed as follows

$$(\Delta u_{x3})_{DDM,\,i} = \pm \frac{\partial u_{x3}}{\partial \theta_i}\bigg|_{\boldsymbol{\vartheta} = \boldsymbol{\mu}_{\boldsymbol{\Theta}}} \sigma_{\Theta_i}; \quad i = 1, ..., 10 \tag{10.8}$$

$$(\Delta u_{x3})_{FD,\,i} = u_{x3}(\boldsymbol{\mu}_{\boldsymbol{\Theta}} \pm \mathbf{I}^{(i)}\boldsymbol{\sigma}_{\boldsymbol{\Theta}}) - u_{x3}(\boldsymbol{\mu}_{\boldsymbol{\Theta}}); \quad i = 1, ..., 10 \tag{10.9}$$

where $\mathbf{I}^{(i)}$ is a Boolean vector of length equal to the number of parameters with 1 in the i-th position and 0's elsewhere and $\boldsymbol{\sigma}_{\boldsymbol{\Theta}}$ is the vector collecting the standard deviation of the random parameters. The two tornado diagrams corresponding to $P_{tot} = 300\text{kN}$ (Fig. 10.6) and $P_{tot} = 450\text{kN}$ (Fig. 10.7), respectively, show that, for low-to-moderate non-linearities in the response, FOSM estimates of the response variability are in good agreement with the ones obtained through finite difference (FD) calculations. Furthermore, in the same range of non-linearities, the response variability due to the variation of ± 1 standard deviation of each parameter is moderate ($\Delta u_{x3} \leq 12.10\,\%$). For large non-linearities ($P_{tot} = 600\text{kN}$, Fig. 10.8), larger differences occur between FOSM and FD results, in particular for parameters to which the response is more sensitive, such as the core and

cover concrete parameters. For these parameters, the FOSM estimate of the variation of the response due to the variation of ± 1 standard deviation of each parameter is very large (more than 50% for $f_{c,\,core}$), while the same estimate using FD, in general, provides lower values for FFD and higher values for BFD. For the parameter $f_{c,\,core}$, which is the parameter to which the response is more sensitive at load level $P_{tot} = 600\text{kN}$, the BFD analysis does not converge and the corresponding finite element models reaches failure due to near singularity of the structure stiffness matrix at the load level $P_{tot,\,fail} = 582\text{kN}$. This result is denoted in Fig. 10.8 as 'BFD NA'. In order to generate the tornado diagrams of Figs. 10.6 through 10.8 using FD analysis, two additional non-linear finite element pushover analyses are required for each random parameter considered. On the other hand, the tornado diagrams using FOSM results are obtained at modest additional computational cost after performing the FOSM analysis. In addition, tornado diagrams using FD do not provide any information about the effects of correlation between couples of random parameters. In contrast with this, FOSM analysis provides information about the dependency of the response variance due to the correlation between parameters, as shown in Table 10.3. The tornado diagrams given in Figs. 10.6 through 10.8 plot also the swing of the response quantity u_{x3} due to the variability of each material parameter. The computed swings provide consistent information in terms of relative importance ranking of the material parameters to the results obtained through FOSM analysis. The only exception is at the load level $P_{tot} = 600\text{kN}$ for parameter f_y, which importance is underestimate by FOSM. In fact, for the lowest values of f_y, the structural system reaches failure at load levels lower

than $P_{tot} = 600kN$ (represented in Fig. 10.8 with the note 'swing NA'), showing that the relation between the response quantity u_{x3} and the parameter f_y is strongly non-linear.

FOSM analysis provides additional information about correlation between different response quantities and between response quantities and random material parameters. As examples, Figs. 10.9 and 10.10 compare the correlation coefficient between the response quantity u_{x3} and the material parameter $f_{c,\,cover}$ and between the response quantities u_{x3} and u_{x1}, respectively, computed by FOSM analysis and by MCS analysis, with MCS results acting as reference solution. The results from the two different methods show good agreement for low-to-moderate non-linearities in the response behavior. Notice that for load levels above $P_{tot} = 450kN$, the MCS results used to compute the correlation coefficient between the response quantities u_{x3} and u_{x1} are conditional to the survival of the structure up to the corresponding load level and, thus, for this specific case, the comparison between FOSM and MCS results is not very meaningful for $P_{tot} \geq 450kN$. On the other hand, computing the correlation coefficient from unconditional MCS results would give completely arbitrary results, since the value of the displacement u_{x1} after failure is achieved is not uniquely defined.

Figs. 10.11 through 10.13 show some results from the simplified procedure proposed to approximate the probability distributions of the response quantity considered as function of the modeling parameters considered as random one at the time. In Figs. 10.11 and 10.12, the PDFs (scaled by a factor 100 and 50, respectively) and CDFs of the displacement u_{x3} for $P_{tot} = 300kN$ and $P_{tot} = 450kN$, respectively, obtained by the pro-

posed approximate procedure considering as variable the parameter $f_{c,\,cover}$, are compared with the corresponding quantities obtained by simulation. In the same Figures, the relations between u_{x3} and $f_{c,\,cover}$ are also plotted. Fig. 10.13 shows the PDFs (scaled by a factor 4000) and CDFs of the displacement u_{x3} for $P_{tot} = 450\text{kN}$ obtained by the proposed approximate procedure considering as variable the parameter f_y are compared with the corresponding quantities obtained by simulation. In addition, the relation between u_{x3} and f_y is also plotted. The response probability distributions obtained by simulation are generated by repeating the non-linear finite element pushover analysis for 20 different values of the parameter considered. The functional relations between values of the parameter considered and response quantity are obtained interpolating with a cubic spline the values obtained through simulation. The response probability distributions obtained by the proposed simplified procedure are generated at a negligible additional computational cost for the parameter $f_{c,\,cover}$, which follows a lognormal distribution completely described by mean and standard deviation, while, for parameter f_y, two additional non-linear finite element analyses (corresponding to the minimum and maximum values of the parameter) are required to determine the corresponding beta distribution. Notice that the simplified procedure assumes a one-to-one relation between values of the parameter considered and response quantity, hypothesis which is satisfied by the functional relations obtained by simulation. From the results presented in Figs. 10.11 through 10.13 and from results corresponding to other random material parameters not presented herein for space limitation, it is found that the proposed simplified procedure can provide approximate probability dis-

tributions which are in good agreement with the ones obtained through simulation for low-to-moderate non-linearities in the response at a very low computational cost. It is also found that, for large non-linearities as the ones encountered at the load level $P_{tot} = 600\text{kN}$, the approximate probability distributions could compare very poorly with the distributions obtained through direct simulation. This disagreement is principally due to two factors: (1) estimates of mean and standard deviation of the response quantity considered are in poor agreement with the corresponding values computed through MCS, and (2) the hypothesis of one-to-one relation between values of the parameter considered and response quantity is no more satisfied.

10.6.2 Two-dimensional SFSI system

The second application example consists of a two-dimensional Soil-Foundation-Structure Interaction (SFSI) system, a model of which is shown in Fig. 10.14. The structure is a two-storey two-bay reinforced concrete frame with section properties given in Fig. 10.14. The foundations consist of reinforced concrete squat footings at the bottom of each column. The soil is a layered clay, with stiffness properties varying along the depth.

The frame structure of this SFSI system is modeled by using displacement-based Euler-Bernoulli frame elements with distributed plasticity, each with four Gauss-Legendre integration points. Section stress resultants at the integration points are computed by discretizing the frame sections into layers. Foundation footings and soil layers are modeled through isoparametric four-node quadrilateral finite elements with bilinear displacement interpolation. The soil mesh is shown in Fig. 10.14. The constitutive behavior of the steel reinforcement is modeled by using a one-dimensional J_2 plasticity model with both kine-

matic and isotropic linear hardening (Conte et al., 2003). The concrete is modeled by using a Kent-Scott-Park model with no tension stiffening (Scott et al., 1982). Different material parameters are used for confined (core) and unconfined (cover) concrete in the columns. The soil is modeled by using a pressure-independent multi-yield surface material model (Elgamal et al., 2003), specialized for plane strain analysis (Fig. 10.14). Different material parameters are used for each of the four layers considered.

Similarly to the previous application example, ten material constitutive parameters are used to characterize the various structural materials involved in the structure, namely four parameters for the confined concrete ($f_{c,\,core}$, $\varepsilon_{c,\,core}$, $f_{cu,\,core}$, $\varepsilon_{cu,\,core}$), three parameters for the unconfined concrete ($f_{c,\,cover}$, $\varepsilon_{c,\,cover}$, $\varepsilon_{cu,\,cover}$) with the fourth parameter $f_{cu,\,cover} = 0\text{MPa}$, and three parameters for the reinforcement steel (f_y, E_0, H_{kin}: kinematic hardening modulus) with the fourth parameter $H_{iso} = 0\text{MPa}$ (isotropic hardening modulus). Notice that, assuming $H_{iso} = 0\text{MPa}$, the one-dimensional J_2 plasticity model reduces to the bilinear inelastic model used in the first application example. These material parameters are assumed to follow lognormal distributions with parameters given in Table 10.4. The correlation coefficients between the couples of parameters are the same as in the first application example. In addition to the material parameters describing the structural materials, eight material parameters are used to model the four soil layers, i.e., the shear strength, τ_i, and the initial shear modulus, G_i, with i = 1, 2, 3, 4. These material parameters are assumed to follow lognormal distributions with parameters given in Table 10.4 (Phoon and Kulhawy 1996). The correlation coefficients between the parame-

ters are assumed as follows: $\rho = 0.4$ for (1) τ_1 and τ_2, (2) τ_1 and G_1, (3) τ_2 and τ_3, (4) τ_2 and G_2, (5) τ_3 and τ_4, (6) τ_3 and G_3, (7) τ_4 and G_4; and $\rho = 0.0$ for all other pairs of parameters. Also in this case, these correlation coefficients are chosen based on engineering judgement, since to the authors' knowledge, precise values of correlation coefficients are not available in the literature.

Similarly to the first application example, after static application of the gravity loads, the structure is subjected to a quasi-static pushover analysis, in which an upper triangular distribution of horizontal forces is applied at the floor levels (see Fig. 10.14). The total base shear force, $P_{tot} = 1.5P$, is considered as deterministic and is assumed to increase linearly during the analysis from 0kN to 750kN. In this analysis, only material non-linearities are taken into account. A response analysis and response sensitivity analysis using the DDM are first performed at the mean values $\boldsymbol{\mu}_{\boldsymbol{\Theta}}$ of the random parameters $\boldsymbol{\Theta}$. A MCS analysis based on 1000 realizations is then carried out based on the Nataf model used as joint PDF of the random parameters $\boldsymbol{\Theta}$. Finally, global sensitivities of the response quantities $\mathbf{R}$ are evaluated through FFD and BFD analysis, perturbing one material parameter at a time by plus and minus one standard deviation, respectively. Finite element response, response sensitivity and probabilistic response computations are performed using the finite element analysis framework OpenSees (Mazzoni et al. 2005), in which the constitutive model for the soil was augmented for response sensitivity analysis (Gu et al. 2007a) and the response sensitivity algorithm for imposing multipoint constraints (in this case required for connecting the frame elements used to describe the structure with the quadrilateral elements employed to model the squat footings) was implemented (Gu et al.

2007b). The results of the analysis are presented in a similar way as for the first application example.

Fig. 10.15 shows a comparison of estimates of the mean and mean ± 1 standard deviation of the force - response curve for the horizontal roof displacement at the top of the central column, u_1, obtained through FOSM analysis using the DDM to compute the response sensitivities and MCS, respectively. Fig. 10.16 displays the standard deviation estimates of u_1 obtained through MCS and FOSM analysis using different methods to compute the response sensitivities. For the given structure subjected to quasi-static push-over, the condition of failure is defined as (near) singularity of the structure stiffness matrix or $u_{1,fail} = 0.28\text{m}$ (i.e., roof displacement over roof height ratio equal to 3.9%), whichever happens first. It is found that, until the load level $P_{tot} = 630\text{kN}$ is reached, no failure case is observed in the MCS performed, while nearly one quarter of the Monte Carlo realizations reach failure below load level $P_{tot} = 750\text{kN}$. In Figs. 10.15 and 10.16, horizontal dashed lines mark the load levels $P_{tot} = 375\text{kN}$ and $P_{tot} = 630\text{kN}$, which denote the load levels below which the response is almost linear and no failure occurs, respectively. In Figs. 10.15 and 10.16, for load levels above $P_{tot} = 630\text{kN}$, both the unconditional (denoted as "MC") and conditional to survival ("MCS cond. surv.") MCS estimates of the mean value and standard deviation of u_1 are plotted. The results obtained using FOSM and MCS are qualitatively very similar to the ones presented for the first application example.

Fig. 10.15 shows that the FOSM approximation is in excellent agreement with the MCS results when the structural response is nearly linear (for load levels below $P_{tot} = 375kN$), while the FOSM results slightly underestimate the MCS results when the structure undergoes low-to-moderate non-linear inelastic deformations (for load levels between $P_{tot} = 375kN$ and $P_{tot} = 630kN$), with differences increasing with increasing non-linearities. In this case, the maximum level of non-linearities reached in the analysis is less pronounced at the global level than in the previous example and the differences between FOSM analysis and MCS analysis are relatively small also for load levels ($P_{tot} \geq 630kN$) for which MCS realizations start to reach failure. It can be concluded that, also for the second application example considered in this paper, FOSM analysis provides, at very low computational cost, very good estimates of the mean of response quantities for low-to-moderate levels of material non-linearity in the structural response.

The different techniques employed for computing response sensitivities used in FOSM and shown in Fig. 10.16 are: (1) DDM; (2) BFD analysis with perturbations $\Delta\theta_i = -\sigma_i \quad (i = 1, 2, \ldots, 18)$; (3) FFD analysis with perturbations $\Delta\theta_i = \sigma_i$ $(i = 1, 2, \ldots, 18)$; and (4) FD average of global sensitivities computed using BFD and FFD. It is observed that these four methods produce similar results, but in this case the estimates of the standard deviation of u_1 obtained using BFD, FFD and FD average slightly overestimate the standard deviation computed through MCS for load levels below $P_{tot} \geq 665kN$, while the DDM estimate is extremely close to the MCS value for load levels up to $P_{tot} \geq 510kN$. For higher load levels, all the four sensitivity-based methods

underestimate the MCS results. As for the mean of the response, FOSM analysis using DDM provides, at very low computational cost, very good estimates of the standard deviation of response quantities for low-to-moderate levels of material non-linearity in the structural response also in the case of probabilistic pushover analysis of SFSI systems.

Fig. 10.17 plots, on a semilogarithmic scale, the coefficient of variation (C.O.V.) of the mean of the response quantity u_1 for different load levels as a function of the number of simulations performed. At 1000 simulations, the C.O.V. for $P_{tot} = 375\text{kN}, 630\text{kN}, 750\text{kN}$ are 0.20%, 0.49% and 0.91%, respectively, and thus the MCS results are very reliable. In this case, the number of simulations required to obtain a C.O.V. lower than 10% are less than 10 for $P_{tot} = 375\text{kN}$ and $P_{tot} = 630\text{kN}$, and about 50 for $P_{tot} = 750\text{kN}$, showing a faster convergence than in the previous application example.

Table 10.5 provides the sensitivities of u_1 to the random material parameters computed at the nominal/mean values of the latter and normalized both in a deterministic sense and probabilistic sense respectively, together with the relative contributions (or marginal contributions) to the variance $\sigma_{u_1}^2$ of u_1 of each of the material random parameters, expressed as per cent of $\sigma_{u_1}^2$ for different load levels. Table 10.6 shows the contributions to the variance $\sigma_{u_1}^2$ of u_1 due to the cross-terms (for all pairs of correlated parameters) expressed as per cent of $\sigma_{u_1}^2$ for different load levels. From Tables 10.5 and 10.6, the following observations can be made:

(1) The parameters $f_{cu,\,core}$ and $\varepsilon_{cu,\,core}$ do not influence the response, since the core concrete does not reach its peak strength at any load level and in any fiber in which the structure is discretized.

(2) The parameter $f_{c,\,cover}$ is the one with largest marginal contribution to the variance of the response for load levels $P_{tot} = 375\text{kN}$ and $P_{tot} = 630\text{kN}$ and is the second most important parameter for $P_{tot} = 750\text{kN}$. The parameter $\varepsilon_{c,\,cover}$ is very important at lower load levels and its importance decreases sensibly for increasing load levels. In fact, at lower load levels, the parameter $\varepsilon_{c,\,cover}$ influences the response mainly through its effects on the stiffness of the cover concrete (i.e., higher values of $\varepsilon_{c,\,cover}$ imply lower stiffness of the cover concrete for a fixed value of $f_{c,\,cover}$ and thus higher displacements), while at higher load levels, when the fibers of cover concrete start to reach their peak strength, higher values of $\varepsilon_{c,\,cover}$ have the effects also of reducing the number of fibers which reach the peak strength for a given load level, thus reducing the displacement. This shows that the structural response behavior strongly depends on the cover concrete material parameters, in particular for low-to-moderate load levels.

(3) The parameter f_y increases its importance for increasing load levels. Its effects are almost negligible for $P_{tot} = 375\text{kN}$, when very few steel reinforcement fibers have reached yielding, while f_y is the second and first most important parameter for load levels $P_{tot} = 630\text{kN}$ and $P_{tot} = 750\text{kN}$, respectively. In particular, for

$P_{tot} = 750kN$, f_y contributes with about 51% of the variance of the structural response u_1.

(4) The variability of the soil properties has a small effect on the variability of the response u_1 and, in general, this effect decreases for increasing load levels. The only parameter which effect is significant at all load levels is the parameter τ_3, which influences the sliding of the foundation over the soil layer on which they are posed.

(5) The effects due to modeling parameter correlation are small and, in general, they decrease for increasing load levels. The only significant effects are due to the correlation between $\varepsilon_{c,\,core}$ and $\varepsilon_{c,\,cover}$ and between $f_{c,\,core}$ and $f_{c,\,cover}$.

Figs. 10.18 through 10.20 provide the tornado diagrams referred to the structural response u_1 for different load levels. These tornado diagrams reproduce the information about the relative importance of the several random material parameters and also show that at higher load levels the amplitude range of the response increases significantly. In fact, varying the most important parameters of ± 1 standard deviation produce a variation in the response of less than 10%, about 10% and almost 50% for load levels $P_{tot} = 375kN$, 630kN and 750kN, respectively. Results obtained through FOSM compare favorably with the one obtained by BFD and FFD for $P_{tot} = 375kN$ (Fig. 10.18) and $P_{tot} = 630kN$ (Fig. 10.19), while differences are evident for $P_{tot} = 750kN$ (Fig. 10.20), in particular because of the strong non-symmetry of the BFD and FFD responses with respect to the mean response which cannot be captured by FOSM. These tornado dia-

grams plot also the swings of the response quantity u_1 due to the variability of each parameter when all the others are kept constant at their mean values. The importance ranking of the parameters obtained considering the swings matches very well the one obtained by FOSM analysis at all the load levels considered.

Figs. 10.21 and 10.22 compare the approximate probability distributions of u_1 as function of $f_{c,\,cover}$ and τ_3, respectively, for load level $P_{tot} = 630\text{kN}$ with the corresponding distributions computed point by point based on the non-linear functional relation between parameters and response obtained through finite element analysis. In these figures, PDFs and CDFs are plotted together with the relation between the response and the parameter considered, when all the other parameters are kept fixed with values equal to the mean values. It is found that the proposed procedure can provide probability distributions in reasonable agreement with the ones computed by repeated finite element analyses at very small computational cost also for SFSI systems for low-to-moderate response non-linearities. For increasing non-linearities, the agreement between probability distributions obtained through the proposed approximation and direct simulations degrades rapidly.

10.7 CONCLUSIONS

This paper presents a comparison between probabilistic response analysis results obtained through Monte Carlo simulation and Mean Centered First-Order Second-Moment (FOSM) analysis using non-linear finite element response and response sensitivity analyses of structural and geotechnical systems subjected to quasi-static pushover. The effects on FOSM analysis results of using different methods for computing response sensi-

tivities are also investigated. It is found that FOSM approximation using the Direct Differentiation Method for computing response sensitivities provides, at very low computational cost, very good estimates of the mean and standard deviation of the response quantity considered herein for low-to-moderate levels of material non-linearity in the response of structural systems and SFSI systems subjected to quasi-static pushover analysis. Furthermore, the relative importance (in both the deterministic and probabilistic sense) of the material parameters on the structural response is obtained as by-product of a FOSM analysis at negligible additional computational cost. In addition, FOSM results can be used to obtain approximate probability distributions of response quantities of interest as function of a single random parameters which are in reasonable agreement (in the low-to-moderate range of non-linearities in the response) with the corresponding distributions obtained through direct simulation at a much higher computational cost. For high non-linearities in the structural system considered, agreement between FOSM and MCS results deteriorates but qualitative information, such as importance ranking of the material parameters in influencing the response variability, can still be obtained. It is noteworthy that in cases where non-convergence of the simulations occur before the failure threshold of the response is reached, estimating of mean and variance of the response using MCS can lead to some difficulties and is not uniquely defined.

It can be concluded that FOSM analysis provides a large amount of probabilistic information at a very low computational cost and can provide satisfactory accuracy for probabilistic analysis of structural and SFSI systems subjected to quasi-static pushover analysis, provided that the level of non-linearities exhibited by the system considered are

low-to-moderate. For large non-linearities, FOSM can be used effectively to obtain qualitative information on the importance ranking of modeling parameters on the system response.

Table 10.1 Marginal PDFs of material parameters for the three-story building (distribution parameters for lognormal distribution: (1) $\lambda = \mu_{\log(X)}$, (2) $\zeta = \sigma_{\log(X)}$; for beta distribution: (1) x_{min}, (2) x_{max}, (3) α_1, (4) α_2)

RV [unit]	Distr.	Par.#1	Par.#2	Par.#3	Par.#4	Mean	c.o.v [%]
$f_{c,core}$ [MPa]	lognorm.	3.5205	0.1980	-	-	34.47	20
$\varepsilon_{c,core}$ [-]	lognorm.	-5.3179	0.1980	-	-	0.005	20
$f_{cu,core}$ [MPa]	lognorm.	3.1638	0.1980	-	-	24.13	20
$\varepsilon_{cu,core}$ [-]	lognorm.	-3.9316	0.1980	-	-	0.020	20
$f_{c,cover}$ [MPa]	lognorm.	3.2975	0.1980	-	-	27.58	20
$\varepsilon_{c,cover}$ [-]	lognorm.	-6.2342	0.1980	-	-	0.002	20
$\varepsilon_{cu,cover}$ [-]	lognorm.	-5.1356	0.1980	-	-	0.006	20
f_y [MPa]	beta	227.53	427.48	3.21	4.28	307.46	10.6
E_0 [MPa]	lognorm.	12.1914	0.0330	-	-	201000	3.3
b [-]	lognorm.	-3.9316	0.1980	-	-	0.02	20

Table 10.2 Normalized sensitivities computed by DDM of u_{x3} to material parameters and their relative contribution to variance of u_{x3} at different load levels (three-story building)

	Deterministic sense			Probabilistic sense			$\Delta(\sigma^2_{u_{x3}})/\sigma^2_{u_{x3}}$ [%]		
P_{tot} [kN]	300	450	600	300	450	600	300	450	600
$f_{c,core}$	-0.230	-0.313	-2.742	-0.046	-0.063	-0.548	6.01	9.22	36.21
$\varepsilon_{c,core}$	0.219	0.284	1.540	0.044	0.057	0.308	5.42	7.44	11.42
$f_{cu,core}$	0	0	-0.006	0	0	-0.001	0	0	<0.01
$\varepsilon_{cu,core}$	0	0	-0.003	0	0	-0.001	0	0	<0.01
$f_{c,cover}$	-0.521	-0.605	-1.737	-0.104	-0.121	-0.347	30.74	33.74	14.53
$\varepsilon_{c,cover}$	0.413	0.305	-0.160	0.083	0.061	-0.032	19.30	8.56	0.12
$\varepsilon_{cu,cover}$	0	-0.006	-1.142	0	-0.001	-0.228	0	<0.01	6.28
f_y	0	-0.063	-2.070	0	-0.007	-0.219	0	0.10	5.80
E	-0.369	-0.417	-0.765	-0.012	-0.014	-0.025	0.42	0.44	0.08
b	0	0	-0.047	0	~0	-0.010	0	<0.01	0.01

Table 10.3 Contribution (%) of the cross-correlation terms to the variance of the response quantity u_{x3} (three-story building)

P_{tot} [kN]		300	450	600
$\varepsilon_{c,core}$	$\varepsilon_{cu,core}$	0	0	-0.04
$\varepsilon_{c,core}$	$\varepsilon_{c,cover}$	16.36	12.77	-1.90
$\varepsilon_{c,core}$	$\varepsilon_{cu,cover}$	0	-0.21	-10.84
$f_{c,core}$	$f_{cu,core}$	0	0	0.12
$f_{c,core}$	$f_{c,cover}$	21.75	28.22	36.70
$\varepsilon_{cu,core}$	$\varepsilon_{c,cover}$	0	0	<0.01
$\varepsilon_{cu,core}$	$\varepsilon_{cu,cover}$	0	0	0.03
$f_{cu,core}$	$f_{c,cover}$	0	0	0.06
$\varepsilon_{c,cover}$	$\varepsilon_{cu,cover}$	0	-0.28	1.41

Table 10.4 Material parameters (with lognormal distributions) for the two-dimensional SFSI system

Structural material parameters			Soil material parameters		
RV [unit]	Mean	C.O.V. [%]	RV [unit]	Mean	C.O.V. [%]
$f_{c,core}$ [MPa]	34.49	20	τ_1 [kPa]	33	25
$\varepsilon_{c,core}$ [-]	0.004	20	G_1 [kPa]	54450	30
$f_{cu,core}$ [MPa]	20.69	20	τ_2 [kPa]	50	25
$\varepsilon_{cu,core}$ [-]	0.014	20	G_2 [kPa]	77600	30
$f_{c,cover}$ [MPa]	27.59	20	τ_3 [kPa]	75	25
$\varepsilon_{c,cover}$ [-]	0.002	20	G_3 [kPa]	121000	30
$\varepsilon_{cu,cover}$ [-]	0.008	20	τ_4 [kPa]	100	25
f_y [MPa]	248.20	10.6	G_4 [kPa]	150000	30
E_0 [MPa]	200000	3.3	-	-	-
H_{kin} [MPa]	1612.9	20	-	-	-

Table 10.5 Normalized sensitivities computed by DDM of u_1 to material parameters and their relative contribution to variance of u_1 at different load levels (two-dimensional SFSI system)

	Deterministic sense			Probabilistic sense			$\Delta(\sigma^2_{u_{x3}})/\sigma^2_{u_{x3}}$ [%]		
P_{tot} [kN]	375	630	750	375	630	750	375	630	750
$f_{c,core}$	-0.039	-0.054	-0.139	-0.008	-0.011	-0.028	0.67	0.56	0.69
$\varepsilon_{c,core}$	0.037	0.048	0.108	0.008	0.010	0.022	0.60	0.43	0.41
$f_{cu,core}$	0	0	0	0	0	0	0	0	0
$\varepsilon_{cu,core}$	0	0	0	0	0	0	0	0	0
$f_{c,cover}$	-0.280	-0.393	-0.943	-0.056	-0.079	-0.189	33.93	29.22	31.65
$\varepsilon_{c,cover}$	0.240	0.249	0.215	0.048	0.050	0.043	24.93	11.76	1.64
$\varepsilon_{cu,cover}$	0	0	-0.027	0	0	-0.005	0	0	0.03
f_y	-0.043	-0.672	-2.260	-0.005	-0.712	-0.240	0.22	24.00	51.11
E_0	-0.462	-0.392	-0.337	-0.015	-0.013	-0.011	2.51	0.79	0.11
H_{kin}	0	-0.003	-0.021	0	-0.001	-0.004	0	<0.01	0.02
τ_1	-0.049	-0.077	-0.091	-0.012	-0.019	-0.023	1.61	1.73	0.46
G_1	-0.017	-0.013	-0.007	-0.005	-0.004	-0.002	0.29	0.07	<0.01
τ_2	-0.053	-0.085	-0.101	-0.013	-0.021	-0.025	1.90	2.11	0.56
G_2	-0.024	-0.018	-0.012	-0.007	-0.006	-0.004	0.54	0.14	0.01
τ_3	-0.087	-0.146	-0.179	-0.022	-0.037	-0.045	5.16	6.32	1.77
G_3	-0.049	-0.048	-0.045	-0.015	-0.014	-0.014	2.34	0.97	0.16
τ_4	-0.030	-0.065	-0.085	-0.007	-0.016	-0.021	0.59	1.23	0.40
G_4	-0.030	-0.036	-0.034	-0.009	-0.011	-0.010	0.87	0.55	0.09

Table 10.6 Contribution (%) of the cross-correlation terms to the variance of the response quantity u_1 (two-dimensional SFSI system)

P_{tot} [kN]		375	630	750
$\varepsilon_{c,core}$	$\varepsilon_{cu,core}$	0	0	-0.13
$\varepsilon_{c,core}$	$\varepsilon_{c,cover}$	6.19	3.61	1.32
$\varepsilon_{c,core}$	$\varepsilon_{cu,cover}$	0	0	0
$f_{c,core}$	$f_{cu,core}$	0	0	0
$f_{c,core}$	$f_{c,cover}$	7.63	6.45	7.46
$\varepsilon_{cu,core}$	$\varepsilon_{c,cover}$	0	0	0
$\varepsilon_{cu,core}$	$\varepsilon_{cu,cover}$	0	0	0
$f_{cu,core}$	$f_{c,cover}$	0	0	0
$\varepsilon_{c,cover}$	$\varepsilon_{cu,cover}$	0	0	-0.33
τ_1	τ_2	1.40	0.28	0.03
τ_1	G_1	0.55	1.53	0.41
τ_2	τ_3	2.51	2.92	0.80
τ_2	G_2	0.81	0.44	0.06
τ_3	τ_4	1.40	2.23	0.67
τ_3	G_3	2.78	1.98	0.42
τ_4	G_4	0.57	0.66	0.16

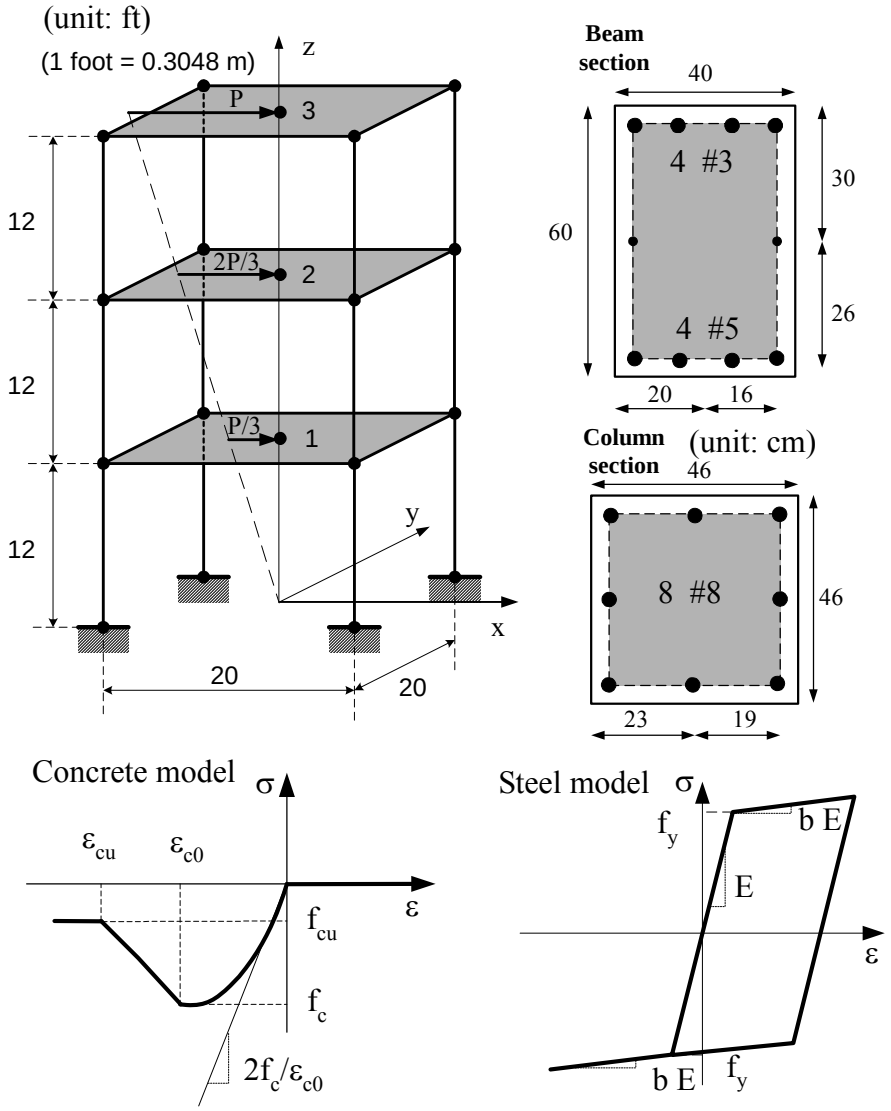

Figure 10.1 Geometry, cross-sectional properties, applied horizontal loads and material constitutive models for the three-story R/C building.

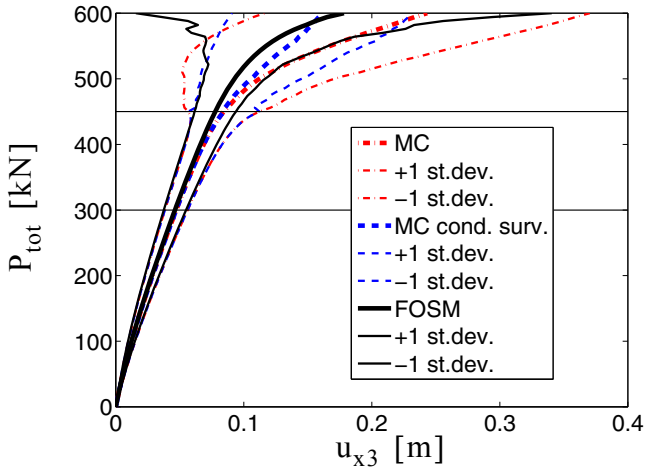

Figure 10.2 Probabilistic response of the three-story R/C building.

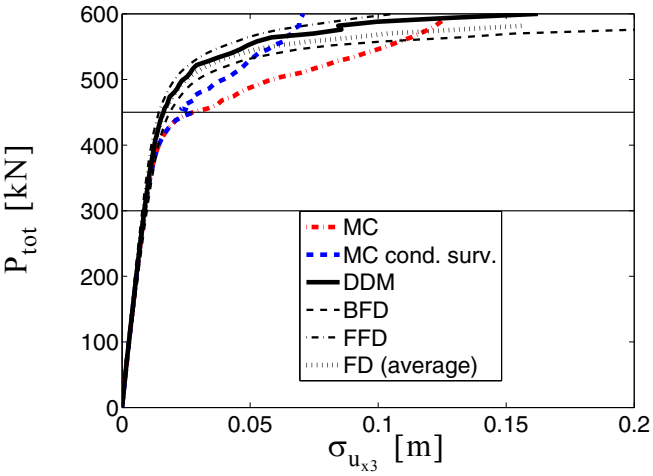

Figure 10.3 Standard deviation of the three-story R/C building.

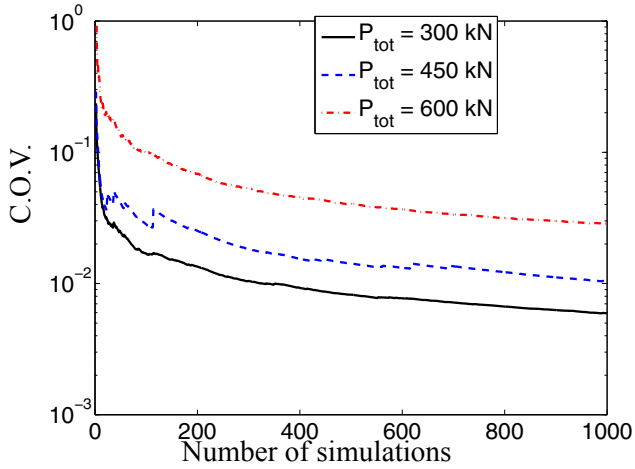

Figure 10.4 Coefficient of variation of the mean response at different load levels computed using MCS for the three-story R/C building.

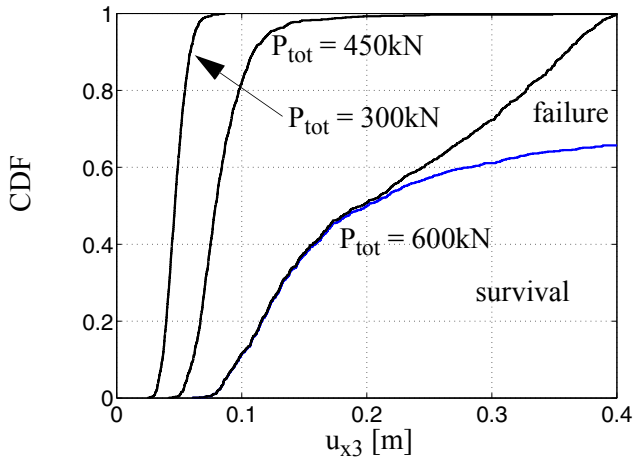

Figure 10.5 CDFs of u_{x3} for different load levels estimated using MCS for the three-story R/C building.

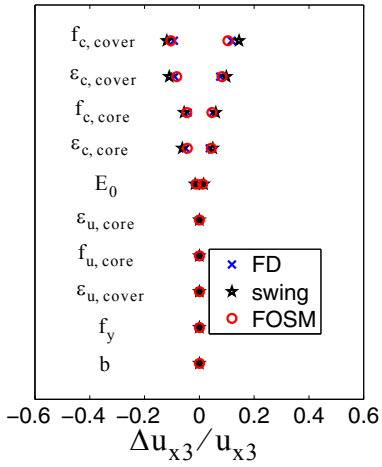

Figure 10.6 Tornado diagram for the three-story R/C building: $P_{tot} = 300\text{kN}$.

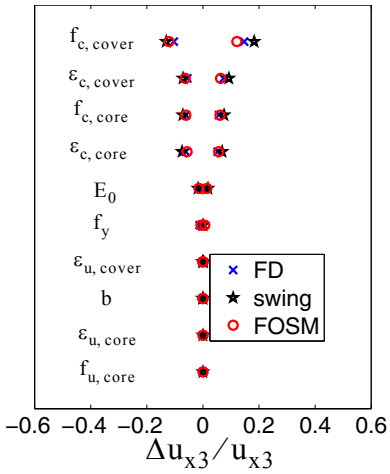

Figure 10.7 Tornado diagram for the three-story R/C building: $P_{tot} = 450\text{kN}$.

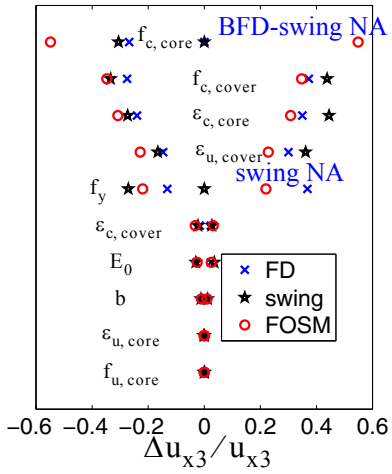

Figure 10.8 Tornado diagram for the three-story R/C building: $P_{tot} = 600\text{kN}$.

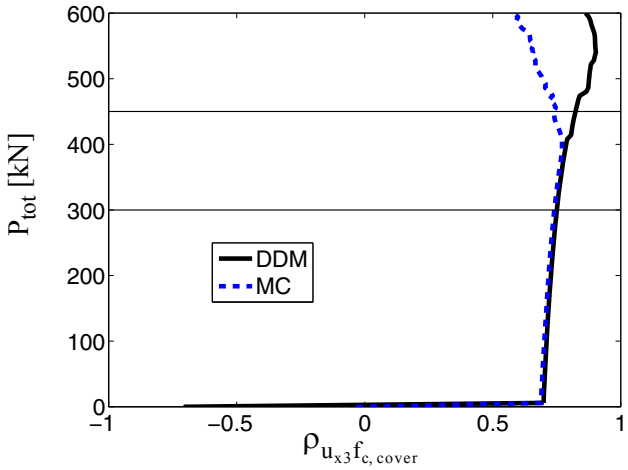

Figure 10.9 Correlation of response quantity u_{3x} with material parameter $f_{c,cover}$ for the three-story R/C building.

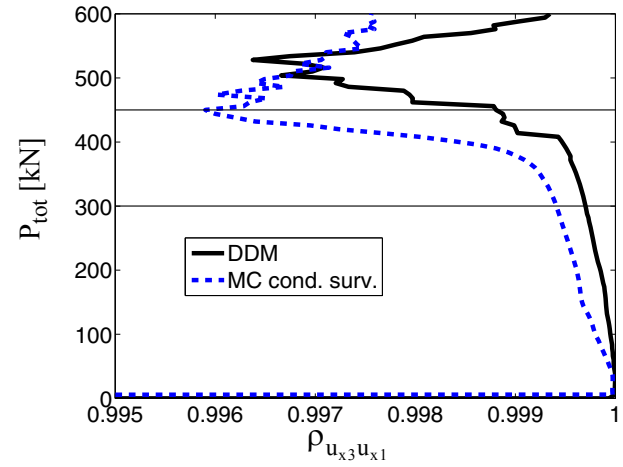

Figure 10.10 Correlation of response quantities u_{3x} and u_{1x} for the three-story R/C building.

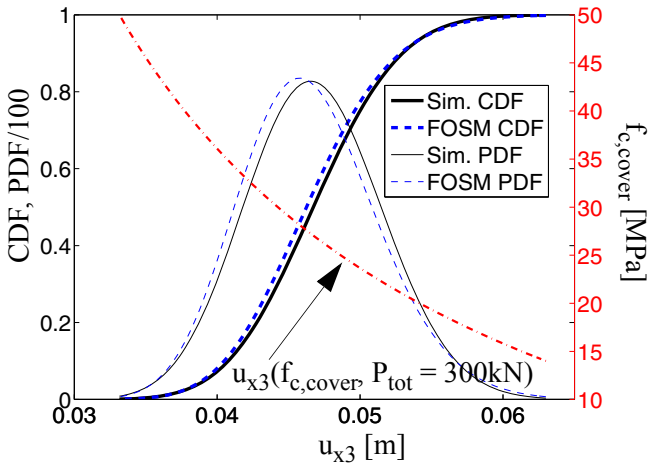

Figure 10.11 CDF, PDF and relation of the response u_{3x} of the three-story R/C building as function of $f_{c,cover}$ for P_{tot} = 300kN.

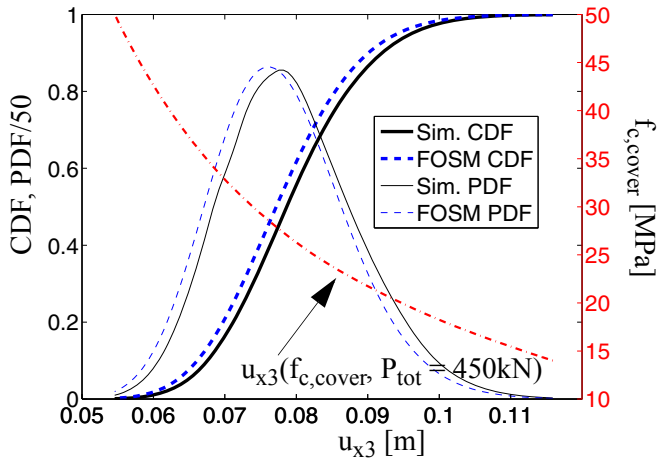

Figure 10.12 CDF, PDF and relation of the response u_{3x} of the three-story R/C building as function of $f_{c,cover}$ for $P_{tot} = 450kN$.

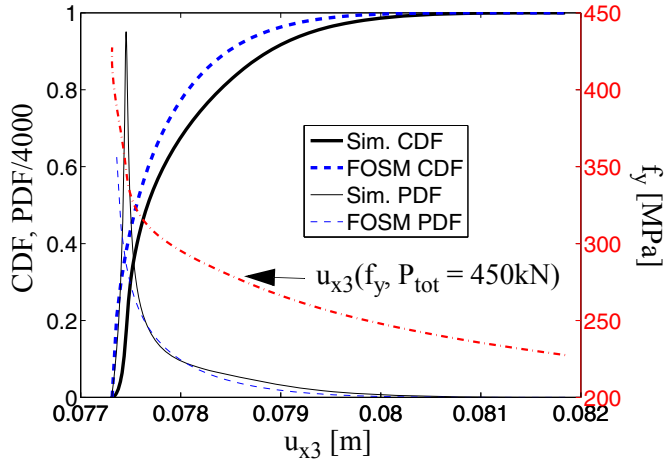

Figure 10.13 CDF, PDF and relation of the response u_{3x} of the three-story R/C building as function of f_y for $P_{tot} = 450kN$.

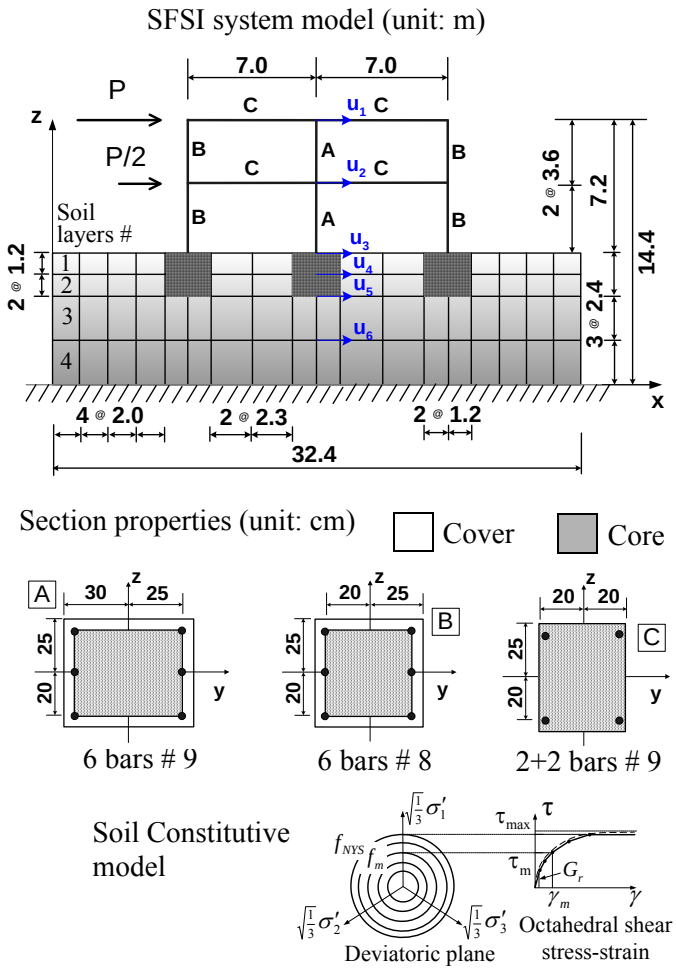

Figure 10.14 2-D model of SFSI system: geometry, section properties and soil model.

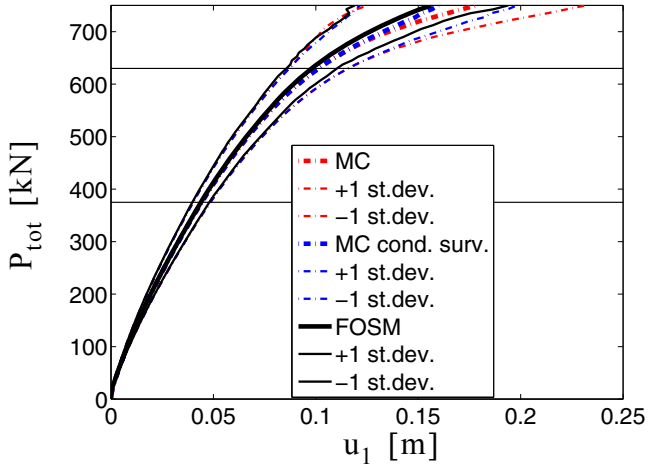

Figure 10.15 Probabilistic response of the two-dimensional SFSI system.

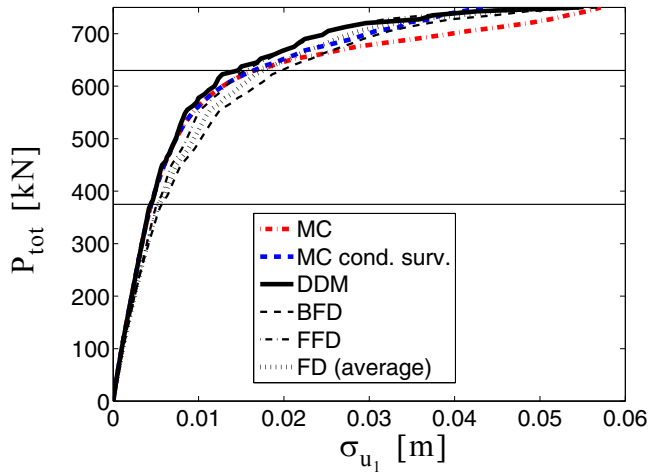

Figure 10.16 Standard deviation of the two-dimensional SFSI system.

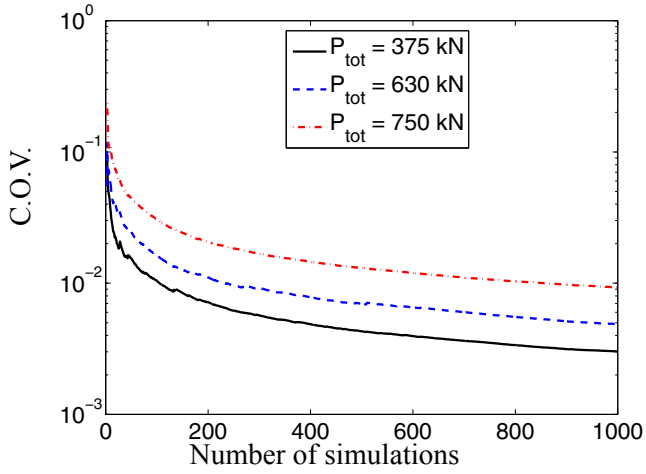

Figure 10.17 Coefficient of variation of the mean response at different load levels computed using MCS for the two-dimensional SFSI system.

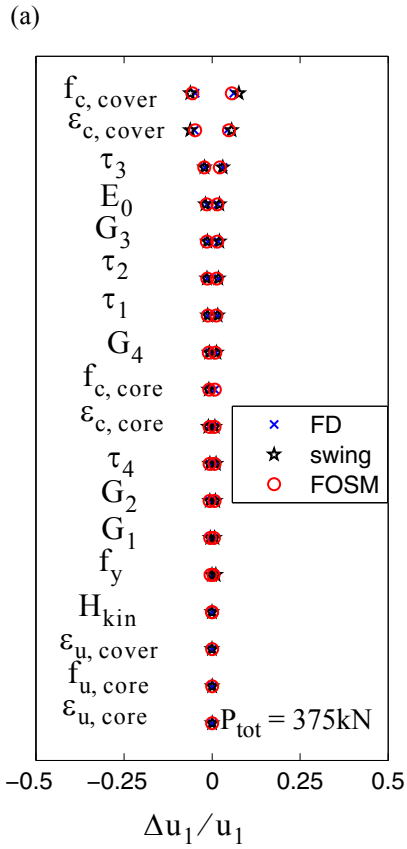

Figure 10.18 Tornado diagram for the two-dimensional SFSI system: $P_{tot} = 375\text{kN}$.

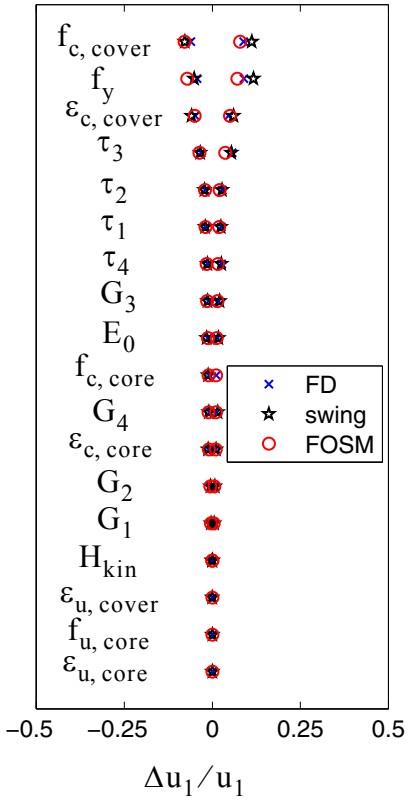

Figure 10.19 Tornado diagram for the two-dimensional SFSI system: $P_{tot} = 630\text{kN}$.

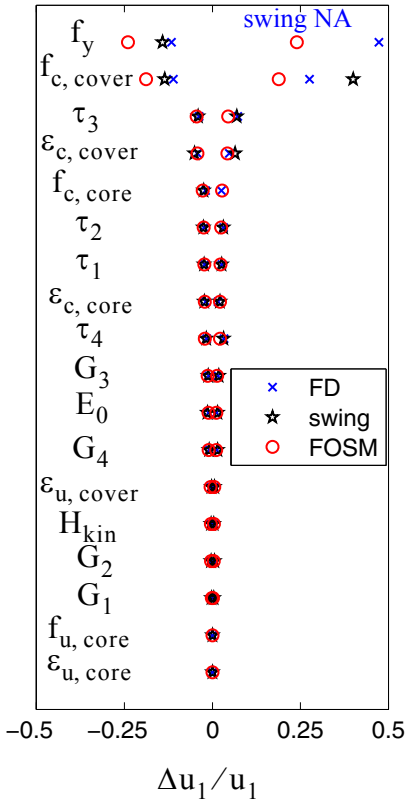

Figure 10.20 Tornado diagram for the two-dimensional SFSI system: $P_{tot} = 750\text{kN}$.

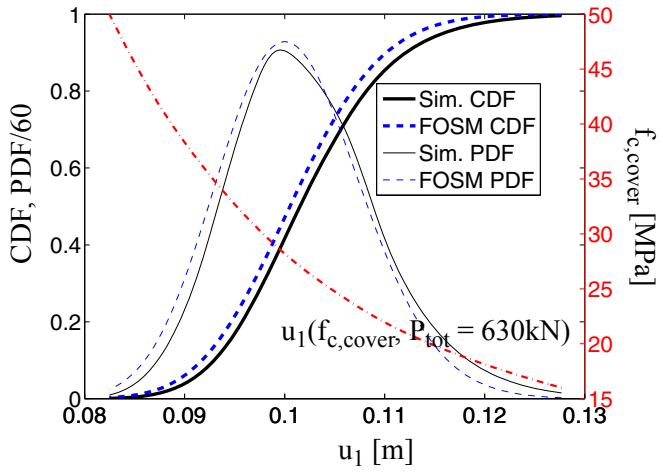

Figure 10.21 CDF, PDF and relation of the response u_1 of the two-dimensional SFSI system as function of $f_{c,cover}$ for $P_{tot} = 630kN$.

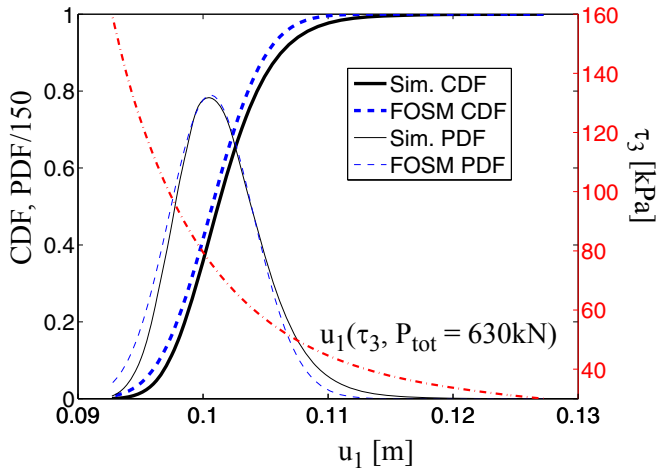

Figure 10.22 CDF, PDF and relation of the response u_1 of the two-dimensional SFSI system as function of τ_3 for $P_{tot} = 630kN$.

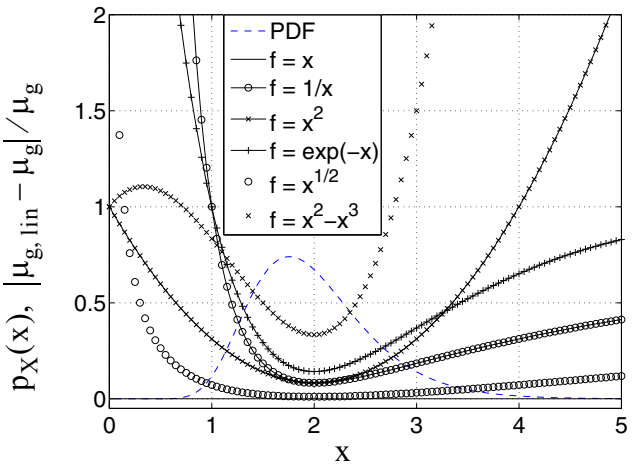

Figure 10.23 Relative error between mean of linearized response and exact mean for lognormal distribution of the parameter and different functional relations.

APPENDIX: OPTIMAL LINEARIZATION POINT OF RESPONSE FUNCTION FOR MEAN RESPONSE ESTIMATE

The problem of finding the optimal point to which linearize the (scalar) response function r for obtaining the best estimate of the mean response can be formulated as follows

$$\min \left| \int_{\boldsymbol{\Theta}} [r(\boldsymbol{\vartheta}_0) + \nabla_{\boldsymbol{\vartheta}} r\big|_{\boldsymbol{\vartheta}=\boldsymbol{\vartheta}_0}(\boldsymbol{\vartheta}-\boldsymbol{\vartheta}_0) - r(\boldsymbol{\vartheta})] p_{\boldsymbol{\Theta}}(\boldsymbol{\vartheta}) d\boldsymbol{\vartheta} \right| \quad \text{subject to: } \boldsymbol{\vartheta}_0 \in \boldsymbol{\Theta};\ \int_{\boldsymbol{\Theta}} p_{\boldsymbol{\Theta}}(\boldsymbol{\vartheta}) d\boldsymbol{\vartheta} = 1 \tag{10.10}$$

The objective function $\left|f(\boldsymbol{\vartheta}_0)\right|$ can be written as follows

$$\begin{aligned} \left|f(\boldsymbol{\vartheta}_0)\right| &= \left| \int_{\boldsymbol{\Theta}} [r(\boldsymbol{\vartheta}_0) + \nabla_{\boldsymbol{\vartheta}} r\big|_{\boldsymbol{\vartheta}=\boldsymbol{\vartheta}_0}(\boldsymbol{\vartheta}-\boldsymbol{\vartheta}_0) - r(\boldsymbol{\vartheta})] p_{\boldsymbol{\Theta}}(\boldsymbol{\vartheta}) d\boldsymbol{\vartheta} \right| \\ &= \left| r(\boldsymbol{\vartheta}_0) + \nabla_{\boldsymbol{\vartheta}} r\big|_{\boldsymbol{\vartheta}=\boldsymbol{\vartheta}_0}(\boldsymbol{\mu}_{\boldsymbol{\vartheta}}-\boldsymbol{\vartheta}_0) - \mu_r \right| \end{aligned} \tag{10.11}$$

Imposing the first order optimality conditions, we obtain

$$\begin{aligned} \nabla_{\boldsymbol{\vartheta}_0} f(\boldsymbol{\vartheta}_0) &= \nabla_{\boldsymbol{\vartheta}_0} r(\boldsymbol{\vartheta}_0) + \nabla_{\boldsymbol{\vartheta}_0}(\nabla_{\boldsymbol{\vartheta}} r\big|_{\boldsymbol{\vartheta}=\boldsymbol{\vartheta}_0})(\boldsymbol{\mu}_{\boldsymbol{\vartheta}}-\boldsymbol{\vartheta}_0) - \nabla_{\boldsymbol{\vartheta}} r\big|_{\boldsymbol{\vartheta}=\boldsymbol{\vartheta}_0} \\ &= \mathbf{H}_r\big|_{\boldsymbol{\vartheta}=\boldsymbol{\vartheta}_0}(\boldsymbol{\mu}_{\boldsymbol{\vartheta}}-\boldsymbol{\vartheta}_0) = \mathbf{0} \end{aligned} \tag{10.12}$$

which is always satisfied for $\boldsymbol{\vartheta}_0 = \boldsymbol{\mu}_{\boldsymbol{\vartheta}}$.

REFERENCES

ATC 1996. *Seismic Evaluation and Retrofit of Concrete Buildings,* ATC-40 Report, Volumes 1 and 2, Applied Technology Council, Redwood City, CA.

Barbato M., Conte J.P. (2005) "Finite Element Response Sensitivity Analysis: a Comparison between Force-Based and Displacement-Based Frame Element Models" *Computer Methods in Applied Mechanics and Engineering*, 194:1479-1512.

Barbato M., Conte J.P. (2006) "Finite element structural response sensitivity and reliability analyses using smooth versus non-smooth material constitutive models" *International Journal of Reliability and Safety*, 1(1-2):3-39.

Barbato M., Gu Q., Conte J.P. (2006) "Response Sensitivity and Probabilistic Response Analyses of Reinforced Concrete Frame Structures" *Proceeding* of 8th National Conference on Earthquake Engineering, San Francisco, CA, USA.

Barbato M., Zona A., Conte J.P. (2007) "Finite element response sensitivity analysis using three-field mixed formulation: General theory and application to frame structures" *International Journal of Numerical Methods in Engineering*, 69(1):114-161.

Bjerager P. (1990) "On computation methods for structural reliability analysis" *Structural Safety*, 9(2):79-96.

Bolotin V.V. (1968) *Statistical Methods in Structural Mechanics*. Holden-Day, Inc., San Francisco, CA, USA.

Conte J.P., Jagannath M.K., Meghella M. (1995) "Earthquake Response Sensitivity Analysis of Concrete Gravity Dams" *Proceedings 7th International Conference on Applications of Statistics and Probability,* 395-402, Paris, France, July 10-13, 1995.

Conte J.P. (2001) "Finite Element Response Sensitivity Analysis in Earthquake Engineering" *Earthquake Engineering Frontiers in the New Millennium*, Spenser and Hu, Swets and Zeitlinger, 395-401.

Conte J.P., Vijalapura P.K., Meghella M. (2003) "Consistent Finite-Element Response Sensitivity Analysis" *Journal of Engineering Mechanics* (ASCE), 129:1380-1393.

Conte J.P., Barbato M., Spacone E. (2004) "Finite Element Response Sensitivity Analysis Using Force-Based Frame Models" *International Journal for Numerical Methods in Engineering*, 59:1781-1820.

Cook R.D., Malkus D.S., Plesha M.E. (1989) *Concepts and Applications of Finite Element Analysis*. Wiley, New York, NY, USA.

Crandall S.H. (2006) "A half-century of stochastic equivalent linearization" *Structural Control and Health Monitoring*, 13:27-40.

Der Kiureghian A., Ke B.-J. (1988) "The Stochastic Finite Element Method in Structural Reliability" *Probabilistic Engineering Mechanics*, 3(2):83-91.

Ditlevsen O., Madsen H.O. (1996) *Structural Reliability Methods*. Wiley, New York, NY, USA.

Dong W.M., Chiang W.L., Wong F.S. (1987) "Propagation of uncertainties in deterministic systems" *Computers & Structures*, 26(3):415-423.

Felli J.C., Hazen G.B. (2004) "Javelin Diagrams: A Graphical Tool for Probabilistic Sensitivity Analysis" *Decision Analysis*, 1(2):93-107.

FEMA 302-303 (1997) *NEHRP Recommended Provisions for Seismic Regulations for New Buildings and Other Structures*.

Ghanem R.G., Spanos P.D. (1991) *Stochastic Finite Elements: A Spectral Approach*. Springer-Verlag, New York, USA.

Grigoriu M. (2000) "Stochastic mechanics" *International Journal Solids and Structures*, 37:197–214.

Gu Q., Conte J.P., Yang Z., Elgamal A. (2007a) "Response Sensitivity Analysis of A Multi-Yield-Surface J_2 Plasticity Model by Direct Differentiation Method", to be submitted to *International Journal for Numerical Methods in Engineering.*

Gu Q., Barbato M., Conte J.P. (2007b) "Handling of Constraints in Finite Element Response Sensitivity Analysis", to be submitted to *Journal of Engineering Mechanics*, ASCE.

Haftka R.T., Gurdal Z. (1993) *Elements of Structural Optimization*. Third edition, Kluver Academic Publishers, Dordrecht, Germany.

Haukaas T., Der Kiureghian A. (2004) "Finite element reliability and sensitivity methods for performance-based engineering" *Report PEER 2003/14*, Pacific Earthquake Engineering Research Center, University of California, Berkeley, CA, USA.

Howard R.A. (1988) "Decision analysis: practice and promise" *Management Science*, 14(6):679-695.

Kleiber M., Antunez H., Hien T.D., Kowalczyk P. (1997) *Parameter Sensitivity in Nonlinear Mechanics: Theory and Finite Element Computation*. Wiley, New York, USA.

Liu J.S. (2001) *Monte Carlo strategies in scientific computing*. Springer Series in Statistics, Springer, Berlin, germany.

Lupoi G., Franchin P., Lupoi A., Pinto P.E. (2006) "Seismic fragility analysis of structural systems" *Journal of Engineering Mechanics* ASCE, 132(4):385-395.

Mazzoni S., McKenna F., Fenves G.L. (2005) *OpenSees Command Language Manual.* Pacific Earthquake Engineering Center, University of California, Berkeley. <http://opensees.berkeley.edu/>

Mirza S.A., MacGregor J.G. (1979) "Variability of Mechanical Properties of Reinforcing Bars" *Journal of the Structural Division*, 105(5): 921-937.

Mirza S.A., MacGregor J.G., Hatzinikolas M. (1979) "Statistical Descriptions of Strength of Concrete" *Journal of the Structural Division*, 105(6):1021-1037.

Phoon K.K., Kulhawy F.H. (1996) "On quantifying inherent soil variability" *Proceedings ASCE GED Spec. Conf. on Uncertainty in the Geologic Environ.: From Theory to Practice*, 1:326-340, Madison, Wisconsin.

Porter K.A., Beck J.L., Shaikhutdinov R.V. (2002) "Sensitivity of Building Loss Estimates to Major Uncertain Variables" *Earthquake Spectra*, 18(4):719-743.

Saltelli A., Chan K., Scott E.M. (2000) *Sensitivity Analysis*. Wiley, Chicester, England.

Scott B.D., Park P., Priestley M.J.N. (1982) "Stress-Strain Behavior of Concrete Confined by Overlapping Hoops at Low and High-Strain Rates" *Journal of the American Concrete Institute*, 79(1):13-27.

To C.W.S. (2001) "On Computational Stochastic Structural Dynamics Applying Finite Elements" *Archives of Computational Methods in Engineering*, 8(1):3-40.

Zona A., Barbato M., Conte J.P. (2005) "Finite Element Response Sensitivity Analysis of Steel-Concrete Composite Beams with Deformable Shear Connection" *Journal of Engineering Mechanics* (ASCE), 131(11):1126-1139.

Zona A., Barbato M., Conte J.P. (2006) "Finite Element Response Sensitivity Analysis of Continuous Steel-Concrete Composite Girders" *Steel and Composite Structures*, 6(3):183-202.

CHAPTER 11

STRUCTURAL RELIABILITY ANALYSIS USING THE CONCEPT OF DESIGN POINT

11.1 INTRODUCTION

The field of structural reliability analysis has seen significant advances in the last two decades (Ditlevsen and Madsen 1996). Analytical and numerical methodologies have been developed and improved for the probabilistic analysis of real structures characterized in general by nonlinear behavior, material and geometric uncertainties and subjected to stochastic loads (Schueller et al. 2004). Reliability analysis methods have been successfully applied to such problems, as the ones encountered in civil engineering and typically analyzed deterministically through the finite element (FE) method (Der Kiureghian and Ke 1988).

Several reliability analysis methods, such as asymptotic methods (First- and Second-Order Reliability Methods: FORM and SORM) (Breitung 1984; Der Kiureghian and Liu 1986; Der Kiureghian et al. 1987; Der Kiureghian 1996; Ditlevsen and Madsen 1996) and importance sampling with sampling distribution centered on the design point(s) (Schueller and Stix 1987; Melchers 1989; Au et al. 1999; Au and Beck 2001a) are characterized by the crucial step of finding the design point(s) (DPs), defined as the most likely failure point(s) in the standard normal space. In particular, asymptotic methods can pro-

vide reliability analysis results with a relatively small number of simulations (often of the order of 10-100 simulations for FORM analysis) and with a computational effort practically independent of the magnitude of the failure probability. Furthermore, these methods provide important information such as reliability sensitivity measures, as by-product of the DP search (Hohenbichler and Rackwitz 1986). Other reliability analysis methods, e.g., subset simulation (Au and Beck 2001b; Au and Beck 2003) and importance sampling with sampling distribution not centered at the DP(s) (Bucher 1988; Ang et al. 1992; Au and Beck 1999), do not use the concept of DP. In general, the computational cost of these methods increases for decreasing magnitude of the failure probability. Thus, for very low failure probabilities, these methods could require a large number of simulations.

In this chapter, structural reliability methods based on the concept of DP are reviewed. Recent improvements (some of which developed in the course of this research) in terms of efficiency and robustness of the DP search process are presented and applications to nonlinear FE models of structural systems are shown in order to highlight capabilities and shortcomings of these methods.

11.2 FINITE ELEMENT RELIABILITY ANALYSIS AND DESIGN POINT SEARCH

In general, the structural reliability problem consists of computing the probability of failure P_f of a given structure, which is defined as the probability of exceeding some limit-state (or damage-state) function(s) (LSFs) when the loading(s) and/or structural properties and/or parameters in the LSFs are uncertain quantities modeled as random vari-

ables. This work focuses on component reliability analysis, that is, we consider a single LSF $g = g(\mathbf{r}, \boldsymbol{\vartheta})$, where $\mathbf{r}$ denotes a vector of response quantities of interest and $\boldsymbol{\vartheta}$ is the vector of random variables considered. The LSF g is chosen such that $g \leq 0$ defines the failure domain/region. Thus, the time-invariant component reliability problem takes the following mathematical form

$$P_f = P[g(\mathbf{r}, \boldsymbol{\vartheta}) \leq 0] = \int_{g(\mathbf{r}, \boldsymbol{\vartheta}) \leq 0} f_{\boldsymbol{\Theta}}(\boldsymbol{\vartheta}) d\boldsymbol{\vartheta} \tag{11.1}$$

where $f_{\boldsymbol{\Theta}}(\boldsymbol{\vartheta})$ denotes the joint Probability Density Function (PDF) of random variables $\boldsymbol{\vartheta}$.

Moreover, it is assumed that the LSF describes a first-excursion problem in one of the following simple forms:

$$g = \begin{cases} u_{lim} - u(\boldsymbol{\vartheta}, \hat{t}); & \text{(up-crossing problem)} \\ u(\boldsymbol{\vartheta}, \hat{t}) - u_{lim}; & \text{(down-crossing problem)} \\ u_{lim} - |u(\boldsymbol{\vartheta}, \hat{t})|; \quad (u_{lim} > 0); & \text{(double-barrier crossing problem)} \end{cases} \tag{11.2}$$

in which $u(\boldsymbol{\vartheta}, \hat{t})$ is a scalar response quantity (i.e., nodal displacement) computed at $t = \hat{t}$, where t is an ordering parameter (loading factor in a quasi-static analysis or time in a dynamic analysis), $\hat{t}$ is a specified value of t (e.g., $\hat{t} = \max(t)$ in a pushover analysis) and u_{lim} is a deterministic threshold. In this case, the time-invariant reliability problem reduces to computing

$$P_f = P[g(\boldsymbol{\vartheta}, \hat{t}) \le 0] = \begin{cases} P[u(\boldsymbol{\vartheta}, \hat{t}) \ge u_{lim}] \\ P[u(\boldsymbol{\vartheta}, \hat{t}) \le u_{lim}] \\ P[|u(\boldsymbol{\vartheta}, \hat{t})| \ge u_{lim}] \end{cases} \tag{11.3}$$

For time-variant reliability problems, an upper bound of the probability of failure, $P_f(T)$, over the time interval [0, T], can be found as (Bolotin 1969)

$$P_f(T) \le \int_0^T \nu_g(t)dt \tag{11.4}$$

where $\nu_g(t)$ denotes the mean down-crossing rate of level zero of the LSF g. In this case, the LSF also depends on the time t and can be expressed, in general, as $g = g(\mathbf{r}(\boldsymbol{\vartheta}, t), \boldsymbol{\vartheta}, t) = g(\boldsymbol{\vartheta}, t)$. An estimate of $\nu_g(t)$ can be obtained numerically from the limit form relation (Hagen and Tvedt 1991)

$$\nu_g(t) = \lim_{\delta t \to 0} \frac{P[(g(\boldsymbol{\vartheta}, t) > 0) \cap (g(\boldsymbol{\vartheta}, t + \delta t) \le 0)]}{\delta t} \tag{11.5}$$

The numerical evaluation of the numerator of Eq. (11.5) reduces to a time-invariant two-component parallel system reliability analysis. It is clear that the term $P[g(\boldsymbol{\vartheta}, t) \le 0]$ in Eq. (11.3) represents the building block for the solution of both time-invariant and time-variant reliability problems (Der Kiureghian 1996).

The problem in Eq. (11.1) is extremely challenging for real-world structures and can be solved only in approximate ways. The conceptually simplest FE structural reliability method is crude Monte Carlo Simulation (MCS), consisting in (1) simulating repeatedly a set of random modeling parameters $\boldsymbol{\vartheta}$ according to the given joint PDF, $f_{\boldsymbol{\Theta}}(\boldsymbol{\vartheta})$,

(2) computing the corresponding structural response or performance function through FE analysis keeping track of the number of times that the limit-state condition is exceeded and (3) estimating the probability of failure as

$$P_f \cong \frac{n_{fail}}{N} = P_{f,\,MCS} \tag{11.6}$$

where n_{fail} denotes the number of recorded failures and N is the total number of simulations performed. A measure of the accuracy of the MCS estimate of the failure probability is given by the coefficient-of-variation (cov) of $P_{f,\,MCS}$ as

$$\mathrm{cov}[P_{f,\,MCS}] = \sqrt{\frac{1-P_f}{N \cdot P_f}} \approx \frac{\sqrt{\dfrac{1}{N(N-1)} \sum_{i=1}^{N} \left(P_i - \dfrac{1}{N} \sum_{j=1}^{N} P_j \right)^2}}{\dfrac{1}{N} \sum_{j=1}^{N} P_j} \tag{11.7}$$

where P_i is an indicator defined such that

$$P_i = \begin{cases} 1 & \text{failure} \\ 0 & \text{otherwise} \end{cases} \tag{11.8}$$

Crude MCS (Liu 2001) is a very robust and general method for structural reliability analysis but, for small probability events, becomes extremely inefficient or even computationally unfeasible since it requires a very large number of computationally very expensive simulations in order to obtain an accurate estimate of the failure probability (e.g., for $\mathrm{cov}[P_{f,\,MCS}] = 0.10$ and $P_f \sim 10^{-4}$, the required number of samples is of the

order $N \sim 10^6$). This crucial drawback justifies and motivates the large amount of research devoted to developing more efficient structural reliability analysis methods.

A well established methodology, alternative to simulation, consists of introducing a one-to-one mapping/transformation between the physical space of variables $\boldsymbol{\vartheta}$ and the standard normal space of variables $\mathbf{y}$ (Ditlevsen and Madsen 1996) and then computing the probability of failure P_f as

$$P_f = P[G(\mathbf{y}) \le 0] = \int_{G(\mathbf{y}) \le 0} \varphi_{\mathbf{Y}}(\mathbf{y}) d\mathbf{y} \tag{11.9}$$

where $\varphi_{\mathbf{Y}}(\mathbf{y})$ denotes the standard normal joint PDF and $G(\mathbf{y}) = g(\mathbf{r}(\boldsymbol{\vartheta}(\mathbf{y})), \boldsymbol{\vartheta}(\mathbf{y}))$ is the LSF in the standard normal space.

Solving the integral in Eq. (11.9) remains a formidable task, but this new form of P_f is suitable for approximate solutions taking advantage of the rotational symmetry of the standard normal joint PDF and its exponential decay in both the radial and tangential directions. An optimum point at which to approximate the limit-state surface (LSS) $G(\mathbf{y}) = 0$ is the "design point", which is defined as the most likely failure point in the standard normal space, i.e., the point on the LSS that is closest to the origin. Finding the DP is a crucial step for approximate semi-analytical methods to evaluate the integral in Eq. (11.9), such as FORM, SORM and importance sampling (Au and Beck 1999; Breitung 1984; Der Kiureghian et al. 1987).

The DP, $\mathbf{y}^*$, is found as solution of the following constrained optimization problem:

$$\mathbf{y}^* = \arg\left\{ \min\left(\frac{1}{2}\mathbf{y}^T\mathbf{y}\right) \middle| G(\mathbf{y}) = 0 \right\} \tag{11.10}$$

The most effective techniques for solving the constrained optimization problem in Eq. (11.10) are gradient-based optimization algorithms (Gill et al. 1981; Liu and Der Kiureghian 1991) coupled with algorithms for accurate and efficient computation of the gradient of the constraint function $G(\mathbf{y})$, requiring computation of the sensitivities of the response quantities $\mathbf{r}$ to parameters $\boldsymbol{\vartheta}$. Indeed, using the chain rule of differentiation for multivariable functions, we have

$$\nabla_{\mathbf{y}} G = (\nabla_{\mathbf{r}} g|_{\boldsymbol{\vartheta}} \cdot \nabla_{\boldsymbol{\vartheta}} \mathbf{r} + \nabla_{\boldsymbol{\vartheta}} g|_{\mathbf{r}}) \cdot \nabla_{\mathbf{y}} \boldsymbol{\vartheta} \tag{11.11}$$

where $\nabla_{\mathbf{r}} g|_{\boldsymbol{\vartheta}}$ and $\nabla_{\boldsymbol{\vartheta}} g|_{\mathbf{r}}$ are the gradients of LSF g with respect to its explicit dependency on quantities $\mathbf{r}$ and $\boldsymbol{\vartheta}$, respectively, and usually can be computed analytically (e.g., for the LSF g given in Eq. $(11.2)_1$, we have $\nabla_{\mathbf{r}} g|_{\boldsymbol{\vartheta}} = -1$ and $\nabla_{\boldsymbol{\vartheta}} g|_{\mathbf{r}} = 0$); the term $\nabla_{\boldsymbol{\vartheta}} \mathbf{r}$ denotes the response sensitivities of response variables $\mathbf{r}$ to parameters $\boldsymbol{\vartheta}$, and $\nabla_{\mathbf{y}} \boldsymbol{\vartheta}$ is the gradient of the physical space parameters with respect to the standard normal space parameters (i.e., Jacobian matrix of the probability transformation from the $\mathbf{y}$-space to the $\boldsymbol{\vartheta}$-space). For probability distribution models defined analytically, the gradient $\nabla_{\mathbf{y}} \boldsymbol{\vartheta}$ can be derived analytically as well (Ditlevsen and Madsen 1996).

For real-world problems, the response simulation (computation of $\mathbf{r}$ for given $\boldsymbol{\vartheta}$) is usually performed using advanced mechanics-based non-linear computational models developed based on the FE method. FE reliability analysis requires augmenting existing FE formulations for response-only calculation, to compute the response sensitivities,

$\nabla_{\boldsymbol{\vartheta}}\mathbf{r}$, to parameters $\boldsymbol{\vartheta}$. An accurate and efficient way to perform FE response sensitivity analysis is through the DDM (Zhang and Der Kiureghian 1993; Kleiber et al. 1997; Conte 2001; Conte et al. 2003; Franchin 2004; Haukaas and Der Kiureghian 2004; Zona et al. 2005, 2006).

The DP search, for FE reliability analysis involving large nonlinear models of real-world structural systems, is itself a formidable task. Some of the difficulties and the ways in which they have been addressed in this work are presented below.

11.2.1 High computational cost

The DP search requires repeated computations of the constraint function and its gradient (at least once at every iteration of the optimization algorithm) through FE response and response sensitivity analyses, the computational cost of which depends on the complexity of the FE model considered.

The use of the DDM for response sensitivity computations allows one to reduce significantly the computational cost of each iteration of the optimization algorithm when compared with the use of the finite difference method (e.g., forward finite difference, FFD). When the number of sensitivity parameters is large, the computational cost of response sensitivity calculations can be predominant over the computational effort of response-only calculations. In particular, response sensitivity analysis using FFD analysis requires performing an additional nonlinear FE response analysis for each sensitivity parameter. On the other hand, the use of the DDM can reduce the computational cost of response sensitivity analysis to only 10%-40% of the CPU time required by FFD analysis.

Chapters 3 through 5 describe new developments and extensions of the DDM to address the state-of-the-art nonlinear FE technology. It is noteworthy that DDM-based response sensitivities are more accurate than FFD sensitivities and are not affected by the "step-size dilemma" (Haftka and Gurdal 1993). In general, these properties are beneficial for the optimization algorithm used in terms of convergence rate and can reduce the number of iterations required to reach the DP within a predefined accuracy.

11.2.2 Complexity of the nonlinear constrained optimization problem

The constrained optimization problem in Eq. (11.10) can be very difficult to solve for strongly nonlinear constraint functions defined in high-dimensional spaces, as is usually the case for realistic structural problems. The DP search for FE reliability analysis requires robust and efficient nonlinear constrained optimization algorithms, as well as their computer implementation and integration with advanced, efficient and robust deterministic FE codes.

In this work, two different algorithms have been used:

(1) the improved Hasofer-Lind Rackwitz-Fiessler (HL-RF) algorithm with line-search (Der Kiureghian and Liu 1986; Rackwitz and Fiessler 1978), available in both computational platforms FEDEASLab-FERUM (Haukaas 2001) and OpenSees (Mazzoni et al. 2005);

(2) the non-linear programming code SNOPT (Gill et al. 2002, 2005), which has been integrated with both FEDEASLab-FERUM and OpenSees in the course of this research.

While the improved HL-RF algorithm is a gradient-based iterative method specialized for structural reliability problems (Liu and Der Kiureghian 1991), SNOPT is a general-purpose optimization code based on Sequential Quadratic Programming (SQP) (Gill et al. 1981). It has been found that SNOPT, when compared to the improved HL-RF algorithm, is more robust and often is able to converge to the DP with a smaller number of iterations. On the other hand, for the same number of iterations, SNOPT requires more CPU time than the improved HL-RF algorithm due to the more general and sophisticated gradient-based algorithm.

11.2.3 Numerical noise in finite element analysis

The use of FE analysis introduces numerical noise in the evaluation of the constraint function and its gradient. This numerical noise may pose severe limitations on the accuracy with which the DP is obtained.

In fact, in a constrained optimization routine, convergence is obtained when the two conditions of feasibility (violation of the constraint) and optimality (gradient of the associated Lagrangian function equal to zero) are satisfied within a specified tolerance. The tolerance for the feasibility condition is related to the accuracy with which the constraint function can be computed (thus to the convergence tolerance in the Newton-based iterative process used in nonlinear FE analysis), while the tolerance for the optimality condition depends on the accuracy in the constraint gradient computation, the order of magnitude of which is equal to the square root of the convergence tolerance used in the response calculations. These relations between the numerical tolerances for the convergence of different iterative algorithms must be taken into account when setting such tolerances in

order to obtain a reasonable compromise between computational effort and attainable accuracy.

11.2.4 Discontinuities in the response sensitivities

The gradient of the constraint function (i.e., the FE response sensitivities) may exhibit discontinuities. In general, gradient-based optimization algorithms do not ensure convergence to a (local) optimum of the objective function in Eq. (11.10) subject to the given constraints (expressed in terms of structural response quantities) if response sensitivities are discontinuous. Typically, non-convergence to an existing optimum may occur if discontinuities in the gradient of the LSF (i.e., response sensitivity discontinuities) exist in a neighborhood of the optimum itself. Even in cases when convergence can be achieved, gradient discontinuities can be detrimental to the convergence rate of the optimization process. In theory, gradient-based optimization algorithms can reach (locally) a quadratic convergence rate, when the Lagrangian function associated with the given problem is second-order differentiable and its exact Hessian is available (Gill et al. 1981). However, this is not the case for structural reliability problems, for which at most exact first-order response sensitivities are available. It can thus be concluded that, for practical purposes in FE reliability analysis, requiring at least continuous FE response sensitivities is a good compromise between convergence rate and computational cost.

Chapter 6 investigates response sensitivity continuity (or lack thereof) and provides:

(1) insight into the analytical behavior of FE response sensitivities obtained from smooth and non-smooth material constitutive models;

(2) the response sensitivity algorithm for a widely used smooth material constitutive model (the Menegotto-Pinto model for steel material);

(3) a sufficient condition on the smoothness properties of material constitutive laws for obtaining continuous response sensitivities in quasi-static FE analysis;

(4) important remarks and observations regarding the dynamic FE analysis case, which suggest that response sensitivity discontinuities can be eliminated/reduced by using smooth material constitutive models and refining the time discretization of the equations of motion.

11.2.5 Non-convergence of the finite element analysis

Nonlinear FE analyses may not converge to equilibrium. In such cases, the constraint function cannot be evaluated numerically and the optimization algorithm may stop before reaching the DP.

In general, non-convergence takes place in two distinct cases: (1) when the combination of parameter values produces a non-physical configuration, and (2) when the computer program stops due to lack of numerical convergence. The first case should happen very rarely if the joint PDF of the random parameters is chosen carefully to represent accurately the physical properties of the structural system considered. The second case is very common in the failure domain, where grossly nonlinear behavior is expected in the structural system response. The optimization algorithm should be enhanced with specific methods to avoid as much as possible the domain in which the constraint function is not defined. SNOPT provides built-in routines to move away from the parameter domain where the constraint and objective functions are not defined.

11.2.6 Multiple local minima

The gradient-based optimization algorithms considered in this work are designed for local optimization. Thus, even when these algorithms converge to a solution, there is no assurance that the obtained point is the global DP for the reliability problem of interest.

This difficulty can be tackled, at least in principle, by using global optimization routines based on gradient-based local optimization. The problem of existence and computation of multiple local minima will not be considered in the sequel since its study is beyond the scope of this work.

11.3 FIRST-ORDER RELIABILITY METHOD (FORM)

FORM analysis provides an approximation of the failure probability P_f as defined in Eq. (11.1) through two main operations: (1) the DP search in the transformed uncorrelated standard normal space, and (2) the approximation of the LSS in the standard normal space with the hyper-plane tangent to the LSS at the DP. The probability content of the half-space defined by this tangent hyper-plane is known in closed-form and is used as first-order failure probability estimate.

The distance from the origin of the standard normal space to the DP is also called "reliability index" and denoted as

$$\beta = \|\mathbf{y}^*\| \tag{11.12}$$

The first-order probability estimate is then found as

$$P_{f,\,FORM} = \Phi(-\beta) \tag{11.13}$$

where $\Phi(\ldots)$ denotes the standard normal CDF.

It is noteworthy that, as a by-product of a FORM analysis, the following valuable parameter importance measures (Hohenbichler and Rackwitz 1986; Liu et al. 1989; Ditlevsen and Madsen 1996) are obtained:

(1) The $\boldsymbol{\alpha}$-vector:

$$\boldsymbol{\alpha} = \nabla_{\mathbf{y}}\beta\big|_{\mathbf{y}^*} = -\frac{\nabla_{\mathbf{y}}G\big|_{\mathbf{y}^*}}{\left\|\nabla_{\mathbf{y}}G\big|_{\mathbf{y}^*}\right\|} \tag{11.14}$$

$\boldsymbol{\alpha}$ denotes the sensitivity of the reliability index with respect to the coordinates of the DP in the standard normal space. The $\boldsymbol{\alpha}$-vector is a unit vector normal to the LSS at the DP and pointing to the failure domain. The absolute values of the elements of $\boldsymbol{\alpha}$ are indicative of the relative importance of the corresponding random variables in the standard normal space.

(2) The $\boldsymbol{\gamma}$-vector

$$\boldsymbol{\gamma} = \frac{\nabla_{\boldsymbol{\vartheta}}\beta\big|_{\boldsymbol{\vartheta}^*}\cdot\mathbf{D}}{\left\|\nabla_{\boldsymbol{\vartheta}}\beta\big|_{\boldsymbol{\vartheta}^*}\cdot\mathbf{D}\right\|} = \frac{\boldsymbol{\alpha}\cdot\nabla_{\boldsymbol{\vartheta}}\mathbf{y}\cdot\mathbf{D}}{\left\|\boldsymbol{\alpha}\cdot\nabla_{\boldsymbol{\vartheta}}\mathbf{y}\cdot\mathbf{D}\right\|} \tag{11.15}$$

where $\mathbf{D}$ is the diagonal matrix of the standard deviations σ_i (i = 1, ..., n) of the original variables in the physical space and $\nabla_{\boldsymbol{\vartheta}}\mathbf{y} = (\nabla_{\mathbf{y}}\boldsymbol{\vartheta})^{-1}$ is the Jacobian matrix of the probability transformation from the $\boldsymbol{\vartheta}$-space to the $\mathbf{y}$-space. The $\boldsymbol{\gamma}$-vector is a normalized (unit dimensionless) importance measure for the vector of the original random variables and corresponds to the sensitivity of the reliability index with respect to the coordinates of the DP in the physical space with components scaled multiplying each

of them by their correspondent standard deviation. It can be shown that for statistically independent random variables $\boldsymbol{\gamma} = \boldsymbol{\alpha}$.

(3) The $\boldsymbol{\delta}$-vector

$$\boldsymbol{\delta} = \nabla_{\boldsymbol{\mu}}\beta \cdot \mathbf{D} = \boldsymbol{\alpha} \cdot \nabla_{\boldsymbol{\mu}}\mathbf{y}^* \cdot \mathbf{D} \tag{11.16}$$

which is a dimensionless importance measure of the means of the random variables. The $\boldsymbol{\delta}$-vector denotes the sensitivity of the reliability coefficient with respect to the means of the random variables in the physical space with components scaled multiplying each of them by their correspondent standard deviation. Each component of the $\boldsymbol{\delta}$-vector equals 100 times the change in β due to a change in the corresponding mean of 1 per cent of the standard deviation.

(4) The $\boldsymbol{\eta}$-vector

$$\boldsymbol{\eta} = \nabla_{\boldsymbol{\sigma}}\beta \cdot \mathbf{D} = \boldsymbol{\alpha}^{\mathrm{T}} \cdot \nabla_{\boldsymbol{\sigma}}\mathbf{y}^* \cdot \mathbf{D} \tag{11.17}$$

which is a normalized importance measure of the standard deviations of the random variables. The $\boldsymbol{\eta}$-vector denotes the sensitivity of the reliability coefficient with respect to the standard deviations of the random variables in the physical space with components scaled multiplying each of them by their correspondent standard deviation. Each component of the $\boldsymbol{\eta}$-vector equals 100 times the change in β due to 1 per cent change in the corresponding standard deviation.

FORM analysis can be extremely efficient and provide a failure probability estimate with a small computational effort practically independent of the magnitude of P_f. On

the other hand, when the LSS is highly nonlinear especially near the DP, FORM analysis can be quite inaccurate.

11.4 SECOND-ORDER RELIABILITY METHOD (SORM)

SORM analysis has been established as an attempt to improve the accuracy of FORM and is obtained by approximating, in the standard normal space, the LSS at the DP by a second-order surface. The SORM estimate of the failure probability, $P_{f,SORM}$, is given as the probability content of the failure side of the second-order surface.

The first comprehensive study on SORM was performed by Fiessler et al. (1979), in which a parabolic surface tangent to the LSS at the DP with the axis of the parabola along the direction of the DP was obtained through second-order Taylor expansion and curvature-fitting. A geometrically insightful and asymptotically exact result for parabolas was derived by Breitung (1984) as

$$P_{f,\,SORM} \cong P_{f,\,B} = \frac{\Phi(-\beta)}{\prod_{j=1}^{n-1} \sqrt{1-\kappa_i \beta}} \tag{11.18}$$

where κ_i are the main curvatures, taken positive for a concave LSS, and n denotes the number of random variables. These main curvatures are computed as the eigenvalues of the following Hessian matrix **A**:

$$\mathbf{A} = \frac{\mathbf{H}_{red}}{\left\| \nabla_{\mathbf{y}} G \big|_{\mathbf{y}^*} \right\|} \tag{11.19}$$

in which $[\mathbf{H}_{red}]_{ij} = [\mathbf{R} \cdot \mathbf{H} \cdot \mathbf{R}]_{ij}$ is the reduced Hessian computed at the DP (with respect to the rotated coordinates in the standard normal space), with i, j = 1, 2, ..., n-1, **H** is the $n \times n$ Hessian matrix of the LSF at the DP (with respect to the original coordinates in the standard normal space), **R** is a matrix of coordinate transformation so that the new reference system has the n-th axis oriented as the DP vector **y***, and $\left\| \nabla_{\mathbf{y}} G \big|_{\mathbf{y}^*} \right\|$ denotes the Euclidean norm of the gradient of the LSF at the DP.

Another simple approximation of $P_{f,\,SORM}$ has been proposed by Hohenbichler and Rackwitz (1988) as

$$P_{f,\,SORM} \cong P_{f,\,HR} = \frac{\Phi(-\beta)}{\prod_{j=1}^{n-1} \sqrt{1 - \frac{\phi(\beta)}{\Phi(-\beta)} \kappa_i \beta}} \tag{11.20}$$

where $\phi(\ldots)$ denote the standard normal PDF.

A more accurate three-term formula has been proposed by Tvedt (1983) and exact results for a paraboloid were derived by Tvedt (1988) and have been extended to cover all the quadratic forms of Gaussian variables (Tvedt 1990). Other extensions of SORM include a point-fitted parabolic algorithm developed by Der Kiureghian et al. (1987, 1991), an importance sampling improvement introduced by Hohenbichler and Rackwitz (1988), new approximations using McLaurin and Taylor series expansions (Koyluoglu and Nielsen 1994; Cai and Elishakoff 1994), and new empirical approximations (Zhao and Ono 1999a, b; Hong 1999).

11.5 IMPORTANCE SAMPLING

Crude MCS can require a large number of samples to obtain sufficiently accurate failure probability estimates, because it employes a sampling distribution centered at the mean point, while failure events tend to occur in the tail regions of probability distributions. A large number of evaluations of the performance function may be computationally costly or prohibitive and this inhibits the use of crude MCS in most FE reliability applications. The importance sampling (IS) method is based on the idea of centering the sampling distribution near the failure domain in order to increase the efficiency of the sampling scheme.

Introducing an indicator function $I(\mathbf{y})$ as

$$I(\mathbf{y}) = \begin{cases} 1 & \text{if} \quad G(\mathbf{y}) \le 0 \\ 0 & \text{otherwise} \end{cases} \tag{11.21}$$

Eq. (11.1) can be rewritten as (Ditlevsen and Madsen 1996)

$$P_f = \int_{\Omega_n} I(\mathbf{y})\phi(\mathbf{y})d\mathbf{y} = \int_{\Omega_n} \left[I(\mathbf{y})\frac{\phi(\mathbf{y})}{f(\mathbf{y})} \right] f(\mathbf{y})d\mathbf{y} \tag{11.22}$$

where Ω_n denotes the entire standard normal space of dimension n, and $f(\mathbf{y})$ is a joint PDF, called the sampling distribution, which must be non-zero within the region where $I(\mathbf{y}) = 1$. It is observed that the last integral in Eq. (11.22) is an expectation of the random variable $Q(\mathbf{y}) = I(\mathbf{y})\frac{\phi(\mathbf{y})}{f(\mathbf{y})}$ relative to the distribution $f(\mathbf{y})$, which can be easily estimated by generating statistically independent realizations of the random variable $Q(\mathbf{y})$

derived from the distribution $f(\mathbf{y})$ and taking their average. Thus, an unbiased estimator of P_f is given by

$$P_f \cong P_{f,IS} = \frac{1}{N}\sum_{i=1}^{N} q_i \tag{11.23}$$

where q_i is the i-th realization of the random variable $Q(\mathbf{y})$ and N is the number of samples.

For IS analysis to be efficient and accurate, the distribution $f(\mathbf{y})$ must be (1) easy to evaluate, (2) non-zero within the region where $I(\mathbf{y}) = 1$, and (3) centered near the failure domain. This is often accomplished using for $f(\mathbf{y})$ a standard normal PDF centered at the DP (Melchers 1989), i.e., $f(\mathbf{y}) = \phi(\tilde{\mathbf{y}})$ where $\tilde{\mathbf{y}} = \mathbf{y} - \mathbf{y}^*$.

A measure of accuracy of the probability estimate is the variance of $P_{f,IS}$, which can be estimated as

$$\mathrm{var}[P_{f,IS}] \cong \frac{1}{N(N-1)}\left[\sum_{i=1}^{N} q_i^2 - \frac{1}{N}\left(\sum_{j=1}^{N} q_j\right)^2\right] \tag{11.24}$$

The coefficient of variation (cov) of the probability estimate can be computed as

$$\mathrm{cov}[P_{f,IS}] = \frac{\sqrt{\mathrm{var}[P_{f,IS}]}}{P_{f,IS}} \tag{11.25}$$

Sampling can be repeated a user-defined number of times, N_{max}, or until $\mathrm{cov}[P_{f,IS}]$ falls below a specified target cov.

11.6 TIME-VARIANT RELIABILITY ANALYSIS

A classical approach to solving time-variant reliability problems makes use of estimates of the mean out-crossing rate $\nu_g(t)$ to compute (1) an analytical upper bound to the time-variant failure probability

$$P_f(T) \leq \int_0^T \nu_g(t)\, dt = P_{f,\,UB} \tag{11.26}$$

and (2) the Poisson approximation of $P_f(T)$

$$P_f(T) \cong 1 - \{1 - P[g(\boldsymbol{\vartheta}, 0) \leq 0]\} \cdot \exp\left(-\int_0^T \nu_g(t)dt\right) = P_{f,\,P} \tag{11.27}$$

where $P[g(\boldsymbol{\vartheta}, 0) \leq 0]$ denotes the probability that the system is initially (at time t = 0) in the failure domain. Thus, the problem reduces to computing the value of the mean out-crossing rate at a discrete number of time instants and numerically estimate the integral $\int_0^T \nu_g(t)dt$.

11.6.1 Out-crossing rate as a two-component parallel system reliability analysis

The mean out-crossing rate may be computed as the zero level down-crossing rate of the scalar process G(**y**, t), using Rice's formula (Rice 1944, 1945), as

$$\nu_g(t) = \int_{-\infty}^{0} |\dot{G}|\, f_{G\dot{G}}(G = 0, \dot{G})\, d\dot{G} \tag{11.28}$$

where $f_{G\dot{G}}(G = 0, \dot{G})$ is the joint PDF of $G(\mathbf{y}, t)$ and its time derivative $\dot{G}(\mathbf{y}, t)$ evaluated at $G(\mathbf{y}, t) = 0$. This joint PDF is extremely difficult or practically impossible to determine for a general nonlinear inelastic system, inhibiting the direct application of Rice's formula in FE structural reliability analysis.

Alternatively, the mean out-crossing rate can be computed from the limit formula in Eq. (11.5) (Hagen and Tvedt. 1991), which can be rewritten in the standard normal space as

$$\nu_g(t) = \lim_{\delta t \to 0} \frac{P[(G_1 < 0) \cap (G_2 < 0)]}{\delta t} \tag{11.29}$$

where $G_1 = -G(\mathbf{y}, t)$ and $G_2 = G(\mathbf{y}, t + \delta t)$. The numerator is the probability that the system is in the safe domain at time t and in the unsafe domain at time $t + \delta t$. A numerical approximation of the out-crossing rate can be obtained by considering a finite δt (sufficiently small to assure that at most one out-crossing event is possible), computing the numerator of Eq. (11.29) and dividing it by δt. The evaluation of the numerator of Eq. (11.29) corresponds to solving a time-invariant parallel system reliability problem of two components with LSFs G_1 and G_2, respectively, at a specific time. For this purpose, a FORM analysis (Ditlevsen and Madsen 1996) can be employed.

11.6.2 FORM approximation of mean out-crossing rate

The numerator in Eq. (11.29) can be computed linearizing the two LSSs $G_1 = 0$ and $G_2 = 0$ at points $\mathbf{y}_1^*$ and $\mathbf{y}_2^*$ in the standard normal space and using a first-order

approximation of the probability $P[(G_1 < 0) \cap (G_2 < 0)]$. The probability content in the failure domain defined by the intersection of the two linearized LSSs is given by (Madsen et al. 1986):

$$P \cong P_{FORM} = \Phi_2(-\beta_1, -\beta_2, \rho_{12}) = \Phi(-\beta_1)\Phi(-\beta_2) + \int_0^{\rho_{12}} \phi_2(-\beta_1, -\beta_2, \rho)\, d\rho \quad (11.30)$$

where $\Phi_2(v_1, v_2, \rho)$ is the bi-variate normal joint CDF with zero means, unit variances and with correlation coefficient ρ, β_1 and β_2 are the reliability indices of the two linearized failure modes, $\rho_{12} = \boldsymbol{\alpha}_1 \boldsymbol{\alpha}_2^T$ is the correlation coefficient between the two linearized failure modes and $\phi_2(v_1, v_2, \rho)$ denotes the bi-variate normal joint PDF with zero means, unit variances and correlation coefficient ρ, i.e.,

$$\phi_2(v_1, v_2, \rho) = \frac{1}{2\pi(1-\rho^2)} \exp\left(- \frac{v_1^2 + v_2^2 - 2\rho v_1 v_2}{2(1-\rho^2)} \right) \quad (11.31)$$

A complete discussion on the choice of the two linearization points $\mathbf{y}_1^*$ and $\mathbf{y}_2^*$ for the LSSs $G_1 = 0$ and $G_2 = 0$ can be found in Li and Der Kiureghian (1995) and Conte and Vijalapura (1998). In general, the requirements in terms of precision in computing the DPs for the two distinct LSSs for small δt can be very strict. In addition, solving Eq. (11.30) requires two DP searches and the solution of a numerically challenging integral, thus resulting in a methodology very expensive computationally. In this work, the following approximate solution of Eq. (11.30) (Koo et al. 2005) is employed

$$\Phi_2(-\beta_1, -\beta_2, \rho_{12}) \approx \Phi_2(\beta, -\beta, \rho_{12}) \approx \frac{1}{2\pi}\exp\left(-\frac{\beta^2}{2}\right) \cdot \left[\frac{\pi}{2} + \arcsin(\rho_{12})\right] \qquad (11.32)$$

Eq. (11.32) relies on the fact that, for small δt, $\beta_2 \approx -\beta_1 = \beta$ and $\rho_{12} \approx -1$. Complete derivation of this approximate formula can be found in Koo (2003). In addition, if the structural system is deterministic and thus the random parameters describe only the excitation, an approximation $\tilde{\mathbf{y}}_2^*$ to the DP excitation at time t + δt, $\mathbf{y}_2^*$, can be obtained through shifting by δt the DP excitation at time t, $\mathbf{y}^*$ (i.e., $(\tilde{\mathbf{y}}_2^*)_i = (\mathbf{y}^*)_i - [(\mathbf{y}^*)_i - (\mathbf{y}^*)_{i-1}] \cdot \delta t / \Delta t$, i = 1, ..., n, $(\mathbf{y}^*)_0 = 0$). Therefore, the computation of ρ_{12} can be performed with sufficient accuracy approximating the vector $\boldsymbol{\alpha}_2$ as

$$\boldsymbol{\alpha}_2 = -\frac{\nabla_{\mathbf{y}} G_2\big|_{\mathbf{y}_2^*}}{\left\|\nabla_{\mathbf{y}} G_2\big|_{\mathbf{y}_2^*}\right\|} = \frac{\mathbf{y}_2^*}{\|\mathbf{y}_2^*\|} \cong \frac{\tilde{\mathbf{y}}_2^*}{\|\tilde{\mathbf{y}}_2^*\|} \qquad (11.33)$$

which requires finding only one DP (for the LSS $G_1 = 0$) and obtains the DP excitation for the second LSS by shifting the DP excitation of the first LSS by the amount δt (Koo et al. 2005).

11.7 APPLICATION EXAMPLES

11.7.1 Time-invariant problem: quasi-static pushover of a R/C frame structure

The first application example consists of a two-story two-bay reinforced concrete frame on rigid base, a model of which is shown in Fig. 11.1. This frame structure is mod-

eled using displacement-based Euler-Bernoulli frame elements with distributed plasticity, each with four Gauss-Legendre integration points along its length. Section stress resultants at the integration points are computed by discretizing the frame sections into layers (i.e., the 2-D equivalent of fibers for the 3-D case). The constitutive behavior of the steel reinforcement is modeled using Menegotto-Pinto constitutive model with kinematic hardening (Menegotto and Pinto 1973; Barbato and Conte 2006). The concrete is modeled using a smoothed Popovics-Saenz model with zero tension stiffening for the envelope curve (Balan et al. 1997, 2001; Kwon and Spacone 2002, Zona et al. 2005). This model is obtained from the model presented in (Zona et al. 2004) smoothing the unloading/reloading branches with third-order polynomials to preserve the smoothness of the monotonic envelope also in the cyclic behavior. Different material parameters are used for confined (core) and unconfined (cover) concrete in the columns. Typical stress-strain cyclic responses of the three material constitutive models used in this application example are shown in Figs. 11.2 (for the confined and unconfined concrete materials) and 11.3 (for the reinforcement steel).

Thirteen material constitutive parameters are used to characterize the various structural materials present in the structure, namely five parameters each for the confined concrete ($f_{c,\,core}$: peak strength, $\varepsilon_{c,\,core}$: strain at peak strength, $f_{cu,\,core}$: residual strength at a control point, $\varepsilon_{cu,\,core}$: strain at which the residual strength is reached, $E_{c,core}$: initial tangent stiffness) and the unconfined concrete ($f_{c,\,cover}$, $\varepsilon_{c,\,cover}$, $f_{cu,\,cover}$, $\varepsilon_{cu,\,cover}$, $E_{c,cover}$) and three parameters for the reinforcement steel (f_y: yield strength, E_0: initial stiffness, b: post-yield to initial stiffness ratio). These material parameters are modeled as

random fields spatially fully correlated, i.e., each material parameter is modeled with a single random variable (RV). The marginal PDFs of these material parameters are given in Table 11.1 and were obtained from studies reported in the literature based on real data (Mirza and MacGregor 1979; Mirza et al. 1979).

The statistical correlation coefficients between the various material parameters are assumed as follows:

(1) $\rho = 0.7$ for (a) $f_{c,\,core}$ and $f_{cu,\,core}$, (b) $\varepsilon_{c,\,core}$ and $\varepsilon_{cu,\,core}$, (c) $\varepsilon_{c,\,cover}$ and $\varepsilon_{cu,\,cover}$, (d) $f_{c,\,core}$ and $f_{c,\,cover}$, (e) $\varepsilon_{c,\,core}$ and $\varepsilon_{c,\,cover}$, (f) $\varepsilon_{cu,\,core}$ and $\varepsilon_{cu,\,cover}$, (g) $E_{c,\,core}$ and $E_{c,\,cover}$, (h) $f_{c,\,cover}$ and $f_{cu,\,cover}$, (i) $f_{cu,\,core}$ and $f_{cu,\,cover}$;

(2) $\rho = 0.5$ for (a) $f_{cu,\,core}$ and $f_{c,\,cover}$, (b) $\varepsilon_{c,\,core}$ and $\varepsilon_{cu,\,cover}$, (c) $\varepsilon_{cu,\,core}$ and $\varepsilon_{c,\,cover}$; (d) $f_{c,\,core}$ and $f_{cu,\,cover}$;

(3) $\rho = 0.0$ for all other pairs of parameters.

These correlation coefficients are chosen based on engineering judgement, since to the authors' knowledge, precise values of correlation coefficients are not available in the literature.

After static application of the gravity loads (assumed as uniformly distributed load per unit length of beam $Q = 42.5 kN/m$ at each floor, corresponding to a uniformly distributed load per unit area $q = 8.5 kN/m^2$ assuming an inter-frame distance of L' = 5.0m), the structure is subjected to a quasi-static pushover analysis, in which an upper tri-

angular distribution of horizontal forces is applied at the floor levels (see Fig. 11.1). The horizontal force applied at the roof level, P, is modeled as lognormal random variable with mean $\mu_P = 350\text{kN}$ and cov = 20% (see Table 11.1), while the horizontal force applied at the first floor level is considered fully correlated with P and with value P_1 = P/2. FE response, response sensitivity and reliability analyses are performed using the FE analysis framework OpenSees (Mazzoni et al. 2005), in which three-dimensional frame elements were augmented for response sensitivity analysis (Barbato et al. 2006) and the response sensitivity algorithm for imposing multipoint constraints was implemented (Gu et al. 2007).

A roof displacement u_{lim} = 0.144m (corresponding to a roof drift ratio of 3.0% and computed from the horizontal displacement of the top of the middle column) is considered as failure condition. Thus, the LSF is given by g = 0.144m - u_{roof}. The DP search is performed with the origin of the standard normal space as starting point using both the improved HL-RF algorithm and SNOPT. The two algorithms yield practically identical results in terms of DP and importance measures at the DP (with the improved HL-RF algorithm performing better than SNOPT in terms of CPU time for this specific case study). The improved HL-RF algorithm requires 9 performance function evaluations and 5 gradient (response sensitivity) computations to find the DP. Fig. 11.4 plots the base shear - horizontal floor displacement (recorded at the top two nodes of the middle column) responses of the considered structural system subjected to quasi-static pushover analysis at the mean point and at the DP of the random modeling parameters. The DP in physical and standard normal spaces and parameter importance measures are provided in Table

11.2. From the parameter importance measures computed at the DP, it is observed that the dominant parameter is the value of the horizontal force applied at the roof level, P, followed by the yield strength of the reinforcement steel, f_y, and the peak strength of the unconfined concrete, $f_{c,cover}$, while the sensitivity of the reliability index to other parameters is almost negligible. The first-order reliability index is $\beta_{FORM} = 2.048$ and the FORM estimate of the failure probability is $P_{f,\,FORM} = 0.0203$. Using an algorithm proposed by Der Kiureghian and De Stefano (1991), the first principal curvature of the LSS at the DP is obtained, which allows one to find a SORM approximation of the failure probability, $P_{SORM,\,1} = 0.0210$, based on Breitung's formula (Eq. (11.18)) considering only the first principal curvature. Computing the Hessian matrix **H** by finite difference applied to the "exact" gradient computed through DDM, all the 13 curvatures of the LSS at the DP are computed (see Subsection 11.4) and the SORM approximation based on the complete Breitung's formula is obtained as $P_{f,\,B} = 0.0223$. The SORM approximation based on Eq. (11.20) (Hohenbichler and Rackwitz 1988) using all the computed curvatures gives $P_{f,\,HR} = 0.0257$. An IS analysis is performed using as sampling distribution a joint standard normal PDF centered at the DP and cov[$P_{f,IS}$] = 0.05 as stopping criterion, yielding $P_{f,\,IS(0.05)} = 0.0266$ (1955 samples). Finally, a second IS analysis is performed using as sampling distribution a joint standard normal PDF centered at the DP and cov[$P_{f,IS}$] = 0.01 as stopping criterion yielding $P_{f,\,IS(0.01)} = 0.0262$ (40830 samples). Considering $P_{f,\,IS(0.01)}$ as reference solution, it is found that both FORM and SORM analyses provide accurate estimates of the failure probability of the subject structural system subjected to

the quasi-static pushover loads considered. The SORM approximation based on the complete Breitung's formula provides a more accurate result, but is computationally significantly more expensive (more than twice) than SORM based on the first principal curvature at the DP and FORM. The SORM approximation based on Eq. (11.20) is very accurate (the most accurate among the semi-analytical approximations) at the same computational cost of the SORM approximation based on the complete Breitung's formula. IS with $\text{cov}[P_{f,IS}] = 0.05$ is computationally very expensive. Failure probability estimates and relative computational times (normalized to the computational time required by FORM) are provided in Table 11.3 for all the reliability analyses performed.

11.7.2 Time-variant case: linear elastic SDOF and MDOF systems subjected to white noise excitation

The methodology presented in Section 11.6 for time-variant reliability analysis has been tested on simple linear elastic SDOF and MDOF systems subjected to white noise excitation from at rest initial conditions. The structural properties of the systems are considered as deterministic quantities. The input ground motion is modeled as a linearly interpolated Gaussian white noise discretized into random variables representing the ground acceleration at instants of time separated by time interval Δt. Mean up-crossing rates are estimated numerically by FORM analysis using Koo's approximation in Eq. (11.32) and then compared with available closed-form solutions (Lutes and Sarkani 2004).

Fig. 11.5 compares analytical and numerical mean up-crossing rates for different time discretization intervals Δt (i.e., Δt = 0.010s, 0.005s and 0.001s, respectively) for a

linear elastic SDOF system representing an idealized a shear-type single-story steel frame with height $H = 3.20\text{m}$, bay length L = 6.00m and made of European HE340A steel columns. The system is defined by the following parameters (taken as deterministic): mass $M = 28800\text{kg}$, damping ratio $\zeta = 0.02$, and stiffness K = 40.56kN/mm, resulting in a natural period of $T_0 = 0.17\text{s}$. The Gaussian white noise has PSD $\phi_0 = 0.007\text{m}^2/\text{s}^3$ and the deterministic threshold defining exceedance of the limit-state is $\xi = 0.016\text{m}$ (single-barrier up-crossing problem). From Fig. 11.5, it is observed that the numerical estimates of the mean up-crossing rate clearly converge to the exact mean up-crossing rate for decreasing values of Δt. In all the analyses, $\delta t = 10^{-5}$s is employed.

The second benchmark example consists of a linear elastic model of a one-bay three-story shear-frame with bay of length L = 6.00m and story height H = 3.20m. A model of this structural system is described in Section 6.3.1 of Chapter 6. The fundamental period of this linear elastic undamped shear-frame is T_1 = 0.38s. Natural frequencies, natural periods and effective modal mass ratios for the undamped structure are given in Table 6.1. Viscous damping in the form of Rayleigh damping is assumed with a damping ratio $\zeta = 0.02$ for the first and third modes of vibration. The Gaussian white noise ground motion has PSD $\phi_0 = 0.029\text{m}^2/\text{s}^3$ and the LSF is defined as $g = \xi - u_{\text{roof}}$, with deterministic threshold $\xi = 0.096\text{m}$ for the horizontal roof displacement, $u_{\text{roof.}}$ Fig. 11.6 plots the DP excitation and DP relative displacement response for the single-barrier up-crossing problem at time $t = 5.0\text{s}$. Fig. 11.7 compares analytical and numerical mean up-crossing rates for different white noise time discretization intervals Δt (i.e., $\Delta t = 0.020$s

and 0.010s, respectively) obtained for the considered linear elastic 3-DOF system subjected to white noise base excitation, from at rest initial conditions, and upcrossing the deterministic threshold $\xi = 0.096\text{m}$. Also in this case, the numerical estimates of the mean up-crossing rate clearly converge to the exact mean up-crossing rate for decreasing values of Δt and $\delta t = 10^{-5}$s. The results presented in Figs. 11.5 and 11.7 show that the mean up-crossing rates obtained using FORM analysis are in very good agreement with the exact results when a sufficiently small time-interval, Δt, is used in discretizing the white noise excitation process.

11.7.3 Time-variant case: nonlinear hysteretic SDOF system subjected to white noise excitation

To incorporate the effects of inelastic structural behavior in FE reliability analysis, mean out-crossing rate computations are performed for a SDOF system with a force-deformation relation modeled using the Menegotto-Pinto (MP) constitutive law. This constitutive law is calibrated to a shear-type single-story steel frame with height H = 3.20m, bay length L = 6.00m and made of European HE340A wide flange steel beams. The system is defined by the following parameters (taken as deterministic): mass M = 28800 kg, damping ratio $\zeta = 0.02$, initial stiffness K = 40.56kN/mm, initial yield force F_{y0} = 734kN and post-yield to initial stiffness ratio (i.e., strain hardening ratio) b = 0.05.

This SDOF system is subjected to two different input ground motions modeled as Gaussian white noise processes with PSD $\phi_0 = 0.035\text{m}^2/\text{s}^3$ and $\phi_0 = 0.25\text{m}^2/\text{s}^3$, respectively. The expected cumulative number of up-crossing events (single-barrier prob-

lem) and time-variant failure probability relative to the roof displacement exceeding the threshold $\xi = 0.016\text{m}$ (roof drift ratio = 0.5%) and $\xi = 0.048\text{m}$ (roof drift ratio = 1.5%), respectively, are computed using FORM and MCS. Fig. 11.8 compares the estimates of the expected cumulative number of up-crossing events obtained using FORM and MCS (with one standard deviation interval as well) for the case $\phi_0 = 0.035\text{m}^2/\text{s}^3$ and $\xi = 0.016\text{m}$, in which the structure behaves quasi-linearly. Fig. 11.8 also compares the time-variant failure probability estimates obtained through the FORM-based Poisson approximation and MCS. Fig. 11.9 plots the shear force-roof drift response at the DP for up-crossing at time t = 5.0s. Fig. 11.10 compares the same estimates as in Fig. 11.8, but for the case $\phi_0 = 0.25\text{m}^2/\text{s}^3$ and $\xi = 0.048\text{m}$, in which the structure yields significantly. Fig. 11.11 shows the force-displacement response at the DP for up-crossing at time t = 5.0s. For quasi-linear structural behavior, the results in terms of expected cumulative number of up-crossings obtained using FORM are in good agreement with the MCS results. In this case, the difference between the FORM-based Poisson approximation and MCS estimate of the time-variant failure probability is mainly due to the relatively high value of P_f, for which the Poisson assumption of statistically independent up-crossing events is not very good. On the other hand, a FORM approximation of the LSS for significantly nonlinear structural behavior provides a very inaccurate estimate of the expected cumulative number of up-crossings and therefore of the time-variant failure probability. Thus, computationally efficient methodologies are needed to take into account the nonlinear nature of the LSS for mean out-crossing rate computation in the case of significant inelastic structural behavior.

11.8 CONCLUSIONS

In this Chapter, the state-of-the-art of finite element structural reliability analysis using the concept of design point (DP) is presented. The search of the DP consists of solving a nonlinear constrained optimization problem for which DDM-based structural response sensitivities are used. Existing methodologies (FORM, SORM, Importance Sampling, time-variant reliability through mean out-crossing rate computation) are reviewed and new improvements (some of which developed in this work) in terms of efficiency and robustness are illustrated.

Examples of both time-invariant and time-variant FE reliability analysis applied to linear elastic and nonlinear hysteretic models of structural systems are presented and the corresponding results are discussed in terms of accuracy and computational efficiency. It is found that the adopted methodologies can often provide results sufficiently accurate for engineering purposes with a small computational effort (compared to MCS) practically independent on the magnitude of the failure probability. On the other hand, these approximate techniques can produce inaccurate estimates of failure probabilities when the structural systems under study exhibit strong nonlinear inelastic behavior. New techniques are needed to understand clearly the reasons for these inaccuracies and to improve the methodologies currently employed.

Table 11.1 Marginal PDFs of material parameters and horizontal loads for the two-story R/C frame

RV [unit]	Distribution	Mean	c.o.v [%]
$f_{c,core}$ [MPa]	lognormal	34.47	20
$f_{cu,core}$ [MPa]	lognormal	25.72	20
$\varepsilon_{c,core}$ [-]	lognormal	0.005	20
$\varepsilon_{cu,core}$ [-]	lognormal	0.020	20
$E_{c,core}$ [MPa]	lognormal	27850	20
$f_{c,cover}$ [MPa]	lognormal	27.58	20
$f_{cu,cover}$ [MPa]	lognormal	1.00	20
$\varepsilon_{c,cover}$ [-]	lognormal	0.002	20
$\varepsilon_{cu,cover}$ [-]	lognormal	0.012	20
$E_{c,cover}$ [MPa]	lognormal	24910	20
f_y [MPa]	lognormal	248.20	10.6
E_0 [MPa]	lognormal	210000	3.3
b [-]	lognormal	0.02	20
P [kN]	lognormal	350	20

Table 11.2 Design point and importance measures from FORM analysis for quasi-static pushover of R/C frame structure

RV [unit]	ϑ^*	y^*	α	γ	δ	η
$f_{c,core}$ [MPa]	31.82	-5.62e-2	-0.0275	-0.0387	0.0427	-0.0189
$f_{cu,core}$ [MPa]	24.13	-8.96e-3	-0.0044	0.0000	0.0000	0.0000
$\varepsilon_{c,core}$ [-]	0.0049	1.23e-2	0.0060	0.0085	-0.0089	0.0017
$\varepsilon_{cu,core}$ [-]	0.0195	0.00	0.0000	0.0000	0.0000	0.0000
$E_{c,core}$ [MPa]	24160	-1.64e-2	-0.0080	-0.0113	0.0119	-0.0028
$f_{c,cover}$ [MPa]	25.10	-3.76e-1	-0.1836	-0.1509	0.1685	-0.0845
$f_{cu,cover}$ [MPa]	0.93	-9.68e-3	-0.0047	-0.0091	0.0100	-0.0042
$\varepsilon_{c,cover}$ [-]	0.0019	-2.86e-2	-0.0139	-0.0056	0.0059	-0.0012
$\varepsilon_{cu,cover}$ [-]	0.0167	-2.93e-2	-0.0143	-0.0204	0.0215	-0.0048
$E_{c,cover}$ [MPa]	26970	-6.26e-2	-0.0306	-0.0228	0.0240	-0.0058
f_y [MPa]	232.5	-5.67e-1	-0.2767	-0.2781	0.2970	-0.1849
E_0 [MPa]	209700	-2.22e-2	-0.0109	-0.0109	-0.0109	-0.0006
b [-]	0.0195	-3.77e-2	-0.0184	-0.0185	0.0195	-0.0043
P [kN]	502.9	1.929	0.9419	0.9469	-0.6313	-1.5991

Table 11.3 Time-invariant reliability analysis results for the quasi-static pushover analysis of the R/C frame structure

Analysis	P_f	Relative CPU time
FORM	0.0203	1
$SORM_1$	0.0210	1.02
$SORM_{all,B}$	0.0223	2.26
$SORM_{all,HR}$	0.0257	2.26
$IS_{0.05}$	0.0266	53.83
$IS_{0.01}$	0.0262	1103.51

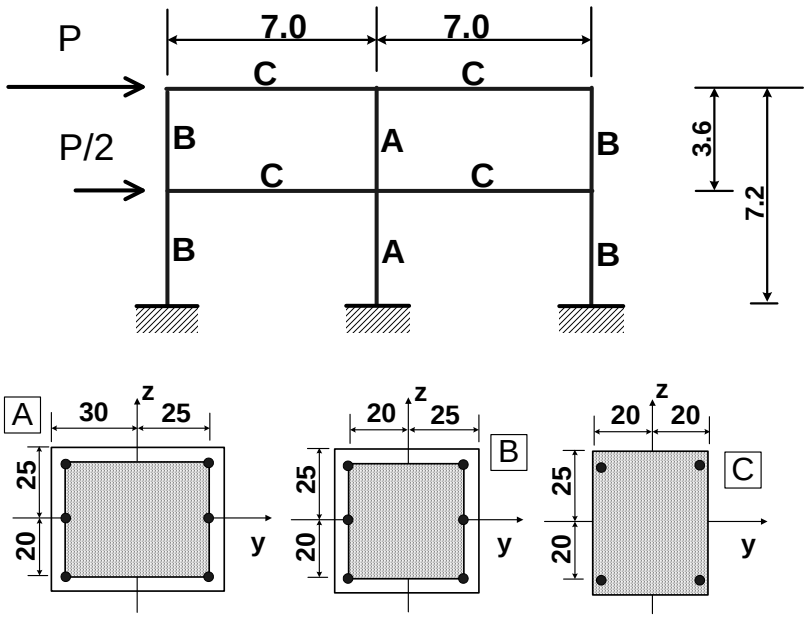

Figure 11.1 Geometry, cross-sectional properties and applied horizontal loads for the two-story R/C frame.

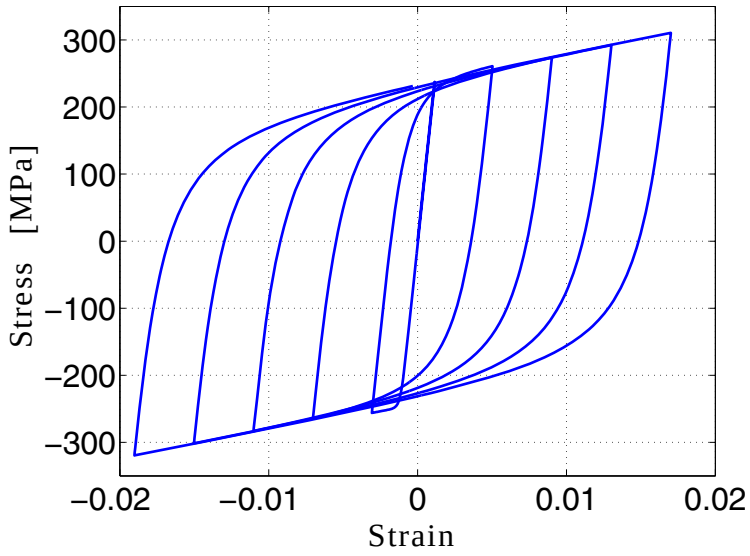

Figure 11.2 Material constitutive model for the reinforcement steel of the two-story R/C frame.

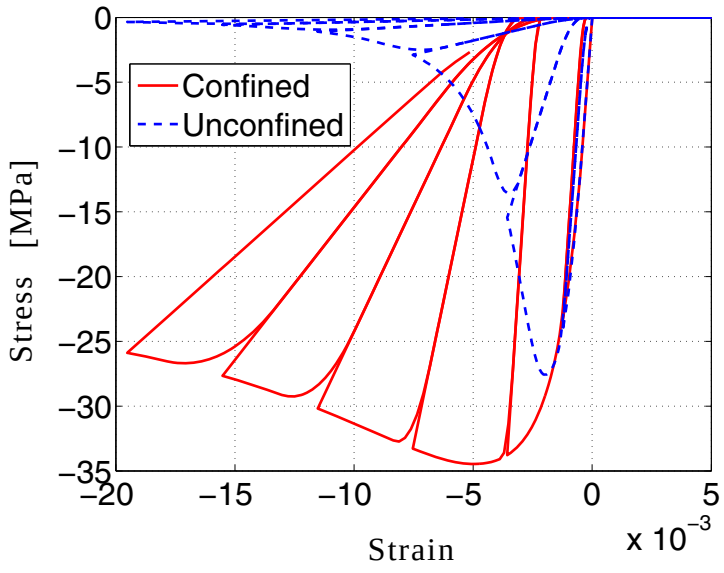

Figure 11.3 Material constitutive model for confined and unconfined concrete of the two-story R/C frame.

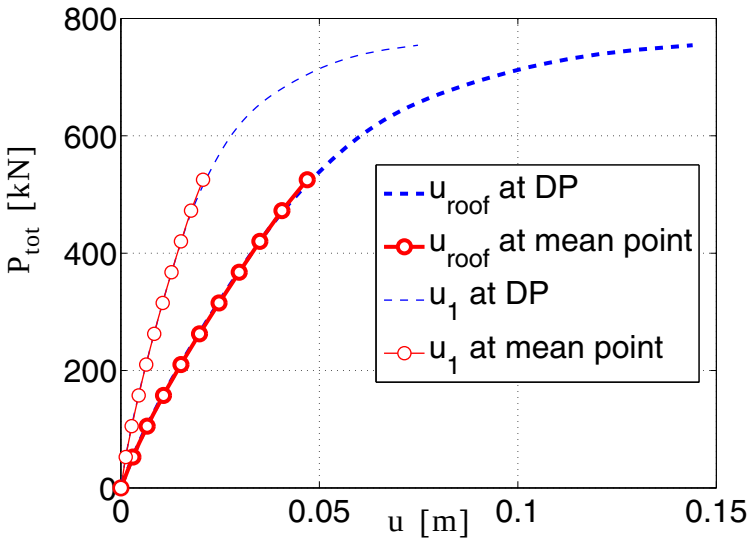

Figure 11.4 Base shear - horizontal floor displacements of two-story R/C frame structure at the mean point and at the DP.

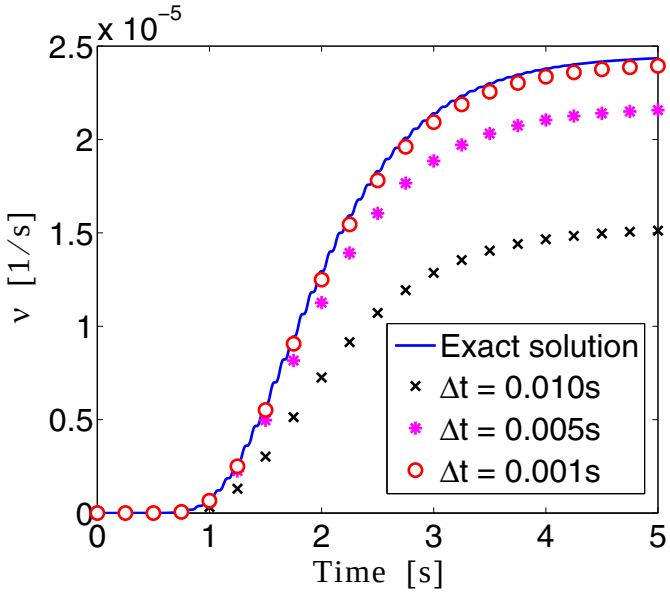

Figure 11.5 Mean up-crossing rate computation for linear elastic SDOF system.

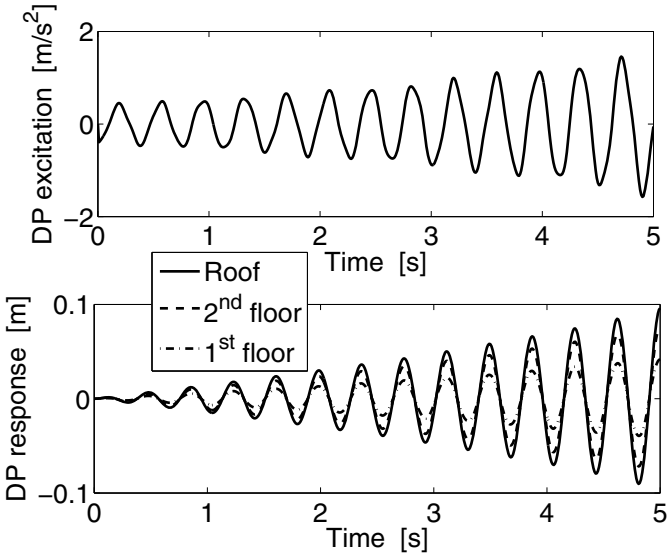

Figure 11.6 DP excitation and DP response of linear elastic 3-DOF system subjected to white noise ground motion.

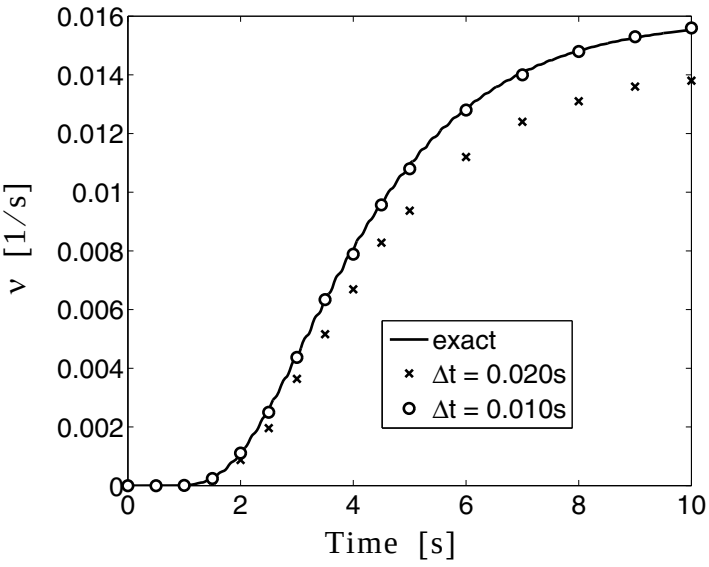

Figure 11.7 Mean up-crossing rate computation for linear elastic 3-DOF system.

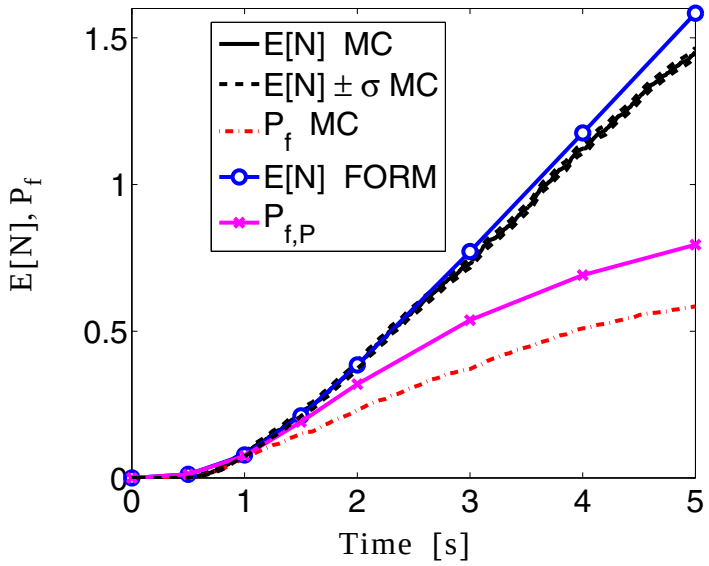

Figure 11.8 Estimates of the expected cumulative number of up-crossing events and time-variant failure probability for the MP SDOF system relative to a drift threshold $\xi = 0.016\text{m}$.

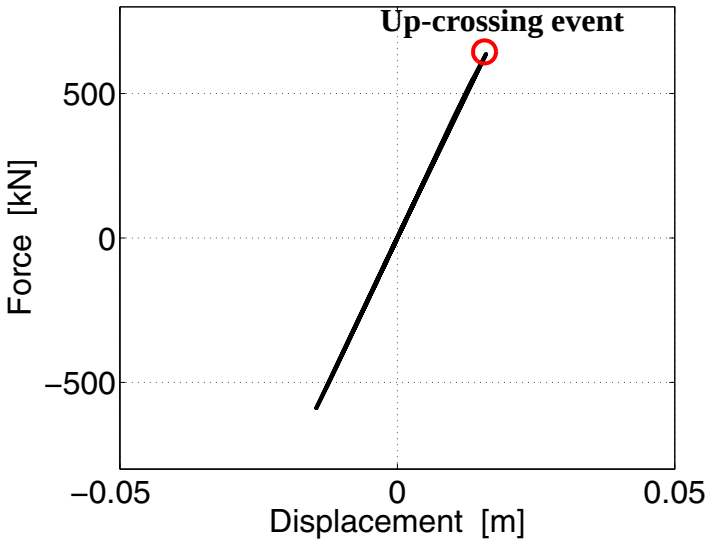

Figure 11.9 Shear force - drift relation at the DP for the MP SDOF system relative to the drift threshold $\xi = 0.016\text{m}$ at time t = 5.0s.

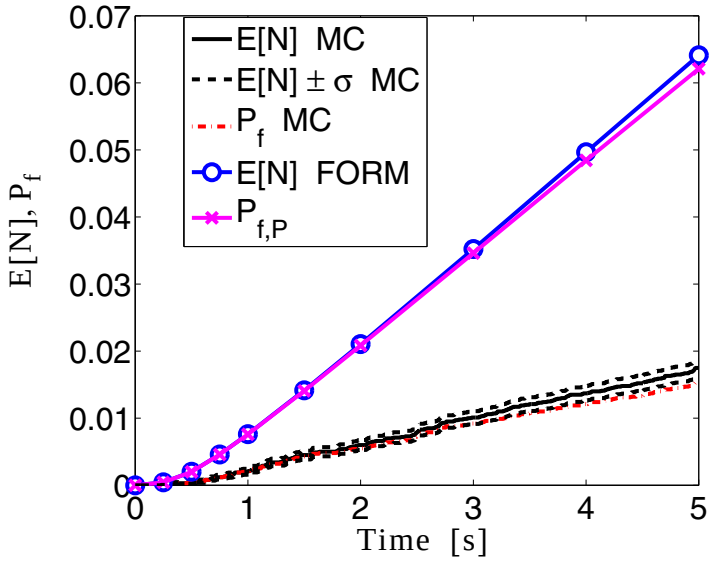

Figure 11.10 Estimates of the expected cumulative number of up-crossing events and time-variant failure probability for the MP SDOF system relative to a drift threshold $\xi = 0.048\text{m}$.

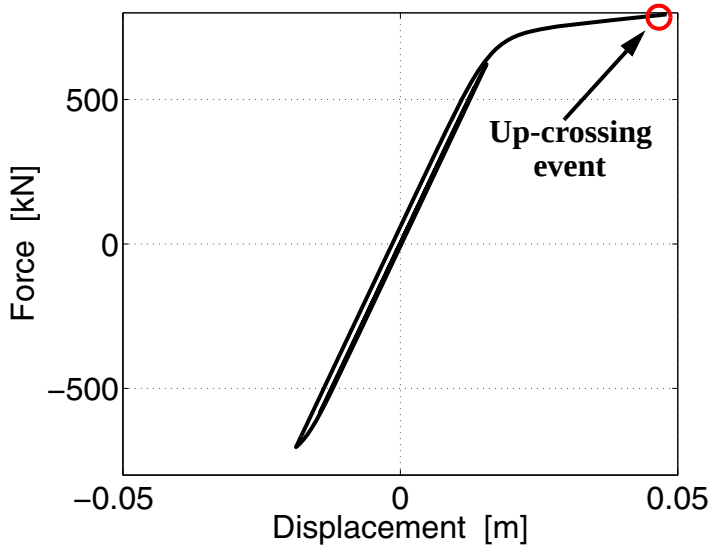

Figure 11.11 Shear force - drift relation at the DP for the MP SDOF system relative to the drift threshold $\xi = 0.048\text{m}$ at time t = 5.0s.

REFERENCES

Ang G.L., Ang A.H.-S., Tang W.H. (1992) “Optimal importance sampling density estimator” *Journal of Engineering Mechanics* (ASCE), 118(6):1146–1163.

Au S.K., Beck J.L. (1999) “A new adaptive importance sampling scheme” *Structural Safety*, 21(2):135–158.

Au S.K., Beck J.L. (2001a) “First excursion probabilities for linear systems by very efficient importance sampling” *Probabilistic Engineering Mechanics*, 16(3):193–207.

Au S.K., Beck J.L. (2001b) “Estimation of small failure probabilities in high dimensions by subset simulation” *Probabilistic Engineering Mechanics*, 16(4):263–277.

Au S.K., Beck J.L. (2003) “Subset simulation and its application to seismic risk based on dynamic analysis” *Journal of Engineering Mechanics* (ASCE), 129(8):901–917.

Au S.K., Papadimitriou C., Beck, J.L. (1999) “Reliability of uncertain dynamical systems with multiple design points” *Structural Safety*, 21(2):113–133.

Balan T.A., Filippou F.C., Popov E.P., (1997) “Constitutive model for 3D cyclic analysis of concrete structures”. *Journal of Engineering Mechanics* (ASCE), 123(2):143-153.

Balan T.A., Spacone E., Kwon M. (2001) “A 3D hypoplastic model for cyclic analysis of concrete structures”. *Engineering Structures*, 23:333-342.

Barbato M., Conte J.P. (2006) “Finite element structural response sensitivity and reliability analyses using smooth versus non-smooth material constitutive models” *International Journal of Reliability and Safety*, 1(1-2):3-39.

Barbato M., Gu Q., Conte J.P. (2006) “Response Sensitivity and Probabilistic Response Analyses of Reinforced Concrete Frame Structures” *Proceeding* of 8th National Conference on Earthquake Engineering, San Francisco, CA, USA.

Bolotin V.V. (1969) *Statistical methods in Structural Mechanics*. Holden-Day, San Francisco, CA, USA

Breitung K. (1984) "Asymptotic approximations for multinormal integrals" *Journal of the Engineering Mechanics Division* (ASCE), 110(3):357–366.

Bucher C.G. (1988) "Adaptive importance sampling – an iterative fast Monte Carlo procedure" *Structural Safety*, 5(2):119–126.

Cai G.Q., Elishakoff I. (1994) "Refined second-order reliability analysis" *Structural Safety*, 14, 267–276.

Conte J.P., Vijalapura P.K. (1998) "Seismic safety analysis of concrete gravity dams accounting for both system uncertainties and excitation stochasticity". *Report ENEL-CRIS*, Rice University, Houston, TX, USA.

Conte J.P. (2001) "Finite Element Response Sensitivity Analysis in Earthquake Engineering" *Earthquake Engineering Frontiers in the New Millennium*, Spenser and Hu, Swets and Zeitlinger, 395-401.

Conte J.P., Vijalapura P.K., Meghella M. (2003) "Consistent Finite-Element Response Sensitivity Analysis" *Journal of Engineering Mechanics* (ASCE), 129:1380-1393.

Conte J.P., Barbato M., Spacone E. (2004) "Finite element response sensitivity analysis using force-based frame models" *International Journal for Numerical Methods in Engineering*, 59(13):1781–1820.

Der Kiureghian A., Liu P.-L. (1986) "Structural reliability under incomplete probability information" *Journal of the Engineering Mechanics Division* (ASCE), 111(EM1):85–104.

Der Kiureghian A., Lin H.-Z., Hwang S.-J. (1987) "Second-order reliability approximations" *Journal of the Engineering Mechanics Division* (ASCE), 113(EM8):1208–1225.

Der Kiureghian A., Ke B.-J. (1988) “The stochastic finite element method in structural reliability” *Probabilistic Engineering Mechanics*, 3(2):83–91.

Der Kiureghian A., De Stefano M. (1991) “Efficient algorithms for second-order reliability analysis” *Journal of Engineering Mechanics* (ASCE), 117(12):2904-2923.

Der Kiureghian A. (1996) “Structural reliability methods in seismic safety assessment: a review” *Journal of Engineering Structures*, 18(6):412–424.

Ditlevsen O., Madsen H.O. (1996) *Structural Reliability Methods*. Wiley, New York, NY, USA.

Franchin P. (2004) “Reliability of uncertain inelastic structures under earthquake excitation” *Journal of Engineering Mechanics* (ASCE), 130(2):180–191.

Gill P.E., Murray W., Wright M.H. (1981) *Practical Optimization*, New York: Academic Press.

Gill P.E., Murray W., Saunders M.A. (2002) “SNOPT: an SQP algorithm for large-scale constrained optimization” *SIAM Journal on Optimization*, 12:979–1006.

Gill P.E., Murray W., Saunders M.A. (2005) “User’s guide for SNOPT version 7, a Fortran package for large-scale non-linear programming” *User’s Guide*, Version 7.0, Available at: http://www.scicomp.ucsd.edu/~peg/.

Gu Q., Barbato M., Conte J.P. (2007) “Handling of Constraints in Finite Element Response Sensitivity Analysis”, to be submitted to *Journal of Engineering Mechanics* (ASCE).

Hagen O., Tvedt L. (1991) “Vector process out-crossing as parallel system sensitivity measure” *Journal of Engineering Mechanics* (ASCE), 117(10):2201–2220.

Haftka R.T., Gurdal Z. (1993) *Elements of Structural Optimization.* Third edition, Kluver Academic Publishers, Dordrecht.

Haukaas T. (2001) “FERUM (Finite Element Reliability Using Matlab)” *User’s Guide*, Available at: http://www.ce.berkeley.edu/~haukaas/FERUM/ferum.html.

Haukaas T., Der Kiureghian A. (2004) “Finite element reliability and sensitivity methods for performance-based engineering” *Report PEER 2003/14*, Pacific Earthquake Engineering Research Center, University of California, Berkeley.

Hohenbichler M., Rackwitz R. (1986) “Sensitivity and importance measures in structural reliability” *Civil Engineering Systems*, 3(4):203–209.

Hong H.P. (1999) “Simple approximations for improving second-order reliability estimates” *Journal of Engineering Mechanics* (ASCE),125(5):592-595.

koo H. (2003) “FORM, SORM and simulation techniques for nonlinear random vibration”, *Ph.D. thesis*, University of California at Berkeley, Berkeley, CA, USA.

Koo H., Der Kiureghian A., Fujimura K. (2005) “Design-point excitation for non-linear random vibrations” *Probabilistic Engineering Mechanics*, 20:136-147.

Koyluoglu H.U., Nielsen S.R.K. (1994) “New approximations for SORM integrals” *Structural Safety*, 13:235–246.

Kleiber M., Antunez H., Hien T.D., Kowalczyk P. (1997) *Parameter Sensitivity in Nonlinear Mechanics: Theory and Finite Element Computation*, New York, Wiley.

Kwon M., Spacone E. (2002) “Three-dimensional finite element analyses of reinforced concrete columns” *Computers and Structures* 80:199-212.

Li C.-C., Der Kiureghian A. (1995) “Mean Out-Crossing Rate of Nonlinear Response to Stochastic Input” *Proceedings ICASP9*, Balkema, Rotterdam, The Netherlands, 295-302.

Liu J.S. (2001) *Monte Carlo strategies in scientific computing*. Springer Series in Statistics, Springer, Berlin, Germany.

Liu P.-L., Der Kiureghian, A. (1991) “Optimization algorithms for structural reliability” *Structural Safety*, 9(3):161–177.

Lutes L.D., Sarkani S. (2004) *Random vibrations - analysis of structural and mechanical systems.* Burlington, MA: Elsevier Butterworth-Heinemann.

Madsen H.O., Krenk S., Lind N.C. (1986) *Methods of structural safety.* Prentice-Hall Inc., Englewood Cliffs, NJ.

Mazzoni S., McKenna F., Fenves G.L. (2005) *OpenSees Command Language Manual.* Pacific Earthquake Engineering Center, University of California, Berkeley. <http://opensees.berkeley.edu/>

Melchers R.E. (1989) “Importance sampling in structural systems” *Structural Safety*, 6(1):3–10.

Menegotto M., Pinto P.E. (1973) “Method for analysis of cyclically loaded reinforced concrete plane frames including changes in geometry and non-elastic behavior of elements under combined normal force and bending” *Proceedings, IABSE Symposium on* ‘Resistance and Ultimate Deformability of Structures Acted on by Well-Defined Repeated *Loads’*, Lisbon.

Mirza S.A., MacGregor J.G. (1979) “Variability of Mechanical Properties of Reinforcing Bars” *Journal of the Structural Division*, 105(5): 921-937.

Mirza S.A., MacGregor J.G., Hatzinikolas M. (1979) “Statistical Descriptions of Strength of Concrete” *Journal of the Structural Division*, 105(6):1021-1037.

Rackwitz R., Fiessler B. (1978) “Structural reliability under combined random load sequences” *Computers and Structures*, 9(5):489–499.

Rice S. O. (1944) “Mathematical analysis of random noise.” *Bell System Technical Journal*, 23:282.

Rice S. O. (1945) “Mathematical analysis of random noise.” *Bell System Technical Jour-*

nal, 24:46.

Schueller G.I., Stix R. (1987) “A critical appraisal of methods to determine failure probabilities” *Structural Safety*, 4(4):293–309.

Schueller G.I., Pradlwarter H.J., Koutsourelakis P.S. (2004) “A critical appraisal of reliability estimation procedures for high dimensions” *Probabilistic Engineering Mechanics*, 19(4):463–474.

Tvedt L. (1983) “Two second-order approximations to the failure probability” *Veritas Rep. RDIV/20-004083*, Det Norske Veritas, Oslo.

Tvedt L. (1988) “Second-order reliability by an exact integral” *Proc., 2nd IFIP Working Conf. on Reliability and Optimization on Structural Systems*, P. Thoft-Chistensen, ed., Springer, New York, 377–384.

Tvedt L. (1990) “Distribution of quadratic forms in the normal space - application to structural reliability” *Journal of Engineering Mechanics* (ASCE), 116(6):1183-1197.

Zhang Y., Der Kiureghian A. (1993) ‘Dynamic response sensitivity of inelastic structures’, *Computer Methods in Applied Mechanics and Engineering*, 108(1-2):23–36.

Zhao Y.G., Ono T. (1999) “New approximations for SORM: Part 1” *Journal of Engineering Mechanics* (ASCE), 125(1):79–85.

Zhao Y.G., Ono T. (1999) “New approximations for SORM: Part 2” *Journal of Engineering Mechanics* (ASCE), 125(1):86–93.

Zona A., Barbato M., Conte J.P. (2004) “Finite element response sensitivity analysis of steel-concrete composite structures.” *Report SSRP-04/02*, Department of Structural Engineering, University of California at San Diego, La Jolla, CA, USA.

Zona A., Barbato M., Conte J.P. (2005) “Finite element response sensitivity analysis of steel-concrete composite beams with deformable shear connection” *Journal of*

Engineering Mechanics (ASCE), 131(11):1126–1139.

Zona A., Barbato M., Conte J.P. (2006) “Finite Element Response Sensitivity Analysis of Continuous Steel-Concrete Composite Girders” *Steel and Composite Structures*, 6(3):183-202.

CHAPTER 12

MULTIDIMENSIONAL VISUALIZATION IN THE PRINCIPAL PLANES

12.1 INTRODUCTION

The geometric properties and interpretation of reliability and random vibration problems are the object of great interest in structural reliability analysis. FORM and SORM analysis are based on geometric approximations of the limit-state surface (LSS) defining the reliability problem at hand (Der Kiureghian 2000). Knowledge of the topology (in both the physical and standard normal spaces) of the LSSs corresponding to a given reliability problem is extremely valuable in:

(1) gaining physical and geometrical insight into the structural reliability problem at hand;

(2) understanding the reason behind possible difficulties encountered in the DP search;

(3) developing more robust and efficient DP search algorithms exploiting the identified physical/geometrical insight;

(4) analyzing the inaccuracies of the FORM/SORM approximations for time-invariant probability of failure and mean out-crossing rate computation; and

(5) pointing to more efficient and accurate computational reliability methods for evaluating the probability content of failure domains typically encountered in structural reliability analysis.

Nevertheless, only a limited amount of research has been devoted to provide useful insight into the geometric properties of nonlinear LSSs typically arising in FE reliability analysis of nonlinear structural models subjected to random loading (Der Kiureghian 2000). This is probably due to the fact that the study of the topology of LSSs is a challenging task and requires visualization of nonlinear hyper-surfaces in high-dimensional spaces (i.e., physical or standard normal space defined by random parameters representing loading, geometric and material parameters). Indeed, only very limited tools (Haukaas and Der Kiureghian 2004) are available to visualize LSSs and LSFs in two- or three dimensional subspaces (defined by sets of two or three axes of the standard normal space in which the reliability problem is cast) of high-dimensional spaces, commonly encountered in time-invariant and time-variant FE reliability analysis. In this work, a new method is developed for the visualization of LSSs in high-dimensional spaces for both time-invariant and time-variant FE structural reliability analysis.

12.2 A NEW VISUALIZATION TECHNIQUE FOR LIMIT-STATE SURFACES IN HIGH-DIMENSIONAL SPACES: THE MULTI-DIMENSIONAL VISUALIZATION IN THE PRINCIPAL PLANES (MVPP) METHOD

The broad interest on the topology of LSSs in structural reliability problems and the lack of a general methodology for visualizing hyper-surfaces in high-dimensional spaces (number of dimensions larger than 3) contribute to make LSS visualization a crucial and interesting topic of research. In this work, a new methodology, herein referred to

as Multidimensional Visualization in the Principal Planes (MVPP), is proposed for visualizing the shape of LSSs near their DP(s) in the context of FE reliability analysis.

The basic idea behind the MVPP method is to visualize the LSS in the neighborhood of the DP(s) in subspaces (planes) of particular interest. In the proposed methodology, these planes are defined as the planes of principal curvatures of the LSS at the DP(s), referred to as Principal Planes (PPs). The MVPP requires finding the traces of the LSS in the PPs in decreasing order of magnitude of the principal curvatures of these traces at the DP(s). In the sequel, the MVPP method is introduced first for time-invariant reliability problems and then is extended to time-variant reliability problems. The method has been implemented in both the computational frameworks Opensees (Mazzoni et al. 2005) and FedeasLab-FERUM (Filippou and Constantinides 2004; Haukaas 2001).

12.2.1 MVPP for time-invariant reliability problems

The MVPP method is based on several analysis components which can be developed and implemented independently. This independence among the different components is an extremely useful property of the method, since it allows its straightforward implementation in an object-oriented computational platform such as OpenSees. In the case of time-invariant reliability analysis, the MVPP method consists of the following major steps: (1) search of the DP(s), (2) change of reference system, (3), determination of the PPs of interest, and (4) visualization of the traces of the LSS in these PPs.

12.2.1.1 Search of the DP(s)

This step consist of solving a nonlinear constrained optimization problem using gradient-based optimization algorithms, as described in Subsection 11.2 of Chapter 11. If more than one DP is found, the subsequent steps can be applied to each of the DPs retained.

12.2.1.2 Change of reference system

A new reference system in the standard normal space is defined so that the n-th axis (with n = number of random variables) is oriented in the direction defined by the DP vector **y*** and the new origin coincides with the DP. A generic vector **y'** in the new reference system is obtained as

$$\mathbf{y}' = \mathbf{R} \cdot (\mathbf{y} - \mathbf{y}^*) \tag{12.1}$$

where the rotation matrix **R** is defined so that

$$\mathbf{R} \cdot \mathbf{y}^* = [0 \ \ldots \ 0 \ \ \beta]^T \tag{12.2}$$

in which β = distance from the origin of the DP (i.e., FORM reliability index). The rotation matrix **R** can be computed using any suitable **QR** decomposition algorithm, e.g., classical Gram-Schmidt orthonormalization, modified Gram-Schmidt orthonormalization, Householder reflections algorithm, Givens rotations algorithm (Stoer and Bulirsch 2002).

12.2.1.3 Definition of the PPs of interest.

Each PP is defined by the DP vector $\mathbf{y}^*$ and one of the eigenvectors (Principal Direction: PD) of the (normalized and reduced) Hessian matrix $\mathbf{A}$ (see Chapter 11, Section 11.4):

$$\mathbf{A} = \frac{\mathbf{H}_{red}}{\left\| \nabla_{\mathbf{y}} G \big|_{\mathbf{y}^*} \right\|} \tag{12.3}$$

in which $[\mathbf{H}_{red}]_{ij} = [\mathbf{R} \cdot \mathbf{H} \cdot \mathbf{R}]_{ij}$ is the reduced Hessian computed at the DP in the $\mathbf{y}'$ space, with i, j = 1, 2, ..., n-1, $\mathbf{H}$ is the $n \times n$ Hessian matrix of the LSF at the DP in the standard normal space, and $\left\| \nabla_{\mathbf{y}} G \big|_{\mathbf{y}^*} \right\|$ denotes the Euclidean norm of the gradient of the LSF at the DP. Herein, the LSF is assumed to be twice differentiable, to ensure existence of the Hessian matrix at the DP. As shown in Chapter 6, the above assumption is satisfied when the constitutive material models are differentiable with respect to the sensitivity parameters, the loading is piecewise continuous and (for reliability problems based on dynamic FE analysis) the time-step used to integrate the equations of motion of the system is sufficiently small.

The PDs are sorted in decreasing order of magnitude (absolute value) of the corresponding eigenvalues (referred to as Principal Eigenvalues: PEs). A limited number of PDs is computed (using any algorithm for finding the eigenvalues/eigenvectors of a real-valued symmetric square matrix) together with the corresponding PPs in which the topological properties of the LSS are of interest.

In this study, the Hessian matrix **H** in the standard normal space is obtained by forward finite difference (FFD) calculations applied to the DDM-based response sensitivities. This computation can be carried out in two different ways: (1) computing the Hessian matrix $\mathbf{H}_{\boldsymbol{\vartheta}}$ in the physical space and then transforming it to the Hessian matrix in the standard normal space, or (2) using finite difference calculations in the standard normal space and obtaining directly **H**.

The second procedure is less prone to numerical difficulties and inaccuracies and is adopted herein. After fixing a perturbation value, Δy, for the standard normal random variables (e.g., $\Delta y = 10^{-3} \div 10^{-5}$), the i-th row of the Hessian matrix is approximated as

$$\mathbf{H}_i \approx \frac{1}{\Delta y}\left[\nabla_{\mathbf{y}} G\big|_{\mathbf{y}^* + \Delta y \cdot \mathbf{e}_i} - \nabla_{\mathbf{y}} G\big|_{\mathbf{y}^*}\right] \tag{12.4}$$

where $\mathbf{e}_i$ denotes the i-th axis unit vector, i.e., a column vector with all zero components except the i-th one which is equal to 1. The row vector $\nabla_{\mathbf{y}} G\big|_{\mathbf{y}^* + \Delta y \cdot \mathbf{e}_i}$ is obtained by: (1) finding the perturbation vector $\Delta\boldsymbol{\vartheta}^{(i)} = \nabla_{\mathbf{y}}\boldsymbol{\vartheta} \cdot \Delta y \cdot \mathbf{e}_i$, (2) computing the perturbed gradient $\nabla_{\boldsymbol{\vartheta}} g\big|_{\boldsymbol{\vartheta}^* + \Delta\boldsymbol{\vartheta}^{(i)}}$ in the physical space, and (3) transforming the obtained perturbed gradient back to the standard normal space, i.e., $\nabla_{\mathbf{y}} G\big|_{\mathbf{y}^* + \Delta y \cdot \mathbf{e}_i} = \nabla_{\boldsymbol{\vartheta}} g\big|_{\boldsymbol{\vartheta}^* + \Delta\boldsymbol{\vartheta}^{(i)}} \cdot \nabla_{\mathbf{y}}\boldsymbol{\vartheta}$. To simplify the calculations, the quantity $\nabla_{\mathbf{y}}\boldsymbol{\vartheta}$ is approximated with its value computed at the DP.

Using the DDM to compute the exact gradients in the physical space, the FFD method presented above is more efficient and more accurate than computing the Hessian

matrix **H** by central finite difference applied directly to the LSF. Nevertheless, for detailed FE models of realistic structural systems characterized by a large number of uncertain model parameters, this approach for computing the Hessian matrix, which is then used to compute the major eigenvalues/eigenvectors, could still be computationally prohibitive. Methods are under study for obtaining computationally affordable approximations of the Hessian matrix able to produce sufficiently accurate major eigenvalues/eigenvectors. In addition, the use of an existing algorithm (Der Kiureghian and De Stefano 1991) for computing eigenvalues (and corresponding eigenvectors) in order of decreasing magnitude without having to compute the Hessian matrix is also being considered.

12.2.1.4 Visualization of the traces of the LSS in the PPs

The visualization can be performed following two methods: (1) simulating the values of the LSF over a grid of points in the PP and obtaining the trace of the LSS in this PP as zero level curve of the obtained surface; (2) employing a standard zero-finding algorithm (for scalar functions of a single variable) to obtain the zero of the LSF along directions parallel to the DP direction and contained in the PP. The starting points for the zero-finding algorithm can be taken on the axis of the PP orthogonal to the DP direction (i.e., along the PD defining the PP). This second technique is, in general, more efficient than the first one if a robust and efficient zero-finding algorithm (e.g., safe-guarded secant or Newton's method, see Gill et al. 1981) is employed.

The visualization is obtained by computing directly LSF values only in the (small number of) PPs corresponding to large absolute values of the principal curvatures. In the

subspace not spanned by the considered PPs, the LSS can be approximated as a (reduced dimension) hyper-plane tangent to the LSS at the DP. The traces of this approximation of the LSS in any other plane of this subspace coincide with the axis orthogonal to the DP direction. The MVPP methodology provides important information on the topology of the LSS at the DP(s), identifying a small number of dimensions which are of interest and thus requiring a limited number of FE simulations to visualize the LSS.

12.2.2 MVPP for time-variant reliability problems

In the case of time-variant reliability problems, focus is on the visualization of the two LSS $G_1 = 0$ (at time t) and $G_2 = 0$ (at time $t + \delta t$) and the domain between these two hyper-surfaces. Indeed, the probability content of this domain is the numerator of the limit relation to compute the mean out-crossing rate (Hagen and Tvedt 1991, see Chapter 11, Subsection 11.6.1). The MVPP method can be extended to time-variant reliability problems simply by adding the visualization of the perturbed LSS $G_2 = 0$ as part of the fourth step of the methodology.

If the trace of the LSS $G_1 = 0$ is obtained by simulating the LSF over a grid of points, the trace of the LSS $G_2 = 0$ can be obtained efficiently by using the approximation

$$G_2 = G(\mathbf{y}, t + \delta t) \approx G(\mathbf{y}, t) + \frac{\partial G}{\partial t}\delta t = g(\boldsymbol{\vartheta}, t) + \nabla_{\mathbf{r}} g \cdot \frac{\partial \mathbf{r}}{\partial t}\delta t \qquad (12.5)$$

where $\mathbf{r}$ is a vector of response quantities used to formulate the LSF (see Chapter 11, Subsection 11.2). This approximation allows to find the trace of $G_2 = 0$ in the PPs of interest

without any additional FE response simulations. If the trace of the LSS $G_1 = 0$ in a PP is obtained from a zero-finding algorithm, an efficient way to obtain the trace of the LSS $G_2 = 0$ in the same PP consists of is using as starting point of the zero-finding algorithm the corresponding zero point of the LSS $G_1 = 0$ in each of the search directions parallel to the DP vector **y***.

12.3 APPLICATION EXAMPLES

The application examples considered in Chapter 11 are revisited here in order to illustrate the MVPP method, its typical results and its capabilities in terms of providing insight into the topology of the LSS at the DP(s). In addition, the MVPP method can suggest ways to develop new structural reliability analysis methods to improve FORM, SORM and mean out-crossing rate computation using FORM approximation. A new hybrid reliability method, suggested by visualization results obtained through the MVPP method, will be presented and illustrated in next chapter.

12.3.1 Time-invariant case: quasi-static pushover of a R/C frame structure

The first application example consists of a time-invariant reliability analysis performed on a 2-bay 2-story R/C frame structure subjected to quasi-static pushover (see Chapter 11, Subsection 11.7.1). The MVPP method is applied to this problem taking full advantage of the results obtained from the previously performed reliability analysis.

The four steps required by the MVPP method are:

(1) Search of the DP(s) (already performed in FORM and SORM analyses).

(2) Change of reference system (already performed in SORM analysis).

(3) Determination of the PPs of interest. The PDs and corresponding PEs of the LSS at the DP are already computed for SORM (curvature fitting) analysis. The results in terms of principal curvatures and corresponding radii of curvature are given in Table 12.1. The only remaining task is deciding in which PPs the LSS needs to be visualized. A useful criterion is to fix a minimum value for the quantity $\beta\kappa_i$ (i = 1, ..., n-1, with n = number of random variables) below which visualization in the corresponding PP is not needed. This criterion is often used in SORM analysis (Der Kiureghian and De Stefano 1991) in order to decide which corrections to apply when using Breitung's Formula (Breitung 1984). Here, this minimum value is taken as $(\beta\kappa_i)_{min} = 0.02$. Therefore, in this particular example, the LSS is visualized in the first three PPs.

(4) Visualization of the trace of the LSS in the PPs. The trace of the LSS in each of the PPs is obtained as zero level curve of the surface obtained by simulating the value of the LSF over a grid of points in the considered PP. Given the coordinates of a grid point in the PP, they are transformed to the original standard normal space coordinates and then to the physical space coordinates. With these values of the random parameters in the physical space, a FE analysis is performed to obtain the value of the performance function. In the current example, for each of the three PPs considered, the employed grid extends from -0.2 to +0.2 in the direction of the DP vector **y*** and from -1.0 to +1.0 in the PD. The LSF is evaluated at 41 grid points in each direction of the PP, for a total of $n_{FE} = 3 \cdot (41^2 - 1) = 5040$ additional FE analyses. The visualization obtained with

this procedure is computationally very expensive, but can be regarded as reference solution for testing more efficient visualization methods and approximation procedures for reliability analysis, which will be presented in next chapter.

Figs. 12.1, 12.3 and 12.5 show the LSS traces in the first, second and third PP, respectively, together with FORM and SORM approximations, contour lines of the LSF in the PP and the domain in which the FE analyses do not converge (in short, non-convergence domain, i.e., the domain in which the performance function is not defined). The trace of the actual LSS in each of the 3 major PPs is very close to the traces of both the first- and second-order approximations of the LSS in this PP. Figs. 12.2, 12.4 and 12.6 provide zoom views of Figs. 12.1, 12.3 and 12.5, respectively, in the range $x \in [-1.0, 1.0]$ and $y \in [-0.0225, 0.0025]$ (with x = coordinate in the PD and y = coordinate in the DP direction), in which the differences between actual LSS traces and FORM and SORM approximations can be better appreciated. Notice that the SORM approximation of the LSS is obtained as the paraboloid tangent to the LSS at the DP with principal curvatures κ_i (i =1, ..., n). Thus, the trace of the SIRM approximation to the LSS in the i-th major PP is given by

$$y = \frac{1}{2}\kappa_i x^2 \tag{12.6}$$

where i = number denoting the order of the PP. The non-convergence domain is contained completely in the failure domain, which is not necessarily the case for very high limit-state thresholds. The visualization of the LSS using the MVPP method explains the good agree-

ment between FORM, SORM and IS results obtained for this problem (see Chapter 11, Subsection 11.7.1).

12.3.2 Time-variant case: linear elastic SDOF system subjected to white noise excitation

The MVPP method is also tested with a time-variant reliability problem involving a linear elastic SDOF system subjected to Gaussian white noise excitation. The example is taken as the first application example in Chapter 11, Subsection 11.7.2. In this case, in theory the Hessian matrix is a zero matrix, but due to numerical noise and finite precision arithmetic, it is not exactly a zero matrix and has non-zero eigenvalues (very small in amplitude). The MVPP method requires: (1) computing a user-defined number of principal eigenvectors and eigenvalues (in general, much smaller than the number of random variables n), (2) sorting them in the order of decreasing absolute value of the eigenvalue, (3) finding the LSS trace using FE analysis in the PPs for which $\beta\kappa_i \geq (\beta\kappa_i)_{min}$, where $(\beta\kappa_i)_{min}$ = user-defined threshold, and (4) visualizing the LSS linearization in the remaining PPs. Here, a closed-form equation (see Appendix) is derived for the trace (in the PPs) of the linearization of the LSS $G_2 = 0$.

Fig. 12.7 shows the traces of the two LSSs at time t = 1.0s and $t + \delta t = 1.005s$, respectively, obtained through FE analysis (setting $(\beta\kappa_i)_{min} = 2 \cdot 10^{-16}$ to capture the first PE), together with other contour lines of the LSF in the first PP. Fig. 12.7 also provides the trace of the LSS at time $t + \delta t = 1.005s$ obtained using the closed-form equa-

tion for the linearization of the LSS. In this closed-form equation, the DP for the perturbed LSS $G_2 = 0$ is obtained through shifting by δt the DP excitation at time t (see Chapter 11, Subsection 11.6.2). The LSS traces obtained by FE analysis and the closed-form equation practically coincide.

12.3.3 Time-variant case: nonlinear hysteretic SDOF system subjected to white noise excitation

As third application example, the MVPP method is applied to the time-variant reliability analysis of a nonlinear hysteretic SDOF system subjected to Gaussian white noise excitation (see Chapter 11, Subsection 11.7.3). In this case, Poisson approximation based on mean up-crossing rates computed by FORM approximation (in short, FORM-based Poisson approximation) provides very inaccurate results compared to MCS (see Fig. 11.10). The FORM-based Poisson approximation suffers from two sources of error: (1) violation of the hypothesis of independence of out-crossing events, which is at the basis of the Poisson approximation, and (2) FORM approximation of nonlinear LSSs in computing the mean out-crossing rate at a given instant of time. It is also observed that, in this case, the inaccuracy of the FORM-based Poisson approximation is due principally to the FORM approximation, which suggests a pronounced nonlinearity of the LSSs at their DP. In this Subsection, the MVPP method is used to investigate the topology of these LSSs and verify the source of inaccuracy in the FORM-based Poisson approximation.

Fig. 12.8 plots the DP excitations at time $t = 1.0$s and $t + \delta t = 1.005$s, respectively. The second DP excitation is obtained through shifting the first one along the time axis by

$\delta t = 0.005s$. These DP excitations are characterized by low values of the ground acceleration for most of the time-history and very high values concentrated at the end of the excitation time-history. In terms of DP response, the SDOF system behaves almost linearly at the exception of the last part of the response time-history, in which the nonlinear hysteretic behavior is concentrated. This behavior has been recognized as typical for structural systems modeled using the Menegotto-Pinto constitutive model (Barbato et al. 2006; Conte et. al. 2007).

Table 12.2 provides the first 10 principal curvatures and corresponding radii of curvature for the considered problem at time $t = 1.0s$. It is observed that: (1) the first three curvatures are very large; (2) the absolute value of the principal curvatures decreases very fast; (3) even if the number of random variables for this problem is quite large ($n = 100$), only a few PPs are needed to visualize the nonlinear behavior of the LSS in the neighborhood of the DP. In this specific case, setting $(\beta\kappa_i)_{min} = 0.05$, the MVPP requires to visualize the LSS using FE analysis in only three PPs. Fig. 12.9 shows the first three normalized PDs, which can be interpreted as the shape of the loadings that, superposed to the DP excitation, produce the largest curvatures in the LSS in the neighborhood of the DP.

Figs. 12.10 through 12.12 show the MVPP-based visualization in the first three PPs of the two LSSs involved in the computation of the mean up-crossing rate at time $t = 1.0s$. From these figures, it is observed that:

(1) The differences between the trace of the actual LSS at time t = 1.0s and the traces of FORM and SORM approximations to the LSS are very pronounced, with FORM defining a much larger and SORM a much smaller failure domain than the actual one.

(2) The FORM approximation of the failure domain for mean up-crossing rate computation is poor, particularly in the first and second PPs.

The MVPP results, presented in Figs. 12.10 through 12.12 for this specific application example, confirm that the inaccuracy of FORM-based mean up-crossing rate computation is strictly connected with the significant difference in shape of the actual LSSs (strongly nonlinear) with their linearizations used in FORM analysis.

12.4 CONCLUSIONS

This Chapter introduces a new visualization technique for LSSs near their DP(s) in high-dimensional spaces: the Multidimensional Visualization in the Principal Planes (MVPP). The MVPP method consists of visualizing a LSS in the neighborhood of a DP in subspaces (planes) of particular interest. These planes are defined as the planes of principal curvatures of the LSS at the DP and are referred to as Principal Planes (PPs). The MVPP requires finding the trace of the LSS in the PPs in decreasing order of magnitude of the principal curvatures.

The MVPP methodology provides important information about the topology of the LSS, identifying a small number of dimensions which are of interest and thus requiring a limited number of FE analyses to effectively visualize the LSS. The newly gained insight into the geometric properties of the reliability problem at hand can be used to develop

more efficient and accurate computational reliability methods for evaluating the probability content of failure domains typically encountered in FE structural reliability analysis.

APPENDIX: TRACE OF THE FORM APPROXIMATION OF THE PERTURBED LSS $G_2 = 0$ IN A GIVEN PP

The hyper-plane tangent to the LSS $G_2 = 0$ at the DP at time $t + \delta t$, $\mathbf{y}_2^*$, can be written in the original standard normal space as

$$\nabla_{\mathbf{y}} G_2\big|_{\mathbf{y}_2^*} \cdot (\mathbf{y} - \mathbf{y}_2^*) = 0 \tag{12.7}$$

where

$$\nabla_{\mathbf{y}} G_2\big|_{\mathbf{y}_2^*} = -\frac{\left\|\nabla_{\mathbf{y}} G_2\big|_{\mathbf{y}_2^*}\right\|}{\left\|\mathbf{y}_2^*\right\|}(\mathbf{y}_2^*)^T \tag{12.8}$$

Thus, Eq. (12.7) can be rewritten as

$$(\mathbf{y}_2^*)^T \cdot (\mathbf{y} - \mathbf{y}_2^*) = 0 \tag{12.9}$$

Introducing the new reference system defined in Subsection 12.3.1 through Eqs. (12.1) and (12.2), and noticing that matrix **R** is a rotation matrix with the following property

$$\mathbf{R}^T\mathbf{R} = \mathbf{R}\mathbf{R}^T = \mathbf{I}_n \tag{12.10}$$

in which $\mathbf{I}_n$ denotes the (n x n) unit matrix, the left-end-side of Eq. (12.9) can be manipulated as follows

$$\begin{aligned}(\mathbf{y}_2^*)^T \cdot (\mathbf{y} - \mathbf{y}_2^*) &= (\mathbf{y}_2^*)^T(\mathbf{R}^T\mathbf{R})(\mathbf{y} - \mathbf{y}_2^*) = [(\mathbf{y}_2^*)^T\mathbf{R}^T][\mathbf{R}(\mathbf{y} - \mathbf{y}_2^*)] \\ &= (\mathbf{R} \cdot \mathbf{y}_2^*)^T[\mathbf{R}(\mathbf{y} - \mathbf{y}^*) - \mathbf{R}(\mathbf{y}_2^* - \mathbf{y}^*)] = (\mathbf{y}_2' + \mathbf{R} \cdot \mathbf{y}^*)^T(\mathbf{y}' - \mathbf{y}_2')\end{aligned} \tag{12.11}$$

where $\mathbf{y}_2' = \mathbf{R}(\mathbf{y}_2^* - \mathbf{y}^*)$, in which $\mathbf{y}^*$ denotes the DP of the LSS $G_1 = 0$ at time t.

If the PD (i.e., the normalized principal eigenvector in the original standard normal space) defining the PP of interest is denoted as $\mathbf{y}_{PD}$, its expression in the transformed reference system is $\mathbf{y}_{PD}' = \mathbf{R} \cdot \mathbf{y}_{PD}$. Notice that the n-th component of $\mathbf{y}_{PD}'$ is equal to zero, i.e., $(\mathbf{y}_{PD}')_n = 0$, since, by the definition of a PD, $\mathbf{y}_{PD}$ must be orthogonal to the DP direction $\mathbf{y}^*$. A new rotation matrix, $\mathbf{R}_2$, can be defined so that

$$\mathbf{R}_2 \cdot \mathbf{y}_{PD}' = [0 \ \ldots \ 0 \ 1 \ 0]^T \tag{12.12}$$

$$\mathbf{R}_2\mathbf{R} \cdot \mathbf{y}^* = [0 \ \ldots \ 0 \ \beta]^T \tag{12.13}$$

and

$$\mathbf{R}_2^T\mathbf{R}_2 = \mathbf{R}_2\mathbf{R}_2^T = \mathbf{I}_n \tag{12.14}$$

A rotation matrix $\mathbf{R}_2$ satisfying Eqs. (12.12) through (12.14) can be obtained by Gram-Schmidt orthonormalization of a (n x n) matrix having the vector $\mathbf{y}_{PD}'/\|\mathbf{y}_{PD}'\|$ as (n-1)-th row, 1's on the main diagonal (with the exception of the (n-1)-th position) and 0's elsewhere. The rotation matrix $\mathbf{R}_2$ identifies a new coordinate reference system with origin centered in the DP, with the n-th axis oriented as the DP direction and (n-1)-th axis oriented as the PD considered. The corresponding transformation is given by

$$\mathbf{y}'' = \mathbf{R}_2 \cdot \mathbf{y}' = \mathbf{R}_2\mathbf{R}(\mathbf{y} - \mathbf{y}^*) \tag{12.15}$$

Substituting Eq. (12.11) into Eq. (12.9) and using Eqs. (12.12) through (12.15) yields

$$(\mathbf{y}_2'' + \mathbf{R}_2\mathbf{R} \cdot \mathbf{y}^*)^T(\mathbf{y}'' - \mathbf{y}_2'') = 0 \tag{12.16}$$

A vector $\mathbf{y}''$ belonging to the considered PP has the first (n-2) components equal to zero, thus the trace of the hyper-plane defined by Eq. (12.16) in the PP can be expressed as

$$[(\mathbf{y}_2'')_1 \ \cdots \ (\mathbf{y}_2'')_{n-1} \ \ ((\mathbf{y}_2'')_n + \beta)] \begin{bmatrix} -(\mathbf{y}_2'')_1 \\ \cdots \\ (\mathbf{y}'')_{n-1} - (\mathbf{y}_2'')_{n-1} \\ (\mathbf{y}'')_n - (\mathbf{y}_2'')_n \end{bmatrix} = 0 \qquad (12.17)$$

Introducing the notation $x = (\mathbf{y}'')_{n-1}$ and $y = (\mathbf{y}'')_n$, Eq. (12.17) becomes

$$-\sum_{i=1}^{n} (\mathbf{y}_2'')_i^2 + (\mathbf{y}_2'')_{n-1} \cdot x + ((\mathbf{y}_2'')_n + \beta) \cdot y - \beta \cdot (\mathbf{y}_2'')_n = 0 \qquad (12.18)$$

Finally, the required trace of the hyper-plane tangent to the LSS at the DP at time $t + \delta t$ in the PP is the line defined by the following equation

$$y = c_1 \cdot x + c_2 \qquad (12.19)$$

where

$$\begin{cases} c_1 = -\dfrac{(\mathbf{y}_2'')_{n-1}}{(\mathbf{y}_2'')_n + \beta} \\ c_2 = \dfrac{1}{(\mathbf{y}_2'')_n + \beta} \cdot \left[\beta \cdot (\mathbf{y}_2'')_n + \sum_{i=1}^{n} (\mathbf{y}_2'')_i^2 \right] \end{cases} \qquad (12.20)$$

Table 12.1 Principal curvatures and radii of curvature for MVPP method applied to the time-invariant reliability analysis of a R/C frame structure subjected to quasi-static pushover

PD	Curvature κ_i	Radius of curvature $1/\kappa_i$	$\beta\kappa_i$
1	-0.0412	-24.25	-0.0845
2	-0.0224	-44.68	-0.0459
3	-0.0137	-73.21	-0.0280
4	-0.0067	-150.2	-0.0136
5	-0.0035	-282.1	-0.0073
6	-0.0021	-480.6	-0.0043
7	0.0013	768.9	0.0027
8	-0.0010	-1002	-0.0020
9	-0.0008	-1188	-0.0017
10	0.0008	1220	0.0017
11	-0.0006	-1709	-0.0012
12	1.6e-007	6.3e+006	3.3e-007
13	-7.1e-010	-1.4e+009	-1.5e-009

Table 12.2 First 10 principal curvatures and radii of curvature for MVPP method applied to the time-variant reliability analysis of a nonlinear hysteretic SDOF system subjected to white noise excitation (t = 1.0s, $\xi = 0.048\text{m}$, $\phi_0 = 0.25\text{m}^2/\text{s}^3$)

PD	Curvature κ_i	Radius of curvature $1/\kappa_i$	$\beta\kappa_i$
1	4.5498	0.22	15.692
2	0.8714	1.15	3.006
3	0.2205	4.54	0.760
4	0.0120	83.11	0.0415
5	-0.0093	-107.1	-0.032
6	-0.0014	-717.2	-0.005
7	-0.0009	-1130	-0.003
8	-0.0003	-2912	-0.001
9	0.0001	9384	3.7e-004
10	-7.5e-005	-13413	-2.6e-004

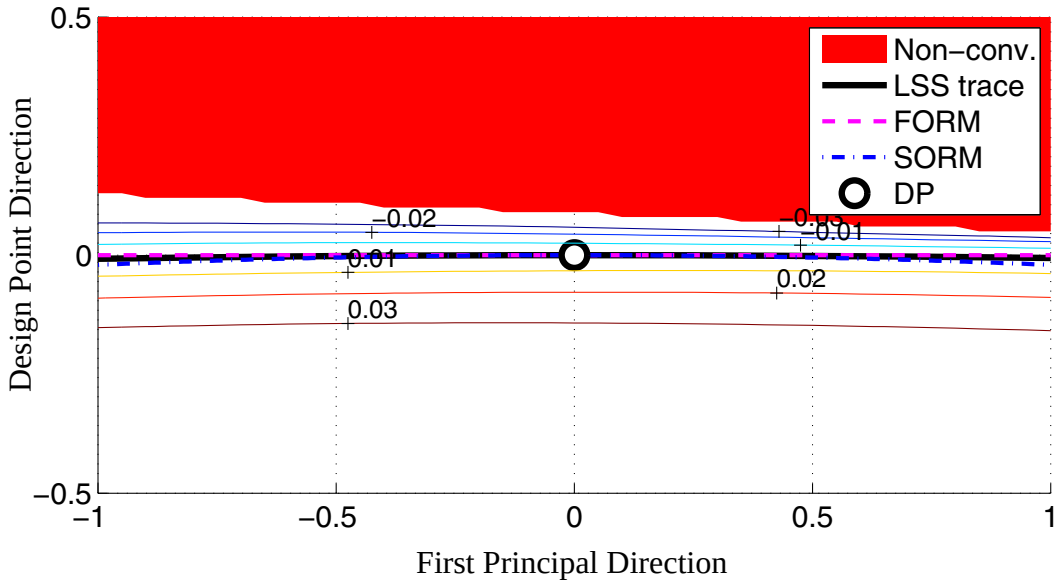

Figure 12.1 MVPP for time-invariant reliability analysis of a R/C frame structure subjected to quasi-static pushover: first PP.

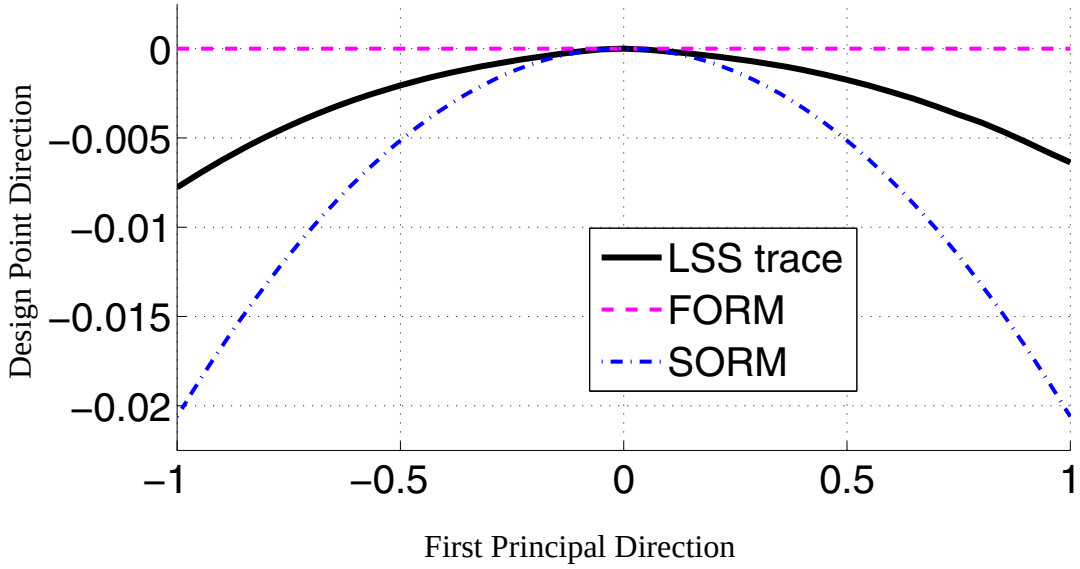

Figure 12.2 MVPP for time-invariant reliability analysis of a R/C frame structure subjected to quasi-static pushover: first PP (zoom view).

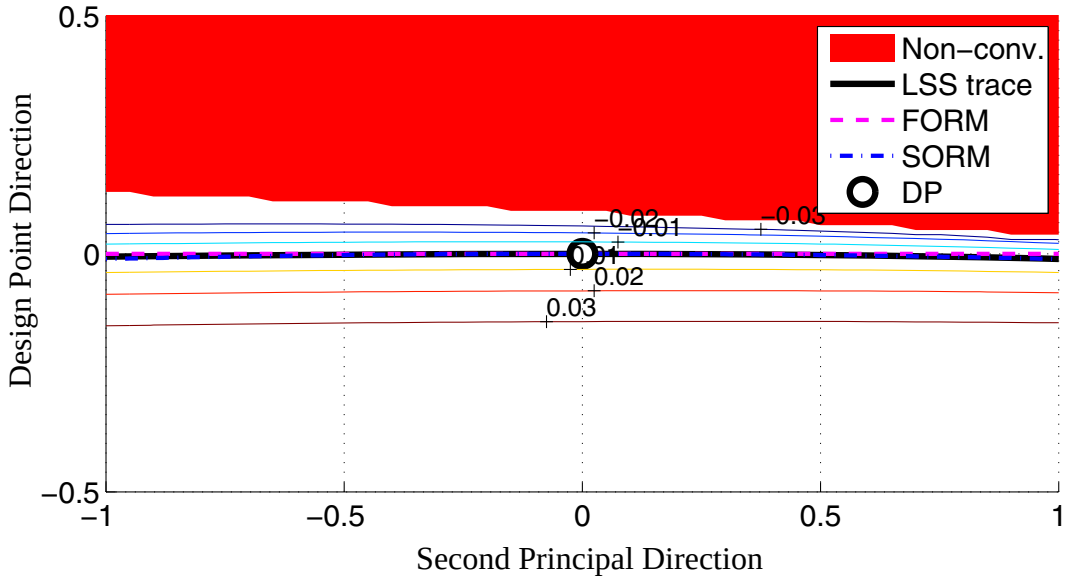

Figure 12.3 MVPP for time-invariant reliability analysis of a R/C frame structure subjected to quasi-static pushover: second PP.

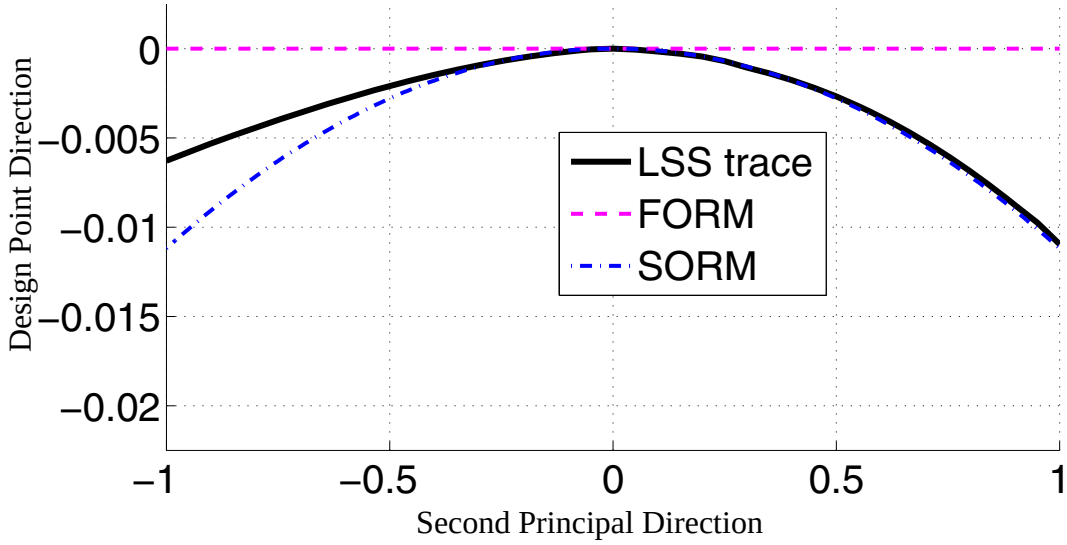

Figure 12.4 MVPP for time-invariant reliability analysis of a R/C frame structure subjected to quasi-static pushover: second PP (zoom view).

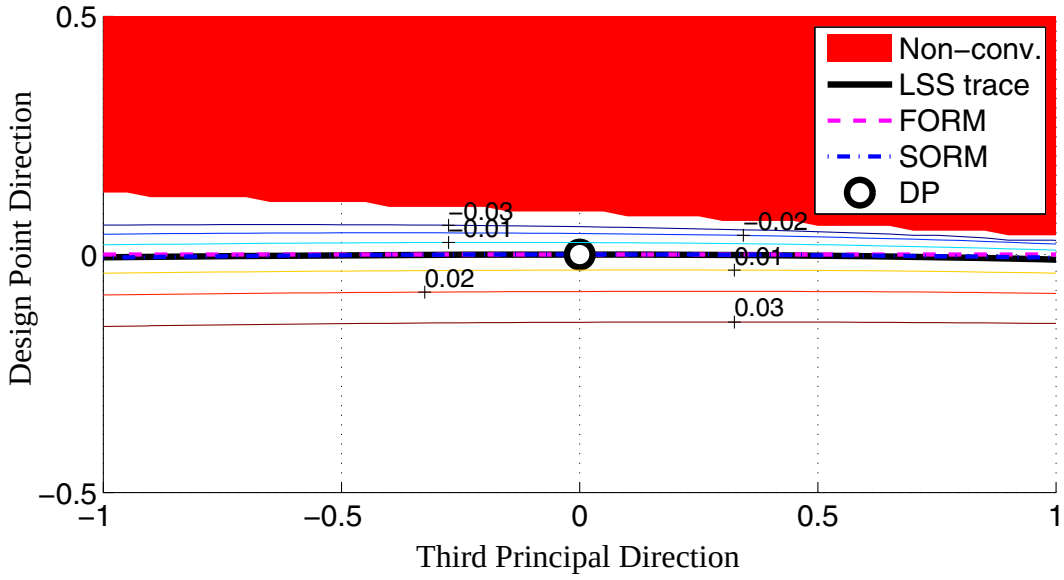

Figure 12.5 MVPP for time-invariant reliability analysis of a R/C frame structure subjected to quasi-static pushover: third PP.

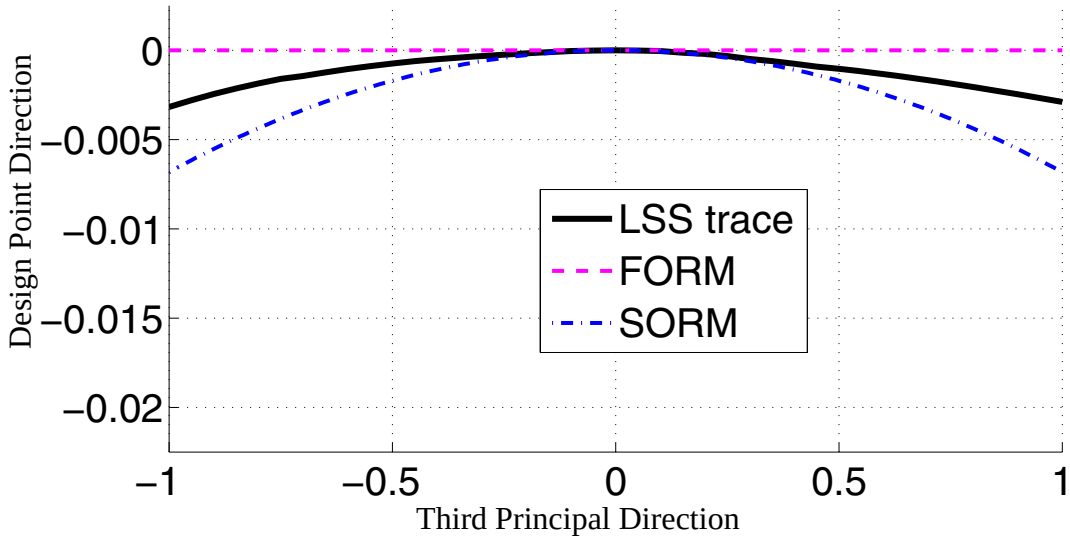

Figure 12.6 MVPP for time-invariant reliability analysis of a R/C frame structure subjected to quasi-static pushover: third PP (zoom view).

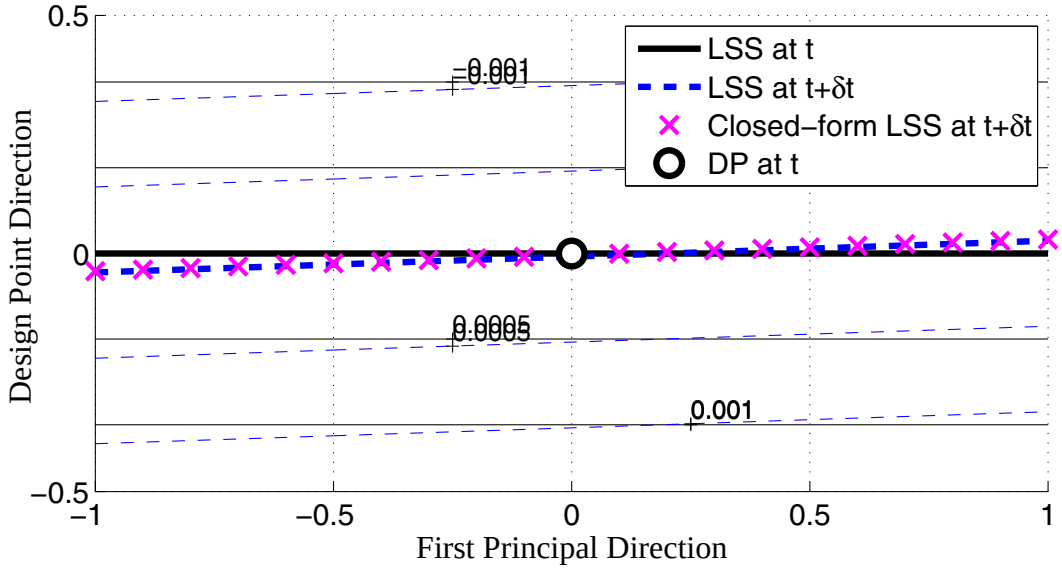

Figure 12.7 MVPP for time-variant reliability analysis of a linear elastic SDOF subjected to white noise excitation: first Principal Plane.

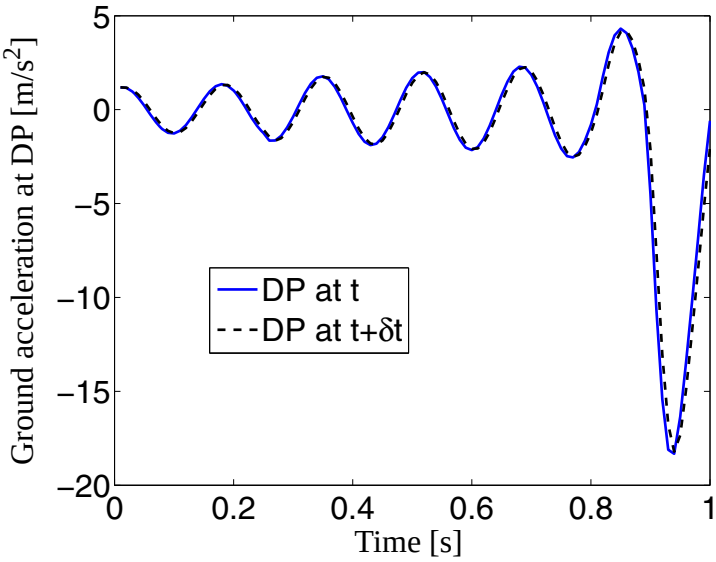

Figure 12.8 Design point excitations at time $t = 1.0\text{s}$ and $t + \delta t = 1.005\text{s}$ for time-variant reliability analysis of a nonlinear hysteretic SDOF system subjected to white noise excitation ($\xi = 0.048\text{m}$, $\phi_0 = 0.25\text{m}^2/\text{s}^3$).

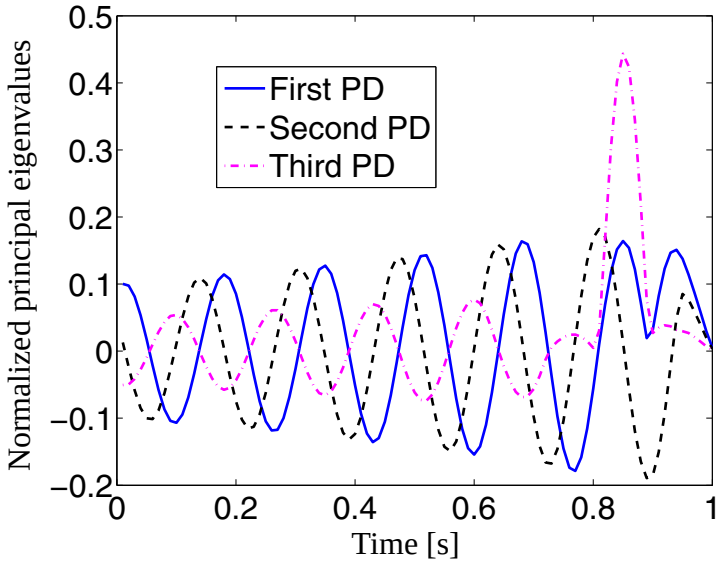

Figure 12.9 Normalized principal eigenvectors for time-variant reliability analysis of a nonlinear hysteretic SDOF system subjected to white noise excitation ($t = 1.0\text{s}$, $\xi = 0.048\text{m}$, $\phi_0 = 0.25\text{m}^2/\text{s}^3$).

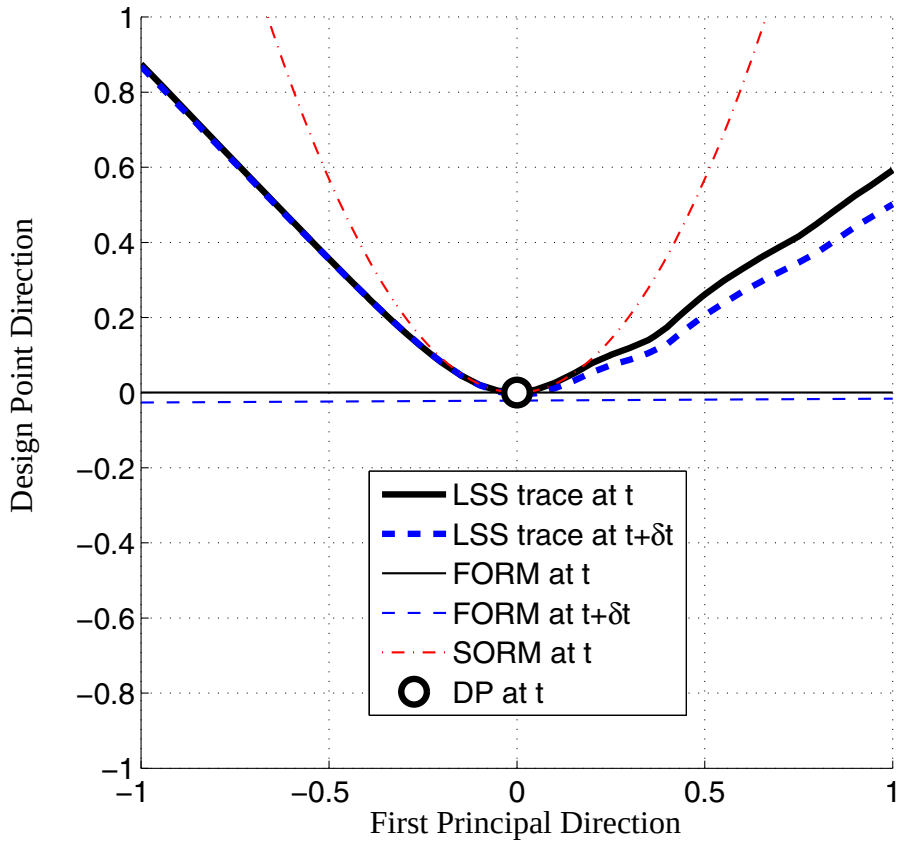

Figure 12.10 MVPP for time-variant reliability analysis of a nonlinear hysteretic SDOF system subjected to white noise excitation ($t = 1.0s$, $\xi = 0.048m$, $\phi_0 = 0.25m^2/s^3$, $\delta t = 0.005s$): first Principal Plane.

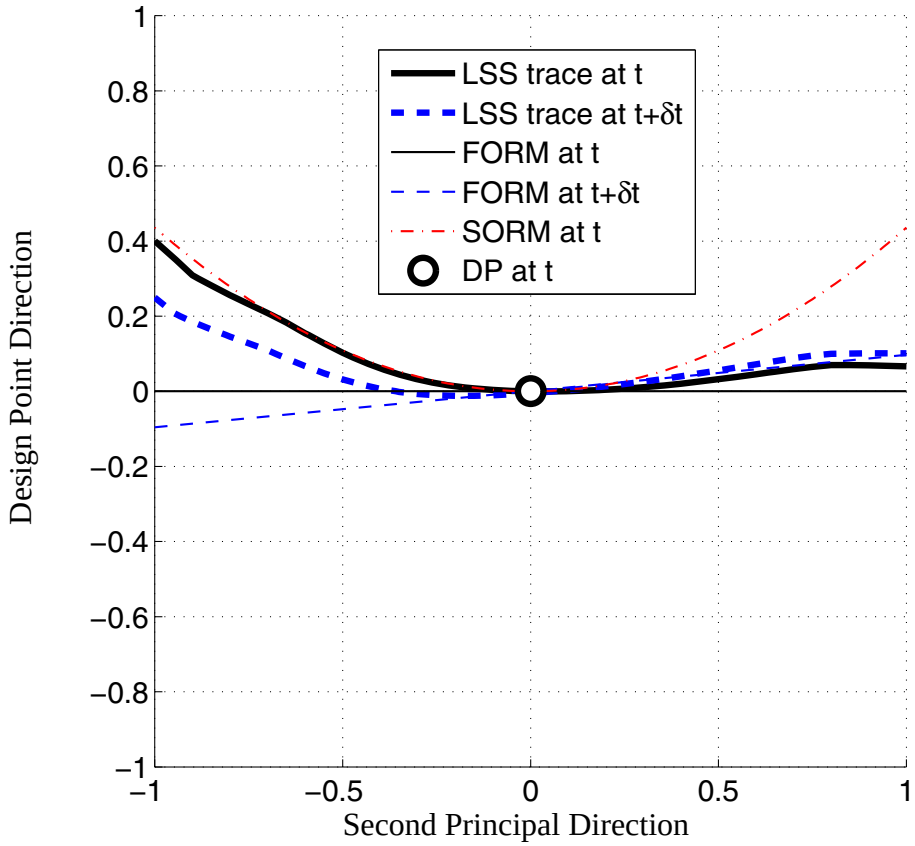

Figure 12.11 MVPP for time-variant reliability analysis of a nonlinear hysteretic SDOF system subjected to white noise excitation ($t = 1.0\text{s}$, $\xi = 0.048\text{m}$, $\phi_0 = 0.25\text{m}^2/\text{s}^3$, $\delta t = 0.005\text{s}$): second Principal Plane.

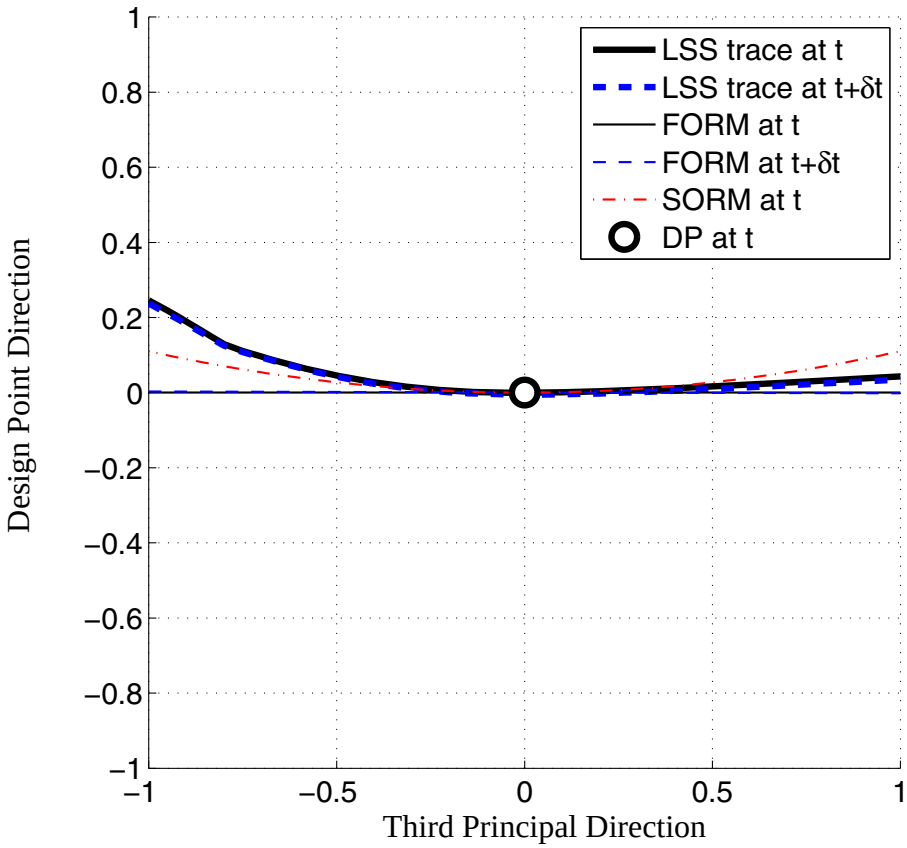

Figure 12.12 MVPP for time-variant reliability analysis of a nonlinear hysteretic SDOF system subjected to white noise excitation ($t = 1.0\text{s}$, $\xi = 0.048\text{m}$, $\phi_0 = 0.25\text{m}^2/\text{s}^3$, $\delta t = 0.005\text{s}$): third Principal Plane.

REFERENCES

Breitung K. (1984) “Asymptotic approximations for multinormal integrals” *Journal of the Engineering Mechanics Division* (ASCE), 110(3):357–366.

Der Kiureghian A., De Stefano M. (1991) “Efficient algorithms for second-order reliability analysis” *Journal of Engineering Mechanics* (ASCE), 117(12):2904-2923.

Filippou F.C., Constantinides M. (2004) “FEDEASLab getting started guide and simulation examples” *Technical Report NEESgrid-2004-22*, 31 August, Available at: http://fedeaslab. berkeley.edu/.

Gill P.E., Murray W., Wright M.H. (1981) *Practical Optimization*, New York: Academic Press.

Hagen O., Tvedt L. (1991) “Vector process out-crossing as parallel system sensitivity measure” *Journal of Engineering Mechanics* (ASCE), 117(10):2201–2220.

Haukaas T. (2001) “FERUM (Finite Element Reliability Using Matlab)” *User’s Guide*, Available at: http://www.ce.berkeley.edu/~haukaas/FERUM/ferum.html.

Haukaas T., Der Kiureghian A. (2004) “Finite element reliability and sensitivity methods for performance-based engineering” *Report PEER 2003/14*, Pacific Earthquake Engineering Research Center, University of California, Berkeley.

Mazzoni S., McKenna F., Fenves G.L. (2005) *OpenSees Command Language Manual*. Pacific Earthquake Engineering Center, University of California, Berkeley. <http://opensees.berkeley.edu/>

Stoer J., Bulirsch R. (2002) *Introduction to numerical analysis*, 3rd ed. Springer.

CHAPTER 13

DESIGN POINT - RESPONSE SURFACE - SIMULATION (DP-RS-SIM) HYBRID RELIABILITY METHOD

13.1 INTRODUCTION

Classical reliability methods such as FORM and SORM have been real breakthroughs toward feasible and reliable methods for integrating probabilistic information and uncertainty analysis into advanced design methods and modern design codes. These methods have been widely used with success in solving challenging reliability problems. Nevertheless, caution should be used in their applications since limits and shortcomings in terms of accuracy are known and documented, e.g., (1) existence of multiple DPs (Der Kiureghian and Dakessian 1998; Au et al. 1999), (2) nonlinearity of the LSS due to non-gaussianess of the input process for random vibration problems (Der Kiureghian 2000), (3) nonlinearity of the LSS due to nonlinearity in the system response (see Chapter 11, Subsection 11.7.3, where an example is presented on time-variant reliability analysis of a structural system exhibiting a strongly nonlinear behavior).

As already seen in Chapter 11, alternative methods, which are not directly based on the concept of DP, have been the object of vast research. Among these methods, attention is focused on Response Surface (RS) methods in this chapter.

The RS method consists of a collection of statistical methods to substitute an unknown function $g(\boldsymbol{\vartheta})$ of some variables $\boldsymbol{\vartheta}$ with an analytical one, $\tilde{g}(\boldsymbol{\vartheta})$, obtained using a limited number of known values of $g(\boldsymbol{\vartheta})$ and referred to as RS. The problem of the determination of $\tilde{g}(\boldsymbol{\vartheta})$ consists essentially of three steps:

(1) Choice of an appropriate analytical form for the RS, i.e., definition of the parameters $\mathbf{p}$ necessary to determine a sufficiently accurate analytical function $\tilde{g}(\boldsymbol{\vartheta}) = \tilde{g}(\boldsymbol{\vartheta}, \mathbf{p})$ representing the major sources of variability/uncertainty in $g(\boldsymbol{\vartheta})$. Generally, in this step, a reduction of the variables to be accounted for explicitly in the RS is performed.

(2) Design of an appropriate experiment, i.e., definition of the most appropriate location in the space of the variables $\boldsymbol{\vartheta}$ for the points (called experimental points) at which $g(\boldsymbol{\vartheta})$ needs to be evaluated. This step is known in the literature as "experimental design" (Khuri and Cornell 1996) and requires two substeps: (a) finding the so-called "center point", and (b) defining the best location of experimental points around the center point to estimate accurately the parameters $\mathbf{p}$.

(3) Estimation of the undetermined parameters $\mathbf{p}$ of $\tilde{g}(\boldsymbol{\vartheta}, \mathbf{p})$ using known values of $g(\boldsymbol{\vartheta})$ at the experimental points and statistical/regression analysis tools.

Once a satisfactory procedure is defined to determine $\tilde{g}(\boldsymbol{\vartheta})$, the reliability analysis can be subsequently carried out using FORM/SORM or Monte Carlo simulation with variance reduction techniques. It is noteworthy that, in the initial stages of the development of the RS methodology (Wong 1984, 1985; Faravelli 1989, 1992; Bucher and Bourgund 1990; Rajashekhar and Ellingwood 1993; Breitung and Faravelli 1996; Yao and Wen

1996; Zhao et al. 1999; Huh and Haldar 2002), the objective of its application in structural reliability was to avoid carrying out a DP search based on FE response and response sensitivity analysis, viewed as too complex and computationally expensive. Large amount of research has been devoted to finding a center point as close as possible to the DP (Bucher and Bourgund 1990; Rajashekhar and Ellingwood 1993; Breitung and Faravelli 1996; Huh and Haldar 2002). As shown in Chapters 2 through 6, FE response sensitivity analysis underwent significant developments in the last decade and is still a very active field of research, overcoming in large part the difficulties encountered in its application to reliability analysis.

Current research trends highlight the importance of structural reliability analysis methodologies able to provide improved estimates of the failure probability without an excessive increase in computational cost when compared with ordinary FORM/SORM analyses. In this work, a new hybrid reliability analysis method, combining the DP search techniques used in FORM/SORM analyses with the RS method and based on the insight gained from the MVPP method (see Chapter 12) is developed, described and illustrated through several application examples.

13.2 A NEW RELIABILITY METHOD: THE DESIGN POINT - RESPONSE SURFACE - SIMULATION (DP-RS-SIM) METHOD

Information about the topology of the LSS(s) near the DP(s) can be used effectively in order to improve on the FORM approximation accounting for nonlinearities in the LSF. The development of a new hybrid reliability method, referred to as Design Point-

Response Surface-Simulation (DP-RS-Sim) method, is presented in this chapter. This method has been suggested by the insight on the topology of typical LSSs gained by using the MVPP method, which indicates that the inaccuracy in FORM/SORM approximations of nonlinear LSS(s) can be the major source of error in estimating time-invariant and time-variant failure probabilities for structural systems exhibiting nonlinear behavior.

The DP-RS-Sim method combines: (1) the concept of DP (basis of FORM and SORM), (2) the RS method to approximate in analytical (polynomial) form the LSF near the DP, and (3) a simulation technique (Sim) to be applied on the RS representation of the actual LSF. The innovative integration of these three methods together with the insight gained through the MVPP method provides several beneficial properties:

(1) The DP is an optimal center point for generating a RS approximation of a LSS. This fact is well known and documented in the literature (Yao and Wen 1996; Carley et al. 2004) and, therefore, several approximate methods have been proposed to find a suitable center point as close as possible to the DP (Bucher and Bourgund 1990; Rajashekhar and Ellingwood 1993; Liu and Moses 1994; Breitung and Faravelli 1996; Yao and Wen 1996; Zhao et al. 1999). In the work of Huh and Haldar (2002), the use of the DP obtained through FORM analysis is directly employed.

(2) In general, the application of the RS method is limited to problems defined in terms of a small number of variables (5-7 at most), due to the fact that the number of samples required to define the RS approximation increases exponentially with the number of dimensions (or basic random variables). Several techniques have been proposed to decrease the total number of parameters to be explicitly considered in the definition of

the RS approximation, neglecting some parameters or lumping parameters in groups (e.g., Schotanus 2002). The proposed method does not require to eliminate parameters at the modeling stage but, based on the decomposition in linear and nonlinear parts of the LSF at the DP suggested by the MVPP method, is able to capture the nonlinearities in the LSF by using a relatively small number of transformed parameters.

(3) Simulation techniques are very general and able to take into account the existence of multiple DPs and multiple failure modes (system reliability) without additional approximations. On the other hand, when sampling requires a FE analysis of a large nonlinear model of a complex real-world structural system, the computational cost of sample generation repeated a large number of times can be unfeasible and inhibit the use of simulation techniques in FE reliability analysis. The capability of accounting for multiple DPs and multiple failure modes is retained by the proposed method, while the relative computational cost of a single simulation is reduced dramatically and consists of a simple polynomial evaluation, making possible the generation of millions of samples in few seconds on a regular personal computer.

Since the proposed method is base on simulation techniques for estimating the failure probability, it is, in principle and with only minor variations, suitable for both component and system time-invariant reliability problems and for component mean out-crossing rate computations.

13.2.1 DP-RS-Sim method for time-invariant component reliability problems

The main steps of the DP-RS-Sim method for time-invariant component reliability analysis involving a LSS with a single DP are:

(1) DP search (step common to FORM, SORM and MVPP method).

(2) Change of the reference system (step common to SORM and MVPP method)

(3) Determination of the principal directions (PDs) of interest (step common to SORM with curvature fitting and MVPP method).

(4) Decomposition of the LSF in a linear and a nonlinear part.

(5) RS approximation of the nonlinear part of the LSF.

(6) Computation of P_f through simulation.

Steps 1 through 3 have already been explained and described in detail (see Chapter 11, Subsection 11.2, for the DP search and Chapter 12, Subsection 12.2, for the change of reference system and the computation of the PDs of interest). Steps 4 through 6 are explained in detail in the following Subsections.

13.2.1.1 Decomposition of the LSF in linear and nonlinear parts

It has been observed (see Chapter 12) that only few of the principal curvatures of the LSS at the DP are non-negligible. The MVPP results confirm that even strongly nonlinear LSSs concentrate their nonlinearity in a few principal directions (PDs) only, while they are almost linear in the subspace defined by the remaining variables. Therefore, it is useful to separate the contribution to the LSF of variables defining a subspace of the standard normal space in which the LSS at the DP is strongly nonlinear from the contribution of the remaining variables, which can then be linearized with little or negligible loss of accuracy in representing the LSF.

Letting n_{PD} = number of PDs of interest (typically $n_{PD} \le 5$), the following three reference systems are used in the proposed method:

(1) the original reference system $\mathbf{R}_n$ in the standard normal space, with generic vector $\mathbf{y} = [y_1 \ \dots \ y_n]^T$;

(2) the transformed reference system $\mathbf{R}_n'$ with origin at the DP and n-th axis oriented in the direction of the DP vector **y***, with generic vector $\mathbf{y}' = [y'_1 \ \dots \ y'_n]^T$; and

(3) the final reference system $\mathbf{R}_n''$, with generic vector $\mathbf{y}'' = [y''_1 \ \dots \ y''_n]^T$, obtained by rotating $\mathbf{R}_n'$ so that the (n-1)-th to (n-n_{PD})-th axes coincide with the first to n_{PD}-th PDs, respectively.

The corresponding transformations between reference systems are

$$\mathbf{y}' = \mathbf{R}(\mathbf{y} - \mathbf{y}^*) \quad \leftrightarrow \quad \mathbf{y} = \mathbf{R}^T \cdot \mathbf{y}' + \mathbf{y}^* \qquad (\mathbf{R}_n \leftrightarrow \mathbf{R}_n') \tag{13.1}$$

$$\mathbf{y}'' = \mathbf{R}_2 \cdot \mathbf{y}' \quad \leftrightarrow \quad \mathbf{y}' = \mathbf{R}_2^T \cdot \mathbf{y}'' \qquad (\mathbf{R}_n' \leftrightarrow \mathbf{R}_n'') \tag{13.2}$$

$$\mathbf{y}'' = \mathbf{R}_2\mathbf{R}(\mathbf{y} - \mathbf{y}^*) \quad \leftrightarrow \quad \mathbf{y} = \mathbf{R}^T\mathbf{R}_2^T \cdot \mathbf{y}'' + \mathbf{y}^* \qquad (\mathbf{R}_n \leftrightarrow \mathbf{R}_n'') \tag{13.3}$$

The LSF G(**y**) can be rewritten in the final reference system $\mathbf{R}_n''$ as

$$G(\mathbf{y}) = G(\mathbf{R}^T\mathbf{R}_2^T\mathbf{y}'' + \mathbf{y}^*) = G((\mathbf{y}'') \cong G_{lin}(\mathbf{y}''_{lin}) + G_{nl}(\mathbf{y}''_{nl})) = G_{nl}(\mathbf{y}''_{nl}) \tag{13.4}$$

where the vector $\mathbf{y}''$ is partitioned as $\mathbf{y}'' = [\mathbf{y}''^T_{lin} \ \ \mathbf{y}''^T_{nl}]^T$, $\mathbf{y}''_{lin} = [y''_1 \ \dots \ y''_{n-n_{PD}-1}]^T$ and $\mathbf{y}''_{nl} = [y''_{n-n_{PD}} \ \dots \ y''_n]^T$. The term $G_{lin}(\mathbf{y}''_{lin})$ is equal to zero since, in the refer-

ence system $\mathbf{R}_n''$, the gradient of the LSF is oriented in the direction of the DP vector **y*** and thus orthogonal to all other variables, i.e.,

$$\begin{aligned} G_{lin}(\mathbf{y}) &= \nabla_{\mathbf{y}} G\big|_{\mathbf{y}^*}(\mathbf{y}-\mathbf{y}^*) = \nabla_{\mathbf{y}} G\big|_{\mathbf{y}^*}\mathbf{R}^T\mathbf{R}_2^T\mathbf{R}_2\mathbf{R}(\mathbf{y}-\mathbf{y}^*) \\ &= -\left\|\nabla_{\mathbf{y}} G\big|_{\mathbf{y}^*}\right\| \cdot [0 \ \ldots \ 0 \ 1] \cdot \mathbf{y}'' = -\left\|\nabla_{\mathbf{y}} G\big|_{\mathbf{y}^*}\right\| \cdot y''_n \end{aligned} \tag{13.5}$$

The approximate expression of the LSF in Eq. (13.4) neglects higher-order terms in the variables $\mathbf{y}''_{lin}$ as well as the interaction terms between $\mathbf{y}''_{lin}$ and $\mathbf{y}''_{nl}$, but also allows to reduce drastically the number of variables to consider for approximating the nonlinear LSF. This step is innovative and unique to the proposed DP-RS-Sim method.

13.2.1.2 RS approximation of the nonlinear part of the LSF

The term $G_{nl}(\mathbf{y}''_{nl})$ needs to be approximated using the RS method. Any of the existing methods can be applied. Herein, the recently proposed Multivariate Decomposition Method (MDM) (Xu and Rahman 2004, 2005; Rahman and Xu 2004; Rahman and Wei 2006; Wei and Rahman 2007) is adopted.

The MDM involves an additive decomposition of an N-dimensional function into at most S-dimensional functions, where $S \ll N$. This work considers the two cases S = 1, for which the MDM reduces to the Univariate Decomposition Method (UDM), and S = 2, corresponding to the Bivariate Decomposition Method (BDM). It is noteworthy that the low computational cost of the RS approximation in the DP-RS-Sim method is mainly due to the decomposition of the LSF into a linear and a nonlinear part, which reduces the number of variables from n (total number of random variables) to $N = n_{PD} + 1 \ll n$. The use

of the UDM or BDM to build the RS approximation of $G_{nl}(\mathbf{y}"_{nl})$ further increases this intrinsic efficiency and allows the use of polynomial approximations of order higher than two in the variables that influence the most the nonlinear behavior of the LSS at the DP.

Considering a nonlinear function G(**y**) of the N-dimensional vector $\mathbf{y} = [y_1 \ldots y_N]^T$, the UDM assumes the approximation $G((\mathbf{y}) \cong \tilde{G}_1(\mathbf{y}))$, in which $\tilde{G}_1(\mathbf{y})$ is given by

$$\tilde{G}_1(\mathbf{y}) = \sum_{i=1}^{N} G_i(y_i) - (N-1)G(\bar{\mathbf{y}}) \tag{13.6}$$

where $\bar{\mathbf{y}} = [\bar{y}_1 \ \ldots \ \bar{y}_N]^T$ = point around which the approximation is done (center point) and $G_i(y_i) = G(\bar{y}_1, \ldots, \bar{y}_{i-1}, y_i, \bar{y}_{i+1}, \ldots, \bar{y}_N)$ = univariate component function.

The BDM assumes the following approximation $G((\mathbf{y}) \cong \tilde{G}_2(\mathbf{y}))$, in which $\tilde{G}_2(\mathbf{y})$ is given by

$$\begin{aligned} \tilde{G}_2(\mathbf{y}) &= \sum_{i_1 < i_2 \le N} G_{i_1, i_2}(y_{i_1}, y_{i_2}) - (N-2)\sum_{i=1}^{N} G_i(y_i) + \frac{(N-1)(N-2)}{2} \cdot G(\bar{\mathbf{y}}) \\ &= \sum_{i_1 < i_2 \le N} G_{i_1, i_2}(y_{i_1}, y_{i_2}) - (N-2)\tilde{G}_1(\mathbf{y}) - \frac{(N-1)(N-2)}{2} \cdot G(\bar{\mathbf{y}}) \end{aligned} \tag{13.7}$$

where $G_{i_1, i_2}(y_{i_1}, y_{i_2}) = G(\bar{y}_1, \ldots, \bar{y}_{i_1-1}, y_{i_1}, \bar{y}_{i_1+1}, \ldots, \bar{y}_{i_2-1}, y_{i_2}, \bar{y}_{i_2+1}, \ldots, \bar{y}_N)$ = bivariate component function.

Xu and Rahman (2004) show that the UDM and BDM provide approximations of the nonlinear function G(**y**) consisting of all terms of the Taylor series expansion around

point $\bar{\mathbf{y}}$ containing one and two variables, respectively, i.e., differing from the original function only by residuals of second and third order, respectively. For sufficiently smooth G(**y**) with a convergent Taylor series, the coefficients associated with higher-dimensional terms are usually much smaller than those with one- or two-dimensional terms. As such, higher-dimensional terms contribute less to the function, and therefore can be neglected.

The basic idea and principal assumption behind the UDM and BDM is that component functions of order higher that one (for UDM) and two (for BDM) will be negligible compared to lower order component functions, i.e., the effects of the interaction between two (UDM) or more than two (BDM) variables are much smaller than the effects deriving from each variable (UDM) or the interaction between two variables (BDM). When this hypothesis is satisfied, the method provides useful lower-variate approximations of a high-dimensional function.

After defining a univariate or a bivariate approximation of the original function, the coefficients defining the univariate and bivariate component functions need to be determined. Xu and Rahman (2004) suggest to obtain the component functions as polynomials with coefficients fitted by using Lagrangian interpolation. It is assumed that n_P = function evaluations are available, i.e.,

$$G_i^{(j)} = G(\bar{y}_1, \ldots, \bar{y}_{i-1}, y_i^{(j)}, \bar{y}_{i+1}, \ldots, \bar{y}_N) = G_i(y_i^{(j)}) \tag{13.8}$$

where $y_i^{(j)}$ (j = 1, ..., n_P) = values of variable y_i at which G(**y**) is computed

Using Lagrangian interpolation (i.e., imposing that the approximating function has exactly the same value as the original function at the experimental points), each univariate component function is given by

$$G_i(y_i) = \sum_{j=1}^{n_p} [G_i^{(j)} \cdot \varphi_j(y_i)] \tag{13.9}$$

in which $\varphi_j(y_i)$ denotes the following shape function

$$\varphi_j(y_i) = \frac{\prod_{k=1,\, k \neq j}^{n_p} (y_i - y_i^{(k)})}{\prod_{k=1,\, k \neq j}^{n_p} (y_i^{(j)} - y_i^{(k)})} \tag{13.10}$$

In a similar way, the bivariate components can be expressed as

$$G_{i_1, i_2}(y_{i_1}, y_{i_2}) \approx \sum_{j_1=1}^{n_p} \sum_{j_2=1}^{n_p} [G_{i_1, i_2}^{(j_1, j_2)} \cdot \varphi_{j_1}(y_{i_1}) \cdot \varphi_{j_2}(y_{i_2})] \tag{13.11}$$

where the coefficients $G_{i_1, i_2}^{(j_1, j_2)}$ are given by

$$\begin{aligned} G_{i_1, i_2}^{(j_1, j_2)} &= G(\bar{y}_1, \ldots, \bar{y}_{i_1 - 1}, y_{i_1}^{(j_1)}, \bar{y}_{i_1 + 1}, \ldots, \bar{y}_{i_2 - 1}, y_{i_2}^{(j_2)}, \bar{y}_{i_2 + 1}, \ldots, \bar{y}_N) \\ &= G_{i_1, i_2}(y_{i_1}^{(j_1)}, y_{i_2}^{(j_2)}) \end{aligned} \tag{13.12}$$

Here, n_P is assumed constant for all variables, even though this is not necessary. Notice also that, in the DP-RS-Sim method, the RS approximation is built in the reference

system $\mathbf{R}_n''$, with center point coincident with the origin of the reference system (i.e., the DP). Thus, $\bar{\mathbf{y}} \equiv \mathbf{y}''^* = \mathbf{0}$, $G(\bar{\mathbf{y}}) = G(\mathbf{y}''^*) = 0$ and Eqs. (13.6) and (13.7) simplify to

$$\tilde{G}_1(\mathbf{y}) = \sum_{i=1}^{N} G_i(y_i) \tag{13.13}$$

$$\tilde{G}_2(\mathbf{y}) = \sum_{i_1 < i_2 \le N} G_{i_1, i_2}(y_{i_1}, y_{i_2}) - (N-2)\tilde{G}_1(\mathbf{y}) \tag{13.14}$$

From Eq. (13.14), it is clear that a bivariate approximation requires to develop first the univariate approximation.

13.2.1.3 Computation of P_f through simulation

The estimate of the time-invariant failure probability is obtained using crude MCS or any other more advanced variance reduction simulation technique (e.g., importance sampling) applied on the analytical RS approximation of the actual LSF. In this work, IS is employed with sampling distribution taken as the standard normal joint PDF centered at the DP. Defining the indicator functions $I(\mathbf{y})$ and $I(\mathbf{y}'')$ as

$$I(\mathbf{y}) = \begin{cases} 1 & \text{if} \quad G(\mathbf{y}) \le 0 \\ 0 & \text{otherwise} \end{cases} \tag{13.15}$$

$$I(\mathbf{y}'') = \begin{cases} 1 & \text{if} \quad G(\mathbf{y}'') \cong G_{lin}(\mathbf{y}''_{lin}) + G(\mathbf{y}''_{nl}) = G_{nl}(\mathbf{y}''_{nl}) \le 0 \\ 0 & \text{otherwise} \end{cases} \tag{13.16}$$

and defining the vector $\mathbf{y} = \mathbf{R}^T\mathbf{R}_2^T\mathbf{y}'' + \mathbf{y}^*$, the failure probability P_f for a time-invariant component reliability problem can be expressed as

$$P_f = \int_{\Omega_n} I(\mathbf{y})\phi(\mathbf{y})d\mathbf{y} = \int_{\Omega_n} \left[I(\mathbf{y}'')\frac{\phi(\mathbf{y})}{\phi(\mathbf{y}'')} \right] \phi(\mathbf{y}'')d\mathbf{y}'' \tag{13.17}$$

where Ω_n denotes the entire standard normal space of dimension n and $\phi(\ldots)$ represents the standard normal joint PDF. Thus, an unbiased estimator of P_f is given by

$$P_f \cong P_{f,IS} = \frac{1}{N}\sum_{i=1}^{N} q_i \tag{13.18}$$

where q_i is the i-th realization of the random variable $Q(\mathbf{y}'') = I(\mathbf{y}'')\dfrac{\phi(\mathbf{R}^T\mathbf{R}_2^T\mathbf{y}'' + \mathbf{y}^*)}{\phi(\mathbf{y}'')}$ according to the sampling distribution $\phi(\mathbf{y}'')$ and N is the number of samples.

13.2.2 DP-RS-Sim method for time-invariant system reliability problems

In time-invariant system reliability analysis, the DP-RS-Sim method requires repeating the first three steps defined above for each of the components/LSFs and applying the fourth step after forming a Boolean indicator which provides correspondence between failures of the single components and failure of the system. Parallel and series systems are relevant particular cases for which the failure domains are defined respectively as

$$\mathbf{D}_p = \bigcap_{i=1}^{n_C} \mathbf{D}_i \tag{13.19}$$

and

$$\mathbf{D}_s = \bigcup_{i=1}^{n_C} \mathbf{D}_i \tag{13.20}$$

where $\mathbf{D}_i$ denotes the failure domain for the i-th component (or failure mode) and n_C is the number of components (or failure modes). Time-invariant component reliability analysis with a LSS characterized by multiple DPs can be interpreted as a special case of a time-invariant series system reliability problem, i.e., with the failure domain given by the union of the failure domains defined by the response surfaces approximating the original LSF in the neighborhood of each of the DPs.

13.2.3 DP-RS-Sim method for time-variant reliability problems

Time-variant component reliability analysis is performed using the DP-RS-Sim method to compute the mean out-crossing rate with the limit relation (Hagen and Tvedt 1991)

$$\nu_g(t) = \lim_{\delta t \to 0} \frac{P[(G_1 < 0) \cap (G_2 < 0)]}{\delta t} \tag{13.21}$$

where $G_1 = -G(\mathbf{y}, t)$ and $G_2 = G(\mathbf{y}, t + \delta t)$. As already seen in Chapter 11, Subsection 11.6, this problem can be solved as a time-invariant two-component parallel system reliability problem, with the two component LSSs given by $G_1 = 0$ and $G_2 = 0$. The specific properties of this problem (in particular the fact that the two LSSs are almost superposed, as indicated by the correlation coefficient between the two linearized failure modes being very close to -1) suggest to approach it in a slightly different way, as already done in the application of the MVPP method.

The modification of the DP-RS-Sim method to deal with the time-variant reliability problem are summarized below:

(1) The DP search is performed only for the DP of LSF G_1, while the DP for G_2 is obtained through shifting the first DP by the small time interval δt.

(2) The RS approximation for the second LSF is performed in the same reference system ($\mathbf{R}_n$") in which the RS approximation to the first LSF is defined. This assumes that the PDs of the second LSS at the DP are close to the corresponding ones for the first LSS. It also implies that the linear part of LSF G_2 in the reference system $\mathbf{R}_n$" is not equal to zero any more and must be accounted for by using the gradient at the DP of the second LSS. This gradient is not computed directly (since it would require to repeat the DP search for the LSS $G_2 = 0$ defined at time $t + \delta t$), but it is approximated by a vector with direction defined by the shifted DP of the first LSS and magnitude equal to the one of the gradient at the DP of the first LSS.

(3) The RS approximation of the second LSF is obtained without additional FE analyses, using the following approximation:

$$G_2 = G(\mathbf{y}, t + \delta t) \cong G(\mathbf{y}, t) + \frac{\partial G}{\partial t}\delta t = -G_1 - \frac{\partial G_1}{\partial t}\delta t \qquad (13.22)$$

(see Chapter 11, Subsection 11.2 and Chapter 12, Subsection 11.2.2) at the same experimental points used to approximate the first LSF, where the values of G_1 and $\frac{\partial G_1}{\partial t}$ have already been computed.

13.3 APPLICATION EXAMPLES

13.3.1 Time-invariant component reliability case: analytical LSF

The first application example is a time-invariant component reliability problem with an analytical LSF depending on three independent standard normal variables y_i (i = 1, 2, 3). This case study is used here to illustrate the methodology step by step, as explained in Subsection 13.2. The analytical LSF is chosen as

$$G(\mathbf{y}) = \frac{61}{80}y_1^2 + \frac{27}{160}(y_2^2 + y_3^2) + \frac{19\sqrt{6}}{80}y_1(y_2 - y_3) - \frac{19}{80}y_2y_3 - \frac{21}{20}(y_2 + y_3) + \frac{41}{40} \quad (13.23)$$

A visualization of the LSS $G(\mathbf{y}) = 0$ is given in Fig. 13.1. The DP is found as $\mathbf{y}^* = \left[0 \;\; \frac{1}{2} \;\; \frac{1}{2}\right]^T$ (Step 1), the rotation matrix $\mathbf{R}$ is obtained via Gram-Schmidt orthonormalization as

$$\mathbf{R} = \begin{bmatrix} 1 & 0 & 0 \\ 0 & \frac{\sqrt{2}}{2} & -\frac{\sqrt{2}}{2} \\ 0 & \frac{\sqrt{2}}{2} & \frac{\sqrt{2}}{2} \end{bmatrix} \quad (13.24)$$

and the new expression for the LSF in the transformed reference system $\mathbf{R}_n'$ (Step 2) is

$$G(\mathbf{y}') = \frac{61}{80}y'^2_1 + \frac{23}{80}y'^2_2 + \frac{1}{20}y'^2_3 + \frac{19\sqrt{3}}{40}y'_1y'_2 - \sqrt{2}y'_3 \quad (13.25)$$

The visualization of the LSS $G(\mathbf{y}') = 0$ in the reference system $\mathbf{R}_n'$ is provided in Fig. 13.2. The norm of the gradient at the DP is $\left\|\nabla_{\mathbf{y}} G\big|_{\mathbf{y}^*}\right\| = \sqrt{2}$ and the normalized and reduced Hessian matrix $\mathbf{A}$ at the DP in the reference system $\mathbf{R}_n'$ is

$$\mathbf{A} = \frac{\sqrt{2}}{80}\begin{bmatrix} 61 & 19\sqrt{3} \\ 19\sqrt{3} & 23 \end{bmatrix} \tag{13.26}$$

The principal eigenvalues are $PE_1 = \sqrt{2}$ and $PE_2 = \frac{\sqrt{2}}{20}$. Since $PE_2 \ll PE_1$, in the RS approximation, the contribution to the LSF of the variable corresponding to the second PD will be linearized (Step 3). The rotation matrix $\mathbf{R}_2$ is given by

$$\mathbf{R}_2 = \begin{bmatrix} \frac{1}{2} & -\frac{\sqrt{3}}{2} & 0 \\ \frac{\sqrt{3}}{2} & \frac{1}{2} & 0 \\ 0 & 0 & 1 \end{bmatrix} \tag{13.27}$$

and the LSF in the final reference system (shown in Fig. 13.3) is given by

$$G(\mathbf{y}'') = y''^2_2 + \frac{1}{20}(y''^2_1 + y''^2_3) - \sqrt{2}y''_3 \tag{13.28}$$

Neglecting the higher-order contribution of the second PD corresponding to variable y''_1, Eq. (13.28) can be approximated as (Step 4)

$$G(\mathbf{y}'') \approx G_{nl}(y''_2, y''_3) = y''^2_2 - \sqrt{2}y''_3 + \frac{1}{20}y''^2_3 \tag{13.29}$$

The RS approximation is obtained by the UDM considering three points (to fit a quadratic function) on each of the two axes (i.e., located at -1, 0 and +1 in the final reference system $\mathbf{R}_n''$ on the axes defined by variables y''_2 and y''_3). Thus, the univariate RS approximation requires only four additional evaluations of function $G_{nl}(y''_2, y''_3)$. In fact, the value of this function at the origin is zero, since the origin coincides with the DP.

The univariate component functions are

$$\begin{aligned} G_3(y''_3) &= \left(\frac{1}{20} + \sqrt{2}\right) \cdot \frac{1}{2}(y''^2_3 - y''_3) + 0 \cdot (1 - y''^2_3) + \left(\frac{1}{20} - \sqrt{2}\right) \cdot \frac{1}{2}(y''^2_3 + y''_3) \\ &= \frac{1}{20} y''^2_3 - \sqrt{2} y''_3 \end{aligned} \tag{13.30}$$

$$G_2(y''_2) = 1 \cdot \frac{1}{2}(y''^2_2 - y''_2) + 0 \cdot (1 - y''^2_2) + 1 \cdot \frac{1}{2}(y''^2_2 + y''_2) = y''^2_2 \tag{13.31}$$

and the univariate RS approximation (Step 5) is

$$\tilde{G}_1(\mathbf{y}'') = G_2(y''_2) + G_3(y''_3) = y''^2_2 - \sqrt{2} y''_3 + \frac{1}{20} y''^2_3 \tag{13.32}$$

Figure 13.4 shows the visualization of the univariate RS approximation of LSS $G(\mathbf{y}'') = 0$.

Finally, IS on the RS approximation is performed to estimate the failure probability corresponding to the failure event $G(\mathbf{y}) \leq 0$, yielding $P_{f,\,\text{Hybrid}} = 0.13322$ (Step 6). This estimate is compared with estimates from FORM, SORM using Breitung's formula (Breitung 1984), SORM using Hohenbichler and Rackwitz (1986) formula, IS using the exact equation for the LSF and crude Monte Carlo Simulation (MCS). Table 13.1 provides

these analysis results and shows that the DP-RS-Sim method results are close to the ones obtained from IS and MCS, while FORM largely overestimates the failure probability and the two SORM analyses improve the FORM results but still overestimate noticeably the failure probability compared to MCS.

13.3.2 Time-invariant component reliability case: quasi-static pushover of a R/C frame structure

The time-invariant component reliability problem consisting of a quasi-static pushover of a two-bay two-storey R/C frame already considered in Chapter 11, Subsection 11.7.1 and Chapter 12, Subsection 12.3.1, is solved here using the DP-RS-Sim method. Three different approximations are considered in the decomposition of the LSF into a linear and a nonlinear part of the LSF, corresponding to retaining the nonlinear contribution of one, two and three variables along PDs, respectively. A univariate decomposition is adopted to obtain the RS approximation of the LSF at the DP. A fourth order approximation over a square grid of side length equal to two units and centered at the DP is used for each of the univariate components (i.e., five points are used in the Lagrangian interpolation, with points positioned at $-1, -0.5, 0, 0.5, 1$ on each axis). The visualization of the trace of the LSS in the first PP is shown in Fig. 13.5 together with the traces of 1-st (FORM), 2-nd (SORM) and 4-th order (RS) approximations of the LSF. The results obtained are compared with the failure probability estimates derived from other reliability analysis methods (see Chapter 11, Subsection 11.7.1) in Table 13.2. It is found that the DP-RS-Sim provides accurate estimates of the failure probability (considering the IS esti-

mates as reference solution) with a small increase in computational cost compared to FORM and SORM analyses.

13.3.3 Time-variant component reliability case: linear elastic SDOF system subjected to white noise excitation

The linear elastic SDOF system used as benchmark example in Chapter 11, Subsection 11.7.2, for FORM-based mean up-crossing rate computation, and in Chapter 12, Subsection 12.3.2, as application example of the MVPP method, is revisited here to verify the applicability of the DP-RS-Sim method to mean up-crossing rate computation. The SDOF system is subjected to Gaussian white noise excitation with PSD $\phi_0 = 0.25\mathrm{m}^2/\mathrm{s}^3$ discretized in time with a fixed time interval $\Delta t = 0.01\mathrm{s}$. The mean up-crossing rate computation is performed at time $t = 1.00\mathrm{s}$ relative to a deterministic roof displacement threshold $\xi = 0.048\mathrm{m}$ (roof drift ratio = 1.5%). In Table 13.3, it is found that the DP-RS-Sim results converge (for decreasing time perturbation δt) to the FORM results obtained using Koo's formula (Koo et al. 2005) with $\delta t = 0.0001\mathrm{s}$.

13.3.4 Time-variant component reliability case: nonlinear hysteretic SDOF system subjected to white noise excitation

The use of the DP-RS-Sim method in the case of a time-variant component reliability problem is illustrated using the nonlinear hysteretic SDOF system defined in Chapter 11, Subsection 11.7.3 (with deterministic parameters) when subjected to white noise base excitation with power spectral density $\phi_0 = 0.25\mathrm{m}^2/\mathrm{s}^3$ and relative to the determin-

istic displacement threshold $\xi = 0.048\text{m}$ (corresponding to a significantly nonlinear behavior of the structural system, for which visualization using the MVPP method is provided in Chapter 12, Subsection 12.3.3).

The DP-RS-Sim method is applied to compute the time-variant failure probability (for T = 5.0s) of the inelastic SDOF system defined above. The time-variant probability of failure is estimated by integrating numerically the mean out-crossing rate computed at given instants of time (t = 0.25s, 0.5s, 0.75s, 1.0s, 1.5s, 2.0s, 3.0s, 4.0s and 5.0s). The Gaussian white noise excitation is discretized with $\Delta t = 0.01\text{s}$ into 25, 50, 75, 100, 150, 200, 300, 400, and 500 random variables for these instants of time. Each of the LSFs is approximated with a RS obtained as the sum of: (1) an 8-th order polynomial in the four transformed variables defined by the direction of the DP vector and the first three principal directions, and (2) a 1-st order polynomial in the remaining variables (i.e., hyperplane tangent to the LSS at the DP in the subspace defined by the remaining n - 4 variables, with n = total number of random variables). The bivariate component functions are obtained using LSF evaluations over a square grid of points of side length equal to four units and centered at the DP (i.e., 9 points are used in the Lagrangian interpolation, with points positioned at -2, -1.5, -1, -0.5, 0, 0.5, 1, 1.5, and 2 on each axis). The probability content of the hyper-wedge defined by the intersection of the two component failure domains is estimated via importance sampling with a sampling distribution taken as the standard normal joint PDF centered at the DP.

Figs. 13.6 through 13.8 provide visualization of the LSSs at times $t = 1.0\text{s}$ and $t + \delta t = 1.005\text{s}$ using the MVPP method in the first through third PPs, respectively. The

traces of these two LSSs (obtained as the zero level contour lines of the LSF simulated over a fine grid of points in each PP) are compared with the corresponding traces of different response surface approximations, namely a 1-st order (FORM), 2-nd order (fitted over a grid of 3x3 points located at -2, 0, +2 along each axis) and 8-th order polynomial approximation. It is seen that the 8-th order RS approximates the actual LSSs fairly well in the first PP (Fig. 13.6) and very well in the second and third PPs (Figs. 13.7 and 13.8).

Fig. 13.9 compares the results obtained through crude MCS for the expected cumulative number of up-crossing events, E[N], and the time-variant failure probability, P_f, with the upper bound approximation of the failure probability obtained through FORM and the DP-RS-Sim method. As seen in Chapter 11, Subsection 11.7.3, the error due to the use of the analytical upper-bound to the probability of failure P_f is small, while the error due to the use of a FORM approximation to E[N] is very large (error = 266% at time t = 5.0s). The DP-RS-Sim method reduces significantly the error compared to FORM, providing a very good estimate of E[N] (error = 16% at time t = 5.0s) with a small additional computational cost compared to FORM.

13.4 CONCLUSIONS

A new hybrid FE reliability method, referred to as DP-RS-Sim method, has been developed and presented. It combines the concept of design point, the response surface methodology and a simulation technique to improve the accuracy of failure probability estimates obtained by classical FORM and SORM analyses. The new method can be used in time-invariant component reliability, time-invariant system reliability and time-variant

component reliability analyses. Some application examples are provided to illustrate the method and its capabilities.

The DP-RS-Sim method is still under development and both its capabilities and limitations need further study to be fully assessed. Nevertheless, the DP-RS-Sim method is very promising since, as shown here, it is able to provide at reasonable computational cost accurate failure probability estimates for FE reliability problems involving advanced nonlinear FE models and a large number of random variables.

Table 13.1 Time-invariant reliability analysis results for the time-invariant component reliability problem with analytical LSF

Analysis Method	P_f	# of simulations	cov
FORM	0.23975	-	-
$SORM_B$	0.16544	-	-
$SORM_{HR}$	0.15334	-	-
IS	0.12741	109894	0.005
MCS	0.12848	271324	0.005
$DP\text{-}RS\text{-}Sim_{(univ,1)}$	0.13387	107987	0.005

Table 13.2 Time-invariant reliability analysis results for the quasi-static pushover analysis of the R/C frame structure

Analysis	P_f	CPU relative time
FORM	0.0203	1
$SORM_1$	0.0210	1.02
$SORM_{all,B}$	0.0223	2.26
$SORM_{all,HR}$	0.0257	2.26
$IS_{0.05}$	0.0266	53.83
$IS_{0.01}$	0.0262	1103.51
$DP\text{-}RS\text{-}Sim_{(univ,1)}$	0.0264	2.63
$DP\text{-}RS\text{-}Sim_{(univ,2)}$	0.0269	2.90
$DP\text{-}RS\text{-}Sim_{(univ,3)}$	0.0269	3.17

Table 13.3 DP-RS-Sim estimates of the mean up-crossing rate (for $\xi = 0.048$m) of linear elastic SDOF system subjected to Gaussian white noise with PSD $\phi_0 = 0.25 m^2/s^3$

		$\nu(t = 1.0s)$ [1/s]	cov	# of simulations
FORM ($\delta t = 0.0001s$)		0.0982	-	-
DP-RS-Sim	$\delta t = 0.010s$	0.1901	0.05	10029
	$\delta t = 0.005s$	0.1354	0.05	15449
	$\delta t = 0.001s$	0.0989	0.05	70044

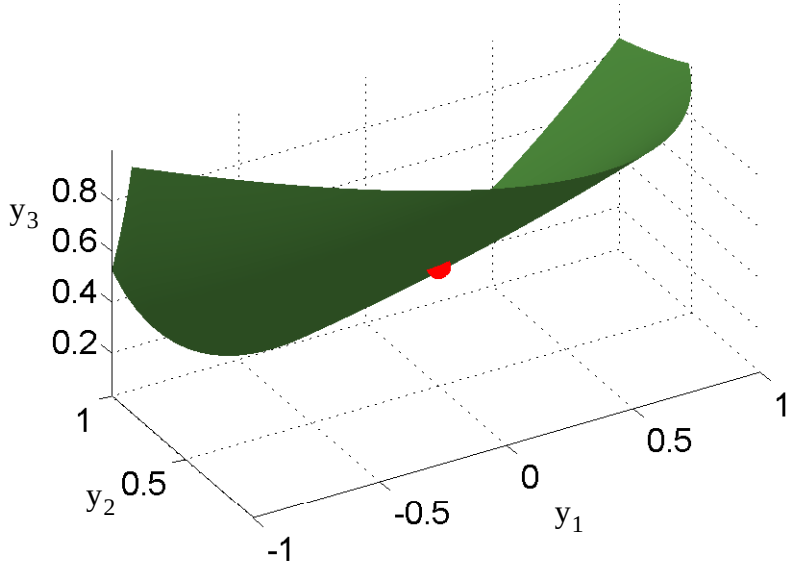

Figure 13.1 Time-invariant component reliability case for analytical LSF: LSS visualization in the original reference system.

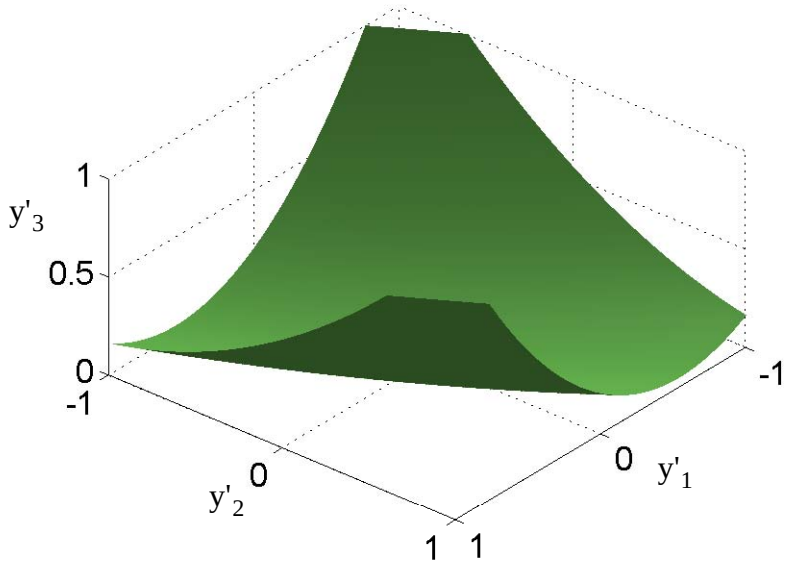

Figure 13.2 Time-invariant component reliability case for analytical LSF: LSS visualization in the transformed reference system.

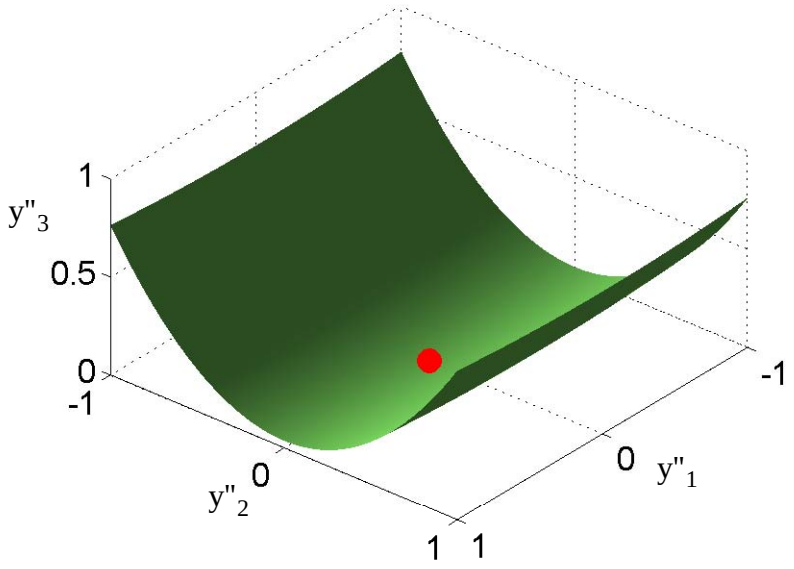

Figure 13.3 Time-invariant component reliability case for analytical LSF: LSS visualization in the final reference system.

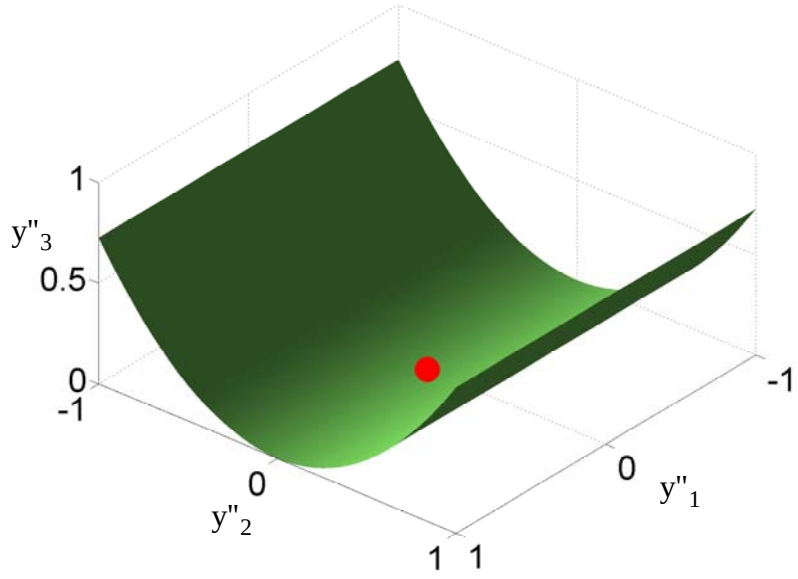

Figure 13.4 Time-invariant component reliability case for analytical LSF: RS approximation of the LSS in the final reference system.

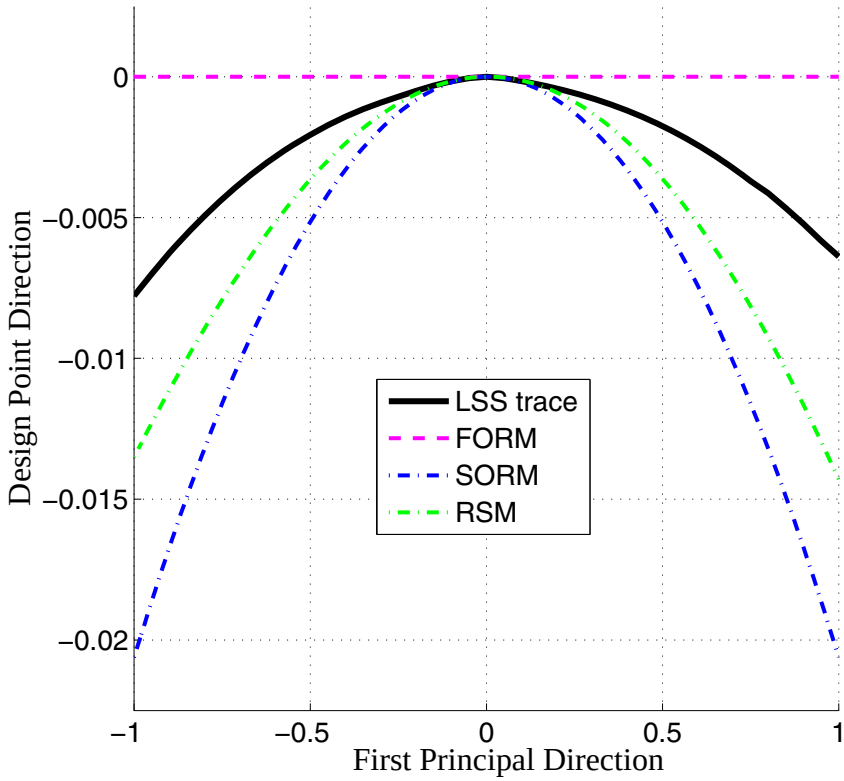

Figure 13.5 MVPP-based visualization of the LSS trace and its different approximations in the first PP for the time-invariant reliability problem of the benchmark R/C frame subjected to quasi-static pushover (vertical axis scaled up by a factor 80).

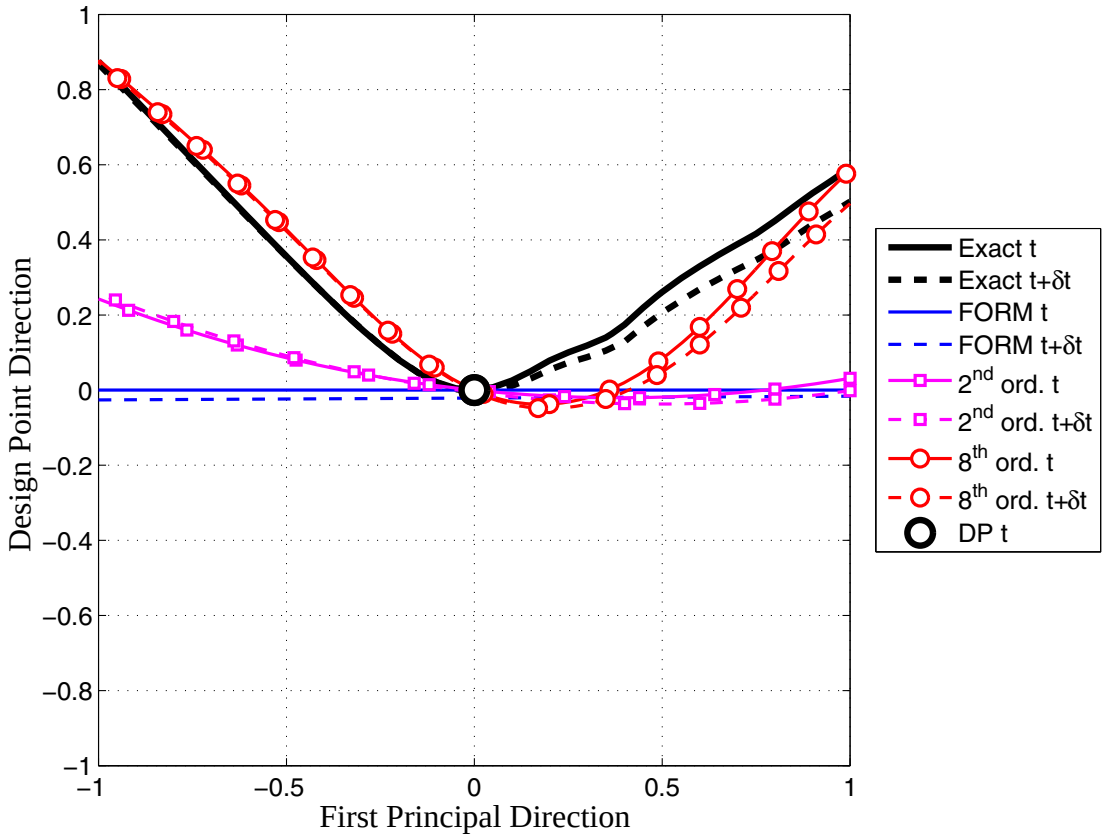

Figure 13.6 Time-variant component reliability case for nonlinear hysteretic SDOF system subjected to white noise excitation: LSSs visualization in the first principal plane.

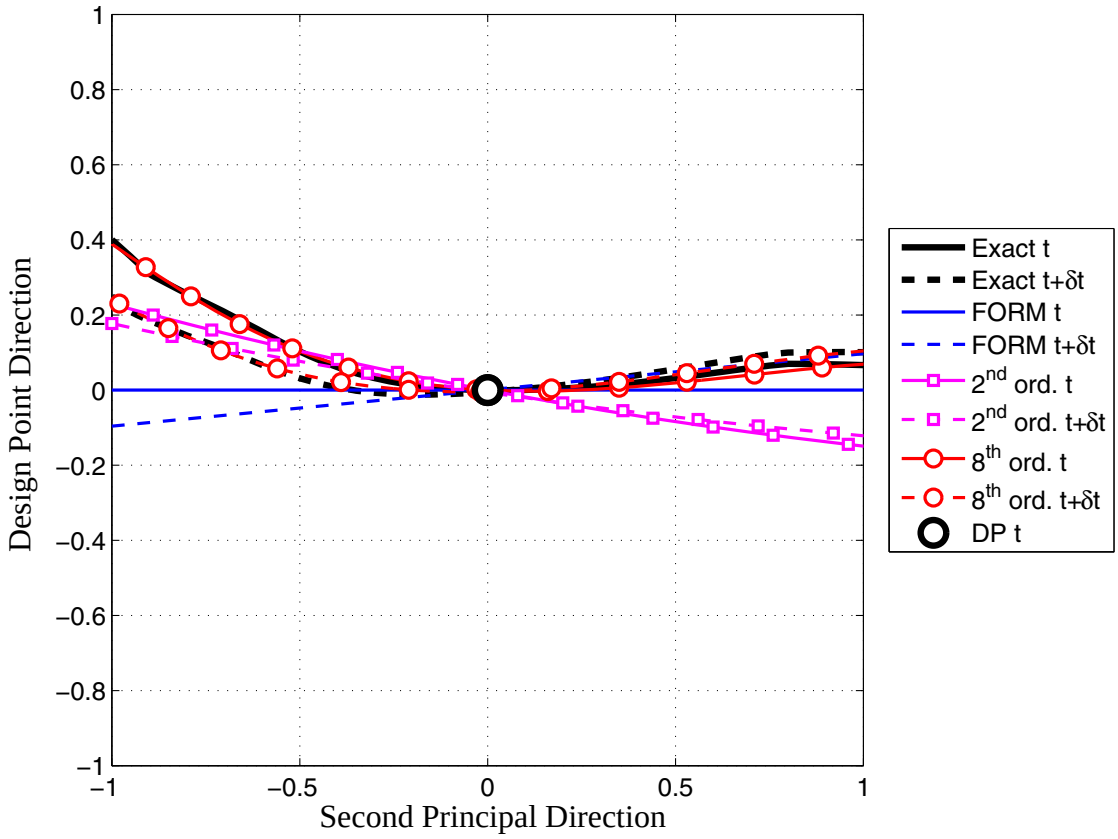

Figure 13.7 Time-variant component reliability case for nonlinear hysteretic SDOF system subjected to white noise excitation: LSSs visualization in the second principal plane.

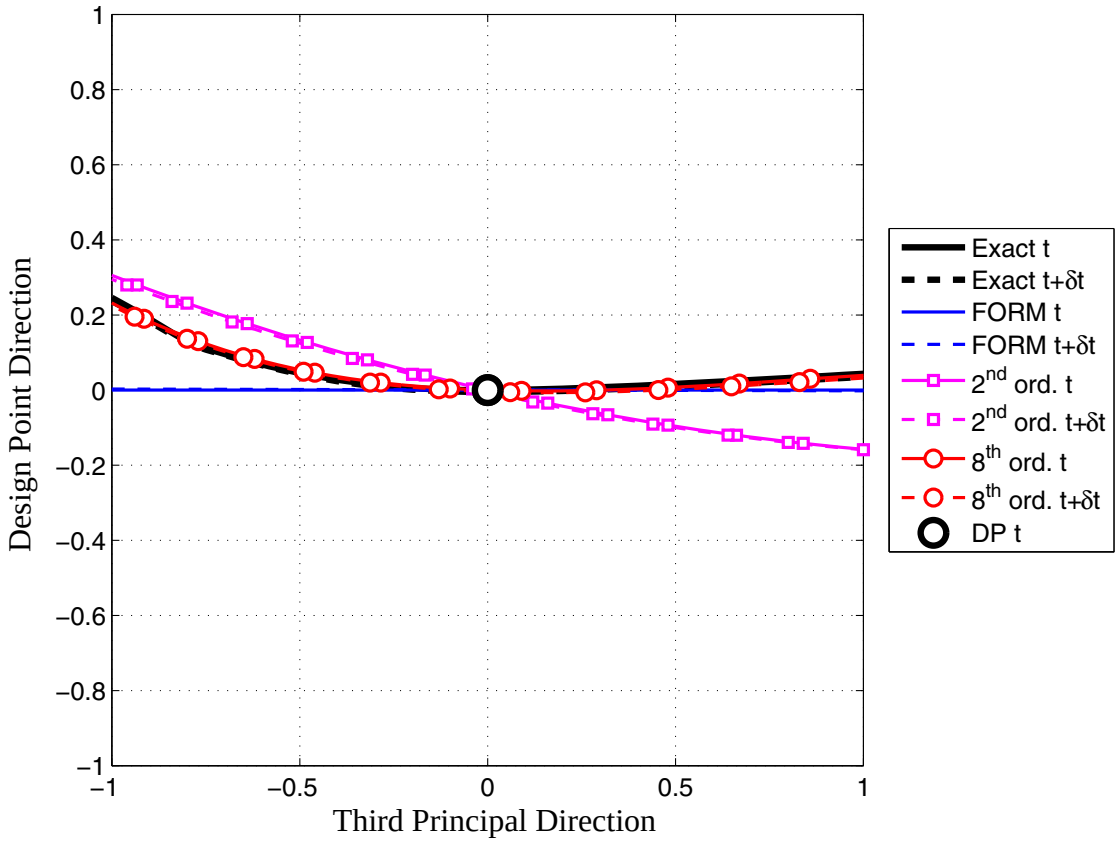

Figure 13.8 Time-variant component reliability case for nonlinear hysteretic SDOF system subjected to white noise excitation: LSSs visualization in the third principal plane.

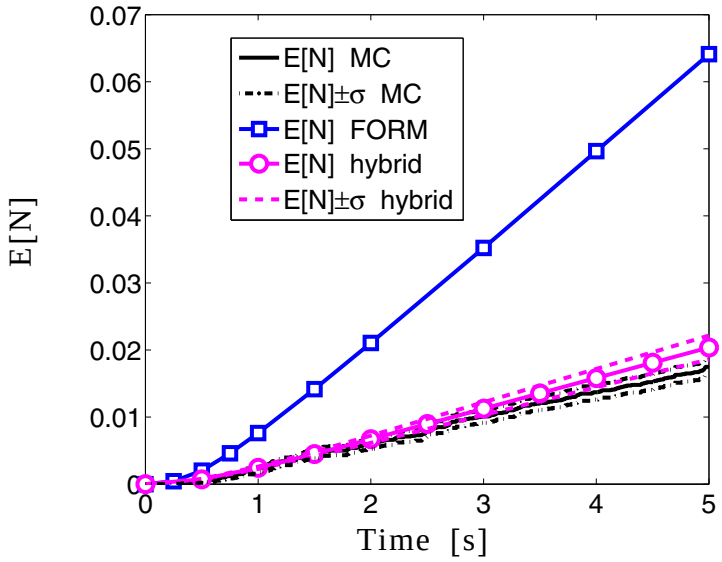

Figure 13.9 Estimates of the expected cumulative number of up-crossing events for the MP SDOF system relative to a roof displacement threshold $\xi = 0.048\text{m}$.

REFERENCES

Au S.K., Beck J.L. (1999) "A new adaptive importance sampling scheme" *Structural Safety*, 21(2):135–158.

Breitung K. (1984) "Asymptotic approximations for multinormal integrals" *Journal of the Engineering Mechanics Division* (ASCE), 110(3):357–366.

Breitung K., Faravelli L. (1996) "Chapter 5: Response surface methods and asymptotic approximations." *Mathematical models for structural reliability analysis*. Casciati F., Roberts J.B., editors, CRC Press, New York.

Bucher C.G., Bourgund U. (1990) "A fast and efficient response surface approach for structural reliability problem." *Structural Safety*, 7:57-66.

Carley K.M., Kamneva N.Y., Reminga J. (2004) “Response surface methodology”. *CASOS Technical Report* CMU-ISRI-04-136, Carnegie Mellon University, Pittsburgh, PA, USA.

Der Kiureghian A., Dakessian T. (1998) “Multiple design points in first and second-order reliability” *Structural Safety*, 20:37-49.

Faravelli L. (1989) “Response-surface approach for reliability analysis.” *Journal of Engineering Mechanics* (ASCE), 115(12):2763-2781.

Faravelli L. (1992) “Structural reliability via response surface.” *Proceedings of the IUTAM symposium on Nonlinear Stochastic Mechanics*, Bellomo N., Casciati F., editors, Springer Verlag, Heidelberg, Germany.

Hohenbichler M., Rackwitz R. (1986) “Sensitivity and importance measures in structural reliability” *Civil Engineering Systems*, 3(4):203–209.

Huh J., Haldar A. (2002) “Seismic reliability of nonlinear frames with PR connections using systematic RSM.” *Probabilistic Engineering Mechanics*, 17(2): 77-190.

Khuri A.I., Cornell J.A. (1996) *Response surface designs and analyses*. Marcel Dekker, New York, NY, USA.

Koo H., Der Kiureghian A., Fujimura K. (2005) “Design-point excitation for non-linear random vibrations” *Probabilistic Engineering Mechanics*, 20:136-147.

Rahman S., Wei D. (2006) “A univariate approximation at most probable point for higher-order reliability analysis.” *International Journal of Solids and Structures*, 43:2820-2839.

Rahman S., Xu H. (2004) “A univariate dimension-reduction method for multidimensional integration in stochastic mechanics.” *Probabilistic Engineering Mechanics*, 19(4):393-408.

Rajashekhar M.R., Ellingwood B.R. (1993) “A new look at the response surface approach

for reliability analysis." *Structural Safety*, 12:205-220.

Schotanus M.I. (2002) "Fragility analysis of reinforced concrete structures using a response surface approach", *Master Degree Thesis*, IUSS, Pavia, Italy.

Wei D., Rahman S. (2007) "Structural reliability analysis by univariate decomposition and numerical integration." *Probabilistic Engineering Mechanics*, 22(1):27-38.

Wong F.S. (1984) "Uncertainties in dynamic soil-structure interaction." *Journal of Engineering Mechanics* (ASCE), 110(2):308-324.

Wong F.S. (1985) "Slope stability and response surface method." *Journal of Geotechnical Engineering* (ASCE), 111(1):32-53.

Xu H., Rahman S. (2004) "A generalized dimension-reduction method for multidimensional integration in stochastic mechanics." *International Journal for Numerical Methods in Engineering*, 61:1992-2019.

Xu H., Rahman S. (2005) "Decomposition methods for structural reliability analysis." *Probabilistic Engineering Mechanics*, 20:239-250.

Yao T.H.-J., Wen Y.-K. (1996) "Response surface method for time-variant reliability analysis". Journal of Structural Engineering (ASCE), 122(2):193-201.

Zhao Y.G., Ono T., Idota H. (1999) "Response uncertainty and time-variant reliability analysis for hysteretic MDOF structures." *Earthquake Engineering and Structural Dynamics*, 28:1187-1213.

CHAPTER 14

CONCLUSIONS

14.1 SUMMARY OF CONTRIBUTIONS AND MAJOR FINDINGS

The research work presented in this thesis contributes to three different research areas: (1) finite element response sensitivity analysis, (2) stochastic process modeling and random vibration theory, and (3) computatonal reliability analysis of structural systems.

The principal contributions and major findings of this research work are summarized below:

(1) An algorithm for DDM-based response sensitivity computation is developed for force-based frame elements and implemented in FEDEASLab.

Previous research has shown that force-based frame elements are superior to classical displacement-based frame elements enabling, at no significant additional computational costs, a drastic reduction in the number of elements required for a given level of accuracy in the simulated response. The present work shows that this advantage of force-based over displacement-based frame elements is even more conspicuous in the context of gradient-based optimization methods, which are used in several structural engineering sub-fields (e.g., structural optimization, structural reliability analysis, finite element model updating) and which require accurate and efficient computation of structural response and response sensitivities to material and loading parameters.

(2) An algorithm for DDM-based response sensitivity computation is derived for finite elements with static condensation of internal degrees of freedom and is implemented in several types of finite elements in FEDEASLab.

It is found that response sensitivity calculations can be performed at the structure level assembling only the sensitivities (with respect to modeling parameters) of condensed element nodal forces and retained (external) element nodal displacements, similarly to response-only calculations.

(3) The DDM is extended to steel-concrete composite frame structures, with implementation in FEDEASLab of several finite element, fiber-discretized section and material constitutive models.

This extension allows efficient and accurate response sensitivity analysis using advanced FE models specifically designed for this type of structures. In particular, the sensitivity of local response quantities such as interlayer slip and shear force between the steel beam and concrete slab components is examined. It is found that local response quantities are very sensitive to material strength parameters when the structural system undergoes large plastic deformations.

(4) A DDM-based response sensitivity algorithm for three-field mixed-formulation finite element based on the Hu-Washizu functional is developed for the general case, including nonlinear geometry and shape sensitivity, and implemented into FEDEASLab for a 10-dof steel-concrete composite frame element.

(5) The effects upon the design point search of gradient discontinuities caused by non-smoothness of material constitutive models in the context of finite element reliability analysis are studied. The response computation algorithms for several smooth/

smoothed constitutive models (e.g., Menegotto-Pinto smooth material constitutive model for steel and smoothed Popovics-Saenz model for concrete) are extended to response sensitivity analysis using the DDM and implemented in both FEDEASLab and OpenSees.

Implications of using smooth versus non-smooth material constitutive models in finite element response, response sensitivity and reliability analyses are analyzed. In general, for both quasi-static and dynamic analysis, gradient-based optimization algorithms do not ensure convergence to a (local) optimum of the objective function subject to the given constraints (expressed in terms of structural response quantities) if response sensitivities are discontinuous. Typically, non-convergence to an existing optimum happens if discontinuities in the gradient of the limit-state function (i.e. response sensitivity discontinuities) occur in the neighborhood of the optimum itself. Even in cases when convergence can be achieved, gradient discontinuities could be detrimental to the convergence rate of the optimization procedure. In theory, gradient-based optimization algorithms can reach (locally) a quadratic convergence rate, when the Lagrangian function associated with the given problem is second-order differentiable and its exact Hessian is available (Gill et al., 1981). However, this is not the case in structural reliability problems, for which at most exact first-order response sensitivities are available. It can thus be concluded that, for general/practical purposes in finite element reliability analysis, requiring at least continuous finite element response sensitivities is a good compromise between convergence rate and computational cost.

A sufficient condition on the smoothness of uni-axial material constitutive models for obtaining continuous finite element response sensitivities is stated and proved for the quasi-static case. The issue of continuity/discontinuity of response sensitivities for the dynamic case is also discussed. It is found that the linear inertia and damping terms in the equations of motion have significant smoothing effects on response sensitivities along the time axis. Nevertheless, discontinuities along the parameter axes are observed for both non-smooth and smooth constitutive models, if the time discretisation of the equations of motion is not sufficiently refined. Several application examples suggest that, for the FE dynamic analysis case, response sensitivity discontinuities can be eliminated by using smooth material constitutive models and refining the time discretisation of the equations of motion.

(6) The efficiency and robustness of different gradient-based nonlinear constrained optimization algorithms is investigated. The general purpose optimization code SNOPT, employing a Sequential Quadratic Programming (SQP) algorithm, is integrated with both FEDEASLab-FERUM and OpenSees, extending the existing options in terms of optimization algorithms available for the DP search.

It is observed that, for cases in which the limit-state surface (constraint function in the optimization problem) is linear or slightly nonlinear, the modified Hasofer-Lind Rackwitz-Fiessler algorithm outperforms other algorithms. When the LSS is very nonlinear, SQP performs better than other algorithms. When the domain in which the FE analyses do not converge at equilibrium is close to the DP, appropriate methods to avoid this non-convergence domain need to be employed. Such methods are built-in into SNOPT, which in general is very robust.

(7) The effect of the convergence tolerance threshold used to measure the convergence of the iterative FE response calculation on the accuracy of the DDM-based FE response sensitivities is investigated.

It is found that the choice of a strict enough convergence tolerance for the iterative response calculation is also important for DDM-based response sensitivity analysis, since the equations of equilibrium/motion are the starting point of the DDM. Use of an inadequate convergence tolerance for response calculation may lead to loss of agreement between response sensitivity results obtained using the DDM and FFD analysis (e.g., an insufficiently small convergence tolerance threshold may lead to erroneous DDM results and very inaccurate FFD results if the perturbation of the sensitivity parameter is “too small” in relation to the tolerance).

(8) A new simulation method is presented for a specific fully nonstationary stochastic earthquake ground motion model which has found wide application in earthquake engineering research. This new method, based on a “physical” interpretation of the considered stochastic model, is limited in scope but outperforms the more general spectral representation method in terms of both accuracy and efficiency.

The new simulation technique is implemented as a stand-alone Matlab-based routine, which is also integrated with FEDEASLab for efficient FE simulation of structural response to stochastic earthquake ground motion excitation.

(9) The definition of the existing non-geometric spectral characteristics (NGSCs) is extended to general complex-valued nonstationary random processes. These newly defined NGSCs are essential for computing the time-variant central frequency and bandwidth parameter of nonstationary response processes of linear systems. The

bandwidth parameter is also used in structural reliability applications, e.g., for obtaining analytical approximations of the probability that a structural response process outcrosses a specified limit-state threshold.

(10) Using the non-geometric spectral characteristics of complex-valued nonstationary processes and employing complex modal analysis, closed-form exact solutions are found for the classical problem of deriving the time-variant central frequency and bandwidth parameter of the response of linear SDOF and MDOF systems, both classically and non-classically damped, when subjected to white noise excitation from at rest initial conditions.

The exact closed-form solutions derived for the linear SDOF oscillator are used to investigate the dependency of the stationary and time-variant central frequency and bandwidth parameter on the SDOF system parameters, i.e., natural circular frequency and damping ratio. These exact closed-form solutions have their own mathematical merit, since to the best of the authors' knowledge, they are new solutions for a classical problem in the field of random vibration theory. These solutions have a direct and important application, since the response of many structures can be approximated by using linear SDOF and MDOF models, and provide valuable benchmark solutions for validating (at the linear structural response level) numerical methods developed to estimate the probabilistic response of non-linear systems subjected to nonstationary excitations.

(11) The non-geometric spectral characteristics of nonstationary random processes are applied to the time-variant first passage problem in structural reliability. The first passage problem consists of computing the probability of a response quantity (linearly

related to the displacement and velocity responses, e.g., absolute displacement, relative displacement, elastic force) exceeding a deterministic time-invariant threshold. This probability is generally known as time-variant probability of failure.

The so-called Vanmarcke failure probability approximations (i.e., classical Vanmarcke and modified Vanmarcke approximations) are computed, by numerical integration of the closed-form solutions of the corresponding hazard functions, for linear elastic single- (SDOF) and multi-degree-of-freedom (MDOF) systems subjected to white noise base excitation from at rest initial conditions. The closed-form expressions for the two Vanmarcke hazard functions are obtained using the closed-form solutions for the time-variant bandwidth parameter relative to the nonstationary stochastic process representing the displacement response.

The results obtained from several application examples indicate that the two Vanmarcke approximations provide greatly improved estimates of the failure probability for the first passage problem as compared to the simpler Poisson approximation. On the other hand, the relative accuracy of the classical Vanmarcke and modified Vanmarcke approximations can be evaluated only on a case by case basis.

(12) A simplified probabilistic response analysis based on the mean centered First-Order Second-Moment (FOSM) analysis using non-linear finite element response and response sensitivity analyses is applied to structural and geotechnical systems subjected to quasi-static pushover. The effects on FOSM analysis results of using different methods for computing response sensitivities are also investigated. It is found that the FOSM approximation using the DDM for computing response sensitivities provides, at very low computational cost, very good estimates of the mean and standard

deviation of the response for low-to-moderate levels of material non-linearity in the response of structural and geotechnical systems subjected to quasi-static pushover analysis.

Furthermore, the relative importance (in both the deterministic and probabilistic sense) of the material parameters on the structural response is obtained as by-product of a FOSM analysis at negligible additional computational cost.

It can be concluded that FOSM analysis provides a large amount of probabilistic information at low computational cost and can provide satisfactory accuracy for probabilistic analysis of structural and geotechnical systems subjected to quasi-static pushover analysis, provided that the level of non-linearities exhibited by the system are low-to-moderate. For large non-linearities, FOSM can still be used effectively to obtain qualitative information on the importance ranking of model parameters on the system response.

(13) The use of state-of-the-art methodologies (FORM, SORM, Importance Sampling, time-variant reliability through mean out-crossing rate computation) in finite element structural reliability analysis based on the concept of design point is investigated for application to realistic nonlinear FE structural models. Several improvements to these methodologies in terms of efficiency and robustness are made and illustrated.

It is found that the adopted methods can often provide results sufficiently accurate for engineering purposes with a relatively small computational effort practically independent on the magnitude of the failure probability. On the other hand, these approximate methods can produce inaccurate estimates of failure probabilities when the structural systems under study exhibit a strongly nonlinear response behavior.

(14) A new technique is developed for visualization of limit-state surfaces (LSSs) near their design point(s) (DPs) in high-dimensional spaces: the Multidimensional Visualization in the Principal Planes (MVPP). The MVPP method consists of visualizing a LSS in the neighborhood of a DP in subspaces (planes) of particular interest. These planes are defined as the planes of principal curvatures of the LSS at the DP and are referred to as Principal Planes (PPs). The MVPP requires finding the trace of the LSS in the PPs in decreasing order of magnitude of the principal curvatures.

The MVPP methodology provides important information about the topology of the LSS, identifying a small number of dimensions which are of interest and thus requiring a limited number of FE analyses to visualize the LSS.

(15) A new hybrid FE reliability analysis method, referred to as Design Point - Response Surface - Simulation (DP-RS-Sim) method, is proposed. The DP-RS-Sim method combines the concept of design point, the response surface methodology and a simulation technique to improve the accuracy of the classical FORM and SORM. The new method can be used in time-invariant component reliability, time-invariant system reliability and time-variant component reliability analyses. Some application examples are provided to illustrate the method and its capabilities.

The DP-RS-Sim method is still under development and both its capabilities and limitations need further study to be fully assessed. Nevertheless, the DP-RS-Sim method is very promising since it is able to provide, at reasonable computational cost, accurate failure probability estimates for FE reliability problems involving advanced nonlinear FE models and a large number of random variables.

14.2 RECOMMENDATIONS FOR FUTURE WORK

Based on the research work performed and presented herein, several research areas have been identified as open to and in need of future work.

(1) In order to fully exploit the advantages of the state-of-the-art FE technology, DDM-based FE response sensitivity analysis must follow closely the advances of FE response-only methods. To date, the gap is still wide. Derivation and implementation of the response sensitivity algorithms are required for new elements, new integration points (e.g., frame section models), new material constitutive models, etc.

(2) The sources of discontinuities in response sensitivities in FE dynamic analysis need to be detected. Finding the reason(s) of the discontinuities along the parameter axes may indicate a method to eliminate them more efficiently than reducing the time-step size in the numerical integration of the equations of motion.

(3) The possibility of coupling DDM-based response sensitivity analysis with the adjoint method should be investigated to exploit the efficiency of the adjoint method for linear elastic structures. In particular, when the nonlinear behavior is concentrated in a small part of the FE model, this combination could provide a very efficient method for FE response sensitivity computation.

(4) Challenges remain in the FE reliability analysis method proposed, in particular for the DP search in very high-dimensional spaces, which is commonly encountered in time-variant reliability problems. More robust and efficient methods for finding the DP are still needed. It is believed that the geometric insight gained using the MVPP method

could be exploited to develop improved optimization algorithms specifically designed for the DP search.

(5) Parallel/distributed computing is a promising approach to alleviate the computational demand in conducting large-scale FE analysis of structural and geotechnical systems. Parallel/distributed computing methods have experienced great development in the last few decades and are very well suited to be applied to certain types of reliability analysis, such as sampling analysis. The study of other applications of parallel/distributed computing to reliability analysis is strongly recommended.

(6) Development of a method for efficient/parsimonious representation of a nonstationary random process is desirable. The nonstationary stochastic earthquake ground motion model considered in this work is able to capture the amplitude and frequency nonstationarities typical of actual earthquake records, but its representation in terms of random variables is far from efficient/parsimonious. There may be more efficient approaches for representation of a nonstationary continuous random process, e.g., frequency domain representation.

(7) Derivation of closed-form expressions for the spectral characteristics of the response processes of linear elastic SDOF and MDOF systems subjected to input processes more realistic than Gaussian white noise (e.g., modulated white noise, filtered white noise, fully nonstationary earthquake ground motion models) can provide important benchmark solutions for numerical methods more generally applicable to nonlinear systems. Research in this direction is recommended.

(8) Numerical methods for the computation of the spectral characteristics of non-Gaussian processes (e.g., response of linear elastic systems subjected to non-Gaussian

input, nonlinear inelastic systems subjected to Gaussian input, nonlinear inelastic systems subjected to non-Gaussian input) are essential to extend the scope of existing improved estimates of the time-variant failure probability (e.g., Vanmarcke approximations).

(9) Parameterization, in terms of seismological variables such as magnitude and site-to-source distance, of stochastic earthquake ground motion models is crucial to propose them as a feasible and meaningful alternative to ensembles of scaled actual ground motion records, which are currently used in structural engineering practice. This parameterization will enable end-to-end probabilistic seismic performance analysis of structural systems, integrating seamlessly seismic hazard analysis, probabilistic demand analysis, damage analysis, and reliability analysis.

(10) The study of simplified probabilistic response methods in dynamic FE analysis is strongly recommended.

(11) The proposed DP-RS-Sim reliability analysis method is still in its embrionic stage of development. Further testing and extensions are needed. In particular, the method could be improved by the development of adaptive algorithms to determine the optimal number of principal directions to be considered in the nonlinear part of the RS approximation, the optimal order of the RS approximation and the optimal size of the grid on which the RS is fitted. The use of other RS approximations needs to be explored as well. Finally, error analysis methods could be extended to the RS approximation used in the DP-RS-Sim method.

(12) FE structural reliability analysis of uncertain systems subjected to random loadings is not addressed in this work. Significant research is needed in this important topic.